AGARD-R-808

AGARD

ADVISORY GROUP FOR AEROSPACE RESEARCH & DEVELOPMENT

7 RUE ANCELLE, 92200 NEUILLY-SUR-SEINE, FRANCE

AGARD REPORT 808

Capsule Aerothermodynamics
(l'Aérothermodynamique des capsules)

This publication was prepared at the request of the Fluid Dynamics Panel. Papers were presented at a Special Course on "Capsule Aerothermodynamics", held at the von Kármán Institute for Fluid Dynamics (VKI) in Rhode-Saint-Genèse, Belgium, 20-22 March 1995.

NORTH ATLANTIC TREATY ORGANIZATION

Published May 1997

Distribution and Availability on Back Cover
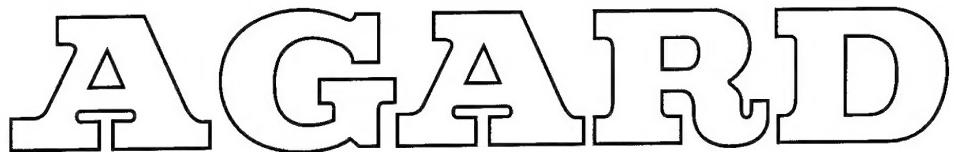
AGARD

ADVISORY GROUP FOR AEROSPACE RESEARCH & DEVELOPMENT

7 RUE ANCELLE, 92200 NEUILLY-SUR-SEINE, FRANCE

AGARD REPORT 808

Capsule Aerothermodynamics

(l'Aérothermodynamique des capsules)

This publication was prepared at the request of the Fluid Dynamics Panel. Papers were presented at a Special Course on "Capsule Aerothermodynamics", held at the von Kármán Institute for Fluid Dynamics (VKI) in Rhode-Saint-Genèse, Belgium, 20-22 March 1995.

DTIC QUALITY INSPECTED 4

North Atlantic Treaty Organization
Organisation du Traité de l'Atlantique Nord

19970703 018

The Mission of AGARD

According to its Charter, the mission of AGARD is to bring together the leading personalities of the NATO nations in the fields of science and technology relating to aerospace for the following purposes:

— Recommending effective ways for the member nations to use their research and development capabilities for the common benefit of the NATO community;

— Providing scientific and technical advice and assistance to the Military Committee in the field of aerospace research and development (with particular regard to its military application);

— Continuously stimulating advances in the aerospace sciences relevant to strengthening the common defence posture;

— Improving the co-operation among member nations in aerospace research and development;

— Exchange of scientific and technical information;

— Providing assistance to member nations for the purpose of increasing their scientific and technical potential;

— Rendering scientific and technical assistance, as requested, to other NATO bodies and to member nations in connection with research and development problems in the aerospace field.

The highest authority within AGARD is the National Delegates Board consisting of officially appointed senior representatives from each member nation. The mission of AGARD is carried out through the Panels which are composed of experts appointed by the National Delegates, the Consultant and Exchange Programme and the Aerospace Applications Studies Programme. The results of AGARD work are reported to the member nations and the NATO Authorities through the AGARD series of publications of which this is one.

Participation in AGARD activities is by invitation only and is normally limited to citizens of the NATO nations.

Capsule Aerothermodynamics
(AGARD R-808)

Executive Summary

This report is a compilation of the edited proceedings for the "Capsule Aerothermodynamics" course held at the von Kármán Institute for Fluid Dynamics (VKI) in Rhode-Saint-Genèse, Belgium, 20-22 March 1995.

At present, on a world scale, different capsules and penetrators are being considered for planetary entry, such as the Huygens probe to Titan, the Intermarsnet to Mars, and a probe attached to the Mercury orbiter to Venus.

In addition, conceptual studies for earth re-entry are in progress for crew transport vehicles. Their geometries vary from low lift-to-drag ratio Apollo type to more advanced and complex bent biconic high lift-to-drag configurations.

Because of the renewed interest in Capsule Aerothermodynamics, this course was organised to stimulate research in this field for young engineers as well as to update expertise for more experienced aerodynamicists.

This series of lectures, supported by the AGARD Fluid Dynamics Panel and the von Kármán Institute for Fluid Dynamics covered all aerodynamic design aspects related to planetary probe and capsule configurations. Critical phenomena occurring during the different regimes of flight from the rarefied through the hypersonic, supersonic, transonic and subsonic portions of flight are reviewed. The impact of real gas and rarefaction on capsule aerothermodynamics, and in particular on forebody and wake flows, is addressed.

In addition, present day computational, and experimental capabilities to assess radiation, blackout, ablation and the characterisation of the dynamic derivatives are discussed.

L'aérothermodynamique des capsules
(AGARD R-808)

Synthèse

Ce rapport rassemble les comptes-rendus du cours sur "l'aérodynamique des capsules" tenu à l'Institut von Kármán de Dynamique des Fluides (VKI) à Rhode-Saint-Genèse, en Belgique, du 20 au 22 Mars 1995.

Présentement, différentes capsules et divers pénétrateurs sont considérés dans le monde entier pour effectuer des entrées planétaires, telle la sonde HUYGENS vers Titan, INTERMARSNET vers Mars, et une sonde attachée à MERCURY ORBITER vers Vénus.

Par ailleurs, des études conceptuelles de véhicules de rentrée terrestre transportant des équipages sont en cours. La géométrie de ces véhicules varie du type Apollo de faible finesse à des configurations biconiques complexes de finesse élevée.

En raison de ce regain d'intérêt dans l'aérodynamique des capsules, ce cours a été organisé pour stimuler la recherche dans ce terrain pour de jeunes ingénieurs, mais aussi pour actualiser l'expertise d'aérodynamiciens plus expérimentés.

Cette série de conférences, avec le soutien du Panel Dynamique des Fluides de l'AGARD et de l'Institut von Kármán de Dynamique des Fluides, couvre tous les aspects de la conception aérodynamique reliés aux configurations de sondes planétaires et de capsules. Le point sur les phénomènes critiques survenant durant les divers régimes de vol depuis le raréfié, à travers l'hypersonique, le supersonique, le transsonique et le subsonique est effectué. L'influence des effets de gaz réel et de raréfaction sur l'aérodynamique des capsules, et en particulier sur les écoulements autour de l'avant-corps et dans le sillage, est analysée.

En outre, les capacités actuelles de calcul et expérimentales permettant d'évaluer le rayonnement, l'occultation radio (black-out) et l'ablation et de caractériser les dérivées dynamiques sont discutées.

Contents

Recent Publications of
the Fluid Dynamics Panel

AGARDOGRAPHS (AG)

Turbulent Boundary Layers in Subsonic and Supersonic Flow
AGARD AG-335, July 1996

Computational Aerodynamics Based on the Euler Equations
AGARD AG-325, September 1994

Scale Effects on Aircraft and Weapon Aerodynamics
AGARD AG-323 (E), July 1994

Design and Testing of High-Performance Parachutes
AGARD AG-319, November 1991

Experimental Techniques in the Field of Low Density Aerodynamics
AGARD AG-318 (E), April 1991

Techniques Expérimentales Liées à l'Aérodynamique à Basse Densité
AGARD AG-318 (FR), April 1990

A Survey of Measurements and Measuring Techniques in Rapidly Distorted Compressible Turbulent Boundary Layers
AGARD AG-315, May 1989

Reynolds Number Effects in Transonic Flows
AGARD AG-303, December 1988

REPORTS (R)

Advances in Cryogenic Wind Tunnel Technology
AGARD R-812, Special Course Notes, January 1997

Aerothermodynamics and Propulsion Integration for Hypersonic Vehicles
AGARD R-813, Special Course Notes, October 1996

Parallel Computing in CFD
AGARD R-807, Special Course Notes, October 1995

Optimum Design Methods for Aerodynamics
AGARD R-803, Special Course Notes, November 1994

Missile Aerodynamics
AGARD R-804, Special Course Notes, May 1994

Progress in Transition Modelling
AGARD R-793, Special Course Notes, April 1994

Shock-Wave/Boundary-Layer Interactions in Supersonic and Hypersonic Flows
AGARD R-792, Special Course Notes, August 1993

Unstructured Grid Methods for Advection Dominated Flows
AGARD R-787, Special Course Notes, May 1992

Skin Friction Drag Reduction
AGARD R-786, Special Course Notes, March 1992

Engineering Methods in Aerodynamic Analysis and Design of Aircraft
AGARD R-783, Special Course Notes, January 1992

Aircraft Dynamics at High Angles of Attack: Experiments and Modelling
AGARD R-776, Special Course Notes, March 1991

ADVISORY REPORTS (AR)

Cooperative Programme on Dynamic Wind Tunnel Experiments for Manoeuvering Aircraft
AGARD AR-305, Report of WG-16, October 1996

Hypersonic Experimental and Computational Capability, Improvement and Validation
AGARD AR-319, Vol. I, Report of WG-18, May 1996

Aerodynamics of 3-D Aircraft Afterbodies
AGARD AR-318, Report of WG-17, September 1995

A Selection of Experimental Test Cases for the Validation of CFD Codes
AGARD AR-303, Vols. I and II, Report of WG-14, August 1994

Quality Assessment for Wind Tunnel Testing
AGARD AR-304, Report of WG-15, July 1994

Air Intakes of High Speed Vehicles
AGARD AR-270, Report of WG-13, September 1991

Appraisal of the Suitability of Turbulence Models in Flow Calculations
AGARD AR-291, Technical Status Review, July 1991

Rotary-Balance Testing for Aircraft Dynamics
AGARD AR-265, Report of WG11, December 1990

Calculation of 3D Separated Turbulent Flows in Boundary Layer Limit
AGARD AR-255, Report of WG10, May 1990

Adaptive Wind Tunnel Walls: Technology and Applications
AGARD AR-269, Report of WG12, April 1990

CONFERENCE PROCEEDINGS (CP)

The Characterization & Modification of Wakes from Lifting Vehicles in Fluids
AGARD CP-584, November 1996

Progress and Challenges in CFD Methods and Algorithms
AGARD CP-578, April 1996

Aerodynamics of Store Integration and Separation
AGARD CP-570, February 1996

Aerodynamics and Aeroacoustics of Rotorcraft
AGARD CP-552, August 1995

Application of Direct and Large Eddy Simulation to Transition and Turbulence
AGARD CP-551, December 1994

Wall Interference, Support Interference, and Flow Field Measurements
AGARD CP-535, July 1994

Computational and Experimental Assessment of Jets in Cross Flow
AGARD CP-534, November 1993

High-Lift System Aerodynamics
AGARD CP-515, September 1993

Theoretical and Experimental Methods in Hypersonic Flows
AGARD CP-514, April 1993

Aerodynamic Engine/Airframe Integration for High Performance Aircraft and Missiles
AGARD CP-498, September 1992

Effects of Adverse Weather on Aerodynamics
AGARD CP-496, December 1991

Manoeuvering Aerodynamics
AGARD CP-497, November 1991

Vortex Flow Aerodynamics
AGARD CP-494, July 1991

Missile Aerodynamics
AGARD CP-493, October 1990

Aerodynamics of Combat Aircraft Controls and of Ground Effects
AGARD CP-465, April 1990

Computational Methods for Aerodynamic Design (Inverse) and Optimization
AGARD CP-463, March 1990

Applications of Mesh Generation to Complex 3-D Configurations
AGARD CP-464, March 1990

Fluid Dynamics of Three-Dimensional Turbulent Shear Flows and Transition
AGARD CP-438, April 1989

Validation of Computational Fluid Dynamics
AGARD CP-437, December 1988

Aerodynamic Data Accuracy and Quality: Requirements and Capabilities in Wind Tunnel Testing
AGARD CP-429, July 1988

Aerodynamics of Hypersonic Lifting Vehicles
AGARD CP-428, November 1987

Aerodynamic and Related Hydrodynamic Studies Using Water Facilities
AGARD CP-413, June 1987

Applications of Computational Fluid Dynamics in Aeronautics
AGARD CP-412, November 1986

Special Course Staff

SPECIAL COURSE DIRECTOR

J. Muylaert
ESTEC
Aerothermodynamic Section\Postbus 299
2200 AG Noordwijk
The Netherlands

LECTURERS

M. Baillion
Aerospatiale
BP 2
78133 Les Mureaux Cedex
France

J.N. Moss
NASA Langley Research Center
M/S 408
Hampton, VA 23681-0001
United States

D. Devezaux
ONERA
BP 72
92322 Châtillon Cedex
France

A. Smith
Fluid Gravity Engineering Ltd
Chiltlee Manor
Haslemere Road
Liphook, Hampshire GU30 7AZ
United Kingdom

G.S. Deiwert
Space Technology Division
NASA Ames Research Center
M/S 230-2/rta
Moffett Field, CA 94035
United States

NATIONAL COORDINATORS

J.M. Charbonnier
von Kármán Institute
Chaussée de Waterloo, 72
1640 Rhode-Saint-Genèse
Belgium

PANEL EXECUTIVE

J.K. Molloy

Mail from Europe:
Attn. FDP Executive
AGARD/OTAN
7, rue Ancelle
92200 Neuilly-sur-Seine
France

Mail from US and Canada:
Attn. FDP Executive
PSC 116
AGARD/NATO
APO AE 09777

CAPSULE AEROTHERMODYNAMICS: MISSIONS, CRITICAL ISSUES OVERVIEW AND COURSE ROADMAP

Jean Muylaert
ESA Technical Directorate,
Aerothermodynamic Section, Postbus 299
2200 AG Noordwijk, NETHERLANDS

Abstract

At present, on a world scale, different capsules and penetrators are being considered for planetary entry such as the Huygens probe to Titan, the Intermarsnet to Mars, and the Mercury orbiter probe to Venus.

In addition conceptual studies for earth reentry are in progress for crew transport vehicles. Their geometries vary from low lift to drag ratio Apollo type to more advanced and complex bent biconic high lift to drag configurations.

Because of the renewed interest in Capsule Aerothermodynamics, this course is organized to stimulate research in this field for young engineers as well as to update expertize for more experienced aerodynamicists.

The course will cover all aerodynamic design aspects related to planetary probe and capsule configurations. Critical phenomena occuring during the different regimes of flight from the rarefied through the hypersonic, supersonic, transonic and subsonic portions of flight will be reviewed. The impact of real gas and rarefaction on capsule aerothermodynamics and in particular on forebody and wake flows will be addressed.

In addition present day computational and experimental capabilities to assess radiation, blackout, ablation and the characterization of the dynamic derivatives will be discussed.

1   Course Road Map

This three day course is devided in 4 parts:

- A first session which reviews the planetary probe missions and the Earth reentry projects and programmes being carried out in Europe, USA and Japan, combined with an overview of the critical points associated with these missions. It basically shows that, on a world scale, quite a lot of activities related to capsule aerothermodynamics are being performed justifying this course.

- The second part of the course contains 3 sessions devoted to fundamental physics, thermodynamics, transport properties, reaction rates, and scaling. In addition ballistic versus lifting reentry strategies will be derived showing the influence of the relevant parameters such as lift to drag ratio and ballistic coefficient.

- The major part of the course i.e. eight sessions, will covers critical points, associated with capsule configurations, such as real gas effects, rarefied flow effects, radiation and blackout, ablation and finally the assessment of the dynamic derivatives. It is the intention that we review for each of these themes the state of the art of the experimental and numerical tools required for best estimation of their impact on the aerothermodynamic design of probes and capsule like configurations.

- The last two sessions of the course will be devoted to two major programmes: the USA Aeroassisted flight experiment and the ESA Huygens probe. For the latter the industrial approach will be reviewed which was followed to come up with the best shape given some stringent mission requirements.

It has to be remarked that within the present three day course not all of the capsule design issues could be addressed. It is realized that issues such as parachute aerodynamics, deployment and stability could not be addressed and that transition as well as reaction and control plume interaction with external flow will only briefly be discussed in the appropriate sessions.

2   Winged versus Unwinged Reentry

The four major classes of hypersonic space transport vehicles and their major aerothermodynamic effects are shown in figure 1 as depicted from reference 1.

- Winged reentry vehicles (RV) such as the space Shuttle, the Buran and the Hermes.

- Hypersonic cruise vehicles (CV) such as the first stage of the Saenger space transportation system.

- Ascent and reentry vehicles (ARV) such as the uper stage Horus of the Saenger system.

- Aeroassisted orbit transfer vehicles (AOTV), also known as the aeroassisted space transfer vehicles (ASTV).

We will concentrate our efforts to reentry of blunt vehicles with low to medium hypersonic lift to drag ratio's. The choise however for ballistic or lifting entry depends on a trade off of many requirements such as : deceleration limits, atmospheric uncertainties, landing site or targetting and recovery, mass limitations etc. These mission requirements will translate into aerothermodynamic requirements during the vehicle design process where at each position in time during flight limits imposed on "g force", dynamic pressure, heatflux, heat load, wall temerature etc are not to be exceeded.

These limits depend of course on the state of the art in space technology. The flight aerothermodynamic loads depend on

- the atmospheric characteristics such as density and temperature,

- the vehicle aerodynamic parameters such as geometry, mass, and aerodynamic coefficients,

- and on flight conditions such as incidence and speed.

The most important vehicle parameters during reentry are :

- the wingloading

- the ballistic coefficient

- and the lift to drag ratio

Configurations with aerodynamic lift, as opposed to ballistic vehicles where the lift is zero, have the advantage to have manoevering capability and therefore enhanced down and crossrange capability; i.e. they can increase there landing region on earth as shown in figure 2 and 3 taken from reference 2.

Figure 4 shows an overview of several vehicle configurations and their corresponding lift to drag ratio's. In session 4 it will be shown that the lift to drag ratio is proportional to the cross range and that stagnation heatflux is inversely proportional to the square root of the nose radius (Fay and Riddell).

It should be noted that with increasing lift to drag one can control also the deceleration forces much better which depending on whether the mission is man rated or not can be a very stringent requirement.

Typical lift to drag ratio's and ballistic coefficients for a range of generic configurations are shown in figure 5 from reference 3. We are concentrating on the low level part of the curve where L/D is lower

than 1 corresponding to the sfere cone shapes. Mercury, Gemini and Apollo command modules were sfere/cone shapes.

For ballistic reentry, the deceleration forces or g forces are very much dependent on the entry speed and the entry angle. Manned ballistic reentry for entry incidences higher than 5 degrees are not possible. This is due to the limitation in negatif "g's" that mankind can tollerate. Figure 6 shows the g forces versus entry angle for some low to medium L/D configurations. For zero entry angle one could obtain acceptable g forces to the expense of landing accuracy and integrated heat load. It is interesting to note that the g forces reduce rapidly even for low L/D vehicles. The 3 g limit can be obtained with L/D configurations of 0.25 as long as their entry angle is lower that 3 degrees. (Apollo has L/D = 0.25 till 0.35).

Lift can be used to reduce the level of deceleration as well as the heating rates during reentry. The effect of L/D on the stagnation point heat transfer rate is shown in figure 7. Lift allows the configuration to decelerate at higher altitudes. The lower value of the free stream density at these altitudes means that the aerodynamic heating will be lower at a given velocity. Note however that despite the decrease in heat flux one can have an increased heat load due to the increase in flight time.

3 Planetary Scientific exploration Probes

3.1 Introduction

ESA and NASA are launching three planetary missions involving entries with very different atmospheric conditions: HUYGENS, to Saturn's satellite Titan, ROSETTA, to a comet and back to earth, and MARSNET, to the planet Mars. Below these three missions will be presented, as well as their aerodynamic characteristics, and some of the aerothermochemical data related to them. Typical entry trajectories are presented. Table 1 shows the Titan, Mars and Earth properties. (reference 17).

The impact of aerothermodynamics on the design and the feasibility of these vehicles is briefly acknowledged. The aerodynamic issues identified for these projects are listed.

The European Space Agency (ESA) is currently studying three scientific probes for planetary missions, reference 4, in conjunction with the National Aeronautic and Space Administration (NASA). For the three missions, NASA will provide the European probes with a launcher, a carrier and communications through their Deep Space Network (DSN). The

aerodynamic shape of the three probes is very similar, based on a 60° sphere-cone for their front heatshield. This choice represents a trade-off between the drag and the stability of the vehicle, but is also supported by the availability of a large aerodynamic database. These three probes involve ballistic atmospheric entries with very different conditions. For manned missions, conservative designs are adopted. For robotic missions, the low cost - low mass approach requires an accurate design, with small margins and a somewhat higher risk. A very good knowledge of the entry environment is needed to fullfill these requirements.

3.2 Huygens

3.2.1 Description of the mission

HUYGENS is a probe designed to perform measurements in the atmosphere of Saturn's giant moon Titan.(reference 5).

The prime contractor for its construction is AEROSPATIALE.

Titan's cold atmosphere is believed to have been preserved in conditions immediately prior to life appearance. HUYGENS' launch is scheduled in 1997. The capsule will fly attached to Saturn's orbiter CASSINI. After 9 years of interplanetary cruise, the composite CASSINI-HUYGENS is inserted in Saturn orbit, and HUYGENS is ejected, approaches Titan and enters its thick atmosphere 22 days later. The Cassini orbiter relays the communications between HUYGENS and the earth.

During the hypersonic phase of its atmospheric entry, the probe is protected by a sphere-cone shaped front heat shield, and a back-cover. When a low supersonic Mach number is reached, the back part of the heat-shield is jettisoned, a pilot chute is opened and finally a large parachute is deployed, to stabilize the vehicle during the transonic phase and to brake more efficiently as seen in figure 8. The front part of the heat shield is then jettisoned, to allow the deployment of the scientific instruments analysing the atmosphere and the planet. The power supply is only sufficient for a descent time of less than three hours. Besides, the orbiter is also available for communications only during a limited time. The minimum descent time required to perform the scientific measurements is two and a half hours. In order to achieve this, the parachute is jettisoned at an altitude of the order of 50 km, and the last part of the descent is free-fall.

When the probe touches the ground, it has accomplished its nominal mission. If the probe survives the impact, it might continue to transmit measurements of the ground structure for a few minutes.

3.2.2 Characteristics of probe's entry

Titan is a planet sized satellite of Saturn. Its surface radius is 2575 km. Its mass is 1.346 10^{23} kg, and the corresponding gravitational constant is $GM = 8.976\ 10^{12}\ m^3 s^{-2}$. The atmospheric composition of Titan is not well known. It is believed to contain 0-20% Argon (Ar), 0-4% methane (CH_4) and 76-100% Nitrogen (N_2) (mole fractions). The winds are unknown, but represent a potential danger for the probe stability. Its topography is presumably known within ± 2 km.

A nominal atmospheric profile, constructed from VOYAGER measurements, is plotted in figure 9 including the associated uncertainties. Titan's atmosphere extends to more than 1200 km, and its surface pressure is higher than the Earth's one.

The diameter of the probe is now 2.7 m, and the mass around 300 kg. The heat shield is made of an ablative material. No significant ablation is expected, but a moderate degasing should occur during Titan's entry, accompanied with some mass loss.

The probe is released from the orbiter with a spin of approximately 5 rotations per minute, and keeps some of it during the hypersonic entry. Typical entry conditions are given in table 2. A corresponding trajectory is shown in figure 10. The convective and radiative heatfluxes are those given by crude engineering correlations. The Mach number is computed with a specific heat ratio value of 1.4 probably different from the real one, which depends on the atmospheric composition. The bump on the Mach curve correspond to the temperature drop around 750 km.

3.2.3 Aerothermodynamics

The accurate prediction of peak and time-integrated heat fluxes is important for the selection and sizing of the Thermal Protection System (TPS) material. Engineering correlations have shown to be completely wrong for the radiative flux predictions. Equilibrium flow calculations seem to overpredict convective heat-fluxes, but underpredict the radiative fluxes, since they underestimate the formation of highly emissive products like CN molecules. The design of the heat-shield requires the use and development of highly sophisticated numerical tools, and the construction of adequate databases, for the aerodynamic properties of the probe and for the plasma chemical, radiative, thermodynamic and transport properties.

The aerodynamic design of the probe relies heavily on early work performed on Titan entry for other entry conditions as shown in reference 6, 7 and 8 and on the properties of its atmospheric components. (reference 9).

A more recent experimental study on nonequilibrium radiation from Park (reference 10) provides also an important element for the non-equilibrium ra-

diation predictions. Non-equilibrium Navier-Stokes calculations are difficult because of the stiffness and complexity of the reactions of decomposition of methane , but they are necessary not only for the heat flux assessment, but also to predict pollutants harmful to on-board scientific instruments.

The prediction of the plasma flow must be performed around the whole probe . The back cover has also a significant mass impact. Again, purely empirical correlations are not sufficient at this stage of the project, and experimental verification is impossible.

In the hypersonic regime, the formation of small amounts of CN induces a more severe heat flux distribution because of a major non-equilibrium radiation contribution. This radiation is highly dependent on the CN electronic temperature, and on the degree of ionization of the flow. Results of nonequilibrium viscous flow calculations are reported in figure 11.

An accurate description of the flow field is necessary for the determination of heat fluxes, and these fluxes have a direct impact on the selection of the material for the thermal protection system. The flight conditions are such that it is necessary to rely on a computational assessment of the heat flux distribution, associated with a sound margin evaluation and an adequate experimental qualification. The non-equilibrium radiative heat-fluxes are several times higher than their equilibrium counterparts.

3.3 MARSNET

3.3.1 Description of the mission

In 2001 or 2003, ESA will launch a cluster of three scientific exploration stations to Mars.(reference 12 and 13).

NASA will provide a Delta 2 class launcher, and carriers as well as Deep Space Network support. The MARSNET probes will form a network of robotic mini-probes on Mars surface.

They will study the atmosphere of Mars, its surface and its internal structure. Their observations will be completed by the informations from the future NASA's MESUR Martian probe network. Their nominal operation will last two years (one martian year) in a very harsh climatic environment. The major design drivers are the cost, the mass and the volume of the probes.

3.3.2 Characteristics of probes' entry

The feasibility of the probes is still being investigated, and their final shapes have not been decided yet. The choice of fitting 3-4 probes in a Delta-2 class fairing restricts their diameter to a maximum of $2m$ and their mass to 120 kg. The material used for the TPS could be the same as HUYGENS' one, or a hot structure solution could be retained (C-SiC or C-C). The Martian atmosphere is very thin (120 km), and

at a low pressure, the ground pressure being typically around 700 Pa. The table 3 summarizes the entry conditions for VIKING, MESUR and Marsnet. It appears that MARSNET will face more severe heat fluxes.

Mars atmospheric pressure experiences large variations. A typical entry is represented in figure 12. Notice that most of the heat flux found by engineering correlations is due to convection. The aerodynamic coefficients of VIKING have shown to be very sensitive to real gas effects. The Marsnet trajectory predictions need to account for it.

3.3.3 Aerothermodynamics

The peak heat fluxes are expected of the same order of magnitude as for the HUYGENS capsule. The shock layer around MARSNET will be at a temperature above 7000 K at peak heat flux altitude. The existing thermochemical database comes essentially from the VIKING tests; it needs to be updated and extended to higher temperatures. The vibrational relaxation of polyatomic molecules at very high temperatures needs to be better understood and included in existing codes. The catalytic effects of the thermal protection materials also need to be investigated as well as their characterisation in the Martian atmosphere. The base flow prediction is also an important aerodynamic issue because of potential hot spots on the protuberant back cover of the martian probe.

The presence of dust in regions of Mars atmosphere where the probe might have a high velocity can lead to some heatshield erosion. and experimental background for the future space exploration missions.

3.4 ROSETTA

3.4.1 Description of the mission

In the first years of the 21st century, the ROSETTA capsule will be launched. Six years later, the probe will land on a comet, and would have returned to Earth with some 20 kg of samples of the comet's nucleus. However, recently it was proposed to cancel the return mission and to transfer the data back to Earth by telemetry. The return to Earth was planned to take more than five years. The most important part of the capsule's mission was to bring back the samples in pristine conditions. To achieve that, the probe should not be subject to decelerations above 50 g. The heat flux and heat soak should be minimum, and the landing dispersion should be moderate.

3.4.2 Characteristics of probe's entry

The probe's shape is similar to Apollo's shape, but no trim angle is planned. A ballistic non-lifting trajectory was chosen. The probe's velocity during entry would have been around 16 km/s and is significantly higher than the maximum earth entry velocity ever experienced, namely Apollo's 11 km/s. At this stage of the study, an entry angle just a little steeper than the skip-out angle was retained to reduce the peak flux and deceleration (table 2). Even so, very severe fluxes were expected during the hypersonic part of its trajectory, around 30 $MW\,m^{-2}$, the major contribution being the radiative one. A strong ionization should be present. A typical trajectory is plotted in figure 13. These levels of heat flux usually require ablative thermal protections. The expected mass of the probe is approximately 300 kg.

3.4.3 Aerothermodynamics

Typically, some shock layer temperatures may be well above 30000 K. The plasma properties at such high temperatures are rather uncertain. Similarly, reaction rates for such high temperatures are not available, and old chemical models such as Dunn and Kang (reference 11) are used.

For these high temperatures, the validity of the Navier-Stokes equations could be questionned. Additional processes probably need to be accounted for; at least the coupling of radiation with the flow field, and the ablation, and possibly electromagnetic effects. Here again, like for HUYGENS, the radiative heat flux will be the major heat exchange process, and ablative processes will have to be accounted for in the heat flux predictions.

3.5 Scientific mission key issues summary

Basic and practical problems remain to be solved and they require improvements for the experimental as well as the numerical tools. Better knowledge of basic physical processes are required especially for the planetary gases. In particular transport and thermodynamic properties, reaction rates and radiative properties need to be investigated.

A proposed real gas validation methodology is shown in figure 14. The thermodynamic coefficients, transport properties , radiation properties and chemical kinetics need to be reassessed using modern shock tubes combined with the latest nonintrusive measurement techniques. Because most of the existing data are comming from older shock tube experiments where the relaxation processes behind a moving normal shock was measured; it is believed that new shock tube experiments combined with the latest nonintrusive measurement techniques are required to reasses these reaction rates and thermo-

dynamic properties. Moreover the validation of the above coefficients need also to be done for expanding flow fields. There is an urgent need to standardize the chemical - and vibrational reaction rates for air and other gases such as CO_2 for specific classes of high enthalpy flows e.g. flows encountered in shock tubes or hot shots which do not necessary require the modelization of ions. Standardization of reaction rates will also take away a source of discrepancies when performing code to code comparisons.

In addition there is an urgent need to improve our understanding of the reaction mechanisms associated with gas surface interactions such as catalysis and ablation. These fundamental experiments could be performed in arc jets or in more clean environments such as solar furnices or induction heated facilities or plasmatrons. Finally figure 15 provides a summary of the key issues related to the above described scientific missions including the latest Mercury orbiter Venus probe.

4 Earth Reentry capsules

4.1 Introduction

There were a lot of Earth reentry flights performed in USA and Russia during the development of the Apollo and Soyuz capsules. It is not the purpose to review all flight experiments and programms but we will only review some of the recent flight experiments as well as describe the most recent capsule programms.

- The Japanese OREX flight programm.

- The ESA Atmospheric Reentry Flight Demonstartor (ARD).

- The ESA Crew Transport Vehicle studies (CTV) which at present are just system studies where different concepts such as the Bent biconic or the Viking type configuration is being studied.

- The German Bremsat which was launched by the Shuttle STS 60 for the purpose of performing low density experiments to explore flow phenomena and to validate flow models and numerical models.

- The Express capsule which was launched in Januari 1995 with the purpose of acquiring low density as well as high enthalpy data in the continuum regime; unfortunately the flight experiment failed.

- The Mirka study performed by Germany.

- Additional studies were performed such as the CARIANE study by CNES France, the CARINA capsule programme by the Italian Space

agency, the LARVE programme by The Netherlands, The Cobra studies by the germans; which will not be adressed further here.

- Finally in view of its importance some Apollo lessons learned will be addressed.

4.2 Orex

On 4 feb. 1994, the Orbital reentry experiment, (OREX) took place. OREX was launched by the first Japanese H2 launcher. Because this is a very recent flight, some of the experimental results will be shown as depicted from reference 13.

Figure 16 and 17 show the location and the specification of the measurement plan. Figure 18 shows the sequents of events. Note the earlier detection of the blackout in flight as compared to the preflight estimation. Figure 19 gives the breakdown of the downrange error :

- 38 Km due to error caused by orbiter injection,

- 47 Km due to error caused by deorbit burn out

- and the remaining 30 Km due to the environmental errors during reentry flight.

Finally figure 20 and 21 show some examples of the data which were taken during flight. It can be concluded that the OREX flight was successfully conducted.

4.3 ARD

The ARD vehicle is based on the Apollo shape, figure 22, with an external diameter of 2.8 m and a maximum mass of 2.8 tons. (reference 14).

It will be launched by the second ARIANE 5 flight as a passenger in april 1996. The mission performed by the vehicle after launch is a suborbital ballistic flight followed by a guided lifting reentry ending with the final phase of deceleration under parachutes and the splach down in the Pacific ocean where the vehicle shall be recovered as seen in figure 23. The heat shield is made of 93 tiles in " Aleastrasil" , a compound of silica randomly oriented short fibers, impregnated with phenolic resin. The conical part and back cover are fitted with " Norcoat - Liege " tiles. The RCS system will ensure the ARD attitude and control during the ballistic and guided reentry phases. It is derived from the ARIANE SCA nozzles (systeme de control attitude). Figure 24 shows the parachute sequence. Figure 25 the ARD measurement plan. The flight conditions will be derived from redundant sources of informations :

- reconstruction of flight trajectory with inertial measuring unit;

- radar traking

- atmospheric characterization with lidar, balloons and rockets(if available),

- pressure measurement on the heat shield,

- total angle of attack.

The aerodynamic coefficients will be derived from the accelerometers and the RCS activation plan will be such as to identify RCS efficiencies as well as alfa derivatives of the aerodynamic coefficient and dynamic stability parameter Cm_q

Figure 26 show the measurememt locations. In addition black out measurements will be performed. Figure 27 and 28 show respectively the wall streamlines and the pressure contours illustrating the complex structures of the separated flow on lee side and at base of the capsule.

The ARD programme will provide a set of usefull data for the qualification of the European design, prediction and development tools.

4.4 Express, Bremsat and Mirka

The simulation of free molecular and transitional effects in windtunnels is not possible due to the limitations in speed and size of present day low density facilities.

Free flight experiments such as the Bremsat and the Express are therefore of major importance for the evaluation of low density effects.

Figure 29 shows the Bremsat dimensions , flight conditions , experiments and equipement. (reference 15).

Two types of experiments will be performed :

- First the gas surface interaction experiment where the accomodation coefficients will be deduced from the panel tangential and normal forces; the density being measured with free molecular ideal orifice probes and flow incidence angle derived from the periodicity of the balance signal output.

- Second the rarefied flow experiment which will be performed in the transitional flow regime. Free molecular sensors , which are mounted on forward facing probe holders will measure the molecular particle flux and kinetic heat flux 100 mm in front of the nose cap. Sensors of the same geometry, which are mounted in the satellite nose cap, will measure the corresponding quantities on the surface. The surface fluxes will be strongly influenced by the evolution of the collision dominated rarefied flow in front of the satellite.

The evaluation of the two types of measurements, i.e. one in the undisturbed free stream and one in the flow field of the nose will give a clear indication of the first collisional processes. They can be a valuable

basis for the validation of Monte Carlo methods at true orbital flight conditions.

Figure 30 shows the Express entry capsule and objectives. Dynamic pressure probes in the nose in order to measure free stream quantities and combined flux probes on the flare are mounted so as to deduce surface pressure, surface partical flux, heat flux and slip velocity.

Finally figure 31 shows the German reentry capsule Mirka which is a 1 m sfere to be launched in 1996, to test new nonablative heat shield material and structure. Figure 32 shows the mirka trajectory in the HEG binary scaling versus speed envelop.

4.5 Apollo

It is considered appropriate to include here some information on the Apollo because of the ongoing European capsule technology programme and because of the many capsule programms which uses the Apollo aerodynamic data base.

We will stress here only the influence of the real gas effects on the trim pitching moment. Figure 33 shows the Apollo command module trim error and comparison with the Space Shuttle. Hassan et al (reference 16) simulated the Apollo at flight conditions and in windtunnel conditions. Figure 34 shows nonequilibrium Navier Stokes computations using a 5 species air model and it can be deduced that the trim angle shift is due to the chemical reactions.

Because of the available data base a technology programme was started in Europe using the Apollo as a reference shape and in support to the above described ARD project. Experiments in low and high enthalpy facilities are planned in this " capsule technology programme " for the study of the influence of real gas and viscous interaction effects on the L/D. In addition critical issues such as RCS interaction, dynamic derivatives, base flow sting support interference, radiation, blackout and ablation are being addressed.

5 CONCLUSION

The present first session of this course addressed the planetary probe entry's for the Huygens, the Marsnet, and the Rosetta missions and reviewed some of the recent Earth reentry capsule programmes. Because of the renewed interest this course was organized to stimulate research for young engineers as well as to update expertize for more experienced engineers. In the following sessions first some fundamentals will be reviewed followed by critical capsule related items and finally some lessons learned wil close this course . It is hoped that the objectives of the course will be met.

6 ACKNOWLEDGEMENT

References

[1] Hirschel, E.H., "Hypersonic Aerodynamics," 2_{nd} Space Course on Low Earth Orbit Transportation Munich, Oct. 1993.

[2] Messerschmid, e. and Schottle, U.M., "Der Wiedereintritt von Kapseln und gefluegelte Fahrzeugen in die Atmosphaere," 3_{nd} Space Course on Low Earth Orbit Transportation Stuttgart, March 1995.

[3] Bertin, J., "Hyersonic Aerothermodynamics ," AIAA Educational Series ISBN 1-56347-036-5, 1994.

[4] Berry, W. and Haeuser, J., "Space vehicle Aerothermodynamics," ESA Bulletin , (64), 1991.

[5] Scoon, G. Whitcomb, G. Eiden, M. and Smith, S. , "Cassini Huygens entry and Descent technologies," Space Technology, 11(4): 167-177, 1991.

[6] Nelson, H. Park, C. and Whiting, E., "Titan atmospheric composition by hypervelocity shock layer analysis," Journal of thermophysics and heat transfer, 5(2): 157-165, 1991.

[7] Tiwari, S. and Chow,H., "Aerothermochemic environment for a Titan aerocapture vehicle.," Technical report NASA CR 168721, NASA, 1982.

[8] Tiwari, S. Chow,H. and Moss, J. , "Analysis of aerothermochemic environment of a Titan aerocapture vehicle," AIAA paper 81-1128, 1981.

[9] Flori, B. and Biolsi, L. , "Transport properties associated with entry into the atmosphere of Titan," AIAA paper 81-0278, 1981.

[10] Park, C., "Assessment of two temperature kinetic model for ionizing air," AIAA paper 87-1574, 1987.

[11] Dunn, M. Kang, S. , "Theoretical and experimental studies of reentry plasma," Technical report NASA CR 2232, NASA, 1973.

[12] Chicarro, A. Scoon, G. and Coradini, M. , "Mission to Mars," Technical Report , ESA SP- 1117, ESA, 1991.

[13] Inouye, Y. , "Orex Flight - Quick report and lessons learned," Second European conference on Aerothermodynamics for space vehicles and fourth European EHVDB workshop, ESA SP-367, ESA , 1994.

[14] Durand, G. Watillon, P. and Cazaux, C., "Atmospheric Reentry Demonstrator (ARD): A Flight Experiemt for technology qualification within the European Manned Space Transportation Programme (MSTP)," Second European conference on Aerothermodynamics for space vehicles and fourth European EHVDB workshop, ESA SP-367, ESA , 1994.

[15] Koppenwallner, G. Johannsmeier D. Mueller-Eigner, R., "Hight Altitude Free Flight Experiment and Instrumentation developed for Bremsat and Express Capsule," Second European conference on Aerothermodynamics for space vehicles and fourth European EHVDB workshop, ESA SP-367, ESA , 1994.

[16] Candler, G. , "A Perspective on Computational Aerothermodynamics: current modelling difficulties," Second European conference on Aerothermodynamics for space vehicles and fourth European EHVDB workshop, ESA SP-367, ESA , 1994.

[17] Marraffa, L. Giordano, D. Huot. J. Smith, A., "Hypersonic Aerothermodynmic aspects of ESA scientific exploration probes," IUTAM conference at Marseille , july, 1992.

Table 1: Titan/Mars/Earth properties

	Titan	Mars	Earth
equatorial radius (km):	2575	3397	6378
rotation period:	15.9 $days$	24h 39mn	24h
mass (kg):	1.35 10^{23}	6.42 10^{23}	5.97 10^{24}
GM $km^3 \, s^{-2}$	8978	42840	398378
atmospheric composition expressed in mole fractions. values less than .001 are reported as 0.			
N_2	.80 → 1.	.027	.79
O_2	0.	.0013	.21
CO_2	0.	.953	0.
Ar	0. → .20	.01	0.
CH_4	0 → .04	0.	0.

Table 2: HUYGENS/MARSNET/ROSETTA typical entry and peak heat flux conditions

	probe:	HUYGENS	MARSNET	ROSETTA
	entry in:	Titan	Mars	Earth
entry	altitude (km):	1270	120	220
	velocity (m/s):	6190	6250 → 6650	16000
	angle:	-64°	-15° → -30°	-10.5^o
peak heat flux	altitude (km):	287	44	63
	velocity (m/s)	5779	5280	14300
	pressure (Pa)	5.75	6.53	15.49
	temperature (K)	145	148	240.1

Table 3: comparison of the different Mars entry probes

|	VIKING	MESUR	MARSNET
cone angle	70°	70°	60°
diameter	3.5 m	2.5 m	2. m
mass	1043 kg	304 kg	120 kg
entry velocity	5. km/s	7. km/s	6.4 km/s
entry angle	-17°	$\geq -20^o$	$\geq -30^o$
guided entry	yes	no	no
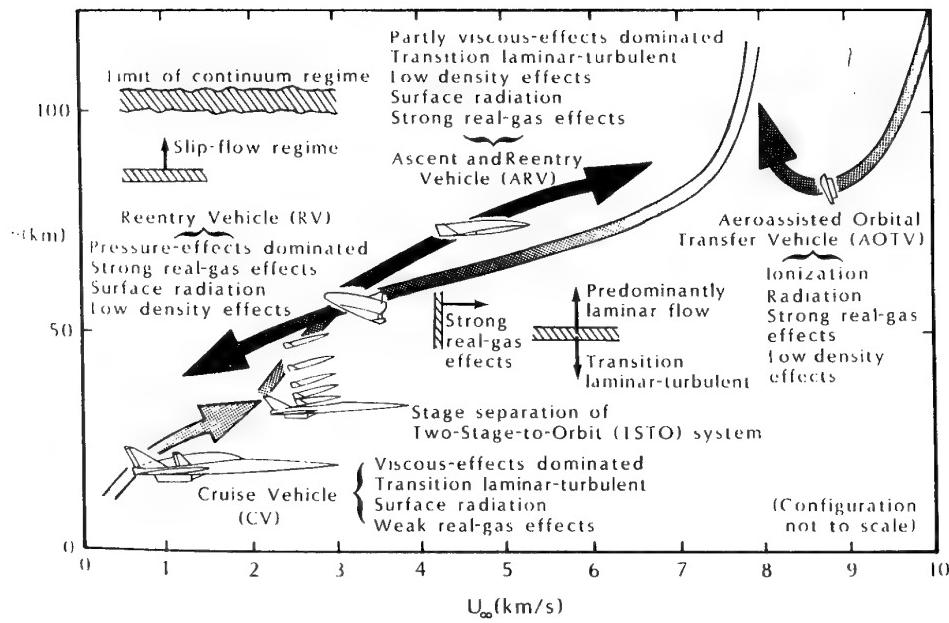
Figure 1: Four major classes of hypersonic space-transport verhicles, and major aerothermodynamic effects.
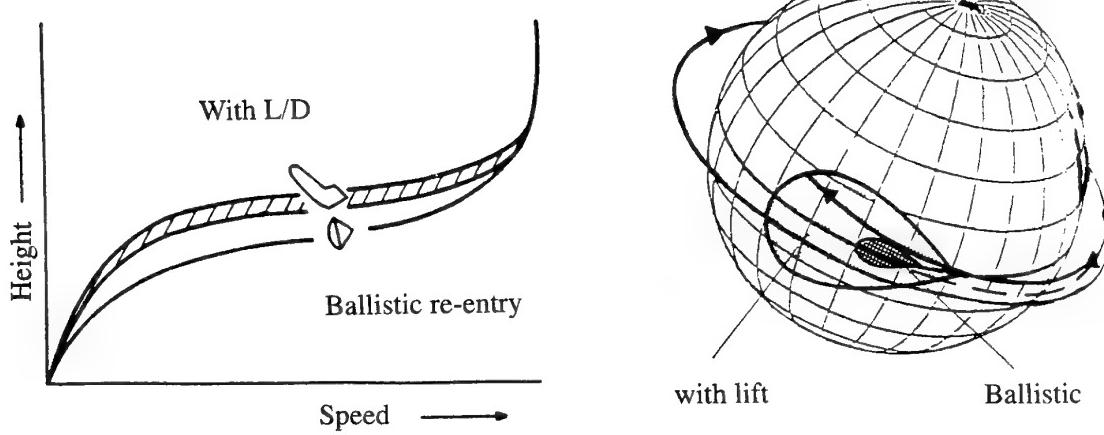

Figure 2: Influence of L/D for different configurations.
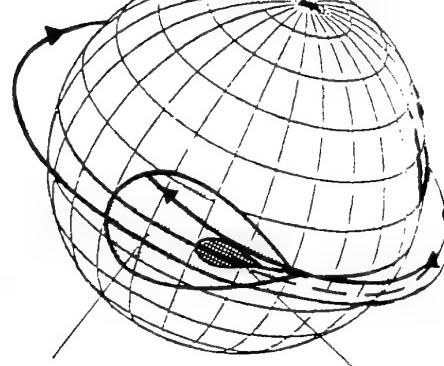
Figure 3: Landing region on earth
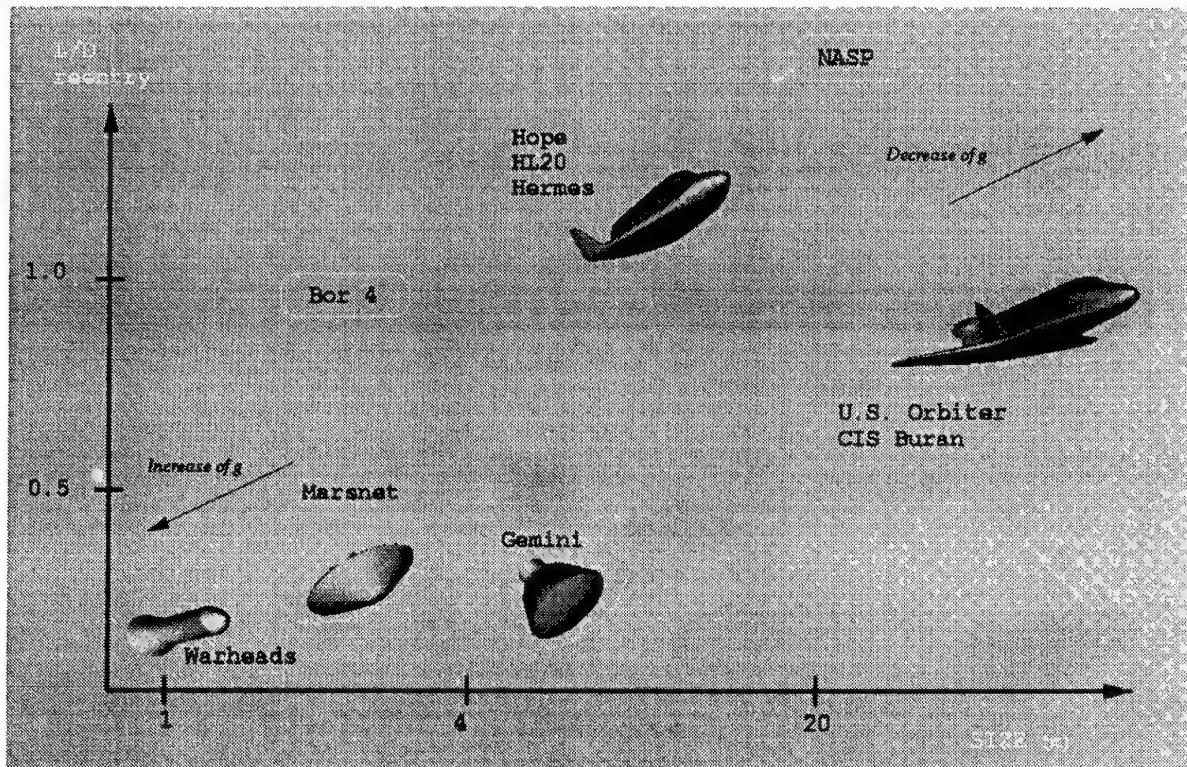
Figure 4: Overview of several verhicle configuration and their corresponding lift to drag ratio
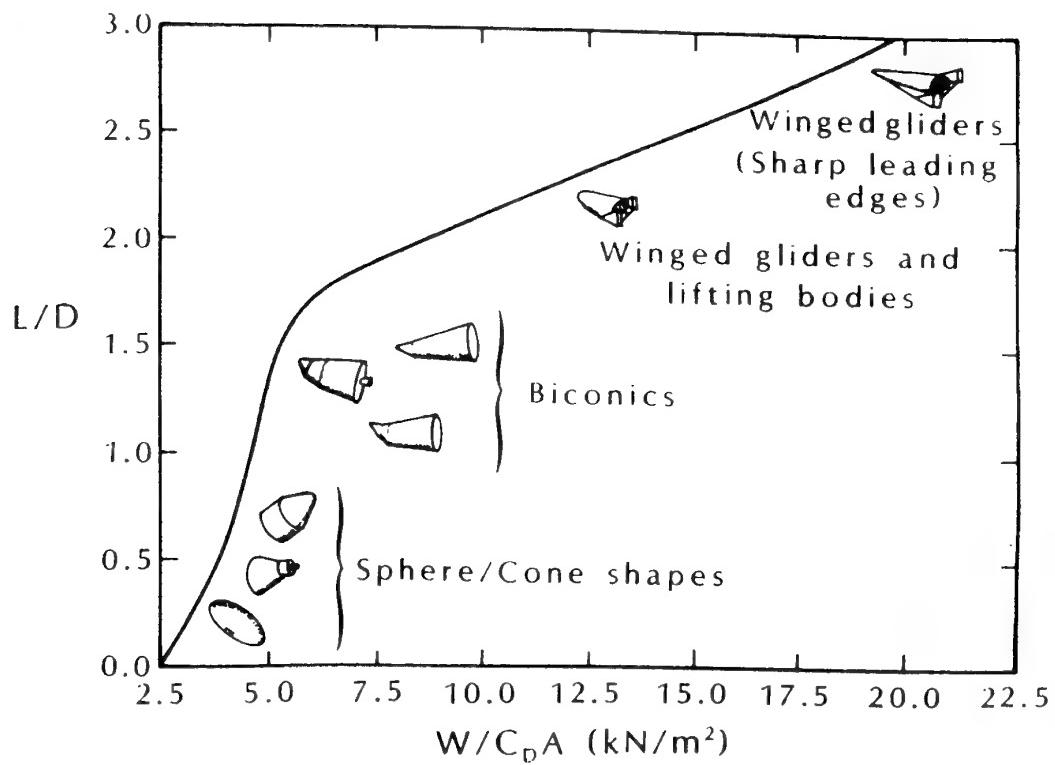
Figure 5: Lift-to-drag ratios (L/D) and ballistic coefficients for er-entry configurations.
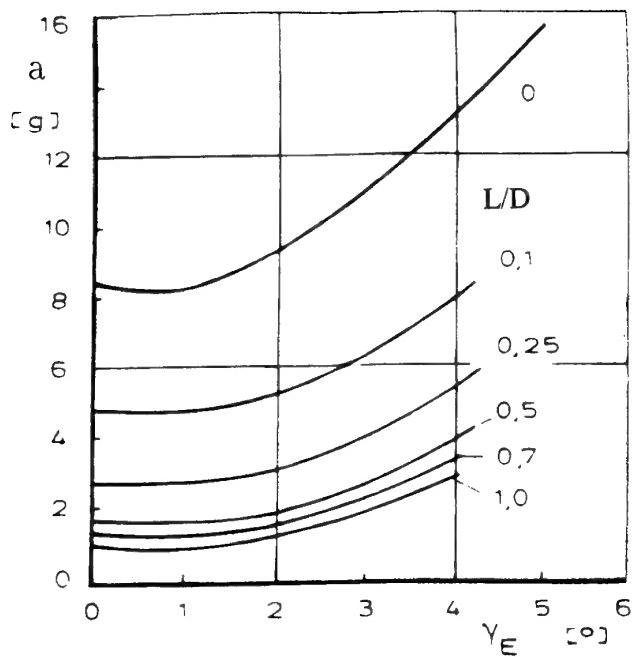
Figure 6: "G"-forces versus entry angle as a function of L/D.
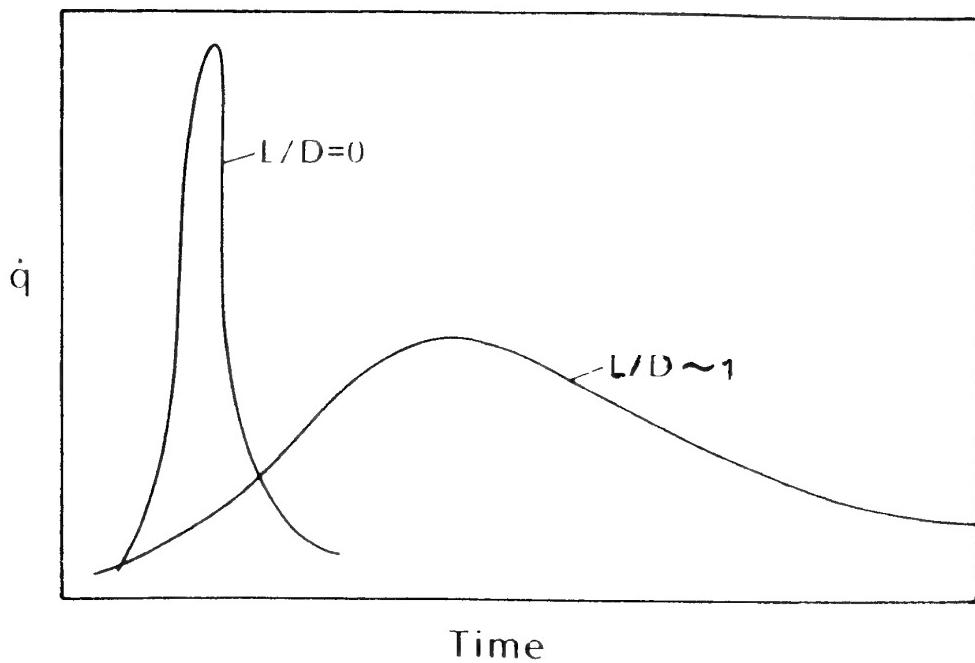
Figure 7: The effect of (L/D) on the reference heating-rate history.

Huygens entry
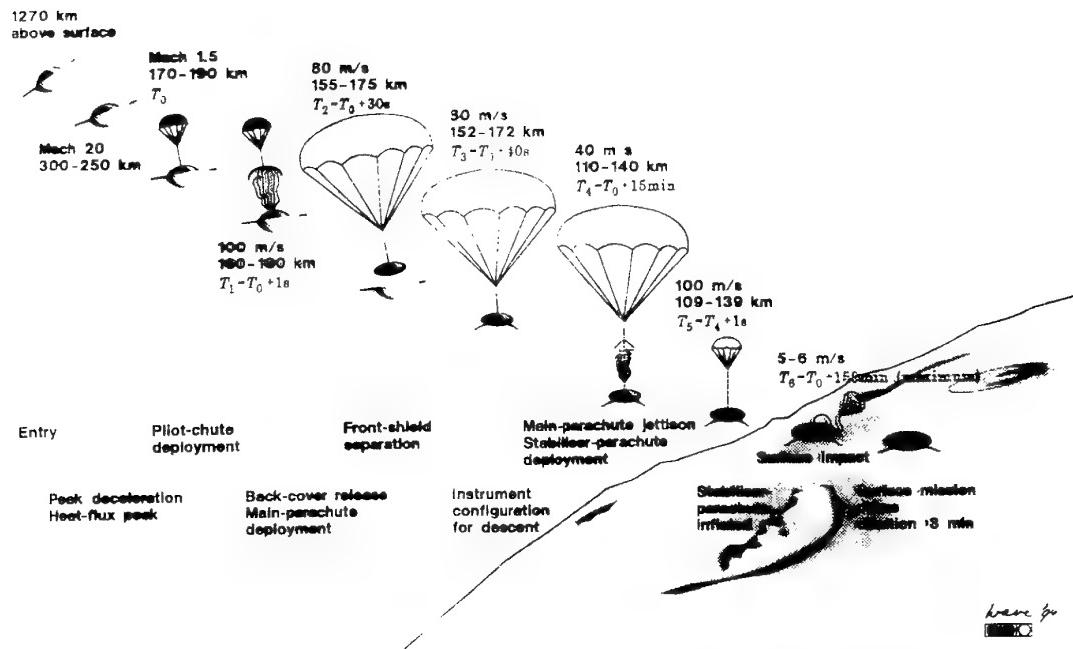
Figure 8: Huygens entry descent scenario
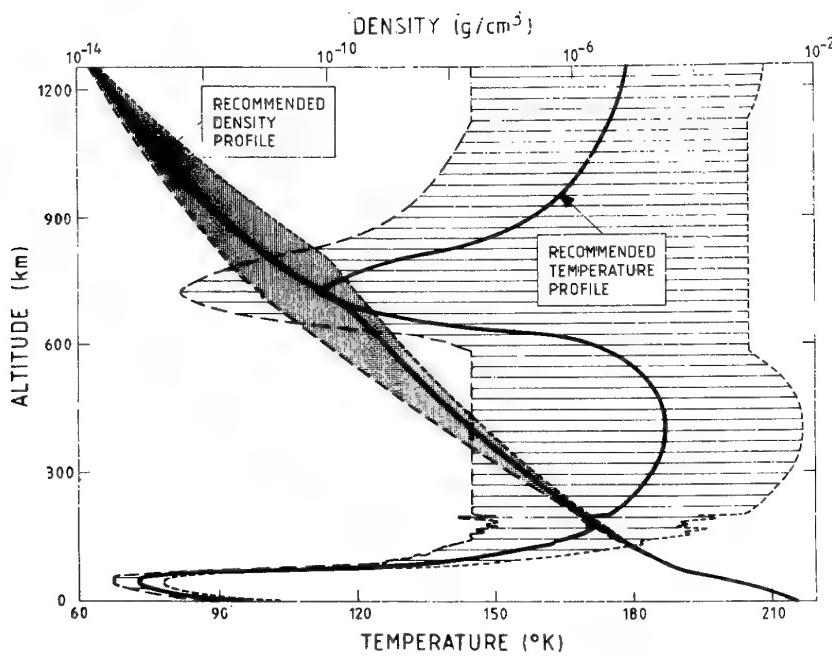
Figure 9: Titan atmosphere characteristics and uncertainties.
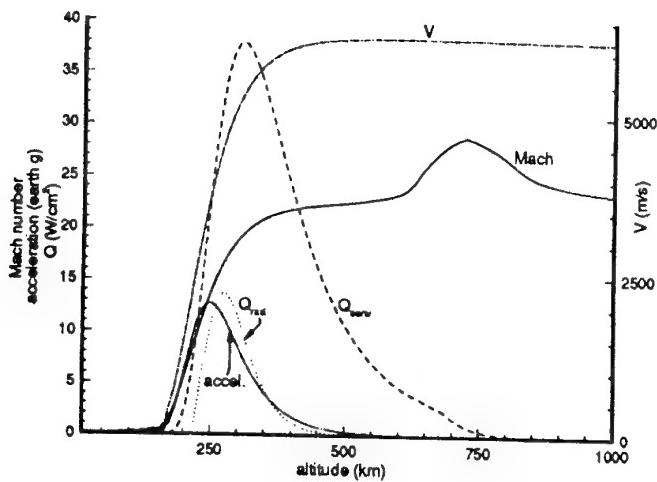
Figure 10: Huygens Entry trajectory
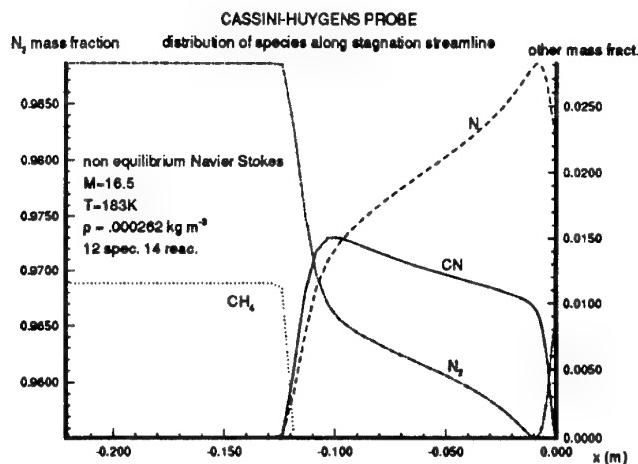
Figure 11: Huygens - non-equilibrium Navier-strokes calculation: concentrations along stagnation
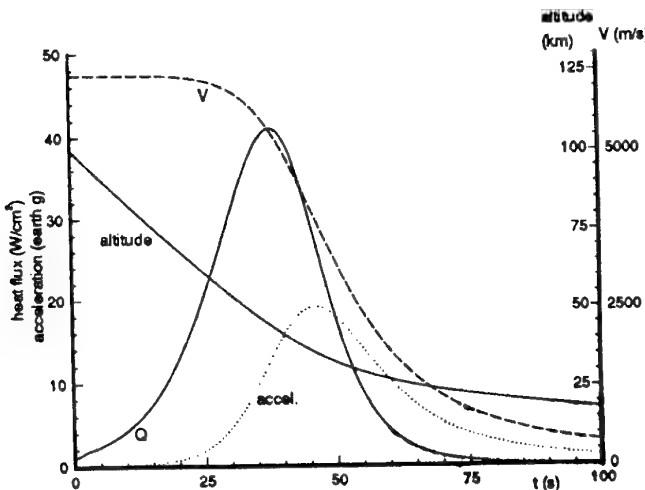
Figure 12: MARSNET Typical entry trajectory
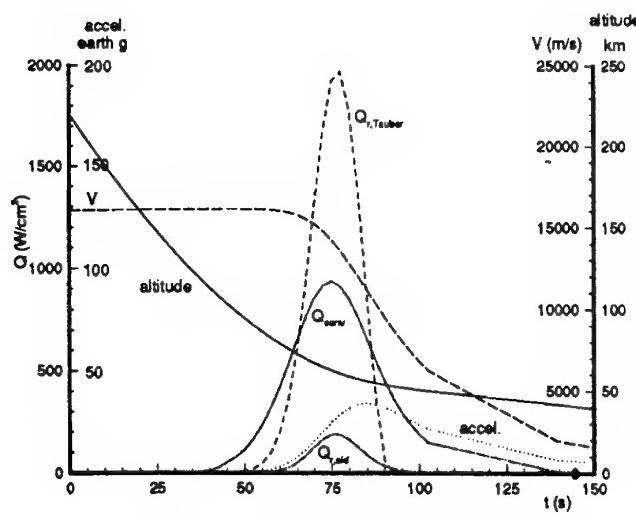
Figure 13: Rosetta entry trajectory
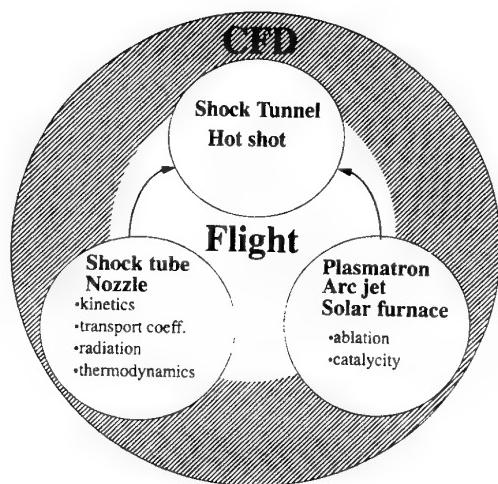
Figure 14: Real gas validation methodology

Project	Conditions	Key Issues and Studies

•Huygens:

- Titan entry
- 6.2 km/sec — radiative heatflux
- N2, CH4, Ar atmosphere

•Rosetta

- return from comet
- 16.5 km/sec — ablation/radiation
- earth reentry — contamination

•Inter Marsnet

- Mars
- 6.2 km/sec — catalycity, CO2 kinetics
- CO2, N2, Ar atmosphere

•Mercury Orbiter

- Probe into Venus atmosphere — ablation/radiation, catalycity
- 15.4 km/sec — turbulence,
- CO2, N2 atmosphere, high press. — convective heat flux,

•For all missions

- — dynamic stability
- — qualification methodology

Figure 15: Overview of scientific mission aerodynamic key issues and challenges

	DOWNRANGE ERROR
(1) ERROR CAUSED BY ORBIT INJECTION ERROR	- 3 8 k m
(2) ERROR CAUSED BY DE-ORBIT THRUST ERROR	- 4 7 k m
(3) ERROR CAUSED BY ENVIRONMENTAL ERRORS DURING REENTRY FLIGHT	- 3 0 k m
TOTAL	- 116 k m

Figure 19: Evaluation of downrange error
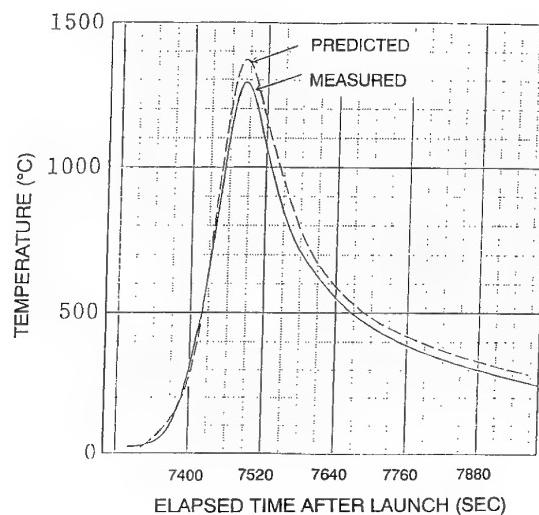
Figure 20: C-C nose cap rear surface temperature at stagnation point


Fig.-14 Gap Heating Effect on Ceramic Tile
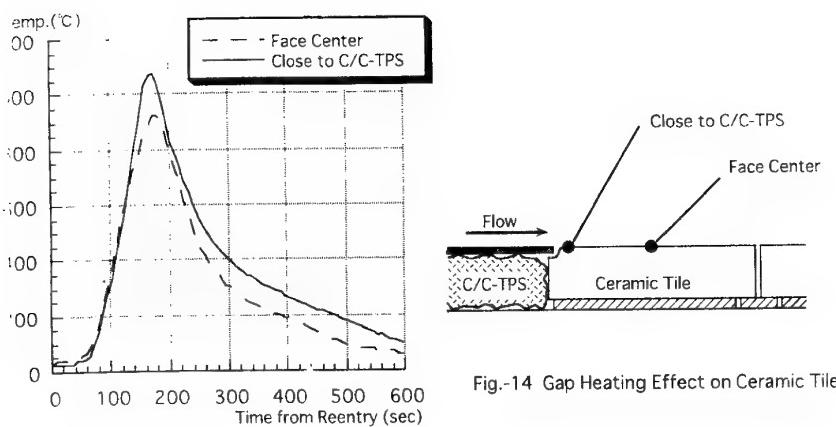
Figure 21: Gap heating effect on ceramic tiles
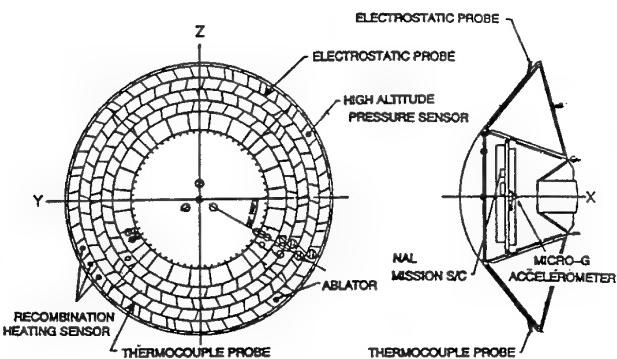
Figure 16: OREX location of measurement mission

Contents of measurement	Means of Measurement	number	Altitude Range	data range	Data Acuuracy
			(km)		
Basic Aerodynamic and Aerothermodynamic Data during Reentry					
• Body Surface Temperature & Pressure	Thermocouple	9	120 – 40	0 – 1600 C	3% FS
	Middle Altitude Pressure Sensor	1	85 – 40	0 – 0.1 atm	0.01 atm
• Temperature for Recombination Heating Measurement	Recombination Heating Sensor, T/C	3	120 – 40	0 – 1700 C	2.5% FS
• micro-G acceleration and wall pressure in rarefied flow	Micro–G Accelerometer,	1	120 – 85	0 – 1.28 G	0.7% FS
	High Altitude Pressure Sensor	1	120 – 75	10^{-1} – 10 Torr	1.9% FS
Basic Data to Evaluate Thermal Structures					
• Temperature at varios points	Thermocouples and resistance	15	120 – 0	0 – 700 C	3% FS
	thermometers	15		0 – 700 C	3% FS
• Temperatures in Ablator	Thermocouples in 3 depths	3	120 – 40	0 – 1400 C	1.8% FS
Basic Data for Communication Blackout					
• Received RF Intensiry Measurement	Antenna at 3 stations near impact pt.	–	–		–
• Electron number density measurement in boundary ly.	Electro–static Probe, currents	5	120 – 80	10^{9} – 10^{14} /cc	3.1% .FS
	Thermocouple Probe, temperatures	3	120 – 80	0 – 1700 C	1.7% FS
Navigation Data by GPSR in orbit and reentry	GPS receiver system	1	–		

Figure 17: Spicification of the measurement system

EVENT	PLANNED (SEC)	FLIGHT (SEC)
SEPARATION FROM H–II	832.7	830.8
START OF DEORBIT	6068.0	6063.5
END OF DEORBIT	6365.3	6348.3
AOS AT CHRISTMAS IS.	7320.0	7290
AOS AT SHIP STATION	7340	7317
START OF BLACKOUT (80km)	7439	7383
END OF BLACKOUT (50km)	7516	7496
PARACHUTE DEPLOY	7630.7	7614.7
SPLASH–DOWN	7986	7982

Figure 18: OREX sequents of events
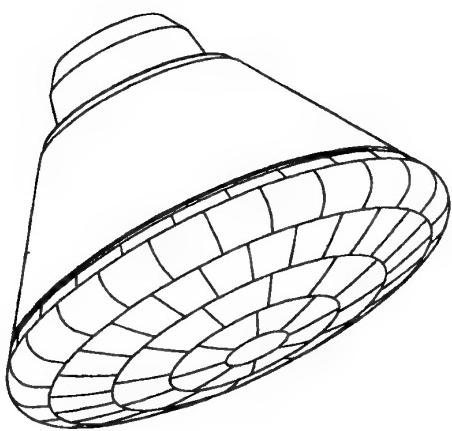
Figure 22: The ARD vehicle
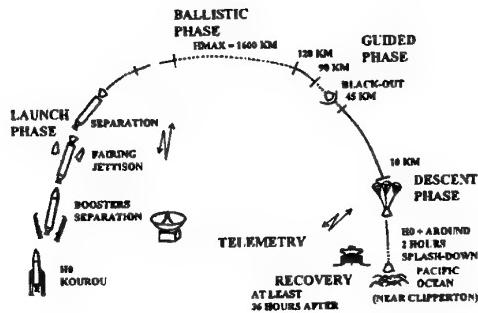
Figure 23: The ARD mission senario
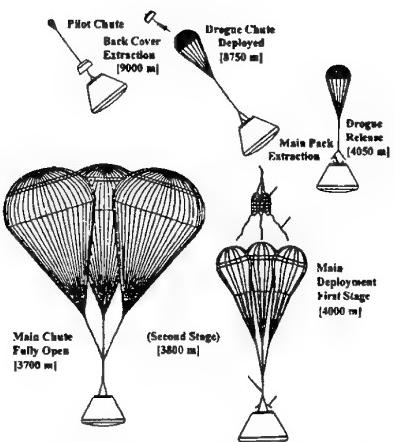
Figure 24: Parachute sequence overview

Measurement	Quantity	Remarks
Thermocouples TPS	50	Thermo-drums: - 4 with 5 Tc - 11 with 3 Tc
Thermocouples TPS	12 (6x2)	Fluxmeters
Thermocouples	24 (6x4)	Material samples
Thermocouples	21	Internal Structure
Thermocouples	14	RCS nozzles
Press. transducers	15	Heat shield
Press. transducers	13	Cone/ back cover
Press. transducers	10	RCS
Tri-axial accelero.	2 (x3)	Flight mechanics (chute deployment/ high altitude aerodynamics)
Accelero./ Gyro.	6 (2x3)	Inertial Measurement Unit (SRI)
Accelero.	2	Vibrations
Reflectometers	2 (x4)	Plasma
Strain gauges	5	Parachute lines
Microphone	1	Acoustics

Figure 25: ARD Measurement plan
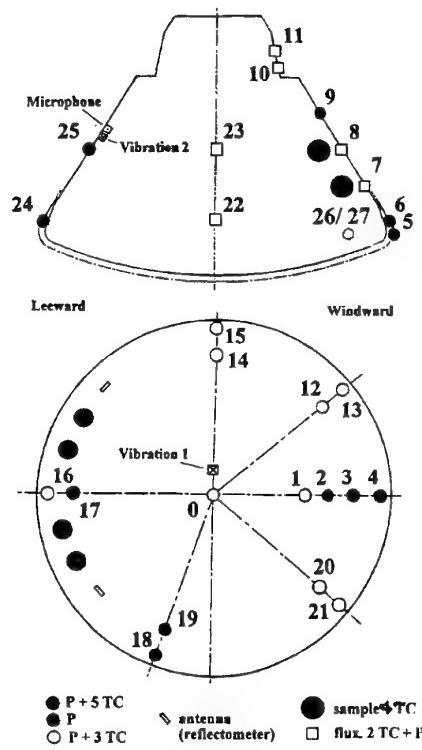
Figure 26: ARD Measurement location on the vehicle

A.R.D : M=23.8 - Z=65.8 km - inc.=20 deg.
Pressure contours

parametre PRESSION (P/Pinf)
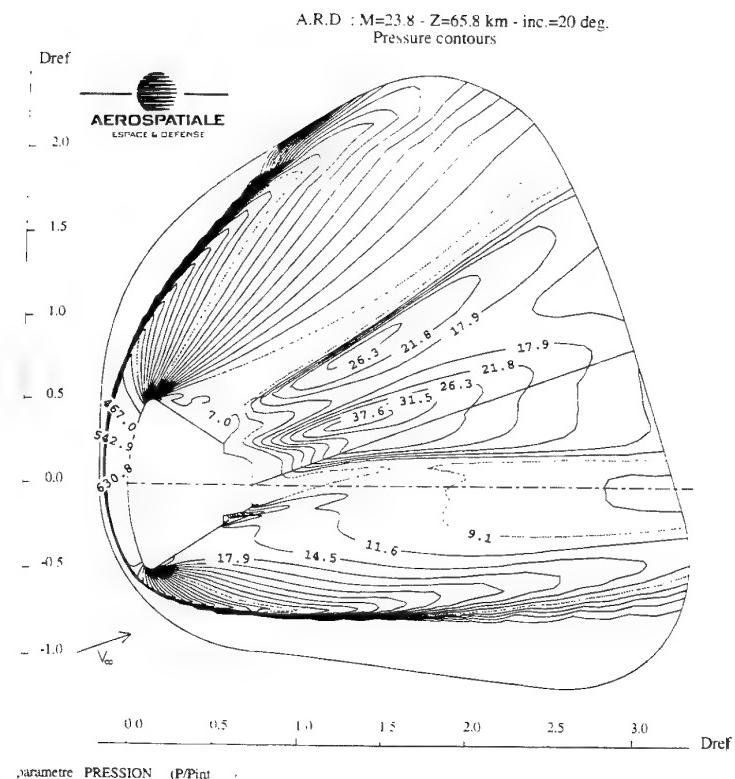
Figure 28: ARD G contours at mach 23
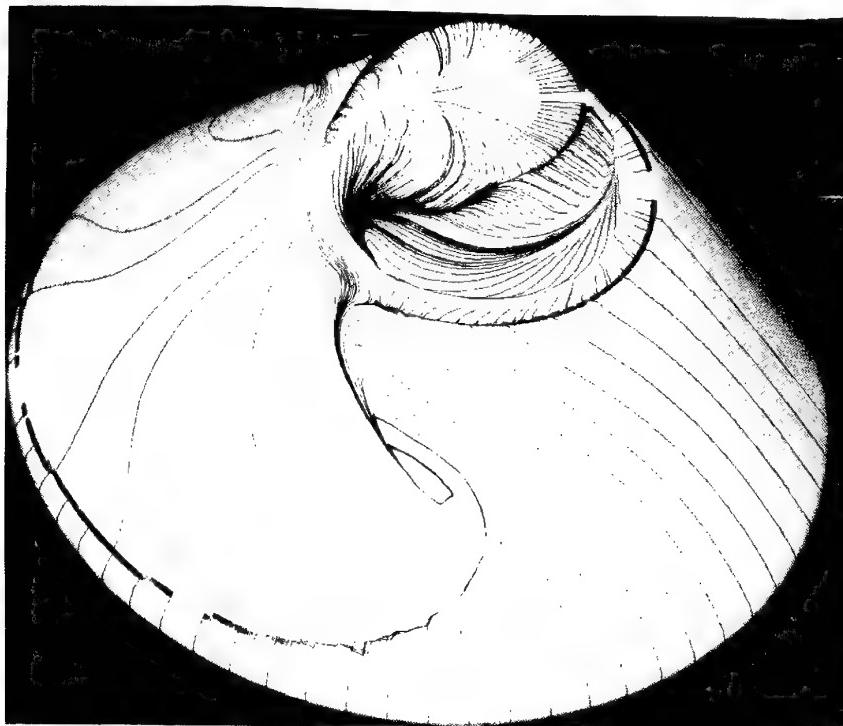
Figure 27: ARD wall streamlines.

Gas Surface Interaction Experiment

Spin stabilized 1 rev/min
Altitude h = 160 -130 km
Free molecular flow

Rarefied Flow Experiment

Stabilization with flaps
Altitude from 120 - 100 km
Knudsennumber Kn = 5 - 0.5
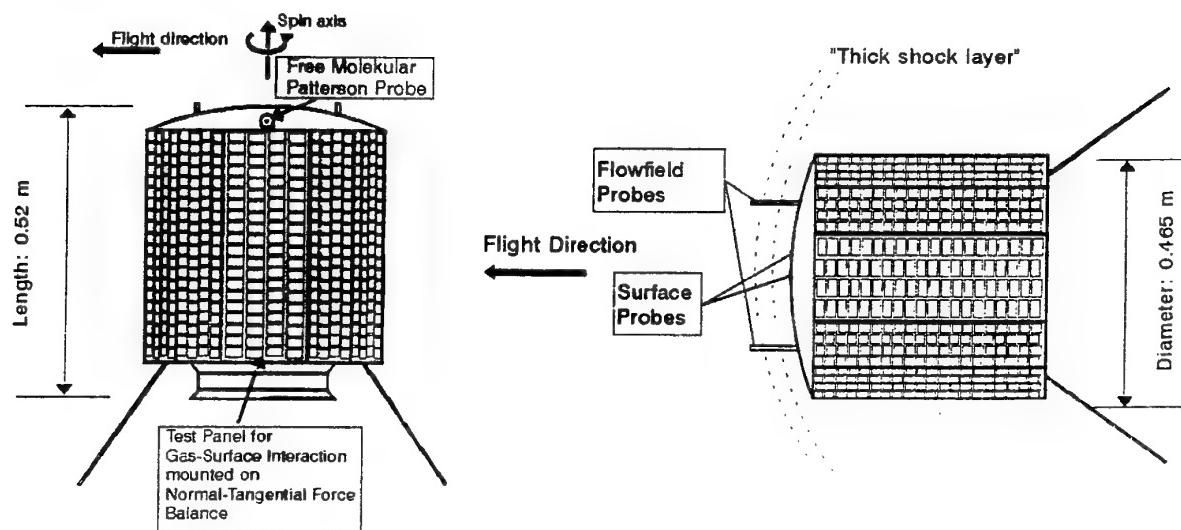
Figure 29: BREM-SAT dimensions, flight conditions, experiments and equipment.
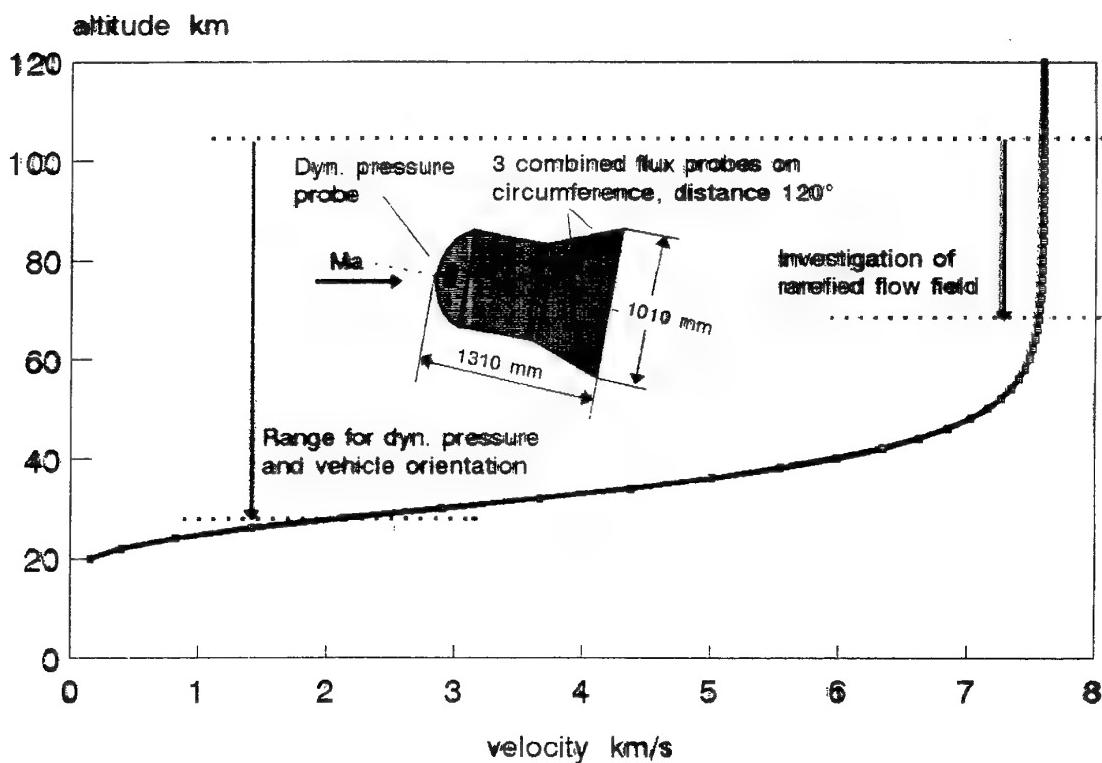
Figure 30: Entry trajectory of EXPRESS- SALYUT-Capsule and objectives.

The German Re-Entry Capsule MIRKA.
MIRKA = Mikro Rückkehr-Kapsel.

Geometry: Sphere with D = 1m

Surface: C-SiC (nonablativ)

Stabilization during reentry: C-G-offset

Task of Mission: Test of new nonablative heat shield structure.

Launch and orbital data:
Piggyback with Russian Photon in 1996
Orbit: 400/250 km
Orbital phase: 14-16 days.
Ballistic cofficient: B = 200 kg/m^2

Experiments during reentry:
Airdata system (HTG)
Surface pressures and heatflux (HTG)
Accelerometers (KT)
Temperature distribution in heat shield (Dornier, TU-Stuttgart)
Pyrometer (TU Stutgart)

Capsule-Team:
DASA-Jena Optronic, DASA-Dornier

	Measurement
Pilot probe	dynamic pressure
1,2,3 combined probes	particle flux heat flux pressure 1+2+3 also freestream incidence

Figure 31: The MIRKA capsule project.
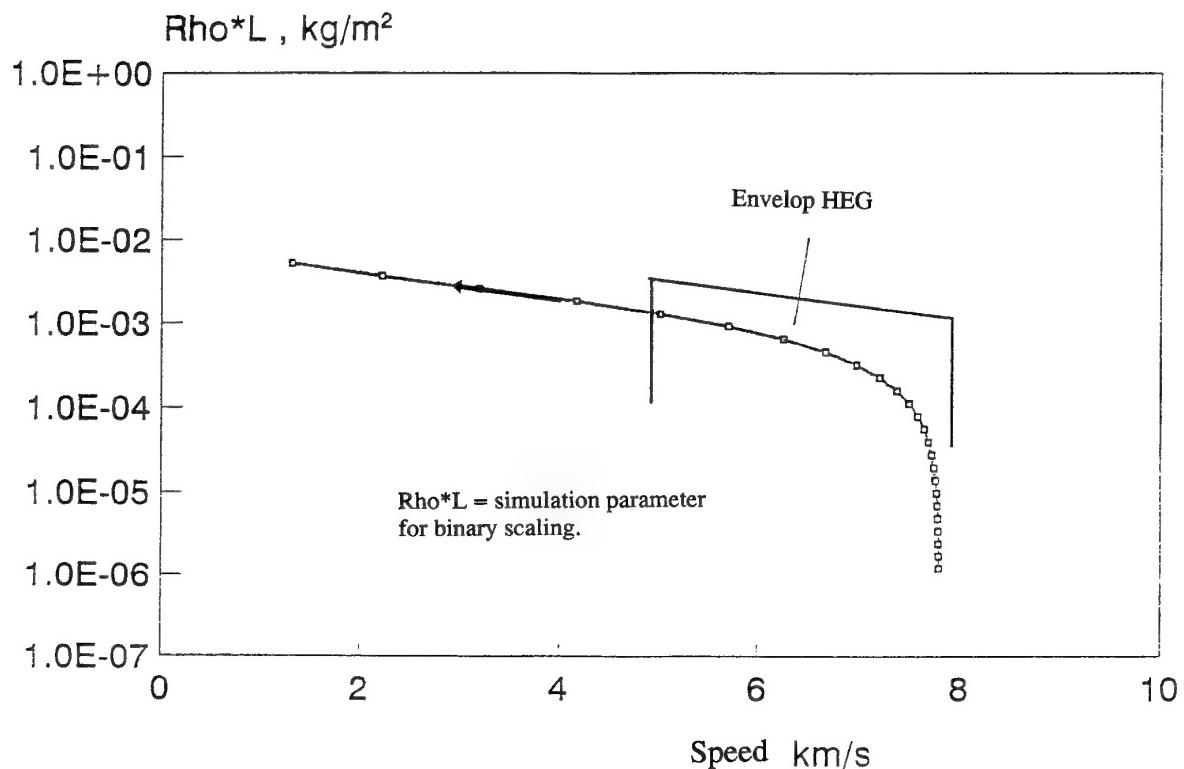
Figure 32: MIRKA re-entry comparison with HEG performance
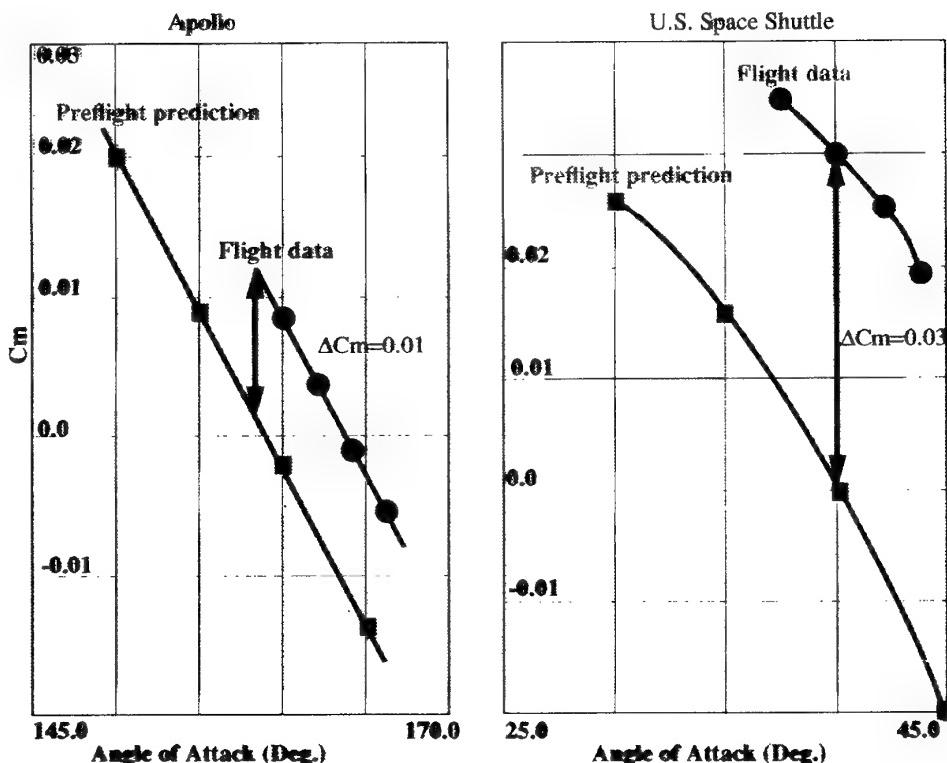
Figure 33: Apollo command module trim Cm Error and comparison with Space Shuttle

Apollo Command Module Aerodynamics

- Hassan et al. simulated the Apollo Command Module at flight
  (8.1 km/s) and wind tunnel conditions

    o 5-species air model, latest thermo-chemical models

	5-species Air	Flight Data	Perfect Gas	Tunnel Data
α (deg)	17.5	17.5	21.0	21.0
C_L	-0.354	-0.33	-0.387	-0.406
C_D	1.397	1.26	1.272	1.27
L/D	-0.253	-0.265	-0.304	-0.32
$C_{M_{cg}}$	-0.001	0.0	-0.012	0.0

- Shows that the trim angle shift is due to chemical reactions

Figure 34: Apollo command module simu lation at flight and windtunnel conditions

PLANETARY ATMOSPHERES, BASIC THERMODYNAMICS AND REGIMES

Arthur Smith
Fluid Gravity Engineering Ltd
Chiltlee Manor
Liphook, Hampshire
GU307AZ, UK

SUMMARY

In Sessions 2 to 4 we shall revue some of the basic phenomena relevant to capsule aerothermodynamics prior to the more detailed Sessions later in the course. Much of the material in these first Sessions is undergraduate material and refers to simple methods in order to introduce the student to the subject with the emphasis on understanding the phenomena rather than a briefing on state of the art techniques. However understanding aerothermodynamics requires understanding of basic mathematics, physics and chemistry which is assumed for this course.

A short list of references is given to each section which has deliberately been kept small such that the student should aim to read all of these in detail. Some of the classic works have been included which although early give good detailed explanations of the subject phenomena.

Session 2 Begins with the atmosphere structure followed by some basic thermodynamics used in aerothermodynamics, and ends with a revue of the classical aerodynamic and aerothermal regimes encountered by a capsule during entry.

2.1 ATMOSPHERE MODELS

Prior to any mission involving an entry into the atmosphere sufficient detail must be known or estimated in order to construct an engineering model of the atmosphere. The model must take account of the extremes of conditions likely to be encountered since this will effect the entry vehicle performance considerably. Even the atmosphere of Earth has large variability and many unknowns particularly in the upper atmosphere. The derivation of a model atmosphere is the first step leading to the engineering models which contain the extreme variability.

2.1.1 Exponential Model Derivation

Using the buoyancy equation

$$dp/dh = -\rho g$$

and the perfect gas equation of state ($p = nkT$) an integration can be performed to determine the atmospheric profile. Most often the temperature varies with altitude and so does the molecular weight and thus a numerical integration is required. The basic variation in the atmosphere is thus derived as:

$$dp/p = -mg/(kT) \, dh$$

The quantity kT/mg (= RT/g) known as the scale height (H) of the atmosphere is therefore a particular characteristic of each planetary atmosphere and therefore:

$$dH/H = dT/T - dg/g$$

When the molecular weight varies as in the upper atmosphere due photo-chemistry effects and lower mixing, the relationship becomes:

$$dH/H = dT/T - dg/g - dm/m$$

Defining the gradient in the scale height

$$B = dH/dh$$

gives the general equation the density in the atmosphere:

$$(d\rho \, g)/(\rho g) = (1+B)/B \, dH/H$$

This equation can only be applied up to a certain limit after which the effect of centrifugal force must be considered due to rotation of the atmosphere and for the light elements such as helium and hydrogen account must be taken of their escape from the atmosphere at the collisionless limit (the exosphere). This extension will not concern us at the present time but is an important consideration for vehicles in low orbits.

Some simple approximations can be made for the comparisons of the planetary atmospheres and the derivation of engineering models of the atmospheres for initial planetary entry analysis. Assuming constant scale height (i.e. constant temperature and constant composition) then the well known barometric height relationship is found:

$$\rho = \rho_0 \, exp(-h/H)$$

Thus the scale height is a measure of the interval in which the density reduces by a factor of e

Accounting for the gravity field then

$$\rho = \rho_0 \, exp\{-r_p h/(H_o(r_p+h))\}$$

Instead of assuming an isothermal atmosphere, with varying gravity we may assume a convective adiabatic atmosphere as occurs at low levels then

$$(\partial T/\partial h)_{ad} = \Gamma = -g/C_p$$

and the scale height becomes:

$$H= RT/(g+R\Gamma)$$

where the temperature drops linearly with altitude and Γ is the dry adiabatic lapse rate.

These models are used in differing layers of the atmosphere to build up complete model atmospheres.

The altitude bands for all atmospheres are typically divided into several bands as for Earth as follows:

• The troposphere exists from ground level where the surface is heated by radiation and decreases with altitude until the tropopause where the temperature reaches a minimum. In the troposphere the temperature exhibits an almost constant lapse rate with altitude and is in convective adiabatic equilibrium.

• Above the tropopause conductive equilibrium occurs and the temperature is nearly constant (isothermal). This is the stratosphere but a very gradual increase in temperature occurs until the stratopause. This temperature increase is associated with solar ultraviolet absorption.

• The third layer is the mesosphere and the temperature gradually falls from the stratopause to the mesopause. Up to the mesopause the atmospheric composition is constant.. This band comprises much of the atmosphere used for capsule entry into the Earth's atmosphere (about 50 to 85km).

• The fourth layer is the thermosphere where the temperature increases with altitude. This is caused by Solar heating causing dissociation and ionisation. and a change in composition. Mixing occurs by diffusion. The thermosphere extends to the exosphere which is the collisionless limit.

Several more regions, the ionosphere and magnetosphere, may be defined but are not of primary interest for entry aerothermodynamics.

For an engineering model the second and third layers are often considered as one nearly isothermal layer.

These bands can be clearly seen in figure 2.1 showing the Earth US1976 standard atmosphere also with temperatures in the Titan (Hunten-Lelouche 1988) Venus (Sieff) and Mars (Sieff) atmospheres. The latter two benefiting from the results of atmosphere probe measurements. Note the data are normalised by the scale height in the stratosphere H_s

In general it is necessary to have knowledge of the planetary constants of radius and mass and rotational period as well as the total mass of the atmosphere (or the conditions at any particular altitude) the atmospheric composition and Solar flux. These values are determined

by astronomical observations in the first instance and are later supplemented by observation spacecraft.
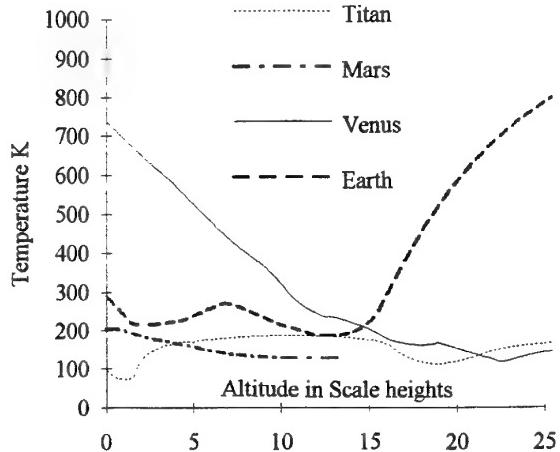
Figure 2.1 Atmosphere Temperature Profiles

2.1.2 Variability

It is interesting to compare and contrast the atmospheres of Venus, Earth, Mars and Titan. Figure 2.2 shows the density of the nominal atmospheres again normalised by the scale height in the stratosphere. Note the similarity in the slopes.
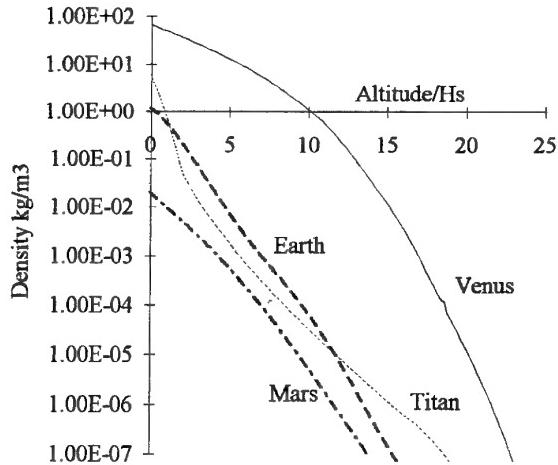
Figure 2.2 Atmosphere Density

Variations in mean density for the atmospheres of Titan and Mars are shown in figure 2.3. Whilst the variability in the density about the mean are shown for Earth in figure 2.4. (re-drawn from the 1966 US atmosphere supplements).

In general the variations in density are quite high, say plus or minus 20% of the seasonal mean for a known atmosphere, and an order of magnitude for the best estimates of unexplored atmospheres. It is clear that for capsule aerothermodynamic design the limits of atmospheric variation must be taken into account.
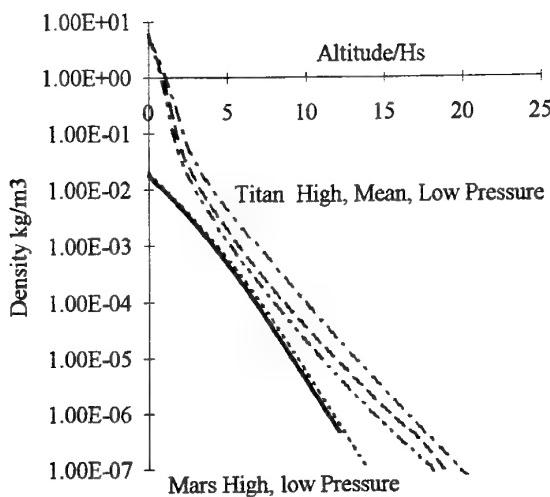
Figure 2.3 Extreme Mean Density Profiles

Figure 2.4 Variation about the mean seasonal density for Earth. (95% range)

2.1.3 Atmospheric Constituents

There are at least eight bodies in our Solar system with atmospheres thick enough to use for aerodynamic deceleration of a capsule. These are shown in table 2.1 with approximate constituents. The constituents of Earth, Mars and Venus are well established from atmosphere probe missions, however there remain quite large uncertainties in the models for the other planets. Estimates of the uncertainty are important criteria for aerothermodynamic design since the chemistry and consequent radiative and convective heat fluxes will change with different atmospheric constituents as will be seen later in the course. The estimation of constituents is made from remote spectroscopic measurements and from geological time-scale modelling.

| Planet/ moon	Mass (Earth = 1)	diameter km	Surface gravity (Earth =1)	Surface Pressure Atm	Scale Height H_s km	Approximate Nominal Atmosphere
Venus	0.815	12104	0.9	95.0	5.3	96% CO2 4% N2
Earth	1.0	12756	1.0	1.0	7.1	78%N2 21%O2 1% Ar
Mars	0.11	6786	0.38	0.0078	7.6	97% CO2 3% N2
Jupiter	317.8	142800				11%He 89% H2
Saturn	95.2	120000				80%He 20%H2
Titan	0.023	5150	0.138	0.0015	38	87%N2 3%CH4 10%Ar
Uranus	14.6	50800				15%He 85%H2
Neptune	17.2	48600				19%He 81%H24

Table 2.1 Some Characteristics of Solar System Bodies with Atmospheres

2.2 BASIC THERMODYNAMICS

During atmospheric entry the passage of the very high kinetic energy freestream gases through the normal and oblique portions of the strong body shock creates very high temperatures in the shock layer between the bow shock and the body particularly close to the stagnation point. Beyond the stagnation region the shock layer gases are cooled by expansion processes.

These elevated temperatures can result in chemical reaction between the various species in the shock layer as well as ionisation and dissociation of polyatomic species.

In its simplest form a shock wave can be considered as a moving, stable front in a fluid, across which the fluid properties (pressure, temperature, density, etc.) change discontinuously. In the frame of the shock, gas flowing through it will experience a rise in pressure and temperature and so its equilibrium properties will change. The gas will attain this new equilibrium by energy

exchange through intermolecular collisions. These require a finite time to occur and in this time the fluid has moved a certain distance downstream of the shock. Hence there will be non-equilibrium region immediately behind the shock front.

It is clear that to understand the processes which occur behind the shock and in the shock layer around an entry capsule that some knowledge of the way atoms and molecules interact and how energy is transferred. It is not possible to proceed very far without introducing the Boltzmann equation:

$$N^*_j = N \, Q^{-1} \, g_j \, exp(-\varepsilon_j/kT)$$

where k is the Boltzmann constant and Q is the partition function :

$$Q = \Sigma_j g_j \, exp(-\varepsilon_j/kT)$$

For atoms or molecules of a given species, quantum mechanics says that a set of well defined energy levels ε_j exists, over which the molecules or atoms can be distributed at any given instant, and that each energy level has a certain number of degenerate states g_j. For a system of N molecules or atoms at a given temperature and density there are N^*_j atoms or molecules in each energy level ε_j when the system is in equilibrium.

The total internal energy is the sum of all the states i.e.

$$E = \Sigma_j \varepsilon_j N^*_j$$

2.2.1 Monatomic gas

Energy is exchanged via translational modes and usually only one or two collisions are needed to raise a molecule to its final state. Typical collision frequencies are about 5 x 10^9 collisions per second and so the shock front is established in 10^{-9} seconds over a distance of a few mean-free paths.

It is possible for strong shocks to produce ionisation of the gas. However, the approach to ionisation is a slow process and takes place over a measurable length scale. The principal processes in the growth of ionisation are (a) atom-atom collisions, (b) photoionisation and (c) atom-electron collisions. Initially (a) and (b) (together with impurity effects) are responsible for the production of electrons. Once these electrons have been produced, further production depends on process (c) whilst the electron gas gains energy via elastic collisions with atoms and ions. Because of the relatively high ionisation potential of the atoms (usually > 10 eV) only singly ionised species are important. Electron - ion collisions are relatively inefficient due to the mass ratio and so the growth of the electron temperature towards the gas (or ion) temperature is slow. Hence there will be a separate electron temperature T_e and a heavy particle atom temperature T. The radiation from the electron gas (free-free and free-bound transitions) might then be important in its interaction with the Thermal Protection System (TPS). Radiation mechanisms are described later.

2.2.2 Polyatomic gas

The situation for a polyatomic gas is more complicated. As well as reaching equilibrium in its translational modes, any polyatomic gas must satisfy the same requirements for its rotational, vibrational and dissociation energies. These processes reach equilibrium more slowly than the translational energy; which can then absorb some of their energy and exceed its equilibrium state before relaxing to its own final value as the slower modes build up.

The efficiency of collisions in exciting a given internal degree of freedom depends upon $e^{-\chi}$ where $\chi = \tau_c /\tau_0$, the ratio of the collision period to the natural period of the degree of freedom. When $\chi <\cong 1$ then the collision period is short compared to the mode period, the probability of energy transfer is high and very few collisions are required to establish equilibrium. In effect the thermal energy is comparable to the mode energy and so a large proportion of molecules can be raised to this new equilibrium. When $\chi >> 1$ a large number of collisions are required for equilibrium since the intermolecular force acting on the mode oscillation changes very slowly and the process is adiabatic in the quantum mechanical sense i.e. it will change states without making any transitions.

The collision period is usually defined as s/v where s is the range over which the molecules may interact and v is the relative velocity of the colliding molecules. We can take a value for s which is about a Bohr radius (0.5 x 10^{-8} cm). For rotational modes, $\tau_0 \cong r/v_r$ where r is the distance of the atom from the centre of gravity of the molecule and v_r is the rotational velocity of the atom around the centre of gravity.

From the equipartition of energy we can take $v_r \cong v$, the translational velocity; r and s are of the same order. The natural period for rotation is $\tau_0 = r/v_r \cong s/v$ and so $\chi \cong 1$. Thus equilibrium between rotation and translation is established after a few collisions. Put another way, the rotational mode spacing for polyatomic molecules is usually small and so the rotational modes are fully excited at moderate temperatures and are able to contribute fully to the specific heats etc. So we can safely assume for a dense gas (many collisions) that $T_r = T$, where T_r is the rotational temperature.. In a rarefied gas this assumption can no longer be made.

For vibrational modes, the natural period is $\tau_0 \cong 1/v$ where v is the vibrational frequency. This is usually rather high and so $\chi >> 1$. In other words, the vibrational modes will only start to contribute at high temperatures i.e. when $kT \cong hv$. From the collision viewpoint, for vibration

$$2\pi\chi \cong 2\pi v \frac{s}{v} = 2\pi v\sigma \left(\frac{M}{2kT}\right)^{\frac{1}{2}}$$

$$= \left(\frac{hv}{2kT}\right)^{\frac{1}{2}} s \left(\frac{4\pi^2 M v}{h}\right)^{\frac{1}{2}}$$

From quantum mechanics we see that the term $(h/4\pi^2 Mv)^{1/2}$ is the amplitude of the molecular vibration in the lowest quantum state e.g. for N_2 this is 3×10^{-10} cm which is very much less than the range s of the interaction forces. It is evident that unless $kT \cong hv$, then $\chi \gg 1$. So a large number of collisions is needed to establish equilibrium and if the state of the gas is changing on a time-scale shorter than that needed for these collisions to take place then the vibrational modes do not contribute to the specific heat etc.

We therefore need to know not only when the vibrational modes will be excited but also on what time-scale these effects are important. Vibrational relaxation times, τ_v depend on temperature and pressure; they are usually described by the Landau-Teller approximation for harmonic oscillators valid to about 5000K:

$$\tau_v = K_1 T^{5/6} \exp\{[K_2/T]^{1/3} /[p(1-\exp(T_v/T))]\}$$

where K_1 and K_2 are constants of the molecule and T_v is the vibrational temperature.

For slow relaxation, the vibrational energy (e_v) equations, for each species, must be added to the gas-phase energy equation. To first order, the relaxation process is linearly dependent on the degree of non-equilibrium:

$$de_v/dt = (e_v(T) - e_v)/\tau_v$$

where $e_v(T)$ is the energy in vibration when the gas is in equilibrium with external temperature T and τ_v is the relaxation time. This is the vibrational rate equation.

At high temperatures this formulation may not be accurate since very energetic collisions may raise the vibrational energy by more than just the single vibrational level assumed in the theory. We then have to consider coupling between vibrational levels and possibly vibrational/radiation coupling.

As with the Arrhenius equation empirical rate data are required to solve the vibrational rate equation and this presents even greater problems concerning uncertainties in these data. Generally a large scatter is found in the data and typical temperature ranges cover 800-6000K which falls short of the expected shock layer temperatures in non-equilibrium conditions. A further problem in the use of the data is that values will vary with the collision partner and data derived from one system will not be applicable to another. This type of expression is only applicable to diatomic harmonic oscillators and only takes account of T-V energy transfer processes. However the largest mole fraction in the Earth and Titan atmosphere by far is Nitrogen, for Mars and Venus however the triatomic carbon dioxide presents a problem, however as a first approximation a similar expression can be used.

It is possible to show that the relaxation time for most diatomic gases is of the form :

$$\tau_v = 1/p \; C_1 \exp (C_2/T)^{1/3}$$

where C_1 and C_2 are constants and p is the pressure.

C_1 and C_2 depend on the particular collision partners and most often the Millikan and White correlation form is used to determine these although other models exits (for example Blackman, Wood and Springfield).

$$C_1 = 0.0016 \; m^{-1/2} \; \theta^{4/3}$$

$$C_2 = \exp(-0.015 C_1 m^{-1/4} -18.42)$$

where m is the reduced molecular weight and θ is the natural vibrational temperature.

These correlations are valid to about 5000 to 8000K above which they predict relaxation times less than the collision time and therefore they must be 'collision limited' or 'diffusion limited' for engineering solutions and this is achieved by adding the collision time from kinetic theory to the relaxation time.

2.2.3 Thermodynamic data

For a perfect gas it is necessary to know the variation of specific heat with temperature, since rotational vibrational and electronic excitation all increase the specific heat. In aerothermodynamics the total specific heat data for each species is most often curve fitted with a polynomial, and it is dangerous to extrapolate from such data, therefore the range of data should cover the range of temperatures in the particular problem. 'Standard' data are available to about 6000K for combustion problems etc., but in aerothermodynamics we may require these data to 10000 or to 100000K depending on the entry velocity and atmosphere.

In principle, one can calculate the temperature dependence of the specific heat by using the techniques of statistical thermodynamics and quantum mechanics. From statistical thermodynamics, we can express the internal energy for a system of N molecules or atoms as:

$$E = NkT^2 \left(\frac{d \ln Q}{dT}\right)_v$$

where Q, the partition function, is written as:

$$Q = \sum_j g_j \exp(-\varepsilon_j / kT)$$

where g_j, ε_j are the degeneracy, total energy of level j and the summation is carried over all energy levels. We note that the energy is measured above the 'zero-point' energy; we mention this as it will be important in the later discussion.

We can express the internal energy as being a sum of the energies of all the possible modes of the system i.e.

$$\varepsilon = \varepsilon_{trans} + \varepsilon_{rot} + \varepsilon_{vib} + \varepsilon_{el}$$

which is the sum of the energies of the translational, rotational, vibrational and electronic modes.

To evaluate the specific heat (at constant volume, which is related to that at constant pressure) we need to calculate the partition function for the system. Since this involves the energy in an exponential form, then it can be calculated as the product of the individual partition functions for each mode of energy. This just involves putting in the correct expression for the mode energy into the equation for Q. One difficulty is that the electronic partition function, unlike the others, has no closed-form expression. However, the summation can be usually truncated after about three or four terms since higher energy levels are only excited at high temperatures (T > 15000K).

From quantum mechanics through the partition function the expressions for each of the energy terms become:

$$\varepsilon_{trans} = 3/2 \; RT$$

$$\varepsilon_{rot} = RT$$

$$\varepsilon_{vib} = (\; h\nu/kT \; /(exp(h\nu/kT) \; -1))RT$$

$$\varepsilon_{el} = \text{data obtained from spectroscopic measurements}$$

We can evaluate the other two thermodynamic properties (entropy and enthalpy) needed for the database from a knowledge of the partition functions and the equations of thermodynamics. However, we can not calculate the true absolute values of enthalpy because of the 'zero-point' energy. This is the energy that the system would possess if it were at 0 K. This cannot be experimentally measured nor calculated since the equations cannot be expressed in fundamental terms - for example, the 'zero-point' vibrational energy is $(1/2)h\nu$ and the vibrational frequency at 0 K cannot be theoretically determined. All is not lost, however, since we can determine the absolute enthalpy using the heat of formation of the system at 0 K; this will not be the same as the 'zero-point' energy but the fact is that one never needs to know the absolute value of enthalpy. In all problems we deal with changes in enthalpy, internal energy and entropy; the changes in these variables will be the same whether we use true 'zero-point' energies or "effective" energies (sometimes called 'chemical enthalpies).

In the absence of experimental data at the higher temperatures, one should be able to extend the database through such thermodynamic calculations. For some complicated species it might be necessary to resort to detailed quantum mechanical calculations to determine the molecular structure (and hence the energy levels).

It is instructive to plot the variation of Cp/R for typical monatomic diatomic and triatomic gases of interest.

Since we know that for a fully excited species from kinetic theory that the energy will be equipartitioned between available modes or degrees of freedom n.

Thus $C_p/R = 1 + n_T/2 + n_r + n_v/2 + h_e/R$

Where n is given in table 2.2. Note for example that CO2 is a linear molecule whereas H2O is non-linear.

Mode \ Species	n_T	n_r	n_v
Atomic	3	0	0
Diatomic	3	1	2
Linear triatomic	3	2	4
Non-linear triatomic	3	3	3

Table 2.2 Maximum Model Energy Contributions

Since rotational equilibrium occurs at low temperature we expect the C_P/R values at room temperature to reflect this, similarly vibrational excitation occurs at medium temperatures and electronic excitation at high temperatures.

Figure 2.5 shows the variation of C_P/R as a function of temperature. Note that for CO_2 one vibrational mode is excited at room temperature. It is seen that the quantum mechanics result for the vibrational energy approaches the kinetic theory limit at high temperature. The rise in electronic energy is just discernable for atomic Nitrogen.
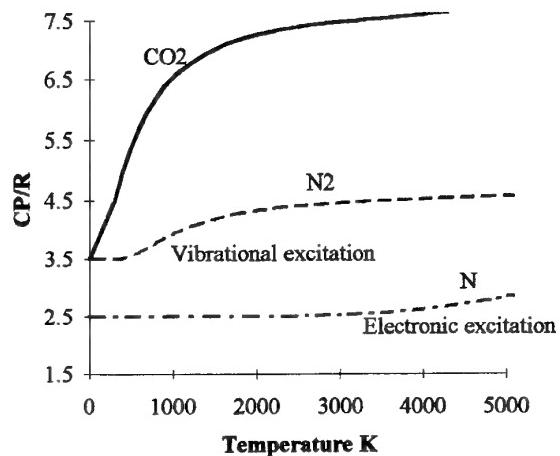
2.5 Specific Heat Variation with Temperature

This also illustrates why the ratio of specific heats for a gas varies with temperature (i.e. $\gamma = C_P/(C_P - R)$)

Partition of the total enthalpy or internal energy of a gas into its modal parts is necessary to compute the thermochemical state in a non-equilibrium flow. Figure 2.6 shows a typical partition between translational plus rotational energy and vibrational energy for a gas in thermal non-equilibrium. The temperature T_v is representative of the Boltzmann distribution of energy ε_v.

This is the basis for many of the simpler 'two temperature' non-equilibrium shock layer solutions.
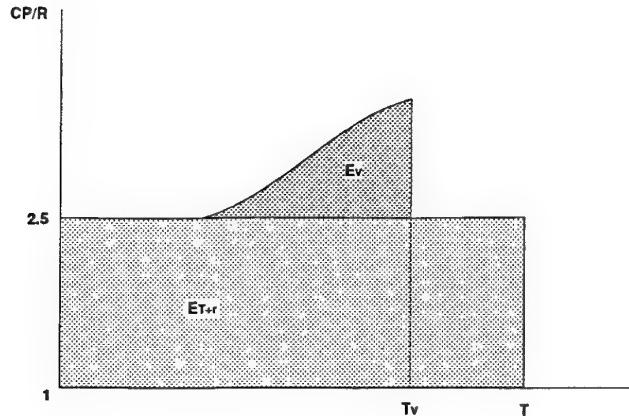

Figure 2.6 Example Energy Partitioning in Thermal Non-equilibrium

2.2.4 Transport Properties

When we speak of transport phenomena, we are referring to the physical processes of viscosity, thermal conduction and diffusion. The essence of these phenomena is the random motion of atoms and molecules. When a particle moves from one location in space to another, it carries with it a certain amount of momentum, energy and mass associated with itself. The transport of this particle momentum, energy and mass through space due to the random motion gives rise to the transport phenomena of viscosity, thermal conduction and diffusion, respectively. Such random motion also applies to electromagnetic radiation; photons, as they traverse a gas, can be repeatedly absorbed and re-emitted as they interact with the gas molecules and so arises the phenomenon of radiation transport. Diffusion is also important in the energy equation, especially for a chemically reacting mixture. We can see this by considering a chemical species, k, diffusing from location 1 to location 2. At the second location the species takes part in a chemical reaction, thus exchanging energy with the gas. That is, as species k diffuses through the gas, it carries with it the enthalpy of species k, and this is a form of energy transport. This is not an energy flux due to convection but arises because of the temperature and concentration gradients.

These phenomena are important since the random motions about an average flow spread gradients, mix materials at sharp interfaces, create motion in the fluid etc. So they are important in the macroscopic as well as microscopic sense.

We can derive the form of the transport coefficients relatively easily. If we consider some mean property, ϕ, carried by particles and that there exists a gradient in space of this property, then the flux of ϕ (in one dimension, for simplicity) is:

$$\Lambda \sim nu\lambda \, d\phi \, /dy$$

where n is the number density of particles, u is mean particle speed $(\sim T^{1/2})$ and λ is the mean-free path $\sim 1/(\sigma n)$ where σ is the collision cross-section). So to get the form of the viscosity, thermal conductivity and diffusion coefficients we substitute $\phi = mv$, kT and X (the mole fraction) to get (resp.):

$$\mu \sim T^{1/2}/\sigma$$

$$k \sim T^{1/2}/\sigma$$

$$D_{ab} \sim T^{1/2}/\sigma \; n \sim T^{1/3}/\sigma p$$

These expressions apply for a pure gas and the diffusion coefficient is that for a binary mixture. We see that the viscosity and thermal conductivity depend only on temperature whereas the diffusion also depends on the density of the gas. The above expressions are derived from a hard-sphere model of the gas in which the details of the intermolecular force field were ignored.

Accurate computation of the diffusive fluxes requires accurate knowledge of the transport coefficients. We replace the hard-sphere model with a picture of particles moving under the influence of an intermolecular force field which varies with the distance, r, from the molecule. One such common model is the Lennard-Jones potential (others are Morse etc. and they differ in their complexity and usage.), which gives the intermolecular force as:

$$F = - \frac{d\Phi_m}{dr}$$

where:

$$\Phi_m(r) = 4\varepsilon \{(d/r)^{12} - (d/r)^6\}$$

and where d is the characteristic molecular diameter and ε is a characteristic energy of interaction between the molecules. This potential is used to calculate the collision integrals which enter all the expressions for the transport coefficients.

For pure species the expressions are relatively simple. For example, viscosity is given by:

$$\mu_k = \frac{5}{16} \frac{\sqrt{\pi m_k kT}}{\pi \sigma_k^2 \Omega_\mu}$$

where σ_k is the Lennard-Jones collision diameter and Ω_μ is the collision integral, which gives the variation of the effective collision diameter as a function of relative energy between molecular collisions. The collision integral depends on the reduced temperature, given by:

$$T_k^* = \frac{kT}{\varepsilon_k}$$

and on the reduced dipole moment, given by:

$$\delta_k^* = \frac{1}{2} \frac{\mu_k^2}{\varepsilon_k \sigma_k^3}$$

In the above expressions, ε_k is the Lennard-Jones potential well depth and μ_k is the dipole moment.

The single component thermal conductivity consists of two parts which arise from molecular collisions and diffusion of the reacting species. The molecular collision terms are treated by considering the separate contribution of all the energy modes that a polyatomic gas may have:

$$k_k = \frac{\mu_k}{W_k} (f_{trans} c_{v,trans} + f_{rot} c_{v,rot} + f_{vib} c_{v,vib} + f_{el} c_{v,el})$$

The binary diffusion coefficients are given in terms of pressure and temperature as:

$$D_{jk} = \frac{3}{16} \frac{\sqrt{2\pi(kT)^3/m_{jk}}}{P\pi\sigma_{jk}^2\Omega_d}$$

where m_{jk} is the reduced molecular mass for the (j, k) species pair and σ_{jk} is the reduced collision diameter. The collision integral Ω_d depends on the reduced temperature which in turn may depend on the species dipole moments and polarizabilities.

Transport Coefficients of Mixtures

One problem is to determine diffusion velocities. Various forms for the diffusion velocity exist. In the case of a chemically reacting mixture, which is a multi-component gas, one can invert the matrix equation

$$G_k = \sum_j \frac{n_j n_k}{N^2 D_{jk}} (v_{dj} - v_{dk})$$

where the source terms, G_k are defined as:

$$G_k =$$
$$grad\left(\frac{n_k}{N}\right) - \left(\frac{\rho_k}{\rho} - \frac{n_k}{N} \frac{grad\ P}{P}\right) - K_k^T \frac{grad\ T}{T}$$

$$= d_k - q_k$$

Physically, this states that concentration gradients can be supported by diffusion velocities, pressure gradients and thermal diffusion effects. However, the matrix algebra involved makes this an expensive operation. A more approximate and simpler approach is the mixture-averaged formulation. In this case the diffusion velocities are related to the species gradients by a Fickian formula:

$$v_{dk} = - \frac{1}{X_k} D_{km} d_k$$

The mixture diffusion coefficient for species i is computed as

$$D_{km} = \frac{1 - X_k}{\sum_j X_j / D_{jk}}$$

where X_k is the mass fraction of species k and D_{jk} is the binary diffusion coefficient. The mixture-averaged thermal conductivity coefficient can be formulated from the single component expression in a similar fashion.

Care must be taken in using the mixture-averaged coefficients. Unlike the multicomponent expressions, the mixture formulae are approximations and are not constrained to require that the net species diffusion flux be zero i.e. the condition

$$\sum_{k=1}^{K} V_k Y_k = 0$$

is not satisfied. This will lead to some non-conservation in the solution of a system of species conservation equations and corrective action will need to be taken.

Another note of caution is that one must be aware that the calculation of the transport coefficients depends critically on the assumption used for the intermolecular force potential (from which we get the collision integrals), which at times can be uncertain or inappropriate. For example, the Lennard-Jones potential is suitable for non-polar molecules; although it can be used to approximate polar molecules over a limited range this is not the case in general. Experimental measurements are also uncertain and difficult to make, especially at high temperature.

In general the assumption of simple mixture laws and binary diffusion coefficients are adequate for most shock layer applications where the species weights to not vary greatly. For example the ratio of masses between carbon and carbon dioxide is about 3.7 and is the maximum for Earth and Mars. Introducing hydrogen increases the ratio to between 12 and 44. Hydrogen occurs in many of the planetary atmospheres and in ablation products.

2.3 CHEMICAL REACTIONS AND RATES

We have discussed the effects of a shock propagating in a gas, namely, ionisation and rotational and vibrational relaxation. In addition to these, as the fluid is heated and compressed on passing through the shock, conditions will be reached whereby chemical reactions will take place. These are of the utmost importance since they can alter the flowfield locally through the production of energy, chemical species etc. and also affect the TPS through radiation, species from the shock layer reactions reaching the TPS and producing further reactions near or with the surface etc. Transport coefficients are therefore also be important as the gas reacts chemically and is ionised.

An important parameter in analysing chemical reactions in a flowing gas is the Damkohler number, Da. This is the ratio of the hydrodynamic time-scale to the characteristic time for chemical reaction. When $Da << 1$, then any chemical reactions take place so slowly compared to the fluid velocity that they do not influence the flowfield and so can be ignored; this is the case of 'frozen' chemistry. At the other extreme $Da >> 1$, and chemical reactions have reached their final state before the fluid has had time to respond; this is the case of 'equilibrium' chemistry, where the forward and backward rates balance each other. In between these two extremes, we have non-equilibrium (finite-rate) chemical kinetics. To analyse the finite rate chemistry processes in gas mixtures it is necessary to know the reaction mechanisms, the rate constants and the appropriate equations. We consider I elementary reversible (or irreversible) reactions involving K chemical species. These can be represented in the general form:

$$\sum_{k=1}^{K} v'_{ki} \chi_{ki} \; \overset{\rightarrow}{\underset{\leftarrow}{}} \; \sum_{k=1}^{K} v''_{ki} \chi_{ki}$$

where v_{ki} are the stoichiometric coefficients and χ_k are the chemical species. The species conservation equations are written as:

$$dn_k/dt = Q_k - n_k L_k$$

where Q_k is the chemical creation rate, L_k is the chemical destruction rate and n_k is the number density of species k.

Often, one does not require knowledge of the individual chemical creation and destruction rates; in such cases these can be substituted by one variable $\dot{\omega}_k$ which now represents the chemical production rate of species k. This can be expressed as:

$$\dot{\omega}_k = \sum_{i=1}^{I} v_{ki} q_i$$

where:

$$v_{ki} = (v''_{ki} - v'_{ki})$$

For frozen chemistry, we have $dn_k = 0$, whilst for equilibrium chemistry, $\dot{\omega}_k = 0$. The rate of progress variable, q_i, for the ith reaction is given by the difference of the forward rates minus the reverse rates:

$$q_i = k_{fi} \prod_{k=1}^{K} [X_k]^{v'_{ki}} - k_{ri} \prod_{k=1}^{K} [X_k]^{v''_{ki}}$$

where $[X_k]$ is the molar concentration of the kth species and k_{fi}, k_{ri} are the forward and reverse rate constants of the ith reaction. It is assumed that the forward rate constants for the I reactions have the following Arrhenius temperature dependence:

$$k_{fi} = A_i T^{\beta i} e^{-E_i/RT}$$

where the pre-exponential factor A_i, the temperature exponent β_i and the activation energy E_i usually come from experiment.

The reverse rate constants are related to the forward rate constants through the equilibrium constants:

$$k_{ri} = \frac{k_{fi}}{K_{ci}}$$

where K_{ci} is the equilibrium constant, which is written as:

$$K_{ci} = \left(\frac{P_{atm}}{RT}\right)^{\sum v_{ki}} exp\left(\frac{\Delta S_i^0}{R} - \frac{\Delta H_i^0}{RT}\right)$$

where ΔS_i^0 and ΔH_i^0 are the changes in entropy and enthalpy due to chemical reaction.

We see that a precise knowledge of reaction rates, which in turn depend on the equilibrium constants, is required to be able to accurately model chemical reactions. The equilibrium constants can be calculated from thermodynamical considerations and so one need only determine the forward reaction rates experimentally. These rates are known for many basic chemical reactions but often they have only been measured up to temperatures of about 6000K. One has to be cautious when extrapolating the Arrhenius equation to higher temperatures since it depends to an extent on the temperature range. That is to say that a particular reaction will have a different reaction path at high temperatures than at low temperatures (e.g. it might form a different activated complex in each case). In addition, a process which might be very well represented at low temperatures by one set of reactions will not be well described at high temperatures by the same set. A different set of reactions will be needed at higher temperatures and these will in general have a different reaction rate. So it is important not only to know the reaction rates at high temperature but to determine which mechanisms are important in different temperature ranges. Figure 2.7, 2.8 and 2.9 show different reaction rates for the dissociation of N_2 O_2 and CO_2. Therefore it is necessary to be extremely careful to select compatible data for the problem at hand, and to understand the effect of data variability on the flowfield.

There are two classes of reaction for which the Arrhenius formulation does not hold. The first is reactions involving low-activation-energy free radicals. Here, the temperature dependence of the pre-exponential term is very important and is not described well by the simple Arrhenius form. The second class is radical recombination, where a third body is required to remove excess energy upon formation of the product. So these third-body recombination

reactions depend heavily on the pressure and again the Arrhenius form is not really suitable. However, sometimes it is possible to attach an enhanced reaction efficiency to these third bodies that takes this into account.
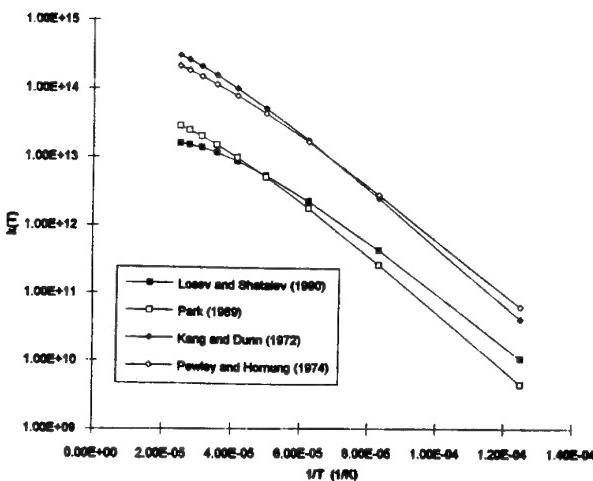

Figure 2.7 N_2 Dissociation Rates with Atoms
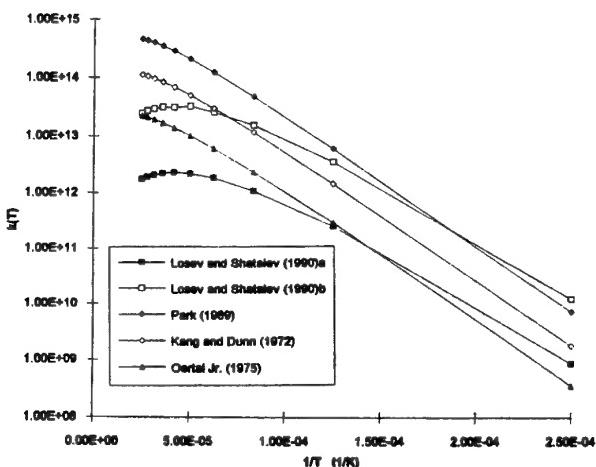
Figure 2.8 O_2 Dissociation Rates with Atoms
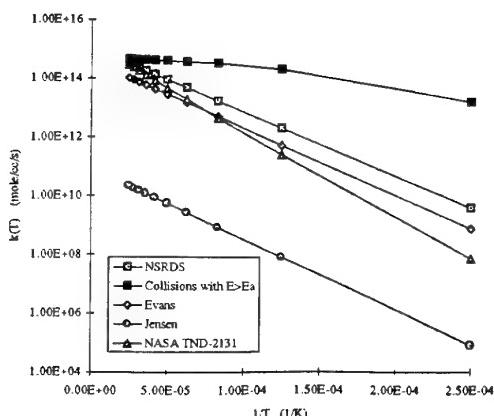
Figure 2.9 CO_2 Dissociation Rates with Diatomics

2.4 VIBRATION -DISSOCIATION COUPLING

The interaction between chemical and thermal rate processes is complicated by the rates of chemical reactions often being strongly dependent on the state of internal excitation as well as the translational energy of the reacting molecules. Therefore, under certain circumstances rates of reactions can be dependent upon the rates of energy transfer between the various energy modes. Under these conditions reaction products, especially of exothermic processes, are formed in a highly non-equilibrium energy distribution thus affecting the reaction path.

Unlike other degrees of freedom, dissociation may become important at temperatures much lower than the characteristic temperature i.e. $kT \ll D$, the dissociation energy per molecule. This occurs because of the large possibility of dissociated states; there is a high probability of dissociation if the relative energy between two colliding molecules equals the dissociation energy. For example, if we consider oxygen and nitrogen, then $D/kT = 59000/T$ & $91600/T$ respectively. However, even at 3000K for oxygen and 5000K for nitrogen, the degree of dissociation is 1.4%, although in each case $D/kT \cong 20$ and the fraction of sufficiently energetic collisions is of the order of 10^{-9}. Dissociation is tied up with vibrational relaxation through the possibility of energy in these modes being made available for dissociation; the rate for this process would then depend on the rate at which the vibrational levels are populated. If n is the number of additional degrees of freedom from which energy may be drawn, then the Boltzmann probability factor $exp(-D/kT)$ is increased by $(D/kT)^{n/2}/(n/2)$. So we see that the interplay between vibration (and rotation) and dissociation might be important, even at relatively low temperatures.

In a gas in thermal equilibrium the energy of reaction is released or taken from the total internal energy of the flow. In a gas which is not in thermal equilibrium, in which we are solving the thermal relaxation equation, the following questions arise,

• How are the chemical kinetics modified ?

• Where does the energy of reaction come from ?

The mechanisms used should satisfy these question simultaneously, i.e. the model should be consistent. Two basic mechanisms for dissociation can be defined:

• Non-preferential dissociation, where recombination occurs to all vibrational levels at the same rate, or in terms of dissociation, molecules can dissociate with equal probability regardless of their vibrational excitation level given a sufficiently energetic collision.

- Preferential dissociation, where recombination occurs preferentially to the upper vibrational levels, or in terms of dissociation, molecules with excited upper vibrational levels will dissociate with greater probability, given a sufficiently energetic collision.

An important result of preferential dissociation is the departure of the energy distribution from the Boltzmann distribution. A plot of the log of number density with energy should be a straight line for a Boltzmann distribution. However if we continually favour the higher levels, these will be relatively depleted in dissociation, and overpopulated in recombination and the number density-energy plot will not be straight. This has an important consequence for radiation.

Considering the vibrational energy drain in a dissociating gas it is clear that more vibrational energy is lost on average for the preferential model. Theoretical and experimental assessment of non-equilibrium flows have led to several models for vibration dissociation coupling.

From thermal relaxation only we have the Landau-Teller model:

$$de_v/dt = (e_v(T) - e_v)/\tau_v$$

Now we need to add the drain on the average vibrational energy due to dissociation. Therefore for a non preferential model this becomes:

$$de_v/dt = (e_v(T) - e_v)/\tau_v - e_v(dn_k/dt)$$

where the second term represents loss of the average vibrational energy of dissociating molecules since $(dn_k/dt) = Q_k - n_k L_k$ (the difference between the species creation rate and destruction rate as before). To be consistent then the temperature used in the Arrhenius equation should be weighted by the energy available in all modes. In situations where the free stream kinetic energy is much larger than the dissociation energy of the molecules then this temperature is heavily weighted towards the translational temperature T.

For a preferential model this second term is modified to account for the fact that proportionately more highly energetic molecules dissociate, and the rate controlling temperature is weighted accordingly.

$$de_v/dt = (e_v(T) - e_v)/\tau_v - E(dn_k/dt)$$

The remainder of the dissociation energy $(D-E)$ is taken from the translational + rotational energy in either case.

Treanor and Marrone
Treanor and Marrone proposed the following mechanism to account for the drain of vibrational energy by dissociation where $E(dn_k/dt)$ is partitioned into forward and backward components:

$$de_v/dt = (e_v(T) - e_v)/\tau_v$$
$$- (E(T,T_v) - e_v) Q_k$$
$$+ (E(T,T) - e_v) n_k L_k$$

where :

$E(T,T_v)$ is the vibrational energy lost by dissociation and $E(T,T)$ is the vibrational energy gained in a recombination.

The second accounts for the loss of average vibrational energy of dissociating species evaluated at the vibrational temperature, and the third adds vibrational energy for newly combined molecules at the heavy particle temperature.

The forward rate k_f is modified to become:

$$k_f = k_f*(Q_v^s(T)Q_v^s(T_F)/((Q_v^s(Tv)Q_v^s(-U))$$

where Q are the vibrational partition functions, k_f* the forward rate constant under thermal equilibrium. and :

$$1/T_F = 1/T_v - 1/T - 1/U'$$

and Marrone and Treanor found that $U' = -E_v/3k$ gave a good result for relaxation behind the shock..

This is quite a complex model. And forms the basis for many extensions and simplifications.

Park
Park has developed a simpler model taking advantage of later computations of population/depopulation rates.

Using a harmonic oscillator assumption, the average vibrational energy removed is shown to be :

$$E = D/2$$

where D is the average dissociation energy, and this is referred to as the CVDV model (coupled-vibration dissociation-vibration).

Since it is expected that the higher levels are densely populated, then in a non-preferential model in the anharmonic case then the range of the energy removal is expected to be:

$$0.5 < E/D < 1.0$$

However detailed solution of the Master equation which describes how number density of individual vibrational states change provides a lower value:

$$E/D = \sim 0.3$$

Since D is much greater than the average vibrational energy, even using 0.3 reduces the average vibrational energy by much more than the average vibrational energy and this is a preferential dissociation model.

In order to correct the reaction rate for non-equilibrium effects, the two temperature model of Park was deduced from experimental data the driving temperatures assuming a mechanism associates a mean temperature of the form:

$$T_m = T^{1-q}T_v^{\,q}$$

where the exponent q takes the value given in table 2.3.

Reaction type	q
Dissociation	0.5
Neutral Exchange	0
Associative ionisation	0
Charge exchange	0
Electron impact ionisation	1
Radiative re-combination	1
Reverse	0

Table 2.3 Typical Exponents in the Park Two Temperature Model.

Alternate values may be found in the literature. In particular for dissociation when $q = \sim 0.3$ the model becomes consistent with harmonic oscillator simulations of dissociation reactions when these are required to produce the same solution as the one temperature rate coefficient when $T = T_v$.

An explanation of the allocation of controlling temperatures can be made as follows:

- Dissociation. T represents the energy of the colliding partner and T_v the vibrational energy of the dissociating molecule. Thus the average vibrational energy of the dissociating species is taken into account.

- Exchange. The colliding partners have equal vibrational energy on average and so the controlling temperature is the heavy particle translational temperature.

- Associative Ionisation. The collision partners are atomic and so the controlling temperature is the heavy particle translational temperature.

- Electron Impact Ionisation. The impacting electron has average temperature equal to T_v equal to the electronic temperature in the two temperature model and so the controlling temperature is T_v

The empirical model of Park contains no direct coupling between the energy disposal and the correction of reaction rates and is thus technically an inconsistent model, although it is probably the widest used model at present.

Vibration-dissociation coupling is a current area of uncertainty and debate in aerothermodynamics and new consistent models and experiments will hopefully lead to progress in this field.

2.5 SHOCK LAYER RADIATION

The magnitude of the thermal radiation from the hot gases in the shock layer is affected by several parameters, primarily these relate to the geometry of the shock layer and the chemical and thermodynamic state of the shock layer. Surface characteristics such as emissivity, absorbtivity and the injection of ablation products (or transpiration gases) into the boundary layer are also important when considering the radiation to the vehicle surface.

For an optically thin gas then the thicker the shock layer the larger the volume of radiating gas, thus as the shock stand-off distance for a bluff body is directly proportional to the radius of curvature in the stagnation (subsonic) region the radiative flux becomes proportional to the radius of curvature of the body.

The more energetic the flow, then the higher the temperature in the shock layer. With increasing Mach number the gases are heated to an extent where dissociation of the molecules begins to occur, this process absorbs a considerable amount of energy, thus the average molecular weight is decreased, specific heats increased and the ratio of specific heats decreased. This results in a lower shock layer temperature and shock stand-off, and of course changes to the chemical composition, including ionisation of some species. It is clear then that the condition of the shock layer gases in terms of whether equilibrium has been achieved or not can greatly effect the radiation.

The thermal radiation is generated by emissions from each of the excited species in the shock layer. Thus at the body surface the heat flux is calculated by summing all the emission and absorption activity from the shock layer gases in view, and this may include absorption and re-emission activity in any ablation products, and indeed from the wall itself.

Some relevant mission examples are given below with TPS type since relatively cool TPS ablation products can cause radiative blockage by absorption and re-emission.

- High speed Earth return representative of a Mars, Lunar or cometary mission at 13 to 16km/s with a mix of equilibrium and non-equilibrium chemistry with carbon surface ablation and phenolic resin pyrolysis gas products injection into the boundary layer. Radiation is significant for these entries and can be equal to the convective flux. The Rosetta entry vehicle has been used as a technology demonstrator within ESA and will be used as an example later. Data are available from Apollo 4 and Fire 1&2 missions at 11km/s. Apollo had an ablative TPS with special provision for radiometry and calorimetry with radiative fluxes about 30% of the total. PAET and the recent UV precursor flights at between 3 and 5 km/s provide detailed radiometry for code phenomenology validation, for selected Earth atmosphere shock layer species

- Venus entry. The atmosphere of Venus is very similar in composition to Mars with a high proportion of carbon dioxide, but entry speeds are much higher at 11 to 12 km/s and the atmosphere is very dense. At this speed there is a considerable radiation from the shock layer and an ablative heatshield is

necessary. Carbon phenolic TPS has been used on Pioneer, but an alternative such as silica phenolic is attractive especially if its reflectivity is taken into account. Many Venera craft have successfully entered the Venus atmosphere.

- Jupiter entry at over 40km/s or Saturn/Uranus entry at 25-30 km/s. Much analysis has been carried out for the Jupiter Galileo mission with its carbon phenolic TPS, and if data is available after the entry, some post test analysis will undoubtedly be undertaken. The hydrogen/helium atmospheres and high ablation rates (30-50% of vehicle mass is TPS) provides challenging radiation dominated cases, of which only a Jupiter mission is underway at present.

- Titan Entry. Although at modest entry velocity of 6km/s, the Huygens probe will encounter a high radiative heat flux due to the unique atmosphere of Titan. The low proportion of methane in a thin nitrogen atmosphere produces a non-equilibrium radiation environment where radiative and convective fluxes are approximately equal. Current efforts of the project team to estimate this environment are of interest. The ablative TPS is low density quartz phenolic.

- Mars Entry. Currently radiative fluxes are considered negligible for direct Mars entry at about 6km/s. At higher entry velocities, i.e. should higher energy trajectories be used, radiation may become important. Nevertheless any Mars entry mission will need to confirm that the radiative environment is low, in particular with ablation products from low density ablators reacting with the atmosphere to enhance the number density of radiating species, or the effect of catalytic surfaces.

The importance of radiation has been illustrated above, but where does it come from? Some of the basic phenomena are summarised below.

2.5.1 Shock Layer Condition

At high entry velocities the temperatures behind the bow shock wave may reach very high values with the freestream chemical species becoming dissociated and in some cases highly ionised. The high shock layer temperatures lead to significant radiation from the hot shock layer gases. For the flowfields considered in entry problems the radiation is mainly due to electronic transitions and is thus in the visible or UV. For typical low ballistic coefficient entries, significant non-equilibrium may exist in regions of the shock layer both in thermodynamic (i.e. species internal energy distribution between rotational, vibrational and electronic modes or states and the translational mode) and chemical processes. The thermal non-equilibrium is commonly expressed as different temperatures for each mode, the internal modes lagging the translational by differing degrees. Chemical non-equilibrium in the entry environment of the forebody means that dissociation reactions are delayed and the mole fractions of molecular species and molecular indermedions

is higher after the shock than in the equilibrium case. This leads to the non-equilibrium overshoot phenomena.

The radiated energy travels in all directions through the flowfield, either being absorbed by the shock layer gases or continuing until it leaves the vicinity of the vehicle or reaches the surface of the vehicle. Radiation that travels upstream of the bow shock leads to heating of the shock precursor region with corresponding increase in freestream enthalpy. Of more significance in general is the radiation that falls on the vehicle surface, or radiative heat flux. In some entry scenarios the radiative heat flux is the dominant mechanism (e.g. for Jovian entry where entry velocities are ~ 40km/s) with the convective contribution becoming insignificant. The forebody flowfield of such vehicles is further complicated by the fact that the only viable material choice for thermal protection systems is a charring ablator type. Pyrolysis gases and subliming or reacting surface species therefore become significant features of the vehicle boundary layer. In general these products will have a beneficial effect in reduction of radiative heat flux since they act to absorb incident radiation. The flux is thus reduced by radiation blockage. On the other hand the absorption of radiation will increase the temperature of the boundary layer gases with a possible associated increase in convective flux. The simulation may be further complicated when ablation products or interaction of these with freestream species gives rise to species which themselves are particularly strong radiators. An example of this is the formation of CN in the boundary layer of carbon heatshields in high enthalpy air flows.

To give an idea of the sensitivity of the radiative fluxes, the intensity of radiative emission is strongly dependent on the shock layer gas pressure and thickness (i.e. nose geometry). In existing engineering correlations for both convective and radiative heat flux, vehicle velocity, nose radius and freestream density are usually independent variables for a given atmosphere. The velocity exponent is typically in the range 5 to 16 for radiative fluxes, whereas for convective flux correlations the velocity exponent is typically 3.
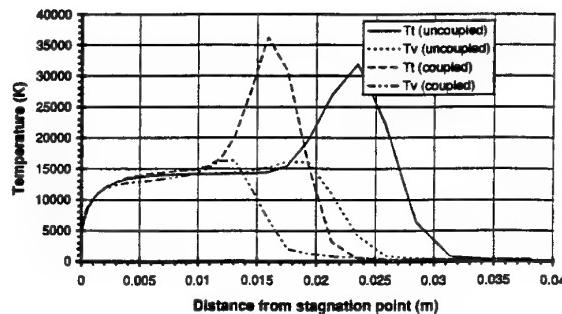

Figure 2.10 Stagnation Streamline temperatures with and without radiation coupling.

The Rosetta entry vehicle provides a good example to illustrate these phenomena. The effects of coupling the radiative transport to the flowfield are shown in figure 2.10 and 2.11 showing stagnation streamline temperature profiles and surface heat fluxes respectively
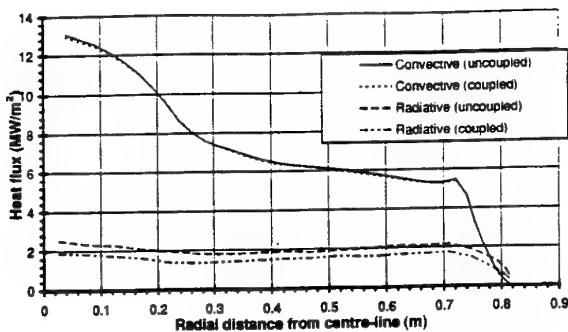

Figure 2.11 Surface Heat fluxes, with and without radiation coupling

2.5.2 Population Distribution

Given the flowfield, the population distributions of excited states (primarily of electronically excited states) for the radiating atomic or molecular species need to be determined prior to determination of radiation emission and absorption phenomena. For the case of thermochemical equilibrium these population densities can be inferred using the Boltzmann distribution for each mode of internal energy. For example this equilibrium approach (i.e. large Damkohler number) is suitable for post-shock conditions of high velocity re-entries at low altitudes into Earth's atmosphere such as for the Rosetta re-entry at peak heat flux and for the pre-shock heating in general. At small Damkohler number (higher altitudes or at lower post shock densities, such as for the Huygens entry near peak heat flux) not only is the gas thermodynamically in non equilibrium, i.e. the internal modes are not at the same temperature as the translational temperature, but the population distributions (including particularly the electronically excited states) are no longer Boltzmann. The total post shock non-equilibrium behaviour causes the phenomenon called radiation overshoot and needs to be considered for an accurate radiation prediction.

The excited states number densities have to be determined by models employing different complexities and accuracies. For the description of the distribution of vibrational and rotational states within a molecule, the equilibrium assumption holds over a broad range. Thus, the number densities of vibrational states within an electronically excited state can be determined using the Boltzmann distribution employing the vibrational temperature. For the calculation of rotational states the Boltzmann distribution using the translational temperature of the heavy particles can be used since the rotational

temperatures equilibrate very fast with the translational degree of freedom of the heavy particles. For the electronically excited states another indicator of the non-equilibrium regime is utilised to determine which assumptions can be made: If the time constant for electronic excitation is small compared to the flow residency time ($Da_e >> 1$), then it is possible to assume that the population and de-population rates are approximately equal, i.e. the distribution is in quasi-steady state (QSS). In the limit of low density it has been shown the time constant approaches the Einstein coefficient for particular transition probability. The QSS assumption greatly simplifies the solution necessary to determine the population of excited states.

2.5.3 Radiative Processes

Once the flowfield and excited state population distributions are known, the radiative processes themselves can be addressed. These processes are described briefly here. In general, these processes are complex and require knowledge of atomic and quantum physics.

The electronic internal energy of a gas is stored in distinct excitation states of the bound electrons, with the addition of vibrational and rotational states for the case of molecules. The emission of a photon occurs when an electron of an atom or molecule falls from a higher to a lower excited state, with absorption causing the opposite process. As only distinct energy states are permitted for the transitions, these processes only occur at distinct points of the wavelength spectrum determined by the energy states. These internal transitions within a particle are referred to as bound-bound radiation, each transition producing a single characteristic line. Certain effects cause a broadening of those lines around their initial wavelength. The strength of the broadening is dependent on the physical effect causing them. Important broadening mechanisms are natural broadening, Doppler-, collision-, and Stark broadening. The change of the emission and the absorption coefficient as a function of the wavelength within a line is called the line profile. Typical profiles found are, each according to the broadening mechanisms, Lorentz profiles (e.g. for collision or pressure broadening), Gauss profiles (for Doppler broadening), or a superposition of both forms Voight profiles.

A sketch of the processes is given in figure 2.12. Arrows pointed upward indicate an absorption process, arrows pointed downward represent emission processes. Bound-bound transitions occur in both atoms as well as ions and molecules. In the latter, however, they are accompanied by vibrational and rotational transitions, so that the resulting multitude of lines or 'band' spectra are very complex. The bound-bound spectrum is typical of atoms and ions. As indicated in Fig. 2.12 the energy difference between adjacent energy levels decreases from the basic level upward to the ionisation level. This means that transitions ranging from the infrared to the ultraviolet range are generally possible. In the applications considered here usually the lower energy levels are closely occupied, and this is the reason why there are many

transitions with the ground state as starting or ending state. These transitions are called resonance transitions, due to the large difference of the energy levels, they are in the ultra violet range. Furthermore the gas in the shock layer is mostly strongly dissociated and partially ionised for high speed entries, so that most of the radiation is released by this atomic radiation mechanism, and ion lines need to be considered. However certain radiating molecules such as CN can be formed in the non-equilibrium overshoot region and these must also be considered.
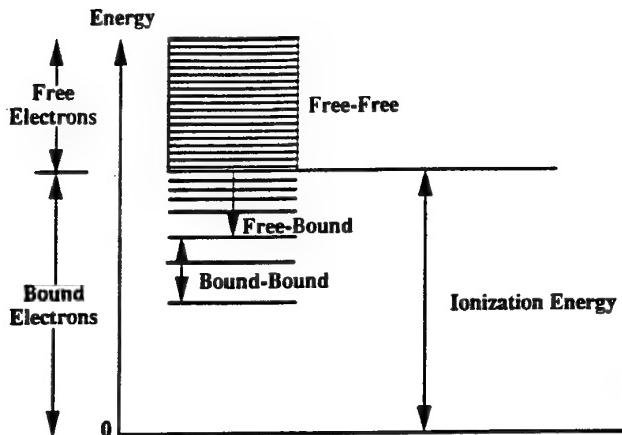

Figure 2.12 Typical Electronic Transitions

The continuum radiation is caused by transitions of the free electrons. It can be divided into the free-free (Bremsstrahlung) and the free-bound radiation, see Fig. 2.12.

For polyatomic gases to be considered the electronic transitions of these molecules are of interest and can be found from the visible to the ultra violet range of the spectrum. These are accompanied by vibrational and rotational transitions. Vibration-vibration, rotation-rotation, and vibration-rotation transitions are only possible for molecules with permanent dipole moment, i.e. hetero-nuclear molecules. Compared to the electronic transitions these transitions are relatively weak and occur in the infra red. These IR rotational and vibrational transitions can be used for diagnostic purposes in ground test facilities, but are not of interest for aerothermal heating..

2.5.4 Classification of Radiative Mechanisms

In summary all relevant radiative processes in radiation gas dynamics can be classified in three categories.

Free-free transitions:

This type of radiation is primarily produced by free (= unbound) electrons that accelerate in the vicinity of ions. Conservation of energy requires them to emit their energy

difference as E.M. radiation, which is known as bremsstrahlung. The spectrum of this radiation is continuous and can be determined from classical elctrodynamic theory.

Bound-free transitions:

A bound-free transition is a transition of an atom or a molecule that results in its ionisation or dissociation.

Bound-bound transitions:

Atoms can transit from one electronic state to another, emitting or absorbing the energy difference as EM radiation. The intensity of the spectral line is proportional to the number of atoms that populate the higher (or lower) energy-state, and to the specific transition probability expressed by an Einstein-coefficient A. (The Einstein coefficients can be computed from Quantum mechanical theory with approximations)

The transition of a diatomic molecule from one electronic state to another will produce a "band" of lines, due to the different possible vibrational and rotational states within an electronic state. The structure of such an electronic transition band results from a selective number of combinations of vibrational and rotational changes within the electronic transition. The intensity of each band as a whole is determined by the oscillator-strength f (determined from spectroscopic measurements), and within one band each vibrational "line"-intensity is given by a Franck-Condon factor (derived from quantum mechanical calculations or from measurements). The intensity of the rotational lines within one vibrational "line" is determined by the population-distribution (rotational temperature) and the degeneration of the rotational states.

2.5.5 Thermodynamics of Radiation

Complete Thermodynamic Equilibrium (CTE)

Molecular processes are in detailed balance leading to Maxwell/Boltzmann distribution of states. All radiation processes occur at the equilibrium temperature of the gas locally. Characteristically the mean free path of the gas particles is much greater than the mean free path of the photons. Absorption and emission are equal locally at all frequencies.

Local Thermodynamic Equilibrium (LTE):

When the gradients of the thermodynamic variables at certain locations are small, the local values of these variables can be used to define thermodynamic equilibrium states that locally approximate the real thermodynamic states at these locations. This approximation is called "the Local Principle", and the gas is said to be in Local Thermodynamic Equilibrium (LTE). At LTE, the excited states of a gas can be described by a Boltzmann distribution.

In LTE as opposed to CTE, the mean free path of the photons can be larger than the mean free path of the gas particles and so emission and absorption processes are not equal across all wavelengths and therefore not in equilibrium.

Non-Local Thermodynamic Equilibrium (NLTE):

When gradients of thermodynamically variables become large, the assumption of LTE no longer can be made, and the flow becomes thermodynamic non-equilibrium and Boltzmann distribution of internal energy is not strictly valid. The radiation is no longer thermal and a more general approach has to be considered.

2.5.6 Optical Thickness of Gases

Optical thickness is a macroscopic quality of a system and implies nothing of local properties, but can be used to classify particular regimes or cases and thus which assumptions are possible

The optical depth for a given wavelength is the integral through the depth of gas (i.e. the shock layer or the computational cell) of the absorption coefficient and density product.

Optically Thick Gases:

The optical depth is much smaller than the slab thickness. A gas in CTE must be optically thick, but a gas which is optically thick is not necessarily in CTE.

For optically thick gases the radiation has the same local character as the molecular gas and can be supposed to be in local equilibrium with the gas. Then LTE is valid and the local radiative emission will be given by Planck's law, but with a local temperature of the gas inserted.

Optically Thin Gases

The optical depth is much larger than the slab thickness. For optically thin gases however, the LTE assumption can not be maintained for the complete system containing gas and radiation, since now the radiation at a point reflects conditions within a large photon mean free path and so violate the local principle. The radiation is then not locally describable by an equilibrium distribution, but has to be determined by solving a radiative transport equation. In order to solve this transfer equation, one has to state the absorptive and emissive properties of the gas at each location, which depend on the local state of the gas.

In general the high temperature plasma region surrounding a re-entry vehicle is optically thin.

2.6 AEROTHERMAL REGIMES

Now that we have an understanding of the atmosphere and the physical and chemical processes in the shock layer it is possible to distinguish particular regimes during an atmospheric entry where particular assumptions can be

made such that the method of solution of problems in these regimes can be determined.

A typical entry trajectory, whether it be through any planetary atmosphere will encompass a number of different flowfield regimes. In the subsequent sections, a brief physical description of these regimes is given in the order in which they will be encountered by an entry vehicle, followed by the boundary definition.

2.6.1 Free Molecular

At extreme altitudes, where the gas is very rarefied, the flow has to be described using kinetic theory. This region is known as the free molecular regime and as the vehicle descends it enters the near free molecular regime. In the near free molecular regime, the molecules reach the body surface after only a few collisions with surface reflected molecules, and in the free molecular regime the molecules are assumed to reach the surface without colliding with any reflected molecules since the molecules are so widely spaced. As the vehicle descends further, it encounters a region of transition from the near free molecular to the continuum, and engineering results can be obtained using bridging schemes between the two regimes.

2.6.2 Merged Layer Regime

As the vehicle descends, the flow begins to exhibit continuum characteristics, but is still influenced by rarefied gas effects. Within the merged layer regime, a boundary can be identified that divides the freestream and the shock-layer, but within the shock-layer, the shock wave and boundary layer are not distinguishable.

The no-slip condition which is assumed to hold for continuum flows does not hold at these high altitudes. Specifically, at low densities the flow velocity at the surface takes on a finite value, and also the gas temperature at the surface differs from the actual surface temperature. The shock wave cannot be described as a discontinuity and the shock layer must now be treated as fully viscous, and conventional boundary layer analysis is no longer applicable.

2.6.3 Slip Flow

As the density increases, as the altitude decreases, the shock wave thins to a point where it can now be treated as a discontinuity in the flowfield, and, as the density increases further, is no longer merged with the boundary layer. The boundary layer remains very thick and hence results in stronger viscous interaction.

As the altitude decreases the discontinuity in temperature and velocity at the wall reduce. Eventually, these effects disappear altogether, and the non-slip condition can be assumed to hold.

2.6.4 Continuum

The assumption of a continuum flowfield requires that the mean free path be very much smaller than the smallest

characteristic length of the flowfield, i.e. the boundary layer thickness, so that sufficient molecular collisions occur to establish continuum conditions within this region at every instance. Viscous effects can now be confined to the boundary layer. In such environments, where the density is high, several assumptions can be made about the flowfield around a bluff body. Due to the entropy increase across the shock, there are strong entropy gradients in the nose region where shock curvature is greatest. The boundary layer grows inside the entropy layer and is effected by it, since it is also a region of strong vorticity.

At the high Mach numbers associated with the high altitude end of the continuum regime, viscous dissipation within the boundary layer causes an increase in temperature within the boundary layer, which in turn causes the boundary layer to thicken. This can exert a major displacement effect on the inviscid flow outside the boundary layer, and the resulting changes in the inviscid flow effect the boundary layer growth. Since the flow behind the near-normal portion of the bow shock is subsonic, the viscous interaction will be strongest away from the stagnation region where the flow has accelerated to supersonic velocities.

The high temperature in the boundary layer due to viscous dissipation and in the shock layer due to the shock wave will mean high heat transfer rates to the surface. Generally, convective heating dominates, but if the temperature is sufficiently high the thermal radiation emitted by the gas itself, radiative heating, can be significant.

As the altitude decreases, viscous dissipation effects are reduced, and the boundary layer thins. At high Reynolds numbers/low Mach numbers, where the boundary layer is very thin, the shock layer is essentially inviscid, and viscous interaction is weak.

2.6.5 Flowfield Boundary Definitions

The various flowfield regimes can be characterised in terms of the Knudsen number, defined as:

$$Kn = \lambda/d = \sim \frac{M}{Re_d}$$

where: λ is the molecular mean free path;
d is a characteristic dimension
(e.g. body length or diameter).

In this form, the Knudsen number is applied to low Reynolds number flows, (typically $Re_d < 10^2$).

When d is set to the boundary layer thickness δ:

$$Kn = \lambda/\delta = \sim \frac{M}{\sqrt{Re_d}}$$

and in this form the Knudsen number is applied to higher Reynolds number flows, (typically $Re_d > 10^2$).

Using these definitions, the boundaries of the various regimes can be specified, albeit somewhat arbitrarily, as:

Free molecule $\qquad\qquad M/Re_d > 10;$

Transitional:
Near Free molecule $\quad 10 > M/Re_d > 1;$
Merged layer $\; 1 > M/Re_d$ to $MRe_d^{-1/2} > 0.1;$

Slip flow $\qquad\qquad 0.1 > MRe_d^{-1/2} > 0.01;$

Continuum flow $\qquad 0.01 > MRe_d^{-1/2}$

Figures 2.13, 2.14 and 2.15 show typical ballistic trajectories Earth return (Rosetta), Mars (Marsnet) and Titan (Huygens).
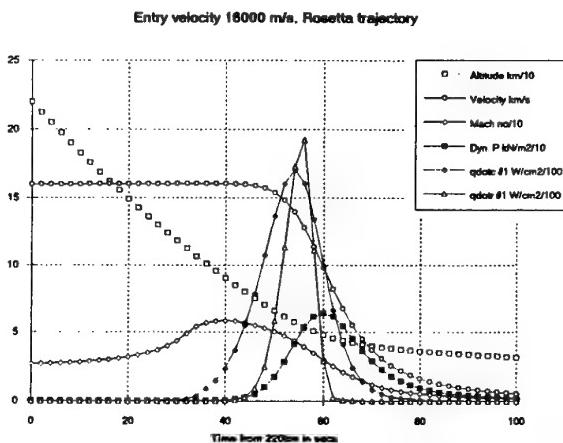

Figure 2.13 Rosetta trajectory parameters
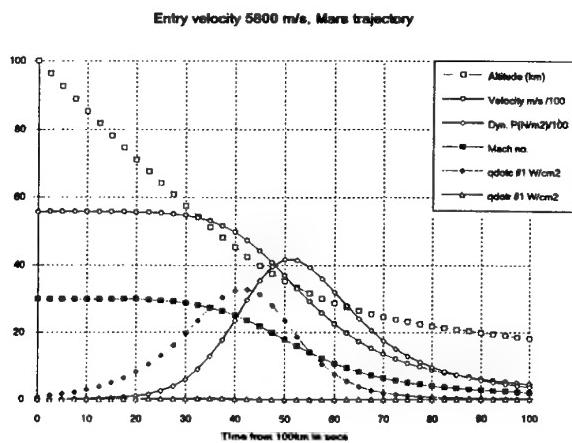
Figure 2.14 Mars trajectory parameters

Figure 2.15 Huygens trajectory parameters
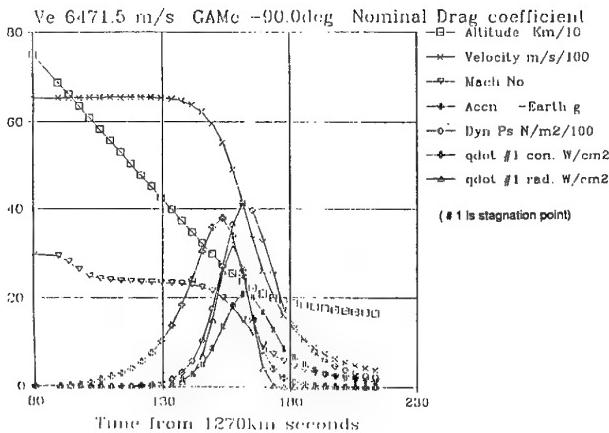
Figures 2.16, 2.17 and 2.18 show the Knudsen number (both definitions from above) Reynolds number, dynamic pressure, stagnation convective heat flux vs. altitude for the same trajectories. It can be seen that the high dynamic pressure portion of the entry where peak deceleration occurs the Reynolds number is greater than about 2×10^5 based on the base diameter and the Knudsen number less than 1×10^{-4}. Therefore, for drag calculation purposes it is quite reasonable to assume continuum flow. Figures 2.19, 2.20 and 2.21 show the boundaries on velocity altitude plots for the three trajectories.


Figure 2.16 Rosetta entry flowfield parameters
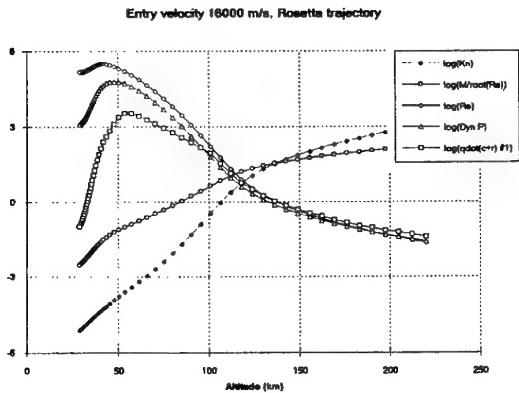
These figures also shows the Knudsen number based on the boundary layer thickness (based roughly on the root of the body Reynolds number) and the convective heating. The definition of the classical regimes is based on this value for the Knudsen number of the entry vehicle and it can be seen that the entry takes place between 1×10^{-1} and 1×10^{-2}, i.e.. slip flow (vorticity interaction effects being negligible on the forward heatshield and only important at the expansion corner). Here we may still use continuum techniques where the effects of boundary layer thickness are accounted for (i.e. Navier Stokes solutions)

and evaluation of the wall conditions undertaken. In practice however the heat transfer rates are over-predicted using no slip and the slip condition becomes another empirical factor.

Figure 2.17 Mars entry flowfield parameters


Figure 2.18 Huygens entry flowfield parameters
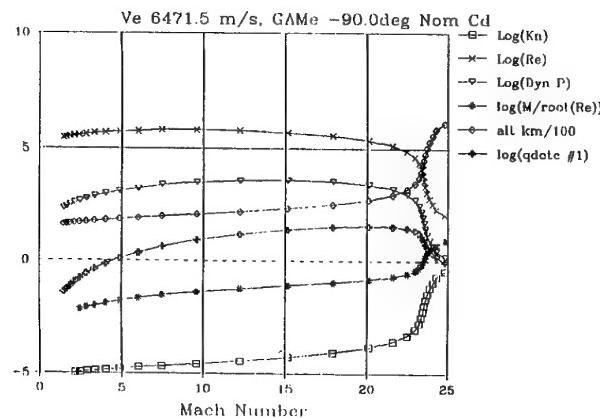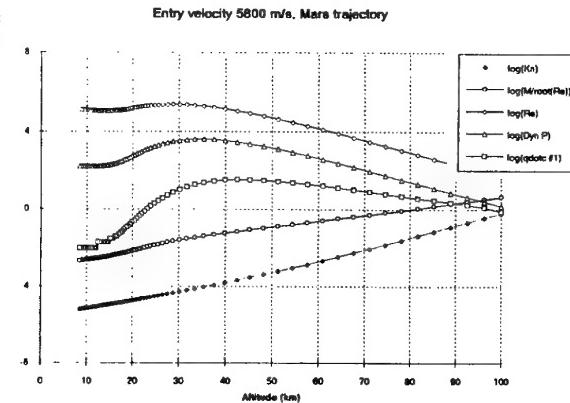
Clearly entry vehicles have geometric features of largely different sizes the base radius to corner radius for example and the definition of regimes need to be treated with caution since continuum flowfields may exhibit rarefied flow effects in particular regions, the corner or base for example. The regimes are a broad guideline therefore.
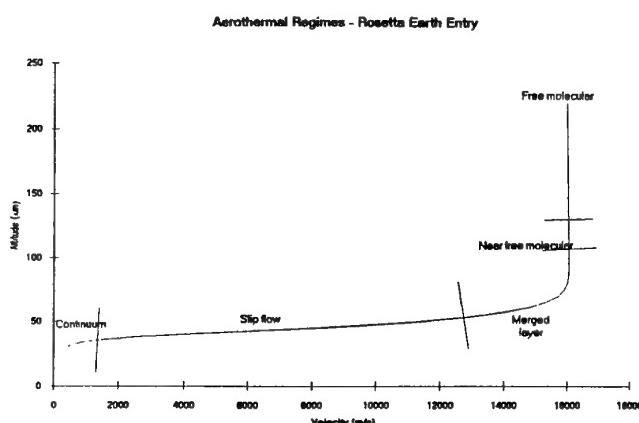
Figure 2.19 Rosetta aerodynamic regimes
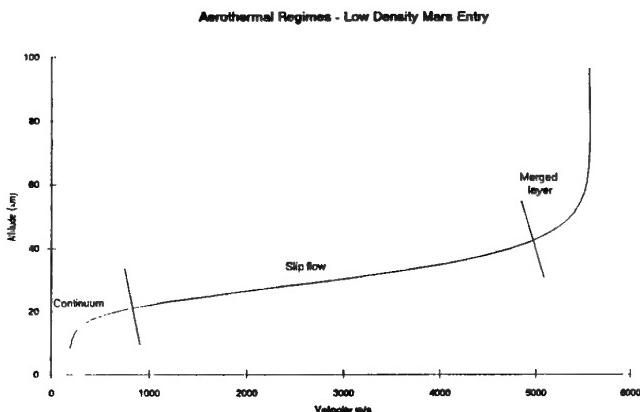
Figure 2.20 Marsnet aerodynamic regimes
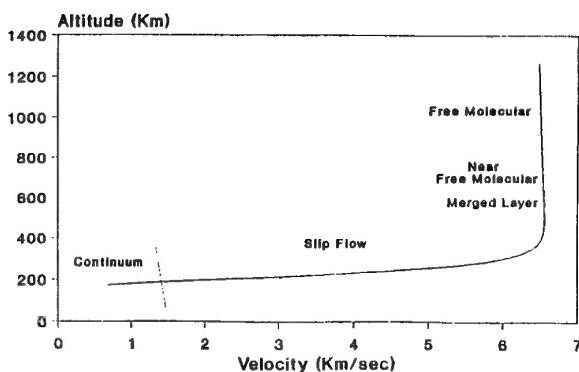
Figure 2.21 Huygens aerodynamic regimes

2.6.6 Thermo-Chemical Boundary Definitions

The parameter which characterises the thermo-chemical regimes is the Damkohler number, Da as described in the discussion of chemistry. This number can be applied to internal degrees of freedom of the molecules or to chemical reactions in the fluids.

The Damkohler number is the ratio of the characteristic time of particles passing a region of the flow t_u to the relaxation time τ in question, where the flow time is usually the ratio of the characteristic dimension L (the shock stand-off distance for instance) and the velocity u

$$Da = L/(u\tau)$$

For chemical reaction we compute the Damkohler number as

$$Da = Ln_k/(\omega_k u)$$

and for thermal relaxation we can define the Damkohler as

$$Da = L/(\tau_v u)$$

The chemical and thermal regimes may be loosely defined as follows:

$Da = 0$	chemically frozen
$0.01 < Da < 1000$	non-equilibrium flow
$Da = \infty$	chemical equilibrium.

At very high altitudes where the densities are very small or at low speeds where temperatures are low, reaction rates are slow compared to the hydrodynamics time-scales (Damkohler number $Da<<1$). This enables the frozen flow assumption to be used and solutions are restricted to those which model the flow of a multi-component fluid as a continuum (or a free molecular) problem utilising an appropriate equation of state and real (i.e. temperature dependent) thermodynamic data. Note that the Damkohler number can be applied equally well to thermodynamic relaxation (vibration, rotation etc.) as to chemical processes and particular reactions. For example a particular reaction may be so fast that it can be replaced by an equilibrium reaction. The dissociation of methane in the Titan atmosphere for example. Or the reaction may be so slow that it can be excluded from the mechanism.

At low altitudes the densities are high and the flow is likely to be characterised by fast chemical reaction whose time-scale is short when compared with that of the fluid velocity (Damkohler number $Da>>1$). In this regime the assumption of equilibrium chemistry in the shock layer is more appropriate.

In the mid-range density regime the assumption of either frozen or equilibrium flow, whilst accurate in some portions of the shock layer, would lead to over (frozen) or under (equilibrium) prediction of temperature in other areas.

In reality between these two regimes the density is such that the flow cannot be accurately characterised as being either frozen or as being in chemical equilibrium. It is in this flight region that non-equilibrium chemical kinetics must be considered.

Thermal non-equilibrium influences the rates at which certain chemical reactions proceed. Translational temperature behind the shock is increased, but vibrational and electronic temperatures are decreased. This implies that the onset of ionisation is enhanced because of the dependence of ionisation reactions (other than electron impact) on the translational temperature, whereas dissociation is diminished because of the dependence of dissociation reactions on the vibrational temperature.

The combination of high thermal energy and ionisation overshoot causes enhancement of radiation, i.e. non-equilibrium processes can also effect the heat transfer distribution. This phenomenon known as non-equilibrium radiation enhancement tends to maintain the radiative heat fluxes to the heatshield surface at a nearly constant value. This is believed to be caused by a region of high temperature and high concentration of excited atoms and molecules that is created during the process of thermal and chemical relaxation behind the shock wave. This non-equilibrium enhancement phenomenon tends to be offset by two phenomena known as collision limiting and truncation.

The chemical Damkohler variation with altitude are shown in figures 2.22, 2.23 and 2.24, with thermal Damkohler numbers in figures 2.25, 2.26 and 2.27. Note that for the formulation employed at one tenth of the distance along the stagnation streamline the regime boundaries were found to be best fitted by lowering the critical values by 10^3.

Approximate chemical and thermal boundaries are shown for the Earth entry in Figure 2.28 and 2.29. These figures are illustrative and use a nitrogen dissociation and vibrational relaxation model only.

For the Mars entry a five species model was used and Vibrational relaxation data appropriate to oxygen Chemical and thermal regimes are shown in figures 2.30 and 2.31.

For Titan entry Figures 2.32 and 2.33 show the chemical and thermal regimes. Since methane dissociates very quickly the thermal regimes are also based on the relaxation of diatomic nitrogen.

It is clear that equilibrium conditions are only appropriate foe the Rosetta entry.

Binary Scaling

For non-equilibrium processes involving two-body molecular collisions, an interesting and important scaling can be obtained for non-equilibrium flowfields, known as binary scaling.

Consider two different flows with the same temperature T_∞ and velocity V_∞ but with differing values of density ρ_∞ and d (characteristic length, the nose radius, say). Plots of mass fraction against distance inside the shock will be the same for the two flows if the product $\rho_\infty d$ is the same between the two flows. This product, $\rho_\infty d$, is known as the binary scaling parameter, and is used for matching wind tunnel conditions to flight conditions.

REFERENCES FOR SESSION 2

Anderson J D Jr., 'Hypersonic High Temperature Gas Dynamics' McGraw Hill, 1989, ISBN 0-07-001671-2

Park C., 'Nonequilibrium Hypersonic Aerothermo-dynamics' Wiley, 1990, ISBN 0-471-51093-9
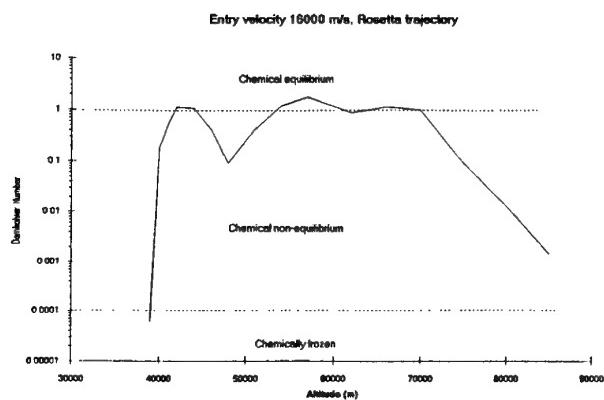
Figure 2.22 Rosetta Chemical Damkohler

Figure 2.25 Rosetta Thermal Damkohler
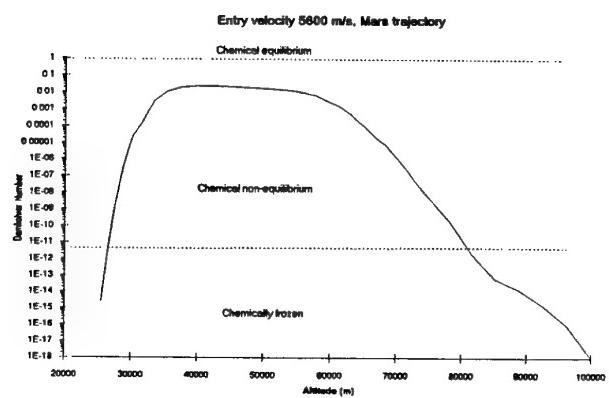
Figure 2.23 Marsnet Chemical Damkohler
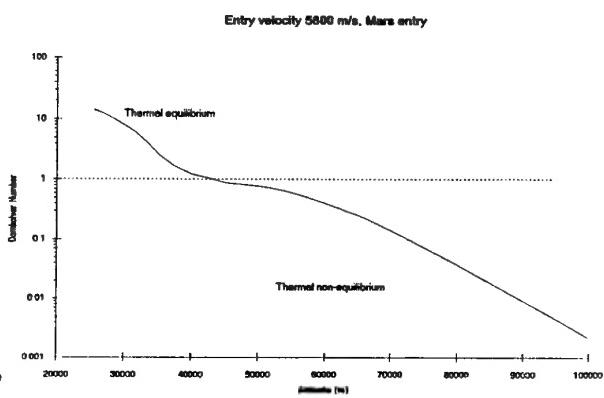
Figure 2.26 Marsnet Thermal Damkohler
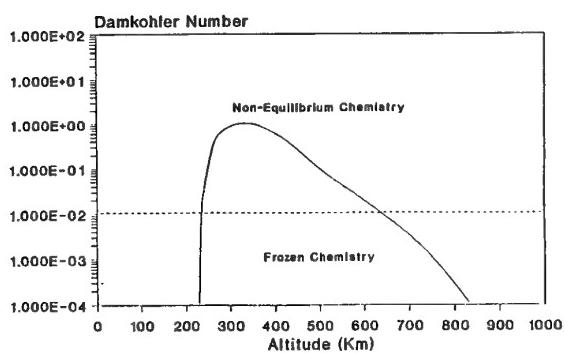

Figure 2.24 Huygens Chemical Damkohler
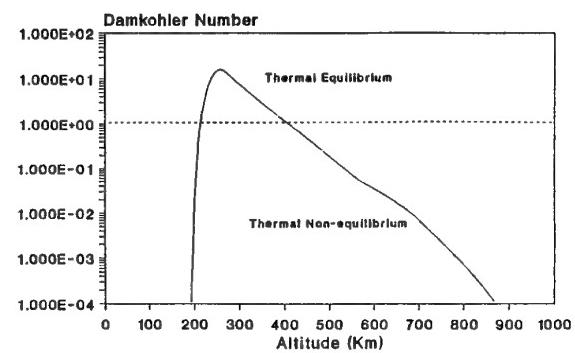

Figure 2.27 Huygens Thermal Damkohler
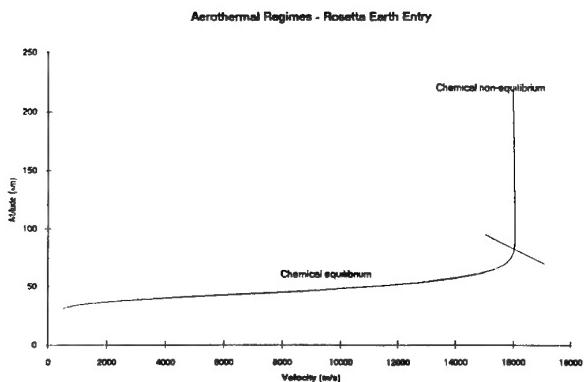
Figure 2.28 Rosetta Chemical Regimes
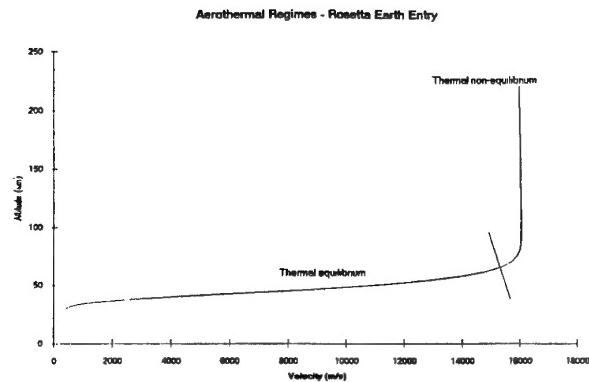
Figure 2.31 Rosetta Thermal Regimes
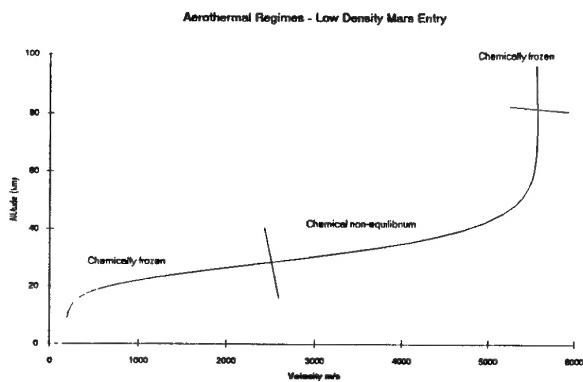
Figure 2.29 Marsnet Chemical Regimes
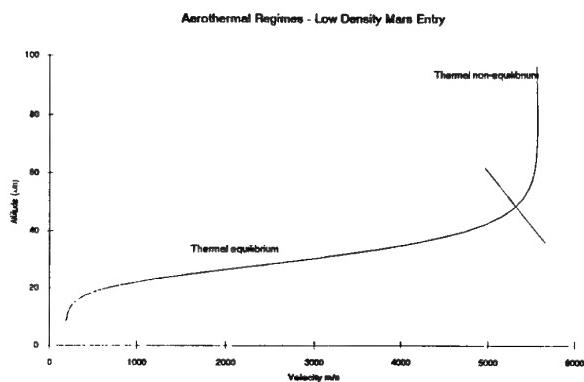
Figure 2.32 Marsnet Thermal Regimes
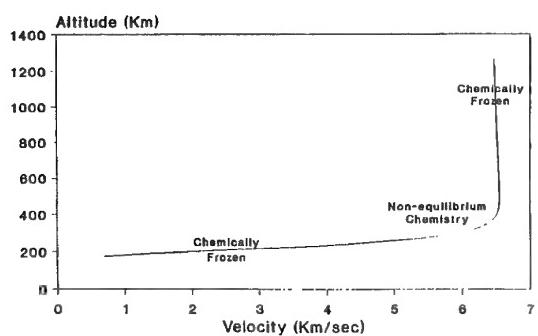
Figure 2.30 Huygens Chemical Regimes
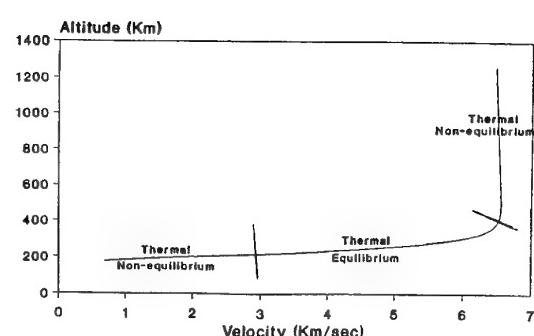
Figure 2.33 Huygens Thermal Regimes

HEAT TRANSFER FOR PERFECT GAS
AND CHEMICALLY REACTING FLOWS

Arthur Smith
Fluid Gravity Engineering Ltd
Chiltlee Manor
Liphook, Hampshire
GU307AZ, UK

SUMMARY

In this section we focus on basic principles and the derivation of some basic relationships used in heat transfer analysis for planetary entry. Catalytic mechanisms and their effect on the thermal protection system is considered, finally radiation transport and regimes are briefly examined.

3.1 PERFECT GAS

The perfect gas equation of state is applicable at pressure below 100bar and/or temperature above 30K when intermolecular forces are negligible. For most entry conditions a perfect gas can be assumed:

$$p = RT/v$$

or $\quad p = \rho RT$

For a perfect gas the internal energy is a function of temperature only, therefore it immediately follows that C_p and C_v are also functions of temperature only.

For a calorifically perfect gas C_p and C_v are constant, i.e. γ is constant.

3.2 REAL GAS

The assumption of a perfect gas may not be valid in some ground test facilities where high pressure gases are expanded to low temperature. When intermolecular forces must be accounted for a real gas equation of state becomes necessary for example Van der Waals equation of state:

$$p = RT/(v\text{-}b) \text{ -}a/v^2$$

where a and b are constants, or by using a compressibilty factor Z

$$pv = ZRT$$

where Z is a function of temperature and pressure, and is available in generalised compressibilty charts.

Often in aerothermodynamics the chemically reacting gas is incorrectly described as a real gas and we try and avoid this confusion.

3.3 NON REACTING FLOWS.

3.3.1 Fouriers Law and Convective Heat Transfer

An empirical observation of one dimensional steady heat flow through a solid between isothermal surfaces shows that the heat flux is proportional to the area of the flow and the temperature difference across the layer and inversely proportional to the thickness and may be expressed :

$$Q = \text{-} kA(dT/dy)$$

or $\quad q = \text{-} k(dT/dy) = \text{-}\rho\alpha C_p\,(dT/dy)$

where α is the thermal diffusivity.

The constant of proportionality k is the thermal conductivity of the material, and the negative sign indicates that the heat flow is positive in the direction of temperature fall. This is Fourier's law and is applicable at all y across the layer

This therefore applies to the stationary gas in a boundary layer next to an isothermal wall, but since the asymptotic gradient is difficult to measure in practice, it is conventional to express the heat flow from the wall to the fluid in the form :

$$q_c = \text{-} h_c(T_{aw}\text{-}T_w)$$

the sign convention is consistent with Fouriers equation, but the temperature change must be written to ensure positive heat flux in the direction of temperature fall.

T_{aw} is the temperature of the gas at the wall if the heat flux is zero, i.e. the adiabatic wall temperature.

The convective heat transfer coefficient h_c , or film coefficient, is not a constant of the fluid but includes the combined effects of conduction and convection in the fluid. h_c is a function of numerous variables such as the transport properties, density and velocity of the fluid.

Before we can use the film coefficient relationship for heat transfer calculations, it is necessary to define T_{aw}. This can be found by solution of the boundary layer equations but in engineering analysis we introduce the recovery factor r defining the amount of energy 'recovered' as the gas is slowed by friction through the boundary layer.

$$T_{aw} = T_e + r u_e^2/2C_p$$

while at the outer edge of the boundary layer:

$$T_o = T_e + u_e^2/2C_p$$

therefore:

$$r = (T_{aw} - T_e)/(T_o - T_e)$$

For incompressible laminar flow over a flat plate $r = Pr^{1/2}$ and for incompressible turbulent flow over a flat plate $r =\sim Pr^{1/3}$. These factors are used well into the hypersonic regime and have accuracy compatible with the simplified engineering analysis. We now call T_{aw} the recovery temperature T_r.

Many non-dimensional groups are used in heat transfer analysis and we shall now explore some of the relationships between them by looking at the nature of h_c.

If we change the temperatures to enthalpies which will be convenient later then:

$$q_c = St\rho_e u_e(H_r - h_w)$$

where for a calorifically perfect gas the Stanton number is

$$St = h_c/(\rho_e u_e C_p)$$

which is the ratio of actual energy transfer rate to the energy flux available.

Multiplying by $x\rho_e u_e C_p/k_e$ gives the Nusselt number:

$$Nu = xh_c/k_e$$

which is the ratio of convective heat transfer to conduction only.

Now the ratio of mass flux to viscosity of the flow is the Reynolds number $Re = \rho xu/\mu$ (i.e. inertial/viscous ratio) and the ratio of ~~thermal to viscous~~ difusivity is the Prandtl number $Pr = \mu C_p/k_e$ therefore: *first is there correl.*

$$Nu = St\, Re\, Pr$$

These groups are used extensively in engineering heat transfer, and consequently in aerothermal analysis. In particular heat transfer is often defined in either Stanton or Nusselt number terms depending whichever is most convenient.

Now since $h_o = h_e + u_e^2/2$

and if $h_r \gg h_w$ then:

$$q_c \sim -0.5St\rho_e u_e^3$$

In hypersonic flow the heat flux is therefore proportional to the cube of the velocity, i.e. in contrast to the drag which is proportional to the square of the velocity. This is the basic reason why heat transfer is so important in hypersonics.

3.3.2 Newtons Law and the Skin Friction Coefficient.

Consider flow over a flat plate where a laminar boundary layer grows due to the viscosity of the fluid. The shear stress at any point in the fluid is proportional to the velocity gradient at that point. The constant of proportionality μ is called the dynamic viscosity of the fluid so that

$$\tau = \mu\, du/dy = \rho\nu\, du/dy$$

This is Newtons law of viscosity. Since the wall asymptotic gradient is difficult to measure as in the heat transfer case, the shear stress at the wall τ_w is usually expressed as a function of the local dynamic pressure:

$$\tau_w = 0.5\rho_e u_e^2\, C_f$$

where C_f is the local skin friction coefficient.

3.3.3 Reynolds Analogy

It is apparent that there is a similarity between the expressions for the heat flux and the shear stress, now if the fluid has a kinematic viscosity ν equal to its thermal diffusivity α then the Prandtl number is unity and dividing q_c by τ, ignoring the sign convention and integrating through the boundary layer gives :

$$q_c/(\tau_w C_p) = (T_e - T_w)/u_e = \theta_e/u_e$$

this is the simple Reynolds analogy. Re-arranging this equation gives :

$$xq_c/(\theta_e k) = \tau_w/(\rho u_s^2)\, x\rho u_s/\mu\, C_p\, \mu/\kappa$$

which in terms of non dimensional groups noting that the Prandtl number is unity is :

$$Nu_x = 0.5\, C_{fx}Re_x$$

where C_{fx} is the local friction factor which is a function of Reynolds number only. Hence the Nusselt number is a function of Reynolds number. Further examination shows that a most useful result of this analysis is :

$$St = 0.5C_f$$

The usefulness of Reynolds analogy lies in this simple relationship which allows first order engineering analysis of many viscous flows where heat transfer is of interest. For example we shall use this result in session 4 to examine the relationships that can be derived between atmosphere, vehicle parameters and heating in simple trajectory analysis.

For non unity Prandtl number, comparing the Blasius incompressible flat plate boundary layer solutions for skin friction and heat transfer, gives the relationship:

$$St = 0.5C_f/Pr^{2/3}$$

This result is also found to be applicable with caution for the hypersonic flat plate laminar boundary layer, and in region of low pressure gradient. However in regions of high gradient, Reynolds analogy is inappropriate.

Often heat transfer results are correlated as functions of the heat transfer parameter $Nu/Re^{1/2}$ since for the classical solution for the laminar incompressible flow over a flat plate:

$$Nu_x = 0.332 \; Pr^{1/3} \; Re_x^{1/2}$$

3.3.4 Stagnation Point Heating

Van Driest performed detailed stagnation point boundary layer solutions with a calorifically perfect gas and correlated the results in the form:

$$q_c = k_s Pr^{-0.6} (\rho_e \mu_e)^{0.5} (h_r - h_w) (du_e/dx)_s^{0.5}$$

where k_s is 0.76 for a sphere and 0.57 for a cylinder. Note that this is a film coefficient formulation. The reason for the higher heat flux in the three dimensional case is in the nature of the flow, in two dimensions the flow can only go in two directions (i.e. up or down), whereas in three dimensions it can also go sideways (left and right). This causes a thinner boundary layer and thus larger dT/dy. In hypersonic flow the shock stand-off is also reduced.

The stagnation point velocity gradient can be determined by assuming a Newtonian pressure distribution at the surface and Eulers equation at the edge of the boundary layer ($dp_e = \rho_e \mu_e \, du_e$) as:

$$(du_e/dx)_s = R^{-1} \{2(p_e - p_\infty)/\rho_e\}^{0.5}$$

Therefore the convective heat flux is inversely proportional to the square root of the stagnation point radius of curvature R. This has a major impact on all capsule designs, dictating large radius of curvature for the forward headshield.

3.4 CHEMICALLY REACTING FLOWS

In a chemically reacting flow the chemical composition may change through the boundary layer, from the boundary layer edge composition to the wall composition since there will be temperature gradients in the boundary layer even for an adiabatic wall. If the gas is in chemical equilibrium the composition in the boundary layer is determined by local conditions only. The species gradients present give rise to diffusion fluxes of species within the boundary layer. These diffusion fluxes provide an effective transport of mass (and energy) and the local equilibrium relies on a balance of these fluxes.

Local equilibrium occurs when the wall temperatures are generally above about 2000K in typical entry situations.

When the wall temperatures are lower the reaction rates are slow even compared to the residency time in the boundary layer and the boundary layer gases are in non-equilibrium. In the limiting case the boundary layer gases

do not react at all and the boundary layer edge composition is maintained to the wall.

Heat transfer in the chemically reacting case is the sum of the Fourier conduction component using the frozen conductivity (i.e. the conductivity that the mixture would posses if no chemical change occurred when a temperature gradient was imposed upon it) plus a chemical term dependent on the diffusion of species towards the wall.

$$q_c = - k(dT/dy)_w + \Sigma \rho c_i V_i h_i$$

$$= - k(dT/dy)_w + D_i \rho \Sigma (h_i \partial c_i / \partial y)$$

where V_i is the diffusion velocity of species i.

When considering the species diffusion terms in engineering analysis it is convenient to introduce two other dimensionless groups, the Lewis number :

$$Le = D_i \rho C_p / k$$

which is the ratio of mass diffusion to thermal diffusion, and the Schmidt number:

$$Sc = \mu/(D_i \rho)$$

which is the ratio of viscous to mass diffusion.

3.4.1 Film Coefficient Approach

The energy equation in the boundary layer for an incompressible constant property low speed flow is :

$$u \partial T / \partial x + v \partial T / \partial y = \alpha \partial^2 T / \partial y^2$$

solutions are generally correlated in the form

$$q_c = - h_c (T_r - T_w)$$

as discussed above. For a high speed chemically reacting flow, if diffusion coefficients are equal and Prandtl and Lewis numbers are unity then boundary layer energy equation becomes:

$$\rho u \, \partial H / \partial x + \rho v \, \partial H / \partial y = \partial / \partial y (\mu \, \partial H / \partial y)$$

where H is the total (sensible + chemical + $u^2/2$) enthalpy. By analogy to the low speed case above, then solutions can be correlated in the form:

$$q_c = - \rho_e u_e C_h (H_e - h_w)$$

and we can define the Stanton number for a chemically reacting flow as :

$$C_h = q_c / (\rho_e u_e (H_e - h_w))$$

and Nusselt number:

$$Nu = x q_c / (k_e (H_e - h_w))$$

The heat transfer equation can now be re-partitioned according to the enthalpy terms into the frozen chemistry 'Fourier' part and the chemical part:

$$q_c = - \rho_e u_e C_h (H_r - h_w)_e - \rho_e u_e C_h (h_e - h_w)_{Tw}$$

In the first term the convective flux is evaluated using the boundary layer edge composition. In the second term, the chemical flux is evaluated at the wall temperature and is driven by the difference between chemical composition of the edge and wall gases at the wall temperature. After partitioning the assumption of unity Lewis number can be relaxed and a mass transfer coefficient C_m used in the chemical flux term

$$q_c = - \rho_e u_e C_h (H_r - h_w)_e - \rho_e u_e C_m (h_e - h_w)_{Tw}$$

If the diffusion coefficients are not approximately equal i.e. when mixtures of widely different molecular weights are present in the boundary layer then the direct chemical enthalpy can not be used and an equivalent enthalpy h^* using a diffusion coefficient weighted average of mole and mass fraction may be employed

$$q_c = - \rho_e u_e C_h (H_r - h_w)_e - \rho_e u_e C_m (h^*_e - h^*_w)_{Tw}$$

3.4.2 Mass Transfer Relationship to Heat Transfer

The mass transfer coefficient is related to the heat transfer coefficient by the frequently employed Chilton-Coburn correlation

$$C_m / C_h = Le^{\phi}$$

where $\phi = 2/3$ is a commonly used value.

The Lewis number Le is the ratio of the Prandtl number to the Schmidt number

$$Le = Pr / Sc$$

For dissociating air, $Pr = 0.71$ and $Sc = 0.5$ then $Le = 1.4$ and $C_m = 1.26\ C_h$. In engineering estimates the Prandtl and Schmidt numbers may be evaluated at a boundary layer reference condition such as defined by Eckert.

3.4.3 Stagnation Point Heating.

Fay and Riddell performed detailed stagnation point boundary layer solutions with a chemically reacting dissociating gas and correlated the results in the form :

$$q_c = 0.76 Pr^{-0.6} (\rho_w \mu_w)^{0.1} (\rho_e \mu_e)^{0.4}$$
$$\{1 + (Le^{\phi} - 1)(h_d / h_e)\}(h_e - h_w)\ (du_e / dx)_s^{0.5}$$

Here h_d is the enthalpy of dissociation the gas mixture. A binary mixture, constant Prandtl and Lewis number and a $T^{1/2}$ viscosity law was assumed for the correlation development.

Comparison with the calorifically perfect gas result shows the only major difference to be the addition of the chemical terms as expected from the partitioning result and gives

the exponent of the Lewis number ϕ for the ratio of mass to heat transfer coefficients.

The condition of the wall and boundary layer give rise to the following parameter values:

boundary layer/wall condition	Parameter
equilibrium	$\phi = 0.52$
frozen with fully catalytic wall	$\phi = 0.63$
frozen with non catalytic wall	$Le = 0.0$

Table 3.1 Fay and Riddell Parameter Values

Note the difference between the equilibrium and frozen fully catalytic wall case is quite small since the gas near the wall is composed of a binary mixture of atoms and molecules such that the diffusion flux, given the same wall condition, is nearly equal and thus independent of the kinetics.

When ionisation becomes important at high velocity (> 9km/s) then the diffusion of electron-ion pairs is greater leading to reduced Lewis number. The ionisation energy must also be taken into account. Overall this leads to an increase in the predicted heat flux. Importantly in this case the heat flux for the frozen boundary layer with fully catalytic wall for a diatomic gas is progressively larger than the equilibrium boundary layer solution with increasing ionisation. This is because in the equilibrium case the mixture is essentially ternary and the large charge-exchange cross section allows a layer of atoms to form which prevent the diffusion of ion-electron pairs towards the wall and thus their recombination energy is not available at the wall. In the case of the frozen boundary layer with fully catalytic wall the recombination take place directly at the wall from ionised to molecular state and thus the insulating atomic layer is not present.

This effect is not seen in singly ionised atomic gases for example Ar or He where the binary nature of the gas would not lead to significantly different fluxes, but recurs in multiply ionised flows.

3.5 SURFACE PROCESSES

Species can stick or adsorb to surfaces generally by one of two processes involving either a physical or chemical interaction, the main features of which are outlined in Table 3.2. Adsorption is the key feature of surface catalysis and presently the process is only partially understood.

3.5.1 Physisorption

In physisorption there is a Van der Waals interaction between the adsorbed molecule and the surface. This is a long range but weak interaction and the amount of energy released when a molecule is physisorbed is of the order of the energy of condensation (~ 25 kJ/mol).

Physical adsorption:	Chemisorption
Heat of adsorption less than about 20 kJ/mole	Heat of adsorption greater than about 200 kJ/mole
Adsorption appreciable only at temperatures below the boiling point of the adsorbate	Adsorption can occur at high temperature
Adsorption increases with increase in pressure	Adsorption decreases with increasing pressure
The amount of adsorption on a surface is a function of the adsorbate	The amount of adsorption is characteristic of both adsorbate and adsorbent
No appreciable activation energy involved	An activation energy may be involved
Multi-layer adsorption	Adsorption leads to, at most, a monolayer.
Small changes in vibrational frequency	Large changes in vibrational frequency
Weak bonding - absorbate removed by evacuation at room temperature or below	Strong bonding - absorbate removed only by evacuation and/or heat usually resulting in decomposition

Table 3.2

This energy can be absorbed as vibrations of the lattice (of the adsorbate) and dissipated as heat, and a molecule bouncing across what is effectively a "cobbled" surface will lose its kinetic energy and stick to the surface in the process known as accommodation. The energy levels associated with the physisorption process are insufficient to lead to breaking of the bonds of surface species. A physisorbed molecule vibrates in its shallow potential well and as the binding energy is low it may shake itself off the surface. This suggests that the molecule has only a short residence time on the surface before returning to the gas. The rate of departure (desorption) can be expected to follow an Arrhenius type law where the inverse of the rate coefficient is a measure of the average lifetime of a molecule on the surface.

It is possible to estimate the order of this time on the surface: If the 'activation energy' of the desorption process (that is the energy acquired from the surface in order to desorb) is say 25 kJ/mol, and assuming that the pre-exponential factor is of the order of a vibrational frequency of the weak molecule-surface bond, say 10^{12} s^{-1}, lifetimes of the order of 10^{-8}s are predicted at room temperature and these decrease to 10^{-11} to 10^{-12} s as the temperature rises to 1000K or 1500K.

3.5.2 Chemisorption

In chemisorption the molecules stick to the surface as a result of the formation of a chemical and usually covalent bond. The energy of attachment is very much greater than in physisorption, typical values being in the region of 200 kJ/mol. It is possible that a molecule undergoing chemisorption may be torn apart as a result of the unsatisfied valencies of the surface atoms. The existence of molecular fragments on the surface as a result of the chemisorption of whole molecules is one of a number of reasons why surfaces can exhibit catalytic activity. The enthalpy of adsorption may change with the extent of surface coverage. This is, in the main, a result of the interaction between adsorbed molecules: if they repel then the enthalpy of adsorption becomes less negative (less exothermic) as coverage increases.

The desorption of a chemisorbed species is always an activated process because the species have to be elevated

from the foot of a potential well as can be seen in Figures 3.1 and 3.2.
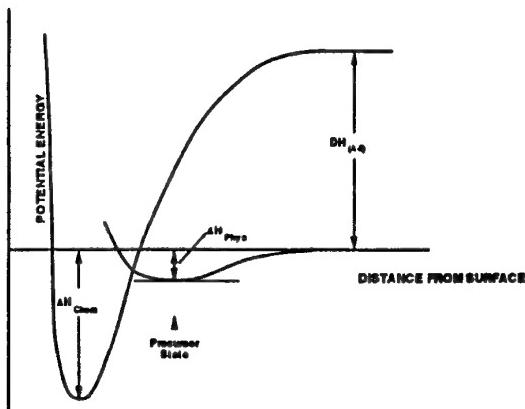
Figure 3.1 Potentail energy Profiles for Chemisorption - zero Adsorption Activation Energy
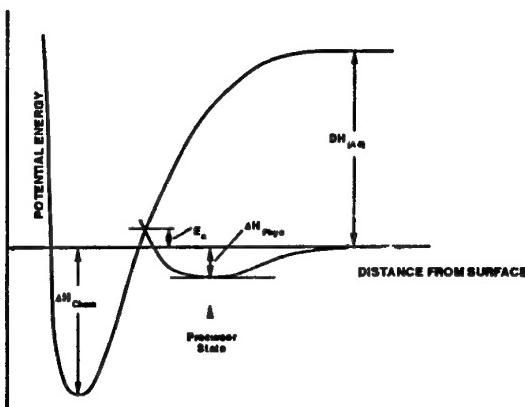
Figure 3.2 Potentail energy profiles for Chemisorption - non-zero Adsorption Activation Energy

The residence time at the surface can be estimated in the same way as for a physisorbed molecule (i.e. with an Arrhenius type law). Here, however, the 'activation energy' is in the region of 100 kJ/mol and an estimate for the pre-exponential factor is of the order 10^{14}s^{-1}. This is justified because the chemisorbed fragments have stiffer bonds to the surface than physisorbed species. This gives a residence time at the surface of the order 3×10^3 s at room temperature and residence times of 2×10^{-9} and 3×10^{-11} s at 1000K and 1500K respectively.

3.5.3 Catalysis

Simply, a catalyst has the effect of increasing the kinetic rate of a reaction without altering the final equilibrium products. In the case of hypersonic flight where high concentrations of dissociated species exist in the shock

layer recombination reactions are likely as the gas cools towards the wall and the presence of a catalyst increases the rate of energy release of the exothermic reaction (although not the total energy release). Where a solid phase catalyst is involved such as a TPS surface then the rate of heat transfer to the catalysis surface will also be increased with a resulting increase in surface temperature which couples back to the rate of the surface reactions. In general this increase in heat flux to the surface is undesirable.

The reason for heterogeneous catalytic activity is the same as for homogeneous catalysis: the catalyst speeds the reaction by lowering the activation energy of the rate-determining step. Therefore, although it does not disturb the thermodynamically determined equilibrium composition of a reaction system, it does increase the rate at which equilibrium is reached, that is it affects the path to equilibrium but not the equilibrium itself. This can be illustrated by reference to Figure 3.3 which demonstrates the possible paths taken by a reaction, catalysed and uncatalysed. Of particular interest here are the activation energies associated with each stage in the catalysed reaction path.
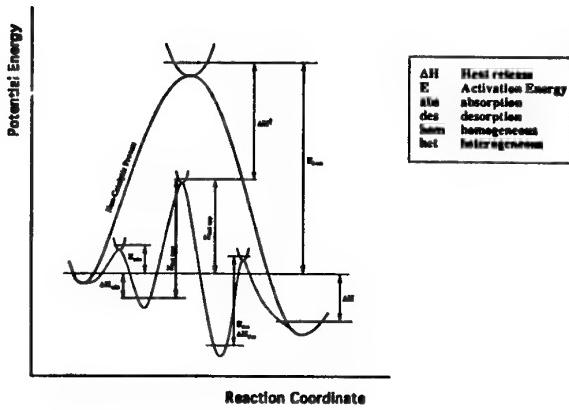

Figure 3.3 Reaction paths for Heterogeneous catalysed and Homogeneous non-catalysed reactions

Illustrated in Figure 3.3 is the fact that adsorption is almost exclusively an exothermic process; that the apparent activation energy of the heterogeneous reaction is less than the actual activation energy as a result of the adsorption step; that the desorption process may be exothermic or endothermic; and that the overall effect of the catalyst is to lower the apparent activation energy.

The basis of much catalytic activity of surfaces is that chemisorption (and sometimes physisorption) organises at least one of the reactant molecules into a form in which it can readily undergo reaction. Often this comes about because the chemisorption process is accompanied by fragmentation. In that case the molecular fragments can be plucked off the surface by an incoming molecule or skip

across the surface until they encounter some other fragment.

Molecular beam studies have shown that catalytic activity of a surface not only depends on its chemical composition but also in some cases on its structure. For instance the cleavage of some bonds appears to depend on the presence of steps and kinks, as illustrated in Figure 3.4, whilst terraces have minimal catalytic activity. The reasons for these effects are not fully understood and are likely to be complex. However they do suggest that catalyst activity may be reduced as these step and kink sites are used up.
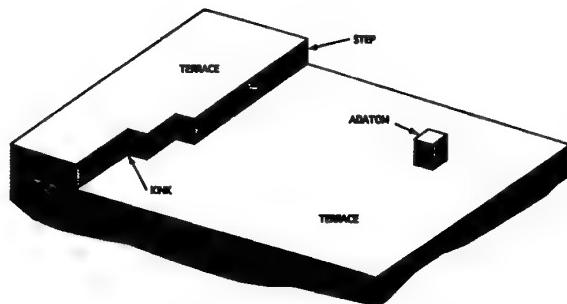
Figure 3.4 Surface defects

The way in which different catalysts act to modify the reaction rates of particular reactions is complex and not always fully understood. Catalysts act in a number of different ways to alter reaction rates. Some simply serve as third bodies carrying away excess energy whilst others serve as templates to hold molecules in certain positions long enough for a rearrangement in molecular structure to occur or for other molecules to find their way to the held species.

Some catalysts act by causing a rearrangement of the reacting species such that their potential energy surface is modified particularly by lowering the potential energy barrier thus altering the activation energy of the reaction. Thus catalysis alters reaction rates but does not affect equilibrium. In hypersonic flight it is the catalytic recombination of dissociated species which is generally of most interest. Recombination of atoms on the surface of the heatshield is seen as a disadvantage in that such reactions are exothermic and the heat of recombination is likely, in part at least, to be deposited into the TPS. Where the boundary layer gases are already in equilibrium then a surface which acts as a good catalyst will have no effect. However as the dissociated atoms approach the cooler body wall then equilibrium will be shifted towards a less dissociated state, i.e. recombination will take place either at the surface or in the boundary layer close to the surface. The heat released from this recombination reaction increases the heat flux to the surface by thermal conduction. Generally the limiting heat flux is associated

with equilibrium conditions and the heat flux to a fully catalytic surface in non-equilibrium flow is approximately the same as this maximum heat flux as has been shown above.

Catalytic effects are closely tied to diffusion processes in that reactions at the surface create a species gradient which drives diffusion to the wall which further increases heat flux.

The main problem here is the scarcity of data for heterogeneous and catalysed reactions.

3.5.4 Mechanisms Of Heterogeneous Catalysis

The classical sequence of events in a surface catalysed reaction comprises:

i) the diffusion of reactants to the surface, usually considered to be fast

ii) adsorption of the reactants on the surface, slow if activated

iii) surface diffusion of reactants to active sites

iv) reaction of the adsorbed species, often rate determining

v) desorption of the reaction products, often slow

vi) diffusion of the products away from the surface.

Processes i) and vi) may be rate-determining where the solid surface is porous. Process ii), the adsorption of the reactants is often rapid, on the other hand process iv), the desorption of the products, must be activated by the heat of adsorption which can be slow particularly at lower temperatures.

One of the reasons why contact catalysis is able to provide a reaction path that is faster than the homogeneous one in the case of bimolecular reactions is that the concentration of the reacting species can be much higher in a surface film than in the gas phase. Consequently a catalysed reaction may be faster purely because of the concentration factor and it is not necessary that the surface reaction is any different in character than the homogeneous one. In many cases however catalysed reactions follow intrinsically different reaction paths and the nature of the solid surface can be unimportant. This is clearly the case with uni-molecular reactions for which the surface concentrations effect is not applicable.

In general the surface geometry of a catalyst appears to affect the activation energies and strengths of adsorption and desorption and to control the nature, concentration and mobility of the surface species. If these surface species are radicals then reaction occurs through various recombination reactions and with a rate enhanced because of the surface concentration effect. Alternatively a catalyst may act by promoting reactions through the formation of intermediates.

More recently the discovery of a third type of adsorbate, neither chemical nor physical (see Table 3.2) but characterised by changes in vibrational frequencies which range from small to very large and by weak bonds have led to a new understanding of catalysis. The quantative description of this third type of adsorbate, the intermedion, requires a new concept of a continuous function relating the vibrational frequencies of molecules and ions to the number of valence or outer shell electrons.

With vibrational frequencies which are intermediate between those of neutral molecules and ions, intermedions have vibrational frequencies which correspond to a non-integral number of electrons, the fraction (perturbation fraction) of which is a constant characteristic of the metallic component and its oxidation state in the adsorbent. Intermedions are thought to be the key to catalysis and have been shown to lead to simple mathematical relationships which designate the catalyst metal, its oxidation state and details of the mechanism of the catalytic reaction. Thus intermedions whilst weakly bonded to a surface as in physical adsorption may show large changes in energy as reflected by the changes in vibrational frequency and consequently may be expected to exhibit significant changes in chemical reactivity. It is the perturbation fraction which is the single property of the metal which is shown to determine its activity as a catalyst, and which has been shown to be the result of the fractional population of the low-lying excited electronic states of metal ions. This theory may well provide an analytical basis for understanding catalytic effects in the future.

Currently in hypersonics, surface catalytic reactions are modelled by assigning to the surface a species recombination probability (γ) and a surface kinetics parameter or catalycity K^w (Figure 3.5). The surface reaction rate is then given as:

$$r = K^w \rho \gamma$$

This recombination probability is the ratio of the mass flux of recombined species to the mass flux of incident dissociated atoms. The γ are temperature dependent and are characteristic of the recombining species and the surface. They are generally independent of pressure and density as most recombination reactions are first order. The γ are generally only available at the elevated temperatures experienced in hypersonic flight for a small number of reactions e.g. nitrogen/oxygen recombination. Data that are available suggests an Arrhenius type expression which leads to an analogy with gas-phase reactions and an energy barrier or activation energy which must be overcome by atoms colliding with the surface. The value of γ are of the order <.01 on ceramic surfaces whilst on metallic, metallic oxide or graphitic surfaces values might be expected to be >0.1 and are normally assumed to be fully catalytic, that is equilibrium exists at the surface.
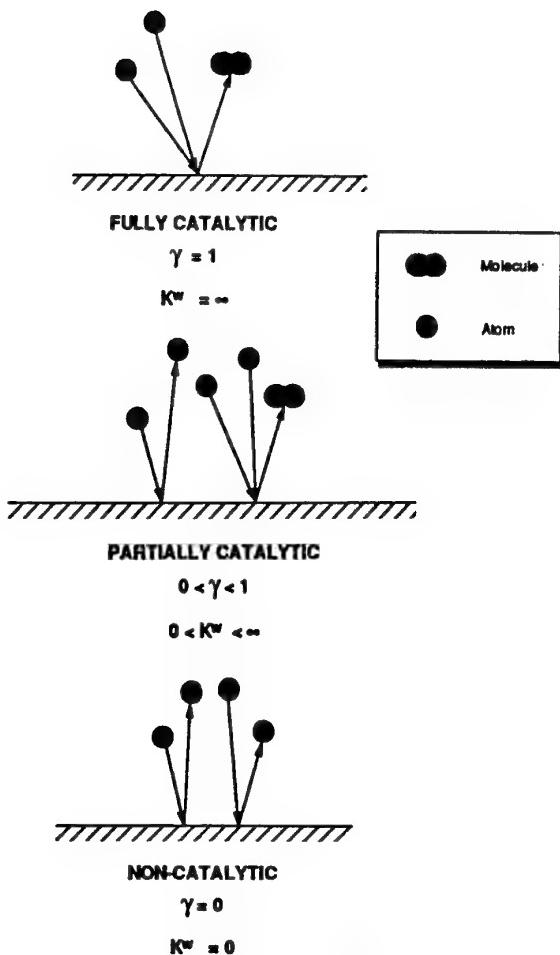
Figure 3.5 Catalyst Surface Recombination

There is evidence to suggest that it is the existence of metal atoms as impurities in otherwise non-metallic TPS which are the primary cause of catalytic activity. Metal atoms need not be present in the surface coating itself as solid state diffusion, which increases exponentially with temperature, would bring these atoms to the surface. This may explain the 'breakaway' phenomena exhibited in the rate of evaporation shown by samples of oxide and nitride coated beryllium when heated as discussed in Section 9. Modelling also needs to take account of incomplete energy deposition when atoms combine on a surface. Observations have shown a lower heat flux than would be expected during surface recombination reactions and that recombined molecules may leave the surface vibrationally or electronically excited. The source of this excess energy is generally thought to be a fraction of the atom recombination energy which remains with the desorbing molecule as internal energy.

To account for this excess energy retained by the desorbing molecules an accommodation factor β is introduced and the energy deposited by the recombination, or other reactions, is thus reduced. β is thus the ratio of the chemical energy deposited into the heatshield to the total energy of dissociation available and can be written as:

$$\beta = \frac{q_{chem}}{m_j \Delta H_{diss}}$$

where q_{chem} is the chemical energy flux, m_j is the mass flux of dissociated species and ΔH_{diss} is the energy of dissociation. Very little is known about β for real space vehicle TPS's consequently restricting its use.

Traditional explanations of surface recombination consider two mechanisms: the Langmuir-Hinshelwood and the Eley-Rideal mechanisms. Both involve the use of 'sites' on the metal surface where clearly defined potential wells or bond locations exist at specific lattice locations. These sites are thought to behave as species in homogeneous reactions with much higher number of degrees of freedom which enable them to dissipate recombination energy very much like third bodies in gas collisions. In the LH mechanism reaction takes place between two adsorbed species whilst the ER mechanism proposes the reaction to be between an adsorbed atom and a gas phase atom. The ER mechanism tends to dominate at lower temperatures due to the low mobility of adsorbed atoms and consequent high probability of collision with in-coming gas atoms.

At higher temperatures where adsorbed atom mobility is high this probability is low and the LH mechanism will tend to prevail. An important conclusion here is that in the ER mechanism the molecule formed by the gas surface collision may leave the surface with a portion of the collision energy. If the time required to break the weak surface-atom bond is shorter than that required to form the molecular bond then the molecule will leave the surface in a state of non-equilibrium. In the LH mechanism the reaction is not one involving collisions and consequently the desorbed molecules will tend to leave in thermal equilibrium and thus the full recombination energy will be deposited into the surface. However there is no way currently of accurately predicting the temperature at which these mechanism switches from ER to LH.

The overall surface reaction involves three steps, adsorption, reaction and desorption. At the elevated temperatures adsorption can be modelled by a first-order Arrhenius process and a half power temperature factor. Until intermedion theory becomes more available realistic predictive techniques for surface reactions will not be possible. Currently surface reactions are modelled by analogy to gas-phase reactions using Arrhenius type expressions. Desorption, particularly at high temperatures, is treated as a second order process. Desorption is then a fast step and often the desorption and reaction processes are considered as one process.

At low temperatures chemisorption is preceded by physisorption and the activation energy is the difference between these two absorption states (see Figure 3.1). At the high temperatures associated with hypersonic flows physical adsorption is much faster and may be neglected. On some metals nitrogen tends to form stable bonds with the metal in an exothermic reaction. In order to desorb from the metal the nitrogen has to climb out of a potential well.

γ for nitrogen recombination on metals can be of the order of 0.1 to 0.2 and metal impurities are thought to be the primary cause of surface reactivity. As previously

discussed solid state diffusion of metal substrata particles through a non-catalysing TPS material can occur at high temperature, a fact which further complicated analysis of catalytic effects.

Typical catalytic recombination reactions and planets where radiative heatshields may be used are :

$CO + O = CO_2$ Mars
$C + O = CO$ Mars
$O + O = O_2$ Mars and Earth
$N + N = N_2$ Earth and Titan

The accommodation coefficient approach allows a specified portion of the energy released in a surface recombination to be imparted to the local flowfield, the remainder forming a diffusive heat transfer component to the wall. The energy released to the flow is assumed to vibrationally excite the gas.

The complete adsorption, surface reaction and desorption properties can be modelled individually:

The adsorption rate w_{ads} is as follows:-

$$w_{ads} = J \, P_{ads} \, (N^*-N)/N^*$$

where:

P_{ads}	is the adsorption probability $(= exp(-E_{ads}/RT))$.
J	is the flux to the surface of
a	toms/molecules undergoing recombinations.
N^*	is the density of surface sites.
N	is the density of occupied surface sites.

This stage is then proceeded by the surface recombination which is described by an Arrhenius form w_r as follows:

$$w_r = k_f [O^*][O^*] \text{ or } k_f [O^*][O]$$

where * denotes a surface adsorbed atom and the absence of * denotes a gas atom.

In the previous equation the case of the surface recombination of oxygen atoms has been considered. The last process to be considered is that of desorption which for the case of oxygen recombination has a rate w_{des} as follows:-

$$w_{des} = k_f [O^*]^2$$

The justification of the form given for w_{des}, when a form such as $w_{des} = k_f [O_2^*]^2$ might have been expected, is that surface recombination and desorption are often thought of as a single process. This assumption simplifies the model and allows an overall form such as that proposed by Langmuir for adsorption to be used.

$$dN/dt = (P_{ads} \, s/(2\pi \, mkT)^{0.5})p(N^*-N)\text{-}f$$
$$exp(-Q/kT)$$

where:

s is the surface area occupied by the adsorbed atom.
m is the mass.
Q is the surface atom/atom bond strength.
f is the desorption probability per unit time.

In summary, of the two approaches described the one most compatible with the gathering of essential empirical data is often preferred. This will most likely lead to the simpler first approach.

Catalytic Computational Example

To illustrate the magnitude of the effects of catalytic activity on the TPS, Figure 3.6 shows for a Marsnet entry vehicle at peak convective heat flux the diffusive and conductive components of heat flux for a fully catalytic wall compared to a non-catalytic wall. The diffusive fluxes caused by the catalytic action are potentially very large. However convincing the TPS designer that this saving can actually be made is quite a different matter and requires extensive materials testing to determine the actual catalytic performance of the TPS in the particular atmospheric environment.
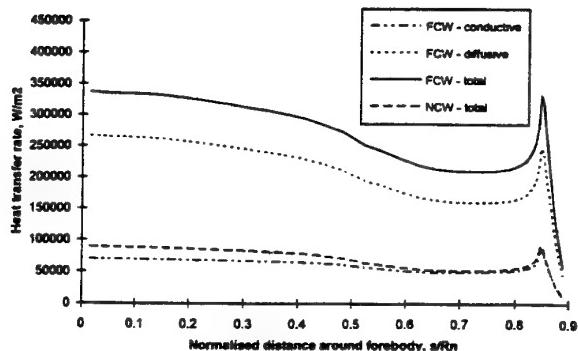
Figure 3.6 Heat transfer rate profile around the Marsnet forebody at peak convective flux

Figures 3.7 and 3.8 compare the species concentrations along the stagnation streamline showing clearly the effect of a fully catalytic wall on the boundary layer chemistry.

Figures 3.9 and 3.10 show the stagnation streamline temperature profiles. It is interesting to note that while the boundary layer temperature profile remains very similar, the shock stand-off increases slightly for the fully catalytic case.
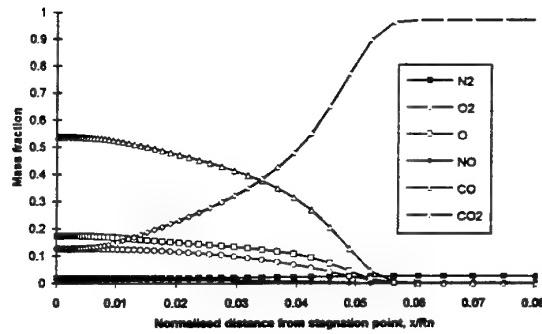
Figure 3.7 Principal species mass fractions along stagnation streamline - non-catalytic wall
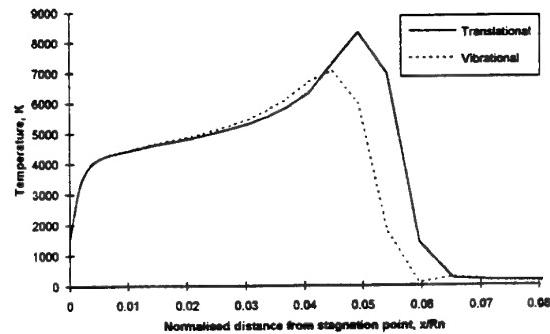
Figure 3.10 Temperature profiles along stagnation streamline - fully-catalytic wall

Finally we note from Figure 3.11 that on the aft cover of such a capsule catalytic activity may be equally important although the magnitude of the fluxes is much lower.
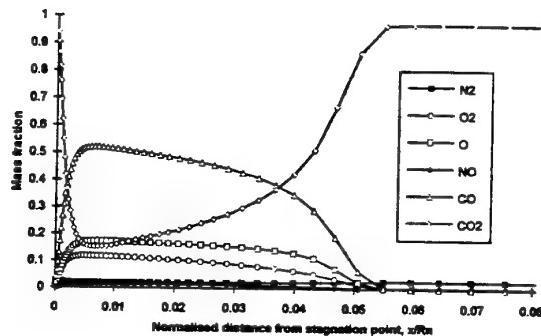
Figure 3.8 Principal species mass fractions along stagnation streamline - fully-catalytic wall
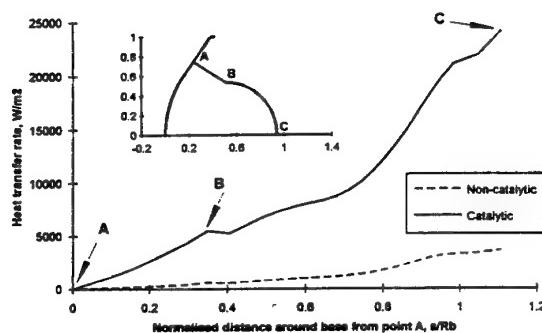
Figure 3.11 Heat transfer rate profile around the Marsnet forebody at peak convective flux

3.6 RADIATIVE FLUX

3.6.1 Radiation Regimes

The determination of the radiative flux incident on the TPS surface is of great importance for capsules during atmospheric entry. The individual radiation mechanisms have been outlined in Section 2, however the emitted energy needs to be transported through the flowfield where it may be re-absorbed prior to reaching the TPS surface or escaping from the shock layer by passing through the bow shock.

Figure 3.9 Temperature profiles along stagnation streamline - non-catalytic wall

Clearly the loss of energy from the flowfield in this way leads to a cooling of the flow, and this energy is taken from the vibrational and electronic energy components. The gas then becomes non-adiabatic in nature. Where

significant absorption is occurring, the flow even if supersonic becomes elliptic in nature because of the upstream transfer of energy.

When the flowfield cooling becomes significant this will alter the chemistry and the resultant radiation thus the processes are truly coupled.

The radiation parameter Γ can be used to determine when coupling is necessary:

$$\Gamma_n = 4\sigma T_s^4 k_s \delta/(\rho_\infty u_\infty h_s)$$

where :

- δ is the shock stand-off distance
- k is the frequency averaged volumetric absorption coefficient
- σ is the Stefan-Boltzman constant
- s subscript are conditions in the shock layer.

Γ_n is the ratio of the radiant energy flux emitted from an optically thin shock layer (the Planck limit) of thickness δ to the enthalpy flux across the shock front. Note that the shock stand-off is proportional to the vehicle radius of curvature so that for stagnation heating, the radiative flux is proportional to the radius of curvature of the TPS (nose radius). This can become a major consideration in entry vehicle design.

For the optically thick cases (known as the Rosseland limit) then:

$$\Gamma_k = 16\sigma T_s^4 k_s/(3\rho_\infty u_\infty h_s)$$

Γ is the ratio of flux to the surface TPS to the enthalpy flux across the shock front.

The approximate radiative regimes are :

$\Gamma < 10^{-3}$	radiation is not important
$10^{-3} < \Gamma < 10^{-2}$	radiation is important but coupling is not necessary
$\Gamma > 10^{-2}$	coupling of radiation to the flowfield is necessary

to evaluate the radiation influence parameter Γ an estimate of k_s is necessary. An approximate relationship is:

$$\tau = \delta k$$

where τ is the optical depth. Since the absorption coefficient is the inverse mean free path until absorption, the optical depth is analogous to an inverse Knudsen number.

Now the transparent gas approximation is acceptable up to an optical depth of about 0.2 while for an optically thick gas the approximation is acceptable until the optical depth of the boundary layer falls below 5.

When the gas is neither thick or thin then the radiant energy flux to the surface is approximated the black body

value, and the ratio of energy flux to the surface to enthalpy flux across the shock is the inverse of the Boltzmann number :

$$Bo^{-1} = \sigma T_s^4/(3\rho_\infty u_\infty h_s)$$

For Earth entry these regime bands are shown in figure 3.12.
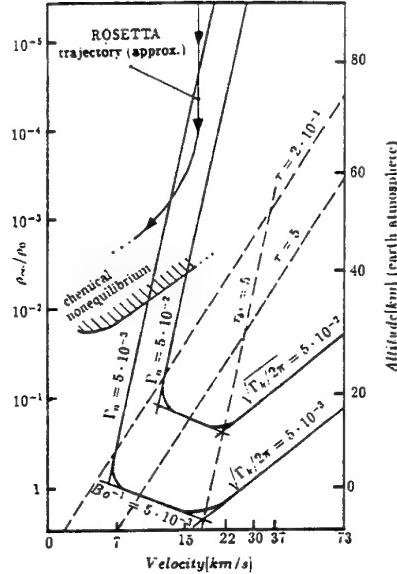
Figure 3.12 Radiative transfer regimes for a blunt body of 0.3m nose radius.

The approximations made to define the radiation interaction are rather sweeping and the effects of non-equilibrium, frequency dependence of the emission/absorption broaden the regime boundaries. Thus this analysis provides an initial guideline. For high speed Earth return, full coupling is required, while for Huygens and Earth-Lunar return radiation is important but full coupling is not strictly necessary, and for Mars entry radiation is not important.

3.6.2 Radiation Transport

The net energy flux at a point in the flowfield is given by the difference between the emission of the gas ε which is a function of local parameters (number densities temperatures) and the absorption of incoming radiation from the surrounding flowfield and is the integral over all wavelengths of the integral over a solid angle of 4π of the absorption coefficient Intensity product $k_\nu I_\nu$

Several simplifications can be made to ease the solution of this relationship:

- assume of an optically thin gas requires only the estimation of emission, but overestimates the flux to the surface.

- assume thermal equilibrium allowing the absorption and emission coefficients to be related through the Planck function;

- treat the shock layer locally as one dimensional - the infinite slab approximation.

However it has been found that the accurate prediction of radiative fluxes is extremely sensitive to the thermal condition of the gas, and thus simplified schemes should be treated with caution.

Assume the radiation from an emitting and absorbing gas is a black body then

$$Bo^{-1} = \sigma T_s^4/(3\rho_\infty u_\infty h_s)$$

and $q_r = \sigma T_s^4/3$

for gas in equilibrium assume:

$$T_s = \sim u_\infty^2/2C_p^*$$

where $h_s = T_s C_p^*$ then:

$$q_r = \sim \sigma\, u_\infty^8/(48\, C_p^{*4})$$

which over predicts for a real situation and therefore

$$q_r \propto u_\infty^8$$

This illustrates then sensitivity of the radiative flux.

3.7 TYPES OF THERMAL PROTECTION SYSTEM

While so far we have considered heat transfer to the surface of the vehicle, one has to consider how to manage this heat load.

The outer layers of the capsule which manage the heat load due to aerothermodynamic heating are called the thermal protection system or TPS. There are several basic mechanisms which are used in the design of the TPS:

- *Re-radiation.* As the surface of the vehicle becomes hotter, much heat can be re-radiated if the surface emissivity is high. TPS systems which rely on this mechanism alone are called Radiative TPS. These are used when the surface temperatures are less than about 2000K, and are usually Carbon or Ceramic based. If the TPS has a very low emissivity/absorbtivity then it acts as a radiative reflector. These type of TPS have been postulated but not used in radiative environments thus far.

- *Conduction.* The hot TPS surface will conduct heat to its interior. Thus for low surface temperatures a high conductivity will enable the surface heat load to be conducted away quickly. Typically these conductive heat shields are metallics such as Beryllium, and due to mass penalties associated with absorbing high heat loads are confined to low heat load regions. Of course the use of high conductivity TPS materials allows the potential use of internal fluids as coolants such as fuel.. For a high surface temperature TPS then the minimum conductivity is required to minimise the heat soaked to the interior.

- *Ablation.* There are three distinct mechanisms of ablation. At very high surface temperature, the surface of the TPS can be expended in sublimation which absorbs energy, at intermediate temperatures however it may oxidise and deposit energy to the surface, additionally the material may thermally degrade in depth absorbing energy and releasing gases which further cool the material as they pass to the surface. Once released from the surface these pyrolysis, and or oxidation and sublimation gases act to block the convective and perhaps the radiative fluxes. This type of TPS is particularly efficient at high surface heat fluxes, and in fact is the only practical solution in many capsule cases.

- *Melting.* Melting of material at the surface followed by its removal due to shear forces removes energy due to the latent heat of fusion, however this is not as efficient as sublimation since the latent heat is lower. Some ablators such as those with Silica may melt at the surface during the ablation process.

- *Blowing.* The introduction of cool gases to the inner boundary layer absorbs heat and thus insulates the surface. These transpiration cooling methods can be particularly useful near sensitive instrumentation ports etc., but generally require too much coolant for whole TPS applications. Also this system is active in that some action needs to be taken to maintain the functioning of the system, and reliabilty and complexity aspects need to be addressed.

These mechanisms may all contribute to a real TPS in part and aerothermodynamic analysis is responsible for the supply of the surface boundary condition to enable the efficient design of a TPS. Since the ablator forms an important class of TPS for capsule entry this will be covered in depth later in the course.

3.8.1 Surface Energy Balance

Of course these mechanisms also exist together, and at the outer surface of the TPS the various heat fluxes to and from the atmosphere and to and from the TPS surface must balance. This surface energy balance may be written using the film coefficient approach as follow:

$k(dT/dy)$ (the conduction from the surface)

$= \rho_e u_e C_h (H_r - h_w)_e$

   (the convective flux to the surface)

$+ \rho_e u_e C_m (h^*_e - h^*_w)_{Tw}$

   (the chemical flux to the surface, including reactions at the surface)

$+ q_r$

   (the radiative flux to the surface)

$+ dm_g/dt\, h_g$

   (the flux from pyrolysis gases arriving at the surface)

$+ dm_c/dt\, h_c$

   (the flux from surface recession arriving at the surface)

. $(\rho v)_w \, h_w$

    (the flux taken by blowing
    from the surface)

- $dm_l/dt \, h_l$

    (the flux taken by liquid phase removal
    from the surface)

$-\sigma \varepsilon T_w^4$

    (the flux leaving by radiation
    from the surface)

Note that from mass continuity at the surface:

$$dm_g/dt + dm_c/dt \, h_c = (\rho v)_w + dm_l/dt$$

The magnitude of the various terms is of primary interest to the TPS designer.

3.8.2 Reduction of Convective Heat Flux by Blowing

The flow of ablation products into the boundary layer provides a boundary condition for the solution of the boundary layer equations whereby a mass flux normal to the wall is present.

For a single perfect gas it is obvious that a component of velocity normal to the wall will decrease the asymptotic gradient of the tangential velocity such that the shear stress at the wall will be decreased:($\tau = \mu \, du/dy$). Also we may expect from Reynolds analogy that the heat flux will also be decreased.

In an ablation or transpiration cooled system the injected gases are most likely to be of different chemical composition to the boundary layer gases. Diffusion and mixing will take place, chemical reactions will occur and energy will be transferred. Thus the process will be complex. For aerothermodynamic assessments it is convenient to use empirical laws and many have been developed. Of course we expect different performance with differing atmosphere and blowing species.

The corrections are made to the Stanton number and are of the form:

$$C_h/C_{ho} = f(B')$$

where C_h is the corrected Stanton number and C_{ho} is the unblown value and B' is the non-dimensional blowing rate:

$$B' = (dm_g/dt + dm_c/dt \, h_c)/(\rho_e u_e C_{ho})$$

A widely used correlation is :

$$C_h/C_{ho} = 2\lambda B'_o/(exp(2\lambda B'_o)-1)$$

where λ is the blowing correction coefficient and is about 0.5 for laminar flows and about 0.4 for turbulent flows. It can be seen that at sufficiently large blowing rates, the convective flux can be significantly reduced. This form is used to correct convective flux if the blowing rate is known. Often the ablation rate is coupled to the heat flux

and so the inverse is of interest to compare blowing effects:

$$C_h/C_{ho} = ln(2\lambda B'+1)/ (2\lambda B')$$

Blowing Regimes can be considered as follows:

- $B'_o < 0.1$, Lightly Blown. Convective fluxes are reduced by less than 5% and the effects can be ignored to first order.

- $0.1 < B'_o < 1$, Moderately Blown. Up to about 40% reduction in convective flux. The flowfield and ablator response can be loosely coupled. ($B' < 2$)

- $1 < B'_o < 4.5$, Highly Blown. The convective flux is reduced by up to 95% and full coupling is likely to be required. ($B' < 100$)

- $B'_o > 4.5$, Massively Blown, These situations occur only in radiation dominated environments such as the highest energy entries to Jupiter etc. Full radiation flowfield TPS coupling is required. ($B' > 100$)

To illustrate this, Figure 3.13 shows the reduction in convective flux for a high speed Earth entry where convective fluxes are reduced by between a factor of 3 and 10. These results were computed in a loosely coupled radiation, fully coupled flowfield and surface ablation.
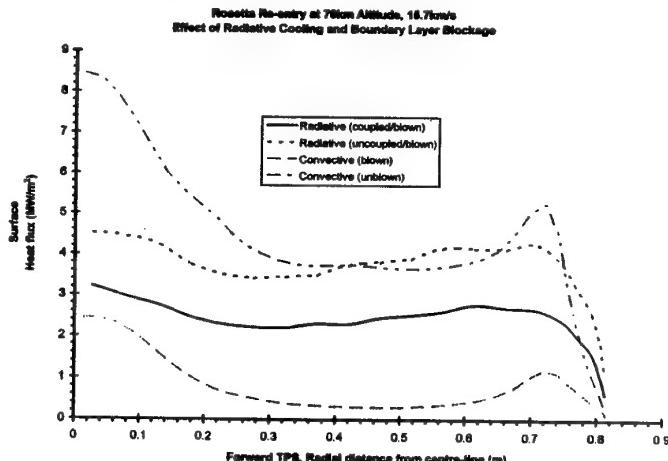
Figure 3.13 Effect of high Blowing rate on the Rosseta entry vehicle.

3.8 ENGINEERING METHODS

For planetary entry assessments simple correlations of the entry flux can be developed based on simplifications of the stagnation flow analysis (of for example Fay and Riddell).

The general form of the correlation is

$$q = k \, \rho^a \, (R_n)^b \, (V/10^4)^c \, (H_r - H_w)/(H_r - H_{300})$$

This may be applied to the radiative flux as well as the convective. Tables 3.3 and 3.4 give typical values of the

constants with limiting conditions. Other values for these constants are abundant in the literature and cover not just the stagnation region but swept cylinders, laminar and turbulent surfaces etc. The accuracy of such correlations can be within 5% of more definitive methods provided sufficient number of ranges are used.

In practice the results of a matrix of boundary layer, full shock layer computations or coupled radiation solutions (usually 1D slab) are curve fitted to provide the constants. In this way the effects of non-equilibrium are taken into account. This may result in altitude (density) and velocity dependant values of the constants.

	k (q in W/cm^2)	a	b	c	range km/s
Venus & Mars	19513	0.5	-0.5	3.04	0 to 16
Earth & Titan	20668	0.5	-0.5	3.15	0 to 8

Table 3.3 Stagnation Convective flux Correlation Constants

	k (q in W/cm^2)	a	b	c	range km/s
Venus	7.7e5	0.52	0.48	9.0	~11
Earth	6.54e6	1.6	1.0	8.5	0 to 8
Mars	3.84	1.16	0.56	21.5	0 to 7
Titan	8.83e8	1.65	1.0	5.6	4 to 7

Table 3.4 Stagnation Radiative flux Correlation Constants

To illustrate the effectiveness of such correlations, it is interesting to look an example. Table 3.5 shows the convective and radiative fluxes at the stagnation point for entry to Venus and Mars.

The velocity at peak convective flux is close to 85% of the entry velocity as expected. The convective correlation developed for Mars entry agrees well with Navier Stokes and boundary layer codes throughout the range but falls below the boundary layer code at high speed due to the influence of ionisation taken into account in the boundary layer code transport properties. This is as expected. The increased effect of blowing on the convective fluxes can be seen, such that for the high speed entry the convective flux can be ignored and the material ablation is radiation driven.

The radiative fluxes agree reasonably well at 11km/s where the correlation was developed from 1D slab equilibrium radiation solutions. The radiative cooling of the flowfield at 14km/s lowers the radiative flux by a factor of about 3 to the value shown.

	Marsnet	Pioneer Large	ESA Venus
V_e m/s	5563	11660	15500
V ($q_{c\ max}$) m/s	4780	9920	13560
q_c W/cm^2 correlation	32	2794	12400
q_c W/cm^2 Integral. b.l. code (ibl)	28	2771	13600
q_c W/cm^2 Navier Stokes	34	2210 (Moss VSL)	
qc W/cm^2 Blown		250(Moss VSL)	184(ibl)
V ($q_{r\ max}$) m/s	5305	10633	13887
q_r W/cm^2 correlation (cooled)	0.21	3635	22170
q_r W/cm^2 coupled (cooled)		2915 (Moss)	

Figure 3.14 Stagnation point heat flux comparison for Entry into CO_2 atmospheres of Mars and Venus

REFERENCES FOR SESSION 3

Fay J.A., Riddell FR., 'Theory of Stagnation Point Transfer in Dissociated Air'
Journal of the Aeronautical Sciences, February 1958.

Fay J.A., Kemp N.H., 'Theory of Stagnation Point Transfer in Partially Ionized Diatomic Gas' AIAA Journal of the Aeronautical Sciences, December 1963.

Kendall R.M. 'A General Approach to the Thermochemical Solution of Mixed Equilibrium - Nonequilibrium, Homogeneous or Heterogeneous Systems'.
NASA CR-1064 June 1968

ENTRY AND VEHICLE DESIGN CONSIDERATIONS

Arthur Smith
Fluid Gravity Engineering Ltd
Chiltlee Manor
Liphook, Hampshire
GU307AZ, UK

SUMMARY

In session 4 we shall look at basic equations of motion of a capsule during its approach and entry and note some relationships between trajectory, vehicle parameters and structural and thermal loads in order to investigate which vehicle characteristics are important in capsule aerothermodynamic design.

Typical entry scenarios are explained including orbital transfer, aerobraking and aerocapture.

Design considerations for a ballistic capsules are explored with reference to Mars, Titan and Earth return, while a lifting capsule trade-off is considered for Earth return.

4.1 ENTRY SCENARIOS

4.1.1 Exo- Atmospheric Trajectory

A spacecraft in the solar system has an absolute velocity V_∞ relative to its launch site dependent on the sum of all the impulses and gravitational effects it has received since launch. When the spacecraft nears a planetary mass, the gravitational field begins to influence the spacecraft, and the spacecraft is accelerated towards the planet. For a simple two body system where velocity is now relative to the new planetary mass the specific total energy is $V_\infty^2/2$ while the local gravity is

$$g = GM_p/(r_p+h)^2$$

This is the differential of the specific gravitational potential function $-M_pG/(h+r_p)$. Thus the specific energy equation for the spacecraft has both kinetic and gravitational potential components:

$$V_\infty^2 = V_e^2 - 2M_pG/(h+r_p)$$

where:

V_∞ is the inertial velocity;

V_e is the entry velocity;

M_p is the planet mass;

G is the universal gravitational constant;

h is the altitude above the surface;

r_p is the planet radius.

Applying this relationship to the launch situation gives the escape velocity :

$$V_{esc} = (2M_pG/r_p)^{0.5} = (2g_or_p)^{0.5}$$

where g_o is the gravity at the planet surface.

Clearly an interplanetary return entry velocity must be equal or greater than the escape velocity. The velocity for a circular orbit is given directly by centrifugal balance as

$$V_{circ} = (M_pG/(r_p+h))^{0.5}$$

Which for low orbit $r_p>>h$

$$V_{circ} = (g_or_p)^{0.5}$$

Which represents 70% of the escape energy.

The amount of energy to be lost in a braking manoeuvre is very large and this must be dissipated by heat. Some of this heat passes into the capsule, but most is given to the atmosphere and this is a necessity given the total specific energy. The total specific energy for several planetary missions is given in table 4.1.

Planet/ moon	Typical entry velocity range V_e km/s	Entry altitude h_e km	Specific energy MJ/kg
Venus	Pioneer 11.5 Mercury orbiter 16	120	66 128
Earth	suborbital: 6 orbital: 8 Lunar return Apollo: 11 Mars/Comet return: 13 to 16.5	120	18 32 61 85 to136
Mars	Viking: 4.5 Marsnet: 6 Mesur: to 8	120	10 18 32
Jupiter	Gallileo: 48		1152
Saturn	25		313
Titan	Huygens: 6 Aerocapture: 8	1000	18 32
Uranus	25 to 26	500	313 to 338
Neptune	24 to 27	450	288 to 365

Table 4.1 Initial specific energy for some atmospheric entry missions

The general form of the energy equation is known as the vis-viva equation :

$$V^2 = M_pG\{2/(h+r_p) - 1/a\}$$

where a is the semi major axis of the trajectory conic.

4.1.2 Aerobraking

To directly sample the atmosphere of a planet or to land on its surface requires the capsule to decelerate from the entry velocity at arrival to a low descent speed. All capsule and probe missions flown to date except the Vikings (lifting entry from orbit) and Apollo Lunar returns (aerocapture to ground) have been of this type.

There are two types of capsule designs, those which are purely ballistic with no means to control the course of the trajectory save changes in drag and those which have a lifting capability where an on-board control system is required to shape the trajectory.

The decision as to whether a ballistic or lifting entry is chosen rests on a trade-off of the requirements:

- deceleration limits (payload sensitivity i.e. instruments, humans or samples);

- atmospheric uncertainties;

- targeting or recovery;

- mass and cost limitations;

- lower ballistic coefficient limit.

It is possible to make a direct aerobraking entry into all of the atmospheres considered subject to the above constraints. For Mars in particular the ballistic coefficient must be low enough to allow a deceleration to the required descent velocity prior to impact. In practice the minimum achievable ballistic coefficient is about 20kg/m2 due to material and complexity constraints.

Thus for the first entries to Mars, Viking had a modest lifting capability to ensure deceleration to parachute deployment velocity at sufficiently high altitude. The Mars atmosphere model had large uncertainties at that time.

For early manned Earth orbital missions a ballistic entry (Mercury, Vostok Voshkod) was used since deceleration levels were endurable (8g) and landing dispersion acceptable for recovery at that time. It should be noted that even Mercury had a control system to initiate spin and maintain zero pitch and yaw to control dispersion and lateral loads. For later missions (Gemini, Apollo) a lifting capsule with roll control was necessary to lower entry deceleration from Lunar return and also provided a means to reduce dispersion and subsequent recovery times due to atmospheric and vehicle performance uncertainties.

4.1.3 Ballistic Entry

We shall now follow the classic approach of Allen and Eggars to examine some of the ballistic entry parameters.

The simple planar equations of motion of a ballistic vehicle are:

$$d^2h/dt^2 = -g + 0.5\rho V^2 AC_d/m \ Sin\gamma$$
$$d^2x/dt^2 = \quad 0.5\rho V^2 AC_d/m \ Cos\gamma$$

where:

x is the downrange direction
A is the vehicle reference area;
C_d is the drag coefficient;
m is the vehicle mass;
γ is the entry angle below the local horizontal.

The ballistic coefficient $m/(C_dA)$ occurs generally in the equations of motion and is shown to be the primary entry vehicle parameter for ballistic entry.

It can be shown that for most ballistic entries the deceleration is much larger than 1g and so to a first approximation the deceleration due to gravity can be ignored. This reduces the equations of motion to a single equation along a straight line trajectory:

$$-dV/dt = 0.5\rho V^2 AC_d/m$$

noting that $dV/dt = -VdV/(dh/Sin\gamma)$ and that for the straight line trajectory $\gamma = \gamma_e$ then the equation of motion becomes:

$$dV/V = 0.5\rho AC_d/(mSin\gamma_e) \ dh$$

assume an exponential atmosphere:

$$\rho = \rho_o \ exp(-Bh)$$

where B is the inverse of the scale height H

then:

$$dV/V = 0.5\rho_0 AC_d/(mSin\gamma_e) \ exp(-Bh) \ dh$$

Integrating and noting that at high altitude
$V = V_e$ the general equation for velocity is determined:

$$V = V_e exp(-0.5\rho_0 AC_d/(Bm \ Sin\gamma_e) \ exp(-Bh))$$

the deceleration is then

$$-1/g_o \ dV/dt = 0.5\rho_0 AC_d V_e^2/(mg_o) \ exp(-Bh)$$
$$exp(-\rho_0 AC_d/(Bm \ Sin\gamma_e) \ exp(-Bh))$$

the altitude at maximum deceleration is therefore:

$$h_m = 1/B \ ln(\rho_0 AC_d/(Bm \ Sin\gamma_e) \ )$$

and the velocity at maximum deceleration is

$$V_m = V_e \ exp(-1/2) = \sim 0.61 \ V_e$$

with maximum deceleration

$$(1/g_o \ dVdt)_{max} = 0.5BV_e^2 \ Sin\gamma_e/(g_o e)$$

It is clear that the maximum deceleration is independent of the physical characteristics of the entry vehicle and depends only on entry speed and flight path angle. The vehicle speed at maximum deceleration bears a fixed relationship to the entry speed (~61%), while the corresponding altitude depends on the physical characteristics and flight path angle but not on the entry speed.

In practice the above equations are limited to entry angles greater than five degrees, since these equations predict zero deceleration for a zero degree entry angle when in fact the minimum achievable is about 8g for an Earth entry. More detailed analysis should be undertaken with a three degrees of freedom simulation of the full equations rather than pursuing higher order closed form solutions since with modern computers numerical simulation is very fast.

Turning attention to heating of the body then if we make the following assumptions for the entry vehicle:

Convective heating only;
Calorifically perfect gas;
Unity Prandtl Number;
Reynolds Analogy,

then the heat transfer coefficient at position x on the vehicle can be determined in relation to the friction coefficient from simple Reynolds analogy.

$$h_{cx} = 0.5\rho_x V_x C_{fx} C_p$$

if we assume that T_r-T_w is constant over the whole vehicle and $T_w \ll T_r$ then

$$q_{cx} = \sim h_{cx} V^2/(2C_p), \qquad dh/dt = VSin\gamma_e$$

and

$$dQ/dh = -0.5V/(2C_p Sin\gamma_e) \rho_x V_x C_{fx} C_p dS$$

where Q is the heat transferred to the whole vehicle and S is the vehicle wetted surface area

rewrite this as

$$dQ/dh = -0.5\rho V^2 SC_f'/(2Sin\gamma_e)$$

If we assume that C_f' is constant then :

$$dQ/dh = -0.5\rho_0 V_e^2 SC_f'/(2 Sin\gamma_e) exp(-Bh)$$
$$exp(-\rho_0 AC_d/(Bm Sin\gamma_e) exp(-Bh))$$

this equation is directly comparable to the deceleration equation.

Total Heat Load

Integrating from entry until impact gives the total heat load to the vehicle:

$$Q = 0.5mV_e^2 C_f'S/(2C_d A)$$
$$(1-exp(-\rho_0 AC_d/(Bm Sin\gamma_e)))$$

From the velocity equation the velocity at impact ($h = 0$) is

$$V_i = V_e exp(-0.5\rho_0 AC_d/(Bm Sin\gamma_e))$$

and so the total heat input may be expressed as:

$$Q = 0.5m(V_e^2 -V_i^2)C_f'S/(2C_d A)$$

however V_i is effectively zero for scientific and manned entries and so

$$Q = 0.5mV_e^2 C_f'S/(2C_d A)$$

Since many simplifying assumptions are made then only comparative remarks can be made for the heating relationships.

To obtain the least heating the factor

$$B = \rho_0 AC_d/ (Bm Sin\gamma_e)$$ is relevant

For a heavy vehicle $B \ll 1$ and

$$Q = \sim 0.5\rho_0 V_e^2 SC_f'/(2BSin\gamma_e)$$

then the entry vehicle passes through the atmosphere with little retardation (ie a slender vehicle), and thus the skin friction is the main contributor and should be minimised.

For a light vehicle $B \gg 1$ and

$$Q = \sim 0.5mV_e^2 C_f'S/(2C_d A),$$

In this case the total heating is reduced by increasing the drag provided that the skin friction does not increase in the same proportion, (i.e. small wetted area S). This physically means that the fraction of kinetic energy given to the missile is $C_f'S/(2C_d A)$, the remainder is transferred to the atmosphere. These are the essential design criteria for the light blunt body entry vehicle.

Heat Transfer Rate

The heat transfer rate to the whole vehicle surface is given by

$$q_c = 1/S dQ/dh dh/dt$$

where $dQ/dh = -0.5\rho V^2 SC_f'/(2Sin\gamma_e)$

therefore

$$q_c = 1/4 \rho V^3 C_f'$$

or in terms of the entry quantities

$$q_c = -\rho_0 V_e^3 C_f'/4 exp(-Bh)$$
$$exp(-3\rho_0 AC_d/(2Bm Sin\gamma_e) exp(-Bh))$$

The velocity for maximum heat transfer rate to the whole body occurs at

$$V = V_e \, exp(-1/3) = \sim 0.72 \, V_e$$

at altitude

$$h = 1/B \; ln(3\rho_0 AC_d/(2Bm \; Sin\gamma_e) \,)$$

Analysis of the stagnation point convective heat flux by assuming a laminar incompressible relation between Nusselt, Reynolds and Prandtl number and a viscosity proportional to $T^{0.5}$ leads to the relationships for maximum stagnation point heat transfer at:

$$V = V_e \, exp(-1/6) = \sim 0.85 \, V_e$$

at altitude

$$h = 1/B \; ln(3\rho_0 AC_d/(Bm \; Sin\gamma_e) \,)$$

The relationships for stagnation heating have been discussed in Section 3 and can be used with the above conditions to give reasonably accurate results.

It is clear that the vehicle speed at maximum heat flux bears a fixed relationship to the entry speed (~72 to 85%), while the corresponding altitude depends on the physical characteristics and flight path angle but not on the entry speed.

Entry Corridor

If the entry angle is too shallow then the entry vehicle may not lose enough energy and the vehicle will pass through the atmosphere and escape to orbit (as in orbital transfer) or escape completely. This critical angle is termed the skipout angle or overshoot boundary. If the vehicle enters too steeply then large deceleration and peak thermal flux may cause failure. This is called the undershoot boundary. The difference between the two can be thought of as the entry corridor for ballistic vehicles.

For a high energy entry the undershoot boundary to limit the deceleration (on a human crew for example) may be above the overshoot boundary thus the entry is not viable with a ballistic vehicle. In this case some means to raise the overshot boundary needs to be found. Clearly reducing the velocity by chemical propulsion may make the corridor width real. However the use of vehicle lift has the same effect since the undershoot boundary may be lowered by employing upwards lift and the overshoot boundary raised by employing downwards lift (i.e. inverted flight).

For the ballistic vehicle it can be shown that once the flight path angle changes sign, the vehicle will skip out.

V_e, γ_e Map

For ballistic entry it is common to express the performance envelope in the form of a V_e ,γ_e map onto which various vehicle design limits can be placed. As an example we shall look at the map developed for an ESA study of a cometary encounter and sample return vehicle 'Caesar' shown in figure 4.1,.
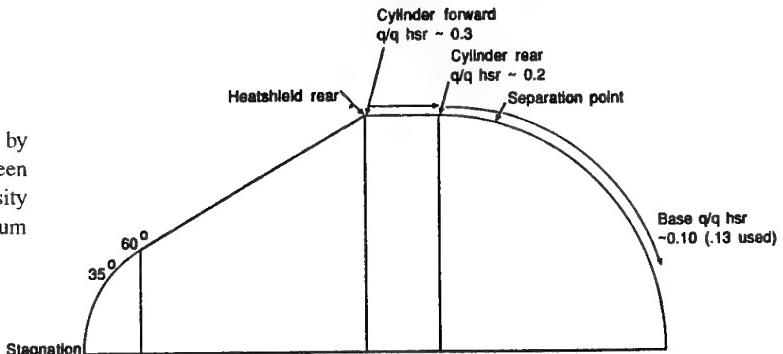

Figure 4.1 Caesar Earth Return Capsule

The initial concern was to limit entry deceleration to 50g to avoid sample crushing. The map of deceleration is shown in figure 4.2 for the range of return velocities being considered. The left hand boundary is the skip out boundary, and the right hand the maximum deceleration. The complete map to -90 degrees is shown in figure 4.3. The entry maximum entry load was increased during the study to 200g.
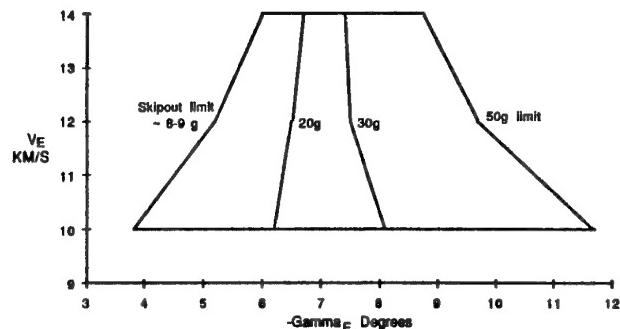

Figure 4.2 Initial Caesar V_e ,γ_e Map

The final design map is shown in figure 4.4. The right hand limit is still the maximum deceleration (now 200g) but considerations of heat soak into the heatshield and consequent TPS and insulation thickness led to the deletion of the shallow entry angles including skip entries. Thus the left hand limit is now a heatsoak limit.

For a given velocity the heat soaked into the vehicle surface is dependant primarily on the re-entry time and thus the shallowest lowest velocities impose this design limit, designated lower left. (LL in figure 4.4). As the entry velocity is increased then the total heat load increases and the maximum occurs for the fastest shallowest entries designated upper left (UL). Finally the maximum heat transfer rate occurs for the fastest steepest entry designated upper right (UR). These are the main aerothermal design cases to be considered for a ballistic

entry vehicle and will determine TPS type and mass, as well as primary structural strength.
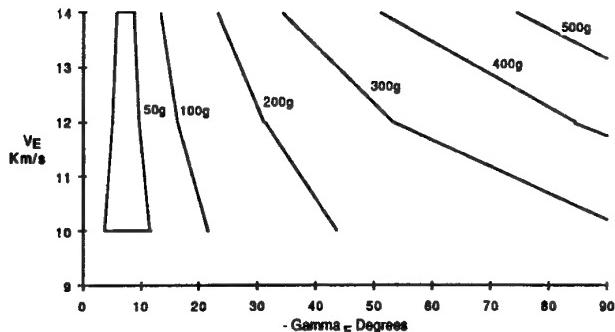

Figure 4.3 Complete Caesar V_e, γ_e Map
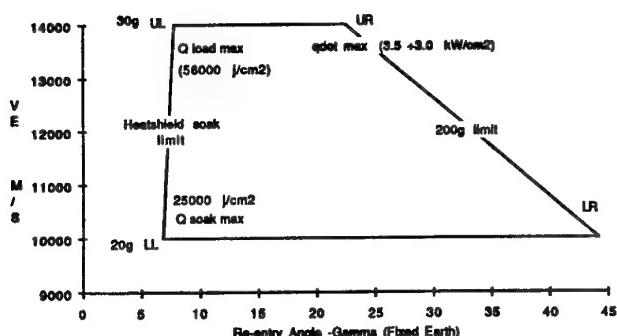
Figure 4.4 Final Caesar Design V_e, γ_e Map

4.1.4 Lifting Entry,

Again follow the classic approach of Allen and Eggars to examine some of the lifting vehicle entry parameters.

The simple equations of motion of a simple lifting vehicle are those of the ballistic vehicle with additional terms for the lift. If we assume that the vehicle has a ratio of Lift to Drag L/D the equations of motion for the lifting vehicle with spherical Earth are:

$$d^2h/dt^2 = -g+V^2/(r_p+h)$$
$$+ 0.5\rho V^2 AC_d(Sin\gamma + L/DCos\gamma)/m$$

and

$$d^2x/dt^2 = 0.5\rho V^2 AC_d(Cos\gamma - L/DSin\gamma)/m$$

these may alternatively be cast as:

$$d(V^2/(g(r_p+h))/d\rho =$$
$$V^2 AC_d/(mg(r_p+h)BSin\gamma) + 2/\rho(r_p+h)B$$

and

$$d(cos\gamma)/d\rho = L/D\, AC_d/(2Bm)$$
$$- (g(r_p+h)/V^2 - 1)Cos\gamma/(\rho B(r_p+h))$$

Simplifying the flight equations for a lifting vehicle by assuming a shallow entry ($sin\gamma = \gamma$ and $Cos\gamma = 1$ and $d(cos\gamma)=\sim0$ give:

$$V^2/(g(r_p+h)) =$$
$$1/[1+0.5(r_p+h)\rho_0 AC_d/m\, L/D\, exp(-By)]$$

This is the equilibrium glide result where the gravitational force cancels the sum of the centrifugal and lift forces. The flight path angle becomes

$$\gamma = -2/[B(r_p+h)(L/D)(V^2/g(r_p+h))]$$

and is typically -1 degrees. The tangential deceleration during equilibrium glide is:

$$a/g = (V^2/g(r_p+h)-1)/(L/D)$$

Note that equilibrium glide is appropriate to entry from orbit since :

$$V^2_{circ} = g(r_p+h)$$

Therefore superorbital entry implies negative lift i.e. inverted flight.

It is seen that the deceleration increases as velocity is reduced and that even moderate L/D can reduce the deceleration significantly. For example the Gemini capsule with L/D about 0.2 enabled the peak load to be reduced to about 5g compared to the 8g of the Mercury ballistic entry along the same initial flight path. For Shuttle with L/D about 1.1, the deceleration is reduced to 1g.

The range of the equilibrium glide phase is determined as:

$$s = 0.5r_p(L/D)ln(1/(1- V^2_e/gr_p))$$

and maximum range is achieved with maximum L/D. A cross range capability is available if the vehicle is rolled through an angle σ and using an equilibrium glide assumption then

$$\phi = (\pi^2/48)(L/D)\, Sin2\sigma$$

where ϕ is the change in latitude relative to the initial great circle entry plane. A bank angle of 45 degrees gives the optimal cross range since half of the L/D is given to cross range and half to keep the vehicle in the air. Again maximum cross range is gained with maximum L/D, and this equation is reasonably accurate for L/D up to 1.5.

The equilibrium glide is not the only lifting entry of interest since at superorbital speed skip trajectories may be used where sufficient energy is lost prior to an exit from the atmosphere at suborbital velocity followed by a second suborbital entry. This is a form of aerocapture and was studied for Apollo.

Alternatively the vehicle lift can be used to keep the vehicle in the atmosphere until velocity is suborbital when the vehicle may be rolled 180 degrees. This was adopted for Apollo and was used in ESA studies for the Rosetta lifting capsule.

Heating relations for the lifting entry can be derived in a similar manner for ballistic entry and for the equilibrium glide vehicle the maximum average heating rate to the whole vehicle occurs at

$$V = (gr_p/3)^{0.5}$$

which if we assume that entry occurs from a circular orbit ($V^2_e = \sim gr_p$)

$$V = 0.55 \, V^2_e$$

This occurs at altitude:

$$h = 1/B \, ln(L/D \, r_p\rho_0 AC_d/(4m))$$

The velocity at maximum heat flux is a fixed ratio of the (glide) entry velocity, while the altitude depends on the ratio of L/D to ballistic coefficient

4.1.5 Orbital Transfer

Studies of orbital transfer techniques to lower energy orbits have been made using atmospheric braking.

In 1990 the spacecraft Magellan used the atmosphere of Venus to circularise its orbit due to a lack of onboard fuel. This was achieved in 840 passes losing only 1.5m/s per pass. Magellan was not designed for this purposed but has demonstrated the feasibility of such manoeuvres to save fuel.

The low velocity decrement on each pass makes the navigation and control of such manoeuvres relatively straight-forward since errors can be corrected in successive passes. Such manoeuvres require only vehicle drag (i.e. a ballistic vehicle) since orbit is assured and a deep entry is avoided in any case. Maximum deceleration using a deployable brake is likely to be in the order of 0.1g for future aerobraking spacecraft designs.

An interplanetary spacecraft would use chemical propulsion to insert itself into a highly elliptic orbit and then use a small apoapsis burn to lower periapsis into the atmosphere after radio occultation data had revealed the atmospheric profile. A chemical propulsion periapsis raise manoeuvre halts aerobraking when the orbit is slightly elliptic (say 5:1). Control becomes more difficult with longer time spent in the atmosphere as the errors due to unknown atmosphere variability mount, and of course complete circularisation within the atmosphere would lead to entry.

The accuracy of prediction of the drag in the rarefied flow regime is sufficient to predict successive periapsis altitudes to within about 1 km for about five orbits ahead. The limits imposed for excess heating at too low a periapsis probably require predictions to within about 3 km altitude. However the analysis can be calibrated accurately by onboard accelerometers.

The disadvantages of orbital transfer by aerobraking are the long time required for multiple passes, and of course an orbital velocity must already have been achieved. Thus the technology is suitable for missions where only a small performance margin over the initial propulsive manoeuvre to orbit is required.

The analysis of orbital transfers with aerobraking is very similar to the analysis using chemical propulsion with the addition of a time varying drag force dependent on velocity and altitude. Such schemes are outside the scope of the present course.

The US AFE was a vehicle design to explore the single pass orbital transfer or low performance aerocapture and had a lifting capability to control the energy lost. For a high margin over propulsive systems and short time scale of operations and indeed for hyperbolic arrival the single pass orbital transfer or aerocapture may save propulsive mass up to twice the payload in orbit.

4.1.6 Aerocapture

On arrival at a planetary destination, the spacecraft may be required to manoeuvre into an orbit in order to make scientific measurements, drop probes or relay information. In all missions to date this has been carried out using chemical propulsion systems in a periapsis retro-burn to slow the spacecraft down to orbital velocity. This may be followed by minor orbital transfer manoeuvres again using chemical propulsion.

The transport of the required propulsion system and more importantly the propellant is a mass expensive solution. Many studies have been carried out into the use of the planetary atmosphere to provide the means to lose the required amount of energy.

Aerocapture is achievable with low L/D provided the entry corridor is large enough. In general a large (compared to capsules) L/D is required to achieve an aerocapture to orbit with large superorbital arrival velocity. Since all the excess energy is taken out in one pass, this requires precise control during the atmospheric pass and a higher level of technology compared to direct aerobraking or orbital lowering.

The vehicle uses its lifting capability to maintain a constant drag in the continuum flow regime until the desired velocity is reached. The vehicle then pulls up above the atmosphere and at apoapsis uses a small chemical propulsion burn to raise periapsis above the atmosphere. Alternatively the vehicle may remain in the atmosphere and decelerate to descent speed. Apollo's Lunar return was an aerocapture to ground from 11km/s and achieved this with $L/D \sim 0.3$ and within 12g deceleration. Aerocapture to Earth of high speed comet or planetary return capsules has also been studied at speeds up to 17km/s and is also possible with modest 0.3 L/D.

The modulation of the lift is achieved by either pitch control or by rolling a fixed *L/D* vehicle. The latter method simplifies vehicle design but requires greater attitude changes because bank reversals must be used to equalise the effects of the out of plane lift on the cross range.

The rationale for following a constant drag profile as opposed to a position, velocity or entry angle profile (i.e. a constant flight path angle also assures entry) is because on-board accelerometers can easily measure drag directly whereas estimates of position require more sophisticated techniques and integrations which may compound errors. Also variations in the atmosphere can be accounted for directly. For aerocapture to orbit then prediction of the time to pull up is also simplified and use of full pull up is desirable to shorten the exit phase in an essentially uncontrolled final manoeuvre.

Aerocapture to orbit in this manner applies to almost all atmospheres but performance advantages diminish for planets with masses larger than Uranus due to the large TPS mass requirements. However this could be overcome to a certain extent at least for Saturn by using an atmosphere bearing moon such as Titan to perform the capture to Saturn orbit.

Three factors determine the aerocapture aerodynamic shape and performance characteristics

- volumetric efficiency

- accuracy

- vehicle mass

The accuracy requirement essentially sets the *L/D*. During the initial entry the vehicle must have sufficient *L/D* for control to keep the drag constant and avoid under or overshoot, either of which would be disastrous. *L/D* defines the width of the corridor, and increasing *L/D* widens the corridor to a certain extent. Aerocapture accuracy increases with increasing *L/D* until it reaches a maximum at about 1.5.

Low ballistic coefficient $(M/(C_dA))$ vehicles generally have low *L/D*. For example the US manned capsules (sphere segment with offset cg) with *L/D* 0.18 to 0.3 (Gemini Apollo), raked cones and cones with offset cg 0.14 to 0.28 (AFE and Viking).

High *L/D* (>1.) vehicles generally have high ballistic coefficients such as Shuttle, Buran. Lifting bodies such as Hermes, Bor HL10/20 etc. are in between.

The vehicles most often proposed for aerocapture missions are bent biconics and assume the geometric ratios of 2:1 for forward/aft cone angle and aft length over forward length for a maximum *L/D* of 1 to 1.5.

In the remainder of the course we shall consider capsules i.e. either ballistic for joint science missions or low *L/D* for manned entry such as ACRV, MSTP Mars return etc.

The entry corridor achieved is the result of exo-atmospheric manoeuvres in response to the onboard guidance, navigation and control system. In general the entry corridor is measured as an altitude band normal to the hyperbolic approach velocity vector asymptote. This is then related to the entry angle γ_e by :

$$Cos\ \gamma_e = B/(r_p+h)\ \{1+2GM_p/((r_p+h)V_e^2)\}^{-0.5}$$

where *B* is the altitude in the B plane to the intersection of the asymptote of the hyperbolic trajectory. The B plane is a plane containing the planet centre and normal to the asymptote of the hyperbolic trajectory.

Thus the navigation, guidance and control system must be capable of delivering the entry vehicle into the corridor for which it is designed. The achievable direct entry corridors range from about a degree for Earth, Mars and Venus to about 10 degrees at Uranus where the scale height of the atmosphere is large due to the low molecular weight.

It is clear that the vehicle maximum *L/D* will be required to perform at and recover from the extremes of the entry corridor.

4.1.6 Manoeuvre During Entry

Manoeuvring systems can be grouped into two main types. Firstly, there are the bank-to-turn concepts, which roll the vehicle and use pitch plane generated lift to provide the manoeuvring capability. Such systems require separate roll control and pitch control devices, an example being the single windward flap designs. In these designs, the roll control can be provided by roll thruster, control surfaces or internal moving mass, and the windward flap itself can be split to generate a roll torque. The second main type of manoeuvring system is the skid-to-turn concept, which use full roll, pitch and yaw control. Examples of this type of system are missiles with cruciform control surfaces. Such systems provide full 6D control of the vehicle attitude in flight, but are usually more complex have aerodynamic heating problems and may be heavier compared to the bank-to-turn concepts. The concepts used for capsules have all been bank to turn

Aerodynamics Of The Manoeuvre

A capsule will generally be designed to fly at maximum L/D, and so the roll control system provides the primary control mechanism for entry.

To achieve the required static incidence two moments must come into balance. These are the control moment and the vehicle restoring moment. The former is generated by the control force comprising normal lateral and axial components, all of which act about the vehicle centre of gravity. Clearly the relative magnitude of the moments at a given attitude depends on both the magnitude of the forces and the length of moment arm.

Here some common systems are described and their limiting characteristics identified.

- **Windward Flap.** The windward flap is conventionally located at the rear of the vehicle usually on a body slice. It is deployed as a reverse acting mechanism in that it is deployed into the flow to achieve zero trim and retracted to achieve a given trim. By splitting the flap roll moments can be induced thus combing pitch and roll control. Hinge moments and aerothermal response are the main design driver interests here. In the case of aerothermal response, this includes non-equilibrium effects, separation and attachment heating (and for an ablator shape change).

- **Bent Nose.** The bent nose vehicle achieves its control by inducing vehicle camber. The nose may be bent by conventional hinge which involves a complex joint or by a simpler rotational mechanism.

- **Jet Interaction.** Here a transverse jet is used to provide the control moment. An augmentation of the control moment is afforded by the interaction of the jet and hypersonic shock/boundary layer. The system has the advantage of also being used for exo-atmospheric attitude control. Accurate analysis of the augmented control force is difficult to estimate but generally a factor of 2 is used.

- **Moving Mass.** By moving the centre of gravity out of the pitch plane, then a roll torque is induced due to the offset lift. This system of course requires a moving internal mass say along a track near the vehicle maximum diameter and accrues no aerothermodynamic penalty.

4.2 BALLISTIC ENTRY VEHICLE DESIGN CONSIDERATIONS

In this section some of the background to the early configuration issues for the Huygens, Marsnet and Rosetta Earth return entry vehicles is given as a guideline to the design considerations for ballistic capsule entry. So far of course only the Huygens Probe is destined to fly.

The forward aeroshell of some ballistic Probes is shown in figure 4.5. Significant differences in geometric features are apparent due to differing design criteria and philosophy.

4.2.1 Vehicle Design Philosophy

The design of the entry vehicle needs to fulfil the demanding requirements of the mission. The mission environment consist of the following phases:

- Assembly and Test
- Transport and Integration

- Launch
- Inter-planetary Cruise
- Hypersonic Entry
- Supersonic/Subsonic Descent
- Landing/Impact
- On-surface performance

The environment effectively imposes engineering constraints on the overall design, and possibly of greatest interest is the hypersonic entry which lasts only a few minutes but can dictate most of the aeroshell configuration and a large proportion of the mass budget.

As well as the environment the remaining engineering constraints are provided by time-scales, both launch opportunity and mission lengths, and most importantly in these times, costs.

The cost driver has become predominant for these tightly budgeted missions and has had a great influence on the designs.

This influence has been subjective at early stages of the projects and has resulted in the adoption of the following philosophy which should allow the maximum confidence in performance at the earliest possible time. This is particularly important at pre-feasibility stage.

- Adoption of ballistic entry where possible (no guidance)

- Simple generic shape to take maximum advantage of existing aerodynamic data, and to simplify analysis.

- Interpolation within the existing data where possible rather than extrapolation. This may lead to sub-optimal design, but higher confidence.

- Maximum commonalty in geometry between missions, such that the confidence in performance is built up and common problems are more likely to be discovered.

4.2.2 Entry Dynamics

Before considering the aerothermodynamic problems, it is instructive to look at the simple rules which contribute to the commonalty in entry design.

Consider the ballistic entry vehicles so far defined for the three missions. All are separated on direct approach to the planet, and to preserve their attitude for entry are spun slowly at separation.

Since the separation can occur several days prior to entry, nutation of the motion is to be avoided, and as such the principal inertial axis should be arranged to be the spin axis.

ESA Venus 45 degree sphere-cone (= Pioneer & Galileo)
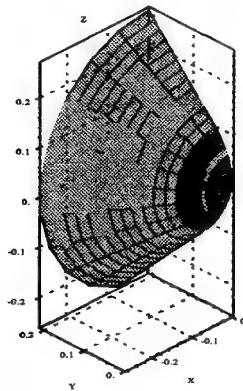
Earth return 60 degree sphere-cone (55g)
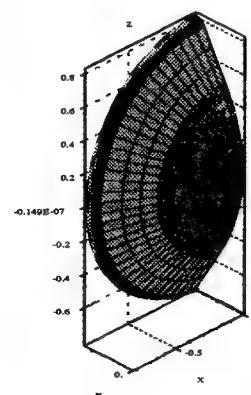
Huygens 60 degree sphere-cone
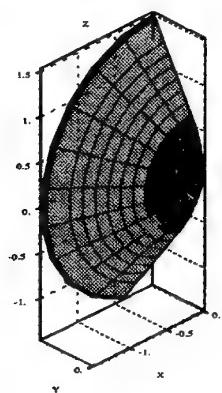
Viking 70 degree sphere-cone
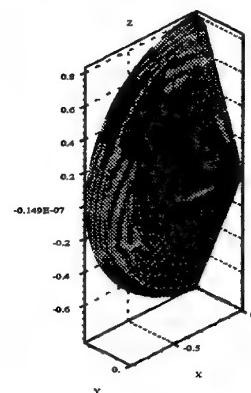
Earth Return 60 degree sphere cone (100g)
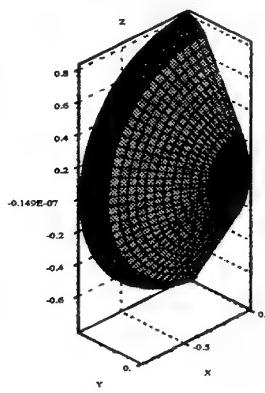
Venus (Mercury Orbiter) Torus
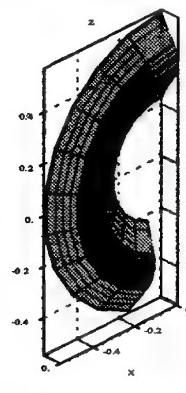
Figure 4.5 Forward Aeroshell of Some Ballistic Vehicle Designs (Note Viking is lifting but similar geometries are studied for ballistic entrty)

The vehicle enters the atmosphere at an angle of attack which is a combination of exo-atmospheric coning motion and the inclination of the coning axis to the trajectory velocity vector. The coning motion is caused by the separation tip-off errors from the spacecraft at spin eject time, combined with the mass characteristics of the body, principally the dynamic imbalance. During entry as the body experiences atmospheric forces, an aerodynamic moment is generated which acts to decrease the angle of attack. The motion becomes gradually more dominated by the aerodynamic forces and less by gyroscopic effects. The entry vehicle begins to respond in a pitching motion. As the aerodynamic stiffness increases, the angle of attack envelope is reduced. This motion is damped by the dynamically induced aerodynamic force generated called the pitch damping force. After peak dynamic pressure the angle of attack envelope would again increase, however due to the damping of the pitching motion, the angle of attack continues to reduce and becomes asymptotic to the static trim angle of attack.

Blunt cones exhibit a pitching reinforcing (positive) damping force in the transonic to low supersonic regime and while this does not effect the hypersonic entry phase, it is important to note that the destabilising coefficients are maximum for the blunter configurations, and the effect must be considered for the supersonic-transonic motion which may include parachute deployment or aeroshell/decelerator jettison sequences. Also of note is that the destabilising coefficients reduce with increasing angle of attack, such that by 20 degrees incidence the damping coefficients again act to reduce the pitching motion.

Structural modes should be well clear of the pitch or spin frequency to prevent any aeroelastic coupling. For the high atmosphere deceleration, low spin rate entries, the frequencies are of order a few Hz, and major structural modes are well above these, for the current designs.

On entering the atmosphere, it can be arranged that the spin axis is aligned with the velocity vector, however a small angle of attack is allowable, 15 degrees maximum has been used for all three missions. This is chosen for several reasons :

- The vehicle aerodynamics are not well characterised above 30 degrees incidence.

- Allowance has been included for exo-atmospheric coning motion.

- Large lateral forces are not desirable.

- Cyclic heat flux variations are not desirable.

- Large pitch angles are not desirable for atmosphere analysis from trajectory data.

Effect Of Asymmetries On Vehicle Motion

a) Centre Of Gravity Lateral Offset

A centre of gravity (cg) lateral offset from the geometric central (spin) axis is normally due to the accuracy of the static balance and leads to both the offset of the principle rotation axis from the geometric centreline and to the generation of a trim angle of attack during atmospheric entry. With the very statically stable entry vehicles considered, (the static margin is about 50-60% of the base diameter) the consequences of cg offset on the trajectory are small and any initial angle of attack is quickly damped to the trim angle of attack. The main consequence of cg offset alone is lateral accelerations which have been shown to be very small, and as a small roll damping effect which always acts to reduce the spin rate. The resultant static trim angle of attack for the Huygens Probe for example is under four degrees for every centimetre lateral cg offset, such that a very small trim should be achievable with a balance within 5mm.

A much larger maximum cg offset was used in Monte-Carlo six degree-of-freedom trajectory stability studies of this vehicle, such that the probe is shown to be statically and dynamically stable during entry.

For Rosetta, sample density and load asymmetry were shown to have a small overall effect on trim.

b) Aeroshell Asymmetry

During manufacture, assembly and flight the aeroshell or decelerator will gain some degree of distortion. The distortion may be in both hoop and axial modes.

Axial symmetric distortions and even harmonic hoop distortions of even large magnitude will have very little effect on the trajectory or entry vehicle (apart from roll moments) and will be well within the predicted accuracy of the ballistic coefficient. However first harmonic hoop distortions and axial body bending modes could produce significant trim moments. These again in isolation produce a trim angle of attack which will act the same as a centre of gravity offset discussed above.

The first harmonic hoop mode on the aeroshell or decelerator (equivalent in effect to first body bending 'shuttlecock' mode) produces the largest trim moment for a given deviation from the nominal shape as may be expected since the higher harmonics are cyclically symmetric. Figure 4.6 shows the static trim angle of attack resultant from first harmonic radial distortion of the decelerator on the Huygens Probe. The distortion is assumed to be zero at the decelerator/probe joint station and linearly increasing to the maximum at the decelerator rear. Also shown in Figure 4.6 are the cg offset effects on trim. The figures for Rosetta are shown for comparison.

Figure 4.6 Static Trim from Asymmetries

Figure 4.7 Change in Huygens Probe Spin to Mach 1
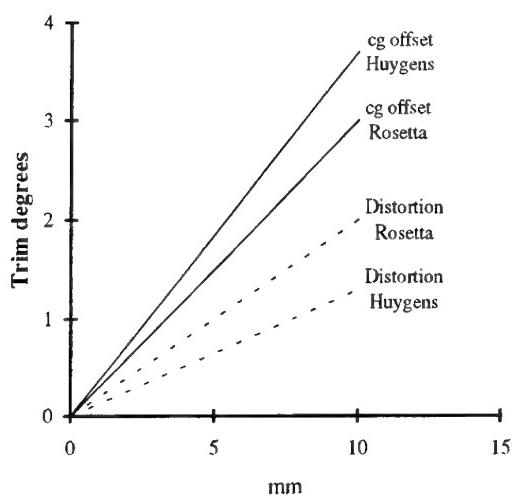
In addition where there is a large amount of surface recession due to ablation, similar asymmetries may occur. For the Rosetta entry vehicle the effect was estimated by allowing the carbon phenolic char layer to 'strip' from one side of the vehicle only, although in practice this is unlikely with the shear forces predicted. The resultant trim was very small (less than one degree).

c) Combined Asymmetries- Spin Rate Limitation.

Mass and geometric asymmetries in combination and depending on their angular relationship can produce significant roll torque's which may either spin the entry vehicle up or down (and through zero roll rate). The angular relationship is critical but for low spin rates an out of plane (90 degree) relationship is close to the worst case. Six degree-of-freedom entry simulations with varying asymmetries are used to produce spin rate histories. Figure 4.7 shows contours of spin rate excursions from the spin rate at the start of the entry phase to Mach 1 for a typical Huygens entry. While these will vary with trajectory, this type of figure serves as a design guide-line for geometric and mass tolerancing. The heatshield roll damping due to skin friction has not been included. The effect is likely to be small for these classes of entry but always acts to reduce the spin rate.

The choice of an adequately low initial spin rate (initially 60 deg/s) ensures that the spin rate at the start of the descent phase is in the desired range for Huygens (i.e. the limiting spin up case), and may be a consideration for Rosetta and Mars entry for parachute deployment.

Only sufficient spin to ensure low exo-atmospheric 'wobble' is necessary. These entry vehicles do not require spin for entry stability, and even spin excursions through zero roll rate do not contribute significantly to 'ground' dispersions when compared with initial trajectory alignment errors and atmosphere density variations.
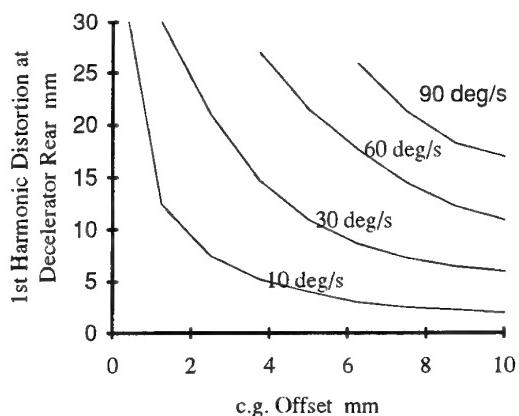
d) Moments Of Inertia

To avoid nutation and consequent tumble during coast, pitching/spin resonance problems during entry, and to relax the tip off error rotation rates budget, the spin or polar moment of inertia Ixx should be larger than the lateral moments of inertia Iyy and Izz. This should also be observed for the Huygens Probe without decelerator as the Probe pitching frequency is quite low after decelerator jettison and should the probe spin rate have increased during entry then a resonance could occur.

The possibility of a resonance is removed (and the need for analysis) if Ixx remains greater than Iyy & Izz. The Huygens Probe for example has acceptable inertia ratios of about 1.4 : 1.

Asymmetry of Iyy and Izz is of little consequence during entry, resulting only in sine squared variation in the spin rate during 'coning' motion. For the missions considered it is desirable to measure roll acceleration to examine the aerodynamic performance and therefore Iyy and Izz should be close.

Non zero products of inertia Ixz and Ixy cause the principal polar axis to be at an inclination to the geometric axis. During exo-atmospheric flight this leads to a coning motion even in the absence of pitch and yaw impulses during spin up and separation from the spacecraft. During the entry phase so long as the entry vehicle spins then an additional 'trim' angle of attack is induced which is dependent both on the spin rate and the aerodynamic pitching frequency. This effect together with c.g offset and trim asymmetries may increase or reduce the roll rate depending again on the phasing, however the effect is small as when the entry vehicle is close to peak dynamic pressure the aerodynamic pitching frequency is highest and the roll rate low even for large asymmetries. Therefore products of inertia are only limited by the initial angle of attack generated by the exo-atmospheric coning motion. The coning motion angle must be added to the inclination of the coning axis to the trajectory to form the total angle of attack. The practical limit of products of inertia are recommended to be less than 2% of the difference between the polar and lateral moments of inertia. This may be

relaxed considerably once the mission trajectories become more firmly established in post feasibility stages of the project.

Dynamic Instability

There are several possible causes of dynamic instability:

- Roll Resonance's. If the spin frequency becomes equal to the aerodynamic pitch frequency then a resonant lock-in can occur. This may case large pitch angle increases and large lateral loads and perhaps failure. Lock in can occur twice, initially as the pitching frequency increases prior to peak dynamic pressure and passes the spin frequency, and then as the pitching frequency decreases after peak dynamic pressure or as the vehicle spin rate increases due to asymmetries. Usually first resonance occurs at high altitude where aerodynamic forces are low, and usually no problem occurs, however at lower altitude especially if the vehicle has an increasing roll rate due to asymmetry, a problem can occur. The resonant phenomena is entirely avoided if the vehicle spin axis is the major inertial axis. This has been the design goal for all three vehicles.

- Pitch Damping. Instability can occur if there is positive pitch damping. This commonly occurs with bluff vehicles at low supersonic and transonic speeds. Axi-symmetric vehicles have this characteristic at zero or small angle of attack, and the bluffer the vehicle the worse the problem. It is therefore avoided by one of 3 methods:

    1. Avoid flying through this flight domain. Supersonic parachute deployment is a possibility but can impose additional problems for the parachute design.

    2. Adapt the geometry to a less bluff shape. This is the common route and is a performance trade-off

    3. Fly at angle of attack where the effect is minimised. A lifting entry requires a guidance system and can increase complexity and costs significantly. This is therefore to be rejected if adequate performance in terms of deceleration/altitude can be achieved with an aerobraking ballistic entry.

- 'Unsteady' Aerodynamic Effects. For example unsteady flows in separated regions can lock in with the vehicle motion. Similarly re-attachment points can move with the vehicle motion, again resonance can occur. Base flows for the vehicles presented here are of concern, and re-attachment is avoided by ensuring that the base aeroshell is within the shear layer up to maximum expected angle of attack. Blowing from ablation is an example where forebody aerodynamics can be effected adversely. The lag in ablation product formation is caused by the heat soak time constant of the material to react and produce pyrolysis gases. This can occur if there is a significant coning motion where the windward meridian is rotating in body co-ordinates. This is avoided by ensuring a low initial angle of attack and low coning motion.

- Aeroelastic effects. Although not strictly dynamic instabilities, a structure - flowfield coupling can occur, for example panel flutter. No aeroelastic analysis has been carried out in the early stages, but natural structural modes have been checked against aerodynamic frequencies.

    For example the decelerator natural frequencies are well above the Probe pitch and spin frequencies, base flow pressure oscillations have been assessed as very low, and forebody acoustic excitation is avoided with a laminar boundary layer, step size minima and roughness criteria being set.

Conclusions From Entry Dynamics Discussion.

The entry vehicle should ideally have the following features :

- Geometric axi-symmetry.

- Inertial axi-symmetry about the geometric symmetry axis (statically and dynamically balanced).

- Spin axis as the major inertial axis.

- Arrange major structural modes away from Aerodynamic modes.

- Small initial angle of attack.

4.2.3 Aerodynamic Configuration

The primary mission requirement which drives the aeroshell geometry is for deceleration at the highest altitude. For Huygens this is so that atmosphere experiments can begin at the highest possible altitude, 170 km is the target, whilst for Mars the atmosphere density is so low that maximum deceleration is required to provide sufficient altitude for parachute deployment at some of the chosen higher altitude sites. For Rosetta the requirement is to provide minimum mass, at a sufficiently steep entry angle to provide acceptable downrange dispersion for recovery, thus the trade-off is between heat flux and TPS thickness and area.

The aerobraking scenario uses a low ballistic coefficient vehicle for a 'direct' entry and aims to lose sufficient energy in the upper atmosphere to achieve the desired velocity and altitude conditions for the later mission phases. For a non lifting ballistic entry no guidance or control is necessary provided that dispersions are acceptable. The aerobraking concept is therefore less costly than its aerocapture equivalent but places emphasis on the design of an acceptably low ballistic coefficient stable aeroshell.

To achieve a low ballistic coefficient, a large area, high drag coefficient, low mass vehicle is required. For all of the missions considered, the mass is critical and the scope for mass reductions below the provisional budget allowable was small. Therefore the design drivers are for a large area and high drag coefficient entry vehicles.

Large drag coefficients are achieved usually at the expense of stability, and since the mass and cost budgets can not provide an onboard stability and control system, the geometric configuration must be sufficiently stable in free flight.

The philosophy of the studies undertaken was to provide a minimum cost solution and the adoption of a simple sphere cone with large half cone angle and sufficient stability can make use of a large amount of existing aerodynamic data and is therefore the natural choice.

Cone Angle

Studies have covered the range of half cone angles, 30 degrees 45 degrees and between 56 and 75 degrees. A cone angle of 70 degrees as used on Viking produced a near maximum drag coefficient, further increasing the cone angle has little effect on drag coefficient. Stability of the large angle cones however is lower and therefore to achieve a nominal zero angle of attack through peak heat flux and peak dynamic pressure during entry, 60 degrees was chosen for Huygens. This configuration has an acceptably large drag coefficient (only 4% less than the 70 degree cone) but a higher static stability. Low supersonic/transonic dynamic stability is also greatly improved.

Figure 4.8 Typical Drag and Moment
Coefficients Varying Cone Angle
(Experimental Results at Mach 9.5)
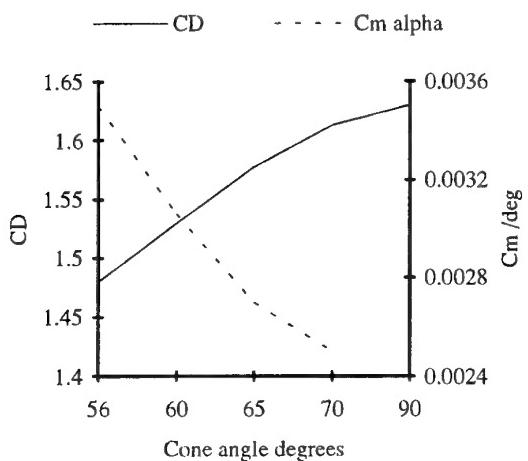
Figure 4.8 shows experimental pitching moment coefficient about the stagnation point and the drag coefficient for a range of cone angles together with the flat disk limit.

Base Diameter

The maximum base diameter vehicle is utilised with Mars entry for three landers and for the single Huygens probe, consistent with the space envelope available on the Spacecraft. Deployable decelerators were rejected in initial studies on grounds of complexity. The base diameter is the single largest contributor to a low ballistic coefficient for these missions. The lowest ballistic coefficient also provides the lowest heat flux.

For Rosetta the choice was complicated by the high heat fluxes which required a dense charring ablator. With a heavy heatshield which is the most massive part of the vehicle, increasing the area increases the mass proportionally since the ablator thickness is only marginally reduced, and thus the performance driver is minimising the mass. A changeover point in TPS material to a lower density may alleviate the situation as the fluxes reduce with decreasing ballistic coefficient. However even increasing the base diameter to the maximum allowable (3m) in the space envelope did not produce a lower mass even with a TPS material change. Therefore given the high drag shape to give lowest fluxes, the total mass may be minimised by reducing the volume to the minimum required for the payload by reducing the diameter, this of course increases the ballistic coefficient but reduces the total heatload. Further optimisation involving the rear TPS was not carried out.

Nose Radius

The nose radius has been chosen as a near optimum for minimum heatshield mass, ease of fitment in the spacecraft and launch envelope, and for maximum drag coefficient.

Although the effect of nose radius on drag coefficient is small a large radius gives a slightly larger drag coefficient and less mass per unit base area.

Huygens. For Huygens phase A with a Carbon TPS, the decelerator and forward heatshield have adequate thermal margins, and thus the mass is governed by the structural loading and by the thermal insulation requirement, therefore the smallest area will give the lowest mass, as the insulation mass is secondary. An instrument cover nose cap had a mass fixed by the ballistic separation requirement, and was independent of the nose radius to a first order.

Therefore the largest nose radius consistent with aerodynamic stability and existing data availability (i.e. certainty in aerodynamic coefficients) should provide minimum insulation thickness for a radiative heatshield concept given the low radiative heating environment (at phase A configuration). The maximum geometric value was 1.5m allowing the decelerator to be conical.

A Beryllium forward TPS was rejected for lack of thermal margin, while a low density ablative design was also rejected due to excess mass.

Boundary layer heat transfer analysis shows that the total convective heat load to the Probe forebody (i.e. less decelerator) reduces with increasing nose radius, this is a combination of reducing stagnation heat transfer and reducing total area. This is achieved despite the fact that the conical section has lower heat transfer rates than the spherical section.

The 1.25m radius chosen was consistent with the limit of bluntness ratio where transonic aerodynamic data is readily available for the Probe less decelerator. This ensures good confidence in the design by using computational methods to interpolate between experimental data rather than relying on extrapolation beyond the available range of data.

Marsnet. No optimisation was carried out in the early studies, the initial geometry was chosen as identical to Huygens in order to utilise the same aerodynamics (factored as necessary for atmosphere differences). Reductions in base diameter have been made for Spacecraft envelope fitment purposes with three landers each with reduced mass. However the maximum nose radius produces the lowest convective coefficient and highest drag and the nose radius remains large at 1.25m. Radiative fluxes were found to be negligible with the low entry velocity and relatively low shock layer temperatures. The current ratio of nose radius to base radius is still within the existing aerodynamic databases for bluntness ratio, and therefore there is room for optimisation in later studies.

Rosetta. For Rosetta since the radiative fluxes are significant, the nose radius was optimised for minimum total radiative plus convective heat load. Two distinct designs evolved, 'Iteration 1' is a steep entry providing close to the maximum deceleration load allowable for the payload of 100g. 'Iteration 2' is a shallower entry designed to give the payload an easier ride at 45-55g and is the shallowest entry with acceptable downrange dispersion. The steep entry has a shorter duration heat pulse and even though the heat fluxes are higher this leads to a thinner heatshield. The nose radius is 0.5m for this case. The shallower entry was preferred by the project team since all structural and payload loadings are the smallest practicable. The nose radius for this case is increased to 1.0m. Nose radius was chosen to give the combined minimum convective plus radiative heat flux since convective flux is proportional to the inverse square root of nose radius while radiative flux is directly proportional to nose radius. . In these selections of nose radius there is uncertainty in the magnitudes of the fluxes particularly for radiation, due to non-equilibrium effects. Although no blockage effects were taken into account recent analysis still supports the initial design. Figure 4.9 shows the effects of convective flux blockage by ablation products and radiative cooling of the shock layer.
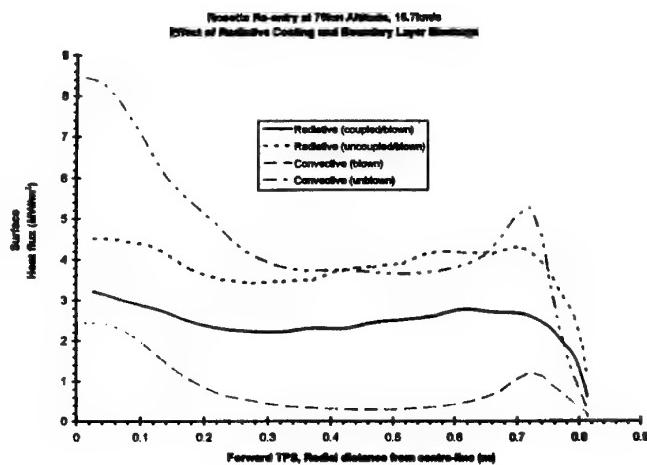

Figure 4.9 Rosetta entry at 70km, 15.7 km/s

Aeroshell or Decelerator Corner Radius

The final geometric feature is a radius to limit heating in the expansion corner region of the decelerator due to flow acceleration. For Huygens and Marsnet, the provisional Carbon-Carbon (C-C) and Ceramic (C-SiC) decelerators of the entry vehicles had a large thermal margin, however the corner heating, similar to the nose convective heating, increases as the corner radius decreases.

For a sharp corner the calculated heat transfer at the corner is very large value. At angle of attack, test data show that the corner heating is further increased, and even the high temperature ability of the Carbon and SiC may be exceeded locally.

Introducing a progressively larger corner radius to the rear of the decelerator produces a lowering heat flux at the corner which at zero angle of attack becomes less than the stagnation heating. This is the criteria used and a 5 cm corner radius has been selected representing a corner to base radius ratio of 0.03 for Huygens. Analysis shows that even at large angle of attack (20°) the heat flux should be limited to less than twice the zero angle of attack stagnation value. This increase in heat flux only increases the surface equilibrium temperature by about 20% and therefore is easily within the TPS capability.

6dof trajectory studies show that angle of attack excursions near peak heating are small, consequently the design assumptions are adequate. A secondary effect of a corner radius is a contribution to hoop stiffness where it is most required, and therefore mass penalties should not accrue from this feature.

Introducing a corner radius reduces the drag coefficient while the centre of pressure is moved forward, static stability is increased by the compensating increase in normal force producing an increase in the moment coefficient. The 5 cm corner radius selection reduces the drag coefficient by about 2.5% over a sharp corner, again the wind tunnel data is scaled by Newtonian

aerodynamics. The corner radius should be reduced to the minimum in to allow the maximum drag coefficient. The adoption of an elliptic corner profile may prove to be more efficient but is outside existing databases. The same corner radius is provisionally selected for Marsnet.

For Rosetta the situation is similar even with a different TPS, here the TPS is ablating and whilst the reduction in drag coefficient is important with increasing corner radius, it was judged more important to preserve a nearly constant thickness of forward TPS in order to lessen manufacturing complexity. A smaller radius thicker TPS may be lower in mass however, but shape change and consequent aerodynamic effects would be larger. The corner radius is thus sized to give a total heat flux equal to the stagnation value at zero angle of attack. Radiative flux uncertainties are also taken into account for this computation. The resulting corner radii are larger than for the radiative TPS of Huygens and Marsnet at 8 cm for the Iteration 2 geometry and 16 cm for the Iteration 1 geometry.

Conclusions from the Aeroshell Geometry Discussion

The entry vehicle geometric features are determined by:

- Minimum ballistic coefficient

- Availability of existing aerodynamic databases

- High drag shapes consistent with stability constraints and existing databases. This leads to the choice of large angle sphere cones.

- Nose radii based on minimum mass, maximum drag. This leads to maximum radius for large margin C-C and C-SiC TPS limited only by Bluntness ratios in aerodynamic databases. The minimum heat load is the criteria for ablators, with equal radiative and convective components.

- Corner radii minimum for maximum drag based on thermo-structural limit for C-C and C-SiC radiator and constant thickness for an ablator.

- Base diameter maximum for minimum ballistic coefficient for maximum altitude missions. Non-deployable decelerators chosen for low cost and low complexity.

Boundary Layer Transition.

Boundary layer transition for all the bluff vehicles is based on the Viking assessments of a boundary layer momentum thickness Reynolds number of 140 as being pessimistic. Using this value, Huygens and Marsnet maintain a laminar boundary layer throughout the entry, whilst on Rosetta the boundary layer becomes turbulent after peak convective flux, such that the total heat load is not greatly affected. This is fortunate for all vehicles since transition uncertainty prior or close to peak heat flux significantly effects the TPS sizing.

No attempt was made to utilise a more sophisticated transition 'law' developed for other vehicles or flow types since extrapolation to this type of vehicle would be dubious considering the small database available.

Conclusions from the Transition Discussion

- Lack of suitable transition data specific to this class of vehicle leads to pessimistic assumptions.

Base Flow

Base flow effects on these class of vehicle need analysis for two main areas :

- Shear layer impingement on the rear cover can cause local heat flux increases, plus re-attached flow can cause stability problems if the attachment point 'locks in' with the dynamic motion.

- The base convective heat fluxes determine the rear TPS design and mass.

For Huygens the rear cover is well clear of any impingement and therefore only recirculation region heating is of interest. Using a thin C-C decelerator TPS also produces a radiant heat flux to the rear. For Rosetta the rear conical heatshield was designed to be inside the shear layer based on flat base computations and a k-ε turbulent model with perfect gas (frozen) flow. The forebody boundary layer input to the shear layer was included, but the large base radius to boundary layer thickness means that the boundary layer state has little effect on the base flow.

For Marsnet the rear cover is also expected to be within the shear layer. The base convective fluxes are generally estimated from flight correlations in the early concept stage. Those from Viking being used for Marsnet giving about 4% of stagnation. For Rosetta with its conical rear TPS, Apollo correlations for the separated regions were used at about 1% of stagnation, and for Huygens 2% of stagnation was used as an estimate from other bluff body correlations.

Conclusions from the Discussion of Base Flow :

- Differing base flow heat flux correlations seem appropriate in differing regions and atmospheres for very bluff vehicles. Further analysis is still required.

- Base impingement and reattachment needs to be assessed with Navier Stokes codes.

- Accurate predictions of the base convective fluxes are elusive.

Catalytic Wall Effects

Catalytic wall effects are expected for both Huygens and Marsnet where non-equilibrium flows are encountered. Fully catalytic walls were assumed in the early analysis, but boundary layer solutions for Huygens and Navier

Stokes Solutions for Marsnet show that significant reductions in convective fluxes can occur for non-catalytic TPS surfaces. However before advantage can be taken of this, the catalytic behaviour of the atmosphere gases on the TPS wall must be known with some certainty, especially if the TPS has been exposed to space environments for example radiation, debris impact, thruster plume impingement and thermal cycling. The reactions for O_2 and N_2 recombination have been studied for some Earth entry TPS, but the data still exhibit large scatter. For Mars the CO_2 recombination is very important to assess. Similarly for Huygens N_2 and CH_X recombination appear important.

Conclusions from the Discussion of Catalytic Effects :

- Catalytic wall reactions are important for Marsnet and Huygens

- TPS lifetime effects need assessment.

Ablation Effects

Ablation is significant for the Rosetta entry where heat fluxes are high and dictate the use of a high density charring ablator such as carbon phenolic. The relatively shallow entry to protect the sample payload leads to a long heat pulse and therefore a thick single layer heatshield to keep the sub-structure cool. A new technology hot structure / hot bond concept is being developed for these type of TPS to reduce the heatshield mass.

Since the shock layer is close to thermochemical equilibrium during the heat pulse, existing chemical equilibrium ablation codes are used to predict the in-depth response. The ablation code also provides the blowing boundary condition for the Navier Stokes and boundary layer codes. This is important since the blowing reduces the wall gradients and therefore reduces the convective flux. The cool carbon laden blowing gases can also absorb some of the radiative flux to the wall, the resulting heated boundary layer gases increasing the convective flux again. Convective and radiation blockage are estimated from engineering correlations in the early stages and later assessed using full Navier Stokes codes. Figure 4.2.5 shows that the effect of blockage can be very large.

- Ablator response is fully coupled to the flowfield and thus TPS sizing.

Contamination

TPS contamination can occur when atmospheric gases dissociate to form potential condensates or absorbents. Such is the case for Huygens where carbon is formed from the cracking of CH_4. Analysis and experiment have shown that the carbon is driven towards the cool wall by diffusion, and condenses on the wall. Since the wall temperature is low compared to the carbon sublimation temperature, it is supposed that the carbon is supercooled and gives up its latent heat on touching the surface. A significant build up of carbon deposits is expected from analysis and experiment for Huygens amounting to 0.3

mg/cm^2. Other hydrocarbons may be absorbed or formed in the deposit or TPS surface.

Absorbents may outgas during descent, and particulates may shear off if the TPS is present. To date it has not been possible to distinguish between particulate and gaseous material removed, but it has been shown that circumstances could exist where the contaminant removed from the heatshield could enter the instruments if the TPS is present. While this is a worst-on-worst analysis, total TPS removal was selected for the Phase B baseline.

- Contamination remained an open issue for Huygens A

- TPS contaminant absorption models no not exist.

- Outgassing models need specific experimental investigation.

4.3 LIFTING ENTRY VEHICLE DESIGN

4.3.1 Lifting Mechanism.

In order to generate lift the vehicle must generate some asymmetry and thus circulation in the flowfield. That is the pressure and friction forces on the vehicle have a non-zero integrand in a plane normal to the velocity vector.

This may be achieved by a flying a symmetric vehicle at angle of attack or by generating an asymmetric vehicle geometry or both.

For the symmetric geometry the means of maintaining an angle of attack is the offset of the centre of gravity. This mechanism was used by the US on Gemini, Apollo and Viking.

Typical asymmetric geometries are perturbations of the symmetric geomtries, for example a sliced cone such as the AFE or a bent biconic. In each of these cases pressure bearing surfaces are effectively removed from one side of the vehicle thus inducing a moment which is trimmed out at angle of attack.

For a symmetric lifting vehicle the pitch moment equation about the centre of gravity is:

$$M = 0.5\rho V^2 A[C_a\, x_{cgo} - C_n\, (x_{cp} - x_{cg}) + C_m]$$

where :

    x_{cg} is the centre of gravity location
    x_{cp} is the centre of pressure location
    x_{cgo} is the centre of gravity offset from the aeroshell centreline
    C_a is the axial force coefficient
    C_n is the normal force coefficient
    C_m is the moment coefficient due to aerodynamic controls or perturbations.

defining $(x_{cp} - x_{cg})$ as the static stability margin k_s and the vehicle in a trimmed condition then
$M = 0$ with $C_m = 0$ and:

$C_a\,x_{cgo} = C_n\,k_s$

re-arranging in terms of C_l/C_d or L/D

$x_{cgo}/k_s = (L/D\,Cos\alpha - sin\alpha)/(cos\alpha - L/D\,sin\alpha)$

for a typical bluff vehicle $L/D = \sim 0.3$ at 20 degrees incidence and k_s is about the vehicle radius R_b and so $x_{cgo} = \sim 7\%\,R_b$. The capsule will thus be able to achieve a mass induced trim at maximum L/D with reasonable tolerance.

For a slender vehicle $L/D = \sim 1.0$ and $x_{cgo} = \sim k_s$
and since k_s is about half the base radius R_b then mass trim at maximum L/D may be difficult to achieve and other devices will also have to be used such as body bend or body shaping.

The choice of vehicle configuration is first made on the L/D requirements which are determine by cross range, entry corridor and if required aerocapture accuracy (to orbit).

Large cross range, high speed or thin atmosphere (low deceleration) and high accuracy all call for high L/D.

Our simple trajectory analysis has shown that heating is minimised for low ballistic coefficient which is achieved with a bluff vehicle and so a small L/D is suitable to provide modest cross range control for recovery purposes, provide reasonable entry load alleviation whilst at the same time providing a low heating.

Table 4.2 gives the L/D of some capsule configurations some of which are shown in figure 4.10.

Capsule	L/D	Geometry
Gemini	0.2	Sphere seg-clyl
Apollo	0.3	Sphere-seg
Viking	0.18	Sphere cone
AFE	0.28	Ellipse/raked cone
'Fat' biconic	0.5	optimal bi-conic
Shuttle	1.1	Wing-body
'slender' biconic'	1.5.	optimal bi-conic

Table 4.2 Some Lifting Vehicle Characteristics

The slender biconic gives optimal aerocapture to orbit accuracy, while the shuttle is a compromise vehicle for low speed handling but presents a maximum radius swept cylindrical lower heatshield during entry at high incidence (low ballistic coefficient attitude) for minimum heat load.

Fat biconics have been considered for many planetary entry missions and their medium L/D give good load reduction and good cross range for accurate landing point selection. This type of biconic was also considered for the Rosetta mission at one stage, prior to the trade-off between low L/D and ballistic capsules.

Of interest when considering the lifting capsule is the direction of lift. For a slender vehicle pitching nose up causes a lift force in the upwards direction. For a bluff vehicle pitching nose up causes a lift force in the downwards direction.

The reason for this change is obvious from the lift equation:

$L = C_n Cos\alpha - C_a sin\alpha$

Lift changes sign when $C_a sin\alpha$ becomes greater than $C_n Cos\alpha$. The bluff capsules have large C_a and small C_n and the opposite is the case for slender vehicles. For Newtonian flow over a conic this occurs at a cone angle of 45 degrees where the net lift is zero at all angles of attack. Thus a 45 degree sphere cone such as Pioneer Venus and Galileo will experience little lateral acceleration but is still stable, thus the internal design may be simplified where very large axial loads are expected.

For the low L/D capsule, geometric design features are similar to the ballistic vehicles, since the ballistic vehicles must allow for incidence excursions during entry, and given the L/D requirement the ballistic coefficient must still be minimised with little surface area as before. However the corner radius heating must be considered more carefully as for high incidence the stagnation region can move to the corner making the corner radius the dominant geometric feature for the convective heating i.e. small radii lead to large convective heating rates.

$(q_c \propto r^{-0.5})$

Pitch damping for bluff vehicles is positive transonically at small incidence but changes to negative at incidence. This is an advantage to the lifting vehicle.

Flow attachment to the rear heatshield is also an issue since this increases the wetted area and thus total heat load and may lead to motion-separation coupling.

The decision between asymmetric and symmetric geometries is made initially based on the L/D. For high L/D we will need vehicle asymmetry and as previously mentioned the generic design rule for biconics is the 2:1 ratio. Nose radius is then optimised against TPS capability. For low L/D capsules we can achieve the required L/D by moving the centre of gravity. Thus the need for asymmetry is removed. Asymmetry in the rear structure is desirable to alleviate attached flow heating and is part of the discussion below.

Apollo Sphere-segment

Slender Bent Bi-conic

AFE Elipse raked-cone

Bent Bi-conic
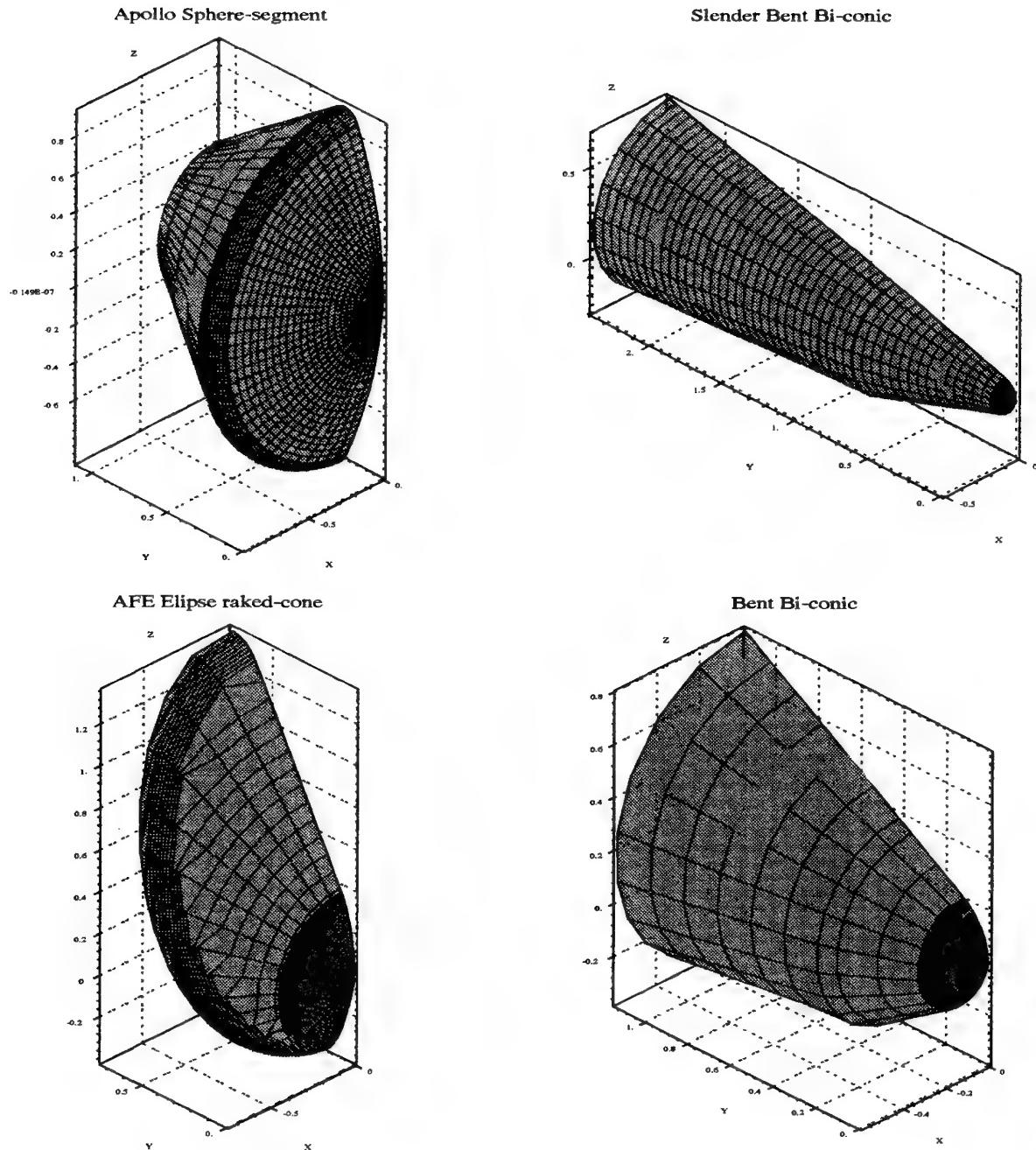
Figure 4.10 Some Lifting Capsule Geometries

Example Comparison Study for High Speed Earth Return

The discussion of lifting vehicles is now confined to capsule candidates, i.e. those which are essentially simple geometries with low to medium L/D.

In the following trade-off, for a high speed Earth return from a comet CNSR-Rosetta, two lifting capsule generic types were selected for analysis. These are the Apollo type and a modest L/D raked cone of the type proposed for the US Aero-assisted Orbital Transfer Vehicle (AOTV) and related AOTV flight experiment (AFE).

Only a low L/D is required to limit the downrange dispersion to acceptable limits, higher L/D giving increased cross range capability. Trajectory studies identified the desire to increase the corridor width and reduce dispersions by both increasing the L/D and reducing the Ballistic Coefficient.

It was possible to consider a higher L/D vehicle such as a biconic for this mission, as the rear sample loading option and low entry loads made this attractive and a precursory

study produced the vehicle shown in Figure 4.11. However this was dropped on the grounds of lack of supporting design data and thus low confidence. Therefore for this study where aerobraking to ground was the goal, only low L/D capsules were studied. In particular advantage was taken of extensive US experience with the Apollo programme, and more recently with the AOTV flight experiment programme which planned to use a raked cone configuration, the generic type of which has been proposed for planetary entry for many years.
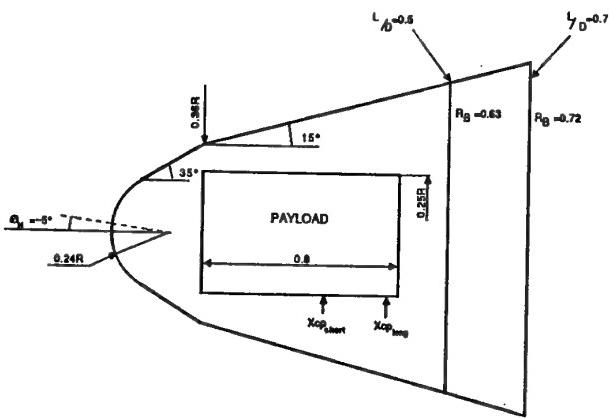

Figure 4.11 CNSR Bent Biconic Early Trade-off Configuration

4.3.2 Apollo Type Capsule

Configuration

The Apollo-like capsule is a sphere segment vehicle having a spherical forward heatshield and conical rear heatshield. The large radius forward heatshield gives the lowest convective heating, and was retained at the largest value for maximum axial length of the vehicle when placed nose out in the side mounted position of the spacecraft. This largest nose radius amounts to the same value as the launch fairing radius. For shallow entries the radiative heating is less as a proportion of the total than for steeper entries and so for the shallowest possible entries, the largest possible nose radius is retained (see aerothermal discussion). The nose radius is thus 2.2m. A body diameter of 1.85m is used for consistency with earlier studies with the intention of scaling the final geometry to give the minimum capsule volume and thus mass for the final container design.

The capsule geometry was scaled from Apollo to make use of the available databases thus increasing the confidence in the capsule design with its demonstrated Earth entry capability.

In order to accommodate the capsule within the spacecraft envelope either nose-in or nose out the after cone is truncated. These changes have a very small computed effect on the capsule aerodynamic coefficients, allowing direct use of the Apollo aerodynamic database.

Aerodynamics

Continuum Coefficients
The Apollo continuum aerodynamic coefficients have been taken directly from the Apollo wind tunnel data. Flight data examination gives an excellent validation of the database

Free Molecule Coefficients
The free molecular drag coefficients are calculated using the standard method with full specular reflection and equal freestream and wall temperatures. The free-molecular L/D is small due to the relatively large shear forces and for the this study can be assumed to be zero.

Damping Coefficients
The damping coefficients are also taken from Apollo wind tunnel data. The damping coefficients are similar in magnitude to the bluff cone values of the ballistic capsule as might be expected, but with some pitch and yaw reinforcing damping at transonic and subsonic velocities which may be of some concern. However this was managed adequately by the Apollo GNC.

Aerothermodynamics

Earth Atmosphere Aerothermochemistry
It is appropriate to mention the aerochemistry environments to be encountered by the Rosetta capsule. These can be divided into the shock layer and its chemistry, and the boundary layer/heatshield chemistry.

The entry velocities are high enough that in the shock layer one can expect very high temperatures and appreciable ionisation of the gases. The high altitude (and thus low density) heating peak due to the shallow entries leads to the chemical and thermodynamic processes not achieving equilibrium in small distances behind any shock . However this is offset to a certain extent by the relatively large size of the capsule geometries such that gases at the boundary layer edge are close to equilibrium. Comparison of equilibrium chemistry boundary layer solutions for convective heating show acceptable agreement with non-equilibrium flowfield/convective heating results in the stagnation region and therefore for this stage of the study equilibrium convective heating results were used. The radiant heating is more sensitive to the shock layer property profile and it was necessary to develop a non-equilibrium radiant heat transfer model.

The stagnation heat transfer rates are large and a dense charring ablator is necessary for all but the shallowest entries, however an empirical blockage correction has been computed which reduce fluxes. The surface temperatures are high and allow the assumption of surface equilibrium chemistry. However at the high altitudes at which peak heat transfer occurs, it was recommended that non-equilibrium reaction of the boundary layer and heatshield products should be undertaken.

Continuum Convective Heat Transfer
The laminar convective heat transfer distribution is based on Apollo data from wind tunnel tests and flight data.

Nine heat transfer locations were chosen on the body windward-leeward plane for TPS assessment.

For the present analysis the stagnation heat transfer was calculated using a correlation based on the theory of Fay and Riddell which is strictly valid only to about 8km/s. However to use the results at higher entry velocity, equilibrium air chemistry boundary layer calculations were undertaken in order to gain confidence in the correlation at velocities up to 17km/s. The agreement between boundary layer calculations and the correlations is within about 10%.

For bluff vehicles the sonic line lies on the corner torroidal regions which are present to reduce the convective heating from the sharp edge value. The acceleration to the sonic line on the decreased radius of curvature increases the velocity gradient close to the stagnation point equivalent to the effect of reducing the radius of curvature or nose radius and thus increasing the convective heat transfer. The effect increases with incidence as the stagnation point approaches the torriodal section. The stagnation heat transfer correlations are thus adjusted for the equivalent stagnation velocity gradient from the usual spherical geometry values, again this agrees well with boundary layer calculations.

Free Molecular Heat Transfer

Free molecular heat transfer has been calculated along each trajectory for each CNSR capsule using established methods, with accommodation coefficients set to unity and with a cold (300K) wall temperature.

In order to bridge between free molecular and continuum heat transfer in the transitional and slip regimes a combination of bridging functions have been used. On windward facing surfaces a minimum of either free molecular or continuum heat transfer is taken. On leeward surfaces a Knudsen number based bridging function is used as with the pressure coefficient. The latter is necessary as free molecular heat transfer to shaded areas is zero for high vehicle speed to molecule speed ratios. Bridging is discontinued in the shaded regions after peak heat transfer for Rosetta.

The use of the bridging functions adequately compensates for high continuum heat transfer in the transition and slip regimes, but as with the aerodynamic coefficients the effect on the total heat transfer is small and so no further refinement of the bridging methodology is justified for this phase of the study.

Boundary Layer Transition

Transition to turbulent flow has been predicted using a suitable bluff body correlation to the boundary layer momentum thickness Reynolds number which is applicable to the attached flow areas. A similar correlation was assumed to apply in the regions of separated flow. This type of procedure was used successfully on Apollo but based on local flow conditions which are considered less reliable when changing scale or geometries.

Radiant Heat Transfer

Radiant heating to the Rosetta capsule forms a significant fraction of the total, particularly for the steeper entries. The radiant heat transfer distribution was based on that used for Apollo but amended for differing angles of attack by an engineering correlation. The stagnation point radiant heating is taken from an air correlation strictly valid only to 8km/s but previously checked against Apollo flight data with good agreement. However Rosetta entry velocities are significantly higher than those for Apollo(11km/s) and comparison with non-equilibrium chemistry predictions showed a potential under prediction using this correlation. On the superorbital Apollo test flight(spacecraft 017) the non-equilibrium radiant heating at about 10km/s was not dominant and equilibrium chemistry theory and flight data agreed well. A new correlation was developed which extends the range of application to 16km/s to cover the non-equilibrium effects and was expected to be accurate to within a factor of 2 for the Rosetta application.

Trajectory

The Apollo type and AFE type trajectory utilised for this study were selected initially as a 20g peak and a 50g peak reference, this assumed a 15km/s entry in the local frame. A minimum flight path angle of 1 degree was set to ensure entry and the guidance algorithm maintained this with alternate left-right roll manoeuvres.

Mass Characteristics And Stability

In order to achieve the desired trim, the centre of gravity must be offset. The Apollo relative centre of gravity position is therefore to be used to give the design nominal trim of 20 degrees. (L/D 0.3). Variations in sample mass and position and ablation asymmetry/mass loss will affect the trim by a few degrees at most and this is expected to be managed by the GNC system.

The static margin is about 1m for the Apollo type capsule with a centre of gravity 0.5m aft of the forward heatshield, thus the vehicle is acceptably stable in the continuum regime.

Heatshield Considerations

Maximum heat fluxes for the shallow 20g entry are small enough on the forward heatshield (1000W/cm2) to consider a lighter heatshield material, however the material choice in this range (Nylon Phenolic) suffers from a low density Char which is stripped under boundary layer shear forces. Rear cone heat transfer is quite low and although transition is predicted, a lightweight ablator (ESM) will be adequate in varying thickness at all locations.

Simulations of entries close to the skipout limit at about 9-11g show heat fluxes less than 500W/cm2 which are in the range of the Apollo ablator and some of the mid density ESM's. Thus a very shallow entry could produce a step reduction in heatshield mass, although the heatsoak time is increased requiring greater insulation thickness.

It should be noticed that the convective and radiant heat fluxes are nearly equal for the 20g 15km/s entry, with convective dominating at shallower angles while at higher entry velocity (for the same g load) the radiative component begins to dominate, illustrating the choice of the largest possible nose radius (Apollo type capsule) for the shallow entries.

4.3.3 Raked Cone Capsule

In order to achieve a modest L/D and low ballistic coefficient a large angle sphere cone can be utilised. Indeed for the Viking missions to Mars this was the geometry chosen (70 degree cone at 11 degrees incidence and L/D 0.18) for maximum drag with modest control. During the period leading up to Viking, there was much testing of simple aerodynamic configurations for planetary entry including raked cones.

In the early 1980's attention was focused on planetary missions where aerobraking is used for descent to ground, whereas aerocapture with a large L/D gives most flexibility for capture to orbit.

Later attention was turned to aero - assisted orbital transfer to save fuel when returning from high to low energy orbits. This effort was re- focused on the raked cone for high drag coefficient and good stability characteristics. The US planned to flight test such a vehicle and this of necessity generated much wind tunnel and computational data which was of use to the Rosetta entry evaluation.

At first glance the requirements seem too dissimilar as the entry energies and mission requirements are quite different, however closer inspection reveals the similarity in design objectives for the aerodynamic configuration. These are;

> Low ballistic coefficient
> Low L/D
> Well understood aerodynamic performance.

Although the size and materials will be quite different the basic geometry serves as a design point from which we may extrapolate if necessary.

Configuration

In order to compare performance with the Apollo capsule the same maximum diameter is chosen which may be scaled to contain the final sample container. The rear heatshield is intended to be in separated flow and an initial 45 degree dividing streamline is taken as the maximum rear heatshield envelope at this stage. The cone half angle is 60 degrees with a rake angle of 73 degrees (90 degrees being symmetric). An expansion corner radius of 10% of the base diameter is used for the AFE vehicle. The nose rather than being spherical is in fact elliptic with a 2:1 major to minor axis ratio. This feature increases the nose radius of curvature over the equivalent sphere and thus reduces the convective heat transfer at zero angle of attack. A slight increase in drag coefficient is also achieved.

Aerodynamics

Continuum And Free Molecule Coefficients
The continuum aerodynamics have been taken from wind tunnel data for 60 degree sphere cones, and a raked cone and factored by Newtonian ratios to the AFE configuration. Data are also obtained from computations in the literature. Only drag coefficient and L/D were developed for this study.

The AFE vehicle is very similar in performance to the Apollo type capsule, but with slightly lower L/D (0.28) at its design angle of attack (17 degrees). However the drag coefficient is higher by about 8% giving a lower ballistic coefficient for equivalent mass. The comparison of basic characteristics is given in. Figure 4.12 which also shows the guided and ballistic capsules to approximately the same scale.


	'Apollo' type capsule	'Apollo' type capsule	Ballistic Capsule
Mass kg	300	300	250
Diameter m	1.85	1.85	1.63
Cd (alpha trim)	1.30	1.36	1.54
L/D (alpha trim)	0.3	0.28	0
Nose Radius m	2.2	~1.5 equiv. (elliptic)	1.0
Selected Entries (Earth g)	10-20	20-50	50-100
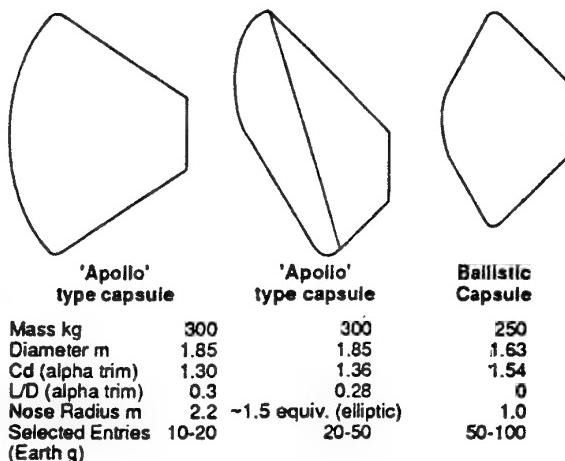
Figure 4.12 Comparison of Trade-off Vehicles

Damping Coefficients
The damping coefficients have been taken as those for an equivalent sphere cone initially and are thus the same as the ballistic capsule. This is adequate for initial trajectory studies and give the capsule good damping characteristics in most of the Mach number. These initial damping coefficients are superior to those of the Apollo type capsule.

Aerothermodynamics

As with the Apollo like capsule the reference stagnation heat transfer is based on the results of Fay & Riddell for equilibrium air, corrected for the local curvature effects. The same radiative and distribution correlations have been used as for the Apollo type capsule but applied to the AFE shape. Seven locations were chosen to represent the heat transfer distribution about the AFE type vehicle for TPS assessment

Trajectory

The same trajectory entry conditions and control law were used as for the Apollo type capsule.

Heatshield Considerations

The AFE vehicle has only slightly higher convective heat flux and lower radiative heat flux than the Apollo vehicle on the forward heatshield. The convective component is dominant at both entry velocities indicating the desire for a larger nose radius, or the use of this type of vehicle at still higher entry velocities or steeper (than 20g) entries . The rear heatshield is all in separated flow allowing an even thickness of low density ablator. This is achieved at the expense of reduced capsule volume for the same capsule diameter.

Mass Properties And Stability

For the AFE vehicle a nominal trim angle of attack of 17 degrees is required but unlike the other capsules considered the AFE is truly asymmetric in geometry, but the c.g position is again located to give the desired trim. The static margin is similar to the Apollo like capsule at 1m assuming a centre of gravity position 0.5m aft of the forward heatshield. However the pitching moment coefficients appear larger than for the Apollo type capsule indicating a greater tolerance to sample mass/position and ablation asymmetries. The AFE type capsule is thus acceptably stable .

4.3.4 Guided Capsule Choice

There is little difference in the performance of the two configurations aerodynamically speaking, however there are advantages and disadvantages to both configurations.

The Apollo shape vehicle has the major advantage of having been proven for Earth entry already, and consequently there is a large volume of aerodynamic and aerothermodynamic data available which will give a high confidence to the capsule design at an early stage and potentially lead to lower costs. The large forward heatshield radius is ideal for the shallow entries where the radiative component of the heat transfer is proportionately lower. However the design of the Apollo rear heatshield does allow attached flow on the windward side at angle of attack leading to a larger rear heatshield mass than for a separated flow design. This may lead to a lighter capsule however if the overall body radius can be reduced.

The AFE design has the potential to achieve similar L/D values given slight modifications to the geometry, i.e. increased rake angle and reduced corner radius, but this would be diverging from the AFE geometry for which there was expected to be much data. Therefore design confidence will be lower initially and costs potentially higher with a larger test programme particularly in the low supersonic, transonic and subsonic range where no AFE data will be available in any case.

The real choice may well be made on heatshield mass which forms a large fraction of the total capsule mass. For very shallow entries close to skipout (around 10-15g) heat transfer rates are reduced to an extent where a change to a light charring ablator may be considered. For this scenario the largest radius of curvature is required in order to minimise convective heating (radiative heating being proportionately lower for the shallow entries). Therefore the Apollo style capsule seems attractive at shallow entries less than 20g.

For the steeper guided entries 20g to about 40g the smaller radius of curvature of the AFE vehicle may make it attractive from the heatshield mass point of view. Additionally a trade-off on increased rear heatshield mass by allowing flow attachment, against reduced body diameter (and thus reduced forward heatshield mass) is possible. Greater than about 40g the ballistic capsule becomes attractive as dispersions reduce.

4.4 'COMPUTATIONAL TOOL SET' REQUIREMENTS

So far the shape of the entry vehicles has generally been defined by simple laws and can be accomplished with relatively simple tool set which is adequate in the very early project stages. This may be designated the 'level one' analysis, using :

- 3dof and 6dof trajectory codes with planetary atmosphere models

- Newtonian aerodynamic code to interpolate existing aerodynamic databases

- Free-molecule aerodynamic code and suitable empirical drag and flux bridging functions

- Heat flux correlation's for convective and radiative fluxes.

- Heatshield sizing algorithms.

However in all but the trajectory codes, detailed knowledge is required to develop or confirm the basis of the engineering solutions.

The determination of accurate aerodynamic coefficients is very important since the atmosphere composition can be determined from the vehicle performance, while stability is always a consideration whatever the mission.

The heat flux distribution and history determine the choice of TPS and geometric ratios.

The first essential analysis is to determine the aerodynamic and aerothermal flight regimes through which the vehicle will pass. This will give the engineer a clear perception of where in the entry particular analysis methods should be used. In the preliminary stages the classical regimes will have become evident from the trajectory analysis which should use both free molecule and continuum drag coefficients with a suitable bridging function. A simple Knudsen based bridge is most common for drag coefficient.

The formal analysis should consolidate the classical regimes and should investigate the thermal and chemical regimes. Most commonly the latter are expressed in terms of the Damkohler number.

To carry out this investigation a chemically reacting shock layer simulation is most useful, and since the whole entry parameter space needs to be investigated the method should be fast.

In this respect a loosely coupled suite consisting of an inverse Euler code for the shock layer, followed by streamtube tracing and chemistry computation along the streamtube may be employed. Chemical source terms are then fed back to the Euler energy equation. The Euler iterations take a few seconds and the chemistry a few minutes for each trajectory point. Shock stand-off may be used as the convergence criteria.

Boundary layer edge conditions are taken as a post process of the Euler solutions for convective heat flux analysis using usually an integral code with frozen or equilibrium chemistry assumptions. Radiation calculations are also performed from the shock layer results as a post process. Both the boundary layer and radiation codes takes a few minutes to compute the solutions for the whole trajectory.

The radiation source terms can also be fed back to the Euler solution, as can boundary layer thickness. However for regime scoping studies an uncoupled procedure is usually sufficient.

Wall conditions can be accommodated in the boundary layer solution in a simple manner, blowing is accommodated with a correlation within the integral boundary layer code, whilst for the frozen boundary layer solution, a 'catalytic' wall can be introduced by substituting the wall enthalpy for equilibrium wall enthalpy at the same temperature.

Parametric investigations using these methods have been carried out to varying degrees in the early stages of all three missions discussed. In general the results are acceptably accurate excepting radiation in highly non-equilibrium flow at present.

Such a suite also allows rapid comparison of the sensitivity of differing thermochemical mechanisms, and allows rapid construction of a viable set prior to more complex computations. These 'level two' results can be used to calibrate the engineering correlations in the level one analysis. The level two codes are therefore :

• Fast inviscid shock layer solution.

• Loosely coupled chemistry solution

• Boundary layer codes.

• Uncoupled or loosely coupled slab radiative solution.

• Charring material ablation code

Once the thermochemical data has been assembled and tested with the level two codes, and the results validated as far as practicable a more sophisticated analysis again must be carried out to verify the simpler results in areas beyond the validation. (here verification is defined as being correct numerical implementation of the physics and chemistry, while validation is the comparison of the models with the real world). For continuum regimes this verification is by a full or thin layer thermo-chemical non-equilibrium Navier Stokes solution. Due to the lack of other suitable methodologies the Navier Stokes codes are used well into the transitional regime, and account can be taken of slip effects. Direct Simulation Monte-Carlo should be used to confirm bridging functions between continuum and free-molecular.

The level three codes are :

• Thermo-chemical non-equilibrium Navier Stokes.

• Direct Simulation Monte Carlo with suitable chemistry and radiation models.

• Full 2D Non-equilibrium radiation code.

Full thermo-chemical non-equilibrium Navier Stokes code solutions for Rosetta, Marsnet and Huygens have been computed and presented in the literature. The level three codes are used sparingly in the early stages due to the costs involved, but must be used in development phases to confirm design viability, whilst experiments provide validation data for these codes. These codes are often the only way to investigate the entry phenomena where no flight data is available, and ground tests are impractical.

4.4.1 Conclusions From The Methods Discussion.

• A three level set of codes is time and cost efficient for vehicle design studies.

• Level one codes are readily available but require careful calibration.

• Level two codes have been widely developed in the past, and are still very useful.

• Level three codes can simulate many situations, but the required level of expertise and time required for use must not be underestimated.

4.5 AEROTHERMAL DATABASE

From the level 2 parametric studies, the extent of the required aerothermal database is determined. This data must be adequate for the entry being considered and often the data require some extension to higher temperatures, and in some cases the data are sparse or non-existent.

The development of high enthalpy facilities is essential for the understanding of, and database generation for aerothermodynamic problems for planetary entry.

4-24

The trend towards increasing cfd analysis to support design is only sustainable if the databases are made available, which means development of the necessary facilities and databases prior to critical design decisions.

4.6 REFERENCES FOR SESSION 4

Allen H.J., Eggars A.J., 'A study of the Motion and Aerodynamic Heating of Ballistic Missiles' NACA TR-1381 1958

Eggars A.J., Allen H.J., Neice S.E., 'A study of the Motion and Aerodynamic Heating of Ballistic Missiles' NACA TN-4046 1957

French J.R., Cruz M.I., 'Aerobraking and Aerocapture for Planetary Missions'. AIAA Journal of Aeronautics and Astronautics February 1980.

Griffin M.D., French J. R., 'Space Vehicle Design' AIAA Education Series, ISBN 0-930403-90-8

Rarefied Flows of Planetary Entry Capsules

James N. Moss
Langley Research Center
Hampton, VA 23681-0001 USA

SUMMARY
The impact of rarefaction on entry capsules and spacecraft aerothermodynamics is emphasized for various aeroassist missions. The capability of the direct simulation Monte Carlo (DSMC) method to simulate such flows is demonstrated through examples of validation studies and applications. Several space flight projects and ground-based experiments are reviewed for which rarefaction effects have significant effect on spacecraft performance or experimental measurements. This review clearly demonstrates the significant role that the DSMC method plays in characterizing such flows.

SYMBOLS

a   speed of sound

A_{ref} reference area

C_D drag coefficient, $2F_X/\rho_\infty V_\infty^2 A_{ref}$

C_H heat transfer coefficient, $2q/\rho_\infty V_\infty^3 A_{ref}$

C_i mass fraction of species i, ρ_i/ρ

C_L lift coefficient, $2F_y/\rho_\infty V_\infty^2 A_{ref}$

C_P pressure coefficient, $2p/\rho_\infty V_\infty^2$

d   diameter

D   drag force

F   force

k   Boltzmann constant

Kn   Knudsen number, λ/L

L   lift force or reference length

m   molecular mass

M   Mach number

n   number density, m^{-3}

$\tilde{n}$ fractional density rise across shock

n_{e^-} electron number density, m^{-3}

p   pressure

q   surface heat flux

Re   Reynolds number

R_N stagnation radius of curvature

s   coordinate along body surface

T   temperature

T_{ov} overall kinetic temperature

V_∞ freestream velocity

u   velocity component tangent to body surface

v   velocity component normal to body surface

X_i mole fraction of species i

x   coordinate measured along body centerline or coordinate for 3-D AFE configuration

y   coordinate measured normal to body centerline or coordinate for 3-D AFE configuration

α incidence angle

γ specific heat ratio

γ_i recombination probabilities for species i

η coordinate normal to body surface

ρ density

τ shear stress

Subscripts

A   axial

i   ith species

N   normal

w   wall value

∞ freestream value

1. INTRODUCTION
Hypersonic flows where rarefaction effects are important occur over a wide spectrum of conditions ranging from low density (high altitudes) situations to relatively high density flows where the characteristic dimension is small. Examples are the overall aerothermodynamics of space

vehicles at high altitude (re-entry flows, satellite contamination, and plume interactions), the heating along the leading edges and wake flows at lower altitudes, and very localized aerothermal loads occurring at even lower altitudes such as that resulting from a shock on cowl lip interaction. The aerothermodynamics of entry capsules encompasses the complete flow spectrum in terms of rarefaction; that is, from free molecular to continuum flows. During the higher altitude portion of entry where the flow is free molecular, only the nature of the gas-surface interactions influence the capsule aerothermodynamics. For the transitional flow regime, bounded by free molecular and continuum regimes, both gas-surface and intermolecular collisions are important in establishing capsule aerothermodynamics.

For the transitional flow regime, the molecular mean-free path in the gas is significant when compared with either a characteristic distance over which important flow-property changes take place or when compared with the size of the object creating the flow disturbance. Since the flow is hypersonic, the flow disturbance that envelopes a capsule will be nonequilibrium; that is, one in which nonequilibrium exists among the various energy modes (translational and internal), the chemistry, and radiation for the more energetic flows. For such flows, the shock-wave thickness can range from a significant portion of the shock standoff distance to no evidence of a shock wave. Furthermore, the flowfield disturbance created by the vehicle is very much larger than that experienced under continuum flow conditions. At the surface of the vehicle, the gas-surface interactions are very important as they significantly influence the aerodynamic forces and heating that the vehicle experiences. Evidence of this is the rather spectacular change in aerodynamic and heating coefficients that occur in the transitional regime.

Furthermore, expansion of the forebody flow into the wake extends to lower altitudes the conditions for which rarefaction effects are important in establishing the near wake closure and the level of heating experienced on capsule afterbody or payload. This is particularly true of aeroassisted space transfer vehicles (ASTV's) where determination of wake closure is a critical issue for aerobrakes because the low lift-to-drag ratio aeroshell designs impose constraints on payload configuration/ spacecraft design. The issue is that the payload should fit into the wake in such a manner as to avoid the shear layer impingement to minimize heating.

Transitional flows present unique difficulties for numerical simulations since the model equations used to describe continuum flows (Navier-Stokes) become deficient as the flow becomes more rarefied. A condition for the validity of the continuum approach is that the Knudsen number (ratio of the mean free path to a characteristic dimension) be small compared with unity. For low density flows, the particulate or molecular structure of the gas must be recognized. The mathematical model of such flows is the Boltzmann equation which presents overwhelming difficulties to computational methods for realistic flows. Consequently, the mathematical models that are readily applicable to both continuum and free molecular

(collisionless) flows experience serious limitations when applied to transitional flows. Fortunately, direct simulation methods have evolved over the past 35 years that readily lend themselves to the description of rarefied flows. These developments have generally been concerned with the direct simulation Monte Carlo (DSMC) method. The DSMC method of Bird[1-9] along with many variants is the most used method today for simulating rarefied flows in an engineering context. The DSMC method takes advantage of the discrete structure of the gas and provides a direct physical simulation as opposed to a numerical solution of a set of model equations. This is accomplished by developing phenomenological models of the relevant physical events. Phenomenological models have been developed and implemented in the DSMC procedure to account for translational, thermal, chemical, and radiative nonequilibrium effects. The present discussion will review the general features of the DSMC method, the numerical requirements for obtaining meaningful results, and applications of the method to calculate the flow about various configurations with emphasis on blunt body flows.

An extensive amount of literature is currently available that provides results of comparison of DSMC solutions with experimental data. Results of these comparisons have in general been very favorable. Four examples of validation studies are reviewed herein that include one dimensional shock wave structure and flow about both blunt and slender configurations.

Some of the earlier DSMC solutions for blunt bodies at entry conditions are reviewed to emphasize the effects of rarefaction on both flowfield and surface quantities. The applications reviewed are the axisymmetric approximation for the Shuttle Orbiter nose region, blunted slender bodies, and the aeroassist flight experiment (AFE) vehicle where both reacting and rarefied flow effects are present.

Attention is then directed to a combined experimental and computational study under the aegis of AGARD Fluid Dynamic Panel Working Group 18. This Working Group is addressing two problems that include rarefaction effects: corner flow/jet interactions and blunt-body/wake flows. The corner flow/jet interaction problem focuses on the issues of reaction control system flow interactions that occur at high altitude. It is important to develop prediction methods that can augment wind-tunnel measurements and to validate these prediction methods against selected experiments. The emphasis of the blunt body/wake studies is the significance of rarefaction and real gas effects on the near wake as it influences the afterbody heating and pressure distributions. Experiments are being conducted in both low density wind tunnels and impulse tunnels. Computations are being made with DSMC and Navier Stokes methods for selected experimental cases and generic flight conditions.

The final area reviewed is that of recent and ongoing flight experiments or projects for which rarefied flows are critical to spacecraft performance and experimental measurements. A very successful application of multipass aerobraking was demonstrated in 1993 by lowering and circularizing Magellan's orbit in Venus' upper atmosphere. During

February of 1994, the Japanese Orbital Reentry Experiment (OREX) was successfully executed and results are becoming available. Near term projects include the Skipper mission to obtain bow shock radiation emission measurements while traversing the transitional to low Reynolds number continuum regimes in the Earth's atmosphere. Also, the Galileo probe will enter Jupiter's atmosphere this December and the results of DSMC calculations supporting the aerothermodynamic definition of the probe during its initial atmospheric encounter are presented.

2. AEROASSIST MISSIONS FOR CAPSULES AND SPACECRAFTS

Almost any mission that involves changes in orbital altitude and/or inclination in the vicinity of an atmospheric-bearing planet is a candidate for aeroassist. In Walberg's[10] survey of aeroassisted space missions in 1985, he categorized the possible mission applications as 1) synergetic plane change, 2) planetary mission applications, and 3) orbital transfer vehicle applications. Figures 1 through 3 illustrate several possible planetary missions and orbital transfer vehicle (OTV) maneuvers between High Earth Orbit (HEO) and Low Earth Orbit (LEO).

Of the many aeroassist options, most have relevance to either capsule or spacecraft aerothermodynamics. These include the orbital transfer vehicle (OTV) maneuvers between High Earth Orbit (HEO) and Low Earth Orbit (LEO) (Fig. 1) as well as lunar return missions, multipass aerobraking (Fig. 2), planetary aerocapture (Fig. 3), and direct atmospheric entry (aerobraked) missions (not shown). Studies in the early 80's showed Aeroassisted Orbital Transfer Vehicles (AOTV's) to have a much enhanced payload delivery capability compared to all-propulsive OTV's. Also, these vehicles would encounter significant rarefied effects,extending potentially to perigee conditions. The central issues are nonequilibrium heating and the nature of the wake closure.

Multipass aerobraking is normally carried out at such high altitudes that highly rarefied flow conditions are encountered. An example[11] of a recent application of such an aeroassist maneuver was the use of multipass aerobraking (730 orbits) to achieve a lowering and circulization of the Magellan spacecraft in Venus' upper atmosphere. Also, the plan for the Mars Global Surveyor spacecraft is to launch in late 1996, insert into an elliptical capture orbit at Mars, and then use multipass aerobraking to achieve a nearly circular, polar mapping orbit with a two hour period.

Planetary aerocapture[12] is an aeroassist mission where the velocity decrement is achieved in a single deep atmospheric pass to transfer the vehicle from its hyperbolic approach trajectory to a target orbit about the planet. For single pass aerocapture, the atmospheric penetration is normally deep in order to deplete the excess velocity. Consequently, the critical loads occur in the continuum flow regime.

The most frequently used aeroassist maneuver is where the capsule or probe is aerobraked by direct atmospheric entry. Examples of aerobraked missions are the Apollo entry capsule, the Galileo Probe scheduled for entry into Jupiter's atmosphere this December, and the Mars Pathfinder mission scheduled for launch in 1996. Again, as for single pass aerocapture, the primary aerodynamic loads and heating occurs under continuum conditions. Consequently, rarefaction effects are of paramount importance when the aeroassist maneuver is designed to produce the desired drag decrement at high altitudes to avoid excessive aerodynamic heating. For aeroassist missions where the deceleration occurs much deeper into the atmosphere, rarefaction plays a secondary role on capsule performance, but would be critical in defining and interpreting expreiments conducted during the transitional portion of entry.

3. RAREFACTION

The degree of rarefaction is generally expressed through the Knudsen number, Kn, which is the ratio of the mean free path λ to a characteristic dimension L, i.e.

$$Kn = \lambda/L. \qquad \text{Eq. (1)}$$

Two very different approaches may be used to define λ and L: an overall Kn where λ might be the freestream mean free path and L an overall body dimension (nose radius or body diameter for blunt bodies), or a local Kn where the value of λ is the local mean free path and L is the scale length of a macroscopic gradient such as

$$L = \frac{\delta}{\frac{d\delta}{dx}}. \qquad \text{Eq. (2)}$$

where δ is a macroscopic flow variable such as density, velocity, or temperature. The value of Kn that provides an indication of the boundary between continuum and transitional flows is approximate at best and differs appreciably depending on which of the two approaches is used for defining Kn (overall or local).

An overall Kn is deficient in terms of characterizing the complexities of the flow enveloping a body due to factors such as local flow conditions (large density variations for hypersonic flight), body configuration (axisymmetric or 2-D for example), and surface conditions. Since an overall Kn is more frequently used to present experimental and computational results, a few additional comments are appropriate. For purpose of discussion, we will consider three flow regimes: continuum, transitional, and free molecular. An inclusive definition of the transitional regime would be 0.001<Kn<50.

A number of variations on the overall Kn are also used, particularly for wind tunnel conditions where the mean free path is evaluated at total temperature conditions (see Ref. 13). Also, the Kn can be expressed in terms of Mach and Reynolds numbers, since $M_\infty = V_\infty/a$ and $Re_\infty = v_\infty \rho_\infty L/\mu_\infty$ where a is the speed of sound and μ is

the coefficient of viscosity. The equilibrium mean free path for a simple hard sphere gas is given[9] as

$$\lambda = \frac{1}{\sqrt{2}\pi d^2 n} \qquad \text{Eq. (3)}$$

or

$$\lambda = \frac{16}{5}\left(\frac{m}{2\pi kT}\right)^{1/2}\frac{\mu}{\rho} \qquad \text{Eq. (4)}$$

Since the most probable molecular thermal speed C_m' is given as

$$C_m' = \sqrt{\frac{2kT}{m}} \qquad \text{Eq. (5)}$$

and related to the speed of sound as

$$C_m' = a\sqrt{\frac{2}{\gamma}} \qquad \text{Eq. (6)}$$

then Eq. (4) can be written as

$$\lambda = \frac{16}{5}\sqrt{\frac{\gamma}{2\pi}}\frac{\mu}{\rho a} \qquad \text{Eq. (7)}$$

with the Kn given as

$$Kn = 1.276\sqrt{\gamma}\frac{M_\infty}{Re_\infty} \qquad \text{Eq. (8)}$$

If one uses the boundary layer thickness, δ, as a characteristic length, then $Kn \sim M_\infty/\sqrt{Re_\infty}$ since $\delta/L \sim 1/\sqrt{Re_\infty}$. This relation has been used extensively in the classical literature[14], even though there are conceptual and practical limitations as discussed in Ref. 15. For $M/\sqrt{Re_\infty} \rangle 0.1$, wall slip effects become important (Ref. 16).

In terms of the local Kn as defined in Eq. (2), Bird[9] makes the case that the number should be less than 0.1 for the Navier-Stokes equations to be valid. Figure 4 (Ref. 9) presents the Kn limits for the mathematical models at both the microscopic and macroscopic levels. The limitation of the macroscopic or continuum description as expressed by the Navier Stokes equations arises from the fact that the conservation equations do not form a determinate set unless the shear stress and heat flux can be expressed in terms of lower order macroscopic quantities. Expressions for the transport terms in the Navier-Stokes equations fail when gradients of the macroscopic variables become so steep that their length scale is of the same order as the average distance traveled by molecules between collisions, or mean free paths. The Chapman-Enskog theory which provides expressions for the coefficients of viscosity, heat conduction, and diffusion also provides the limits of validity of the expressions since it assumes that the velocity distribution function f is a small perturbation of the equilibrium or Maxwellian function f_0. As discussed in Ref. 9, for the special case of a flow in the x-direction with gradients only in the y-direction, the Chapman-Enskog distribution can be written

$$f = f_0\left[1 - \alpha_1\frac{\lambda}{T}\frac{dT}{dy} - \alpha_2\frac{\lambda}{u}\frac{du}{dy}\right] \qquad \text{Eq. (9)}$$

where the specific expressions for α_1 and α_2 are given in Ref. 9 (page 3). The local Knudsen numbers appear explicitly in the terms attributable to the shear stress and heat flux, respectively. Since the Chapman-Enskog results is the first term expansion about the local Knudsen numbers, the theory is valid only when they are small in comparison with unity.

Results shown in Fig. 5 demonstrate the importance of the transport properties in the shock wave and the conditions adjacent to the surface along the stagnation streamline for the Shuttle Orbiter at 93 km. The overall Kn based on an effective nose radius of 1.296 m is 0.028. Figure 5 compares the density profile calculated with the viscous shock layer (VSL) method[17] with that calculated by the DSMC method. Evident is the inadequacy of the continuum assumption to describe the overall flowfield for this case.

The shock thickness is greater than the stand-off distance and the shock wave structure merges with that of the thermal boundary layer. At the same time, the surface pressure and heat transfer rates given by the continuum method are in good agreement with those from the DSMC method.

Also shown in Fig. 5 is the variation of the local Kn based on density scale length. As discussed in Ref. 3, the behavior of the local Kn parameter within the shock is no surprise because it is well known that continuum methods cannot be applied to the structure of strong shock waves. The local Kn near the surface is rather large, being an order of magnitude larger than the overall Kn and larger than the limiting value for the validity of the continuum transport equations. The surface temperature is approximately 1043 K while the gas temperature adjacent to the surface is approximately 1400 K. The fractional temperature jump is of the same order as the local Kn.

This example indicates that continuum theories can give useful results for hypersonic flow about the forebody of blunt bodies with cold surfaces when the overall Kn is about 0.05 or less (Ref. 3).

3.1 Requirement for a Discrete Particle Model
As previously discussed, the continuum model as represented by the Navier-Stokes equations becomes deficient when the local Kn exceeds 0.1. For this level of rarefaction and higher, a particulate model which recognizes the gas as a collection of discrete particles is required.

The classical formulation for a gas as a set of individual particles is the Boltzmann equation.[9] The left-hand side of this equation can be regarded as a conservation equation for the velocity distribution function f, with convective and nonstationary terms. The velocity distribution function essentially describes the way in which the particles are arranged in velocity space. The right-hand side of the Boltzmann equation is called the collision term and describes the manner in which molecules can jump from

one point to another in velocity space as a result of collisions. Conventional finite element and finite difference methods can be applied to the left-hand side of the Boltzmann equation, but while the number of dependent variables is reduced to one (the velocity distribution function), the number of independent variables increases from those of physical space to those of phase space. This leads to almost overwhelming difficulties. For example, a steady, one-dimensional flow involves an axially-symmetric distribution function in velocity space so that the solution of the Boltzmann equation is a three-dimensional problem. Almost all of the space-related applications involve flows with at least two spatial dimensions and a three-dimensional distribution function in velocity space. This leads to a five-dimensional grid, and direct numerical solutions can hardly be contemplated. Unsteady boundary conditions with internal degrees of freedom all add to the severity of the problem. The addition of chemical reactions would mean that the Boltzmann equation would be difficult to formulate, let alone solve! The alternative to a formal numerical solution is to take advantage of the discrete structure of the gas and conduct a direct physical simulation of the flow in the computer. As a consequence of the need for an alternative approach, Monte Carlo procedures (any method that employs random numbers) have been developed. Of the various techniques for the Monte Carlo simulation of gas flows, the direct simulation Monte Carlo (DSMC) method is the one that is most readily applied to complex problems. The DSMC method has evolved over the past 35 years, during which time the applications of the method have advanced from idealized or generally artificial test cases to problems of specific engineering applications.

The application of the DSMC simulation method has been aimed primarily at the transition regime that is characterized by Knudsen numbers that are above the upper limit for the validity of the Navier-Stokes equations but below the level at which the flow falls into the collisionless flow or free-molecule regime (see Fig. 4). The current paper focuses on the transitional regime, with special emphasis on calculations at or near conditions for which continuum solutions remain valid.

4. DSMC METHOD

The DSMC method[1-9], is a technique for the computer modeling of a real gas by thousands to millions of simulated molecules. The velocity components and position coordinates of these molecules are concurrently followed through representative collisions and boundary interactions in simulated physical space.

The principal computational tasks associated with the DSMC method are movement of the molecules, indexing molecules into cells, molecular collisions, and sampling of flowfield and surface quantities. The molecules used in the analyses are simulated molecules, each of which represents a very large number (on the order of 10^{10} to 10^{15}) of physical molecules. Thus, scaling the density by a very large factor has the effect of substantially reducing the number of molecular trajectories and molecular

collisions that must be calculated. Remember, however, that the physical velocities, molecular size (diameter of cross section), and internal energies are preserved in the simulation.

Another major aspect of the DSMC method is the uncoupling of the molecular motion and molecular collisions. The validity of this dichotomy is assured by requiring that the computational time step be small when compared with the real physical collision time $[\Delta t < \left(n \overline{\sigma c_r}\right)^{-1}]$. In addition to the time discretization, a cell structure is required for two purposes: first, the selection of potential collision pairs and second, the sampling of flow properties. The simulation becomes more exact as the cell size and time step tend to approach zero.

The cell dimensions must be small in comparison with the scale length of the macroscopic flow gradients. The simulated molecules in the cell are then regarded as representative of the real molecules at the location of the cell, and the relative location of the molecules within the cell is disregarded in the selection of collision partners. As shown previously,[18] the cell size must be small in comparison with the local mean free path in regions of large gradients. For problems with large density variations, the use of variable cell sizes assists in resolving the flow gradients and also minimizing the computational requirements provided that the flow is steady. Since the flow is always calculated as an unsteady flow starting from some initial specified state (usually a uniform freestream or vacuum), any steady flow becomes the large time state of the unsteady flow. For boundary conditions where the flow is steady, the overall computational effort can be substantially reduced by subdividing the flowfield into an arbitrary number of units (regions) where the time step Δt and the scaling factor F_N (the number of physical molecules represented by each simulated molecule) remain constant within a region, but can vary from region to region. Of course, such simulations are not time consistent solutions, but they provide steady state solutions with a substantial reduction in computational requirements. The combination of subdividing the flowfield into regions along with the use of variable cell sizes provides the flexibility to substantially reduce the total number of molecules used in the simulation and also resolve the flow gradients. Recall that in the DSMC method of Bird, the procedures are specified such that the computational time is linearly dependent on the number of molecules.

There is some lower limit on the number of simulated molecules per cell because the cell-sampled density is used in the procedures for establishing the collision rate. The number of molecules per cell should be as large as the order of ten. The other function of the cell besides sampling is the selection of collision pairs. During this process, the mean separation distance of the collision pairs (pairs are selected without regard to position within the cell) should be reduced to minimize the smearing of gradients. This requirement is normally addressed by subdividing the sampling cell into an arbitrary number of sub-cells for the selection of collision pairs. The sub-cells are chosen to contain on average two or three molecules, so that all collisions approach the "nearest-neighbor" ideal.

Should there be only one molecule in a sub-cell, the potential collision partner is selected from an adjacent sub-cell within the cell. With this procedure, the molecular sampling is still done on a cell basis, while the collision pairs are selected within the sub-cells.

The basis for much of the comments on the DSMC method has centered on the way in which a representative set of collisions are selected for each cell at each discrete flow time step Δt so that the appropriate collision frequency is maintained. Prior to 1988, the collision sampling technique that had been recommended by Bird[1] was the "time-counter" method where advantage is taken of the fact that the computational time is linearly proportional to the number of molecules. The collision pairs are accepted with probability proportional to the product of the magnitude of the relative velocity $\bar{c}_r$ and the total collision cross section σ . [This is accomplished by normalizing the $c_r\sigma$ product by the maximum value that has ever occurred within the particular cell and then using an acceptance-rejection procedure (see Appendix C, Ref. 9) to accept or reject the collision pair that was selected at random.] For each collision pair selected, a "cell time" is advanced by

$$2/(N\langle n \rangle \sigma c_r) \qquad \text{Eq. (10)}$$

for a simple gas (see page 121 of Ref. 1 for the corresponding expression for inverse power law molecules), where N is the number of simulated molecules in the cell, and <n> is the time-averaged (steady flow) or ensemble-averaged (unsteady flow) number density in the physical flow. Sufficient collisions are calculated to keep the cell collision time concurrent with the flow time.

In Ref. 7, Bird introduced a replacement for the time-counter method calling it the no-time-counter (NTC) method. The NTC method is obtained by modifying the "direct" or Kac method. In the direct method, all possible pairs in each cell are considered, and the probability of collision within the time step is equal to the ratio of the volume swept out by the cross section (moving with the relative velocity) to the cell volume V_c. The disadvantage is that the computation time is very nearly proportional to the square of the number of molecules. The direct method can be modified by reducing the number of sampled pairs by some factor and increasing the collision probabilities by the same factor. If the factor is such that the maximum collision probability of any pair is unity, the number of pairs to be sampled is

$$0.5N \langle N \rangle F_N (\sigma c_r)_{max} \Delta t/V_c \qquad \text{Eq. (11)}$$

and the collision probability for each selection is

$$(\sigma c_r) / (\sigma c_r)_{max} \qquad \text{Eq. (12)}$$

The selection criterion of equation (12) is identical to that used in the time-counter method. The only change with this method is that the number of collision pair selections is given deterministically [Equation (11)] rather than probabilistically through the operation of the time counter.

4.1 Molecular Models

During the development and extension of the DSMC method, there has been a remarkable increase in the gas complexity for which numerical simulations are possible. The modeling has advanced from a simple hard sphere model to models that include inelastic effects such as rotation, vibration, chemical reactions, electronic excitation, and radiation. The routines used to compute the molecular interactions may be exercised millions of times during the course of a simulation, and it is essential for them to be brief. In developing a model and its numerical algorithm, a careful balance has to be struck between the realism of the physical representation and the computational efficiency. Reference 9 discusses many of the current models available for simulating molecular collisions, internal degree of freedom (rotational and vibrational), chemical reactions, electronic excitation, radiation, and gas-surface interactions.

4.2 Validation with Experiments

When the DSMC calculations are performed carefully (particular attention is given to the numerical requirements of cell size and time step and to the interaction modeling of the viscosity coefficient of the real molecules), the method appears to yield results that agree very precisely with experiments. For example, Harvey and associates[19-21] have made numerous comparisons between experiments and DSMC results primarily for hypersonic nitrogen flows where internal translational energy exchange is a feature of importance. Results of comparisons for surface forces, heat transfer, and flowfield profiles (density and rotational temperature) have been reported for flow about sharp as well as blunt configurations. Four examples of efforts to validate the DSMC technique with experimental results are presented in this section that includes fundamental data concerning shock wave structure, overall aerothermodynamic coefficients for slender and blunt configurations, and separated flows as induced by a compression surface. Section 7 will include results of current studies of comparisons of experimental and computational results for blunt cone configurations.

4.2.1 One-Dimensional Shock-Wave Structure

In Ref. 22, Fiscko and Chapman calculated the one-dimensional shock-wave structure for argon and showed that the calculated shock density thickness was in good agreement with the measured values of Alsmeyer.[23] More recent studies[24-26] also investigated the shock wave structure of argon (Mach 7) and helium (Mach 1.59, 20, and 25) flows using the DSMC method. In these studies, the comparisons between calculation and experiment are done at a very fundamental level in that the comparisons are made for the molecular-velocity distribution function in the shock wave. The measurements (Fig. 6) of the molecular velocities inside a hypersonic normal shock wave, where the gas experiences rapid changes in macroscopic properties, show a highly nonequilibrium molecular motion (translational nonequilibrium) and a bimodal velocity distribution in the direction parallel to the flow. For the experimental conditions, the DSMC method

of Bird provided accurate quantitative prediction of the molecular motion. These calculations and comparisons with measurements represent an important, detailed test of the DSMC method for elastic interatomic collisions.

Figure 6 presents a comparison of the calculated and experimental velocity distributions at one location (ñ denotes the fraction of the density rise across the shock wave) within the normal shock wave. (See Ref. 25 for additional data.) Shown are the velocity distributions both parallel and normal to the flow for Mach 25 helium. Since the flow was produced in a free-jet expansion, the freestream was not in equilibrium (temperature perpendicular to the flow was about 1.1 K while that parallel to the flow was 2.2 K), and this fact was accounted for in the simulation. The calculated results shown in Fig. 6 used the Maitland-Smith intermolecular potential with a distance parameter of 2.976 Å and a well depth of 10.9 K. Similar results using the variable hard sphere (VHS) model for Mach 20 helium are presented in Ref. 24.

4.2.2 Hypersonic Flow About a Delta Wing

In the study of Ref. 27, a general three-dimensional (3-D) DSMC code using a body fitted grid is used to simulate rarefied flows about a delta wing (Fig. 7). As shown in this figure, the top of the wing is flat, the bottom is v-shaped, and the edges are rounded with a constant radius, $R = 0.0632$ mm. The shape of the nose from the side view is elliptical although it appears sharp from the top view. The origin of the coordinate system is located at the tip of the nose, and the x axis is parallel to the top surface and is normal to the base plane. The angle of incidence is measured with respect to the top surface of the model.

The flow simulated is for a wind-tunnel experiment[28] using nitrogen in which the flowfield freestream conditions are $T_\infty = 17.4$ K, $V_\infty = 756$ m/s, $M_\infty = 8.89$, and ρ_∞ varied from 0.172×10^{-5} to 38.033×10^{-5} kg/m^3. According to the VHS collision model (with $T_{ref} = 300$ K, $d_{ref} = 4.07 \times 10^{-7}$ m, and the temperature exponent of the viscosity coefficient of 0.75), the calculated overall freestream Knudsen number ranged from 3.5 to 0.016. The body surface is specified to be at a uniform temperature of 293 K. Full thermal accommodation and diffuse reflection are assumed for the gas-surface interaction.

The flow is quite rarefied for the range of conditions considered, and no evidence of separation is observed at 30° incidence or for $Kn_\infty = 0.389$ and incidence angles ranging from 15° to 60°. As shown in Figs. 8 and 9 for the drag and overall heat transfer coefficients

$(C_D = \text{Drag}/ \frac{1}{2}\rho_\infty V_\infty^2 A$ and $C_H = Q/\frac{1}{2}\rho_\infty V_\infty^3 A$ where $A =$

is the plane view area of the wing with a value of 8.6 mm^2 and Q is the total heat transfer rate), the calculated data are in good agreement with the measurements and within the estimated[28] experimental uncertainty.

4.2.3 Shuttle Orbiter Aerodynamics

In the study of Ref. 29 an evolved version of Bird's F3 code[8] is used to compute the aerodynamics of the Shuttle Orbiter during entry. Computations are made for five nominal altitudes ranging from 170 to 100 km. The computational grid is both Cartesian and unstructured in that the unstructured cells consist of one or more cubic elements defined on a uniform background Cartesian mesh. The VHS intermolecular collision model is used while accounting for internal energy transfer and chemistry among colliding molecules. The gas-surface interactions are modeled as diffuse with complete thermal accommodation.

Micro-g accelerometers have been used[30-32] to measure the axial and normal forces during entry in the altitude range of 160 to 60 km. The ratio of these two forces is of special interest in that it is independent of dynamic pressure. When the computed and flight results are compared (Fig. 11, Ref. 29) good agreement is observed over the entire range of the calculations. Figure 10 presents the data of Ref. 29 in terms of the lift-to-drag ratio as a function of altitude. The L/D ratio can be derived from the normal and axial forces since the incidence angle α is known:

$$L/D = \frac{F_N/F_A - \tan \alpha}{1 + F_N/F_A} \qquad \text{Eq. (13)}$$

The band of flight data shown in Fig. 10 corresponds to a series of shuttle flights occurring under varying atmospheric conditions. Agreement between computed and flight data are good. The modified Newtonian limit, corresponding to a hypersonic inviscid flow, is shown to be L/D = 1.10, which is very close to the value of L/D = 1.06 computed[33] using a Navier-Stokes code. Also shown in Fig. 10 are the results obtained with the DSMC code run in a collisionless mode.

4.2.4 Open Hollow Cylinder-Flare Results

An experimental test program has been completed[34] by the Office National d'Etudes et de Recherches Aerospatials (ONERA) to investigate shock boundary layer interactions induced by a hollow cylinder-flare configuration (Fig. 11). An objective of the experiment was to obtain data where separation and reattachment occurs under fully laminar conditions with a flare angle of 30°. Two aspects of this experiment make it very attractive for code validation studies. First, the flow is axisymmetric, thereby reducing the computational burden of a three-dimensional simulation. Second, the surface measurements include heat transfer, pressure and oil-flow data. Shown in Fig. 11 is a cross section, when rotated about the centerline axis generates the model. As shown, the leading edge is sharp with a bevel angle of 15° and a thickness of 10 mm. The compression surface is inclined 30° to the oncoming flow. The experiments were conducted in the ONERA R5 wind tunnel at the following conditions: Mach 9.9 air with $V_\infty = 1430$ m/s, $\rho_\infty = 4.226 \times 10^{-4}$ kg/m^3, $T_\infty = 51.9$ K, and the wall temperature was 295 K. The flow conditions along the model are primarily in the strong interaction region where the effect of viscous interactions on surface quantities is significant ($Kn_\infty = 0.001$ where the length scale is the distance from the model leading edge to the compression surface).

DSMC calculations[35-36] were made using the general two-dimensional/ axisymmetric code of Bird[37]. A two species

nonreacting gas model was employed. Full thermal accommodation and diffuse reflection are assumed for the gas-surface interactions. The calculations[35] made prior to the experiments yielded results that was in good qualitative agreement with previous experimental findings for hypersonic laminar flows. Good agreement between experimental and calculated values is evident in Figs. 12 and 13 for heat transfer distributions and the extent of the flow separation region, respectively.

5. RAREFIED HYPERSONIC BLUNT BODY FLOWS

Several applications of the DSMC method will now be discussed to highlight some of the physical aspects of hypersonic blunt body flows under low-density conditions. The first is the flow about the nose region of the Shuttle Orbiter; the second is the flow about blunt slender cones and wedges; and the third is the flow about an Aeroassist Flight Experiment (AFE) vehicle that was to be flown in the mid 1990's to simulate the atmospheric encounter of an aeroassisted orbital transfer vehicle (AOTV). Even though the AFE was cancelled in 1991, the AFE served as a focal point for blunt-body experimental and computational studies during the late 80's and early 90's. For the first two applications, the entry velocity is 7.5 km/s, while that for the AFE is 10 km/s. Figure 14 includes the altitude and velocity conditions that are the focus of these applications. Details of the flowfield structure and surface conditions as calculated with the DSMC method are presented and comparisons are made for some applications between the DSMC results and that obtained using Navier-Stokes (NS) and viscous shock-layer (VSL) methods.

5.1 Shuttle Orbiter Calculations

5.1.1 Flowfield Structure

An example of the flowfield structure in the nose region of a blunt reentry vehicle is discussed in Refs. 18 and 38 where axisymmetric calculations were made using the DSMC method to simulate the reentry conditions encountered by the nose region of the Space Shuttle Orbiter. An "equivalent axisymmetric body" concept was used in this study to model the windard centerline of the Shuttle at a given angle of attack with an appropriate axisymmetric body at zero angle of attack. The axisymmetric body was a hyperboloid with a nose radii of approximately 1.36 m and asymptotic body half angle of approximately 42.5° (see Ref. 18). The altitude range considered was 150 to 92 km where the freestream Knudsen number range was 23 to 0.03. The DSMC calculations accounted for translational, rotational, vibrational, and chemical nonequilibrium effects for a 5-species reacting air model. Even for the lowest altitude case considered, the DSMC results show that the shock wave is merged with the shock layer and that the shock thickness is of the same order as the shock layer. Figures 15 (a) through 15 (f) show details of the calculated flowfield structure and provide a comparison of the DSMC and continuum results as obtained with a VSL analysis.[34] The results show that the maximum temperatures for the VSL and DSMC solutions differ only by about 6 percent. [Note that two different temperatures are being compared in Fig. 15 (a). For the VSL calculations, local thermal equilibrium is assumed, and therefore, only one

temperature describes the translational and internal energy states. This is not necessarily the case for the DSMC calculation where nonequilibrium effects are modeled. The temperature shown for the DSMC solution is an overall kinetic temperature, T_{ov}, defined as the weighted mean of the translational and internal temperature. (See Ref. 9)]. The overall temperature begins to rise appreciably at a distance of about 0.4 m from the body, while the VSL calculation, using a discontinuous shock, has a total shock layer thickness of 0.1 m. When the individual temperature components are examined for the DSMC solution [Fig. 15 (b)], the rotational and vibrational temperatures are seen to lag far behind the translational temperatures. The differences between the translational and internal temperature modes increase with altitude, since the collision rate decreases. In the region adjacent to the surface, the slope of the temperature profile resulting from the two computational methods [Fig. 15 (c)] is slightly different, and the temperature jump predicted is 350 K.

The density rise will always lag behind the temperature rise as evidenced by the results in Figs. 15 (a) and 15 (d). In fact, if one assumes that the center of the shock for the DSMC calculation is at the location where the density equals the mean of the freestream and postshock continuum values, then the continuum and DSMC shock locations are in good agreement.

The chemical composition profiles along the stagnation streamline resulting from the DSMC and VSL solutions are presented in Figs. 15 (e) and 15 (f) for O_2 and N_2, and N, respectively. The profile resulting from the two solutions has the same general shape; however, the DSMC results show a significant influence of the thick shock wave on the chemical composition within the shock layer. A significant number of chemical reactions occur in the shock wave, producing atomic mass fraction in excess of 20 percent at the shock location, as given by the continuum solution. By including shock slip boundary conditions in the VSL solution, the chemical composition profile would compare more favorably with the DSMC results within the shock layer, as is demonstrated by the study of Shinn and Simmonds.[39]

The effect of increasing the altitude is to create a more rarefied situation in which the shock layer and shock wave merge [Figs. 16 (a) and 16 (b)]. As the altitude increases, the extent of the flowfield disturbance continues to increase, as evidenced by the results shown in Fig. 16 (c). Shown are the stagnation locations for the maximum value of overall temperature and the location where the density is six times the freestream density (perfect gas condition) as a function of freestream density. Since the collision rate is proportional to the square of the density, the rate of chemical reactions decreases with increasing altitude, and the present calculations show little chemical activity occurring above 105 km.

To make calculations well into the continuum flow regime using the DSMC method is computationally demanding for multidimensional problems. For example, if the altitude is decreased from 92 to 75 km for the previous axisymmetric

calculation, then the freestream density increases by an order of magnitude and the freestream mean-free path decreases by an order of magnitude. As a minimum, if one were to decrease the cell size only in the direction normal to the body to maintain a cell thickness that is less than the local mean-free path, then the number of computational cells would have to be increased by an order of magnitude (the number of particles in the simulation would also increase by an order of magnitude) and the time step reduced by an order of magnitude. At the higher density condition, the collision frequency increases. This results in increased computing time since the time required to calculate the collisions appropriate for a time step is more demanding than the time to move the particles. The combined effects of an increase in the number of particles, a decrease in the time step, and an increase in the collision frequency would increase the time requirement more than two orders of magnitude and the storage requirements by an order of magnitude.

Currently, two-dimensional and axisymmetric versions of the DSMC method can be used to simulate flow conditions well into the continuum regime. Prior to the current computational capabilities, a quasi-one-dimensional code was developed to simulate stagnation streamline flows about blunt bodies well into the continuum regime. Details of the method are described in Ref. 40 and applications of the method to Shuttle entry conditions are given in Refs. 41 and 42. Figure 17, taken from Ref. 41, shows a comparison of the DSMC and VSL calculations for density and overall temperature profiles for Shuttle entry at 75 km altitude. For this simulation, the freestream Knudsen number based on nose radius was approximately 0.002 and the freestream velocity was 7.2 km/s. The VSL calculation is based on a discontinuous shock-wave assumption, whereas the DSMC calculation accounts for a finite shock-wave thickness, and the location of the center of the shock wave, which was specified (as is necessary for the quasi-one-dimensional DSMC method) to be the location where the density is equal to $6\rho_\infty$, was the same as the VSL shock stand-off distance. The profiles at 75 km show an entirely different behavior from those at 92 km in that there is a distinct shock layer preceded by a shock wave that comprises a much smaller portion of the body-induced flowfield disturbance.

The previous comparisons with VSL calculations have been for discontinuous shock crossing with no-slip wall boundary conditions. The effect of integrating through the shock wave and including surface slip boundary conditions has been reported in Refs. 43 and 44. Figures 18 (a) and 18 (b) show the impact of these modifications on the density profiles at 92 km along with results at 115 km. For the 92-km case, the previously discussed VSL and DSMC results are shown along with the stagnation streamline results obtained by solving the NS equations. When shock wave structure is accounted for in the continuum formulation, improved agreement in flowfield properties is observed; yet, the NS calculation underpredicts the extent of the flowfield disturbance. This is no surprise because it is well known that continuum methods cannot be applied to the structure of strong shock waves as evidenced in Ref. 22. For a more rarefied condition [Fig. 18 (b)] which occurs at 115 km altitude, the discrepancy between the NS and

DSMC results is large away from the surface where the NS model is not expected to be valid. A fairly good agreement between the NS and DSMC results is obtained near the surface if the NS-profiles with surface slip are displaced away form the surface a distance equal to a local mean-free path.

5.1.2 Surface quantities
Quantities of particular interest in the transitional flow regime are the heating and aerodynamic forces experienced by the vehicle. Reference 18 provides details concerning the effect of rarefaction on heating and drag for the hyperboloid used to model the nose region of the Shuttle Orbiter. Comparisons (Fig. 19, from Refs. 43, 44) between the DSMC and VSL calculations showed good agreement in the stagnation surface heat transfer at an altitude of 92 km. Both solutions were also in good agreement with the Orbiter flight-measured value. However, as the altitude increased, the VSL results, without slip boundary conditions, began to depart rapidly from the DSMC results for λ_∞/R_N values greater than 0.03. Results of continuum calculations[44] using the NS equations for the stagnation streamline are also compared with the DSMC data for altitudes of 92 to 115 km. The NS and VSL results presented are for altitudes as low as 74.98 km. The NS results agree better with DSMC values for more rarefied conditions than the VSL results. When the NS calculations are made with surface slip boundary conditions, the agreement with the DSMC values is substantially improved, and the agreement is good for the range of conditions for which the comparisons are made. Even though all three numerical methods are in good agreement with respect to stagnation-point heat transfer at an altitude of 92 km, there are substantial differences in the flowfield structure as previously discussed and these differences increase with increasing rarefaction.

If the hypersonic flow conditions are such that dissociation occurs, then the surface convective heating rate can be significantly affected by the extent to which the surface promotes atom recombination. This effect is demonstrated in Fig. 20 where the calculated stagnation-point heating rate is presented as a function of the surface recombination probability γ_i. In the calculation, the recombination probability was assumed to be the same for both atomic oxygen and nitrogen even though different values could be specified for the respective species. For the noncatalytic surface ($\gamma_i = 0$, the heating rate is 65 percent of the fully catalytic value ($\gamma_i = 1$), which indicates the advantage of having a surface that is basically noncatalytic.

Another important factor in rarefied flows that directly impacts the surface forces and heating is the nature of the gas-surface interactions. For most low enthalpy flows over technical surfaces the diffuse scattering model for wall interactions seems quite adequate.[45] However, there are indications that the model of full thermal accommodation and diffuse scattering is not correct at orbital velocities. In Ref. 18, the DSMC method was used to study the sensitivity of rarefied gas flows over a surface to changes in the wall interaction model. An example of the sensitivity of the surface heating and temperature jump was considered in the calculations simulating Shuttle entry. For an altitude of 110 km, a calculation was made

assuming that half of the particles that interact with the surface do so in a diffuse manner with full thermal accommodation, and half interact in a specular manner (elastic collisions) with no thermal accommodation. The net result is a thermal accommodation of 0.5. The results of this calculation were compared with those from the diffuse calculation. The stagnation point heating is 60 percent of that for full accommodation. Similar reductions in heating were evident at other locations downstream of the stagnation point.

Altering the gas-surface interaction model produces a substantial change[18] in the state of the gas adjacent to the surface. The impact on the overall temperature adjacent to the surface is to produce a temperature jump that is about 4.5 times that for the diffuse surface with full accommodation. However, the slope of the temperature profiles adjacent to the surface is very similar for both calculations.

5.2 Blunt Slender Body Calculations

5.2.1 Flowfield Structure
References 46 and 47 reported on studies of the hypersonic low-density flow about slender wedges and cones, where the body half-angles were either 0°, 5°, or 10°. The focus was on the 5° half-angle bodies in the altitude ranges of 110 to 70 km, velocity of 7.5 km/s, and body nose radius of 0.0254 m. Since the nose radius was much smaller than that for the Shuttle Orbiter calculations ($R_N \approx 1.3$ m), the rarefaction effects are evident at much lower altitudes. For example, at 70 km the shock wave and shock layer are merged (Fig. 21) along the stagnation streamline (spherical nose). The DSMC calculation for density shows that the upstream influence of the body is more than three times that predicted by the VSL calculation. This is expected since the VSL shock stand-off distance is only about two freestream mean-free paths.

Figure 22 provides information concerning the chemical activity along the stagnation streamline as a function of altitude for the two-dimensional and axisymmetric configurations. The extent of the flowfield disturbance is significantly greater for the two-dimensional configuration, and this directly impacts the flowfield chemistry. An indication of this effect is presented in
Fig. 22 where the maximum value of the atomic mass fractions along the stagnation streamline is shown as a function of altitude for both the cone and wedge. The onset (atomic mass fraction exceeds 1 percent) of oxygen dissociation occurs at about 96 km for the wedge and at about 90 km for the cone. Therefore, below 96 km, there is significant difference in the level of dissociation for the two configurations.

As the flow expands about the nose region on to the slender afterbody, the density decreases substantially. For example, the 5° cone at 80 km has a stagnation point density that is 70 times the freestream value (constant wall temperature of 1000 K) but decreases very rapidly downstream of the stagnation point (Fig. 23). Figure 23 shows the density profiles along the body normal (η) at

three locations along the conical flank: $s/R_N = 2.3$, 4.1, and 6.3. Large differences are obvious in two flow regions: at the wall and at the shock. The wall temperature is specified as 1000 K in both calculations, yet the temperature predicted by the DSMC method for the gas adjacent to the wall is 2850, 2942, and 2994 K, respectively, for the three body stations. The large temperature jump calculated by the DSMC method produced a much smaller value of wall density.

As for the shock wave structure, major differences are observed in the density profile comparisons. Both calculations show that the extent of the flowfield disturbance increases with increasing downstream distance. Yet, the outward extent of the flowfield disturbance and the magnitude of the compression within the sock wave are substantially different. The DSMC results show that the shock wave is very thick (the initial density rise occurs over a significant spacial extent as opposed to the discontinuous jump used in the VSL calculations) with maximum ρ/ρ_∞ values of 1.8 to 1.5, whereas the VSL predicts corresponding values of 6.9 to 5.8. These results have important implications as to possible flight measurements concerning shock layer properties and shock wave location.

The differences between the DSMC and VSL calculations are further amplified in Fig. 24 where temperature profile comparisons are presented. For the DSMC calculations, an absence of equilibrium between the internal and translational modes exists as the wall is approached (not shown). The same was true of the stagnation results where the differences between the translational and internal kinetic temperature were small; however, at $s/R_N = 4.1$, large differences exist where the internal kinetic temperature is about one half the translational kinetic temperature. Consequently, the overall kinetic temperature shown in Fig. 24 is not to be interpreted as a thermodynamic temperature, which is the quantity shown for the VSL calculation.

5.2.2 DSMC Calculations for binary scaling assumption
Birkhoff[48] has pointed out a similitude which applies when the chemical kinetics are governed by two-body collisions. This binary scaling requires that the characteristic length remain inversely proportional to the freestream density. Favorable conditions for binary scaling exist at high altitudes where three-body collisions, required for recombination, are rare. Consequently, attention can be restricted to the two-body dissociation or exchange processes under rarefied conditions. At these conditions, scaling to another body size at the same velocity may be accomplished by holding the product of ambient density and body size constant, so that the ratio of a characteristic body size is unchanged. The calculations concerning binary scaling were made with the DSMC method for transitional flow conditions ($Kn_\infty = 0.07$), and the results are presented in Figs. 25 (a) and 25 (b) for surface heating. (See Ref. 47 for pressure results.) The conditions for the calculations were $V_\infty = 7.5$ km/s, $T_w = 1000$ K, finite catalytic surface, and the product of the nose radius and freestream density equal to a constant value of 1.01 x 10^{-6}

kg/m^2 for an altitude range of 70 to 90 km. For 75 km altitude, the nose radius was 0.0254 m. [Other values of nose radii are tabulated in Fig. 25 (b).] The results of the numerical simulation are in agreement with the binary scaling assumption as evidenced by the results presented for surface heating. The dimensional surface heating rate distributions for hemispherically blunt bodies are presented in Fig. 25 (a). The corresponding values in coefficient form are presented in Fig. 25 (b). Both the heat-transfer and pressure (not shown) coefficient distributions are invariant with altitude. The temperature jump at the stagnation point remained constant with altitude at a value of 0.75, and the maximum level of dissociation along the stagnation streamline was approximately constant with altitude ($C_O \approx .11$ and $C_N \approx .045$).

6. AFE CALCULATIONS
In the 1980's, extensions[40,49] were made to the DSMC method to include ionized species and thermal radiation for the more energetic flows such as can be encountered by ASTVs. Several applications of the DSMC method were made using axisymmetric,[50,51] and three-dimensional[52,53] codes. The three-dimensional calculations have been made only for the more rarefied portion of the entry trajectory where ionization and radiation effects would be negligible; that is, in the altitude range of 200 to 100 km.

6.1 Three Dimensional Calculations
A side view of the AFE vehicle is shown in Fig. 26. The aerobrake is an elliptically blunted elliptic cone raked off at the base and fitted with a skirt-type afterbody. The three-dimensional configuration has a base length of 4.25 m.

Figure 26 shows the computational grid used for the 120-km-altitude case. In this figure, both cells and subcells are shown on the outer freestream boundary. (For the three-dimensional applications, the cells are deformed hexahedral, and each cell is further divided into six tetrahedral subcells.) However, on the plane of symmetry, only the cell structure is drawn for clarity. Only the forebody and the experimental carrier are included in the calculation since the solid rocket motor was to be ejected during entry near 130 km.

Reference 52 describes in some detail the highly nonequilibrium flow that surrounds the AFE vehicle at these high altitude conditions and the resulting surface pressure and heat transfer distributions. The results of this study show that dissociation is important at 110-km altitude and below (a 5-species gas model was used) and that the flow approaches the free-molecular limit very gradually at higher altitudes. Even at 200 km, the flow is not completely collisionless. This is clearly evident in Fig. 28 where the aerodynamic coefficients (C_D = drag coefficient, C_L = lift coefficient, L/D = lift-to-drag ration) are presented at selected altitudes for an angle of incidence of 0° (using the present coordinate system shown in Fig. 26). The forces are normalized with respect to 1/2 $\rho_\infty V_\infty A_{ref}$ where ρ_∞ and V_∞ are the freestream density and velocity, respectively, and A_{ref}, the reference area,

equals 14.1 m^2. Figure 28 also shows the calculated free-molecule and modified Newtonian results, along with experimental wind-tunnel data. The experiments were conducted in the NASA Langley Research Center Mach 10 air and Mach 6 CF_4 (freon) wind tunnels using high-fidelity models.[54] The wind-tunnel values presented in Fig. 28 are recommended values for zero incidence based on the Mach 10 air and Mach 6 CF_4 results. Clearly, the DSMC results approach the free-molecule limit very slowly at higher altitudes, and even at an altitude of 200 km, the flow is not completely collisionless. Prior to these studies using DSMC, it was generally acknowledged that free-molecule flow existed for the AFE vehicle for altitudes near 150 km, but these studies show that the transitional effects are significant at these altitudes and influence the overall aerodynamic coefficients. These results have important implications for the interpretation of aerodynamic coefficients extracted from flight measurements under rarefied conditions. It has been recognized[55] that transitional effects rather than specular reflection might be influencing the interpretation of flight measurements; however, no calculations were available to establish the fact. The conventional procedure[56] had been to interpret the flight measurements using the free molecule flow calculations. Such procedures are used to establish what fraction of the gas-surface interaction is specular. But it can be seen from these calculations that the transitional effects persist even at very high altitudes (150 km and above).

Figure 28 also contains the results of the Lockheed bridging formula which empirically connects the axial and normal aerodynamic force coefficients between the continuum and free-molecule limits. This is accomplished with a sine-square function by assuming continuum flow at a Knudsen number $Kn_\infty = 0.01$ and free-molecule flow at $Kn_\infty = 10$, which correspond to altitudes of 90 and 150 km, respectively. The bridging formula results are plotted to show the general trend even though they are in error for the conditions considered in the present study. Figures 28(a) and 28(b) also show effects of the pressure and shear forces on the total drag and lift coefficients. Clearly, the pressure contributions are fairly constant for the altitudes considered and are approximately equal to the measured continuum wind-tunnel values. However, the shear contribution increases with altitude, and in effect, increases the drag and reduces the lift. Reference 52 provides a tabulated list of calculated values for stagnation point heating rate and surface pressure.

6.2 Stagnation-Streamline Results
References 50 and 57 describe results of flowfield structure and surface quantities obtained using the quasi-one-dimensional and axisymmetric simulations for altitudes between 130 and 78 km. Comparison of the stagnation flowfield quantities at 90 km (Fig. 29) and 78 km (Fig. 30) provides an indication of the nature of the flow for AFE entry conditions. These results[57] were calculated with the one-dimensional code where the surface was noncatalytic to atom recombination. At 90 km, the normal velocity and density [Fig. 29 (a)], temperature [Fig. 29(b)], species mole fraction [Fig. 29(c)], and electron number density [Fig. 29(d)] profiles show no evidence of a distinct shock

wave, only a gradual merging of the shock wave and shock layer. This behavior is expected at 90 km since the extent of the profiles shown in Fig. 29 is only 13 λ_∞ distance from the surface, which is only slightly greater than the expected thickness of a free-standing shock wave. The corresponding profiles at 78 km (Fig. 30) show an entirely different behavior in that there is a distinct shock layer preceded by a shock wave that comprises a much smaller portion of the body-induced flowfield disturbance. At 90 km, the extent of thermal nonequilibrium is large [Fig. 29(b)], and it is only near the surface that thermal nonequilibrium is achieved. At 78 km, [Fig. 30(b)] most of the shock layer is in thermal equilibrium, and the translational, rotational, and vibrational temperatures are of the order of 10,000 K for much of the shock layer, noticeably lower than the value at 90 km. The peak temperatures within the shock wave are somewhat lower than the corresponding values at 90 km, and the temperatures drop very rapidly behind the specified center of the shock wave (0.11 m).

For both altitudes, much of the chemical activity occurs within the shock wave [Figs. 29(c) and 30(c)]: all of the oxygen dissociation and an appreciable amount of nitrogen dissociation. The atomic nitrogen concentration continues to increase until it reaches a maximum value near the surface. The maximum concentration of atomic nitrogen is greater for the lower altitude case ($X_N = 0.71$ versus 0.60). The maximum electron concentrations were 1.6 and 1.3 percent at 90 and 78 km, respectively. Figures 29(d) and 30(d) present the electron number density profiles for both altitudes where the number densities are of the order of 10^{19} and 10^{20} m^{-3} for the 90- and 78-km conditions, respectively. The fact that the mole fraction of electrons is of the order of two percent or less for these calculations means that the number of simulated electrons and ions is very small in the computation, and there is considerable scatter in the data associated with the ions and electrons. [The curves in Figs. 29(c) and 30(c) are smoothed values.] Furthermore, the surface boundary condition of complete recombination of ions and electrons had no impact on the respective profiles because no ions or electrons ever struck the surface in the simulation. That is, the gas phase reactions are responsible for the depletion of electrons and ions as the relatively cool surface is approached.

6.3 Axisymmetric Calculation with Thermal Radiation
An axisymmetric representation of the AFE vehicle was used in Ref. 51 to calculate the surface convective and radiative heating. The upper rather than the lower portion of the AFE vehicle was considered so that the most severe heating would be calculated for the carrier panel which is shadowed by the aerobrake. Details of results are given in Ref. 51. Only a limited number of solutions were obtained for the AFE type of flow environment. However, recent attention has been refocused on radiation for air shock layers modeled with DSMC, and Ref. 58 provides an indication of current interest and capabilities of the research at Imperial College.

7. CURRENT GROUND-BASED EXPERIMENTAL AND COMPUTATIONAL STUDIES
The AGARD Fluid Dynamics Panel WG 18 began in late 1991 to focus on several problem areas associated with hypersonic fllows. A number of test cases were identified for which experimental and computational studies would be organized. Two test cases for which rarefaction is important and relevant to entry and aeroassist vehicles were selected. The first problem is concerned with the forces generated on surfaces as a result of the interaction between a reaction control jet and the flow field surrounding a vehicle while the second problem is concerned with the near wake structure of blunt bodies and how its closure is influenced by rarefaction. A brief review of the corner-flow/jet interaction is provided by describing the nature of the problem and recent experimental and computational contribution. This will then be followed by a discussion of the blunt body/wake closure studies.

7.1 Corner-Flow/Jet Interaction
Most space vehicles are controlled with reaction thrusters during atmospheric entry. These reaction control system (RCS) jets can be used independently or in conjunction with moveable aerodynamic surfaces depending on the specific vehicle configuration and flight conditions. The exhaust plumes of these control jets act as barriers to the external flow creating an effect that can change the pressure distribution along the vehicle surface containing the jet, as well as on surfaces surrounding the exhaust plume. These surface pressure perturbations lead to interaction forces which must be accurately predicted in order to obtain the desired vehicle performance. The use of RCS jets becomes vital at higher altitudes where the density is low enough to render the control surfaces ineffective. As the altitude increases and the freestream flow becomes more rarefield, the level of interaction between the control jet and the freestream diminishes and is practically nonexistent when the freestream mean free path is very large. Therefore, it is crucial to accurately model RCS firings at intermediate altitudes where reaction controls are needed and significant control jet interactions are expected.

In an effort to gain further insight into the control jet interaction problem, an experimental study[59–60] was conducted by the European Space Agency (ESA) at the SR3 low-density wind tunnel of CNRS in Meudon, France. As shown in Fig. 31, the corner-flow model is made of two perpendicular flat plates with sharp leading edges. A transverse jet is issued from a hypersonic nozzle located in the horizontal plate. This under expanded jet interacts with the external flow and with the surrounding surfaces.

The data base resulting from the experiments are serving as a basis for testing elements of the numerical simulation tools. The problem addressed is fundamental and complex in that the problem has both rarefield and continuum components—the rarefied external flow interacting with a

jet whose central core is at continuum conditions. The ultimate objective of the numerical studies is to provide a methodology for accurately simulating control jet interactions for hypersonic low density flows. Results of recent numerical studies for the SR3 test conditions (see Table 1 for freestream conditions) are presented in Refs. 61–66. In general, the DSMC simulations show good agreement with experimental results for the cases without the jet and show qualitative agreement with the cases with the jet. However, as discussed in Ref. 66 for the most rarefied test case, the calculated surface pressures were greater than the measured values in the region where the jet-induced pressures are greatest. Possible reasons for the discrepancies have been suggested, but not validated.

7.2 Blunt Body/Wake Closure
The second problem concerns the wake closure which is important for entry probes and aerobrakes. A number of fundamental issues exists concerning such flows: how does the wake structure change as a function of rarefaction, what role does thermochemical nonequilibrium play in the near wake structure, and to what limits are continuum models realistic as rarefaction in the wake is progressively increased. Computations are being conducted for both wind tunnel[67–77] and flight[78–80] conditions for the same forebody configuration: a 70° blunted cone with a nose radius equal to one-half the base radius (Fig. 32). Details concerning model configurations and the experimental and computational program are discussed in Chapter 3 of Ref. 81.

7.2.1 Wind Tunnel and Computational Comparisons
The nominal test conditions for the low density wind tunnels participating in the AGARD WG 18 study are listed in Table 1. Also included are the test conditions for one test that has been run in the Large Energy National Shock Tunnel (LENS) facility[82–84] at a low pressure condition to produce Mach 15.6 nitrogen flow. Figure 33 displays the test conditions in terms of rarefaction as indicated by constant lines of $M_\infty/\sqrt{R_\infty}$.

7.2.1.1 SR3 Conditions
The CNRS test for the three freestream conditions listed in Table 1 have been completed.[85,86] Measurements included aerodynamic forces and moments, surface heat transfer, and flow field density with models having base diameters of 5.0 cm. An extensive number of computations have been made for test condition 2 (Table 1) since it was a test case of the 4th European High-Velocity Database Workshop, ESTEC, Noordwijik, The Netherlands, Nov. 1994. Results shown in figure 34 are indicative of the type of agreement achieved between the DSMC simulations and measurements for the surface heat transfer distribution. The DSMC results are the 3-D solutions of Pallegoix[76] for incidence angles of 0°, 10° and 20°. Heat transfer measurements were made only along the windward ray. The present author has made calculations for the three SR3 test conditions at zero incidence, and a comparison of the DSMC and experimental results are presented in Fig. 35. The agreement along the sting $(s/R_n \geq 3.82)$ is very good. Along the cone forebody, the agreement is not as good and deteriorate with decreasing rarefaction. This is particularly evident for test condition 3, when even the qualitative

agreement is poor. Along the forebody, the experimental heating rate values decreases more with distance from the stagnation point than does the computed results, showing little evidence of the corner expansion on the last heat transfer measurement $(s/R_n = 1.56)$. For test condition 3, the experimental value at this location is 55 percent of the DSMS value. When the DSMC results along the forebody are compared with a NS calculation (Ref. 68), the agreement is 10 percent or better along the forebody.

In the study of Ref. 68, the Navier-Stokes solutions were obtained with and without slip boundary conditions. In general, the inclusion of slip boundary conditions provided improved agreement with the DSMC results. This study showed substantial differences between the NS and DSMC computations for the near wake flow field structure and surface results at a Knudsen number of 0.03. As the density of the freestream flow was increased (decreasing Knudsen number), the agreement between the two methodologies improved. For the smallest Knudsen number case (0.001), the overall agreement between the two methodologies was good with the exception of the heating rate to the sting where differences as large as a factor of two are observed. As shown in Fig. 35, the DSMC simulations are in excellent agreement with the experimental data.

7.2.1.2 V3G Conditions
An experimental test program[13] has also been conducted for the 70-deg blunted cone with the V3G free-jet facility of the DLR, Göttingen. Drag, lift, global heat transfer, and recovery temperature were measured in a Mach 9 nitrogen free-jet flow. These measurements were made for various degrees of rarefaction by including most of the transitional regime $(0.03 < Kn_0 < 6)$ for stagnation temperatures of 300 K and 500 K. The wall-to-stagnation temperature ratio was varied between 0.8 and 1.5. The copper model with a base diameter of 5 mm was suspended with a thermocouple at angles of attack of $\alpha = 0$, 20, 40 deg. Details concerning the experiments, data reduction, data accuracy, and results are included in Ref. 13.

Results for $T_0 = 300K$, $T_w/T_0 = 1.0$ and zero incidence are presented in Figs 36(a) and 36(b) for the drag and overall heat transfer coefficient ($C_H = 2Q/\rho_\infty V_\infty^3 A$), respectively. The overall accuracy of the experiments was estimated[13] to be ± 8 percent for these conditions. The DSMC solutions of Refs. 72 and 73 are in very good agreement with the experimental results.

7.2.1.3 LENS Conditions
A series of experiments have been conducted at Calspan with a blunted cone model having a base diameter of 15.24 cm. Tests were made with the LENS facility[84] using both nitrogen and air as test gases. Test at both the 5 and 10 MJ/kg conditions have been completed. Measurements consist of surface pressure and heating rates along the forebody, base, and sting. Most of the instrumentation is concentrated along the sting. The focus of these tests are at continuum conditions; however, one test has been made at low pressure conditions where rarefaction effects should be evident in the wake. The specifics of this test condition are listed in Table 1. Results of the experimental

measurements for the low pressure test were presented in Ref. 84 and DSMC results for this test condition have been reported in Refs. 71 and 72. Figures 37(a) and 37(b) show comparisons of measured and calculated values for heat transfer and pressure coefficient $\left(C_p = 2p_w/\rho_\infty V_\infty^2\right)$ distributions, respectively. As evident in Fig. 37, there is good agreement between the calculations and experiments, both in the separated region and toward the end of the recompression process, indicating[84] that the size of the base flow region is well predicted. The measured forebody pressure coefficients appear excessively high ($C_p = 3.0$ at the stagnation point) for the present flow conditions.

The DSMC results[71] presented in Fig. 37 are time averaged results between time steps 59,520 and 81,546 where the computational domain contained 22,808 cells and 489,146 molecules. For this calculation, the rotational relaxation collision number was set to a constant value of 5 while the vibrational collision number was treated as a variable [Eq. (A6) and using the constants for nitrogen given in Table A6 of Ref. 9] that models the Millikan and White[87] expression for vibrational collision number. For this calculation, a high degree of thermal nonequilibrium exists for both the forebody and wake flow as is discussed in Ref. 71.

7.2.2 Flight Conditions
The flight test cases consists of four individual cases to provide code-to-code comparisons. No experimental results are available for these test cases. The test cases are for both Earth and Mars entry using both reacting and non reacting gas models. The freestream and surface boundary conditions are specified in Ref. 81. Only results for Earth entry conditions have been reported (Refs. 78–80). Reference 78 presents results for both reacting and non reacting air using the DSMC model and results for reacting air using an axisymmetric 3-temperature, 5-species implicit Navier-Stokes code.[88] In addition, DSMC solutions for a reacting 5-species air model have been obtained by Celenligil.[80]

The DSMC and Navier-Stokes results (Ref. 78) were in close agreement for the wake flow field quantities. Also, the size of the vortex as measured from the base of the blunted cone to the wake stagnation point is identical for the two solutions (Ref. 78). However, there are some noticeable differences in the chemical composition within the wake. The most significant difference between the two solution methodologies is in the surface heating calculations along the base plane (Fig. 38). The Navier-Stokes results are 25 to 200 percent greater than the DSMC results, while good agreement exists along the forebody. Also, the two DSMC calculations using 5-species reacting air gas models (Refs. 78 and 80) are in good agreement for the surface heating rates. When the calculation is made with a non reacting gas model as was done in Ref. 78, the results when compared with the reacting air solution shows: much higher surface heating rates, particularly along the base plane (240 percent higher); a smaller vortex; similar values for the wake density contours and essentially the same value for drag.

Two conclusions are readily evident from the recent studies concerning the blunt body/wake flows. First is the demonstrated capability of the DSMC method to calculate the near wake flow feature and the base and afterbody (sting) heating values to good accuracy when compared to experimental measurements. The second point is that the NS computations agree with the DSMC results for quite large overall Knudson numbers along the forebody, but yield significant differences for the base and afterbody when compared with either DSMC or experiment.

8. RECENT AND NEAR-TERM AEROBRAKING MISSIONS
This section highlights several flight projects for which rarefied gas dynamics is critical to spacecraft performance and experimental measurements. The primary tool used to support these projects and experiments has been the DSMC method.

8.1 Multipass Aerobraking
Spacecraft that employ aerobraking to perform efficient orbit modifications has been recently demonstrated by both the HITEN[89,90] and Magellan[11] spacecraft. Both activities involved multipass atmospheric encounters at highly rarefied conditions in the Earth's and Venus' atmospheres, respectively. Skipper is a scientific satellite that will be placed into a highly elliptical orbit and make multiple passes in the Earth's upper atmosphere. As the satellite is progressively lowered from free molecular conditions to altitudes as low as 130 km, instruments onboard the satellite will measure the blow shock ultraviolet radiation. Following this phase of the mission, a controlled re-entry will be executed and bow shock measurements will be conducted from about 150 km down to an altitude where the aerodynamic heating will terminate the measurements.

8.1.1 HITEN
The HITEN[89,90] experiment was successfully conducted during 2 Earth atmospheric encounters (perigee altitudes of 125 and 120 km) at about 11 km/s during March 1991. HITEN was cylindrical in shape with a flat faced forebody having a diameter of 1.4 m and a length of 0.7 m. A thermal blanket developed to withstand heating rates of about 2 W/cm^2 or an equilibrium temperature of about 900 K covered the flat surface exposed to stagnation conditions. At perigee, this surface was normal to the velocity vector. The freestream Knudsen numbers for the two perigee altitudes (based on cylinder diameter) were 3.9 and 2.1, indicating that the flow was transitional. The initial discrepancy reported for measured and predicted heat flux values has been resolved[90] by accounting for lateral heat flux to the two onboard calorimeters.

8.1.2 Magellan
Between May 25 and August 3 of 1993, aerobraking was successfully used to modify the orbit of the Magellan spacedraft in the upper atmosphere of Venus without the need for large propulsive burns. These maneuvers required 730 orbits to halve the orbit period and to modify the orbit

from a highly elliptic (eccentricity of 0.39) to a near-circular orbit that multiplies Magellan's science return.[11] Since Magellan was not designed for atmospheric flight, the multiple-pass method was required to ensure low temperatures and small aerodynamic forces. Major aerodynamic concerns were overheating of the high gain antenna (HGA) and melting the solder connecting the solar cells. Periapsis altitude was controlled throughout aerobraking to keep the solar panels below 433 K, where damage would start to occur.

Magellan consisted of a central body (Fig. 39) which supported two large solar panels (each 2.50 m high by 2.53 m wide) on struts aligned along an axis transverse to the central axis of the vehicle. The flow was directed along the central body axis such that the high gain antenna was aft. The solar panels in this configuration were normal to the flow, but could have been canted at any angle (about the strut axes) to form an effective "windmill."

The initial DSMC simulations of Ref. 91 examined the heating and forces that Magellan would encounter for an altitude range of 125 to 140 km at a perigee velocity of 8.6 km/s. Results of this study revealed that allowable surface temperatures occur at the higher altitudes. The subsequent studies of Refs. (92, 93) provided pre-aerobraking aerodynamic forces, moments, and heating for altitudes near 140 km at a speed of 8.6 km/s. The analysis of Ref. 92 included altitudes of 136 to 140 km where the freestream Knudsen number (based on the HGA diameter of 3.7 m) ranged from 2.8 to 6.3. At altitudes near 140 km, molecular collisions tended to reduce the aerodynamic forces, moments, and heating below the free molecular value by 7–10 percent.[92] Results of these simulations were key inputs to establishing the feasibility of aerobraking Magellan.

With the success achieved in aerobraking Magellan, other planetary missions are expected to make use of this technology and provide opportunities for measurements and experiments that are of interest to the RGD community. Such is the plan for the Mars Global Surveyor (MGS) which will be a polar orbiting spacecraft at Mars with a mission to fulfill the major objectives of the failed Mars Observer Missions. Subject to funding approval, the MGS will be launched with a Delta II vehicle in November 1996, inserted into an elliptical capture orbit at Mars, and then aerobraked to reach a nearly circular, polar mapping orbit with a two hour period. The MGS is the first mission of a new, decade long program of robotic exploration of Mars—the Mars Surveyor Program.

8.1.3 Skipper

Skipper is a Ballistic Missile Defense Organization sponsored mission to characterize the aerothermal chemistry of a low orbiting/reentering spacecraft. Skipper is the third flight in a series of bow shock experiments aimed at making spectrally resolved measurements of shock layer emission. The first two experiments were launched on sub-orbital launch vehicles and made measurements of aerothermal chemistry at speeds up to 5.5 km/s. The Skipper mission (Fig. 40) will extend the

measurements to higher altitudes and higher velocities (8 km/s). This is accomplished in two phases: first, with multiple elliptical orbits (perigee of about 150–130 km) from which spacecraft glow measurements can be made followed by a controlled reentry. The flexibility of Skipper provides an opportunity to progressively map a broad region of rarefied aerothermodynamics as well as to provide an overlap with data obtained from the two previous sounding rocket experiments. The primary goal is to obtain data in the high altitude rarefied flow regime where the modeling uncertainties are high. Multiple passes through part of the altitude region of interest provides a better ability to measure weak signals. The second goal is to penetrate sufficiently low on reentry to overlap with data from the second Bow Shock Ultraviolet flight (65 to 100 km).

The Utah State University Space Dynamics Laboratory is the prime contractor on Skipper and the Moscow Aviation Institute and NPO Liavotchkin serve as sub-contractors for the spacecraft propulsion system, power system, and launch. Skipper is a cylindrical spacecraft having a length of 1.1 m and a diameter of 0.772 m. The end of the cylinder exposed to stagnation conditions has a 1-meter nose radius dome. More details concerning the spacecraft and experiments are given in Ref. 94. The 1-meter nose radius spacecraft dome provides a large number of viewing opportunities in the stagnation region. The Skipper payload will carry a large set of instruments (Ref. 94): 20 photometers, 4 VUV photometric instruments (2 used as ionization cells and 2 as photon counting detectors), and 2 scanning spectrometers.

Quantification of spacecraft heating remains an ongoing activity as does the pre-flight radiance predictions. Since the potential flight regime of interest ranges from 160 to 80 km, both DSMC[95] and continuum[96] methods are being utilized. With flow field solutions from these two models, the NEQAIR model[97] is used to calculate the spectral radiance. Predicted radiance as a function of freestream density for a photometer centered at 230 ± 25 nm suggest that the continuum methods breaks down at about 100 km (Fig. 41).

Axisymmetric and 3-D DSMC solutions have been obtained by the present author using a 5-species reacting air gas model to assess the aerodynamic and heating rates experienced by Skipper during both the elliptic and reentry phases.

8.2 Aerobraking during entry

8.2.1 OREX
On February 4, 1994, the Orbital Reentry Experiment (OREX) was successfully launched into Earth orbit by the H-II rocket and its reentry was essentially as planned. This was the first Japanese entry experiment from orbit and an initial report[98] indicates that the data is of good quality. Extensive aerothermodynamic measurements were made with the objective of providing a data base that can be used to establish the reliability of computational design tools for Earth-Space transportation systems. OREX was a

50° spherically blunted cone with a 1.35 m nose radius of curvature and a base diameter of 3.4 m (Fig. 42). Measurements made in the 120 to 80 km altitude range cover much of the transitional flow regime. Measurements at these altitudes include body surface temperature and pressure, temperature for recombination heating measurements, micro-G acceleration, and electron number density.

DSMC capability developed[99] at the National Aerospace Laboratory, Tokyo, is being used to simulate the higher altitude portion of entry. Figure 43 presents results of accelerometer output and the DSMC simulation of Koura.[99] The accelerometer outputs for the fine-range provide data in the 140 to 100 km altitude range while that for the coarse range extends the measurements to lower altitudes of about 80 km. Additional results have been reported[98] for drag coefficient and surface pressure. The surface temperature and inferred heat transfer rates to the different thermal protection materials will be of particular interest in the transitional flow regime.

8.2.2 Galileo

Galileo is a NASA spacecraft mission to Jupiter, designed to study the planet's atmosphere, satellites, and surrounding magnetosphere. The mission consists of both an orbiter and a probe. In late 1995 after more than a 6 year flight time, the orbiter and probe will separate 150 days prior to Jupiter encounter and both will continue along independent trajectories toward the encounter. When the probe enters the hydrogen-helium atmosphere, it will be traveling at a relative velocity of about 48 km/s. Most of the kinetic energy at entry will be dissipated within 30 s (Ref. 100). After a very harsh aerothermal encounter, the probe will eject what remains of its heat shield and deploy a parachute. During descent, the probe will make several in-situ measurements of atmospheric properties and transmit that data to the orbiting spacecraft. The Atmospheric Structure Experiment, one of six experiments flown on the probe, will measure deceleration during the high-altitude entry phase. This experiment can deduce atmospheric density, pressure, and temperature from deceleration measurements so long as the vehicle drag coefficient is known. The instrument is sufficiently sensitive to detect deceleration exceeding 10^{-5} m/s^2. Consequently, meaningful properties can be assessed[101] for the Jovian upper atmosphere where the probe encounters highly rarefied flow during entry prior to peak heating and ablation of the heat shield.

Accuracy of the experiment depends upon the accuracy with which the probe drag coefficient is determined. Haas[101] recently used DSMC to assess the drag coefficient for the Galileo probe during entry from 750 km down to 350 km altitude in the Jovian atmosphere (most of the transitional regime). A unique aspect of this study was the coupling of the flow field simulation with a modeled response of the carbon phenolic heat shield. Simulations initially employed a simple radiative-equilibrium model for gas-surface interactions. Since the surface heating rates can be substantial for such an entry even under rarefied conditions, the heat shield can potentially pyrolyze, ejecting gas into the flow from the surface. To capture this

behavior, simulations were also made by coupling the material response directly into its surface model by using routines from the Charring Material Thermal Response and Ablation (CMA) program.[102] The CMA model accounts for transient convective heating, radiation, in-depth conduction, heat capacity, and the flow of pyrolysis gases through the porous material. For the altitude range and entry velocity (47.45 km/s) considered by Haas, the freestream Reynolds number based on the probe diameter of 1.265 m ranged from 0.1 to 1000. The forebody of the probe is a 45-deg blunted cone with a nose radius of 0.222 m. The impact of pyrolysis on drag coefficient (Fig. 44) was evident for $Re_{\infty} > 34$. While the transport of momentum due to the emitting pyrolysis particles from the front of the vehicle tends to increase drag, the influence of these particles on the incoming flow tends to reduce the incident momentum imparted to the surface. Whether these competing effects would lead to a net increase or decrease in overall vehicle drag would be difficult to predict without performing simulations. For $Re_{\infty} > 103$, the simulation indicates that the flow is sufficiently rarefied that the pyrolysis gas has very little influence on the incident flow, and the drag coefficient is greater than when neglecting pyrolysis. However, as the low density and pyrolysis emission increased, molecular collisions in front of the probe caused a marked decrease in the convective heat transfer and the incident momentum flux, resulting in a lower drag coefficient for higher Reynolds number cases.

9. SUMMARY

The computational and experimental studies reviewed demonstrate the rather spectacular change in aerodynamic and heating coefficients that can occur for an entry capsule as it makes the transition from a free molecular flow environment to that of continuum flow. Results presented demonstrate convincingly the ability of the Direct Simulation Monte Carlo (DSMC) method to simulate transitional flows for both nonreacting and reacting (dissociating) gases. Examples cited of ongoing projects and programs demonstrate the important role that the DSMC tool plays in aerospace applications where rarefied gas dynamics is an issue. This capability can be used to establish the feasibility of conducting a mission or the development of a data base that can be used to address operational implications, material requirements, and strategies to realize mission objectives. Experiments that provide insight to the physics of complex flows including fundamental data on gas-gas and gas-surface interactions are essential for continued improvement and validation of the physical models used.

10. REFERENCES

1. Bird, G. A.,"Molecular Gas Dynamics", Clarendon Press, Oxford, 1976.

2. Bird, G. A., "Monte Carlo Simulation in an Engineering Context", AIAA Progress in Astronautics and Aeronautics: Rarefied Gas Dynamics, vol. 74, Part 1, edited by S. S. Fisher, AIAA, New York, 1981, pp. 239–255.

3. Bird, G. A., "Low-Density Aerodynamics", Progress in Astronautics and Aeronautics: Thermophysical Aspects of Re-entry Flows, edited by J. N. Moss and C. D. Scott, vol. 103, 1986, pp. 3–24.

4. Bird, G. A., "Nonequilibrium Radiation During Re-entry at 10 km/s", AIAA Paper 87-1543, June 1987.

5. Bird, G. A., "Direct Simulation of Gas Flows at the Molecular Level", Communications in Applied Numerical Methods, vol. 4, 1988, pp. 1165–172.

6. Bird, G. A., "Computation of Electron Density in High Altitude Re-Entry Flows", AIAA Paper 89-1882, 1989.

7. Bird, G. A., "Perception of Numerical Methods in Rarefied Gasdynamics", Progress in Astronautics and Aeronautics: Rarefied Gas Dynamics: Theoretical and Computational Techniques, edited by E. P. Muntz, D. P. Weaver, and D. H. Campbell, vol. 118, 189, pp. 221–226.

8. Bird, G. A., "Application of the Direct Simulation Monte Carlo Method to the Full Shuttle Geometry", AIAA Paper 90-1692, June 1990.

9. Bird, G. A., "Molecular Gas Dynamics and the Direct Simulation of Gas Flows", Clarendon Press, Oxford, 1994.

10. Walberg, G. D., "A Survey of Aeroassisted Orbit Transfer", Journal of Spacecraft and Rockets, vol. 22, no. 1, Jan.–Feb. 1985, pp. 3–18.

11. Curtis, H. H., "Magellian: Aerobraking at Venus", Aerospace America, January 1994.

12. Cruz, M. I. "The Aerocapture Vehicle Mission Design Concept—Aerodynamically Controlled Capture of Payload Into Mars Orbit", AIAA Paper 79-0893, May 1979.

13. Legge, H., "Heat Transfer and Forces on a Blunted 70 Deg. Half Angle Cone Measured in Hypersonic Free Jet Flow", DLR Report IB 222-93 A 33, November 1993.

14. Schaaf, S. A., and Chambré, P. L., "Flow of Rarefied Gases", Div. H. of Fundamentals of Gasdynamics, edited by H. W. Emmons, Vol. III of High Speed Aerodynamics and Jet Propulsion, Princeton Univ. Press.

15. Liepmann, H. W., and Roshko, A., "Elements of Gasdynamics", Wiley, New York, 1957.

16. Gebhart, B., "Heat Transfer", McGraw-Hill, 1961.

17. Shinn, J. L., Moss, J. N., and Simmonds, A. L., "Viscous-Shock-Layer Heating Analysis for the Shuttle Windward Symmetry Plane With Surface Finite Catalytic Recombination Rates", Progress in Astronautics and Aeronautics, vol. 85, 1983, pp. 149–180.

18. Moss, J. N. and Bird, G. A., "Direct Simulation of Transitional Flow for Hypersonic Reentry Conditions", Progress in Astronautics and Aeronautics: Thermal Design of Aeroassisted Orbital Transfer Vehicles, edited by H. F. Nelson, vol. 96, 1985, pp. 113–139.

19. Harvey, J. K., "Direct Simulation Monte Carlo Method and Comparison with Experiment", Progress in Astronautics and Aeronautics: Thermophysical Aspects of Re-Entry Flows, edited by J. N. Moss and C. D. Scott, vol. 103, 1986, pp. 25–43.

20. Harvey, J. K., Celenligil, M. C., Dominey, R. C., and Gilmore, M. R., "A Flat-Ended Circular Cylinder in Hypersonic Rarefied Flow", Journal of Thermophysics and Heat Transfer, vol. 6, no. 1, Jan.–Mar. 1992, pp. 35–43.

21. Celenligil, M. C., "Rarefied Flow Simulations About a Blunt-Ended Cylinder at Incidence", Progress in Astronautics and Aeronautics: Rarefied Gas Dynamics: Space Science and Engineering, edited by B. D. Shizgal and D. P. Weaver, vol. 160, 1994, pp. 323–330.

22. Fiscko, K. A., and Chapman, D. R., "Comparison of Burnett, Super-Burnett, and Monte Carlo Solutions for Hypersonic Shock Structure", Progress in Astronautics and Aeronautics: Rarefied Gas Dynamics: Theoretical and Computational Techniques, edited by E. P. Muntz, D. P. Weaver, and D. H. Campbell, vol. 117, 1989, pp. 374–395.

23. Alsmeyer, H., "Density Profiles in Argon and Nitrogen Shock Waves Measured by the Absorption of an Electron Beam", Journal of Fluid Mechanics, vol. 74, 1976, pp. 497–513.

24. Pham-Van-Diep, G. C., and Erwin, D. A., "Validation of MCDS by Comparison of Predicted with Experimental Velocity Distribution Functions in Rarefied Normal Shocks", Progress in Astronautics and Aeronautics: Rarefied Gas Dynamics: Theoretical and Computational Techniques, edited by E. P. Muntz, D. P. Weaver, and D. H. Campbell, vol. 118, 1989, pp. 271–283.

25. Erwin, E. A., Muntz, E. P., and Pham-Van-Diep, G. C., "A Review of Detailed Comparisons Between Experiments and DSMC Calculations in Nonequilibrium Flows", AIAA Paper 89-1883, June 1989.

26. Pham-Van-Diep, G. C., Eriwn, E. A., and Muntz, E. P., "Nonequilibrium Molecular Motion in a Hypersonic Shock Wave", Science, vol. 245, August 1989, pp. 624–626.

27. Celenligil, M. C., and Moss, J. N., "Hypersonic Rarefied Flow About a Delta Wing—Direct Simulation and Comparison with Experiment", AIAA Journal, vol. 30, no. 8, August 1992, pp. 2017–2023.

28. Legge, H., "Force and Heat Transfer on a Delta Wing in Rarefied Flow", Workshop on Hypersonic Flows for Reentry Problems, Pt. II, Antibes, France, April 1991.

29. Rault, D. F. G., "Aerodynamics of the Shuttle Orbiter at High Altitudes", Journal of Spacecraft and Rockets, vol. 31, no. 6, Nov.–Dec. 1994, pp. 944–952.

30. Blanchard, R. C., Larman, K. T., and Barrett, M., "The High Resolution Accelerometer Package (HiRAP) Flight Experiment Summary for the First 10 Flights", NASA Pub. 1267, April 1992.

31. Blanchard, R. C., "Rarefied Flow Lift-to-Drag Measurements of the Shuttle Orbiter", 15th Congress of International Council of Aeronautical Sciences (ICAS), Paper ICAS-86-2, Sept. 1986.

32. Blanchard, R. C., Larman, K. T., and Moats, C. D., "Rarefied-Flow Shuttle Aerodynamics Flight Model", NASA TM-107698, Feb. 1993.

33. Weilmuenster, K. J., Gnoffo, P. A., and Greene, F. A., "Navier-Stokes Simulations of Orbiter Aerodynamic Characteristics with Emphasis on Pitch Trim and Body Flap", AIAA Paper 93-2814, 1993.

34. Chanetz, B., "Personal Communication", June 1994, ONERA, 8 rue des Vertugadins, 92190 Meudon, France.

35. Moss, J. N., Dogra, V. K., and Price, J. M., "DSMC Simulations of Viscous Interactions for a Hollow Cylinder-Flare Configuration", AIAA Paper 94-2015, June 1994.

36. Moss, J. N., Dogra, V. K., and Price, J. M., "Comparison of DSMC and Experimental Results for Hypersonic External Flows", AIAA Paper 95-2028, June 1995.

37. Bird, G. A., "The G2/A3 Program System Users Manual",Version 1.7, March 1991.

38. Moss, J. N., and Bird, G. A., "Monte Carlo Simulations in Support of the Shuttle Upper Atmospheric Mass Spectrometer Experiment", Journal of Thermophysics and Heat Transfer, vol. 2, April 1988, pp. 138–144.

39. Shinn, J. L., and Simmonds, A. L., "Comparisons of Viscous Shock-Layer Heating Analysis with Shuttle Flight Data in Slip Flow Regime", Progress in Astronautics and Aeronautics: Thermal Design of Aeroassisted Orbital Transfer Vehicles, edited by H. F. Nelson, vol. 96, 1985, pp. 491–510.

40. Bird, G. A., "Direct Simulation of Typical AOTV Entry Flows", AIAA Paper 86-1310, June 1986.

41. Dogra, V. K., Moss, J. N., and Simmonds, A. L., "Direct Simulation of Stagnation Streamline Flow for Hypersonic Reentry", AIAA Paper 87-0405, January 1987.

42. Dogra, V. K., Moss, J. N., and Simmonds, A. L., "Rarefaction Effects for Hypersonic Re-entry Flow", AIAA Journal, vol. 26, April 1988, pp. 392–393.

43. Gupta, R. N. and Simmonds, A. L., "Hypersonic Low-Density Solutions of the Navier-Stokes Equations with Chemical Nonequilibrium and Multicomponent Surface Slip", AIAA Paper 86-1349, June 1986.

44. Gupta, R. N., "A Continuum Analysis of Chemical Nonequilibrium Under Hypersonic Low-Density Flight Conditions", Proceedings of the 15th International Symposium on Rarefied Gas Dynamics, edited by V. Boffi and C. Cereignani, Vol. II, 1986, pp. 432–441.

45. Hurlbut, F. C., "Sensitivity of Hypersonic Flow Over a Flat Plate to Wall/Gas Interaction Models using DSMC", AIAA Paper 87-1545, June 1987.

46. Cuda, V., and Moss, J. N., "Direct Simulation of Hypersonic Flows Over Blunt Wedges", Journal of Thermophysics and Heat Transfer, vol. 1, April 1987, pp. 97–104.

47. Moss, J. N., and Cuda, V., "Nonequilibrium Effects for Hypersonic Transitional Flows", AIAA Paper 87-0404, January 1987.

48. Birkhoff, G., "Fact, Logic, and Similitude", Princeton University Press, Princeton, p. 109, 1960.

49. Bird, G. A., "Nonequilibrium Radiation During Re-entry at 10 km/s", AIAA Paper 87-1543, June 1987.

50. Dogra, V. K., Moss, J. N., and Simmonds, A. L., "Direct Simulation of Aerothermal Loads for an Aeroassist Flight Experiment Vehicle", AIAA Paper 87-1546, June 1987.

51. Moss, J. N., and Price, J. M., "Direct Simulation of AFE Forebody and Wake Flow with Thermal Radiation", Progress in Astronautics and Aeronautics: Rarefied Gas Dynamics: Theoretical and Computational Techniques, edited by E. P. Muntz, D. P. Weaver, and D. H. Campbell, vol. 118, 1989, pp. 413–431.

52. Celenligil, M. C., Moss, J. N., and Blanchard, R. C., "Three-Dimensional Rarefied Flow Simulations for the Aeroassist Flight Experiment Vehicle", AIAA Journal, vol. 29, no. 1, January 1991, pp. 52–57.

53. Celenligil, M. C., and Moss, J. N., "Three-Dimensional Hypersonic Rarefied Flow Calculations Using Direct Simulation Monte Carlo Method", Theoretical and Experimental Methods in Hypersonic Flows, AGARD CP-514, April 1993, Paper 27.

54. Wells, W. L., "Wind Tunnel Preflight Test Program for Aeroassist Flight Experiment", AIAA Paper 87-2367, August 1987.

55. Blanchard, R. C., and Rutherford, J. F., "Shuttle Orbiter High Resolution Accelerometer Package Experiment: Preliminary Flight Results", Journal of Spacecraft and Rockets, vol. 22, no. 4, July–August 1985, pp. 474–480.

56. Blanchard, R. C., "Rarefied Flow Lift-to-Drag Measurements of the Shuttle Orbiter", 15th Congress of International Council of Aeronautical Sciences, Paper ICAS-86-2.10.2, London, England, September 7–12, 1986.

57. Moss, J. N., Bird, G. A., and Dogra, V. K., "Nonequilibrium Thermal Radiation for an Aeroassist Flight Experiment Vehicle", AIAA Paper 88-0081, January 1988.

58. Gallis, M. A., and Harvey, J. K., "Atomic Species Radiation From Air Shock Layers Modelled With DSMC", AIAA Paper 94-2018, June 1994.

59. Allègre, J., and Raffin, M., "Experimental Study on Control Jet Interaction", SESSIA Report 608/91.1043/CNRS Aerothermique RC-91-11, December 1991.

60. Allègre, J., and Raffin, M., "Experimental Study on Control-Jet/Corner-Flow Interaction", ESA Contract, CNRS Report RC92-7, November 1992.

61. Hendriadi, R., "Etude de simulation numérique d'un écoulement hypersonique de gaz raréfié limité par deux plans perpendiculaires avec jet transversal", CNRS Report RS 93-3, Juin 1993.

62. Tartabini, P. V., Wilmoth, R. G., and Rault, D. F. G., "Systems Approach to a DSMC Calculation of a Control Jet Interaction Experiment", To be published in the Journal of Spacecraft and Rockets, 1995.

63. Dupuis, D., and Chauvot, J. F., "Validation du Code JMC3D Sur un cas Experimental d'interaction Entre un Jet et un Ecoulement Hypersonique", Aerospatiale/Hermes Contract, Report HERMES HNT 1253 ASPM, June 1993.

64. Chauvot, J. F., Dumas, L., Dupuis, D., "Corner Flow Jet Interaction: Computations and Experiments", Paper presented at the 19th RGD Symposium, Oxford, England, July 1994.

65. Coron, F., Pallegoix, J. F., and Sportisse, B., "DSMC Computations of Complex Test Cases and Industrial Configurations", Paper presented at the 19th RGD Symposium, Oxford, England, July 1994.

66. Wilmoth, R. G., and Tartabini, P. V., "Three-Dimensional DSMC Calculations of Jet/Corner Flow Interactions", Paper presented at the 19th RGD Symposium, Oxford, England, July 1994.

67. Dogra, V. K., Moss, J. N., and Price, J. M., "Near-Wake Structure for a Generic Configuration of Aeroassisted Space Transfer Vehicles", Journal of Spacecraft and Rockets, vol. 31, no. 6, Nov.–Dec. 1994, pp. 953–959.

68. Moss, J. N., Mitcheltree, R. A., Dogra, V. K., and Wilmoth, R. G., "Direct Simulation Monte Carlo and Navier-Stokes Simulations of Blunt Body Wake Flows", AIAA Journal, vol. 32, no. 7, 1994, pp. 1399–1406.

69. Wilmoth, R. G., Micheltree, R. A., Moss, J. N., and Dogra, V. K., "Zonally Decoupled Direct Simulation Monte Carlo Solutions of Hypersonic Blunt-Body Wake Flows", Journal of Spacecraft and Rockets, vol. 31, no. 6, Nov.–Dec. 1994, pp. 971–979.

70. Moss, J. N., Dogra, V. K., and Wilmoth, R. G., "DSMC Simulations of Mach 20 Nitrogen Flows About a 70° Blunted Cone and its Wake", NASA TM-107762, August 1993.

71. Moss, J. N., Price, J. M., and Dogra, V. K., "DSMC Calculations for a 70° Blunted Cone at 3.2 km/s in Nitrogen", NASA TM-109181, January 1995.

72. Gallis, M. A., and Harvey, J. K., "Comparison of the Maximum Entropy DSMC Code with Flowfield Measurements, AIAA Paper 95-0413, 1995.

73. Gallis, M. A., and Harvey, J. K., "Validation of DSMC Computations for the Flowfield Around a 70° Blunted Cone", Paper presented at the 19th RGD Symposium, Oxford, England, July 1994.

74. Gilmore, M. R., Owen, A. K., and Jones, T. V., "70° Aerobarake Vehicle Plus Afterbody in Hypersonic Rarefied Nitrogen Flow", Paper presented at the 19th RGD Symposium, Oxford, England, July 1994.

75. Marriott, P. M., and Bartel, T. J., "Comparison of DSMC Flow Field Predictions Using Different Models for Energy Exchange and Chemical Reaction Probability", Paper presented at the 19th RGD Symposium, Oxford, England, July 1994.

76. Pallegoix, J.F., "Workshop ESTEC—Test Case No. 6—Rarefied Spherically Blunted Cone", Paper presented at 4th European High-Velocity Database Workshop, ESTEC, Noordwijk, The Netherlands, November 1994.

77. Gilmore, M., "Test Case 6—Rarefied Flow Over a Blunt Body", Paper presented at 4th European High-Velocity Database Workshop, ESTEC, Noordwijk, The Netherlands, November 1994.

78. Dogra, V. K., Moss, J. N., Wilmoth, R. G., Taylor, J. C., and Hassan, H. A., "Effects of Chemistry on Blunt Body Wake Structure", AIAA Paper 94-0352, January 1994.

79. Dogra, V. K., Moss, J. N., Wilmoth, R. G., Taylor, J. C., and Hassan, H. A., "Effects of Chemistry on Blunt Body Wake Structure", AIAA Paper 94-0352, January 1994.

80. Celenligil, M. C., "Personal Communication", Middle East Technical University, Ankara 06531, Turkey, 1993.

81. Anon., "Hypersonic Experimental and Computational Capabilities: Improvement and Validation", AGARD AR-319, To be published in 1995.

82. Anon., "Large Entry National Shock Tunnel (LENS) Description and Capabilities", Calspan-UB Research Center, February 1991.

83. Holden, M., "Recent Advances in Hypersonic Test Facilities and Experimental Research", AIAA Paper 93-5005, Nov.–Dec. 1993.

84. Holden, M., Kolly, J., and Chadwick, K., "Calibration, Validation and Evaluation Studies in the LENS Facility", AIAA Paper 95-0291, 1995.

85. Allègre, J., and Bisch, D., "Experimental Study of a Blunted Cone at Rarefied Hypersonic Conditions", CNRS Report RC 94-7, November 1994.

86. Allègre, J., and Bisch, D., "Experimental Density Flowfields, Heat Transfers and Aerodynamic Forces for a 70° Blunted Cone at Rarefied Hypersonic Conditions", Paper presented at 4th European High-Velocity Database Workshop, ESTEC, Noordwijk, The Netherlands, November 1994.

87. Millikan, R. C., and White, D. R., "Systematics of Vibrational Relaxation", J. Chen. Phys., vol. 39, pp. 3209–3213, 1963.

88. Olynick, D. R., and Hassan, H. A., "New Two-Temperature Dissociation Model for Reacting Flows", Journal of Thermo-physics and Heat Transfer, vol. 7, no. 4, Oct.–Dec. 1993, pp. 687–696.

89. Abe, T., Kawaguchi, J., Saito, S., Ichikawa, T., and Uesugi, K., "The World's First Cis-Lunar Aerobrake Experiment Preliminary Report of the Results", ION 47th Annual Meeting, Williamsburg, USA, Paper 1A-4, 1991.

90. Abe, T., Suzuki, K., and Kawaguchi, J., "Aerothermo-dynamic Flight Environment of HITEN Spacecraft at the Aerobrake Experiment", Symposium on Aerotherm-ochemistry of Spacecraft and Associated Hypersonic Flows", Marseille, France, 1992.

91. Haas, B. L., and Feiereisen, W. J., "Particle Simulation of Rarefied Aeropass Maneuvers of the Magellan Spacecraft", Journal of Spacecraft and Rockets, vol. 31, no., 1994, pp. 17–24.

92. Haas, B. L., and Schmitt, D. A., "Simulated Rarefied Aero-dynamics of the Magellan Spacecraft During Aerobraking", Journal of Spacecraft and Rockets, vol. 31, no. 6, Nov.–Dec. 1994, pp. 980–985.

93. Rault, D. F. G., "Aerodynamic Characteristics of Magellan Spacecraft in Venus Upper Atmosphere", AIAA Paper 93-0723, 1993.

94. Levin, D. A., Finke, R. G., Candler, G. V., Boyd, I. D., Howlett, C. L., Erdman, P. W., and Zipf, E. C., "In-Situ Measurements of Transitional and Continuum Flow UV Radiation From Small Satellite Platforms", AIAA Paper 94-0248, 1994.

95. Boyd, I., and Gocken, I., "Computation of Axisymmetric and Ionized Flows Using Particle and Continuum Methods", AIAA Paper 93-0729, 1993.

96. Candler, G. V., and MacCormack, R. W., "The Computation of Hypersonic Ionized Flows in Chemical and Thermal Nonequilibrium", Journal of Thermophysics and Heat Transfer, vol. 5, no. 3, 1991, pp. 266–273.

97. Park, C., "Calculations of Nonequilibrium Radiation in the Flight Regimes of Aero-Assisted Orbital Transfer Vehicles", AIAA Progress in Astronautics and Aeronautics: Thermal Design of Aero-Assisted Orbital Transfer Vehicles, vol. 96, edited by H. F. Nelson, AIAA, New York, 1985.

98. Inouye, Y., "OREX Flight—Quick Report and Lessons Learned", Invited Paper 4, 2nd European Symposium on Aerothermodynamics for Space Vehicles, ESTEC, November 1994.

99. Koura, K., "In Study of HOPE", Report of HOPE Joint Study by NAL/NASDA, no. 10, sec. 7, 1991, (in Japanese).

100. Moss, J. N., and Simmonds, A. L., "Galileo Probe Forebody Flowfield Predictions," AIAA Progress in Astronautics and Aeronautics: Entry Vehicle Heating and Thermal Protection Systems, vol. 85, edited by P. E. Bauer and H. E. Collicott, AIAA, New York, 1983, pp. 419-445.

101. Haas, B. L., and Milos, F. S., "Simulated Rarefied Entry of the Galileo Probe into the Atmos-phere of Jupiter", AIAA Paper 94-2043, 1994.

102. Anon., "User's Manual Aerotherm Charring Material Thermal Response and Ablation Program CMA87", Report UM-87-11/ATD, Acurex, Corp., Mountain View, CA, 1987.

Table 1. Low-Density Test Conditions

Test Conditions	$T_O(K)$	P_O(bars)	M_∞	Re_∞/cm	$\rho_\infty \times 10^5$ (kg/m³)	V_∞ (m/s)	$T_\infty(K)$	λ_∞(mm)	Nozzle	Gas
(a) SR3 Wind Tunnel, CNRS Meudon									
1	1100	3.5	20.2	285	1.73	1502	13.3	1.05	conical	N2
2	1100	10.0	20.0	838	5.19	1502	13.6	0.35	conical	N2
3	1300	120.0	20.5	7277	46.65	1633	15.3	0.04	conical	N2
(b) V2G Wind Tunnel, DLR Göttingen									
1	575	2	15.6	715	6.65	1082	11.6	0.33	conical	N2
2	675	5	16.5	1210	10.80	1174	12.2	0.21	conical	N2
3	775	10	16.9	1910	16.90	1257	13.3	0.13	conical	N2
(c) V3G Wind Tunnel, DLR Göttingen									
1	295	0.163	9.0	859	14.22	759	17.2	0.16	free jet	N2
2	295	0.0549	9.0	286	4.74	759	17.2	0.48	free jet	N2
3	295	0.0163	9.0	86	1.42	759	17.2	1.60	free jet	N2
4	295	0.0054	9.0	29	0.47	759	17.2	4.80	free jet	N2
(d) RGWT, University of California, Berkeley, (UCB)									
1	300	11.1	22.0	1469	14.40	760	3.1	0.45	free jet	N2
2	1000	20.3	24.5	399	4.19	1450	8.6	1.60	free jet	N2
3	2000	28.4	27.0	214	2.33	2000	14.3	3.00	free jet	N2
(e) LDWT, University of Oxford									
1	290	0.067	6.0	1090	41.7	763	35	0.08	contoured	N2
2	523	0.067	6.0	450	23.1	1025	63	0.19	contoured	N2
3	290	0.020	6.0	325	12.4	763	35	0.27	contoured	N2
4	523	0.020	6.0	124	6.9	1025	63	0.64	contoured	N2
5	290	0.009	7.5	84	2.2	734	24	1.25	free jet	N2
(f) LENS, Calspan Buffalo									
1	4351	74.1	15.6	578	13.06	3246	103.7	0.35	contoured	N2
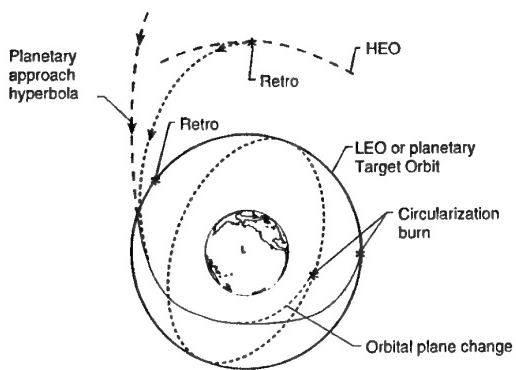
Fig. 1   Aeroassisted maneuvers for synergetic plane change, orbital transfer vehicle, and planetary aerocapture missions.[10]
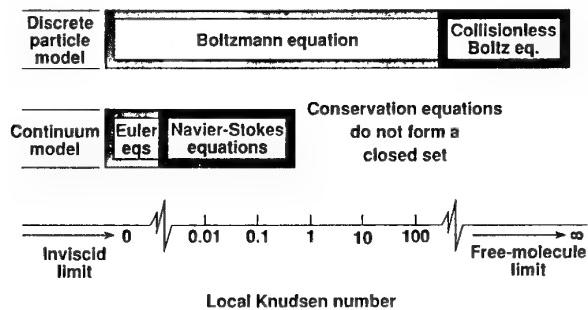
Fig. 4   The Knudsen number limits on the mathematical models.[3,9]
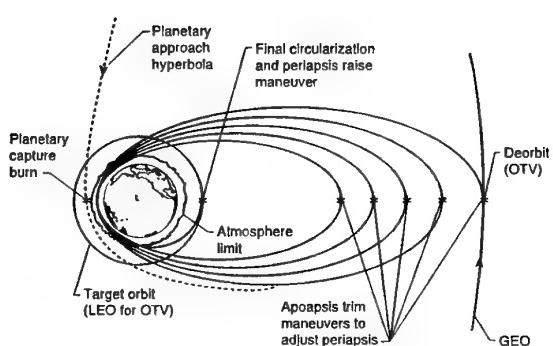
Fig. 2   Multipass aeroassisted maneuvers for planetary aerobraking and orbital transfer vehicle mission.[10]
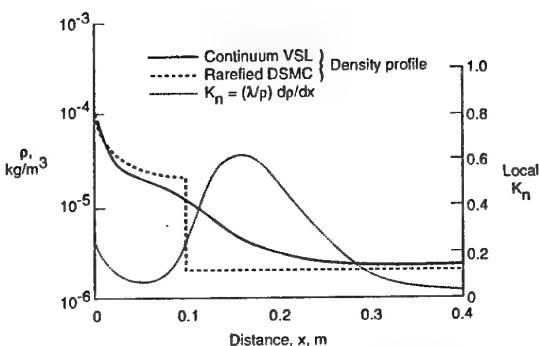
Fig. 5   Density distribution along the stagnation streamline of the re-entering Shuttle Orbiter at 93 km altitude.[3]
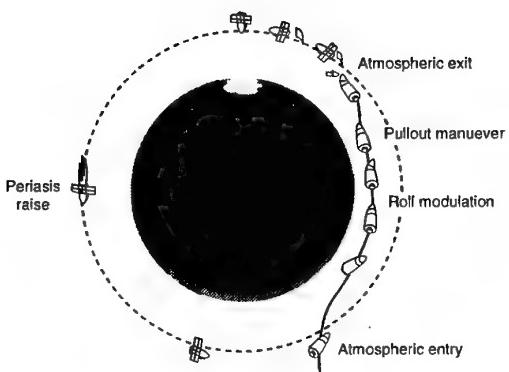
Fig. 3   Planetary aerocapture maneuver.[12]
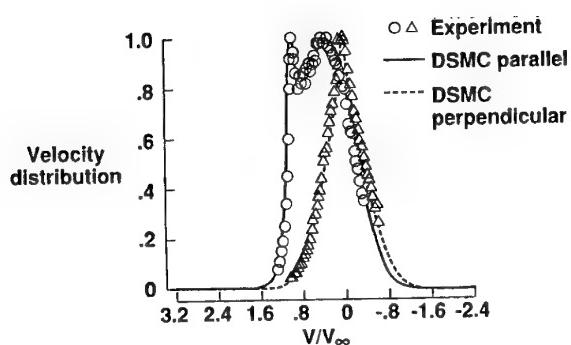
Fig. 6   Comparison of molecular velocity distributions (normal shock, Mach 25 helium, $\bar{n} = 0.565$).[26]
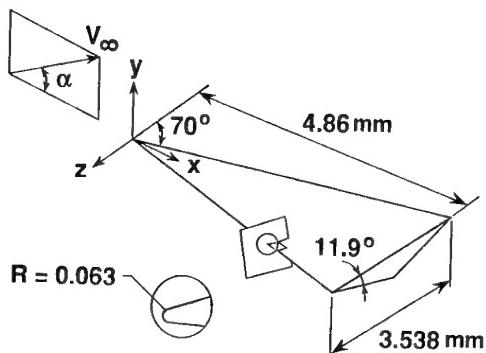
Fig. 7   Schematic of the delta wing (dimensions in millimeters.) [27,28]
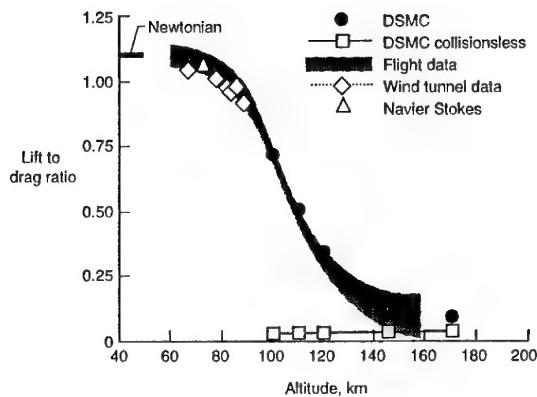
Fig. 10   Shuttle Orbiter lift-to-drag ratio.[29]
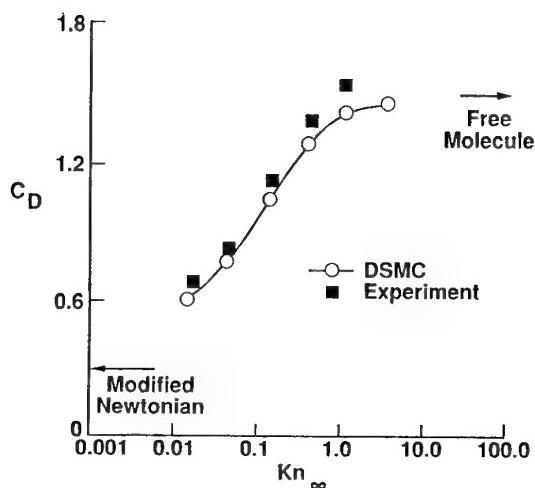
Fig. 8   Delta wing drag coefficient for α = 30 deg.[27]
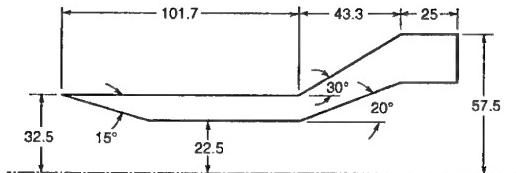
Fig. 11   Hollow cylinder-flare model (dimensions in mm).[35]
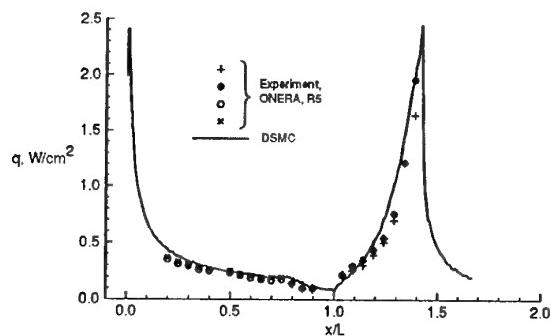
Fig. 12   Calculated and measured heating rate distributions for hollow cylinder-flare model.[36]
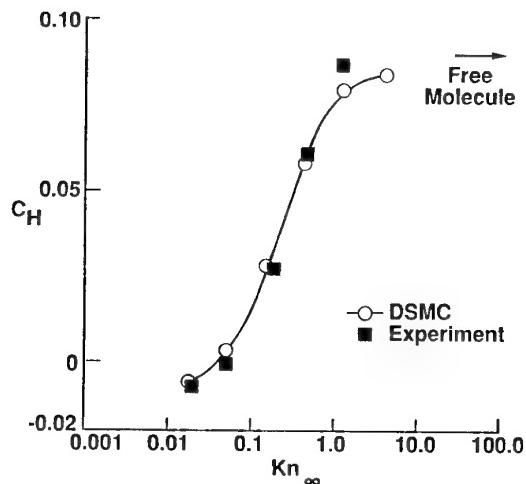
Fig. 9   Delta wing overall heat transfer coefficient for α = 30 deg. [27]
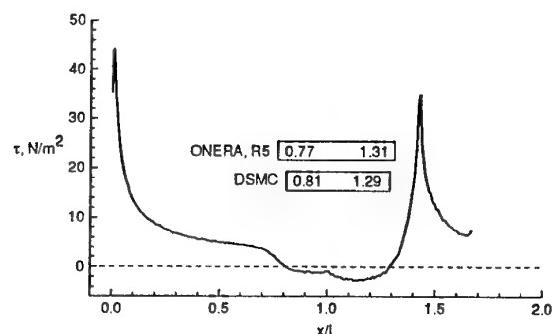
Fig. 13   Calculated shear stress and calculated and measured extent of separation for hollow cylinder-flare model.[36]
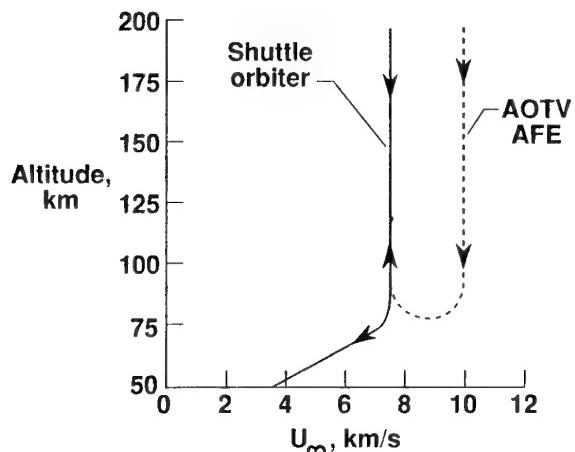
Fig. 14   Entry trajectories.
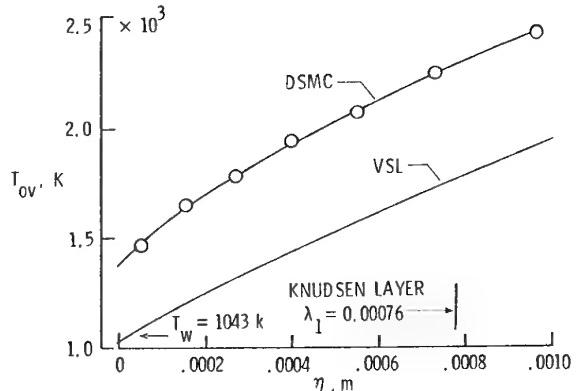
(c) Comparison of temperature profile adjacent to surface.
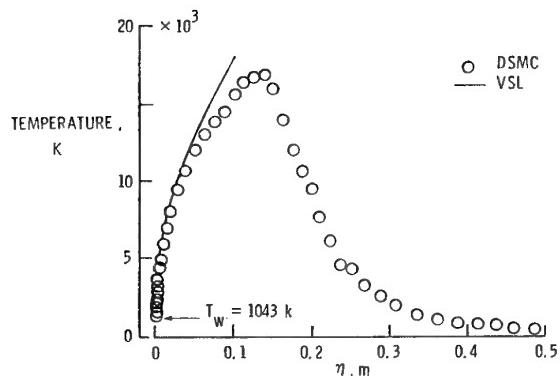
(a) Comparison of temperature.
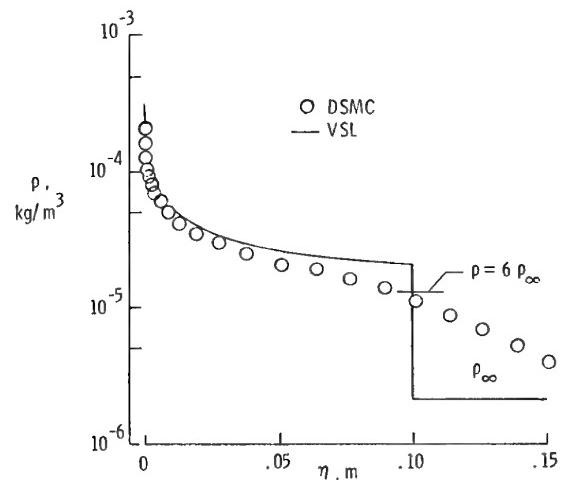
(d) Comparison of density profiles.
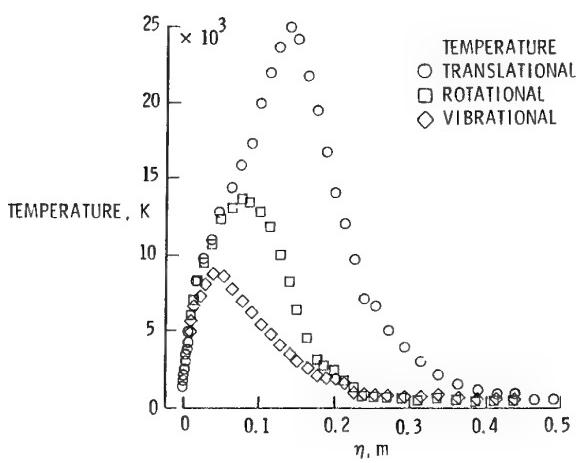
(b) Extent of thermal nonequilibrium (DSMC).
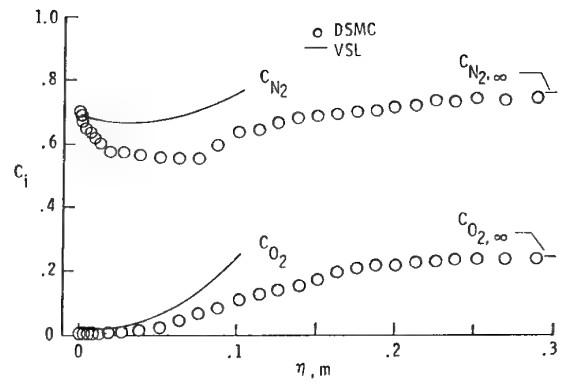
(e) Comparison of species mass fraction profiles for O_2 and N_2.

Fig. 15   Flowfield structure along stagnation streamline of Shuttle Orbiter at 92.3 km. [18]
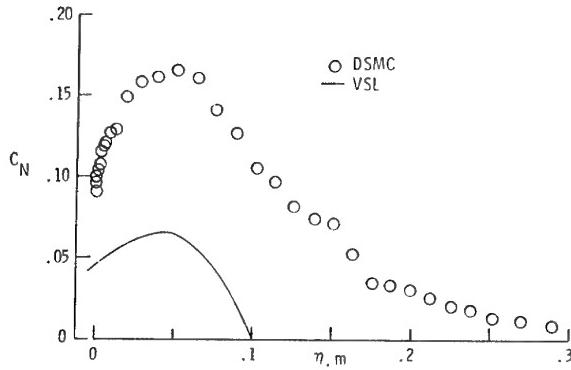
(f) Comparison of species mass fraction profiles for atomic nitrogen.

Fig. 15 Flowfield structure along stagnation streamline of Shuttle Orbiter at 92.3 km. [18]
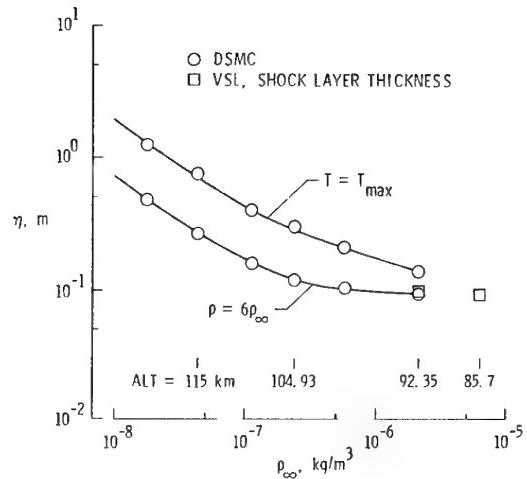
(c) Location of stagnation streamline quantities.

Fig. 16 Effect of rarefaction on flowfield structure (stagnation streamline for Shuttle Orbiter). [18]
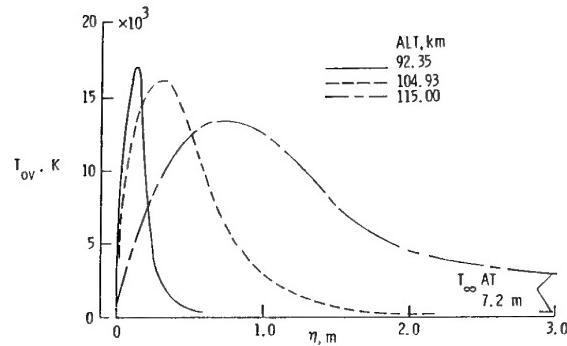
(a) Overall kinetic temperature.
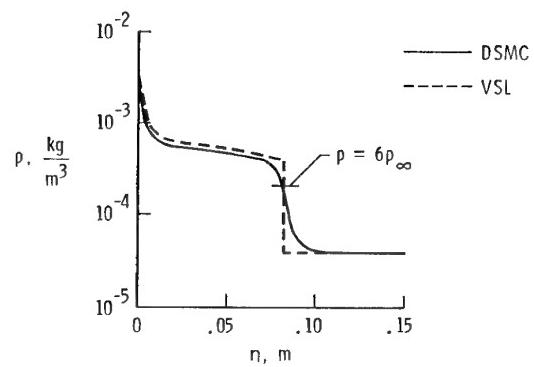
(a) Density.
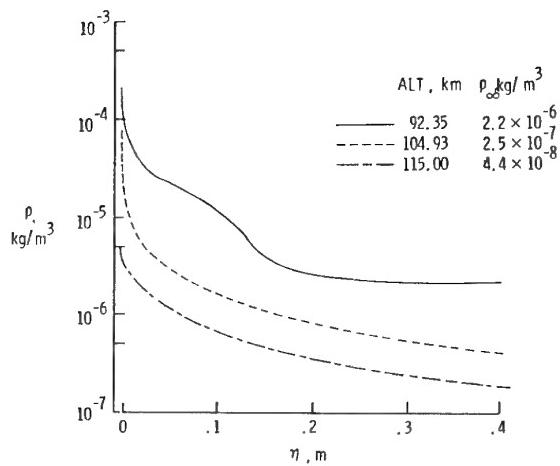
(b) Density profiles.
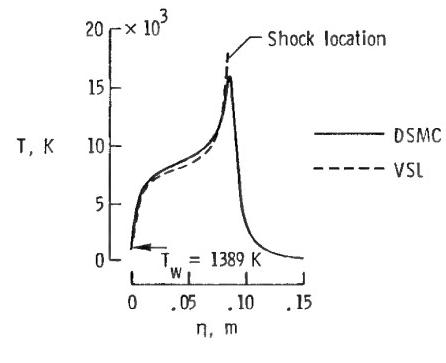
(b) Temperature.

Fig. 17 Comparison of calculated stagnation streamline flow structure (Shuttle Orbiter at 74.98 km, $\eta_s = 0.083$m). [41]
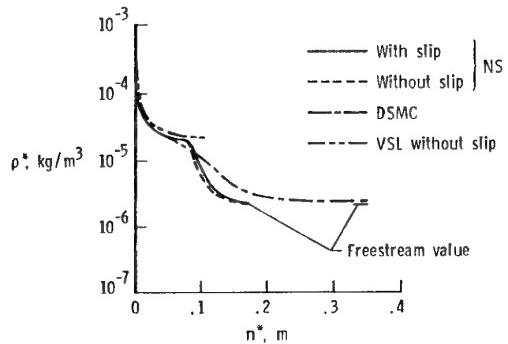
(a) Altitude = 92.35 km.
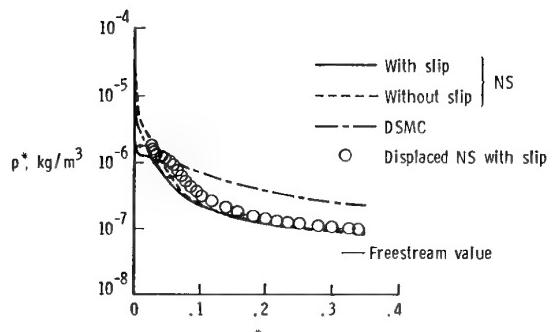
(b) Altitude = 115 km.

Fig. 18 Comparison of stagnation streamline density profiles (Shuttle entry conditions).[44]

Fig. 19 Comparison of calculated heat transfer coefficient for Shuttle entry conditions.[44]
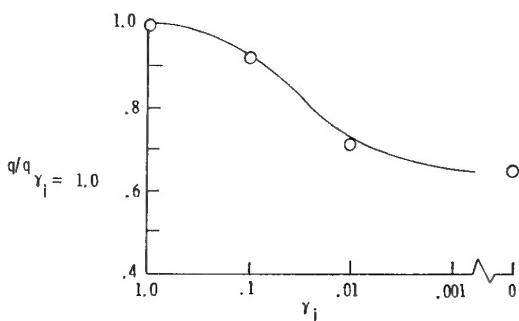
Fig. 20 Effects of surface catalysis on heating (Shuttle entry at 92.35 km, stagnation point).[18]
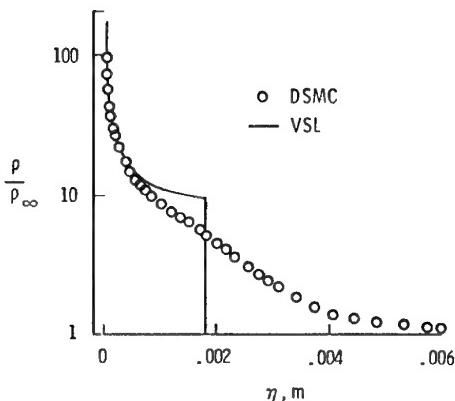
Fig. 21 Comparison of calculated density profiles along stagnation streamline (R_n = 0.0254 m, V_∞ = 7.5 km/s, Alt = 70 km).[46]
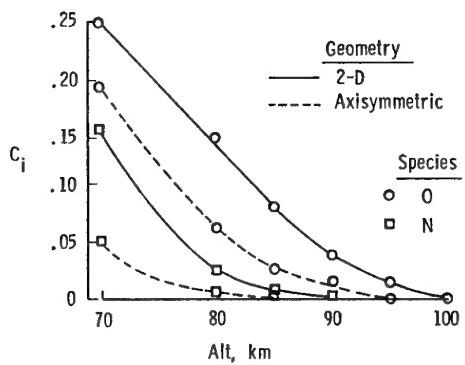
Fig. 22 Maximum atomic mass fraction values along stagnation streamline (R_n = 0.0254 m, V_∞ = 7.5 km/s).[46]
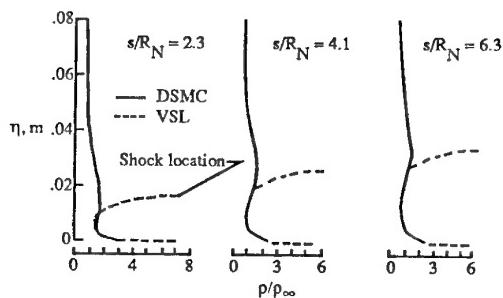
Fig. 23   Comparisons of calculated density profiles
(Alt = 80 km, V_∞ = 7.5 km/s, 5° cone).[46]
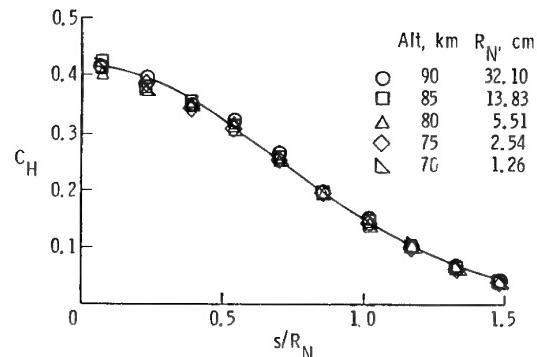
(b)   Heat transfer coefficient.

Fig. 25   Distributions along hemispherical nose
(V_∞ = 7.5 km/s, $\rho_\infty R_n$ = 1.01 x 10^{-6} kg/m^2).[47]
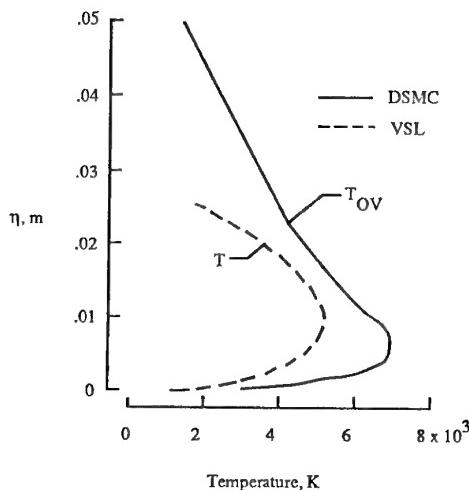
Fig. 24   Comparison of calculated temperature profiles
for 5° blunted cone at s/R_n = 4.1 (Alt = 80 km,
V_∞ = 7.5 km/s).[46]
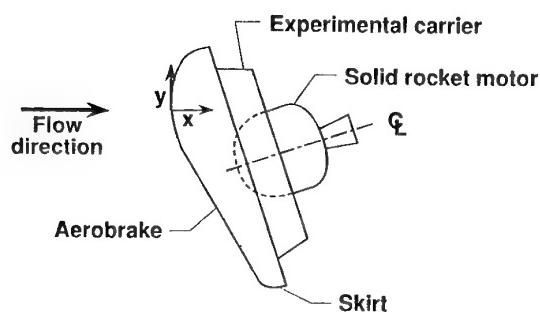
Fig. 26   AFE Configuration.
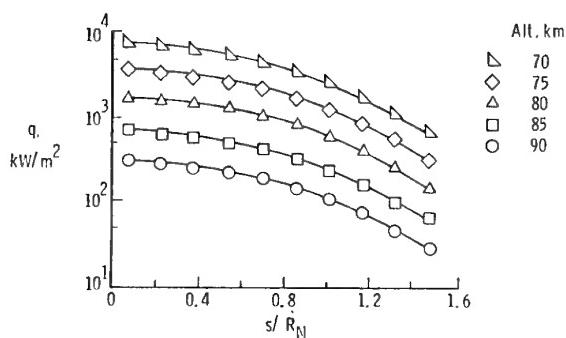
(a)   Heat transfer.

Fig. 27   Computational grid for 3-D AFE calculation at
Alt = 120 km.[52]
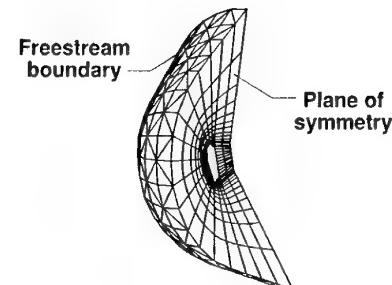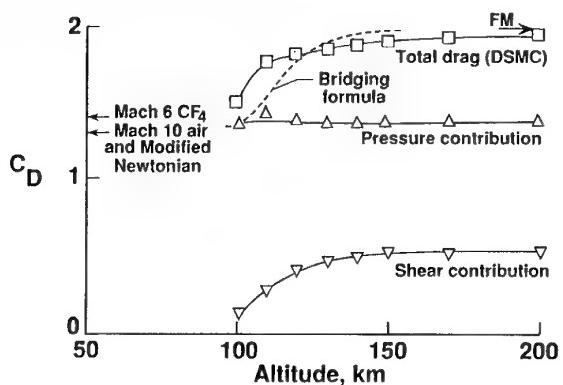
(a) Drag.
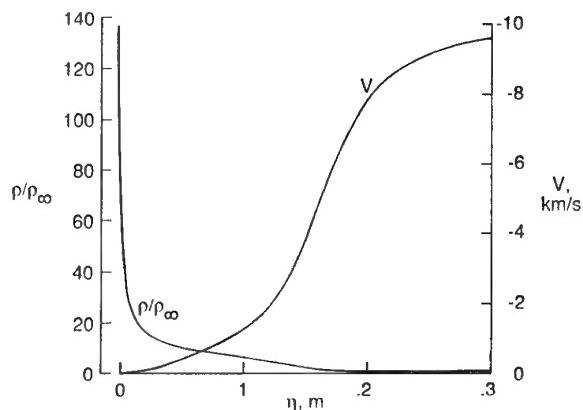
(a) Density and velocity profiles.
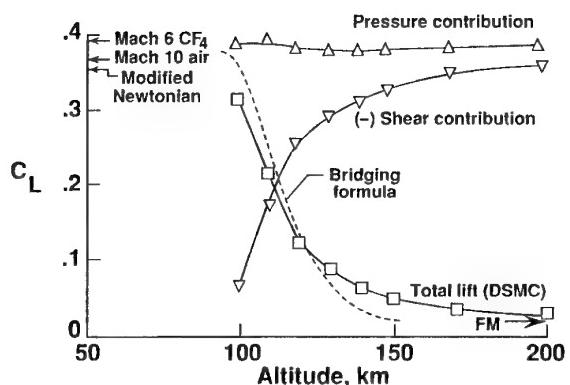
(b) Lift.
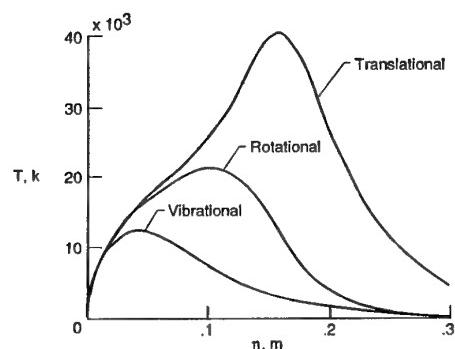
(b) Extent of thermal nonequilibrium.
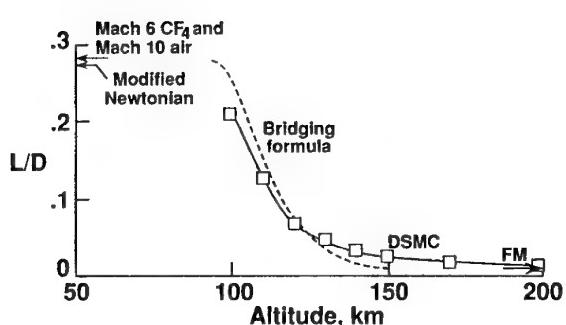
(c) Lift/Drag.
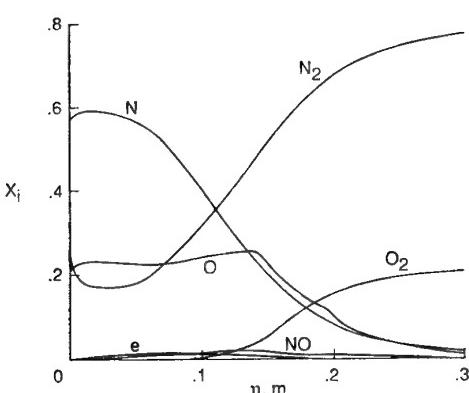
(c) Species mole fraction profiles for neutrals and electrons (ions not shown).

Fig. 28 Aerodynamic coefficient variations with altitude (AFE vehicle, FM denotes free-molecule value).[52]

Fig. 29 Calculated flowfield structure along stagnation streamline of AFE for Alt = 90 km and $V_\infty = 9.9$ km/s.[57]
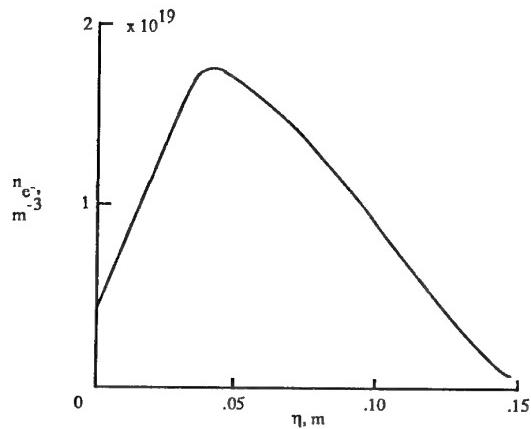
(d) Electron number density profiles.
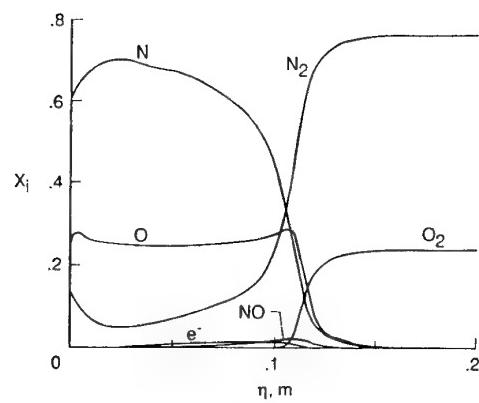
(c) Species mole fraction profiles for neutrals and electrons (ions not shown).

Fig. 29 Calculated flowfield structure along stagnation streamline of AFE for Alt = 90 km and V_∞ = 9.9 km/s.[57]
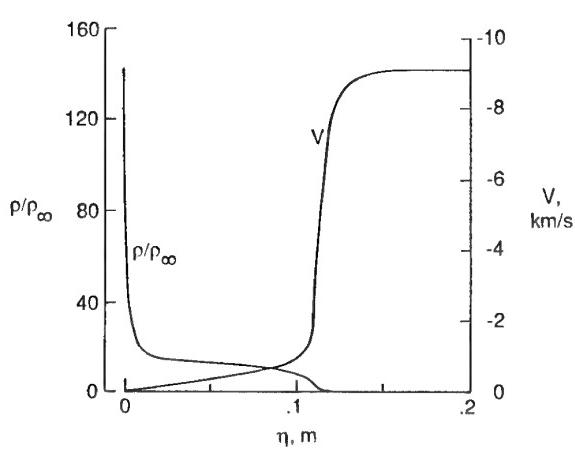
(a) Density and velocity profiles.
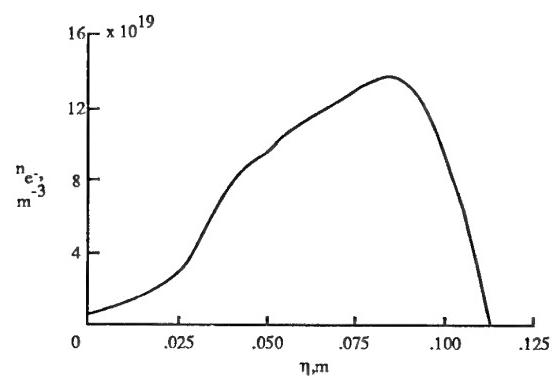
(d) Electron number density profile

Fig. 30 Flowfield structure along stagnation streamline for AFE at Alt = 78 km and V_∞ = 9.1 km/s.[57]
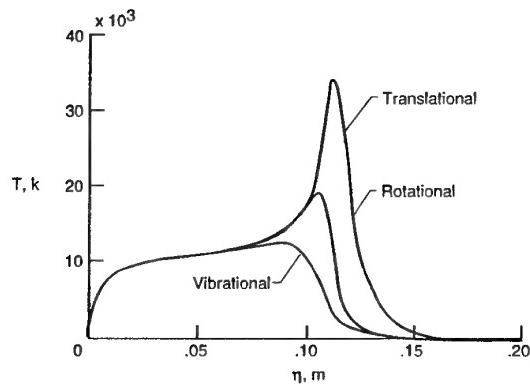

(b) Extent of thermal nonequilibrium.
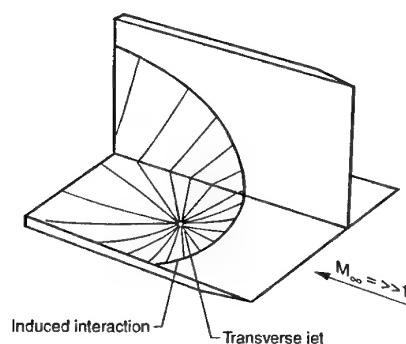

Fig. 31 Schematic of corner-flow/jet interaction model.
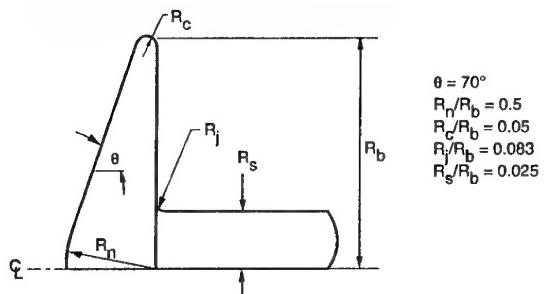
Fig. 32   Blunt-body/wake-closure test model.
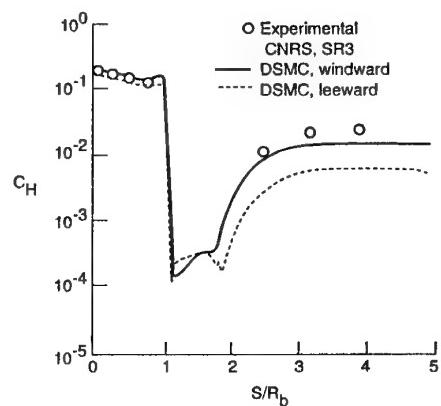
(b) Incidence = 10°.
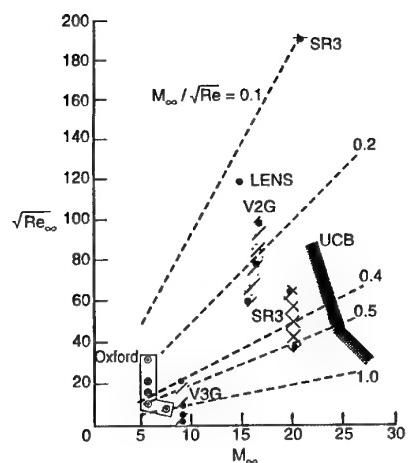
Fig. 33   Low-density test conditions in terms of the
rarefaction parameter $M_\infty / \sqrt{Re_\infty}$.
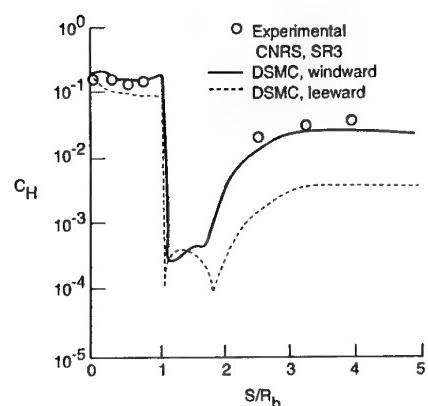
(c) Incidence = 20°.

Fig. 34   Heat transfer coefficient distributions for CNRS
test condition 2. (R_b = 2.5 cm).[76]
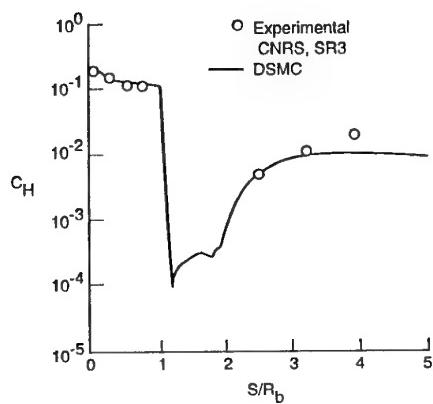
(a) Incidence = 0°.
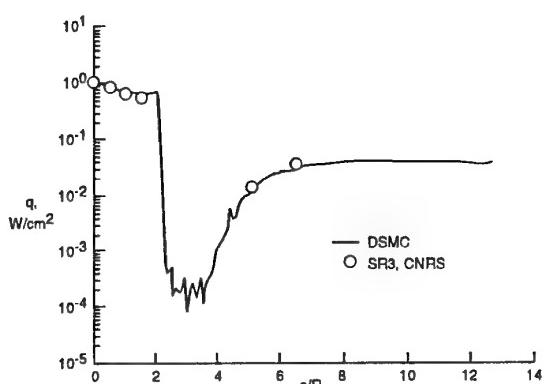
(a) Test condition 1 (Table 1).

Fig. 35   Comparison of SR3 experimental[85] and DSMC[36]
heating rate results (R_n = 1.25 cm and α = 0°).
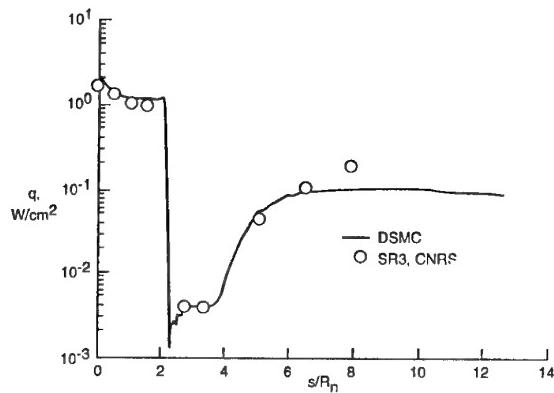
(b) Test condition 2 (Table 1).
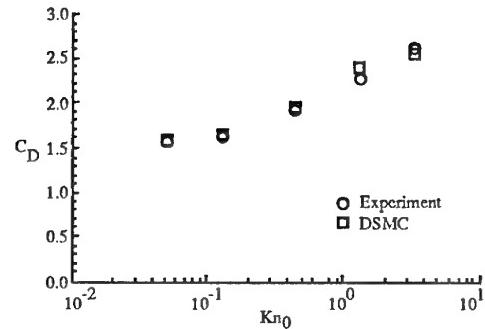
(b) Overall heat transfer coefficient.

Fig. 36   Comparison of experimental [13] and DSMC [72-73] results for V3G tests with 5mm diameter model at zero incidence.
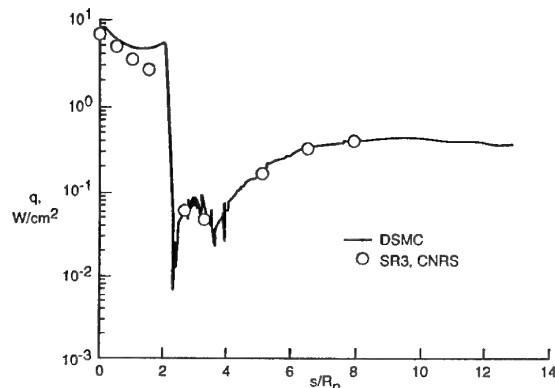
(c) Test condition 3 (Table 1).
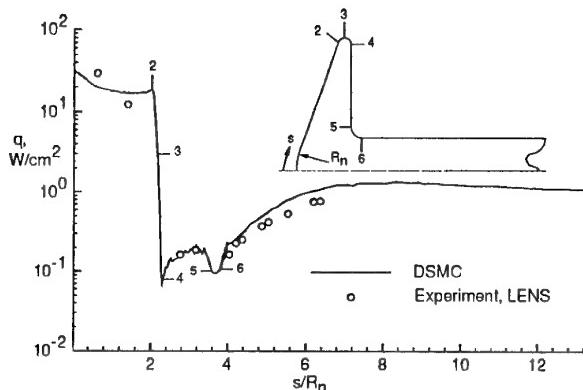
Fig. 35   Comparison of SR3 experimental [85] and DSMC [36] heating rate results ($R_n = 1.25$ cm and $\alpha = 0°$).


(a) Heat transfer.
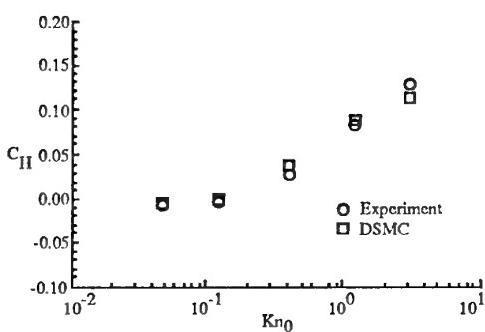
(a) Drag coefficient.
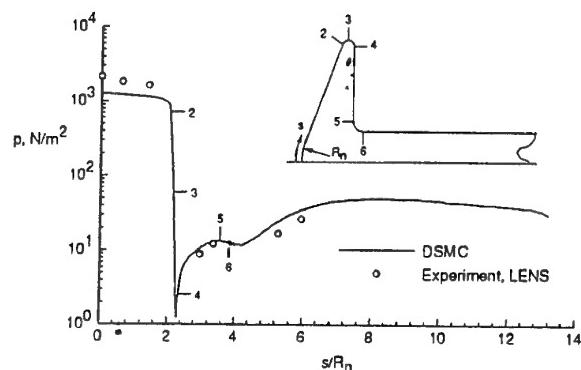
(b) Pressure.

Fig. 37   Comparison of experimental [84] and DSMC [71] results for LENS test ($R_n = 3.81$ cm).
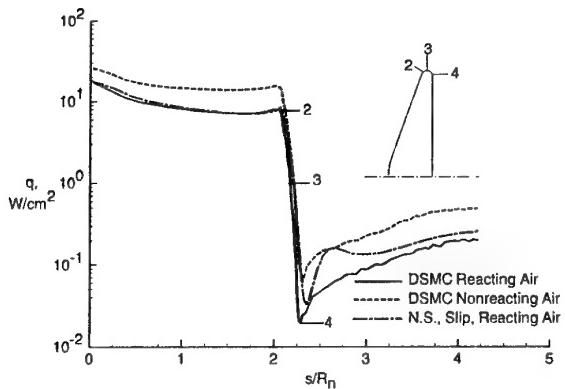
Fig. 38   Computed surface heating rate distribution
for a 70° blunted cone in air (Alt = 85 km,
V_∞ = 7.0 km/s, R_n = 0.5 m).[78]
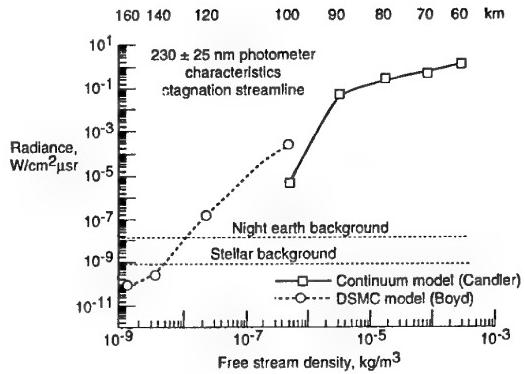
Fig. 41   Calculated radiance levels in the 230 ± 25 nm
photometer passband.[41]
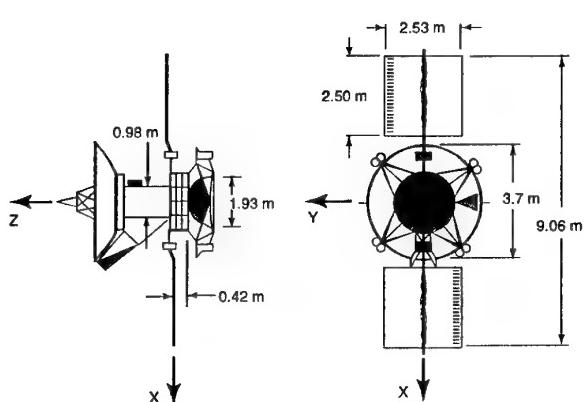
Fig. 39   Magellan spacecraft configuration.
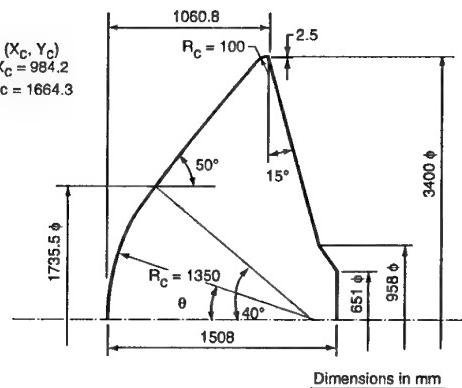
Fig. 42   OREX configuration.
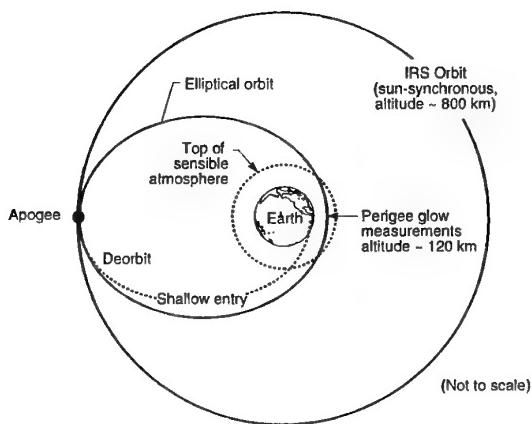
Fig. 40   Skipper orbital and reentry mission.
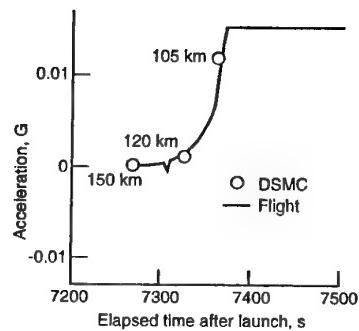
(a) Fine range.

Fig. 43   OREX axial acceleration at high altitude.[98]

(b) Coarse range.
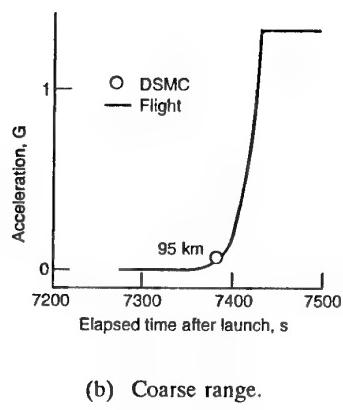
Fig. 43 OREX axial acceleration at high altitude.[98]
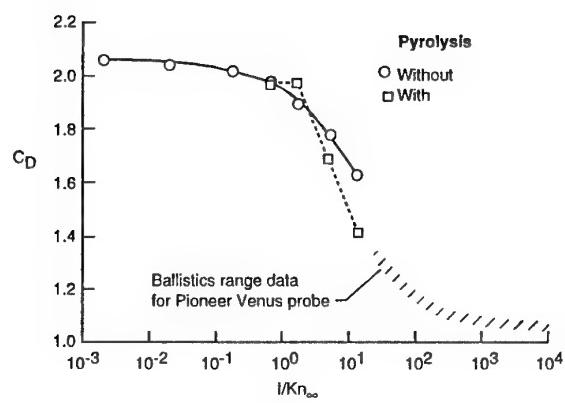
Fig. 44 Effect of pyrolysis injection on Galileo probe drag coefficient.[101]

Real Gas: CFD Prediction Methodology

Flow Physics for Entry Capsule Mission Scenarios

by

George S. Deiwert
Space Technology Division
NASA Ames Research Center, Moffett Field, California 94035
United States

SUMMARY

Mission and concept studies for space exploration are described for the purpose of identifying flow physics for entry capsule mission scenarios. These studies are a necessary precursor to the development and application of CFD prediction methodology for capsule aerothermodynamics. The scope of missions considered includes manned and unmanned cislunar missions, missions to the minor planets, and missions to the major planets and other celestial objects in the solar system.

VEHICLE CONCEPTS FOR SPACE EXPLORATION MISSIONS

To develop and apply CFD prediction methodology for capsule aerothermodynamics it is necessary to have some a priori knowledge of the expected aerothermodynamic flow environment. This will permit the proper choice of the most appropriate form of the conservation equations to be solved and the proper choice of phenomenological models and gas properties necessary to capture the critical flow environment features. To guide detailed CFD studies of capsule aerothermodynamics it is useful to first perform mission and concept studies to scope the important flow phenomena. Such mission and concept studies can be performed with the use of simple engineering computational techniques and empirical correlations.

Space exploration mission requirements will dictate the generic vehicle configuration. Illustrated in Fig. 1, slender, winged vehicles with high L/D will be required when the maximum aeromaneuverability is required. High drag bluff vehicles with low L/D will be required when maximum deceleration is required such as for direct entry aerobraking or aerocapture maneuvers. Such low L/D configurations are the capsules which are the subject of study in this special course. By the very nature of their use they will generate significant aerothermal loads as they are used to convert the kinetic energy of the capsule in to thermal energy in the surrounding medium. In a later section the flow features of this thermally excited environment about a re-entry capsule will be discussed.

For the present, however, it is useful to understand some of the mission drivers for space exploration which require entry capsules, and to look at some typical mission scenarios.

Some of the first order considerations in defining an entry capsule are determined by its intended use. Summarized in Table I are just some of the more obvious major considerations. First is the decision of whether the capsule is to be manned or just a cargo carrier. Design for manned flight requires stringent constraints on deceleration (g) loads, missions of minimal duration and hence, higher speeds, higher factors of safety to assure adequate design tolerance for manned missions, etc. Another major consideration is reusability. Expendable, single use vehicles, such as the Apollo capsules, can be designed with ablative heat shields and will experience a considerably different aerothermal environment than a vehicle that is designed for multiple use and long life cycle. Such reusable capsules will have non-ablative, reflective heat shields. Another consideration is vehicle size and associated in-space construction constraints. Small capsules can be launched in tact, but large cargo carrying vehicles will require some in-space construction.

Table I Re-entry Capsule Design Considerations

> Manned or Unmanned
> Reusable or Disposable
> Large or Small Payload
> Atmospheric Environmant
> GN&C Maneuverability (L/D)
> Entry Speed Range

Guidance, navigation and control (GN&C) considerations will set the L/D requirements for a vehicle. The L/D, in turn, determines the flight angle of incidence which, in turn, determines wake impingement angle. The vehicle ballistic coefficient determines the maximum heating and dynamic pressure loads, and the heating load sizes the thermal protection system and capsule size and structure.

Direct entry capsules utilizing ballistic entry trajectories require very little GN&C control and hence can be designed to maximize drag characteristics. Aerobraking or aerocapture, on the other hand, will require somewhat more control and a variety of considerations must be balanced to define an optimal configuration. Shown in Fig. 2 is a schematic illustrating the concept of aerobrake entry corridor. If the vehicle flies outside this corridor, or if its lift is either too small or too large, the vehicle will either crash to the surface or skip out of the desired orbit. As the vehicle L/D is increased, controllability, and hence, corridor width is increased. Increase in allowable g-load and in allowable maximum temperature also lead to increased allowable corridor width. Increased entry speed, increased capture orbit energy, and uncertainties in atmospheric density, however, reduce corridor width.

Perhaps the most important consideration in determining aerothermal environment is the mission itself. Missions involving cislunar space will differ greatly from missions to the minor planets, missions to the major planets, and missions to

other solar system features such as the sun and comets. Several typical examples of mission scenarios are given below to illustrate the influence of mission requirements on determination of aerothermal environment:

Cislunar missions

One example of a cislunar mission is typified by the direct entry Apollo missions from either Earth (entry speed about 10.5 km/sec) or lunar (entry speed about 11.5 km/sec) orbits. Here, a relatively small expendable capsule is flown a ballistic trajectory directly to the Earth's surface. Because it is manned, human g-loads were a constraint on the maximum deceleration. A high drag (low L/D) configuration was utilized to maximize the dissipation of kinetic energy, and single-use ablative heat shields were utilized to dissipate the aerothermally induced heat loads during entry. The Apollo capsules themselves were designed with large safety margins due to lack of refined design tools and the overriding concern for human safety.

Another example of a cislunar mission, which will require highly refined design tools, is reusable AeroSpace Transfer Vehicles (ASTVs). ASTVs would be space freighters for transporting large payloads when time is not a constraint in the mission requirement. ASTVs would use aerobraking to perform orbit change maneuvers, utilizing aerodynamic drag in the far-outer extent of the atmosphere to alleviate surface heat fluxes and pressure forces, therefore minimizing weight penalties for the aero-assist apparatus. Extensive design and mission-performance analyses for operations encompassing cislunar space have been performed in recent years for ASTV designs in this category. A typical near-Earth orbital transfer mission would be between a geosynchronous Earth orbit (GEO, 35,841 km altitude) and an equatorial LEO. The location of a space station at GEO is a future probability, and low-cost orbital-change maneuvers between GEO and LEO (or Space Shuttle orbits) for personnel and material will be a requirement. The advantages of aerobraking provide substantial savings in propulsion fuel mass for this mission. This is illustrated in Fig. 3 by a typical mission profile for a single-pass ASTV maneuvering between GEO and equatorial LEO. Multiple passes are possible and appropriate for unmanned missions. The constraints on the mission are a re-entry mass of 12 tons (to conform with other studies) and the use of a liquid rocket engine with a specific impulse of 420 sec to make the ASTV reusable and refuelable. The mission scenario is as follows: 1) the ASTV with initial mass of 30 tons (the approximate capacity of the Space Shuttle cargo bay) is inserted into LEO; 2) a propulsive thrust of 2395 m/sec is required to transfer from circular LEO to and elliptical orbit with apogee at GEO and perigee at LEO; 3) this consumes a propulsion fuel mass of about 45% of the initial ASTV total mass; 4) a propulsive thrust of 1456 m/sec is required to achieve the circular GEO from the elliptic transfer orbit; 5) this maneuver consumes an additional 30% of the initial ASTV mass; 6) a payload of 5.5 tons is picked up for transfer to LEO so that a re-entry mass of 12 tons will be obtained subsequently; 7) a retropropulsive thrust of 1490 m/sec is required for transfer to an elliptical orbit with perigee in Earth's atmosphere to take advantage of aerodynamic braking; 8) this maneuver expends 30% of the remaining ASTV mass in fuel and provides the desired re-entry mass of 12 tons; 9) aerodynamic braking occurs with the ASTV, achieving a new elliptical orbit with apogee at LEO; and 10) a final small propulsive thrust of 90 m/sec is required for insertion into LEO, which burns a fuel mass of 2.5%. Thus, aerobraking conserves essentially all of the fuel mass that would be required for return to LEO using all-propulsive maneuvers, which is about 45% of the ASTV mass (the difference between steps 2 and 10).

Manned Mars Missions

Recent studies of manned exploration missions to Mars have considered four different scenarios. These include a short, 330 day, "sprint" mission, a medium length, nominal 500 day mission, a long, nominal 1000 day mission, and a cycler mission. Each of these missions demands multiple vehicles and will involve entry and aerocapture maneuvers both at Mars and at Earth on the return. Entry velocities both at Mars and at Earth can vary greatly depending on the mission duration and whether the aerocapture vehicle is manned or unmanned. Shown in Fig. 4 are Mars and Earth entry velocity envelopes for various missions. For Mars aerocapture the highest entry velocities will be experienced by the cycling missions followed by the sprint down to the 1000 day mission having the lowest approach speeds, which increases as transit time decreases. For the Earth return, all the approach speeds are greater than those for cislunar missions.

A sprint mission scenario is illustrated in Fig. 5. Here an advanced unmanned vehicle with an initial mass of 2040 tons is sent on a low energy trajectory with an initial thrust from Earth orbit of 4.4 km/sec, requiring the expenditure of 1317 tons of fuel. This 723 ton vehicle would arrive at Mars in 259 days with an approach velocity of 5.7 km/sec for aerocapture into an orbit around Mars. The atmosphere of Mars consists essentially of carbon dioxide with small amount of nitrogen and trace amounts of argon. This vehicle would be followed by a smaller, manned vehicle with an initial mass of 1240 tons thrust from Earth orbit at 10.2 km/sec. This would require 1117 tons of fuel leaving a 123 ton vehicle approaching Mars 150 days later at a speed of 14.6 km/sec. This vehicle will be aerocaptured and docked with the larger unmanned vehicle already in Mars orbit. From this docking orbit, a smaller, manned entry vehicle will be sent to land on the Martian surface. After 30 days the Mars lander would return to the docking orbit in preparation for the return of the crew to Earth. The manned Earth return vehicle will leave the Martian orbit with an initial mass of 485 tons and a thrust of 8.3 km/sec, requiring 442 ton of fuel. The 43 ton return vehicle will reach the vicinity of Earth 150 days later, at which time a 5 ton manned capsule will be jettisoned for Earth aerocapture with an entry speed of 13.8 km/sec. The remaining unmanned, expendable 38 ton return vehicle would continue on in space.

Giant Planet Missions

Mission scenarios to the giant planets include 1) the Galileo probe which will be on a direct entry ballistic trajectory through the atmosphere of Jupiter (primarily hydrogen and helium) with an entry speed of about 48 km/sec and a mass of 338 kg as illustrated in Fig. 6. This capsule probe has an ablative heat shield (which comprises 43% of the probe's total mass), has been launched, and is scheduled to arrive at Jupiter on Dec. 7, 1996. 2) The Cassini mission to Saturn includes the Huygens probe which will directly enter the atmosphere of Saturn's moon (composed of nitrogen, methane and argon), Titan, at a speed of about 5.75 to 6.5 km/sec. as illustrated in Figs. 7 and 8. 3) A probe to the planet Neptune has been proposed that would enter the atmosphere (comprised primarily of hydrogen (81%) and helium (19%)) directly at a speed of 24.5 km/sec., illustrated in Fig. 9. At these conditions the flow will be turbulent and, in the light-gas atmosphere, radiation will not be a consideration. A similar study has been performed for the planet Uranus, also illustrated in Fig. 9.

Other Missions

Other missions would include visits to other solar system members and return to Earth. For example, the proposed comet nucleus sample return mission, illustrated in Fig. 10, would return to Earth with an entry speed of 15.5 km/sec. Here the heating rates would be radiation dominated and quite high, the order of 3 kw/cm^2.

FLOW PHYSICS

The purpose of outlining the above example mission scenarios is to provide the basis for illustrating the vast differences in flow physics, and hence aerothermal environment, that must be considered in developing and applying CFD analysis methods to analyze and describe the aerothermodynamics for the respective capsules. While it may be possible to attempt to devise a universal prediction methodology that could be used for all possible mission scenarios, it is more practical to first identify the important physical processes and to apply simpler CFD methods and models that are tailored to describe the essential processes for a particular application.

Major differences exist between the atmospheres of celestial objects in our solar system. The atmospheric composition of Earth is fairly well known. The atmosphere of Mars, which consists primarily of carbon dioxide at a relatively low barometric pressure, is also fairly well defined, although there are observed seasonal variations. Carbon dioxide is a tri-atomic gas and exhibits substantially different radiative characteristics than observed in air. Also, the Martian atmosphere is subject to major dust storms that can significantly affect the aerothermal environment about a vehicle. The atmospheres of the major planets are comprised primarily of helium and hydrogen which are not strong radiators.

Considering only Earth entry missions, a variety of flight environments can be identified. Shown in Fig. 11 is a comparison of vehicle flight regimes in Earth's atmosphere. The direct entry Apollo trajectory is seen to pass rapidly through the high altitude regime where ionization effects may be important. The space craft experiences the bulk of its deceleration, and hence aerothermal heating, in the lower atmosphere (about 40 km altitude) where the flow is continuum and radiation from the bow-shock layer is in equilibrium. A reusable ASTV undergoing an aeropass maneuver, however, has its trajectory in the upper atmosphere where the gas is less dense and nonequilibrium processes, including radiation, are important. A vehicle returning from Mars, or the far solar system, on the other hand, flies a significant part of its trajectory in the lower altitude (about 50-65 km) where the shock layer gas, while in equilibrium, is highly ionized. Peak heating is expected to occur in this regime as the high kinetic energy of the vehicle is being converted to thermal energy.

A schematic which illustrates the difference in shock layer physics between an ASTV cislunar mission and a Mars return mission is shown in Fig. 12. Here, a typical ASTV entry speed is about 10 km/sec at an altitude of 80 km. The gas is heated as it passes through the bow shock, and at that altitude the density is low enough that the shock layer is essentially in thermochemical nonequilibrium and the boundary layer is laminar. Ionization levels will be small, < 1% and the radiation from the shock heated gas cap will be nonequilibrium and will provide a heat flux to the surface comparable to the convective heat load.

A capsule on return from Mars, however, will be characterized by a speed greater than 12 km/sec. at an altitude of about 65 km. Here the gas behind the bow shock will be essentially in equilibrium as will the gas cap radiation. At the high kinetic energy associated with the higher speed entry, however, there

will be substantial levels of ionization (up to 30%). Radiative heating will be quite high and will dominate the total heating to the space craft. Ablative heat shields will be required to accommodate the high radiative heat loads and will, in turn, create a highly turbulent flow near a rough ablating surface. The ablation products will affect the gas composition near the capsule surface and in the wake.

A table has been assembled, Table II, which, in a qualitative sense, characterized some of the important capsule aerobraking parameters and essential flow physics for typical cislunar and Mars missions. Included is a recently considered ASTV flight experiment, AFE (Aero-assist Flight Experiment), direct entry lunar return, unmanned Mars return (reusable), manned Mars return (expendable capsule), unmanned Mars aerocapture, and manned Mars aerocapture. Listed aerobraking parameters and flow features include entry speed, altitude at maximum deceleration which corresponds closely with peak heating, stagnation pressure, convective and radiative peak heating, required TPS, shock layer ionization level, fraction of shock layer thickness in nonequilibrium state, and boundary layer character. Also identified are important physical issues such as radiation/ablation interaction, wall catalysis, and boundary layer transition. It can be seen from this table that the gamut of physical phenomena associated with capsule aerothermodynamics is quite large and that the only viable means to reduce analysis requirements and optimize designs using the most refined CFD tools is to consider problems on a mission by mission basis.

CFD CONSIDERATIONS

To treat all possible mission scenarios, CFD tools must be developed that account for flow regimes that range from free molecular through transitional to continuum. Turbulent flows, including transitional flows and flows with massive wall turbulence can be encountered, as well as unsteady phenomena. Real gas phenomena will encompass thermal and chemical equilibrium and nonequilibrium processes and ionization. Aerodynamic heating will be due both to convective and radiative (equilibrium and nonequilibrium) processes, and material responses will include catalycity, gas/surface accommodation, ablation and transpiration. Complex flow features, such as shock/shock, shock/surface, vortex, and shear layer interactions may also be encountered. And finally, gas properties (thermodynamic, transport, reaction rates and cross sections, and energy exchange mechanisms) for the various atmospheric compositions and shock heated states.

CFD methods, themselves can range in complexity from fairly simple one-dimensional engineering analysis methods and correlations, to viscous shock layer methods, to Euler plus boundary layer methods, to parabolized Navier-Stokes and Reynolds-averaged Navier-Stokes methods. Multiple species and multiple energy modes (temperatures) will require their own conservation equations, and phenomenological models describing species production and depletion and energy exchange processes will be required in addition to transport models for mass momentum and energy require definition.

Once the equation set and phenomenological models have been selected to analyze a given vehicle class for a given mission scenario, a numerical scheme (algorithm) must be employed to solve the equations. Validation of these models and simulations must rely on critical experiments. The development of full flow-field equations, a solution algorithm, illustrative examples, and validation experiments and processes are the subject of subsequent sections of this course.
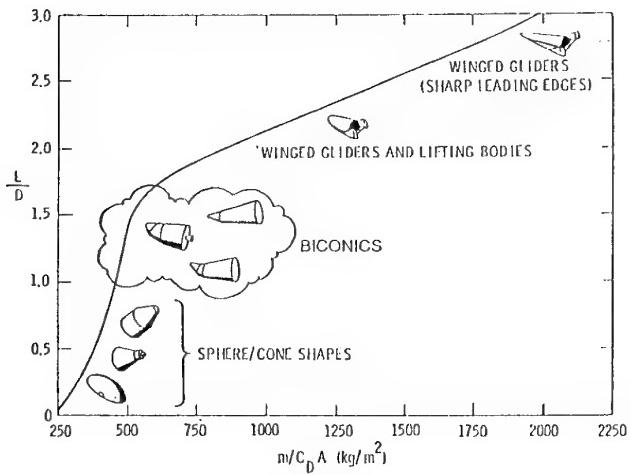
Fig. 1 Typical re-entry configurations: L/D vs. Ballistic Coefficient for 5000 kg mass
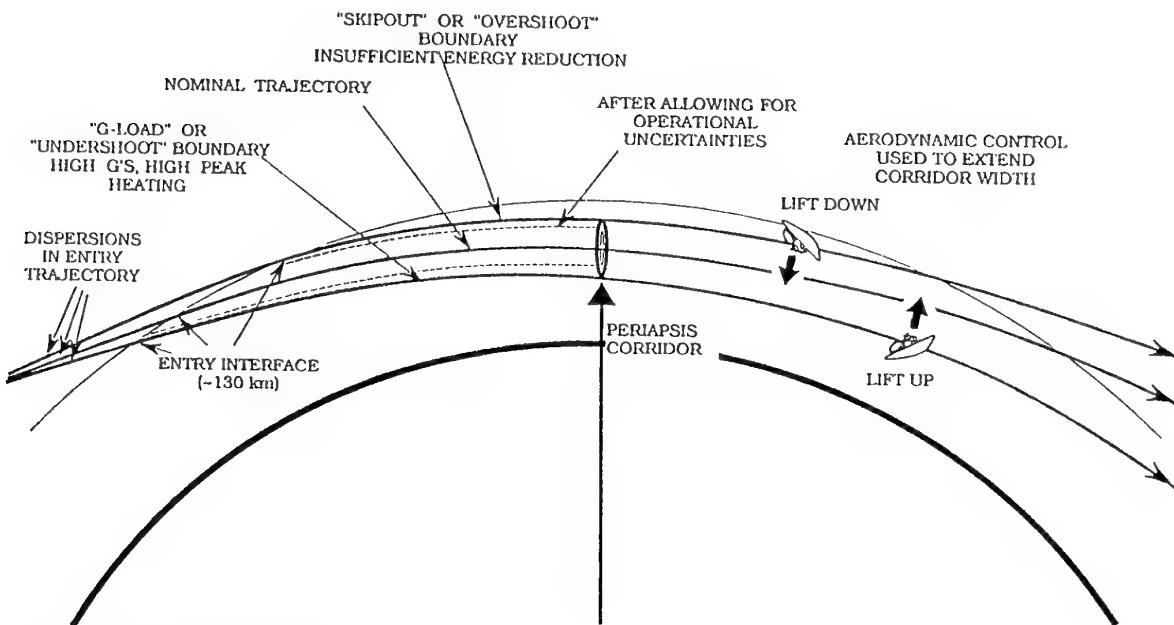
Fig. 2. Aerobraking "Corridor " Concept
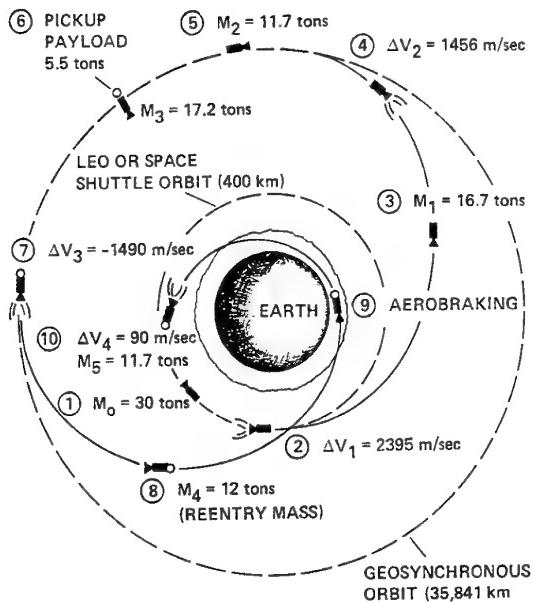
Fig. 3. Mission schematic for ASTV in coplanar maneuver between LEO and GEO. (Masses computed for isp = 420 sec)
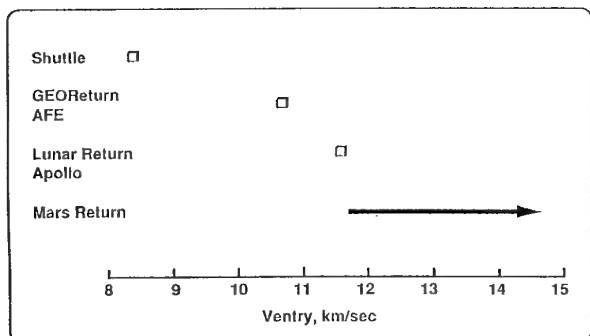
a) Earth Entry
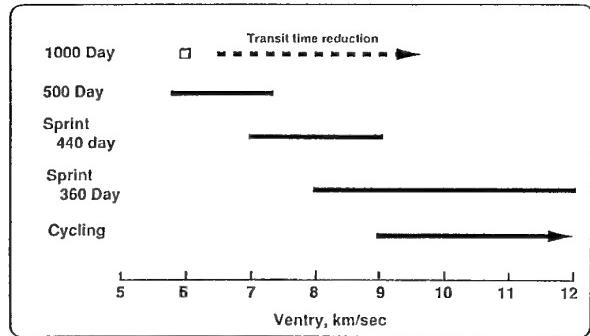
b) Mars Entry

Fig. 4. Entry velocity envelopes for Mars mission with return to Earth

OPTIMUM 330 DAY MANNED MARS MISSION

NASA SP-35, 1962
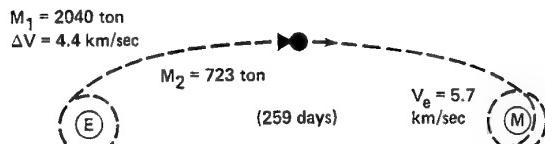
(a) ADVANCED UNMANNED
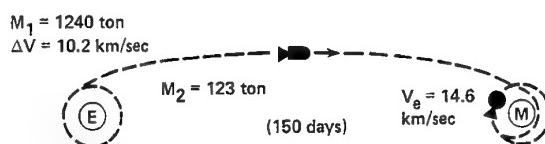
(b) MANNED EARTH-TO-MARS
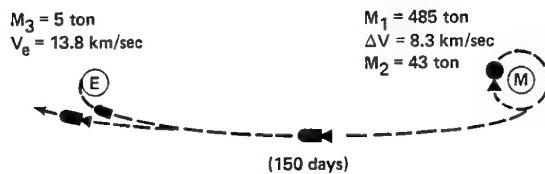
(c) MANNED MARS-TO-EARTH

Fig. 5. Sprint mission schematic to Mars
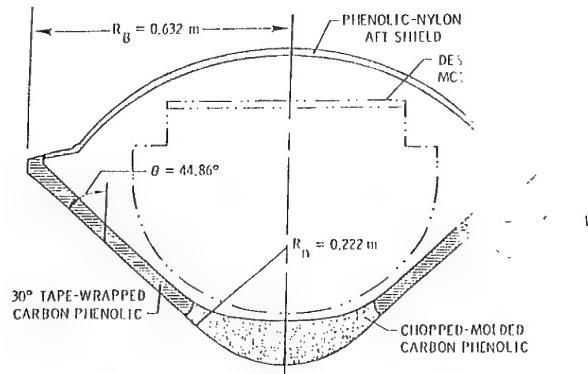
Fig. 6. Galileo entry probe
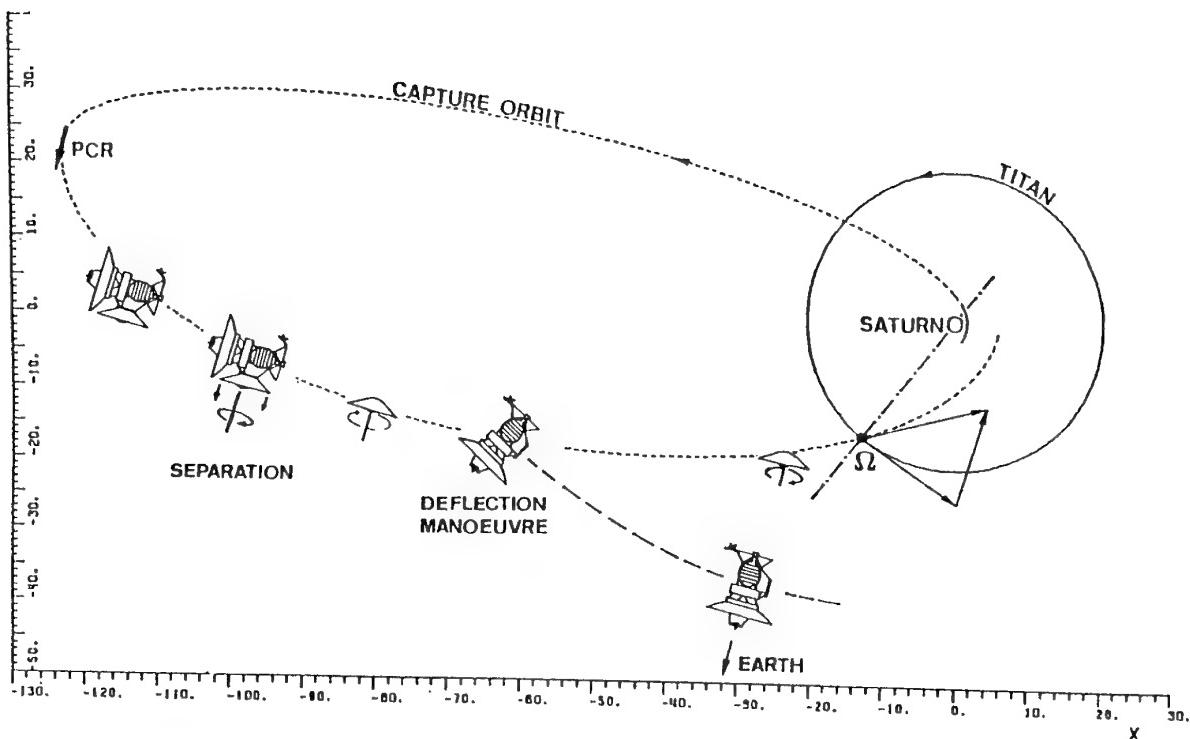
Fig. 7 Cassini mission spacecraft maneuvers from Saturn orbit insertion to Titan encounter

ALTITUDE
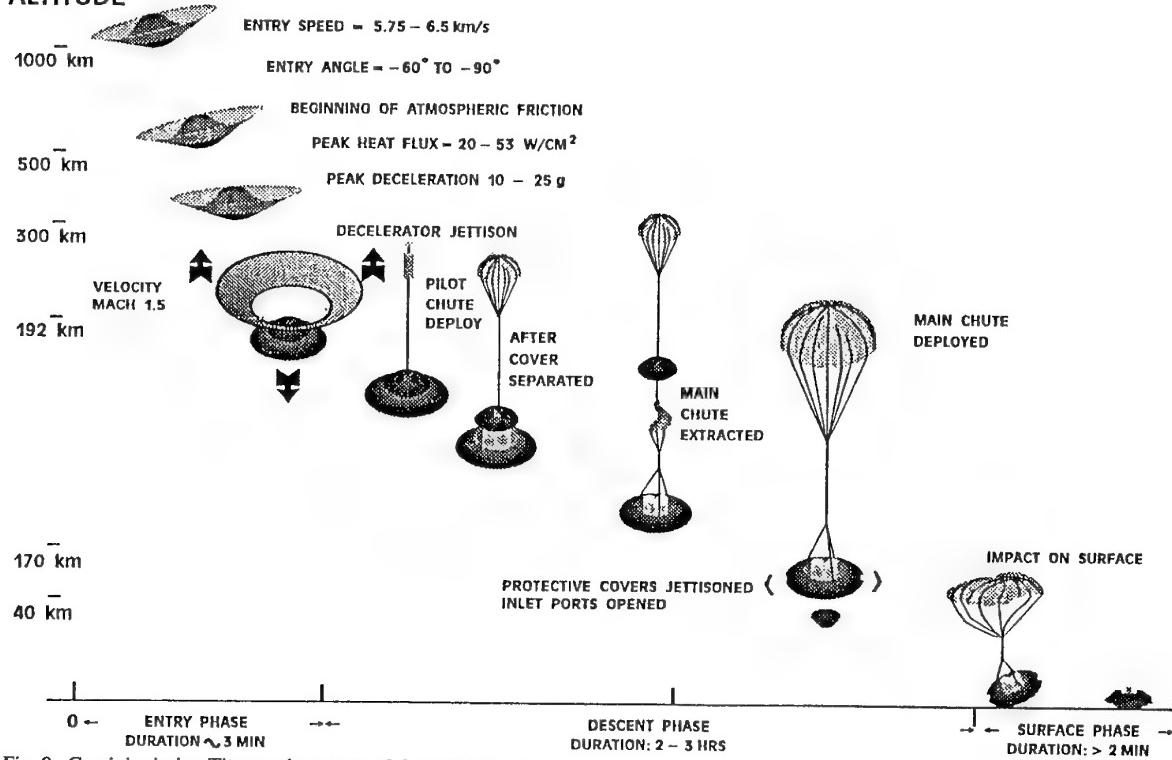
Fig. 8. Cassini mission Titan probe entry and descent scenario

a) Uranus

b) Neptune
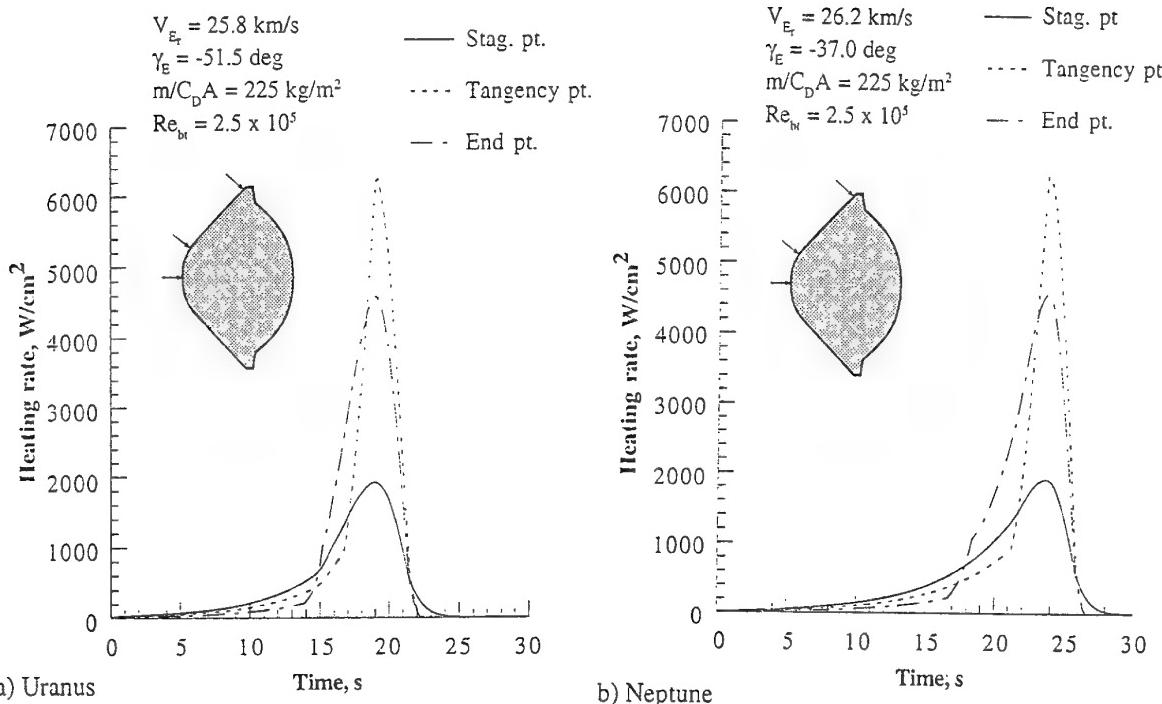
Fig. 9. Heating pulses for nominal giant planet entries

$V_E = 15.5$ km/sec $\gamma_E = -8^o$
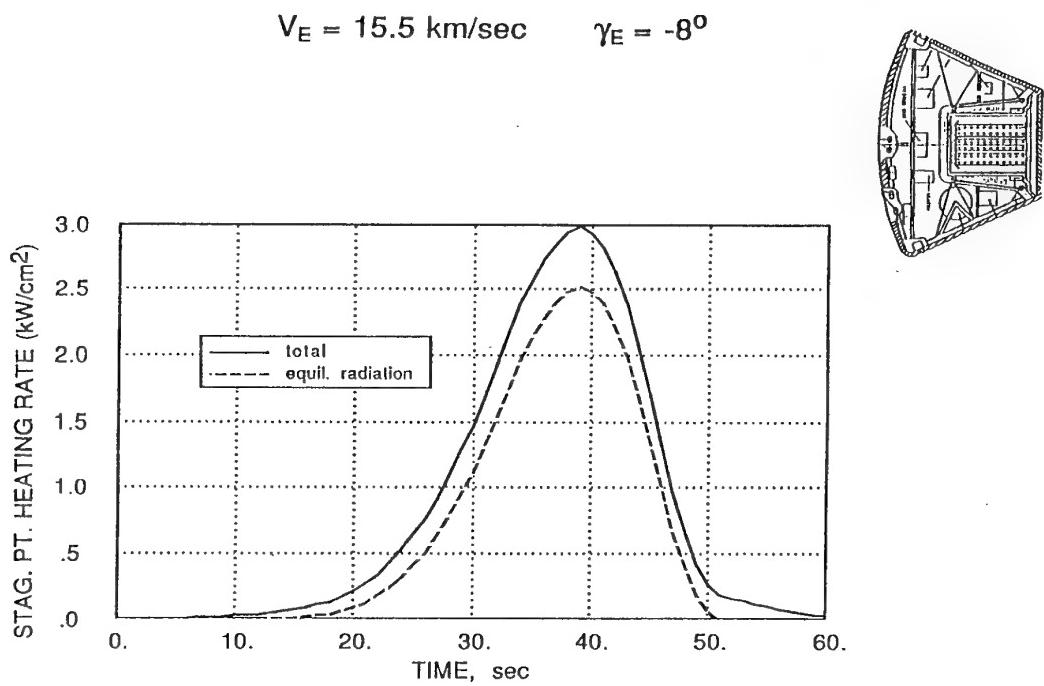
Fig. 10. Comet sample return vehicle "cold wall" heating rates
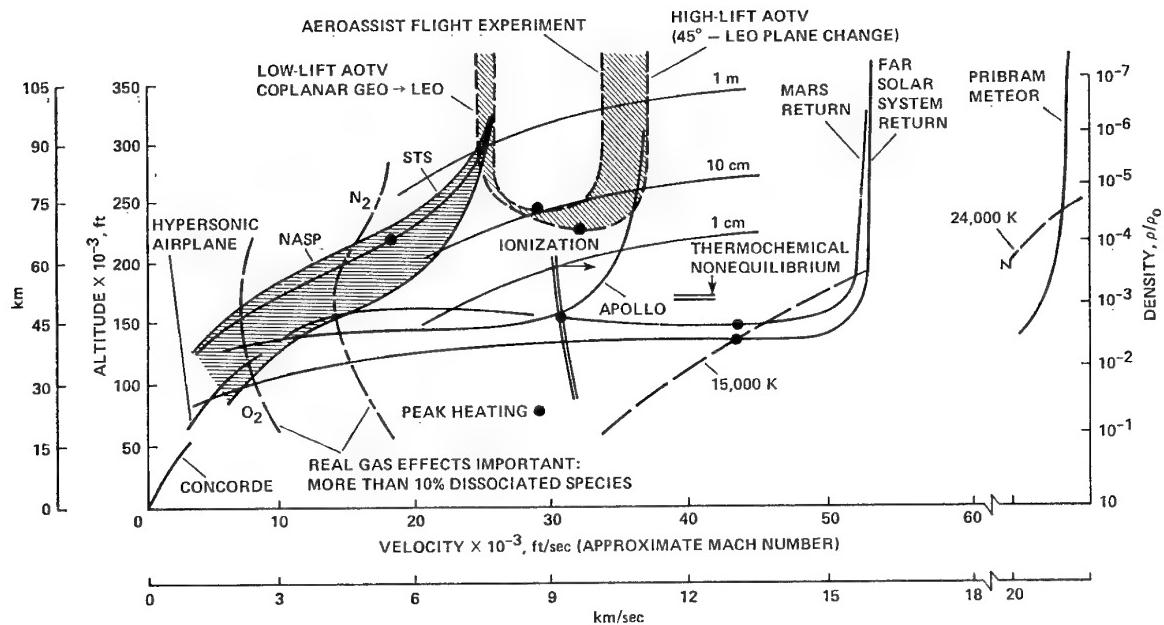
Fig. 11 Comparison of vehicle flight regimes in Earth's atmosphere
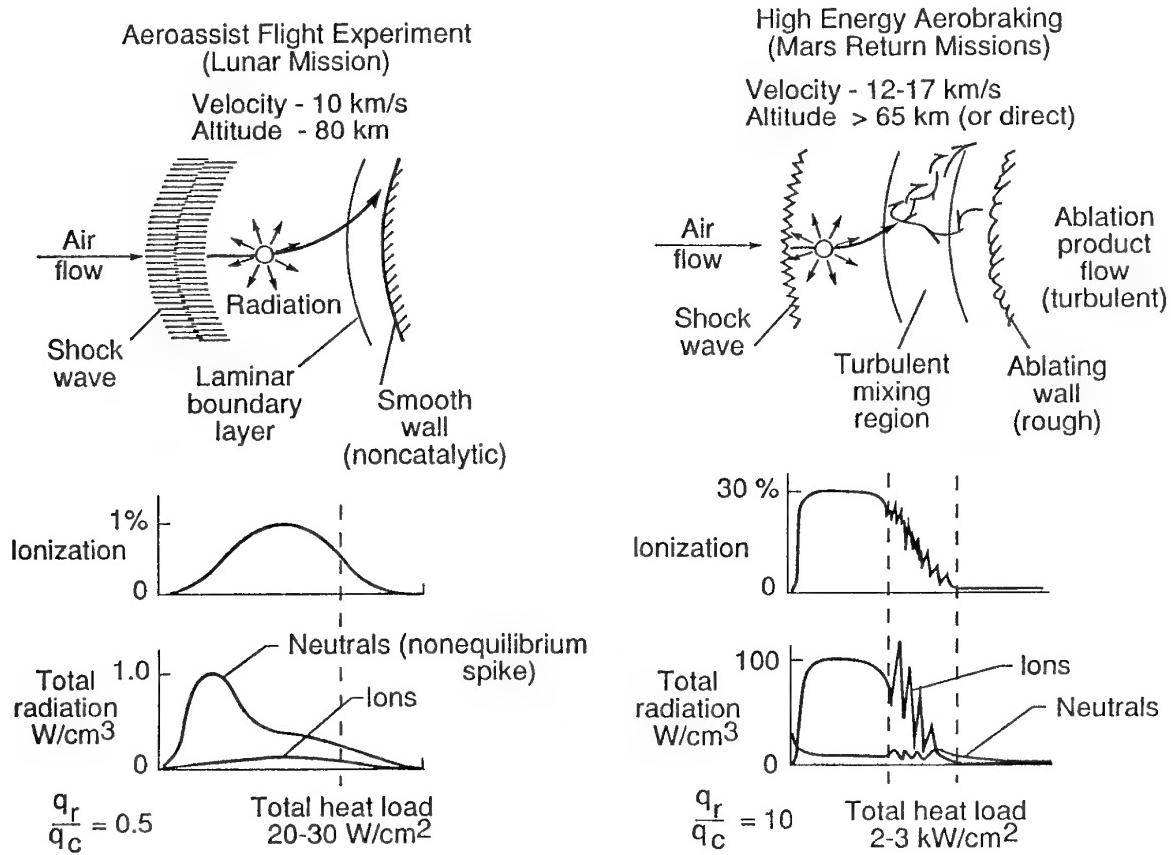
Fig. 12. Comparison of low energy and high energy re-entry shock layer flow physics

Table II. Aerobraking Parameters for Space Exploration Missions

MISSION	AFE	LUNAR RETURN	MARS RETURN REUSABLE	MARS RETURN CAPSULE	MARS ENTRY UNMANNED	MARS ENTRY MANNED
ENTRY SPEED (km/sec)	10	11	13	14	6 to 8	7 to 9
DECELERATION ALTITUDE (km)	75	75	66	65	40	40
STAGNATION PRESSURE (atm)	0.03	0.05	0.20	0.30	0.1 to 0.15	0.1 to 0.2
PEAK HEATING (Conv/Rad) (w/cm2)	40 / 7	50 / 30	150 / 500	500 / 900	100 / 10	100/10 (L/D=1) 30/50 (L/D=.3)
THERMAL PROTECTION SYSTEM	Reflective	Reflective or Ablating	Ablating	Ablating	Reflective or Ablating	Reflective or Ablating
% IONIZATION	0.5 to 1	5 to 10	15	25	0 to 1	0 to 2
NONEQUILIBRIUM STANDOFF %	0.4	0.2	0.2	0.1	Large	Large
BOUNDARY LAYER CHARACTER	Laminar	Laminar	Turbulent	Lam / Turb	Turbulent	Turbulent
IMPORTANT PHYSICS						
RADIATION/ABLATION INTERACTION	None	Small	Large	Large	Small	Small
WALL CATALYSIS	Yes	Yes	No	No	Yes	Yes
BOUNDARY LAYER TRANSITION	No	No	Yes	Yes	Yes	Yes

Data Base for CFD Validation

by

George S. Deiwert
Space Technology Division
NASA Ames Research Center, Moffett Field, California 94035
United States

INTRODUCTION

The flow behind the shock wave formed around objects which fly at hypervelocity behaves differently from that of a perfect gas. Molecules become vibrationally excited, dissociated, and ionized. The hot gas may emit or absorb radiation. When the atoms produced by dissociation reach the wall surface, chemical reactions, including recombination, may occur. The thermochemical phenomena of vibration, dissociation, ionization, surface chemical reaction, and radiation are referred to commonly as high-temperature real-gas phenomena. The phenomena cause changes in the dynamic behavior of the flow and the surface pressure and heat transfer distribution around the object.

The character of a real gas is described by the internal degrees of freedom and state of constituent molecules; nitrogen and oxygen for air. The internal energy states, rotation, vibration and electronic, of the molecules are excited and, in the limit, the molecular bonds are exceeded and the gas dissociated into atomic and, possibly, ionic constituents. The process of energy transfer causing excitation, dissociation and recombination is a rate process controlled by particle collisions. Binary, two-body, collisions are sufficient to cause internal excitation, dissociation and ionization while three-body collisions are required to recombine the particles into molecular constituents. If the rates of energy transfer are fast with respect to the local fluid dynamic time scale the gas is in, or nearly in, equilibrium. If the energy transfer rates are very slow the gas can be described as frozen. In all other instances, wherein any of the energy exchange rates are comparable to the local fluid time scale, the gas will be thermally or chemically reacting and out of equilibrium.

Each of the definitive states of a real gas, equilibrium, frozen, reacting, can be applied to a gas undergoing compression and heating, such as the gas flowing through a strong shock ahead of a bluff body, or to an expanding and cooling gas, such as a gas flowing away from a stagnation region of a bluff body or a gas expanding into a base region. In the first case the gas will be thermally excited and dissociate and ionize; in the second, the atomic constituents will recombine and internal energy states will relax to lower energy levels.

A real gas implies the existence of any, or all, of the above states. This includes the possibility that a real gas can look identical to a perfect gas or a chemically frozen gas. In a real gas flow the model scale is a primary parameter. The possibility exists to generate a spectrum of "real gas" test conditions at a single geometrically similar test point. These flows can vary from frozen to equilibrium flow.

In the limit of chemically frozen flow there is little value to "real gas" experimentation on the nose region; if the flow is frozen at the stagnation point it will remain frozen as it expands about the blunt nose and over the afterbody where it may equilibrate. Nose region information for such a flow will be identical to

perfect gas wind tunnel results and can be predicted reliably within the limits of our knowledge of thermodynamic and transport properties. Afterbody data, however, may be of somewhat greater interest, particularly data describing flow over secondary surfaces which may induce further chemical activity.

Similarly for chemical equilibrium flow, "real gas" experiments are not required. In this case, the extrapolation from a perfect gas to a real gas is straightforward, involving appropriate thermodynamic and transport properties for the reacting gas species.

Between the two limits, in the region of reacting gas flows, is the greatest uncertainty and the greatest need for test data. Facilities required for CFD validation of high enthalpy flows, and for developing and verifying phenomenological models, are devices capable of generating a reacting gas flow over configurations of interest and must have sufficient diagnostics to describe the character and behavior of the flow.

Ground facilities which, although they have serious limitations in simulating full scale flight conditions, are capable of examining selected aspects which are expected to be vital to success in the full-scale flights. Theoretical analyses of the real-gas phenomena, based on quantum and statistical mechanics, require experimental verification in order to assure that the analyses correctly account for all vital phenomena. The ground-test facilities offer the advantage of observations, such as optical flow visualization, which are impractical in actual flight. For these reasons impulse tunnels, which include shock tubes, shock-tube wind tunnels (shock tunnels), and hot-shot wind tunnels (hot-shot tunnels), ballistic ranges, and arc-jet wind tunnels, have been built and operated since the 1960s. The experiments made therein have been effective in verifying to a first-order the results of some of the theoretical works. But neither analysis nor test has approached the level of maturity achieved by those for the lower flight speed ranges.

REAL GAS FLOW PHYSICS

Forebody Heating/Heat Transfer

Real gas thermochemical nonequilibrium processes are important in the determination of aerodynamic heating; both convective (including wall catalytic effects) and radiative heating. To illustrate this we consider the hypervelocity flow over a bluff body typical of an atmospheric entry vehicle or an aerospace transfer vehicle (ASTV.)

The qualitative aspects of a hypersonic flow field over a bluff body are discussed in two parts, forebody and afterbody, with attention to which particular physical effects must be included in an analysis. This will indicate what type of numerical modeling will be adequate in each region of the flow.

A bluff forebody flow field, illustrated schematically in Fig. 1., is dominated by the presence of the strong bow shock wave and the consequent heating, and chemical reaction of the gas. At high altitude hypersonic flight conditions the thermal excitation and chemical reaction of the gas occur slowly enough that a significant portion of the flow field is in a state of thermo-chemical nonequilibrium. A second important effect is the presence of the thick boundary layer along the forebody surface. In this region there are large thermal and chemical species gradients due to the interaction of the gas with the wall. Also at high altitudes the shock wave and the boundary layer may become so thick that they merge; in this case the entire shock layer is dominated by viscous effects.

A gas is in thermal nonequilibrium if, for a given density and internal energy, it is in a thermodynamic state where the internal energy modes cannot be characterized by a unique temperature, and is in chemical nonequilibrium if its chemical state does not satisfy chemical equilibrium conditions. As was asserted above, a portion of the forebody flow field is in thermo-chemical nonequilibrium. This can be seen by considering the trajectory of a control volume of air that enters the shock layer. The translational modes of this volume of gas are heated strongly as it passes through the bow shock wave. The translational modes transfer their energy to the other internal energy modes of the molecules through inter-molecular collisions. Also chemical reaction of the gas species occur such as dissociation and ionization. These processes require a series of intermolecular collisions for equilibrium to be reached. Thus as the volume element of gas is convected through the shock layer, these energy exchanges and chemical reactions occur at a finite rate until, at some point on the streamline, equilibrium is achieved. Therefore, there will be significant thermo-chemical nonequilibrium near the bow shock wave and equilibrium will be approached a large distance along the fluid element's pathline. The rate at which equilibration is realized is dependent on the free-stream density and speed, or altitude and Mach number. A parameter that quantifies the degree of chemical nonequilibrium for a particular condition is the Damköhler number, the ratio of the fluid time scale to the chemical time scale; a similar parameter may be derived for the relaxation of energy modes.

The second important effect in the forebody region is the interaction of the wall with the thermally excited and reacted gas in the boundary layer. At the high altitudes the Reynolds number is relatively small (typically on the order of 10^4 based on free-stream conditions and nose radius). Thus the boundary layer will be thick and viscous effects will dominate much of the flow field. Also, as the boundary layer is influenced by the cool wall, chemical reactions can be slowed or halted in the vicinity of the wall. The wall can also interact chemically with the flow field due to catalytic effects that promote the recombination of reacted species at the wall. Thus the inclusion of viscous effects for hypersonic bluff forebody flow field analyses is mandatory. At high altitudes, the usual assumption of perfect thermal accommodation and no-slip at the wall breaks down. Therefore, for some conditions, temperature and velocity slip effects must also be included.

Lee and Base Flow

The flow about an afterbody, illustrated in Fig. 2., is dominated by two phenomena; the presence of the rapid expansion as the highly compressed gas flows around the shoulder of the vehicle and the related initiation of separation of the gas near the vehicle corner. These two effects require specific modeling approaches and capabilities.

The expansion, which is dominated by inviscid effects, has the effect of rapidly lowering the translational temperature, density and pressure of the gas. However, the chemical state of the gas and the temperatures that characterize the energy in the internal modes will tend to remain constant, or frozen. This results in a flow where the vibrational and electronic temperatures of the gas are far higher than the translational temperature and where the gas is more dissociated and excited than predicted by equilibrium conditions. As the gas flows downstream, recombination occurs slowly and the vibrational temperature rises still higher; a result of a portion of the chemical energy of recombination being put into the higher vibrational modes of the gas. This can cause the gas to radiate significantly in the afterbody region. Another important effect present in the inviscid, expanded region is the presence of species gradients across the wake. This is caused by some portion of the gas having passed through a relatively weak oblique shock wave where reactions are weak, and another part of the gas having passed through the strong forebody shock where reactions are strong. Thus the gas near the center of the wake tends to be more dissociated than that in its extremities and consequently g, the ratio of specific heats, varies across the wake.

A second inviscid effect associated with the wake structure is the presence of a wake shock. As the flow expands around the shoulder of the vehicle, some of it is directed toward the centerline of the body. However, this supersonic flow must change direction and a reflecting shock and an oblique shock wave is formed. The gas becomes compressed in this region, yet the vibrational and electronic temperatures remain high due to freezing, and the gas may radiate significantly.

The location of the separation on the back face of the bluff body is affected by: the state of the boundary layer on the shoulder, the Reynolds number, whether the flow is turbulent or laminar, the ratio of specific heats, and the body geometry. For many cases of interest, particularly at high altitude, the flow can remain attached over a significant portion of the vehicle's afterbody. The location of separation influences the dimension of the recirculation zone and the strength of the shear-layer that forms between the recirculating gas and the external, rapidly expanding, supersonic flow. The recirculation zone entrains gas that was in the forebody boundary layer which was cooled during expansion into the base region, but remains highly dissociated. This recirculation zone will be unsteady, the magnitude of which depends on how the shear-layer behaves and the feedback between the body motion and the state of the gas in the separated region.

The modeling of the free shear-layer must account for large gradients of velocity, temperature, density and species concentration across it, and for the possibility that the flow may be turbulent and unsteady. The numerical treatment of the problem is particularly difficult because of these effects and also due to the uncertain location of this structure.

The afterbody flow field is characterized by the presence of thermo-chemical nonequilibrium, large gradients in thermodynamic quantities and chemical state, and a large separated region. The combination of these factors stretches computational fluid dynamics beyond it current capabilities.

GROUND TEST FACILITY REQUIREMENTS

Ground Test facilities are required to provide meaningful data for the real gas issues previously identified are discussed with particular emphasis on the particular merits of different types of facilities and their capability to best simulate the various aerothermodynamic problems.

In principle, there are two ways to create relative motion between the test article and the air; accelerate the air as in a shock or wind tunnel or accelerate the model as in a ballistic range. Both techniques are being employed at present and both are needed to give insight into real gas phenomena. The two concepts can be combined to create even higher relative speeds whereby a large shock tunnel can be utilized to provide counterflow to an aeroballistic range.

Ballistic ranges represent a unique capability for real gas testing of configurations. They present the only experimental technique by which real gas viscous interaction effects can be observed. Shock tunnels, because of the nature of their expansion process, do not generate sufficiently high test Mach numbers where viscous interaction phenomena would be important.

To date, most data presented from ballistic range facilities have been integrated aerodynamic data on simple geometric configurations. Early efforts by Welch[1] demonstrated a significant real gas effect on the center-of-pressure and moment data. More recent data by Strawa[2-4] continue these studies. Aerodynamic coefficient data are determined through the motions of the model down the length of the tube. Drag and static moment can be determined in about half a period of motion, lift coefficient requires 1.5 to 2 cycles, and damping coefficients require even more. Recent advances (Yates[5]) in automated data taking and data reduction techniques have resulted in significant improvements in the accuracy of aerodynamics coefficients and in the efficiency through which they are determined. Validation requires not only such overall aerodynamic data but also distributions of local flow field quantities within the shock and boundary layer of the tested configuration.

In-stream flow field data can be determined from in-flight shadowgraphs and laser holographic interferometry[6,7]. These data provide quantitative information on shock shape and position, turbulence onset, and instream density variation and provide complementary data to the integrated aerodynamics coefficients to provide data for CFD validation purposes. An obvious advantage of ballistic range testing is that the free stream is accurately characterized and can precisely simulate the flight environment.

Shock tunnels, including expansion tube/tunnels, currently offer the only means of producing both the total enthalpy and pressure levels representative of flight beyond Mach 10. Shock tubes and shock tunnels do not precisely simulate flight environment, however, and flow accelerated test facilities require the free stream to be defined. In supersonic test facilities this has been accomplished through the use of isentropic flow expansion models. However, real gas accelerations are *not* isentropic. Realistic CFD models of the expansion process must be used in conjunction with critical (but not exhaustive) instrumentation to fully define the free stream. The fluid-dynamic and thermodynamic state of chemically reacting air (including the species N, O, N_2, O_2, and NO) should be characterized accounting for viscous effects in the nozzle. Complete calibration of a real gas nozzle expansion process can only be achieved through this collaboration between insightful, limited measurements and increasingly accurate CFD models of the expansion process. Complex real gas flows require the use of full test section calibrations with the key measurements being the free stream density and static temperature. CFD validation must include facility simulation; we must not pretend to simulate flight with flow accelerated ground tests.

Measurement of Aerodynamic Parameters

There are two approaches to experimentally determining the aerodynamic parameters such as lift and drag coefficients and pitching, yawing, and rolling moment coefficients. In the first, the pressure distribution over a test model can be measured. The aerodynamic parameters are obtained by integrating the measured pressures over the surface area. If only the raw experimental data are used in the integration, the procedure is liable to lead to a fairly large numerical error. However, a fairly accurate result could be obtained, at least for simple shapes, if computational tools are used appropriately. In such an approach, the aerodynamic parameters are calculated from the computational-fluid-dynamic (CFD) solution of the flow field studied, and the experimental data on the flow properties, such as pressure or density, are used to provide anchor points for the calculated values. In this approach, the imperfection of the test facility, such as spatial nonuniformity of the test flow or presence of dissociated species, can be accounted for.

In the second approach, lift, drag, and moments of a model can be measured as integrated quantities. Shock tunnels, hot-shot tunnels, and expansion tubes are usually inappropriate in measuring forces and moments. Shock tunnels and expansion tubes cannot produce test flows of sufficiently long duration to enable accurate force measurements for complex models. Hot-shot tunnels produce test times sufficiently long for force measurements, but the flow produced is generally unsteady. Even so, progress in measurement techniques is being made that appears now to permit such direct measurements. The hot shot tunnel, F4, provides such direct measurement capability. Also, the development of such techniques are currently being explored in the United States and in Australia in facilities like the Calspan 96 inch shock tunnel, the Ames 16-Inch shock tunnel, and the University of Queensland T4 tunnel. At the present time, however, there is not a standard procedure for direct measurement of these forces in an impulse facility.

In order to determine the real-gas effects in an experiment, it is imperative first that the facility produces a flow of an enthalpy sufficiently high to produce the real-gas effects. Preferably, the results obtained in such a facility should be compared with those obtained in a perfect-gas facility in order to isolate the real-gas effects. Secondly, the test stream should be in a chemical state close to equilibrium. As is well known, the flow in the expanding nozzle of a high enthalpy, high Mach number shock tunnel or arc-jet wind tunnel undergoes freezing of chemical reactions. Therefore, the appropriateness of a facility for the aerodynamic testing depends on the extent and influence of the chemical freezing in the nozzle on the measured quantities.

Theoretical calculations can be performed to estimate, for a given set of thermodynamic conditions in the reservoir and the given nozzle geometry, the thermodynamic state of the test gas flow and the density ratio across a shock wave in this flow. The density ratio value can then be compared with that expected in flight, to assess how closely the facility simulates the flight condition. Two extreme cases can be used to illustrate this: the normal shock which occurs over the blunt nose, and an oblique shock wave of modestly small angle that will occur over the wings or other components. An oblique shock angle of 30° or smaller may be used. If the flow produced in a laboratory reproduces density ratios in flight for these two extreme cases, then one can assume that the pressure field is simulated reasonably well in the experiment.

Freezing of chemical reactions in the nozzle produces generally smaller density ratios than in flight, which leads to thicker shock layers than in flight, as long as the flow behind the shock wave is in equilibrium. In most experimental conditions, the flow behind the shock is probably not in equilibrium. The presence

of atomic species, and possible elevated vibrational temperature, in the shock tunnel flow induces faster equilibration (due to a decrease in induction time required for excitation and dissociation) of chemical reactions than when the free stream is in equilibrium. This leads to a thinner shock layer than when the free stream is in equilibrium. Thus, the nonequilibrium effect mitigates the discrepancy in density ratios seen between the laboratory and the flight cases.

Freezing occurs mostly at Mach numbers greater than 3. As the reservoir pressure is decreased, freezing occurs at smaller Mach numbers. To minimize the extent of dissociation in the test section stream, one might consider adopting the non reflecting shock tunnel scheme in which the initial levels of dissociation in the driven tube reservoir are considerably lower than those for a reflected shock tunnel where the gas has stagnated.. However, since the Mach number of the flow behind the driven tube primary shock is always less than 3, the flow at the entrance of the expansion region in a non reflecting shock tunnel has a greater degree of dissociation than the flow in a regular shock tunnel at the freezing point. Thus, the flow produced in the nozzle of a non reflecting shock tunnel undergoes a same freezing process as in a shock tunnel. The resulting degree of dissociation in the test section of a non reflecting shock tunnel is nearly identical to that produced in a regular shock tunnel, and, therefore, the scheme has no advantage over the regular shock tunnel in this regard.

A similar argument is applicable to the expansion tube. Since the flow at the beginning of the expansion is at a Mach number below 3, the freezing occurs in an expansion tube in the same fashion as that in the regular or non reflecting shock tunnel. This would lead to the same degree of dissociation at the test section of an expansion tube as in the shock tunnels, if it were not for the fact that the expansion tube has a long acceleration section. Because of the large length of the expansion section, the facility provides a large flow residence time for chemical reactions to proceed, and therefore the extent of free stream dissociation in the test section is usually less than in either shock tunnels. Thus, an expansion tube can produce density ratios across shock waves closer to the flight values than the shock tunnels. In addition, the expansion tube attains an enthalpy higher than the shock tunnels, because the acceleration process in the acceleration section increases enthalpy.

The most appropriate method of measuring forces and moments is by a flight experiment conducted in a ballistic range. In such a test, the model flies freely through a quiescent atmosphere, and the aerodynamic parameters are deduced by analyzing the time history of the flight path and the attitude of the model[6] Models of relatively simple geometry can be tested in a ballistic range for this purpose.[8]

In aeroballistic range studies of the aerodynamic properties of hypervelocity vehicles, it is a common practice to duplicate the flight speed and Reynolds number of full-scale vehicle. This is done by setting speed and the range pressure to match the Reynolds number $R_e = \rho VL/\mu$ in the test as close as feasible to those of full scale flight. This matching of both speed and Reynolds number results in matching the density-length product, ρL, because viscosity is inherently closely matched. Since the flow residence time in the flow field around a model varies directly with scale and the time required for a chemical change resulting from binary collisions varies inversely with density, the characteristic Damköhler number is automatically preserved in such a domain. Depending on test goals, the test pressure and speed may be adjusted slightly to offset the moderate effects of density on the extent of equilibrium dissociation and ionization or for the small effect of free stream temperature on viscosity.

Measurement of Forebody Heating/Heat Transfer

With a certain degree of compromise, heat transfer measurements over complex geometries in the real-gas enthalpy regime can be made also in an impulse tunnel. A model made of the materials of known surface catalytic characteristics can be tested in such a facility much easier than in a ballistic range. Since the test flow stream produced by an impulse tunnel contains certain amounts of dissociated species, the aerothermal simulation in the facilities is not as good as that in a ballistic range. However, as long as the relative concentrations of the dissociated species are small, such tests provide meaningful results that can be compared against CFD calculations.

The thermochemical state of the free stream is known most accurately in a ballistic range. Therefore, it becomes attractive to conduct tests in a ballistic range. Models can be made with materials of known surface catalytic properties, though they may not be the same as in the flight vehicle, and be instrumented with heat transfer gages. The heat transfer rate values measured in flight can either be telemetered or, if the model can be recovered, be recorded on an on-board recorder. Since the time history of heating of the model in a ballistic range test is so different from that in full-scale flight, the thermo-mechanical behavior of the material cannot be correctly replicated. However, the heat transfer rate distribution measured over the surface of known catalytic efficiency should be useful. At the present time the ballistic range/instrumentation capability to perform such testing is extremely limited.

Measurement of Lee and Base Flows

The flows in the leeward side of a slender body at an angle of attack or base region of a blunt body are affected mostly by Mach number, Reynolds number, enthalpy, turbulence, and temporal instability of the flow. The influence of the Mach number and Reynolds number are easily understandable. Enthalpy of the flow affects the effective γ, which in turn affects the turning angles in the expansion area. Turbulence affects the momentum and energy transfer in the shear layer, which in turn influences the pressure in the region. These flows are known to be intrinsically unsteady.[9] Simulation of unsteadiness requires a quietness of the free stream flow over a substantial length of time. For meaningful experimentation of these phenomena, therefore, free-flight type ballistic ranges are the most desirable. For bluff body base/wake flows large scale shock tunnels can be used for real gas flow simulations. Difficulties here include instream instrumentation for the low density wake region and quantification of the unsteady nature of the flow. Such a test campaign will be described later.

In the lee or base region of a vehicle, the dominant chemical reactions are recombinations. The time required for such processes is inversely proportional to the square of density. If ρL is properly simulated in a test, $\rho^2 L$ becomes larger than in flight, resulting in a lee-side/base flow closer to equilibrium than in flight. This will probably produce a substantial error in the flow properties in the region. This point will be elaborated on later.

TEST CASES FOR CFD VALIDATION

The development of validated analysis tools for hypersonic flows involves a process in which real-gas CFD development and application and experimental testing are performed hand-in-hand, synergistically, until the validation is complete. Hypersonic flows inherently involve real gas phenomena. The validation of CFD tools requires considerations associated with

perfect gas CFD validation *plus* consideration of additional complexities associated with real gas phenomena. These complexities include thermal and chemical time scales, multiple gas species, internal energy flow variables and properties, and coupled fluid/chemical processes.

It is equally important to identify the important issues to be studied and to identify the best procedure to use to perform such studies. This is, in part, the purpose of this discussion, and has been treated in some detail by Sharma and Park[10] and Neumann[11].

That it is not possible to fully simulate real gas hypersonic flight conditions in ground test facilities is axiomatic. Ground test experiments must be carefully selected to validate basic principles and concepts in CFD codes. It is necessary to use CFD in the design of experiments, in the definition of the test environment, in the development, application and interpretation of diagnostics, and in the analysis of the test results as a whole. The resulting test data will then form a basis for validating the process and the CFD tools. The CFD codes can be used to extrapolate to flight conditions. And, finally, flight experiments are required to confirm the process as a whole.

As previously mentioned, to acquire data necessary to validate and/or calibrate real gas code capability to predict aerodynamic performance, the aeroballistic range is appropriate. Ballistic range data will include visual flow field data indicating shock shape and location relative to the body (i.e. by way of shadowgraphs) and density distribution (i.e. by holographic interferograms) as well as quantitative information in the form of aerodynamic coefficients including lift, drag and pitching moment. The use of a combination of CFD with experiment has proven most effective in the interpretation of free-flight data. For example, in a recent study on trim angle for the NASA Aeroassist Flight Experiment (AFE) vehicle[5], there was insufficient free-flight data for determining high order terms for series expansion representation of aerodynamic coefficients . In order to extract information from the experimental data, the curvature of the function describing the moment coefficient was required. This curvature was developed using CFD. For the analysis of data from the aeroballistic range the higher order terms in the aerodynamic coefficient expansion were determined from CFD simulations; only the lower order terms were found using a six-degree-of-freedom, weighted, least squares procedure. The resulting experimental aerodynamic coefficients and trim angles agree with those computed by CFD. The effective specific heat ratio was determined by matching the bow shock shape and stand-off distance with CFD perfect gas, constant effective γ, flow field simulations at the test conditions. Results of these comparisons are shown in Fig. 3. in which the CFD simulation bow shock is identified by a coalescence of isobars.

Moment coefficient ballistic range (HFFAF) data for an AFE model are compared with data from two NASA Langley hypersonic cold flow facilities, the 31-inch Mach 10 tunnel and the CF_4 tunnel, in Fig. 4. Results of two test entries each are shown for the Langley tunnels. Each of the three facilities can be represented by an effective γ: 1.2 for HFFAF, 1.34 for the Mach 10 tunnel, and 1.11 for the CF_4 tunnel. The measured trim angles are 14.7, 17 and 12 degrees, respectively.

By minimizing the uncertainty in trim angle, design tolerances can be tightened and vehicle configurations can be optimized for specific mission requirements. By using a combination of CFD analysis and ground-based experiments, the real-gas effects can be simulated, analysis tools validated, and flight conditions can

be estimated with some confidence. In many cases the aeroballistic range can be used to simulate actual flight conditions and reasonable estimates of aerodynamic trim angle and pitching moment for flight can be determined directly. The agreement shown herein between experimental and computed results for the blunt AFE configuration at the ground test conditions indicate that, at these test conditions, the moment coefficients and trim angles can be computed using efficient ideal gas solvers with an appropriate choice for γ; the appropriate value of this parameter can be determined by shock shape comparison. This is not necessarily the case, however, for slender or high lift vehicles. In cases where actual flight conditions cannot be replicated in ground test facilities, real gas solvers must be used to determine if constant effective γ approximations are appropriate. As mentioned previously, the variations in γ at flight conditions can have a sizable influence on aerodynamic moment coefficient and trim angle.

Existing test data for validation of instream flow quantities include (1) flow past a cylinder where shock shape, shock stand-off distance, and density fringe patterns are measured in a shock tunnel[12], (2) ballistic range flow field shadowgraphs of a blunted slender cone with shock generators[3,4].

Ballistic Range Tests

Ballistic ranges can be used to achieve flight velocities where real gas effects are important. They offer an advantage over other hypersonic facilities in that the free stream conditions are known and there are no model supports to cause interference, particularly in the base region. This simplifies boundary and initial conditions and eliminates one source of ambiguity between computational and experimental results.

Tests in such facilities can be conducted in ambient pressures greater than atmospheric (in pressurized ranges) to pressures as low as about 0.02 Torr, and in gases including air, CO_2, H_2, He, Kr, Ar, and Xe. In addition to providing information about aerodynamic coefficients, detailed flow quantities (such as density, temperature, and species concentration) are feasible using modern diagnostic methods.Laser holographic techniques can be used to provide interferogram fringe patterns from which the density field can be deduced. Model wall temperature can be estimated using temperature sensitive paint and infrared photography. Telemetry can be used to transmit data from surface instrumentation. Instream species information can be developed from resonant laser iterferometric methods.

Galileo Tests:

Ballistic ranges have been used to support all of the United States' probe missions to other planets. These include the 1976 Viking mission to Mars, the 1978 Pioneer Venus mission, and the current Galileo probe launched last year, which will arrive at Jupiter next year. The Galileo probe will make in situ measurements as it decends through the Jovian atmosphere prior to its eventual destruction caused by the extreme external pressures.

Although the probe aerodynamics were needed only for initial design purposes, more accurate aerodynamics were needed in support of the Atmospheric Structure Experiment carried on board the probe. This experiment is designed to determine the state properties (i.e., density, pressure, and temperature) of an unknown planetary atmosphere as a function of altitude from measurements made during the entry and descent of the probe. The experiment consists of a three-axis accelerometer, plus pressure and temperature sensors. During the high speed

portion of the trajectory, from an entry velocity above 47 km/sec to sonic speed, direct measurements are impractical and accelerometers are used to determine state properties. This requires a precise knowledge of the probe aerodynamics, in particular the vehicle lift and drag coefficients as functions of Mach number and Reynolds number, The aerodynamic characteristics plus the measured decelerations allow the probe attitude to be determined and the atmospheric density to be deduced. Integration of the density gives pressure, and the temperature is deduced from the equation of state (given the molecular weight, which is measured by another on-board experiment). Ballistic range facilities are well suited to providing the accurate aerodynamic data over a wide range of conditions.

A typical shadowgraph of a Galileo model in flight obtained in the NASA Ames Hypersonic Aerodynamic Free Flight Facility (HFFAF) is shown in Fig. 5. The screw on the model base is for attachment to its sabot prior to launch The verical wires are plumb lines for reference, and the irregular markings are imperfections in the facility windows caused by past debris impacts. These tests were performed in air at a flight Mach number of 14.

Low Reynolds-Number Tests Tests were also conducted to precisely define the drag characteristics of the Galileo probe at Reynolds numbers, based on model diameter, of about 500 to 250. Obtaining drag at these low Reynolds numbers is important because the drag is expected to increase markedly as the slip-flow and free-molecule flow regimes are approached. This dramatic increase in drag occures below a Reynolds number of about 1000.

The importance of obtaining drag at various Reynolds numbers is shown in Fig. 6. Shown are Pioneer Venus data[32] down to a Reynolds number of about 250. The drag coefficient increases continuously below a Reynolds number of 1 million, but the decrease becomes most dramatic below 1000.

ASTV Tests

Ballistic range tests have been conducted for two ASTV configurations: a symmetric and a raked-elliptic-cone configuration. These tests were conducted to: 1) provide experimental data and good flow-field definition against which computational aerodynamicists could validate their computer codes, 2) define bow shock wave shape and shock standoff distance, 3) investigate flow impingement on the afterbody, 4) compare the aerodynamics of several configurations, 5) investigate how minor changes in corner geometry affect the flow field, and 6) determine the trim angle of attack of the trimmed vehicle.

A shadowgraph for thesymmetric configuration[32] is shown in Fig. 7 and for the raked elliptic cone[32] in Fig. 8. These flow visualizations along with drag data from these tests are used cor computer code calibration. With the newer holographic techniques, density data can also be used for code validation.

Other Tests

Simple shapes (such as sharp and blunt cones, bi-cones, and blunt bodies) are used in the ballistic ranges and sting mounted in shock tubes and tunnels to study the effect of real gas properties. Real gas thermodynamic and transport properties and finite rate chemical reactions have a pronounced effect on shock and Mach wave positions and shapes, emitted radiation, and aerodynamic drag. A detailed survey of simulation and diagnostic techniques used for these studies was presented by Sharma and Park[20].

Fundamental Processes

Basic Phenomenon - Compressive & Expanding Flows

To study the nonequilibrium processes in a compressive flow typical of the stagnation region of a bluff forebody, the detail of a gas relaxing after being heated by an incident shock wave is studied. By acquiring a normal shock in a spectrally clean facility, the thermo-chemical state of the gas can be quantified as a function of time and position. By this means such processes as vibration-dissociation coupling, vibration-translation exchange, vibration-rotation coupling, etc., are studied[13-15]

The dominant real gas phenomena is the relaxation process occurring in the flow around hypersonic vehicles. Considerable effort has been expended in recent years to model and numerically compute this behavior (e.g. refs. 16-19). The accuracy of such calculations needs further improvement and there are still many physical parameters that are unknown for high temperature real gases. Three types of experimental data are needed in this model development process: 1) data which will enhance our phenomenological understanding of the relaxation process, 2) data on rates for the relevant reactions, and 3) data on bulk properties, such as spectral radiation emitted by the gas, for a given set of aerodynamic conditions. Such data has been acquired by simulating the required aerothermochemical conditions in an electric arc driven shock tube[20-21]. The NASA Ames' electric arc driven shock tube facility (EAST) is powered by a 0.6 MJ, 40 kV capacitor bank and is capable of producing shock velocities in the range of 2-50 km/sec. The radiation diagnostic system available at the facility, consists of 1) a linear intensified 700 element diode array and a 2-D intensified CCD array with 576 x 384 active elements, both gateable within a time range of 30 ns - 2.5 ms and both with a 2000-8000 A spectral response. A photomultiplier tube (PMT) is used to record the total radiation from the test gas as well as from the driver gas as they pass through the test section. The signal from the PMT is used to estimate the test time and to trigger the diode array system at a given moment during the test history. A Nd:YAG laser based, double exposure, single plate interferometer is also available at the facility. A schematic of the experimental test setup is shown in Fig. 9.

A one-dimensional real-gas flow code for thermo-chemical nonequilibrium (Park[22]) is used to predict the thermochemical state of the shock heated gas behind the incident shock. This code uses a multiple temperature description to model the nonequilibrium behavior of the internal state of the gas and to describe the rate processes. From the predicted thermochemical state of the gas synthetic emission spectra can be generated. Several modeling steps are involved in this process. First are the chemical rate expressions themselves in which there is always some uncertainty in the Arrhenius rate constants, second is the multiple temperature model used to describe both the internal energy states of the gas and the reaction rates, and third is the quasi-steady state model and peripheral approximations used to generate the synthetic spectra. By maintaining a coordinated effort between the modeling activity and the experimental effort it is possible both to improve and refine the phenomenological models as well as validate them. These models will then, in turn, be used in multidimensional flow codes to predict and analyze real gas behavior in more complex flow environments.

To date two sets of experiments have been conducted: 1) measurements at a shock velocity of 6.20 km/sec in 1 Torr nitrogen[23] and 2) measurements at a shock velocity of 10.2 km/sec in 0.1 Torr air[24]. In both the sets, using the linear diode array, the equilibrium and nonequilibrium spectra covering the 3050-5500 A range were recorded.

Measurements in Nitrogen (6.2 km/sec, 1.0 Torr):

For the nitrogen case, the equilibrium temperature of the test gas based on $N_2(2^+)$ band system was found to be 6500 K. The rotational temperature at the point of peak radiation in the nonequilibrium region, based on the intensities at 3143.7 A and 3159.1 A, was found to be about 8800 K. The vibrational temperature, based on the first vibrational level and the ground state of the $N_2(2^+)$ band system was found to be about 6900 K. The vibrational temperatures of higher vibrational levels were lower than this value.

The equilibrium temperature of the test gas based on the $N_2^+(1^-)$ band system was found to be 7200 K. The rotational temperature at the point of peak radiation in the nonequilibrium region was deduced to be about 8800 K, which is consistent with the value found by using the $N_2(2^+)$ band system. Comparisons of rotational temperature with prediction and with earlier data from Allen et al[25] are shown in Fig. 10. The vibrational temperature as measured based on the $v(1,2)/v(1,0)$ levels of the $N_2^+(1^-)$ band system was found to be about 9500 K, with the value decreasing for higher vibrational levels. The temperature based on the $v(7,8)$ vibrational level was about 8500 K. Comparisons of vibrational temperature with prediction and with earlier data are shown in Fig. 11.

Measurements in Air(10.2 km/sec, 0.1 Torr):

For shock heated air the equilibrium temperature was estimated to be 9620 K. The equilibrium emission spectra observed is shown in Fig. 12. By using two different sets of points on the rotational envelope of the $N_2(2^+)$ band system, the rotational temperature, corresponding to the point of peak radiation, was estimated to be about 4400 K and 3990 K respectively, making a mean rotational temperature of 4195 K. Such a low value of rotational temperature was a surprise. The overshoot observed in the nitrogen tests at 6.2 km/sec was absent here. The rotational temperature seems to rise very slowly to reach the equilibrium value. The emission spectra observed at the point of peak radiation is shown in Fig. 13.

The vibrational temperature at the point of peak radiation was deduced using the (2,1) and (3,2) bands of $N_2^+(1^-)$ system at 3564.1 and 3548.2 A respectively and was found to be about 9465 K. There were no other vibrational temperature data available for these conditions   The measured vibrational temperatures based on $N_2^+(1^-)$ as well as based on $N_2(2^+)$ band systems are in line with the theoretical values as predicted by Park's model[18]. Sharma[20] shows further details and analysis of the experimental data and comparisons with theory.

Expanding flows

To study the nonequilibrium processes in an expanding flow as typified by the flow over the shoulder of a bluff body and into the base, or near wake, region, a test gas is shock heated in the Ames EAST facility to high temperature and pressure and allowed to expand rapidly in a two-dimensional nozzle. By using optical diagnostics such as laser holographic interferometry and Raman scattering[26], the thermo-chemical state of the gas during the expansion process is quantified. Nonequilibrium vibrational populations are measured for levels up to v=13, in an expanding flow, using spontaneous Raman scattering technique. A nozzle insert has been installed in the driven section operating in a reflected shock mode. The density flow field was mapped by laser based holography. The results are shown in Fig. 14. where good agreement can be observed between computer simulated and experimental fringe interferograms.

Configuration Study

In addition to characterizing the thermochemical process in an expanding flow, a blunt body base flow test configuration is being developed as part of the Working Group 18 activity. The basic configuration, shown in Fig. 15., is a 20 cm dia., 70^0 spherically blunted cone representative of a planetary entry capsule aeroshell. Models have been fabricated as follows: (1) two uninstrumented brass free flying model to be used for flow visualization studies without the presence of a sting support, and (2) an instrumented sting mounted chromel model for which both the model and the sting support are instrumented with pressure and heat flux gauges (flow visualization can be realized for comparison with the free flight model,) and (3) an uninstrumented sting mounted stainless steel model with a slot in the sting for optical access in the near base region. The uninstrumented stainless steel model has been instrumented with a modest number of surface instruments at Calspan and at DLR. As part of the AGARD FDP WG18 activity the free-flight and sting mounted chromel configurations will be tested in the NASA Ames 16-Inch combustion driven shock tunnel, only sting mounted models will be tested in the DLR free piston shock tunnel, HEG, and only stainless steel sting mounted model will be tested in the Calspan LENS. Each facility will be operated at the same enthalpy and the same Mach and Reynolds numbers(H_0=10 MJ/kg, M=7, and p_0=500 bar). In addition, tests in the Ames facility will be performed at total enthalpies of 5 and 14 MJ/kg at total pressures of 100 bar, in the DLR HEG facility at enthalpies of 20 MJ/kg and total pressures of 500 and 1000 bar, and in the LENS at enthalpy 5 MJ/kg and pressures of 500 and 2000 bar. The lower enthalpy levels produce only modest levels of dissociated oxygen and no dissociated nitrogen. At 10 MJ/kg there will be substantial oxygen dissociation and negligible nitrogen dissociation. At 20 MJ/kg there will be substantial dissociation of both oxygen and nitrogen. Nitrous oxide (NO) will be produced under all test conditions. The test matrix is shown schematically in Fig. 16. In-stream laser induced fluorescence (LIF) data will be acquired at DLR to determine NO temperature and concentration distribution over the shoulder expansion region. Sodium line reversal imaging and high speed schlieren photography will be performed at Ames to identify the wake structure with and without sting support. The stingless model will be suspended in the facility test cabin by nylon threads prior to facility operation. The threads will vaporize upon facility start-up leaving a "free flying" model. The model inertia will maintain the model in an essentially motionless position during the test period.

Test entries have been completed in both the HEG facility and the LENS facility. Preliminary reports of these tests were presented at the recently held workshop on hypersonics held 24-25 November, 1994 at the ESTEC, Noodwijk, The Netherlands.

The purpose of the experiments are to quantify the shear layer separation point, turning angle and wake closure in the presence of flows exhibiting real gas and/or low density behavior. The unsteady character of the near wake will also be characterized, if possible using high speed schlieren and surface heat flux data.

Body surface instruments will provide data for CFD simulation and calibration/validation. Both sting mounted and free flight models will be necessary to assess and quantify the influence of the sting on the instrumented model.

FLIGHT EXPERIMENTS

RAM-C

During the late 1960s three experimental probes were flown into the atmosphere at approximately satellite speed.[27-28] These probes, which were called the RAM-C tests, were sphere-cone configurations with a 0.1524 m nose radius, 9 deg cone half-angle, and a total length of 1.295 m. They were instrumented to measure electron number densities in the flow field. The second test, RAM-C II, is of particular interest because no ablation products were produced. This probe had a beryllium heat-sink nose cap and a Teflon-coated afterbody. Electron number densities were measured at four axial locations using microwave reflectometers and in the boundary layer using an electrostatic rake.

Computations have been performed to replicate the RAM-C II tests at altitudes of 61, 71, and 81 km. This altitude range approximately spans a region of neat-thermo-chemical equilibrium at 61 km to strong nonequilibrium at 81 km. The wall temperature was fixed at 1500 K, which is an approximation to the experimental wall temperature which is unknown. The wall was assumed to be fully non-catalytic which is also an approximation to the RAM-C II test. In each case the free stream velocity was 7650 m/sec.

The computations[16] were performed on body-fitted meshes with 35 points axially along the sphere-cone and 50 points in the flow field normal to the body. Fig 17. shows a typical mesh used for one of the test cases. The computations were performed using shock-capturing techniques for all cases.

Each case was computed using two different chemical models. One set of results was obtained considering five chemical species (N_2, O_2, NO, N, and O), and three vibrational temperatures (*i.e.*, one vibrational temperature per diatomic species). There are a total of eleven coupled equations to be solved. The number density of electrons may be approximated with the use of the quasi-steady-state (QSS) assumption. A second set of results was computed for this gas with NO ionized. In this case there are seven species (N_2, O_2, NO, NO^+, N, O, and e^-), four vibrational temperatures, and the electron temperature, for a total of fifteen equations to be solved. The purpose of performing both sets of calculations is to compare the effects of electrons on the flow field.

The computed results are first compared to the peak electron number density measured along the body at each altitude. These results are presented in Figs. 18-20. They show that the electron number density is highest at the nose and falls off rapidly around the shoulder of the body. The QSS approximation and the nonequilibrium approach follow this trend, but the latter method predicts the data much better. The QSS technique works best at lower altitudes because the flow field is closer to equilibrium for these cases. Conversely, the agreement between the experiment and the nonequilibrium results is best for the higher altitude, nonequilibrium cases. The differences between the two computed results indicate the nature of a nonequilibrium flow field. As the gas expands around the shoulder of the sphere-cone, the translational temperature falls rapidly. The fluid carries with it a large number of electrons that have been produced near the nose but have not yet recombined. Thus, although the local temperature is relatively low, the number of electrons remains high in the shoulder region. This effect is captured by the seven-species solution. However, if we assume that the reaction producing the electrons is governed by the local temperature as in the QSS approach, we predict too few electrons.

Figure 21 compares the computed results using a seven-species model to the measured electron number density near the body surface at $x/r_n = 8.10$ for altitudes of 71 km and 81 km. The results are approximately the right magnitude but do not show the correct behavior near the wall. The problem is likely caused by the uncertainty in wall boundary conditions. The surface of the probe was probably catalytic for the electron-ion recombination reaction and thus would cause a lessening of the electron number density near the wall. This wall effect is not currently included in the calculations. Alternatively, the fixed-wall temperature used for the calculations may be too high which would result in an excessive number of electron near the wall.

The electron number densities computed using the seven-species gas model are in good agreement with the RAM-C II flight experiment. The use of a QSS assumption to derive the electron density from the five-species model predicts the correct trend. However, this approach yields results that are typically at least an order of magnitude in error, especially in highly nonequilibrium cases. The computations also indicate that the heat transfer to the body in the nose region is about 50% greater for a reacting gas than for a perfect gas. The heat transfer results also show that for the cases studied, the flow field is adequately described by the five-species model unless an accurate representation of the electron density distribution is required. The vibrational state of the flow field may be approximated with only one vibrational temperature.

These results and others not discussed here demonstrate that the models used for the translation-vibration and electron-vibration energy exchange mechanisms are adequate in the regime of the test cases. Further research is required to improve these models for high temperatures so that the vibrational and electron temperatures may be computed correctly.

Other Flight Experiments

Other flight experiments include the Fire 2[29] project where radiative emission power was measured at the stagnation point during the flight, and the PAET[30] flight where the radiation intensity in several narrow wavelength channels was measured at the stagnation point of a spherical nose re-entry body. Comparisons between each of these flight experiments and computed results by Park[22] (in which a two-temperature thermochemical nonequilibrium model for dissociating and ionizing air was used) are shown in Figs. 22. and 23., respectively.

Other, more recent flight experiments include the series of Bow Shock Ultra Violet (BSUV) experiments flown by the Utah State University. These flights, however, are at typically much lower speeds than satellite speed and represent a flight regime more representative of a ballistic missile than a re-entry capsule.

Aeroassist Flight Experiment

A recently studied NASA flight experiment called the Aeroassist Flight Experiment (AFE) was planned for this decade. A large base of radiometric data for high altitude, high velocity thermochemically nonequilibrated flow conditions was anticipated. The AFE was to be carried to obit by the Space

Shuttle and then deployed for the atmospheric pass. Accelerated by an 18,000-LB thrust solid rocket motor, the vehicle would enter the atmosphere at nearly 10 km/sec and then experience approximately 500 sec of aerodynamic deceleration, during which a variety of flight data, including radiative and convective heating rates, would be gathered. The vehicle was intended to exit the atmosphere at orbital speed and be recovered by the Shuttle Orbiter for return to Earth for post-flight evaluation. As a preliminary to the design of a radiometer for this experiment, an approximate method for predicting both equilibrium and nonequilibrium radiative surface fluxes was developed[31]. Spectral results for one trajectory state, a velocity of 10 km/sec at an altitude of 85 km, are shown in Fig. 24., where the spectral surface flux at a distance of 20.9 cm behind the shock front is plotted as a function of wavelength in the spectral region from 0.2 to 2.0 mm. An inspection of the figure reveals that the spectrum appears to be composed of a background continuum with a color temperature in the range of 7,000 K TO 8,000 K (based on a flux maximum in the vicinity of 0.4 mm) on which is superimposed a complex structure of molecular bands and broadened atomic lines. The radiation calculation included 11 species (O_2, N_2, NO, O, N, N^+, O^+, N_2^+, NO^+, O_2^+, and e^-); some of the more apparent band-heads and lines from these species are identified in the figure. The results, and others like them, were used to develop instrument parameters for the three different radiometers proposed for the experiment. In a subsequent set of lecture notes, the lessons learned from this proposed flight experiment activity will be described..

References:

1. Welch, C. J., Lawrence, W. R. and Watt, R. M., "Real-Gas Effects on the Aerodynamics of Blunt Cones as Measured in a Hypervelocity Range", AEDC TR 79-33.

2. Strawa, A.W., Chapman, G.T., Canning, T.C., and Arnold, J.O., "The Ballistic Range and Aerothermodynamic Testing," AIAA Paper 88-2015.

3. Strawa, A.W. and Prabhu, D. K., "A Comparison of Experimental and Computational Results for 5 and 10 Degree Cones at High Mach Numbers," AIAA Paper 88-2705.

4. Strawa, A. W., Molvik, G., Yates, L., and Cornelison, C., "Experimental and Computational Results for 5 Degree Blunt Cones with Shock Generators at High Velocity," AIAA Paper 89-3377.

5. Yates, L. A. and Venkatapathy, E., "Trim Angle Measurements in Free-Flight Facilities," AIAA Paper 91-1632, June 1991.

6. Strawa, A. W., and Cavolowsky, J. A., "Development of Non-Intrusive Instrumentation for NASA-Ames' Ballistic Range and Shock Tunnel," AIAA Paper 90-0628.

7. Tam, T. C., Brock, N. J., Cavolowsky, J, A., and Yates, L. A., "Holographic Interferometry at the NASA-Ames Hypervelocity Free-Flight Aerodynamic Facility," AIAA Paper 91-0568.

8. Chapman, G. T., "The Ballistic Range - Its Role and Future in Aerothermodynamic Testing," AIAA Paper 92-3996, July 1992.

9. Behren, S. W., and Ko, D. R. S., "Experimental Stability Studies in Wakes of Two-Dimensional Slender Bodies in Hypersonic Speeds," AIAA Journal Vol. 9, No. 5, May 1971, pp. 851-857.

10. Sharma, S. P., and Park, C., "Survey of Simulation and Diagnostic Techniques for Hypersonic Nonequilibrium Flows," AIAA *Journal of Thermophysics and Heat Transfer*, vol/ 4, No. 2, pp 129-142, April 1990.

11. Neumann, R.D., "Requirements in the 1990's for High Enthalpy, Ground Test facilities for CFD Validation," AIAA Paper 90-1401

12. Hornung, H. G., "Nonequilibrium Dissociating Nitrogen Flow Over Spheres and Circular Cylinders," Journal of Fluid Mechanics, vol. 53, pp. 149-176, 1972

13. Park, C., "Two-Temperature Interpretation of Dissociation Rate Data for N_2 and O_2," AIAA Paper 88-0458

14. Sharma, S., Huo, W., and Park, C., "The Rate Parameters for Coupled Vibration-Dissociation in a Generalized SSH Approximation," AIAA Paper 88-2714.

15 . Park, C., "A Review of Reaction Rates in High Temperature Air," AIAA Paper 89-1740.

16. Candler G. V. and Park C., "The Computation of Radiation from Nonequilibrium Hypersonic Flows," AIAA Paper 88--2678.

17. Candler, G. V. and MacCormack, R. W., "The Computation of Hypersonic Ionized Flows in Chemical and Thermal Nonequilibrium," AIAA Paper 88--0511.

18. Gokcen, T. and MacCormack, "Nonequilibrium Effects for Hypersonic Transitional Flows Using Continuum Approach," AIAA Paper 89-0461.

19. Candler, G. V.,"On the Computation of Shock Shapes in Nonequilibrium Hypersonic Flows," AIAA Paper 89--0312.

20. Sharma, S. and Park, C., "A Survey of Simulation and Diagnostic Techniques for Hypersonic Nonequilibrium Flows, " AIAA Paper 87-0406.

21. Sharma, S. and Park, C., "Operating Characteristics of a 60 cm and a 10 cm Electric Arc-Driven Shock Tube, " AIAA Paper 88-0142.

22. Park, C., "Assessment of Two-Temperature Kinetic Model for Dissociating and Weakly Ionizing Nitrogen," J. Thermophysics and Heat Transfer, Vol. 2, No. 1, Jan. 1988, pp 8-16.

23. Sharma, S., "Nonequilibrium and Equilibrium Shock Front Radiation Measurements," AIAA Paper 90-0139.

24. Sharma, S., Gillespie, W. D. and Meyer, S. A., "Shock Front Radiation Measurements in Air," AIAA Paper 91-0573.

25. Allen, R. A., Camm, J. C. and Keck, J. C., "Radiation from Hot Nitrogen," AVCO-Everett Research Laboratory Report 102, April 1961.

26. Sharma, S., Ruffin, S., Meyer, S. A., Gillespie, W. D. and Yates, L. A., "Density Measurements in an Expanding Flow Using Holographic Interferometry," AIAA Paper 92-0809.

27. Grantham, W. L., "Flight Results of 25,000 Foot per Second Reentry Experiment Using Microwave Reflectometers to Measure Plasma Electron Density and Standoff Distamce," NASA TN D-6062, 1970

28. Jones, W. L. Jr. and Cross, A. E., "Electrostatic Probe Measurements of Plasma Parameters for Two Reentry Flight Experiments at 25,000 Feet per Second,"NASA TN D-6617, 1972

29. Cauchon, D. L., "Radiative Heating Results from the Fire 2 Flight Experiment in a Reentry Velocity of 11.4 Kilometers per Second," NASA TM-X 1402, 1967.

30. Whiting, E. E., Arnold, J. O., Page, W. A., and Reynolds, R. M.., "Composition of the Earth's Atmosphere by Shock-layer

Radiometry During the PAET Entry Probe Experiment,"J. Quantitative Spectroscopy and Radiative Transfer, Vol. 9, Sept. 1973, pp. 837-859.

31. Davy, W. C., Park, C., Arnold, J. O., and Balakrishnan, A., "Radiometer Experiment for the Aeroassist Flight Experiment," AIAA Paper 85-0967, Williamsburg, VA., June, 1985.

32. Intreri, P. F. and Kirk, D. B., "High-Speed Aerodynamics of Several Blunt-Cone Configurations," AIAA Paper 86-0300, Reno, NV, Jan. 1986.
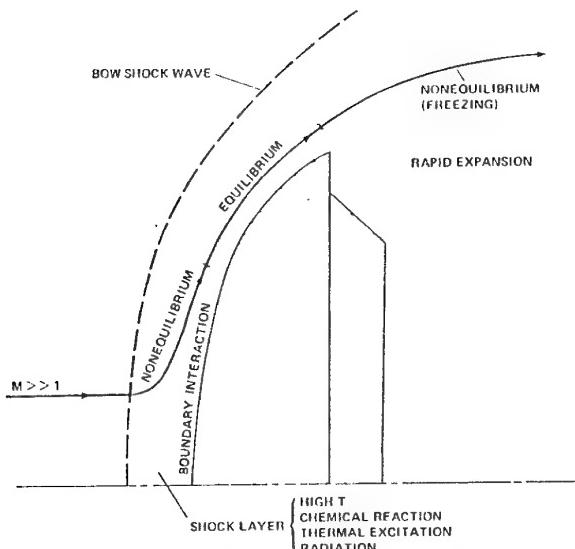
Fig. 1. Schematic of hypervelocity bluff forebody flowfield.
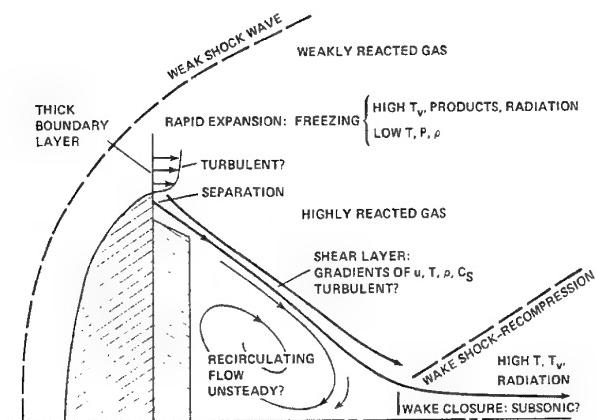

Fig. 2. Schematic of hypervelocity bluffbody near-wake flowfield.

Shadowgraph $\gamma = 1.4$, coarse grid solution $\gamma = 1.2$, coarse grid solution $\gamma = 1.2$, adapted grid solution
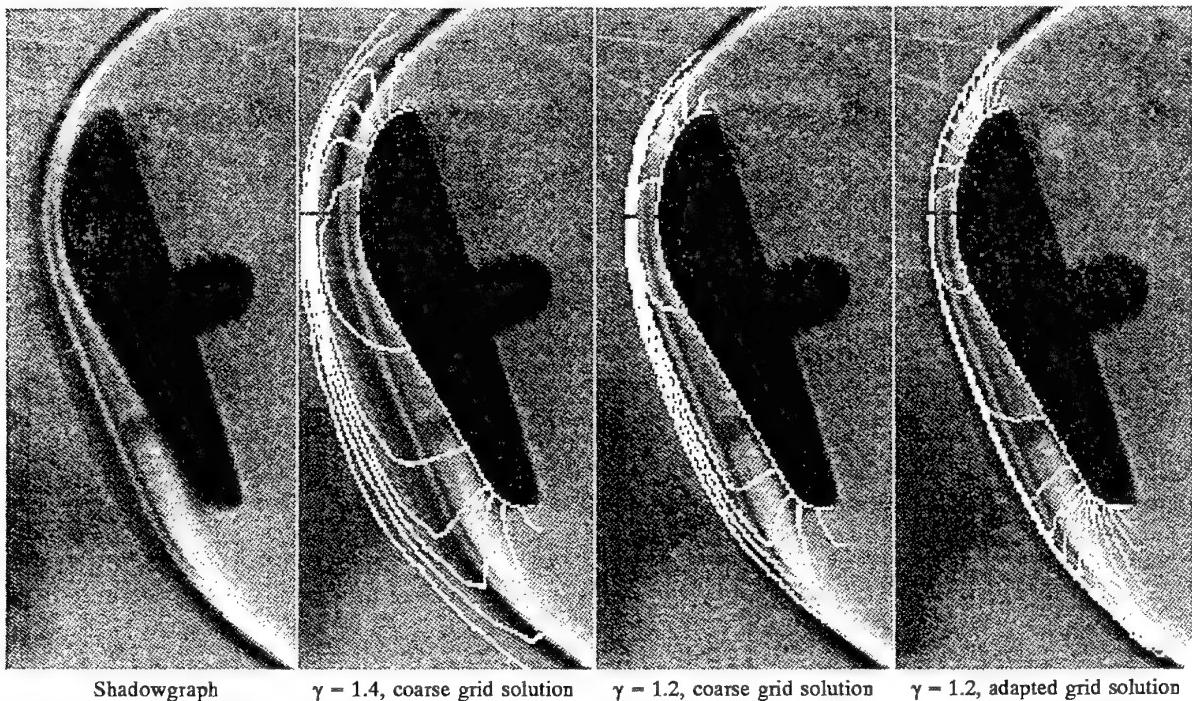
Fig. 3. Experimental and computed AFE bow shock
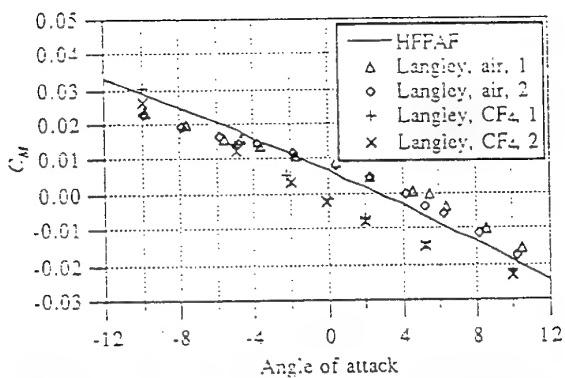
Fig. 4. AFE moment coefficient comparison
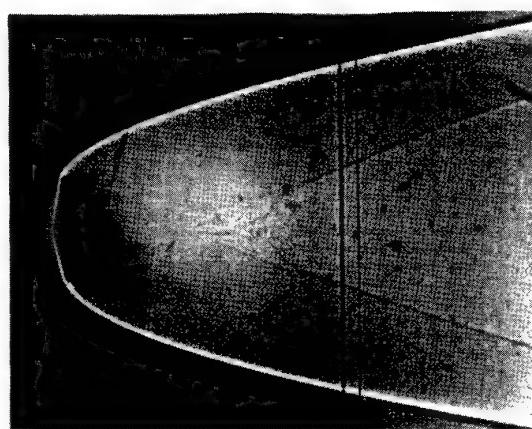
Fig. 7. Shadowgraph of symmetric ASTV

Fig. 5 Shadowgraph of Galileo Probe Model
M = 14, Re = 100,000
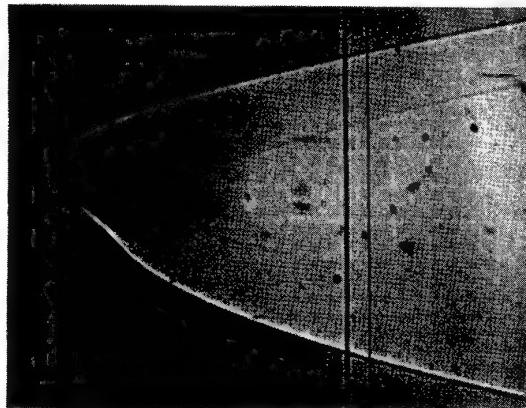
Fig. 8 Shadowgraph of raked elliptic cone
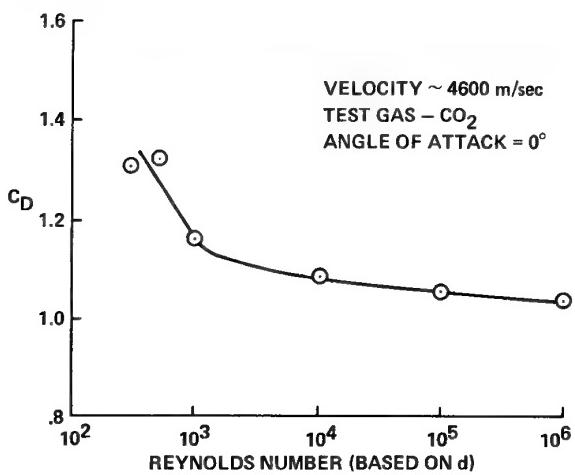
Fig. 6 Effect of Reynolds number on drag characteristics of Pioneer Venus Probe
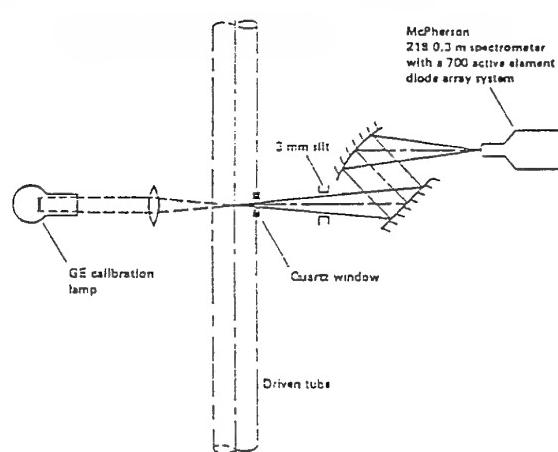
Fig. 9. Schematic of shock tube emission spectra collection optics for diode array system.
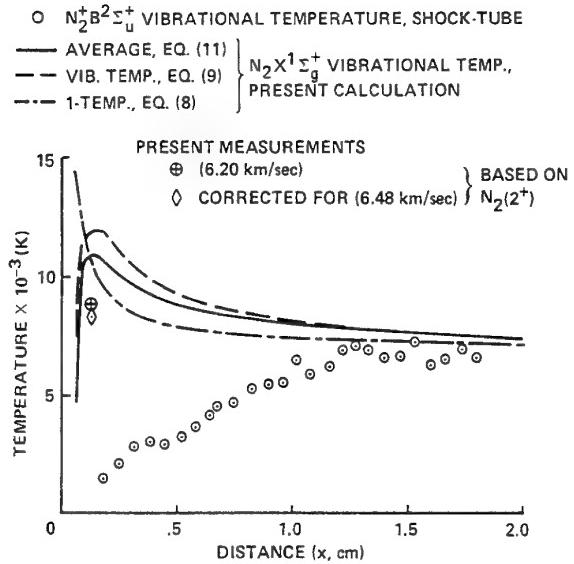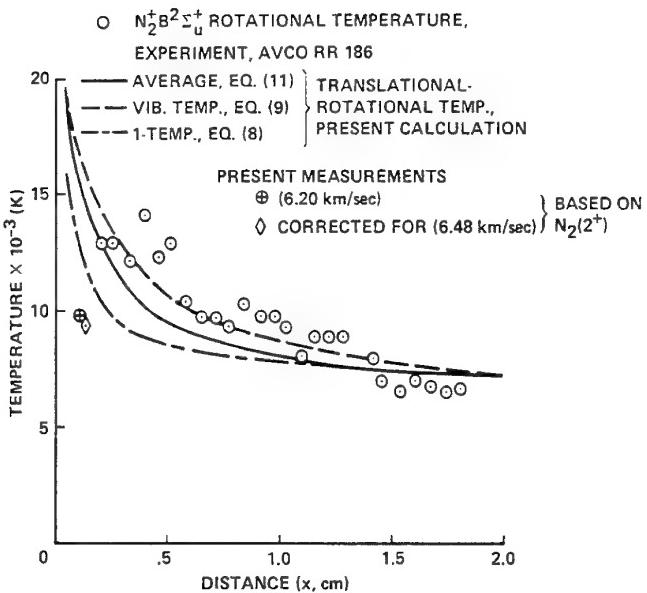
Fig. 10. Rotational temperature behind normal shock in nitrogen: U_s=6.2 k/s, p_1=1.0 torr

Fig. 11. Vibrational temperature behind normal shock in nitrogen: U_s=6.2 k/s, p_1=1.0 torr.

Fig. 12 Equilibrium emission spectra behind normal shock in air: U_s=10.2 k/s, p_1=0.1 torr, gate=1.0 ms, slit=60 m m
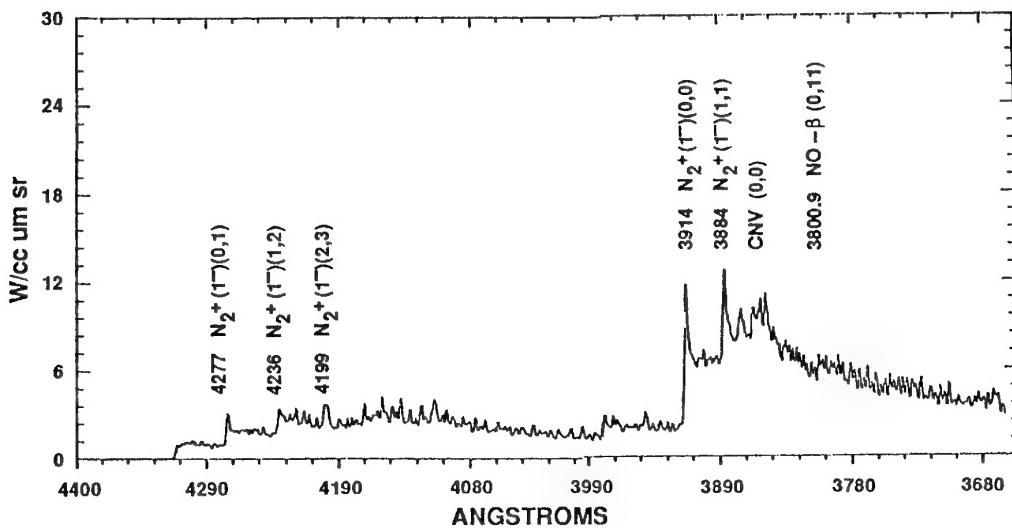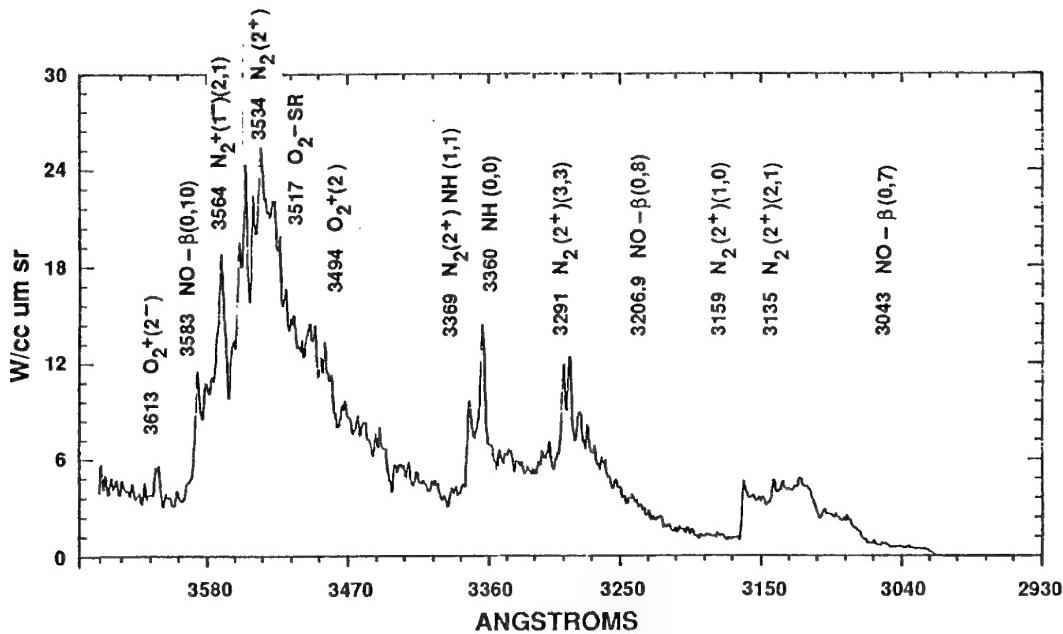
Fig. 13 Nonquilibrium emission spectra behind normal shock in air: U_s=10.2 k/s, p_1=0.1 torr, gate=200 ns, slit=60 m m

$\delta = 70°$
$Rb = 3.000$ In. (76.20 mm)
$\delta = 2Rb = 6.000$ In. (152.40 mm)
$Rn/Rb = 0.5$
$Rc/Rb = 0.05$
$Rs/Rb = 0.25$

Note: T = Tangent points
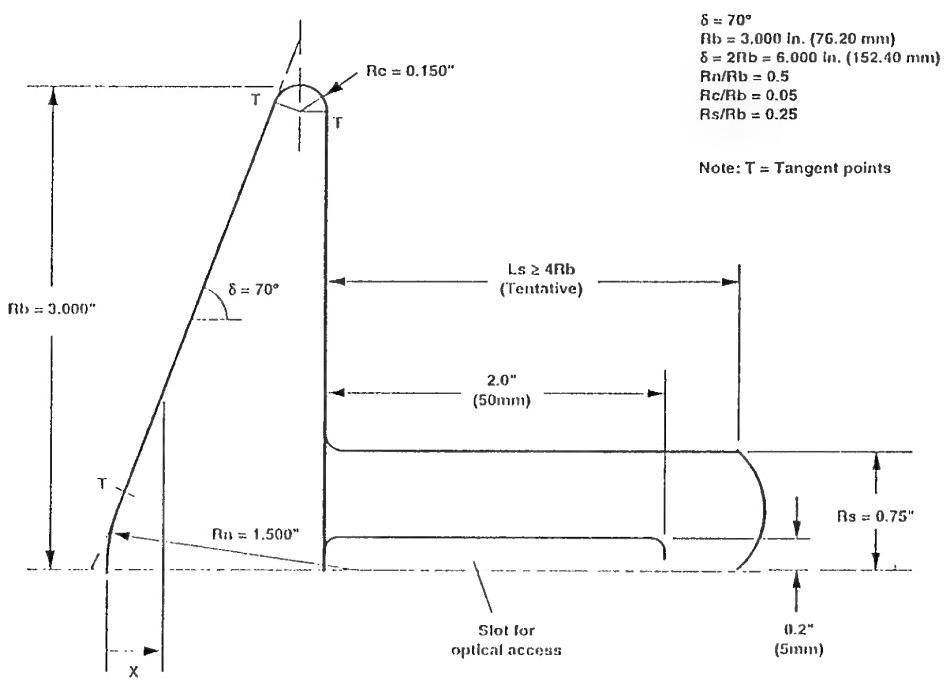
Fig. 15 Blunt Cone Model for Forebody and Base Flow Tests
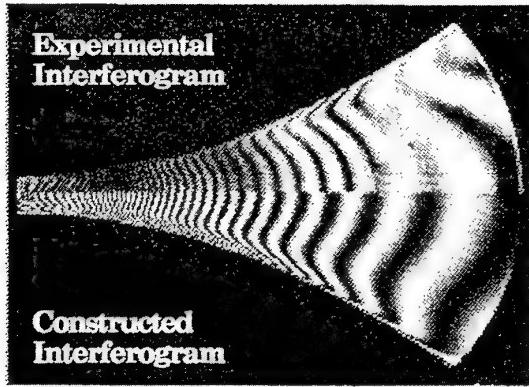
Fig. 14. CFD generated synthetic interferogram compared with experimental observation: P_0=1530 PSI, T_0=7200 K.

Fig. 18. Comparison of peak electro number density, 61 km alt., M = 23.9
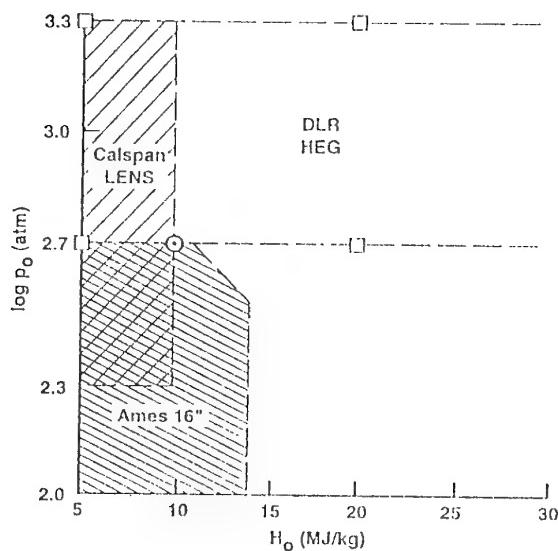
Fig. 16. Test Matrix for Blunt Cone Test Campaign

Fig. 19. Comparison of peak electro number density, 71 km alt., M = 23.9
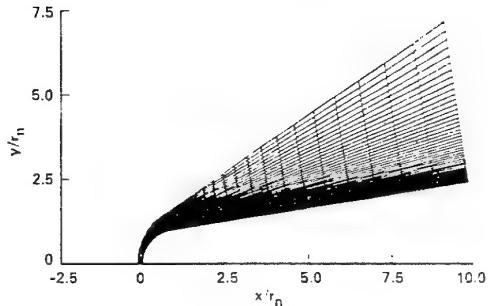
Fig. 17. Computational grid for Ram-C
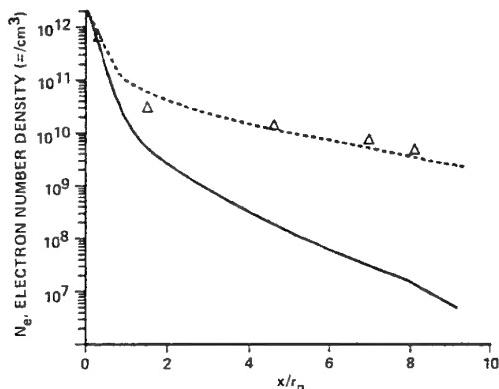
Fig. 20. Comparison of peak electro number density, 81 km alt., M = 28.3
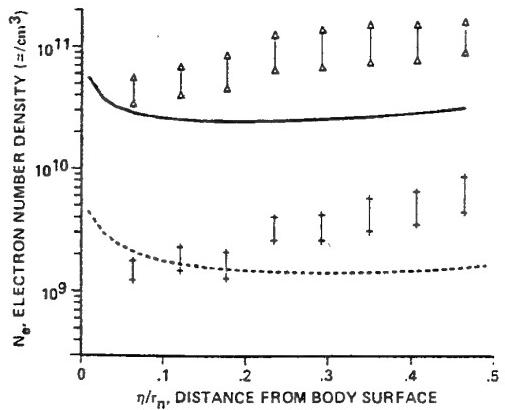
Fig. 21. Comparison of electro number density distribution at x/r_n = 8.1
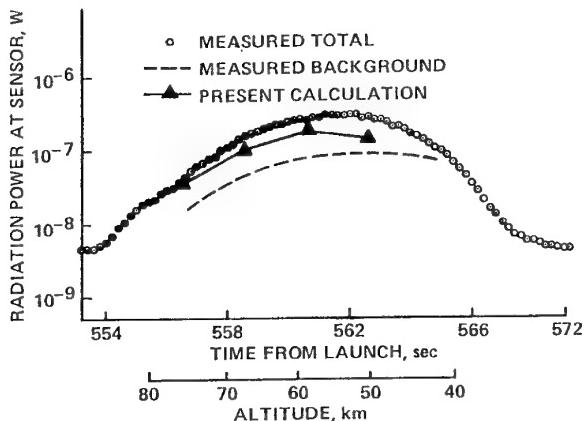
Fig. 23. Comparison between calsulated and measured radiation intensities at 391 nm in PAET experiment
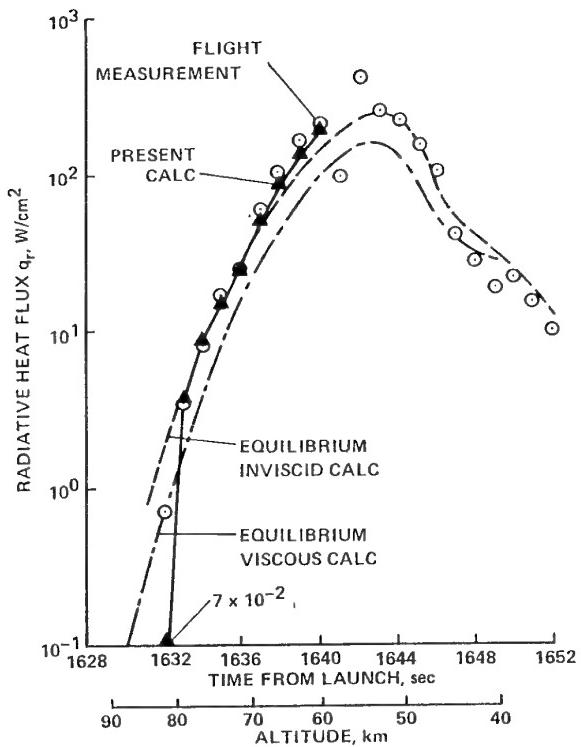
Fig. 22. Comparison between calculated and measured stagnation-point radiative heat fluxes for Fire 2.
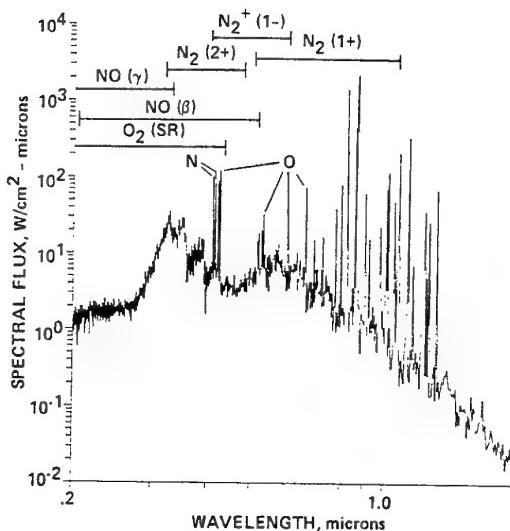
Fig. 24. AFE nonequilibrium flow spectral flux: shock layer depth = 20.9 cm

BLUNT BODIES DYNAMIC DERIVATIVES

M. Baillion
Aerospatiale Branche Espace & Défense
Centre Opérationnel Systèmes
Département Aérodynamique & Electromagnétisme
BP 2
78133 Les Mureaux Cédex
France

SUMMARY

This document addresses the aerodynamic damping coefficients of capsules and planetary entry probes.

First, the general item of dynamic coefficients will be described, and the specificity of large drag, blunted shapes will be described. A tentative description of the dynamic instability of the capsule type shapes will be shown.

This dynamic instability has strong consequences at system level, in the frame of the development phase of both capsules and planetary entry probes, which will then be depicted.

The determination of the dynamic coefficients will be addressed, both by theoretical and experimental ways.

Finally, the HUYGENS enrty module case will be detailed.

LIST OF SYMBOLS

C_A	Axial force coefficient, (-Axial force)/Q S
C_N	Normal force coefficient, (-Normal force)/Q S
C_D	Drag coefficient, $C_N \sin \alpha + C_A \cos \alpha$
C_L	Lift coefficient, $C_N \cos \alpha - C_A \sin \alpha$
C_m	Pitching moment coefficient, (Pitching moment)/Q S d
$C_{mq} + C_{m\alpha}$	Pitch damping coefficient, $\partial Cm/\partial(qd/V)) + \partial Cm/\partial(\alpha' d/V))$
Cp	pressure coefficient (p-pinf)/Q
d	Diameter of the capsule, m
f	frequency of oscillation, Hz
m	Mass of the capsule, kg
M	Moment about y axis, $N.m$
M_θ	$\dfrac{\partial M}{\partial \theta}$
$M_{\theta}\cdot$	$\dfrac{\partial M}{\partial \dot{\theta}}$
S, or A	Reference surface, m^2
V	Freestream Velocity, m/s
Q	Dynamic pressure, $\dfrac{1}{2}\rho V^2$, Pa
R	Local radius of curvature of capsule trajectory, m
X	Longitudinal position in wind tunnel, m
Z	Altitude, km

|	
α	Angle-of-attack, rad
θ	Instantaneous angular displacement from the reference flight condition, rad
γ	Flight path angle, rad
ξ	Dynamic stability parameter
ϕ	arbitrary phase angle, rad
ρ	Density, kg/m^3
ω	angular frequency, rad/s
$(\cdot),(\cdot\cdot)$	First and second derivative with respect to time, s^{-1}, s^{-2}

subscripts

a	Aerodynamic
t	Tare
0	Zero incidence condition
α	Static derivative with respect to incidence, *per rad*
X	Refered at position X in the wind tunnel
m	model
s	sting
w	wake

1. INTRODUCTION

In the frame of the development phase of a capsule, the dynamic behaviour has to be investigated, as it has strong influence on the design of the descent subsystem (parachute), and possibly the Reaction Control System (R.C.S).

Very blunted shapes, like APOLLO, or planetary entry probes, like HUYGENS have been shown to be dynamically unstable, in the sub- trans- and even supersonic Mach number range. This behaviour seems to be due to the nature of the separation zone, in the case of APOLLO, and to the unsteady characteristics of the near wake recirculating flowfield in the case of planetary probes like HUYGENS, or VIKING.

This type of characteristics is constraining for the determination of the dynamic stability parameters, which put strong reliance on experimental measurements, as the numerical way for dynamics of large separated flowfield is not yet mature.

Indeed, the support of the wind tunnel model interferes with the wake, for either forced or free oscillation test techniques. However, free flying tests avoid this problem, but provide however with a less direct insight on dynamic coefficients.

The HUYGENS program provided the opportunity to investigate this dynamic stability problem, at experimental and system level.

2. DESCRIPTION OF THE PROBLEM

2.1 Definitions

When entering atmosphere, the incidence evolution of a blunt body behaves like an oscillator response which is submitted to static and dynamic forces and moments, i.e. the aerodynamic ones.

In the case of a statically stable shape, the aerodynamic static torque results in trimming the incidence through a sinusoidal motion.

The shape is dynamically stable if the amplitude of the incidence oscillatory motion decreases with decreasing altitude. Incidence is then reaching asymptotically its trim value. A further perturbation of incidence is damped.

At the opposite, if the shape is dynamically unstable, incidence amplitude of the oscillatory motion increases, and incidence diverges.
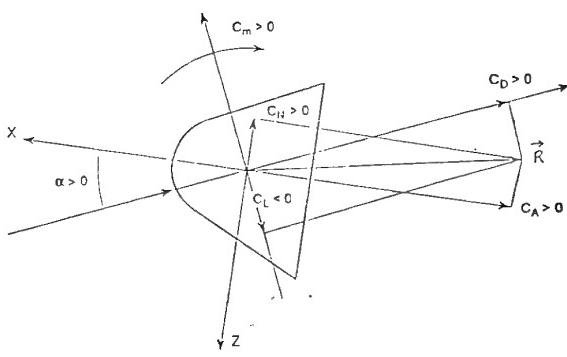
The aerodynamic efforts are fully described by:

- a force vector $\vec{R}$, which is the vectorial resultant of all the aerodynamic forces which act on the body,

- a torque $\vec{m}$ given at a certain location, the center of gravity for example $\vec{m}_G$.

In a body fixed axis:

$$\vec{R} = \begin{vmatrix} - C_A \, \bar{q}_\infty S \\ + C_Y \, \bar{q}_\infty S \\ - C_N \, \bar{q}_\infty S \end{vmatrix} \qquad \vec{m}_G = \begin{vmatrix} + C_l \, \bar{q}_\infty SL \\ + C_m \, \bar{q}_\infty SL \\ + C_n \, \bar{q}_\infty SL \end{vmatrix}$$

where:

- $\bar{q}_\infty$ is the upstream dynamic pressure,

- L,S are respectively the reference length and reference surface,

- C_A, C_Y, C_N are the force coefficients,

- C_l, C_m, C_n are the moment coefficients.

In the case of an axisymmetric shape, like HUYGENS entry module:

- C_m $(\alpha = \alpha_o, \ \beta = 0) = C_n$ $(\alpha = 0, \ \beta = \alpha_o)$ (pitch and yaw moment coefficients),

- C_N $(\alpha = \alpha_o, \ \beta = 0) = C_Y$ $(\alpha = 0, \ \beta = \alpha_o)$ (side and normal force coefficients).

The pitching moment coefficient is usually linearized:

- $C_m = C_{m_\alpha} \cdot \alpha + C_{m_{\dot\alpha}} \dfrac{\dot\alpha L}{V_\infty} + C_{m_q} \cdot \dfrac{qL}{V_\infty}$,

where:

- $C_{m_\alpha} = \dfrac{\partial \, C_m}{\partial \, \alpha}$,

- $C_{m_{\dot\alpha}} = \dfrac{\partial \, C_m}{\partial \left(\dfrac{\dot\alpha L}{V} \right)}$,

- $C_{m_q} = \dfrac{\partial \, C_m}{\partial \left(\dfrac{qL}{V} \right)}$,

q is the pitching rate.

Finally, the shape is statically stable if the aerodynamic torque tends to decrease α, i.e., $C_{m\alpha} < 0$, indeed, an incidence increase results in a torque which will oppose to this angular displacement.

It will be demonstrated in the next paragraph, that the shape is dynamically stable if :

$$\xi = C_D - C_{L\alpha} + \left(\frac{L}{r}\right)^2 \cdot (C_{mq} + C_{m\dot\alpha}) < 0$$

where:

- $C_D = C_A \cos \alpha + C_N \sin \alpha$ is the drag coefficient (see picture above),

- $C_L = - C_A \sin \alpha + C_N \cos \alpha$ is the lift coefficient,

- $C_{L\alpha} = \dfrac{\partial C_L}{\partial \alpha}$,

and $r^2 = \dfrac{I_t}{m}$ transverse radius of giration:

- I_t is the transverse inertia,

- M is the mass of the vehicle.

ξ is called the dynamic stability parameter.

2.2 Analytical description of the dynamic stability

The equilibrium in a direction normal to the trajectory of the vehicle may be expressed as follows:

$$mV^2/R = - mV \, d\gamma/dt = - Q \, S \, C_{L\alpha}\alpha$$

which can be expressed with respect to a small variation around the parameters α and γ :

$$d(\delta\gamma)/dt = Q \, S/mV \; C_{L\alpha}\delta\alpha \qquad (1)$$

The attitude θ is the angle between the longitudinal axis of the vehicle and the local horizontal direction and we have

$$\theta = \gamma + \alpha$$

Considering small variations, it comes

$$\delta\theta = \delta\gamma + \delta\alpha \qquad (2)$$

If I is the transverse inertia of the vehicle, the equilibrium condition about the center-of-gravity leads to:

$$I \, d^2(\delta\theta)/dt^2 = Q \, S \, L \, [\, C_{mq} \, L/V \, d(\delta\theta)/dt$$
$$+ C_{m\alpha} \, \delta\alpha \; + C_{m\dot\alpha} \cdot L/V \, d(\delta\alpha)/dt] \qquad (3)$$

The C_{mq} term is the aerodynamic damping of the rate of change of attitude θ of the vehicle, the term $C_{m\dot\alpha}$ is the damping of the rate of change of the angle-of-attack α. The term $C_{m\alpha}$ represents the aerodynamic stiffness due to the angle-of-attack $\delta\alpha$.

It is then possible to combine the relations (2) and (3) in order to get a second relation between $\delta\gamma$ and $\delta\alpha$:

$$d^2(\delta\theta)/dt^2 = Q \, S \, L/I \, \{ \; C_{mq} \, L/V \, [d(\delta\gamma)/dt + d(\delta\alpha)/dt] +$$
$$C_{m\alpha} \, \delta\alpha + C_{m\dot\alpha} \cdot L/V \, d(\delta\alpha)/dt\} \qquad (4)$$

expression (1) can be derived with respect to time, which gives

$$d^2(\delta\gamma)/dt^2 = Q \, S/mV \; C_{L\alpha}d(\delta\alpha)/dt$$
$$+ \delta\alpha \; d/dt \, (Q \, S/mV \; C_{L\alpha}) \qquad (5)$$

The expression for $d(\delta\gamma)/dt$ and $d^2(\delta\gamma)/dt^2$ are then replaced in equation (4), which gives :

$$Q \, S/mV \; C_{L\alpha}d(\delta\alpha)/dt + d^2(\delta\alpha)/dt^2 =$$
$$(Q \, S \, L^2/I \, V) \, C_{mq} \, [\, Q \, S/mV \; C_{L\alpha}\delta\alpha + d(\delta\alpha)/dt]$$
$$+ (Q \, S \, L/ \, I) \, C_{m\alpha} \, \delta\alpha + Q \, S \, L^2/IV \, C_{m\dot\alpha} \cdot d(\delta\alpha)/dt$$
$$- d/dt \, (Q \, S/mV \; C_{L\alpha}) \, \delta\alpha \qquad (6)$$

Which is equivalent to :

$$d^2(\delta\alpha)/dt^2 \; + d(\delta\alpha)/dt \, [\; Q \, S/mV \; C_{L\alpha}$$
$$- Q \, S \, L^2/IV \, (C_{mq} + C_{m\dot\alpha})]$$

$$- \; \delta\alpha \, [\, Q^2 \, S^2L^2/m \, I \, V^2 \, C_{mq} \, C_{L\alpha} + (Q \, S \, L/ \, I) \, C_{m\alpha}$$
$$- d/dt \, (Q \, S/mV \; C_{L\alpha}) \,] \; = 0 \qquad (7)$$

This equation can be written as :

$$E(t) = d^2(\delta\alpha)/dt^2 \; + A_1(t) \, d(\delta\alpha)/dt + A_0(t) \, \delta\alpha \; = 0 \quad (7')$$

where
$$A_1(t) \; = \; Q \, S/mV \; C_{L\alpha} \; - Q \, S \, L^2/IV \, (C_{mq} + C_{m\dot\alpha})$$

$$A_0(t) \; = - Q^2 \, S^2L^2/m \, I \, V^2 \, C_{mq} \, C_{L\alpha} - (Q \, S \, L/ \, I) \, C_{m\alpha}$$
$$+ d/dt \, (Q \, S/mV \; C_{L\alpha})$$

The ALLEN hypothesis enable the velocity to be expressed as follows :

$$V = V_d \exp \, [\, - K_0/2 \; \exp \, (-Z/Z_0) \,]$$

where Vd is the velocity at beginning of entry, if the density atmospheric profile can be modelised as :

$$\rho = \rho_0 \exp(-Z/Z_0)$$

where ρ_0 and Z_0 are constant, and

$$K_0 = \rho_0 Z_0 S C_D / m \sin \gamma_d$$

Where γ_d is the entry flight path angle.

It is then possible to transform the equation (7') by a variable change, which substitutes the time t to non dimensioned altitude Z/Z_0.

And finally, it comes :

$$\alpha/\alpha_0 = \alpha*/\alpha_0 \cos(2 K_2^{0.5} \exp(-Z/2Z_0) - \pi/4)$$

Where $\alpha*/\alpha_0$ represents the amplitude of the incidence oscillations, that can be expressed as :

$$\alpha*/\alpha_0 = 1/\{\pi K_2^{0.5}\}^{0.5} \exp(K_1 \exp(-Z/Z_0)) \exp(Z/4Z_0) \qquad (8)$$

Where

$$K_2 = K_0/2 C_D (C_{L_\alpha} - C_{m\alpha} L/\beta \sin\gamma_d r^2)$$

Where r is the transverse gyration radius ($r^2 = I/m$), and

$$K_1 = \rho_0 Z_0 S/4 m \sin \gamma_d [C_D - C_{L_\alpha} + L^2/r^2 (C_{mq} + C_{m\alpha}.)]$$

It then turns out that :

If $K_1 < 0$, then $\alpha*/\alpha_0$ decreases when Z decreases, the amplitude of incidence oscillations is damped.

If $K_1 > 0$, then two different cases must be distinguished, according to the magnitude of Z with respect to $Zc = Z_0 Log(4K_1)$:

If $Z > Zc$ then the incidence oscillations are damped

If $Z < Zc$ the oscillatory incidence motion is divergent.

It is therefore the K_1 parameter which enables the body dynamic behaviour to be appreciated.

The parameter K_1 is equal to :

$$K_1 = C \xi$$

with C being a constant, ξ has been defined in §2.1.

It should be pointed out that the C_{mq} and $C_{m\alpha}$. terms are different, although they are used as a sum in the above equation, and measured as a sum in the fixed axis oscillation tests. Indeed, for a free-flying entry vehicle, the varations in the angle of pitch and in the angle-of-attack can occur independently of each other, and result in different longitudinal distribution of the normal velocity. The distribution due to the angle-of-pitch variation, i.e. the pitching velocity q, varies along the chord and intersects zero at the axis of rotation, while the distribution due to the angle-of-attack variation is constant along the chord.

In the case of an oscillation around a fixed axis, both variations occur at the same time, and even if the numerical value of α' and q are equal, their effects are different and are superimposed.

3. BLUNT BODY DYNAMIC BEHAVIOUR

The dynamic behaviour of large drag blunt bodies has been investigated for manned re-entry and for planetary exploration missions. From these experiments, it was shown that this kind of shape is dynamically unstable in the sub-, trans- and even supersonic regimes.

The following part lists some examples of these investigations, and a tentative description of the physical phenoma which contribute to this trend.

3.1 Large angle cones

The dynamic behaviour of large drag sphero-conical shapes was first investigated in the frame of planetary entry probe programs which was foreseen at NASA Ames in the 1960's.

The entry vehicles were required both to be statically stable, and to provide with large drag coefficient, in order to insure efficient deceleration of the probe in the thin Martian atmosphere.

As the deceleration itself was foreseen to provide with informations on the structure of the explored atmosphere, the drag coefficient had to be characterised accurately, while the attitude of the probe had to be known precisely.

Among the wind tunnel tests investigations, ballistic range tests were performed at NASA Ames (see [R1]). The preliminary shape investigations led to selection of sphero-conical 55 and 60° half angle cones (see fig.1). The ballistic range tests were conducted on flat base models and several different rear part geometries.

The sphero-conical shapes were shown to be dynamically unstable in the transonic range, with a similar behaviour for either the flat or modified rear base, while the general dynamic behaviour in hypersonics or subsonics was found to be favourable (see [R2], [R3])

The dynamic stability parameter ξ was positive from Mach $0,8 < M < 1,4$., with a peak of instability at $M=1.1$,

ξ being positive for incidence up to $\alpha > 20°$ at M=1.1 (see fig.2).

Several geometrical modifications were tried to assess the sensitivity of dynamic behaviour with respect to the probe configuration. A toroidal part at the maximum diameter location had no effect on the dynamic behaviour of the models.

In an attempt to understand the origin of the dynamic instability, a spherical after part was added, with the center of the sphere which coincides with the center-of-gravity of the model. In this case, the contribution of the pressure forces acting on the rear part of the model to the aerodynamic moment is zero. This model was shown to be dynamically stable (see figure n°3).

This clearly indicates that the rear part pressure is responsible for the destabilizing moment. The spherical rear part can however modify slightly the front face pressure distribution, through the boundary layer. Indeed, the axial force coefficient appeared to be slightly modified with/without spherical rear part. However, this drastic change of dynamic behaviour seems to be an evidence of the destabilizing trend due to the rear pressure field.

The nature of the near wake must therefore be unsteady, at least in transonic regime.
This phenomenum leads to experimental difficulties for the investigation of the dynamic derivatives of blunted large drag shapes.
Indeed, as the near wake seems to be responsible for dynamic instability, this near wake must be carefully simulated in test conditions, in order to be able to characterise the damping coefficients of the models.
In the case of sting mounted test technique (free or forced oscillation method), the sting is located in the wake, and therefore disturbs the damping coefficient measurements. L.E. Ericsson and J.P.Reding have carefully analysed this problem (see for example [R4]).

Some other candidates for Mars investigations, one 70 and two 60° half angle cones were tested in free flight tests in wind tunnel (see description of the method in §5.3.3.3) (see reference [R5]). The geometries of the tested models are shown on figure n°4.
All of these shapes were shown to be dynamically unstable in the range 0.8 (approximately) to a Mach number between 2 and 3.

Within the large drag large angle cone shapes, the VIKING vehicle aerodynamic behaviour has been widely investigated. The VIKING program was dedicated to the exploration of Mars atmosphere, and has actually achieved several missions (Viking 1 entered the atmosphere of Mars on July 20 1976, Viking 2 on September 3 1976), and had therefore, the same requirement to be fully characterised, in term of trim and damping characteristics.

VIKING is a blunted nose 70° half angle cone with a ratio of nose radius to base radius of 0.5. The center-of-gravity was offset from the axis of symmetry to make it a lifting configuration (zcg/d=0.0134, L/D=0.18) (see [R9]) (see fig.5).
A complete set of dynamic tests were performed on VIKING shapes, as several modifications were made until the final geometry was defined, from sting mounted tests, forced and free oscillation techniques, ballistic range tests and free flight investigations (see reference [R6],[R7],[R8],[R11]).
The VIKING shape was shown to be dynamically unstable in the range M=0.8 to a Mach number slightly larger than 2. One interesting feature is the presence of a double peak of dynamic instability at M=1.1 and M=2.1 (see figure n°6) (see [R8]).

The figure n°7 shows a typical damping parameter Cmq versus incidence, at Mach number M=1.76. It turns out that the damping parameter is positive (negative damping) for angle-of-attack less than 2°, and becomes negative (positive damping) for higher angle-of-attack, and remains roughly constant for $\alpha > 4°$.

It should be pointed out that the VIKING rear part is bulbous (see figure n°8 a comparison between Viking, Huygens and shapes from [R1]), which could improve its dynamic behaviour, like the spherical rear part shape investigated in [R1], although it is eventually dynamically unstable in the transonic range. However, the dynamic instability zone is much smaller in term of angle-of-attack range, than the 60° and 55° flat base shapes.

During the two VIKING Martian entries, the dynamic behaviour was almost the same, and showed that at mortar fire, which occurred at Mach number about 1, the VIKING vehicle was actually dynamically unstable. A significant growth of the oscillation amplitude was measured, while the onboard reaction control system fired a number of times during this period, in an attempt to limit the yaw rate (see [R9] and fig.9).

3.3 Capsules (APOLLO, GEMINI, MERCURY)

The capsule like shapes, like APOLLO, SOYUZ, MERCURY and GEMINI, have been shown to be dynamically unstable too in the sub- transonic regime and in some cases in supersonic regime (see reference [R10],[R12][R13][R14][R15]).

The geometry of these vehicles consists in a front spherical face, characterised by the nose radius ratio R_1/d, where d is the maximum diameter of the capsule, followed by a conical rear part, characterised by the angle between the longitudinal axis of the vehicle and the conical meridian angle θ (see figure n°10 APOLLO and SOYUZ geometries).

The end part of the vehicle consists in a blunt spherical part in the case of APOLLO and SOYUZ, characterised by the rear end radius ratio R_2/d. In the case of GEMINI and MERCURY, the vehicle rear part is a cylindrical part, characterised by its length and local diameter ratio d_c/d.

In the case of APOLLO and SOYUZ, a toroidal part takes place between the sphero-conical front part and the conical rear part, and is characterised by its radius ratio r/d.

The flowfield over such capsule shapes is complex (see fig.11 a Navier Stokes computation in hypersonics, on an APOLLO-like shape). For moderate angle-of-attack, the stagnation point is located on the spherical front part, and the flowfield is attached on all the spherical front face for nearly all the speed regime, from subsonic to hypersonic. At the maximum diameter location, the flow is accelerated, and the boundary layer separates both at windward and leeward sides for small angle-of-attack, and for Mach number regime from subsonic to hypersonic.

When incidence increases, the windward streamlines reattach at a certain location on the conical part. Thus creates a closed separated zone. The same effect can be observed with increasing Mach number, at both the windward and leeward side.

This flow pattern is very unstable in nature, and together with the unsteady near wake, generates the dynamic instability.

Within the APOLLO program, intensive wind tunnel tests were performed, in order to characterize the aerodynamic coefficients of the vehicle in the whole range of flight conditions, in terms of Mach number and Reynolds number mainly. The simulation of high enthalpy conditions could not be performed, while it has important consequences on trim angle-of-attack.

The dynamic test technique which were used on APOLLO were forced-oscillation, limited free-oscillation, and free-to-tumble test technique.

All showed the APOLLO shape to be dynamically unstable in the subsonic regime for Mach number lower than 0.7 (see reference [R10]).

GEMINI models were tested in ballistic range (see reference [R12]). These tests showed stability parameters ξ to be highly positive at Mach number 3 and for low incidence.

Some tests were performed with rounded maximum diameter, and carborandum on the maximum diameter location. Both did ease the reattachment of the boundary layer to occur on the rear cone, and both showed to increase the dynamic instability.

This seems to indicate once more that the rear part flowfield is responsible for the dynamic instability.

The large recirculating near wake of probes, while for the capsules the type of reattachment, either closed or open type recirculation zone on the rear cone, are thought to be responsible for dynamic instability.

Although these phenomena occur at different Mach numbers, they all have impacts at system level, and require specific devices, or mission modifications, to be implemented.

This will be discussed in next paragraph.

4. CONSEQUENCES OF DYNAMIC BEHAVIOUR AT SYSTEM LEVEL

It has been shown that the blunt bodies with large drag are dynamically unstable in the sub, trans and even supersonic Mach number range.

This dynamic instability has consequences at system level, and has therefore to be taken into account in the design of a vehicle, during the vehicle development phase.

Two types of vehicles shall be considered here, the planetary probes, like HUYGENS, or VIKING, and the manned capsules such as APOLLO, or capsules which prefigure manned capsule, and which therefore have the same requirements that the actual manned capsule, i.e. the Atmospheric Re-entry Demonstrator (A.R.D.).

4.1 Probes

In the first case, the planetary entry probe has to decelerate through the atmosphere, from its release velocity imposed by the arrival of an Orbiter (approximately 7000m/s in the case of HUYGENS, 4600m/s for VIKING) close to the target planet, down to a velocity compatible with either scientific experiments to begin (HUYGENS), or landing conditions (VIKING).

The HUYGENS case will be detailed from here.
 Once this deceleration phase has finished, the scientific payload must operate its characterisation goal of the TITAN atmosphere, and the descent module must be extracted from the kernel, which is constituted by the entry shell (see Special Course part *"Aerothermodynamic requirements and Design of the Huygens Probe"*).

A parachute with a larger ballistic coefficient than the entry decelerator is deployed from the descent module, and the connection between the descent and entry modules is cut. The descent module is then extracted naturally by the main parachute.

In order to operate a safe and reliable deployment phase, the incidence of the entry module prior to the mortar fire, has to remain smaller than 10°.

Usual parachute deployment conditions occur in the subsonic regime. Indeed, at supersonic conditions, some shocks occur in the bridles and in the inflated parachute, which may result in unsteady behaviour of the parachute inflated shape. Furthermore, as Mach number increases, the heat fluxes may damage the parachute or the bridles which may result in a mission loss.

However, in the HUYGENS case, because the entry module is dynamically unstable, the incidence increases very quickly in the transonic regime. Therefore, a subsonic deployment would result in an incidence at deployment, which would be larger than the maximum 10° upper limit.

The consequence of the HUYGENS dynamic instability is the need of a supersonic Mach number parachute deployment.

The maximum Mach number deployment condition is derived from the heat flux constraint, plus the fact that a mechanical shock is induced by the inflation of the parachute, as the drag of the system descent module plus parachute increases when the parachute is deployed.

The bridles and the textile material of the parachute can withstand a limited level of stress. This latter one is proportional to the dynamic pressure, and is maximised at parachute inflation shock load.

A second requirement for parachute deployment conditions arises then from this load limit, i.e. the dynamic pressure at deployment must remain lower than 440 Pa.

Finally, the parachute deployment conditions for the HUYGENS probe was selected to be M=1.5 , because of dynamic instability.

4.2 Manned capsules & demonstrator ARD

The blunted capsule shapes have been shown to be dynamically unstable in the sub trans and supersonic Mach number range.

The large drag of the capsule provides with a reasonable maximum deceleration load during hypersonic entry, acceptable by the crew, whereas a center of gravity offset provides with limited level of fineness, which ensures some lateral range capabilities, and load factor control during entry.

Once the deceleration during entry has occurred, some additional subsystem of descent control must provide with the capability to achieve a terminal velocity of roughly less than 10m/s, compatible with soft landing, or water drop conditions. A parachute is therefore used, with a deployment which was achieved in subsonic regime in the case of APOLLO and SOYUZ for example. As in the case of the atmospheric probes, the attitude of the capsule must be such that the incidence remain acceptable with respect to the parachute deployment conditions. Furthermore, angular transverse rate must remain limited.

Now, the capsule shapes like APOLLO are dynamically unstable in the subsonic regime. Without any attitude control device, the capsule would tumble and its incidence may increase up to 180° (spherical front face heat shield rearward position). This unexpected position is furthermore very stable, both statically and dynamically.

A Reaction Control System (R.C.S.) is therefore used, which provides with damping of the angular transverse rate of the capsule. This R.C.S. consists in at least 6 thrusters, located on the rear cone, in the case of APOLLO. They are associated by pair, and provide with pitch (nozzles in the center-of-gravity offset plane), yaw and roll (out of the center-of-gravity offset plane).

The roll nozzles are dedicated to bank angle control, which provides with lift vector orientation (out of trajectory plane for lateral range capability), while the pitch and yaw thrusters provides with damping of the angular transverse rate, which is needed during transonic and subsonic regime, because of dynamic instability.

The opening of the parachute is a mission failure case. Therefore, the R.C.S. was redundant in the case of APOLLO (12 thrusters), while the shape of the SOYUZ capsule is specially designed to reach a single heat shield forward position, in case of R.C.S. failure.

This reliability effort, which is driven by dynamic instability presence, led to large efforts in terms of characterisation, accommodation and mass penalties in the case of the redundant R.C.S. of APOLLO, and extensive wind tunnel tests and shape modifications, in the case of SOYUZ.

Once the parachutes are deployed, the dynamic instability level constraints the design of the descent control system. Indeed, the type of fixation of the parachute, i.e. the number of attachment points of the bridles to the capsule, the length of the bridles, have to be tuned to provide with an efficient damping of the oscillations of the capsule, when it is suspended under the parachute.

5. DYNAMIC STABILITY CHARACTERISATION

Both for planetary probes and manned capsules, the determination of the dynamic derivatives is necessary, in order to respectively, assess the reliable deployment conditions of the parachute, and determine the design of the thrusters, in order to insure an efficient damping of the oscillatory motion of the capsule.

The determination of the damping coefficients could theoretically be determined either from theoretical, numerical or experimental means. In fact, the theoretical, numerical, way is not yet suitable in the case of the large drag shapes, such as large angle cones or capsules shapes. The feature of the near wake flowfield of this kind of shape which is responsible for the dynamic instability is so complex, that in practice the wind tunnel tests are the basic way to investigate large drag shapes dynamic behaviour. However, the experimental investigation is made difficult due to the nature of these capsule dynamic behaviour.

The following part will describe the different methods which are commonly used, their advantages and drawbacks.

5.1 Dynamic stability similarity parameters

Like for the static aerodynamic coefficients, the Mach number and Reynolds number must be reproduced, when wind tunnel tests dedicated to dynamic stability investigations are to be performed.

In addition to these parameters, the frequency of oscillation in relation to full scale conditions must be simulated. The additional parameter $\omega d/V$, is called the reduced frequency parameter, must therefore be reproduced, where ω is the rotational frequency (rad/s), d is a characteristic length of the vehicle, and V is the upstream velocity. This parameter contains the frequency of oscillation, and represents the ratio of a characteristic length of the vehicle, to the wavelength of the oscillation.

5.2 CFD & theoretical prediction

Within the hypersonic region (4<M<10), theoretical methods are available for estimating derivatives for bodies of revolution and relatively simple lifting configurations. The Newton Busemann method for example provides with estimation of the dynamic derivatives in a limited CPU time, with limited numerical developments (see Ref. 16 to 21).

However, in the sub, trans and supersonic flow regime, theory yet fails to predict the dynamic derivatives on large drag shapes. Indeed, the dynamic behaviour of this kind of body is driven by the large recirculating near wake, where viscous effect are predominant.

A correct determination of the dynamic derivatives would then consist in a full Navier Stokes, time dependent simulation of the whole surrounding flowfield of the capsule.

This approach is however necessary to be developed and improved, in order to reduce significantly the CPU time consumption.

The prediction of capsule dynamic behaviour during the atmospheric re-entry undergoes knowledge of the aerodynamic answer to a limited number of given characteristic motions. Each of these motions allows to isolate the answer for one damping parameter each time.

The pitching moment can be derived as follows :

$$C_m(\alpha,q) = C_m(\alpha_0,0) + C_{m\alpha}(\alpha - \alpha_0) + C_{m\dot{\alpha}} \cdot \dot{\alpha} + C_{mq} \cdot q$$

Where α is the instantaneous angle-of-attack, close to the reference position α_0,

Then, it is intended to find the motions for which certain terms of relation above are cancelled out. These motions, shown on the figure n°17 , will allow to extract certain terms separately.

Movements 1 and 2 (movements with constant incidence and rotation with constant incidence) are two different ways to calculate C_{mq}.

Movement 3 allows extraction of $C_{m\dot{\alpha}}$.

With movement 4, the sum of $C_{mq}+C_{m\alpha}$ can be calculated and thus enables the correlation of results.

Very often, complex wind-tunnel testing is required to extract these aerodynamic damping coefficients. This brings to light the interest of numerical computations as they allow the evaluation of dynamic answers regarding a body for any movement, without technological limitations as it is the case in wind-tunnels. Sting effects , which disturb capsule wake, where subsonic areas have a significant influence on the dynamic behaviour, are also avoided.

Furthermore, it is interesting to compare test results with computation (or other) cross-checking.

Today, numerical code validations have been done for wing profiles as well as for 3 D axisymmetric configurations in movement for stiff and bending bodies. However, studied shapes and incidence tested, caused neither separation nor recirculations areas. Thus, this computations allow the use of EULER-type modelisation.

The results have successfully been compared to wind-tunnel testing.

For high separation level bodies and configurations, few computations have been done. This remains a study theme at research stage. Some applications have been undergone in the United States on 2D wing profiles with high incidence pitching movement. Flow conditions remain at low Mach (subsonic) and low Reynolds (2 X 10^6 are reached)(see Ref. 28).

The main difficulty for these computations is linked to the choice of the turbulence model as well as to high computation costs. The first difficulty can also been applied to static computations. Improvements done in turbulence models for static computations will directly benefit to dynamic cases.

The second difficulty concerns computation costs generated. Solvers will have to be time consistent in order to take into account unsteady phenomena (advance in time of the solution will be done in a global way, which means that the same time increment will be used for all grid cells). This constraint is all the more important since grids are thin in turbulent computations.

Two ways have been developed to compensate the disadvantage of the global time step.

The first concerns unstructured solvers. It is a zonal time step, which is similar to the local time step, but remains consistent in time.

The second is the one of structured solvers, it is the technique of implicit 3D resolution. This resolution makes it possible to get free from the CFL constraint which limits the time step. Several implicitation techniques exist, the most consistent must be retained (3DAI, LU, SGS, LERAT-SIDES, etc.).

Methods exist, the important work consists in the validation of these computation methods with a good turbulence model and in making validation tests for configurations with the capsule shape. Thus, it seems that at mean term (until 5 years), methods will be completely operational but will remain expensive with regard to the cost of computations.

5.3 Experimental determination of dynamic derivatives

A complete classification of the experimental means used for dynamic derivatives determination may be found in reference 22 and 23.
The following description will be limited to those which have been employed in the frame of capsule vehicle development phase.

5.3.1Captive model testing

The first kind of methods which will be considered here consists in model fixed on a sting. The techniques which shall be considered here are limited to those where the model has one degree of freedom in pitch.
The model may then be able to oscillate freely, or is constrained to a given imposed motion.
In the first case, the technique is called free-oscillation technique, the second one is forced oscillation technique.

5.3.1.1 Free oscillation test technique

This test technique is the simplest and most direct method usable for providing with informations on the dynamic behaviour of a model.

Indeed, the model is fixed on a sting by a flexure, and is displaced from the trim conditions. The test measurement consists in the recording of the model incidence oscillations versus time.

If the model is dynamically stable, the decay of the incidence amplitude provides with the damping of the mechanical set up, due to internal damping in the flexure, and friction, plus the aerodynamic damping of the model. The same release in wind-off condition is performed, and provides with the measurement of mechanical, or tare, damping. The aerodynamic damping is obtained by the difference between the two.
This technique can however be limited in the case of unstable, or marginally stable shape, like HUYGENS entry module, as no control of the model amplitude is possible. Indeed, if the maximum amplitude of the model oscillation is reached, no quantitative damping information can be derived from a fast divergence incidence. However, this would be the evidence of a strong instability. Furthermore, in the HUYGENS case, the amplitude shape can be erratic, and a simple derivation of the damping coefficient under the form of a logarithmic decrement is not applicable.

The free oscillation technique is advantageous for blunt large drag model dynamic investigation. Indeed, neither balance nor forcing mechanism have to be accommodated in the model. The flexure can be easily inserted in this typically short models, and the center-of-oscillation of the model is therefore possible to be located at the scaled center-of-gravity location. This condition is absolutely needed for capsule like-shapes.

The following part describes the basic equations for derivation of the damping coefficient :

The equations of motion for a body in pitch may be found in reference 22 and has the same general form as the

equations of motion for a body in yaw or roll. For free-oscillation systems, the equation of motion has the form

$$I_y \ddot{\theta} - (M_{\dot\theta a} + M_{\dot\theta t})\dot\theta - (M_{\theta a} + M_{\theta t})\theta = 0 \qquad (9)$$

After introducing new nomenclature for simplification of the derivation of the solution to equation (9), it becomes

$$I_y \ddot\theta + C\dot\theta + K\theta = 0 \qquad (10)$$

The general solution of this equation describing free-oscillation motion can be written as

$$\theta = A_1 \exp(r_1 t) + A_2 \exp(r_2 t) \qquad (11)$$

where A_1 and A_2 are arbitrary constants and r_1 and r_2 are the roots of the characteristics equation. These are obtained as

$$r_{1,2} = -C/(2I_y) +/- ([(C/(2I_y))^2 - K/I_y])^{0.5} \qquad (12)$$

But, since the undamped natural circular frequency is $\omega = (K/I_y)^{0.5}$, and letting $C/(2I_y) = a$, equation (12) becomes

$$r_{1,2} = -a +/- (a^2 - \omega^2)$$

Depending on the relative magnitude of a and ω , three homogeneous solutions to equation (10) are possible.

a>ω or the overdamped case
The two roots are real, and the homogeneous solution to (10) may be written

$$\theta = e^{-at}\left[A \cdot e^{\sqrt{a^2 - \omega_n^2}\cdot t} + B \cdot e^{-\sqrt{a^2 - \omega_n^2}\cdot t} \right]$$

it represents an aperiodic motion, which after an initial disturbance approaches zero.

a=ω or critical damping
The two roots are equal and the general solution to (10) is

$$\theta = e^{-at}\left[A + Bt \right]$$

The case of interest is a < ω
The case of interest is $a < \omega$, where the roots are complex, representing the condition where the system will oscillate. The general solution to equation (10) for this case is

$$\theta = A_1 \exp(a+bi)t + A_2 \exp(a-bi)t \qquad (13)$$

where $r_{1,2} = a +/- bi$

$$a = -C/2I_y$$

$$b = ([K/I_y - (C/2I_y)^2] = \omega_d \text{ (damped natural frequency)}$$

Equation (13) can also be written as

$$\theta = \theta_0 \exp[(-C/2I_y)t] \cos(\omega_d t +/- \phi) \qquad (14)$$

θ_0 and ϕ being arbitrary constants. Equation (14) represents a harmonic oscillation with damping. When $\cos(\omega_d t +/- \phi) = 1$, the envelope encompassing the points of tangency with the displacement is described by

$$\theta = \theta_0 \exp[(-C/2I_y)t]$$

From this relationship, the logarithmic decrement $\log_e(\theta/\theta_0)$ is used to obtain the damping term C. The average damping coefficient can be derived from the time required to damp to a particular ratio. Letting θ_1 and θ_2 represent amplitudes occurring at times t_1 and t_2, respectively, and letting $\theta_2/\theta_1 = R$, we obtain the following equation for the damping moment :

$$C = -2I_y \ f \ \log_e R/Cyr \qquad (15)$$

since $t_2 - t_1 = Cyr/f$

from equation (13) for the natural damped frequency, the static moment is

$$K = I_y \omega_d^2 + I_y(C/2I_y)^2 \qquad (16)$$

The term $I_y(C/2I_y)^2$ is usually very small and can be neglected.

As shown in equations (9) and (10), the dynamic damping and static moments consist of moments due to the aerodynamics and moments produced by tares in the mechanical system. The tares are evaluated from wind-off measurements. The pressure in the tunnel is usually decreased, and the tare damping is extrapolated to zero pressure condition, to derive the vacuum damping. The final aerodynamic dynamic damping and static moments are given by

$$C = -M_{\dot\theta w} = -(M_{\dot\theta a} + M_{\dot\theta t})_w$$

$$M_{\dot\theta a} = (M_{\dot\theta a} + M_{\dot\theta t})_w - (M_{\dot\theta t})_v$$

$$K = -M_{\theta w} = -(M_{\theta a} + M_{\theta t})_w - (M_{\theta t})_v$$

where the subscripts w and v denote wind-on and vacuum respectively.

The structural damping moment parameter varies inversely as the frequency of oscillation. The tare damping term has to be corrected, in order to take into account the fact that the wind-on and wind-off

measurements are performed at different frequencies. Equations (15) and (16) combined with the equations above gives

$$M_{\theta}{}'_a = -2 I_y \, \log_e R \, [\, (f/Cyr)w - (f/Cyr)v \, fv/fw \,]$$

$$M_{\theta a} = I_y \, [\, (\omega_d)_w{}^2 - (\omega_d)_v{}^2 \,]$$

The derivatives, when reduced to a non dimension form for pitching motion, become

$$C_{mq} + C_{m\alpha}{}^{\cdot} = M_{\theta}{}'_a \, (2 \, V/QAd^2)$$

$$C_{m\alpha} = M_{\theta a} \, /QAd$$

Advantages

This method is simple, and provides with real time indications on the dynamic behaviour of the model.

Drawbacks

The necessary reduced frequency parameter simulation may not be easily reached. Indeed, for various Mach number conditions, the flight reduced frequency parameter will vary as a function of aerodynamic frequency $\omega_a = \sqrt{(Q \, S \, d \, C_{m\alpha}/I_t)}$, which will therefore vary with upstream dynamic pressure, and aerodynamic stiffness versus Mach number. In wind tunnel conditions, the dynamic pressure variations with Mach number will not follow the flight ones, and moreover the frequency is driven by the sum of aerodynamic plus flexure stiffness. The reduced frequency parameter will then be hardly be reached for all Mach number conditions. This will be made more difficult if the flexure stiffness is large compared to the aerodynamic one. This is the case when non trimmed conditions are to be tested.

5.3.1.2 Forced oscillation test technique

The model is fixed on a flexure and forced to oscillate by a mechanism. The forcing moment has the form of a sinusoidal torque M cos ωt, where M is the amplitude of the torque, ω is the frequency of oscillation. A strain gage is located on the flexure, and indicates the model angular displacement. A strain gage is also located on the input torque arm. The frequency of oscillation of the forcing torque can be tuned, so that a phase shift between the forcing torque and the displacement is 90°, this corresponds to the resonance condition, i.e.

$$\omega = \sqrt{(K / I)}$$

Where K is the total stiffness of the system (aerodynamic plus flexure), and I is the transverse inertia of the model. In this case, the inertia term balance the stiffness ones, and the forcing torque is compensating for the damping moment. Thus, the amplitude of the oscillation, the

frequency and the torque magnitude provide with the damping of the system. Wind-off tests provide with mechanical part.

The following part shows the basic equation for deriving the damping coefficients from forced oscillation test technique (more details can be found in Ref. 22).

The motion of a model which is rigidly suspended in an airstream and forced to oscillate in one degree of freedom (pitch) as a sinusoidal function of time may be expressed as

$$I_y \ddot{\theta} - (M_{\theta}{}'_a + M_{\theta}{}'_t)\dot{\theta} - (M_{\theta a} + M_{\theta t})\theta = M \cos \omega t \quad (17)$$

where the subscript a refers to the aerodynamic values and the subscript t refers to the tare contribution of the model balance system.

If we denote

$$- (M_{\theta}{}'_a + M_{\theta}{}'_t) = C$$

$$- (M_{\theta a} + M_{\theta t}) = K$$

Equation (17) becomes

$$I_y \ddot{\theta} + C \dot{\theta} + K \theta = M \cos \omega t \qquad (18)$$

The complete solution of this equation is the sum of the general and particular solutions.
When M = 0, the general solution is equation (14), for the case of the free oscillation system.

The particular solution, which is necessary for the steady state case, after the decay of the initial transients, is assumed to be of the form

$$\theta = \theta_0 \cos(\omega_d t - \phi)$$

By substituting $\dot{\theta}$ and $\ddot{\theta}$ in equation (18), and equating coefficients yields

$$\theta_0 = M / [\, (K - I_y \, \omega^2) \cos\phi + C \sin\phi \,]$$

$$\tan \phi = C \omega / (K - I_y \, \omega^2) \qquad (19)$$

Equation (19) shows that for constant amplitude motion, when the forcing frequency is equal to the natural frequency of the system ($\phi = 90°$), the inertia term balances the restoring moment term and the damping moment is precisely equal to the forcing torque,

$$C \, \theta_0 \, \omega = M$$

Under these conditions, the knowledge of the forcing moment M, the angular frequency ω and the system

amplitude θ_0 enable the damping parameter C to be determined.

Introducing the relations for C and K, the aerodynamic damping moment and the equation for M_{0a} become

$$M_{\theta'a} = (M_{\theta'a} + M_{\theta't})_w - (M_{\theta't})_v$$

$$M_{\theta a} = (M_{\theta a} + M_{\theta t})_w - (M_{\theta t})_v$$

where v and w indicate the vacuum and wind on conditions, respectively. In terms of the measured quantities, moment, amplitude and frequency

$$M_{\theta'a} = 1 / \omega_w [(M/\theta_0)_w - (M/\theta_0)v]$$

$$M_{\theta a} = I_y [\omega_w^2 - \omega_v^2]$$

The derivatives when reduced to a non dimension form become

$$C_{mq} + C_{m\alpha'} = M_{\theta'a} (2 V/QAd^2)$$

$$C_{m\alpha} = M_{\theta a} /QAd$$

In the case where the resonance condition is not reached, the expression for the particular solution , its first and second order time derivatives, are substituted into equation (18), which yields to

$$M_{\theta'a} = [M/\omega\theta_0 \sin\phi]_w - [M/\omega\theta_0 \sin\phi]_v \omega_v / \omega_w$$

$$M_{\theta a} = [I_y \omega^2 + M/\theta_0 \cos\phi]_w - [I_y \omega^2 + M/\theta_0 \cos\phi]_v$$

And the non dimension forms, as before.

Advantages
In the case of the forced oscillation test technique, the amplitude of the model motion is fixed by the driving mechanism. This kind of test is therefore adapted to dynamically unstable shapes, like the large drag models capsule shapes.

The need for simulating the reduced frequency parameter may be more easily reached with a forced oscillation technique, because the frequency of oscillation can be tuned, while in the case of free oscillation, the frequency is fixed by the stiffness of the flexure.

Drawbacks
In the case of forced oscillation technique, a forcing mechanism has to be accommodated in the sting, in order to oscillate the model at a constant amplitude. The sting is therefore larger than in the case of the free oscillation tests technique. Moreover a balance may have to be accommodated, which further increases the

accommodation problems, i.e. result in a larger sting diameter.

The center-of-oscillation is difficult to locate at the vehicle scaled center-of-gravity location, which is very important for blunt body dynamic testing.

In the forced oscillation test technique, the damping characteristics of the model put reliance on torque measurements. In the case where the resonance condition is reached, the accuracy of the measurement is expected to be maximum, however, the applied torque is as a result very small. The balance is then required to have a very good accuracy , in order to have a reliable torque measurement. The determination of the amplitude and of the frequency are also part of the damping coefficient measurement algorithm. The final accuracy of the damping depends on the accuracy of at least three independent measurements, while in the case of the free oscillation tests, the only incidence measurement is needed.
It is therefore more difficult to obtain accurate measurements with the forced oscillation test technique than with the free oscillation test technique.

5.3.1.3 transverse rod

During the development program of APOLLO, dynamic derivatives investigations were performed by the use of free-to-tumble test technique. This method allows statically balanced models, mounted on a transverse rod through the center-of-gravity, to tumble freely through a range from 0° to 360° (see typical mounting on figure n°12). Some difficulties were encountered to avoid significant friction and interference from the test set-up. Gas-bearing failed, and precision ball bearings proved to be satisfactory.
The tare damping of the model being negligible, the aerodynamic damping can be derived from the simple second order derivative equation :

$$I_y\theta'' + (C_{mq} + C_{m\alpha'})QAd^2\theta'/2 V + C_{m\alpha} QAd\theta = 0 \tag{20}$$

If C_m is measured from static tests and I_y is measured in advance, the damping coefficient is the only variable, and can be found from iterative simulation of θ time history, until the computed and measured curves fit together.

This test technique was used in the frame of APOLLO development program, and showed the model to be dynamically unstable in the subsonic Mach number range (M<0.7).

As this technique has not been widely and thoroughly used except in APOLLO program, a better knowledge of this technique should be needed to list its advantages/drawbacks. However, one can remark that, as in the general case of sting mounted technique, the interference from the sting may have significant effects on the results, with the specific feature in this particular case of a sting which is protruding from the side of the model into the external flowfield.

5.3.2 Specific problems related to sting-mounted dynamic tests

5.3.2.1 Wake interference

It turns out that the sting support interference problem is still more critical in the dynamic tests than in the static ones. Indeed, the sting must be stiff enough to avoid unwanted vibrations of the test set up, while the sting is excited by both the dynamic unstable shapes and by the motion of the model relative to the sting. A compromise must then be found between the necessary minimum diameter of the sting, related to the required stiffness, and the need to minimize the sting diameter, in order to minimize the interference of this suspension mechanism.

In the frame of the VIKING project, a very large wind-tunnel test campaign has been dedicated to the dynamic behaviour assessment (see Ref. 11).

Very large data uncertainties had been measured by experimenters, and then, it was decided to use different test techniques in order to improve data accuracy and understand the origin of the discrepancies.

Hence, forced oscillation technique tests were performed at the ARNOLD Development Center between $0.6 < M < 3.0$, free oscillation tests were made at AEDC VKF facility, and ballistic, range tests were performed at AEDC VON KARMAN Gas Dynamics Facility in the range $1.6 < M_\infty < 3.0$.

Moreover, during the free oscillation tests, several sting diameters and lengths were used in order to investigate the sting interference effect on damping coefficients measurement (see on figure n° 13).

Besides the sting effect on the damping parameters, schlieren pictures were made during the free flight and the free oscillation tests, in order to assess the influence of the sting on wake geometry.

Even if it is not possible to correlate damping coefficients with the wake geometry, a wake disturbance is for sure responsible for damping coefficients modification.

Figure n° 14 shows wake geometries, both in terms of minimal wake diameter $\left(\dfrac{d_w}{d_m}\right)$ and wake length $\left(\dfrac{\ell_w}{d_m}\right)$ (see figure n° 15 for wake definition), divided by model diameter d_m.

Sting configuration and Mach number have a large influence on wake geometry. Free flight wake geometry lies below the sting-supported results because the sting is forcing the wake diameter outward, while wake lengths are shorter with a sting because less length is required for wake contraction with a larger diameter.

Finally, it turns out that a sting with a diameter ratio $\dfrac{d_s}{d_m} = 0.183$ and a length ratio $\dfrac{l_s}{d_m} = 3.55$ does not disturb significantly the wake geometry.

The further step in VIKING experiments was dedicated to damping coefficients sensitivity with respect to sting geometry.

The largest sting support influences were found to occur at the lowest test Mach number (1.76) for which this interference study was made.

"In fact, the data obtained at $M = 2.23$ show small effects of effective sting length and diameter while the data at $M = 3.0$ showed no interference effects for the tested conditions" (from Ref. 11).

The detailed results of VIKING investigations are shown on figures n° 7 and n° 16.

There is an unstable damping trend as effective sting length increases at very low angle of attack (see $(C_{m_q} + C_{m_{\dot\alpha}})\left(\dfrac{ls}{dm}\right)$ curve slopes on figure n° 7).

The same unstable trend can be observed when the diameter of the sting is decreased (see figure n° 16). However this sting diameter effect can be observed at low angle of attack, for all test REYNOLDS numbers. It is believed that a further diameter ratio decrease would not have altered the results.

Two conclusions arise from these interference studies,

Long, small diameter sting, which provides minimal interference, increases the unstable damping spikes. This is a further evidence that a blunt body wake is the major contributor to unstable damping.

The interference effects are experienced, in the VIKING case, in the angle of attack range where dynamic instability occurs, i.e. where the contribution of the wake to the damping prevails.

5.3.2.2 Transport formula

When the center-of-oscillation cannot be accomodated at the scaled center-of-gravity of the vehicle, a transport formula has to be used, in order to derive the damping coefficients from the flexure to the flight scaled center-of-gravity (see Ref. 34).
A lot of difficulties have been met by experimenters who have tried to apply this formula to capsule model dynamic test results.

In Reference 10, it is pointed out that the first APOLLO dynamic tests were conducted with such a balance and oscillation set up, that the center-of-oscillation could not be accomodated at the cog (Ref.31,32,33). Therefore the tests were made for different center-of-oscillation, and people tried to correlate the resuls, in order to transfer the data to the center-of-gravity. The result were inconclusive.

5.3.3 Free model test techniques

5.3.3.1 Ballistic range tests

A complete description of ballistic range technique can be found in reference 24.
The ballistic range tests consist in launching a scaled model in a tunnel, the recording of the motion pictures along the ballistic range provides with the capability to derive the static and dynamic aerodynamic coefficients of the tested models (see Ref. 1,2,3). Indeed, pictures of the model are taken at regular distance along the ballistic range, while the time corresponding to the recorded picture is accurately known. The deceleration of the model in the ballistic range provides with the drag coefficient, while the attitude of the model is used to derive the damping coefficient from the second order equation of the angular motion of the model. The frequency of oscillation indicates the pitching moment slope.

The capabilities of ballistic range facilities are wide and able to cover from hypersonics to subsonics. The main advantage of this test technique is the absence of interference with a support. The only interference is between model and tunnel wall, which can vary depending on the tunnel geometry (octogonal, cylindrical,...).The size of the model is tuned to this end, and interference is almost negligible (see [R1]).

The limitation of this test technique consists in the difficulties to master the initial conditions of the launch, in terms of initial attitude of the model. Indeed, the models are adapted to the gun by the mean of two, or more pieces sabots. This sabot has to be separated from the model at the entry in the ballistic range itself, this is made by a mechanical deviation of the sabot, which results in hardly predictable kinematic behaviour prior to the tunnel entry. However, with sufficiently long ballistic range, a single shot provides with various model attitude informations, as it flies along the tunnel.

One other difficulty is that the model dynamic derivatives are deduced from full oscillation amplitude motions, and consist therefore in effective damping coefficients (mean value over a cycle). Techniques exist to go from effective to local value of damping coefficients, i.e. the damping coefficient which is actually applicable to a 6 Degree-of-freedom computation. Indeed, a vehicle passes instantaneously through various angle-of-attacks, and needs therefore to know about the instantaneous damping at a given incidence.
The reference 29 provides with formula, derived from energy considerations : the work over a complete oscillation performed either from the local damping times the instantaneous angle-of-attack variation is the same than the work performed by the effective damping times the amplitude variation (see also Ref. 30).

However, it must be pointed out that this transformation from effective to local value is difficult to undergo, in the case of highly non linear damping coefficient variations versus incidence, which is the case for blunt bodies in the transonic regime for example (see [R5]).

From model manufacturing point of view, strong constraints are put on the model, because it has to withstand very high acceleration level during launch in the case of high velocity tests (more than 100 000 g's for hypersonics). The material of the model, and possibly the geometry of the model has to be designed in such a way that the shape remains unchanged.

Besides the considerations on blunt vehicles, it is difficult to test with high Lift over Drag ratio models, because the model may damage the tunnel, as its trajectory is curved during the flight along the ballistic range.

5.3.3.2 Free flight tests in wind tunnel

As said earlier, the main disadvantage of either the forced or free oscillation tests technique, is the presence of a sting in the near wake of the vehicle. This makes the results questionable, as this near wake is thought to be responsible for the transonic dynamic instability.

The free flight tests in a conventional wind tunnel avoids this problem, as it consists in the release of a scaled model in a conventional wind tunnel. The recording of the pictures of the model motion enables the dynamic characteristics of the model to be determined. The models are either sustained in the wind tunnel upstream of the viewing window, or launched by a pneumatic launcher in the upstream direction.

The model launch velocity is tuned so that the model reaches the upstream edge of a viewing window. The incidence time history of the model is recorded, along with the model position in the wind tunnel, versus time.

The accuracy of the analysis is improved if the model oscillates with increased number of cycles in front of the viewing window. The mass of the model must therefore be kept as large as possible, while the model diameter should be reduced, in order to reduce its total drag. On the other hand, its transverse inertia must be reduced, by manufacturing a dense inner core, with an external thin outer shell. In reference [R5], the outer shell consisted in thick polystyrene plastic, while the inner core was powdered tungsten. This enables the model to be destroyed in the wind tunnel, with no damage for the wind tunnel.

The derivation of the damping coefficient is briefly described hereafter (see [R5]):

If one assume the aerodynamic coefficients to be linear function of angle-of-attack [i.e. $C_m = C_{m\alpha} \alpha$; $C_L = C_{L\alpha} \alpha$; $C_D = C_{D0}$], the solution to the equation of planar angular motion :

$$I_y \ddot{\theta} = 1/2 \rho V^2 A d C_m + 1/2 \rho V^2 A \{C_{mq} + C_{m\alpha\cdot}\} (\dot{\theta} d/V) \qquad (21)$$

is

$$\alpha = \alpha_0 \exp(\lambda X) \cos \left\{ \left[(-\rho A d / 2I)C_{m\alpha} + \lambda^2\right]^{1/2} X \right\} \qquad (22)$$

where

$$\lambda = \rho A/4m \left[C_{D0} - C_{L\alpha} - md^2/I \{C_{mq} + C_{m\alpha\cdot}\} \right] \quad (23)$$

It is usually assumed that $[-\rho A d / (2 I)]C_{m\alpha} >> \lambda^2$ and the effective pitching moment slope can be derived from the distance frequency of oscillation from the following

$$C_{m\alpha \ eff} = - 2I\Omega^2/(\rho A d) \qquad (24)$$

where Ω is the distance frequency of oscillation. The damping coefficient may be obtained from equation (22) in terms of the amplitude envelope as

$$\{C_{mq} + C_{m\alpha\cdot}\}md^2/I = 4m /\rho A 1/(X - X_0) Ln (\theta_x/\theta_0) + C_{L\alpha} - C_{D0}$$

For general application these hypothesis are too much restrictive, and more applicable solutions must be found. Unrestricted integral equations for determining the dynamic stability coefficient from energy considerations has been developed in 25 and 26.

In particular, the non linearity of pitching moment versus angle-of-attack must be taken into account.

A more general solution, assuming that the pitching moment, lift and drag may be expressed as

$$Cm = C_{m\alpha} \alpha + 2r_m \theta^3 \qquad C_L = C_{L\alpha} \alpha + k \theta^3$$
$$C_D = C_{D0} + K \theta^2$$

it comes

$$\{C_{mq} + C_{m\alpha\cdot}\}md^2/I = 4m /\rho A 1/(X - X_0) Ln (\theta_x/\theta_0)R + (C_{L\alpha} + 3/4 k \underline{\alpha}_0^2) - (C_{D0} + 1/4 K \underline{\alpha}_0^2)$$

R is the pitching moment correction ratio, and is closed to 1 for small values of r_m associated to blunt bodies.
The corrections for C_L and C_D have small effect on damping coefficient analysis, because they contribute to a small extent to the amplitude of the oscillatory motion.

The derivation of general energy equation to asymmetric and axisymmetric with a center-of-gravity offset may be found in 27. The case of either linear, cubic, bi-linear (two different slopes for positive and negative incidence) and bi-cubic cases are analysed.

Advantages
No sting interference
The initial attitude conditions of the model can be easily tuned
The model motion is fully representative of the flight motion
The test provides with pictures of the model surrounding flowfield in a non disturbed aerodynamic environment.

Drawbacks
The damping coefficient, as derived from the aforementioned analysis corresponds to an effective value of damping over a full oscillation amplitude.
The analysis and derivation of the damping coefficient is complex, especially in he case of non linear pitching moment curve, or model with center-of-gravity offset.

6. HUYGENS CASE

The HUYGENS mission is described in the document *Aerothermodynamic requirements and design of the HUYGENS Probe.*
When entering the TITAN atmosphere, the HUYGENS entry module (see figure n°8) is submitted to aerodynamic torque, which results in the case of a statically stable vehicle, to precession of the elliptic motion of probe longitudinal axis around the velocity vector (see figure n°18). The total incidence (angle beween the probe longitudinal axis and the probe center-of-gravity velocity vector) of the Entry Module (EM) describes then an oscillatory motion, with first a converging amplitude towards a constant trim angle-of-attack.
The angle-of-attack at beginning of entry is less than 10° at Mach number M>20, which becomes less than 2° in supersonics. .
This convergence is the result of the static stability of the 60° half angle entry module in hypersonics (see fig. n° 19).

Early in the project,a complete aerodynamic database, including static and dynamic coefficients,was needed in order to perform 6 degree-of-freedom trajectories.
The preliminary database was built from literature on tested shapes as close as possible to the entry module (EM) shape. Some ballistic range tests which had been performed in the 60's at NASA Ames, provided us with dynamic coefficients of 55°-60° half angle cones, with flat base (see Ref. 1).
Experimenters from these tests did conclude that a dynamic instability was evidenced in transonic regime, but for Mach number M>1.4, the shapes were found to be dynamically stable.

However, no test had been performed for low incidence at M>1.4, and furthermore, the HUYGENS probe has a partially empty afterbody, which could have influence on dynamics (see figure n°8).

Early in the project, dynamic stability tests were therefore performed in sub-trans and supersonic Mach number range, in order to derive a database which should be applicable to HUYGENS probe.

The previous experience of European aerodynamic facilities was limited to aircraft and slender cones, which led to some compromise to find between the existing material and the requiremens connected to blunt bodies dynamic coefficients measurements (mainly issued form VIKING experiments, see Ref. 11).

The HUYGENS dynamic tests were performed:
in Defense Research Agency (DRA at Bedford, Great Britain, past Royal Aircraft Establishment RAE) for the Descent Module (DM) in low subsonics (M=0.2), in the 13 x 9 ft wind tunnel.
in FFA (Swedish Aeronautical Research Institute, at Stockholm, Sweden) for the Entry Module (EM) in sub, trans and supersonics (0,5 < M< 2.0), in the S4 wind tunnel.
A complementary test program was foreseen at Aircraft Research Association (ARA in Bedford) at M=4 and 5, to assess the high supersonic dynamic stability of the Entry Module.

The subsonic tests on the DM were performed with the forced oscillation technique with a so called flexible sting (see Ref. 35).

These tests on the EM were performed with forced oscillation test technique for small amplitude oscillations (1.2° amplitude) with existing rig adapted to aircraft dynamic stability investigation (see figure n°20).
As a result, the sting was large, which resulted in interferences with the flowfield. Moreover, the center-of-oscillation of the tests could not be accommodated inside the model. Therefore, dedicated transport formulae had then to be used in order to derive the damping coefficients at the model scaled center-of-gravity location (see reference n°34) and led to poor accuracy of the results, and finally the sensitivity of the balance was not adapted to the aerodynamics of blunt bodies (large axial force, small normal force and pitching moment).

These FFA tests showed that the entry module was dynamically unstable for Mach number 2 and lower at moderate angle-of-attack ($\alpha \leq 15°$, see figure n°21), with an increasing instability with decreasing Mach number.

The VIKING tests had shown that interference effect were significant for Mach numbers lower than 2 (see Reference n°7), and Schlieren pictures of the EM tests at small incidence did not show evidence of near wake disturbance, in terms of neck diameter and/or neck distance to the base of the EM, when compared to CFD Navier Stokes computations (these two parameters were investigated in VIKING dynamic tests sensitivity studies with respect to sting interference).

Consequently, this unexpected dynamic instability was taken into account in dynamic database used for 6 degree-of-freedom computations of EM entry into TITAN atmosphere.
The dynamic stability of the EM for Mach numbers larger than 2 up to hypersonic regime was fitted to VIKING one, which predict a stabilising trend in the range Mach number 2 to 3 (see Ref. n°6,7).
A conservative slight instability was however kept in super-hypersonic for very small incidence ($\alpha < 2°$), based on free flight of flat base 60° half angle cones (see Ref. n°2).

This unexpected supersonic dynamic instability had a large negative impact on the system.

Indeed, 6 degree of freedom simulations showed that hypersonic to supersonic dynamic instability resulted in a small limit cycle, associated with a transverse rate in high supersonic. These conditions revealed to be very unfavourable in low supersonic, because the dynamic instability peak in transonic resulted then in a fast rise of incidence, up to unacceptable value for safe parachute deployment (more than 30° at Mach number M=1.5).

Further experimental investigations were needed, in order to verify the supersonic stabilising trend, and the actual dynamic behaviour of the EM in high supersonics.

A different facility and test set up were used in ARA (Bedford), in order to avoid the identified sources of discrepancies, and add confidence in results which should be measured by two different ways. Furthermore the Mach number range of the investigations was extended up to Mach 3, in order to verify the stabilizing trend observed on VIKING.

The free oscillation test technique was used. This technique provides the experimenter with a simple and reliable way to assess the dynamic behaviour of a model. Indeed, no balance is used, the sting is then far simpler and smaller. The flare interface was designed to minimize interference with the flowfield, while the diameter of the sting was reduced to reach the VIKING indications : ds/dm<0.18 and Ls/dm>3.5, where ds and dm are respectively the sting and model diameters, and Ls is the sting parallel length (see figure °22, ARA test set up).

Moreover, the direct output of strain gage located on the flexure which is the center-of-oscillation of the tests, and is designed to be placed at the scaled center-of-gravity of the model, gives the incidence versus time history, and so far, immediate evidence of dynamic stability or instability.

Figure n°23 shows the incidence versus time of the EM at Mach number M=2.9.

The quickly damped amplitude of oscillations shows that the EM is dynamically stable at this Mach number, with a Cmq+Cmα.=-0.19.

The analysis of the tests is performed by computing the simple second order differential equation of angular displacement versus time :

$$I \cdot \ddot{\theta} + C \cdot \dot{\theta} + K\theta = 0$$

θ is the angular displacement of the model,

I is the transverse inertia of the model

C is the damping of the system (aerodynamic plus mechanical tare damping)

$$C = M_{\dot{\theta}a} + M_{\dot{\theta}.t} = QSd^2/V(Cmq + Cm\alpha.)(\theta) + M_{\dot{\theta}.t}$$

K is the total stiffness of the system (aerodynamic plus mechanical, i.e. flexure stiffness)

$$K = M_{\theta a} + M_{\theta t} = QSdC_{m\alpha}(\theta) + M_{\theta t}$$

The only unknown is the aerodynamic part of C.

Therefore, the $\theta(t)$ evolution is computed for different value of $(C_{mq} + C_{m\alpha}\cdot)(\theta)$, until the experimental $\theta_E(t)$ and computed $\theta_C(t)$ fit together. Figure n°23 shows $\theta_E(t)$ and $\theta_C(t)$, for at Mach number M=2.9 ($\theta_C(t)$ in fine line).

The free oscillation tests have shown that the EM is actually dynamically unstable for Mach numbers M≤2.4, with an increasing instability for decreasing Mach numbers, for very small range of angle-of-attack ($\alpha \leq 3°$). The stabilising trend from Mach number M=2 to M=3 was confirmed, and a very small dynamic instability is kept in the hypersonic database for very small angle-of-attack ($\alpha \leq 2°$).

The complete new issue of the dynamic database was then used to compute EM trajectories in the TITAN atmosphere, and led to a safe angle-of-attack less than 5° at parachute deployment (M=1.5).

CONCLUSION

The dynamic stability of blunt bodies, like capsule shapes, or planetary entry probes, has been shown to be poor, and at some times unstable in super, trans and subsonics. The rear flow field pattern, and the near wake recirculation zone are thought to be responsible for this dynamic behaviour. This feature results in a difficult investigation of the dynamic characteristics of capsules, either from numerical or experimental way. Indeed, the expected unsteadiness of the rear flowfield, and its sensitivity to interference, make it difficult to respectively, use Navier Stokes codes in largely separated area, and to locate a sting, in the case of sting mounted models in wind tunnel.

At present time, the dynamic derivatives investigations put strong reliance on experiments. However, wind tunnel tests have limitations, in terms of similarity parameters, Mach, Reynolds number, reduced frequency

parameter, which are difficult to meet simultaneously, and in terms of interferences.

The numerical developments allow significant improvements to be foreseen in the next future, which would enable, at least, to have comparisons with experiments.

At system level, the dynamic instability constraints the parachute system, the Reaction Control System, in case of controlled entry, and must therefore be taken into account very early in the development phase of a vehicle.

REFERENCES

1. Sammonds, R.I., "Dynamics of high-drag probe shapes at transonic speeds",NASA TN D-6489,Sept. 1971

2. Sammonds, R.I., "Aerodynamics of Mars entry Probe-Lander Configurations at a Mach number of 10.",NASA TN D-5608, 1970

3. Krumins, Margonis, V., "Drag and Stability of Mars Probe/lander Shapes",*J.Spacecraft and Rockets*,Vol 4,No 8,Aug. 1967,pp 1052-1057 (see also *AIAA paper*,No 67-167, Jan. 1967)

4. Ericsson,L.E.,Reding,J.P.,"Review of support interference in dynamic tests", *AIAA journal*, vol.21, n°12, pp.1652-1666.

5. Marko, W., "Dynamic stability of high-drag planetary entry vehicles at transonic speeds", *AIAA paper*, n°69-105, presented at AIAA 7th Aerospace Sciences meeting, New York, Jan 20-22, 1969.

6. Uselton, B.L., Shadow, T.O., Mansfield, A.C., "Damping-in-pitch derivatives of 120- and 140° blunted cones at Mach numbers from 0.6 through 3", AEDC TR-70-49, April 1970, Arnold Air Force Station, Tennessee.

7. Steinberg, S., Siemers, P.M. III,"Transonic and Supersonic Experimental Pitch Damping Derivatives for Candidate Viking Configurations", 35th Meeting of the Supersonic Tunnel Association, Dallas, Texas, March 8-9, 1971.

8. Sammonds, R.I., Kruse, L., "Viking Entry Vehicle Aerodynamics at M=2 in Air and Some Preliminary Test Data for Flight in CO2 at M=11", NASA TN D-7974, June 1975.

9. Kirk, D.B., Intrieri, P.F., Sieff, A., "Aerodynamic Behavior of the Viking Entry Vehicle: Ground Test and Flight Results",*Journal of Spacecraft*, Vol 15, No 4, pp 208-212.

10. Moseley, W.C., Moore, R.H. Jr, Hughes, J.E., "Stability Characteristics of the Apollo Command Module", NASA TN D-3890.

11. Steinberg, S., Uselton, B., Siemers III, P.M., "VIKING Configuration Pitch Damping Derivatives as influenced by Support Interference and Test Technique at Transonic and Supersonic Speeds",

AIAA paper, N°72-1012, 7th Aerodynamic testing Conference, Sept. 1972.

12. Sommer, S.C., Short, B.J., Compton, D.L., "Free-Flight Measurements of Static and Dynamic Stability of Models of the Project MERCURY Re-Entry Capsule at Mach Number 3 and 9.5", NASA TM-X 373.

13. Igoe, W.B., Hillje, E.R., "Transonic Dynamic Stability Characteristics of Several Models of Project Mercury Capsule Configurations, NASA TM X-554, Aug. 1961.

14. Sammonds, R.I., Dickey, R.R., "Effectiveness of several Control Arrangements on a Mercury-type Capsule", NASA TM X-579, Aug. 1961.

15. Sowman, J.S., "Dynamic Model Tests at Low Subsonic Speeds of Project Mercury Capsule Configurations With and Without Drogues Parachutes", NASA TM X-459.

16. Hui, W.H. and Tobak, M., "Unsteady Newton-Busemann Flow Theory, part I:Airfoils",*AIAA Journal*, Vol 19,March 1981, pp 311-318

17. Hui, W.H. et al, "Unsteady Newton-Busemann Flow Theory, part II:Bodies of revolution", *AIAA Journal*, Vol 19,Oct 1981, pp 1272-1273 (also NASA TM-80459,Oct 1981).

18. Hui, W.H. et al, "Unsteady Newton-Busemann Flow Theory, part III:Frequency Dependence and Indicial Response", *Aeronautical Quarterly*, Vol 33, Nov 1982

19. Hui, W.H. and Van Roessel, H.J., "Unsteady Newton-Busemann Flow Theory, part IV:Three Dimensional",*AIAA Journal*, Vol 22,No 5, May 1985, pp 577-578.

20. Hui, W.H. et al, "Three-Dimensional Unsteady Newton-Buseman Flow Theory", AIAA-82-1305, *9th Atmospheric Flight Mechanics Conference*, August 1982

21. Ericsson, L.E., "Extension of Unsteady Embedded Newtonian Theory", *J.Spacecraft and Rockets*, Vol 30,No 3,May-June 1993,pp 316-322.

22. Schueler, C.J., Ward, L.K. and Hodapp, A.E. Jr, "Techniques for measurement of dynamic stability derivatives in groung test facilities, *AGARDograph 121*, Oct 1967.

23. Orlik-Rückemann, K.,J., "Review of techniques for determination of dynamic stability parameters in wind tunnels", *AGARD-CP-235*, Fluid Dynamics Panel Symposium, Athens, May 22-24, 1978

24. Canning, T.N., Seiff, A., James, C.S., "Ballistic Range Technology", *AGARDograph 138*, Ch.7., Aug. 1970.

25. Dayman, Jr., Bain, "Simplified Free FlightTesting in a Conventional Wind Tunnel", Technical Report No32-346, Jet Propulsion Laboratory, Pasadena, California, Oct. 1962.

26. Prislin, R.H., "Free-Flight and Free-Oscillation Techniques for Wind-Tunnel Dynamic-Stability Testing", Technical Report No32-878, Jet Propulsion Laboratory, Pasadena, California, March 1966.

27. Prislin, R.H., Wilson, M.B., "Determination of Aerodynamic Damping Coefficients from Wind-Tunnel Free-Flight Trajectories of Non-Axisymmetric Bodies", Technical Report No32-1159, Jet Propulsion Laboratory, Pasadena, California, Oct. 1967.

28. Ekaterinaris, J.A., Menter, F.R., "Computation of Oscillating Airfoil Flows with One- and Two-Equation Turbulence Models", *AIAA Journal*, Vol 32, N°12, December 1994

29. Redd, B., Olsen, D.M., Barton, R.L., "Relationship between the Aerodynamic Damping Derivatives Measured as a Function of Instantaneous Angular Displacement and the Aerodynamic Damping Derivatives Measured as a Function of Oscillation Amplitude", NASA TN D-2855, 1965

30. Billingsley, J.P., Norman, W.S., "Relationship between local and effective aerodynamic pitch-damping derivatives as measured by a forced-oscillation balance for preliminary Viking configurations", AEDC-TR-72-25, May 1972

31. Averett, B.T., Kilgore, R.A., "Dynamic Stability Characteristics of Proposed APOLLO Configurations at Mach numbers from 0.30 to 1.20", NASA TM X-912, 1964

32. Averett, B.T., Wright, B.R., "Some Dynamic-Stability Characteristics of Models of Proposed APOLLO Configurations at Mach numbers from 1.60 to 2.75", NASA TM X-971, 1964

33. Averett, B.T., "Dynamic-Stability Characteristics in Pitch of Models of Proposed APOLLO Configurations at Mach numbers from 0.30 to 4.63", NASA TM X-1127, 1965

34. Wehrend Jr, W.R., "An experimental Evaluation of Aerodynamic Damping Moments of Cones with Different Centers-of-rotation", NASA TN D-1768, March 1963

35. O'Leary, C.O., "Wind Tunnel Measurements of Aerodynamic Derivatives using Flexible-Sting Rigs", *AGARD Lecture Series*, AGARD-LS-114
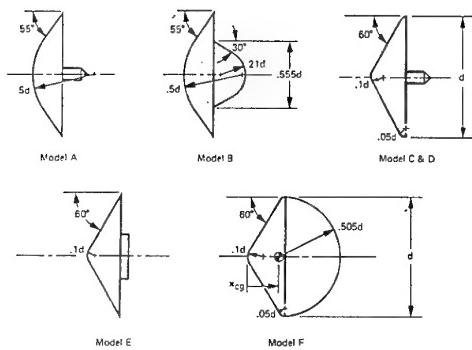
Figure n°1

NASA Ames Ballistic Range Models (from Ref. 1).
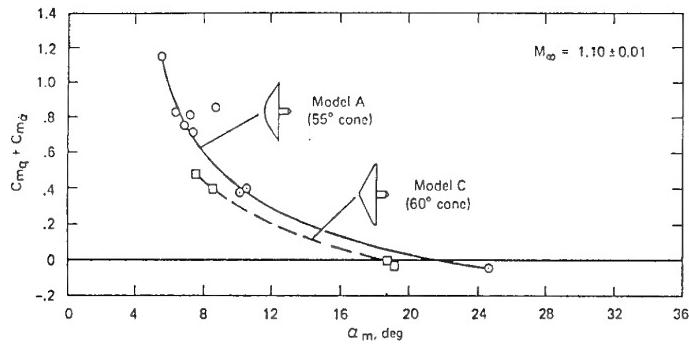
Effect of pitch amplitude on the dynamic stability of models A and C.
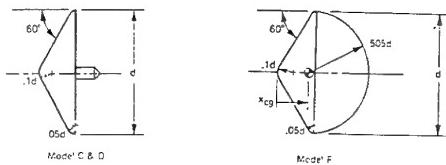
Figure n°2

Dynamic Stability Parameter $\xi(\alpha)$ at M=1.1 (from Ref. 1).

Effect of afterbody shape on the dynamic stability ($C_{m_q} - C_{m_{\dot\alpha}}$) of a 60° half-angle cone at a Mach number of 1.05.

Figure n°3   Dynamic Stability Parameter $\xi(\alpha)$ spherical base model (from Ref. 1).

Figure n°4   Ballistic Range Models (from Ref. 5)

Sketch of Viking entry vehicle.
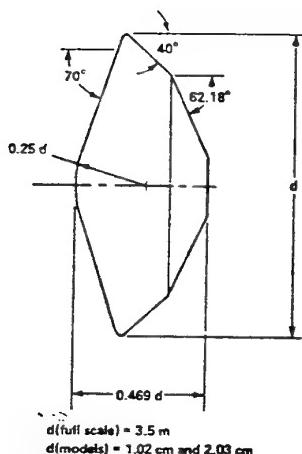
Figure n°5

VIKING geometry (from Ref. 9)

Variation of the dynamic stability $(C_{m_q} + C_{m_{\dot{\alpha}}})$ with Mach number for model A in air
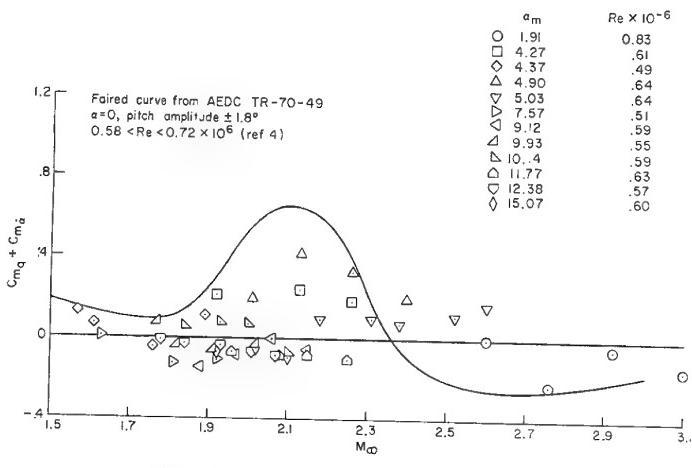
Figure n°6   VIKING Damping Derivative vs Mach number (from Ref. 8).

Dynamic Damping Parameter Comparison at Two Sting Length Ratios as a Function of Angle of Attack; M = 1.76
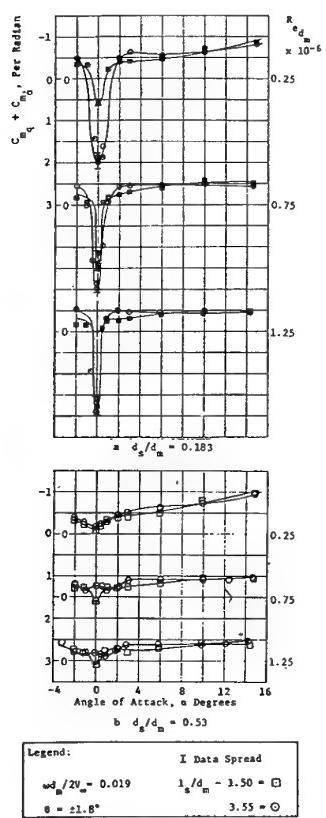
Figure n°7

VIKING Damping Derivative vs α
at Mach number M=1.76 (from Ref. 8)

HUYGENS entry module
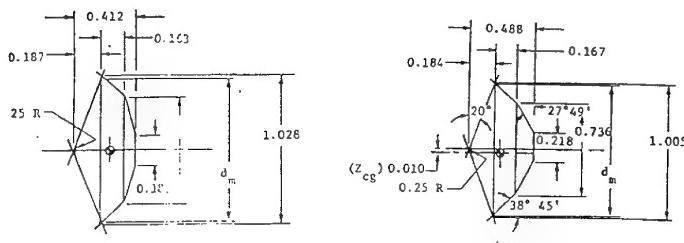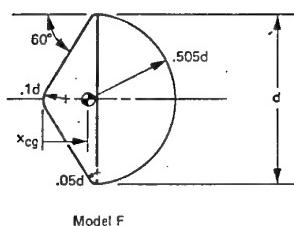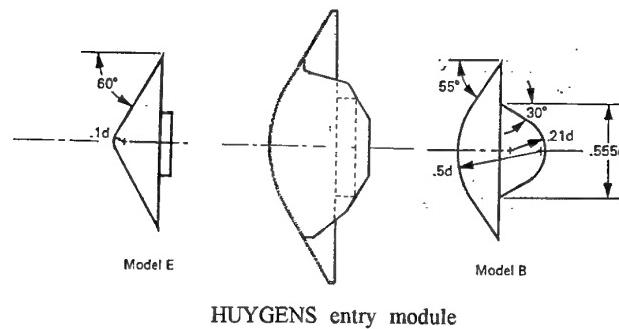
Model F

Figure n°8

VIKING / HUYGENS / Ballistic Range Models Geometry Comparison
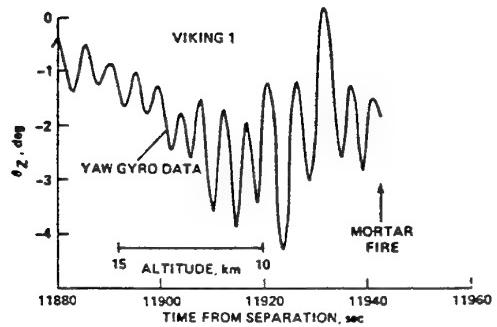
Figure n°9   VIKING 1 Angle-of-Attack Increase in Transonics (from Ref. 9)

APOLLO TYPE SHAPE

Φ	2800 mm	
R_N	3360 mm	1.20 Φ
R_C	140 mm	0.05 Φ
R_b	166.4 mm	0.059 Φ
θ	33°	

D ,m	L ,m	l_κ ,m	d ,m	R_c ,m
2.2	2.142	1.778	0.98	2.235

R_{cp} ,m	$r_{c\kappa p}$,m	l ,m	θ_c ,deg	θ_κ ,deg	$\theta_{\kappa l}$,deg
0.978	0.05	0.936	60.0	7.0	11 0
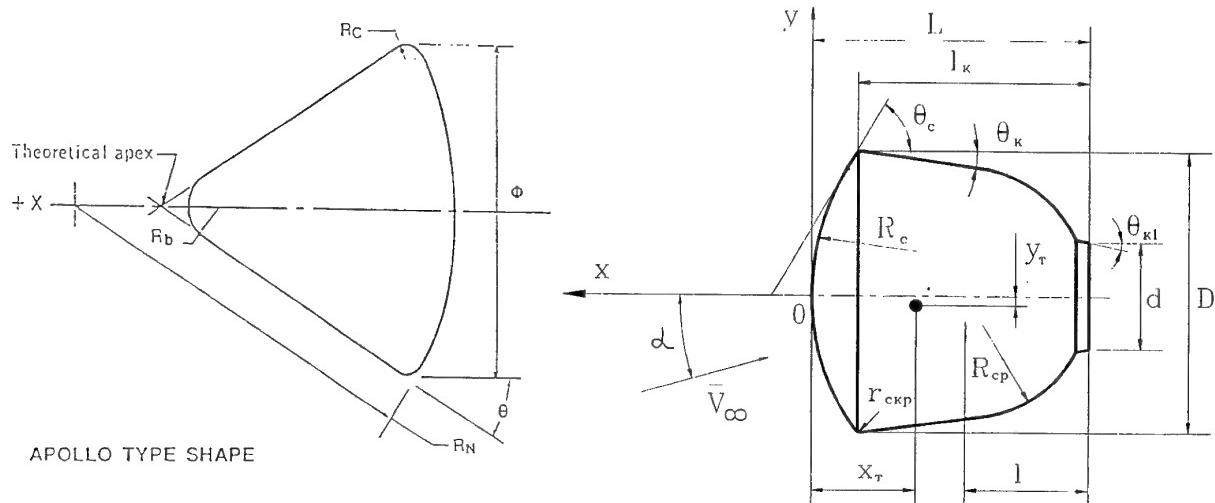
Figure n°10   APOLLO & SOYUZ Geometries
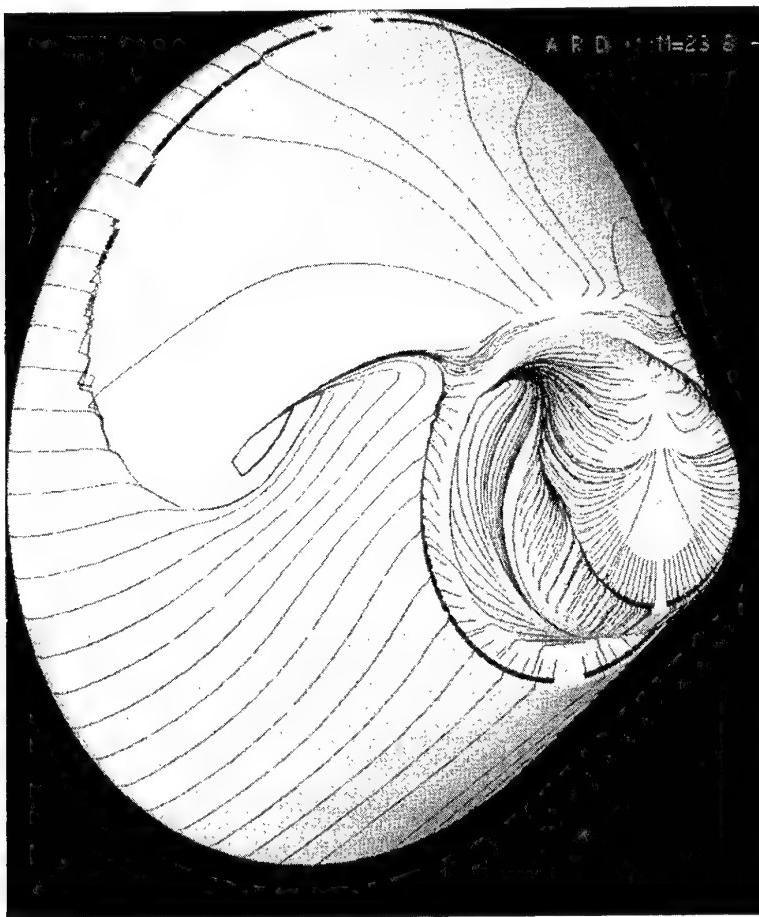
Figure n°11   Navier Stokes Calculation on ARD
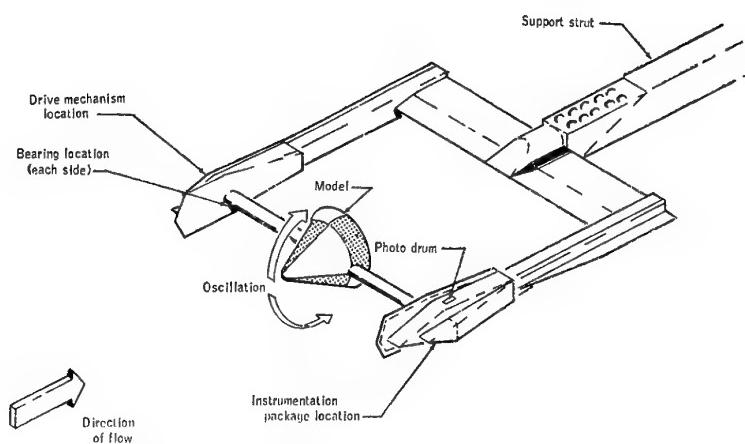
Sketch showing model installation for free-to-tumble dynamic tests.

Figure n°12   APOLLO Free-to-Tumble Set-up (from Ref. 10)
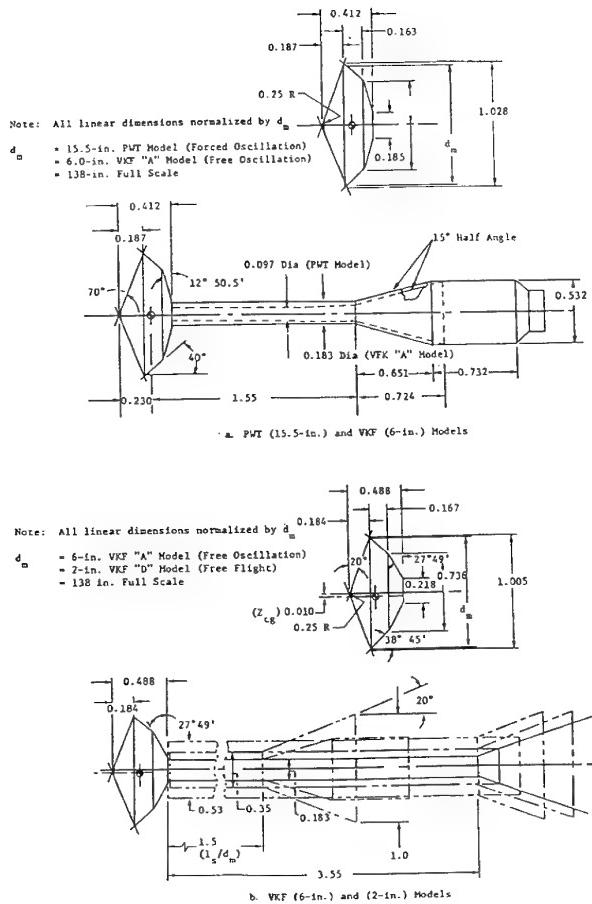
Figure 1 Model and Support Sting Geometry

Figure n°13   VIKING Model and Support Geometry (from Ref. 7)
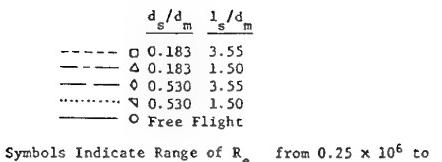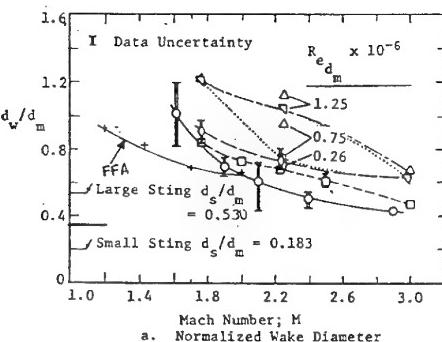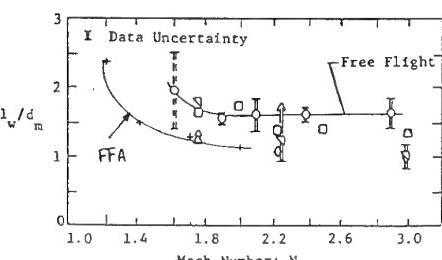
Figure n°14   VIKING Wake Geometry
as a Function of Mach number (from Ref. 7)
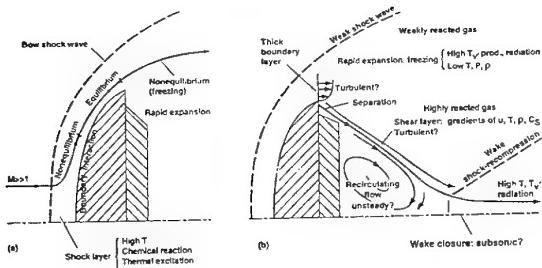
Blunt-body high-speed, high altitude flow field phenomena. a) Forebody, b) afterbody and wake

Figure n°15   Blunt Body Flow Field Phenomena
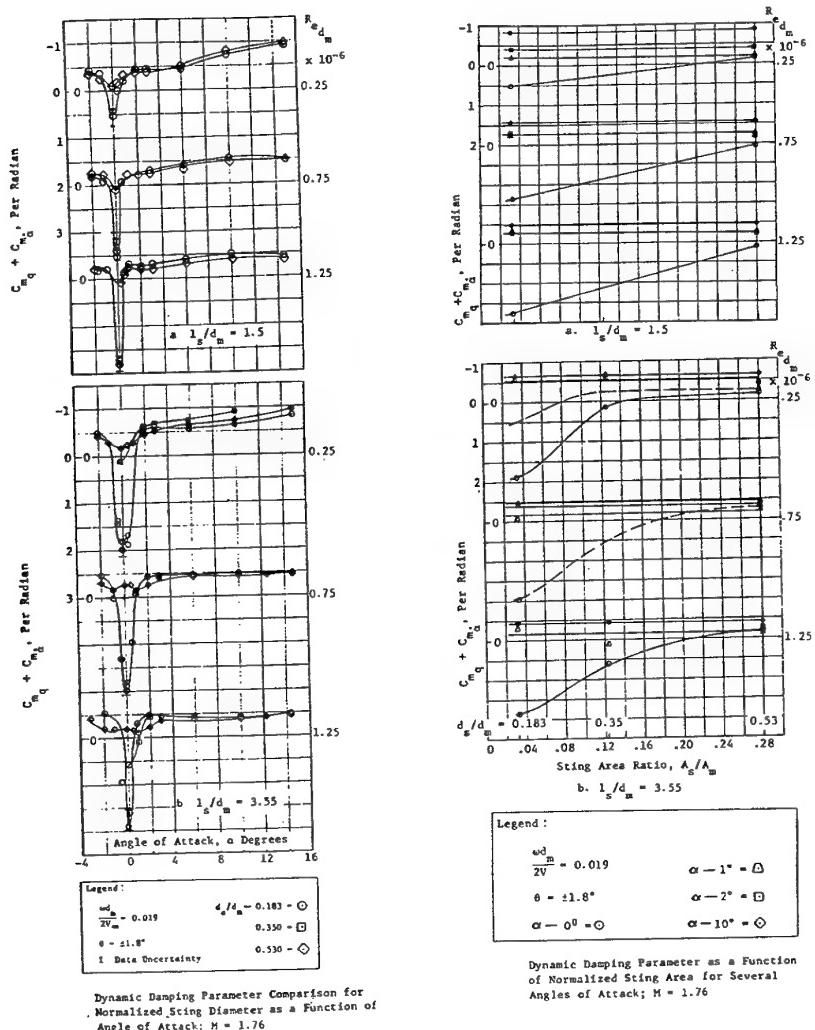
Figure n°16

VIKING Damping Derivative

as Function of Sting Geometry

(from Ref. 8)
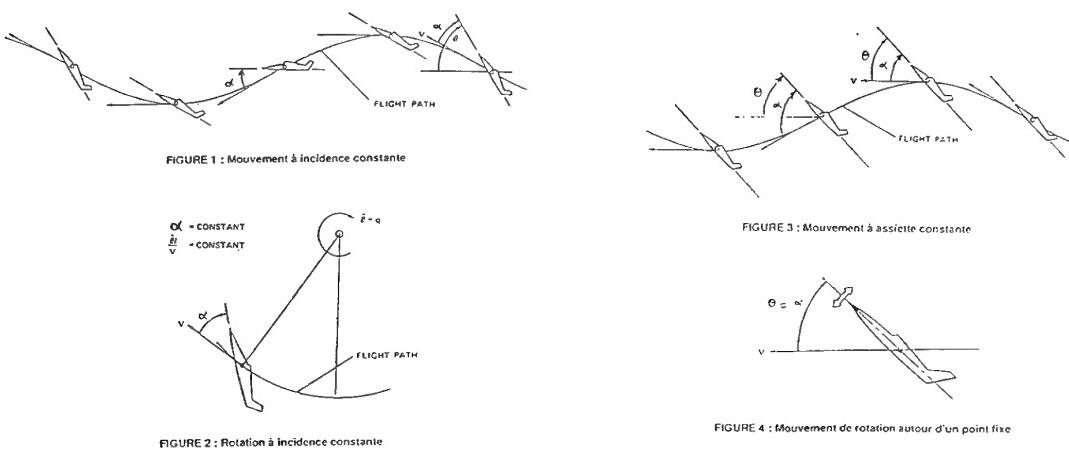
Figure n°17   Different Types of Motions about Center-of-Gravity
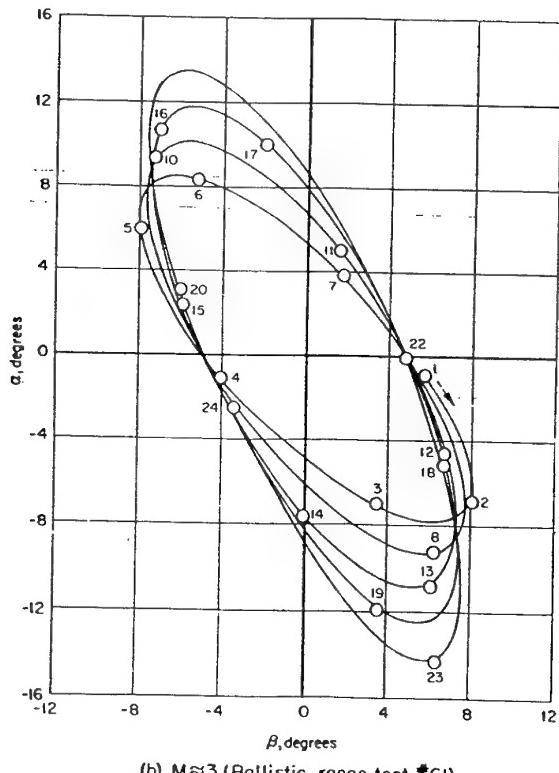
Figure n°18

Angle-of-Attack Typical Evolution (from Ref. 12)

(b) M≈3 (Ballistic–range test #61)

Incidence 10 deg. P=5 rpm
Xg=442.7 mm Yg=14 mm Zg=0 mm tetai=0.5 deg.
no angular transverse rate

HUYGENS - 3.0m diameter
Ve=6190 m/s Pe=-64. deg.
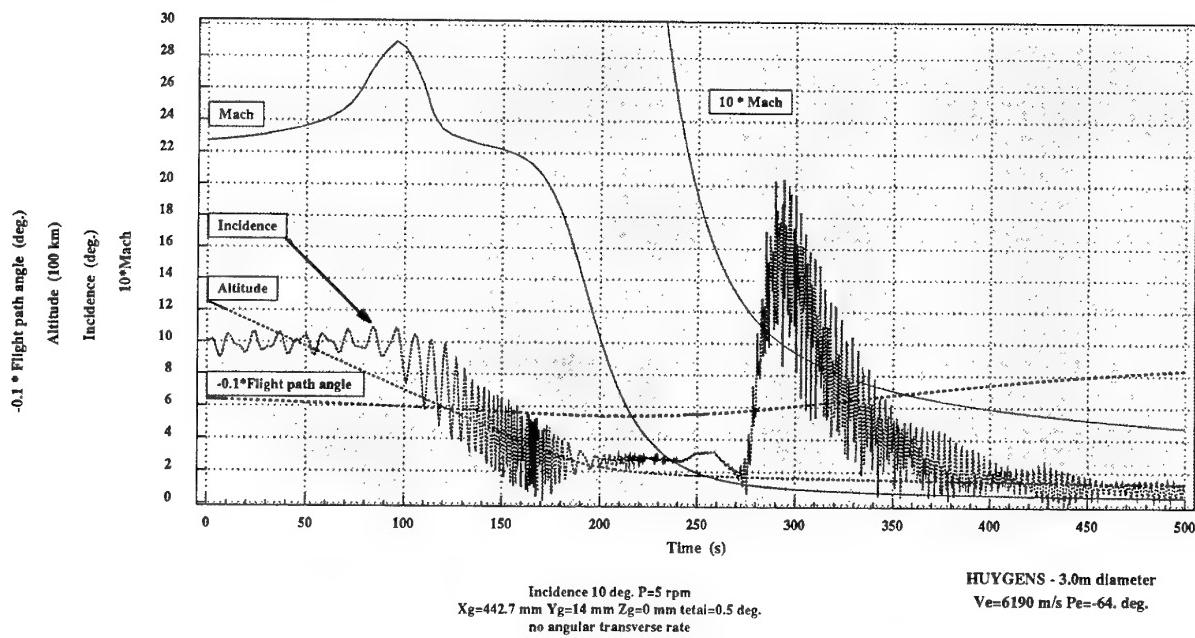
Figure n°19   HUYGENS Entry Module Angle-of-Attack Evolution during Titan Entry
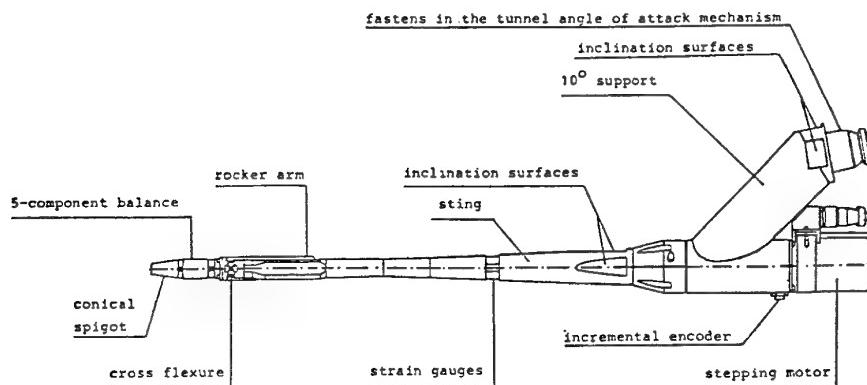
Overview
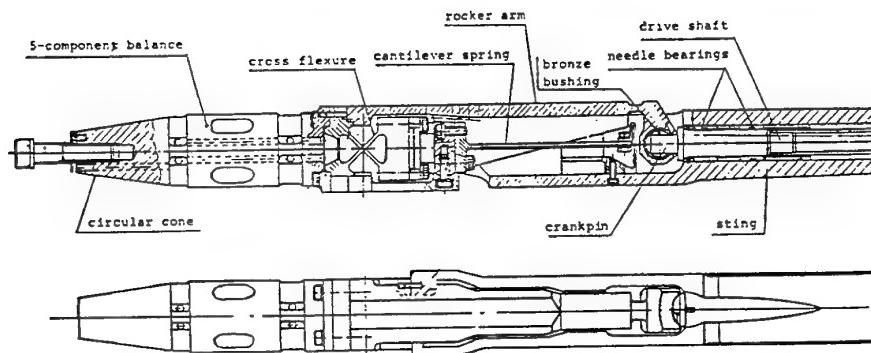
Details

Figure n°20   FFA Dynamic Rig
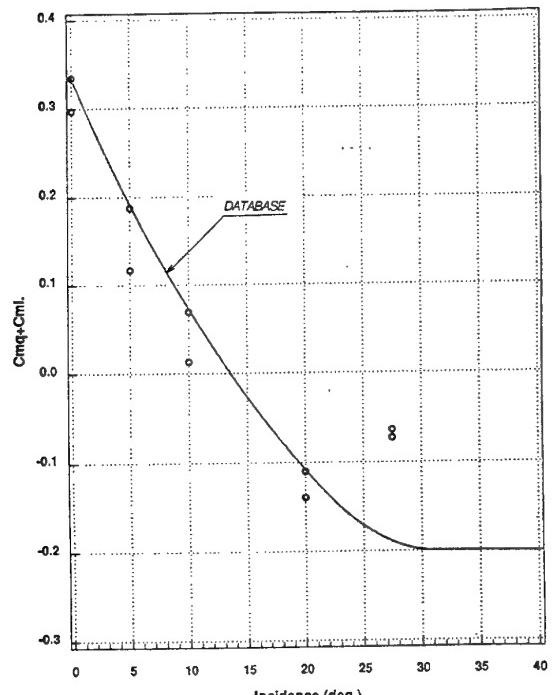
Figure n°21
HUYGENS Entry Module Cmq+Cmα˙
vs Angle-of-Attack at M=2.0

o FFA measurements
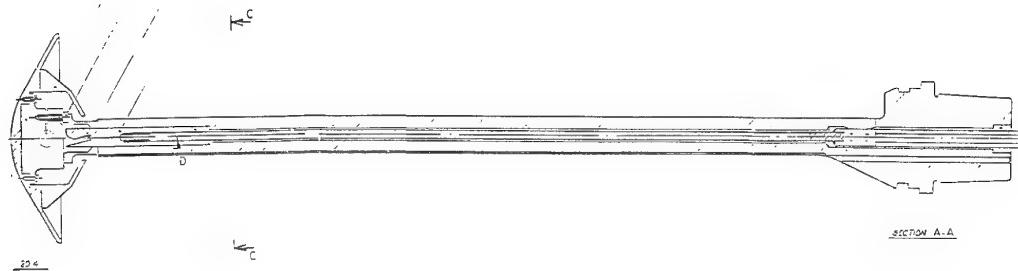
Figure n°22   ARA Dynamic Rig
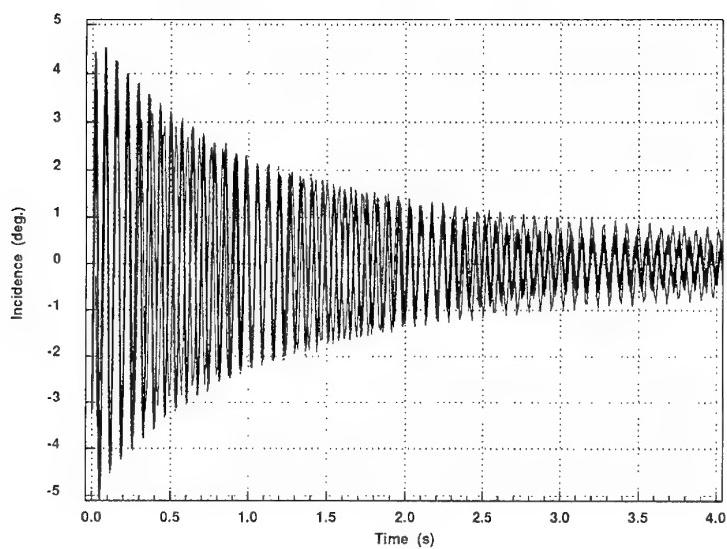
Figure n°23   HUYGENS Entry Module Cmq+Cmα˙ vs Angle-of-Attack at M=2.9

RADIATIVE HEAT FLUX
THEORETICAL AND EXPERIMENTAL PREDICTIONS FOR TITAN ENTRY PROBE

M. Baillion
Aerospatiale Branche Espace & Défense
Centre Opérationnel Systèmes
Département Aérodynamique & Electromagnétisme
BP 2
78133 Les Mureaux Cédex
France

G. Taquin
Aerospatiale Branche Avions
Centre Opérationnel Airbus
Département Avant-Projets
316 Route de Bayonne
31060 Toulouse Cédex
France

SUMMARY

This document presents the rationale of radiative heat flux predictions which were performed in the frame of the HUYGENS probe project.
Due to the particular nature of TITAN atmosphere, associated to the entry velocity of the probe, the radiative heat flux is almost half of the total heat flux.
In the thermal protection design process, accurate radiative heat flux calculations are needed in order to design a secured environment for onboard experiments, while mass penalties of thermal protection must be avoided.

This document describes the theoretical and experimental investigations of the radiative heat fluxes which were performed in the frame of the HUYGENS program.

1. INTRODUCTION

The CASSINI mission is a NASA/ESA program planned to explore the SATURNIAN system , and consits of a Saturn Orbiter sending the on-board HUYGENS probe to TITAN during its fly-by of SATURN.
The HUYGENS probe, which is under ESA responsability, with Aerospatiale Space & Defense as prime contractor, is a 60° half angle blunted cone, which uses aerobraking and decelerates through TITAN atmosphere from 6190 m/s at 1250 km altitude down to 400 m/s near 170 km. This extremely high velocity results in dissociation and ionization in the forebody shock layer. Moreover, the relaxation times of chemical and thermal processes involved are of the same magnitude than the characteristic time of the flowfield, the shock layer being so in full non equilibrium. As the TITAN atmosphere major constituants are N_2 (more than 77% in molar fraction), CH_4 (from 0 up to 3,5%) and Argon which may exist up to 20%, non equilibrium reactions result in CN creation which is known to be a strong radiator.
Dedicated calculations show that, for certain flight conditions, radiative heat flux may exceed the convective one. In the thermal protection design process, accurate radiative heat flux calculations are needed in order to insure a conservative design and to avoid mass penalties of thermal protection.

It is so desirable to validate radiative calculations by comparing theoretical results with experiments. Early in the HUYGENS program, comparisons have been undergone with existing shock tube tests performed by C.Park in a TITAN representative atmosphere gas medium.

However, the sensitivity of the radiative heat flux with respect to the upstream gas mixture had to be experimentally checked, and more insight in the non equilibrium region behind the shock was necessary, in order to add confidence in the radiative heat flux calculations for flight conditions.

Therefore, dedicated shock tube tests have been performed in the TCM2 facility at Université de Provence, Marseille, in France, for different upstream gas mixtures.

This document describes the rationale of the radiative heat flux predictions which have been performed in the frame of the HUYGENS program.

2. SHOCK LAYER PLASMA MODELISATION

Computations of radiative or convective heat fluxes require the plasma modelisation of the shock layer surrounding the entry probe. This paragraph describes the different techniques used.

### 2.1 Physico-Chemical formalism description
2.1.1 Chemical kinetics

A non equilibrium chemistry is assumed in the flowfield. A 3-temperatures model has been used and different relaxation schemes have been considered.

Chemical kinetics
At first the flowfield is assumed to be in vibrational equilibrium with the translation.
We consider s chemical species reacting together according to r reactions such as:

$$\sum_{j=1}^{s} \gamma'_{ij} M_j \xrightleftharpoons[K_{fi,eq}; K_{bi,eq}]{} \sum_{j=1}^{s} \gamma''_{ij} M_j$$
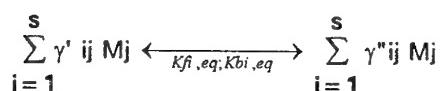
where γ''_{ij} and γ'_{ij} are the stoechiometric coefficients for the species j during the reaction i. Furthermore, $k_{fi,eq}$ and $k_{bi,eq}$ represent the chemical rates for the forward and backward reactions, respectively.

The chemical rate of change of the species j, taking into account the reaction i, is given by:

$$\left[\frac{dc_j}{dt}\right]_i = \beta_{ij}\left[K_{fi,eq} \cdot \prod_{j=1}^{s} c_j^{\gamma'_{ij}} - K_{bi,eq} \cdot \prod_{j=1}^{s} c_j^{\gamma''_{ij}}\right]$$

where $\beta_{ij} = \gamma''_{ij} - \gamma'_{ij}$ and c_j is the molar concentration of the species j [$= \rho_j / \hat{M}_j$].

The total chemical rate of change of the species j is obtained by summation over the r reactions.
The chemical rates are linked together by the following formula: $K_i = k_{fi,eq}/k_{bi,eq}$
where K_i is the equilibrium constant, i.e. the constant which enables, at equilibrium conditions, to calculate, together with conservation equations, the molar fractions of species.
This equilibrium constant K_i can be calculated from power series curve fit, within a certain range of temperature and pressure. However, in the HUYGENS case, where complete thermal non equilibrium occurs, the equilibrium constant is derived from the partition functions Q of the different chemical species implied in the reaction.

These partition functions describe the fraction of molecules in any excited state of the different modes of internal energy storage :

$$N_j^i = \frac{N_j}{Q} C_i \exp\left(\frac{-\varepsilon_i}{kT}\right)$$

Where N_j is the total amount of particle j
N_j^i is the number density of particles j in a given quantic energy ε_i level for translation, vibration, electronic or rotation, C_i is the number of possible representations of ε_i, k is the Boltzmann constant.
T is the corresponding temperature (for translation, vibration, electronic or rotation respectively), and the partition function Q is

$$Q = \sum_i \exp\left(\frac{-\varepsilon_i}{kT}\right)$$

The expression of these partition functions is derived from statistical mechanics (see Ref. 1).

Typically, one of the two reaction rates is given by a ARRHENIUS law, e.g. the forward rate, such as $k_f = aT^b e^{-c/T}$.

Vibration dissociation coupling modelisation
If we now assume a vibrational non equilibrium, we have to modify the previous formulation in order to take into account vibration dissociation coupling. Indeed, it has been experimentally checked that, when two atoms recombine for giving a diatomic molecule, this one is in a more excited vibrational state than the other molecules inside the flowfield. Reversally, the more a diatomic molecule is vibrationaly excited, the more probable this one can dissociate.
For a diatomic species dissociation reaction i, we write :

$$k_{fi} = k_{fi,eq} \cdot \prod_{j=1}^{s} V_j^{A_{ij}} \text{ and } k_{bi} = k_{bi,eq}$$

The exponent A_{ij} is a binary coefficient equal to 1 if the species j is present during the reaction i and if we consider its vibrational non equilibrium; if not, A_{ij} is equal to 0.

The term Vj corresponds to the vibration dissociation coupling factor for the species j. If we assume the equi-probability of dissociation whatever the vibrational energy level considered (see Ref. 2,3), we obtain :

$$Vj = \frac{Qv(T) \cdot Qv(Tmj)}{Nj\ Qv\ (Tvj)}$$

Where Qv is the partition function associated with the vibration. Tmj is a mean temperature given by

$$1/Tmj = 1/Tvj - 1/T$$

Nj represents the number of vibrational levels for the species j.

Translation-vibration energy exchanges

The rate of change in the population of the vibrational states at low temperature is well described by the LANDAU-TELLER formulation where it is assumed that the vibrational level of a molecule can change only one quantum at a time (see Ref. 1). The resulting energy exchange rate is :

$$QT\text{-}v,j\ =\ \rho j\ \frac{ev_j^{\,eq}(T)\ -\ ev_j}{\tau j}$$

where $ev_j^{eq}(T)$ is the vibrational energy per unit mass in local equilibrium with the translational temperature and τj is the vibrational relaxation time for the species j.

$$\left[ev_j^{\,eq}(T)\ = \frac{\hat{R}}{\hat{M}_j} \cdot \frac{\theta_{vj}}{\exp(\theta_{vj}/T)-1} \right]$$

When we take into account the effect of the dissociation on the vibrational energy history, this equation is modified according to :

$$Q_{T\text{-}v,j} = \rho_j \cdot \frac{ev_j^{\,eq}(T)\ -\ ev_j}{\tau_j} - \rho_j \cdot \frac{E_v(T,T_{vj})-ev_j}{C_j}\left[\frac{dC_j}{dt}\right]_f$$
$$+\rho_j \cdot \frac{G_v(T)-ev_j}{C_j}\left[\frac{dC_j}{dt}\right]_b$$

where Cj is the mass fraction of the species j. The second term represents the loss of vibrational energy due to the dissociation whereas the third term represents the gain of

vibrational energy due to the recombination. Ev and Gv are developed in Ref. 2,3.

An expression developed by MILLIKAN and WHITE yields the vibrational relaxation time, τj (Ref. 4). Two others laws have been checked: WOOD and SPRINGFIELD (see Ref. 5) and PARK's modification: at high vibrational temperature, the vibrational ladder climbing process due to heavy particles collisions is diffusive in nature, PARK (see Ref. 6,7) proposes an empirical bridging function between the LANDAU TELLER and diffusive rates.

A second modification is made to take into account the limiting cross section at high temperatures. PARK proposes a new relaxation time $\tau c,j$ to correct this unadequacy. Hence, we get

$$\tau j = <\tau j> \text{ (Millikan \& White)} + \tau c,j$$

Translation-electron energy exchanges

The energy transfer rate between the heavy particle and the electron translational modes is given by LEE (see Ref. 8)

$$Q_{T\text{-}e} = 3\hat{R}\rho_e(T-T_{e-})\sqrt{\frac{8\hat{R}T_{e-}}{\pi\hat{M}_{e-}}}\sum_{j\ne e-}\frac{\rho_j\hat{N}_o}{\hat{M}_j^{\,2}}\sigma_{ej}$$

where σej is the collision cross section for electron-species interactions.

$\hat{N}_o$ is the Avogadro number.

Electron-vibration energy exchanges

The rate of energy transfer between electron translational modes and nitrogen vibrational modes is given by:

$$Q_{ev,j} = \rho_e \frac{\hat{M}_j}{\hat{M}_e}\frac{ev_j^{\,eq}(T_{e-})-ev_j}{\tau_{ej}}$$

for j=N$_2$

where $ev_j^{eq}(Te)$ is the vibrational energy per unit mass in local equilibrium with the electronic temperature.

The relaxation time of electron-vibration energy transfer $\tau e,j$ is given by Ref. 8.

Conservation equations set

The resolution of the different conservation equations(mass, momentum, species mass fraction, vibrational and electronic energy) leads to the evolution of the characteristic thermochemical parameters along any flowfield streamline.

The vibrational energy conservation equation may be written under the form

$$\frac{dev_j}{dx} = \frac{ev_j^{*eq}(T) - ev_j}{u \cdot \tau_j} + \frac{E_v(T,T_{vj}) - ev_j}{u \cdot C_j}\left[\frac{dC_j}{dt}\right]_f$$

$$-\frac{G_v(T) - ev_j}{u \cdot C_j}\left[\frac{dC_j}{dt}\right]_b + \frac{\rho_e}{\rho_j}\frac{\hat{M}_j}{\hat{M}_e}\frac{ev_j^{*eq}(T_{e-}) - ev_j}{u \cdot \tau_{ej}}$$

The three first terms of the equation represent QT-v,j/(ρju), the last term corresponds to Qe-v,j/(ρju).
The electronic energy conservation equation may be written under the form

$$\frac{3}{2}\frac{\hat{R}}{\hat{M}_e}\frac{\partial T_e}{\partial x} = -\frac{p_e}{\rho_e u}\frac{\partial u}{\partial x} + \frac{Q_{T-e}}{\rho_e u} - \frac{Q_{e-v,j}}{\rho_e u}$$

$$-\frac{\sum_s\left[\frac{\partial C_s}{\partial t}\right]_f \hat{I}_s}{\rho_e u}$$

The second and third terms represent respectively the energy exchange between electronic and translational, and electronic and vibrational energies, the last term represents the change of electronic energy due to ionization reactions.

2.1.2 Thermochemical models

The gas within the shock layer of the HUYGENS probe is assumed to be a perfect gas mixture of 20 species: CH_4, CH_3, CH_2, CH, H_2, C_2, N_2, CN, NH, N_2+, $CN+$, H, C, N, Ar, $H+$, $C+$, $N+$, $Ar+$ and $e-$.

These chemical species can react together according to 30 chemical reactions (see table n° 1: "Complete chemistry").

This table gives the coefficients of the ARRHENIUS formula for the forward reaction rates: it has been established by using data from NELSON (see Ref. 9) and PARK (see Ref. 10,11).

Sensitivity studies have been done with this complete set of chemical reactions, particularly dealing with ionization reactions which control the electron production rate (important parameter for the flowfield radiative emissivity).

Hence, in Ref. 9, ionization of N, C, H and Ar is catalysed by electrons and heavy particles whereas in Ref. 10 and 11, Argon ionization is catalysed by electrons and Argon, whereas Nitrogen, Carbon and Hydrogen ionizations are catalysed only by electrons.

Simpler chemical reactions sets have also been used, particularly for non-equilibrium NAVIER-STOKES flowfield calculations around the stagnation point, for reasons of cost and time saving. The code is the Aerospatiale's FLU3NEQV (see Ref. 21). These other chemical reactions sets are listed in table n° 2: "Reduced chemistry".

Only N_2 vibrational non-equilibrium is modelized in the shock layer plasma.

For N_2 vibrational relaxation time modelisation, 3 types of law have been tested:

WOOD and SPRINGFIELD (see Ref. 5)

$$p \cdot \tau_v(N_2) = \frac{A \cdot T^B \cdot \exp(C \cdot T^{-0.333})}{(1 - \exp(\frac{-\theta_v}{T}))}$$

with　　$A = 6.4 \ 10^{-13}$ atm.s
　　　　$B = 0.5$
　　　　$C = 192 \ K^{1/3}$
　　　　$\theta v = 3 \ 353.5 \ K.$

MILLIKAN and WHITE (see reference 4)

$$p \cdot \tau_v(N_2) = A \cdot \exp(C \cdot T^{-0.333})$$

with　　$A = 1.69 \ 10^{-11}$ atm.s
　　　　$C = 220 \ K^{1/3}.$

MILLIKAN and WHITE with PARK correction (see Ref. 6,7)
In these expressions, p is the pressure in atm.

2.2 Plasma modelisation along the stagnation streamline

Computations of the forebody radiative or convective heat fluxes require the bow shock layer plasma to be modelised.
This type of calculation can be very expensive, in term of computer time, and must moreover be performed along the entry module trajectory, in order to size the Thermal Protection System (TPS). The methodology consists therefore in

deriving stagnation heat flux all along the trajectory, while the evolution over the front heatshield is completed by multiplying a nondimensionned profile f(s) by the stagnation value ,

$$f(s) = Q(s,M)/Q,st(s,M)$$

where s is a curvilinear abscissa, M is the Mach number, subscript st stands for stagnation condition and Q is either radiative or convective heat flux.

The computation of the stagnation condition can be assessed by a stagnation line computation, if diffusion process inside the bow shock layer is not too important. The following part describes comparisons between complete bow shock layer computations, and stagnation line ones.

2.2.1 Numerical approaches description

The methodology used for computing stagnation heat flux is based on a decoupled approach: first, a perfect gas, bidimensional inviscid flowfield is computed by a finite differences, explicit, unsteady EULER code around the entry module in order to get the pressure field.

Then, non-equilibrium chemistry is calculated along the stagnation streamline by using the pressure profile coming from the EULER output and by assuming a total enthalpy conservation across the shock and in the shock layer.

N_2 vibrational relaxation and electronic temperature profiles are computed, also, along the stagnation streamline.

The EULER computations are performed with an upstream specific heat ratio $\gamma = 1.4$ and a $\gamma = 1.3$ in the shock layer in order to take into account real gas effects occurring behind the shock at high Mach numbers.

This uncoupled approach has been compared with coupled approaches based either on non-equilibrium NAVIER-STOKES computations assuming thermal equilibrium or on non-equilibrium EULER computations assuming N_2 vibrational relaxation. These comparisons are the subject of the following paragraph.

2.2.2 Chemical non-equilibrium NAVIER-STOKES/EULER computations presentation

NAVIER-STOKES computations

NAVIER-STOKES computations are performed on a sphere-cone shape (Rn = 1.25 m, cone angle = 40 deg.) representative of the HUYGENS entry module geometry in the stagnation region. These computations assume chemical kinetics non-equilibrium but thermal equilibrium (no species vibrate; only, one temperature is considered).

Two simplified chemical kinetics are considered (they are detailed as set n° 1 and n° 2 of table n° 2).

For the chemical set n° 1, we consider the following species:

CH_4, N_2, CH, CN, H_2, H, N, C, Ar.

For the chemical set n° 2, we consider the following species:

N_2, CN, H_2, H, N, C, Ar.
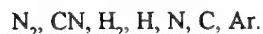
For computations dealing with chemical set n° 2, we assume that CH_4 is immediately dissociated at the shock in carbon and hydrogen atoms: the energy consumption involved in this reaction is taken into account in the total energy balance at the shock (this assumption of instantaneous dissociation of the methane is clearly justified due to the dissociation rate magnitude of methane compared to other species).

The flowfield viscosity and conductivity are obtained by using the semi-empirical formula of WILKE and the EUCKEN's formula, respectively.

We assume a 1.4 constant LEWIS number for the diffusivity modelisation.

Computations have been done for the following upstream conditions:

Z= 253.751 km   M= 19.75
P= 13.37 Pa   T= 145 K

(which is a representative point for TITAN entry: maximum heat flux point for - 75° slope entry with a 270 kg probe mass and nominal density).

Two chemical upstream compositions have been tested: (2 % CH_4, 98 % N_2) and (2 % CH_4, 78 % N_2, 20 % Ar), in volume.

Figures n° 1 and n° 2 represent the pressure and density profiles along the stagnation streamline: the evolutions are quite similar between the different cases.
Figure n° 3 represents the temperature profile along the stagnation streamline; Argon presence increases a bit the temperature level: Argon, being an inert gas, doesn't react and so doesn't consume any flowfield energy which tends to increase the flowfield energy (temperature) with respect to the case without Argon.

By increasing the temperature level, Argon presence decreases the density level and so tends to increase the shock-stand off distance: this increase is rather small (5 %).

When assuming no Argon, the two chemical sets give very close results, except near the shock: with the complete chemical set, the energy consumption due to the methane dissociation occurs along a certain distance behind the shock whereas with the simplified chemical set, this one is instantaneous.

Figures n° 4 and n° 5 represent the CN and C molar fraction profiles along the stagnation streamline, respectively. Argon presence tends to decrease CN and increase C concentration: in fact, Argon presence, by increasing N concentration, make the exchange reaction evoluate in the direction
$N + CN$ gives $C + N_2$, resulting in a CN decrease and C increase.

Conclusions
Argon presence increases shock layer temperature and shock-layer stand off distance.
Argon presence decreases shock layer CN concentration.

EULER computations

Comparisons have also been done with EULER computations assuming both thermal and chemical non-equilibrium on the nominal geometry of the HUYGENS entry module.

Comparisons are shown for the following upstream conditions:

$Z = 253.751$ km, $M = 19.75$ ($\gamma c = - 75°$, 270 kg mass, nominal density)

Two chemical upstream compositions have been tested for the EULER comparisons: (2 % CH_4, 78 % N_2, 20 % Ar) and (3.4 % CH_4, 75.6 % N_2, 21 % Ar) in volume.

For the EULER computations, a chemical set very close to the complete chemistry one (see table n° 1) has been used.

Figures n° 6 represents the CN molar fraction profiles along the stagnation streamline: the CN comparisons are particularly good except near the wall where a boundary layer effect in the NAVIER-STOKES computation explains the differences.

Conclusions
The comparisons between non-equilibrium chemical EULER and NAVIER-STOKES computations give coherent trends with respect to chemical effects.

2.2.3 EULER + Chemistry along stagnation streamline
Comparisons with the coupled approach

The uncoupled approach is based on a non-equilibrium chemistry computation along the stagnation streamline, assuming a total enthalpy conservation across the shock (and in the shock layer).

The uncoupled approach assumes the chemical set given in table n° 1 (complete chemistry).

Temperature comparisons (on figure n° 7) show also very good agreement between both methods: NAVIER-STOKES gives a slightly greater value in the shock layer because no ionisation is modelised.

Chemical species comparisons are indicated on figures n° 7: they are quite satisfactory, except near the wall because of the boundary layer effect.

Conclusions

These comparisons clearly demonstrate that the uncoupled approach is fully coherent with the coupled approach EULER or NAVIER-STOKES (assuming the same kind of thermo-chemical modelisations).

Hence, for heat flux computations, the uncoupled approach is extensively used for reasons of cost and time saving.

Figure n° 8 represents the translational temperature, the N_2 vibrational temperature and the electronic temperature profiles along the stagnation streamline for the Mach 19.76 case assuming (77 % N_2, 3 % CH_4, 20 % Ar) as upstream chemical composition.

After the shock, the electronic temperature increases slowly because it is driven by the free electrons production which is rather small (for these conditions).

However, as electron is its own catalycist for the ionisation reactions, as soon as there are a certain quantity of electrons in the shock layer, there is an "avalanche" type process which greatly increases the electronic production. Then, when the electronic energy has achieved a certain level, the N_2 - vibrational energy coupling becomes prominent and both curves (N_2 vibrational temperature/electronic temperature) collapse in an unique one.

Figure n° 8 also shows the temperature sensitivity with respect to the N_2 vibrational relaxation time modelisation.

The two extreme cases are the WOOD and SPRINGFIELD correlation (biggest relaxation time) and the MILLIKAN and WHITE correlation (smallest relaxation time). The MILLIKAN and WHITE correlation with the PARK correction gives an intermediate solution.

2.3 Plasma modelisations before the entry module

Plasma modelisations of the shock layer before the entry module is required for radiative heat flux profile along the forebody geometry. Shock layer plasma modelisations have been obtained with a shock capturing EULER code assuming N_2 vibrational temperature and non-equilibrium chemistry. The chemical set used is very close to the complete chemistry one (see table n° 1). For the N_2 vibrational law, we assume the MILLIKAN and WHITE N_2 vibrational relaxation time modelisation.

Concerning the (2 % CH_4, 78 % N_2, 20 % Ar) computational case, figure n° 9 show N_2 iso-vibrational temperature lines patterns which remains at a rather high level before the conical part of the frontshield ($Tv(N_2) \geq 7\,000$ K).

On figures n° 10 the iso-CN molar fraction lines pattern is shown. Again, CN molar fraction tends to keep levels which are close to stagnation region ones on the conical part of the frontshield; furthermore, in the expansion region around the corner tip, chemical species tend to keep their molar fractions levels: this is due to a freezing type process characteristic of quick expansion area where the chemical production rates tend to cancel (due to sharp density decrease).

2.4 Plasma modelisation around the entry module

2.4.1 Perfect gas NAVIER-STOKES computations

Plasma modelisation around the entry module, and particularly the knowledge of the near-wake structures, is required for assessing the radiative heat flux loads applied on the back-cover.

Laminar NAVIER-STOKES computations (Aerospatiale code FLU3PNS, see Ref. 22) have been carried out around the entry module shape for the worst thermal protection system material case trajectory (Ve = 6.19 km/s, γe = -66.1°, Entry Probe Mass = 301 kg, minimum density and temperature atmosphere), which corresponds e.g. to the following conditions :

Altitude = 259.940 km

P $\quad$ = 11.41 Pa
Mach $\quad$ = 20.55
T = 145 K

A perfect gas modelisation is considered here; however, a specific heat ration γ =Cp/Cv equal to 1.2 is assumed in order to take into account the temperature decrease in the shock layer due to real gas effects.

Figures n° 11 represents the iso-pressure lines pattern. The wake main structures can be clearly identified: the shoulder expansion region around the tip corner, the free shear layer between this expansion area and the recirculation region, the neck recompression zone characterized by high temperature levels followed by the recompression shock.

Figure n° 12 shows a flowfield streamlines pattern picture; one can identify two main regions:

> -an "inviscid" region characterized by streamlines which are generated from the upstream conditions (before the bow shock).

> -a "viscous" region constituted by the recirculation region and a part of the neck and the recompression region.

It is also interesting to note the presence of two vortices in the recirculation region.

2.4.2 Wake plasma computations

For modeling radiative heating in base region of the GALILEO JOVIAN entry probe, PARK (see Ref. 12) has derived a theoretical model which determines the average thermodynamic properties in the shoulder expanding region, recirculation region, and neck region through application of one-dimensional conservation equations. The shoulder expanding region was treated in thermal and chemical non-equilibrium whereas the recirculation and neck regions, where average velocity was relatively low, were considered in thermodynamic equilibrium.

Hypersonic wake flows behind the Aeroassist Flight Experiment (AFE) are carefully studied for assessing radiative and convective base heat loads in low REYNOLDS environment. The analysis of the non-equilibrium solutions of

PALMER (Ref. 13) and GNOFFO (Ref. 14) show the afterbody flow, soon after the shoulder expansion, to be both chemically and thermally frozen: the species concentration and the vibrational temperature along the streamlines did not change significantly after the shoulder expansion. This result is confirmed by recent studies from VENKATAPATHY, PALMER and PRABHU (Ref. 15).

For TITAN HUYGENS entry probe, three different ways have been investigated:

Chemical equilibrium computation

The simplest way is to perform a chemical equilibrium computation for the entire near-wake flowfield, by considering as inputs data the pressure and temperature values from the perfect gas NAVIER-STOKES calculations.

Non-equilibrium LAGRANGIAN type computation

The flowfield around the body is nearly constituted by the "inviscid" region which is characterized by the highly reactive shock layer before the front shield and the expansion region, from the tip corner down to the neck region, associated with chemical and vibrational freezing phenomena. This region can be considered to be nearly fully inviscid: the only dissipative zones are limited to narrow frontier regions like the boundary layer along the forebody, or the shear layer which makes the separation with the recirculation region. Hence, for plasma computation, it is valid to adopt a LAGRANGIAN type approach where chemical and thermal non-equilibrium is performed along different streamlines.

Figure n° 13 shows that the static temperature levels are close between both methods; however the non-equilibrium modelisation tends to give lower static temperature with respect to the equilibrium one (in the non-equilibrium modelisation, a certain part of the flowfield energy is conserved inside the N_2 vibrational energy levels which tends to freeze; hence, there is less available energy for the translational modes with respect to the equilibrium computation).

Figure n° 14 represents the CN molar fraction distribution inside the near-wake flowfield. The upper part comes from the equilibrium

chemical computation from the NAVIER-STOKES results whereas the lower part comes from the non-equilibrium LAGRANGIAN modelisation. It is striking to observe the important differences between both cases. In the shock layer before the forebody, the equilibrium computation gives very low level of CN compared with the non-equilibrium one: this is now a well-known result since PARK and NELSON works, the CN molecule is not stable at high temperature. Hence, a chemical equilibrium computation will give small levels of CN concentration whereas, if non-equilibrium chemistry is considered, CN molecules is first highly produced at the shock by the exchange reaction $C + N_2 \leftrightarrow CN + N$ and then (very) slowly consumed in the shock layer by the dissociation reaction $CN \leftrightarrow C + N$.

In the near-wake flowfield, the situation is inverted: the equilibrium computation tends to give (relatively) high CN concentration due to the low temperature level, whereas, in the non-equilibrium modelisation, during the shoulder expansion, the CN species is quickly consumed by the (rapid) exchange reaction $CN + N \leftrightarrow C + N_2$ and then freezes at very low levels ($< 10^{-3}$) in the entire afterbody flowfield.

Non equilibrium Navier Stokes computations
The most complete, but is very CPU-time consuming

After having reviewed the calculation techniques of the flowfield kinetics surrounding the entry module, the radiative characteristics must be checked, and the calculation of the emissivity of the shock layer and wake, must be confirmed by comparison with experience.

3. ANALYSIS OF EXISTING EXPERIMENTAL RESULTS
3.1 Scope of the work

Chung Park (Ref. 20) has performed shock tube experiments with a gas mixture representative of a TITAN atmosphere in order to measure radiative emissivities.
When the upstream quiet gas comes across the shock wave, its kinetic energy and the different modes of internal energy (rotational,vibrational,electronic) are excited. This enthalpy increase results in the starting up

of a complex chemical process which transforms, via very quick reaction rates, the upstream gas mixture in a plasma which evolves towards an equilibrium state where the new chemical species are stable. In a similar trend, the storage of internal energy is shared in such a way that it tends towards an equilibrium partition, at a rythm imposed by the exchanges between the different energy modes.
This relaxation process results in the creation of strong radiator molecules such as CN, at very high electronic temperature in the first part of the downstream flowfield which is in thermal and chemical non equilibrium, and then, in an equilibrium zone where radiation vanishes.

The condition of Park's tests are : p=266Pa ; V=5750m/s T=300K
and the upstream chemical composition is 95.7% N_2, 3%CH_4, 1%Ar, 0.3% H_2 in molar fractions.
The experimental outputs in the thesis consist of the measurements of several monochromatic emissivities behind the shock, corresponding to the main transitions of the strongest radiators in the plasma.We shall focus only on the main transitions of CN.

The scope of this step of the radiative studies is to numerically simulate the plasma, and then to calculate the quantities equivalent to the experimental data. The comparison with the experimental values will give us an appreciation on the deviation between the total calculation process used to get emissivities, and the actual behaviour of the plasma in shock tube conditions, in order to derive a best estimate radiation model with associated margins.

3.2 Methodology

We first have to solve the basic equations of motion and the conservation equations of mass and energy for the different species. The species number densities, used with pressure and temperatures are then used to compute the population of excited molecules, with a quasi steady state approach, and compute radiative emissivities.
It is then clear that comparison experiment/calculation is available to test the validity of the whole numerical process, but the

difficulty is that a discrepancy from anyone of the numerical step may be compensated by another one , and thus not be detected.

3.3 Comparison calculation/experiment

Several theoretical hypothesis have been checked in order to simulate the plasma behaviour behind the shock.

Each one of the theoretical hypothesis is considered as an option in our numerical approach, which is switched on/off for the simulations in order to check the sensitivity of the radiative properties of the plasma with respect to the physical process of interest. The final goal is to decrease (ε - ε_{exp}) where ε is a monochromatic emissivity integrated over the spectral area corresponding to the slit area, and ε_{exp} is the experimental measured value.

3.3.1 Comparisons calculation/experiment

Figure n°15 shows the three temperatures and the molar fractions of the different species behind the shock for a particular set of hypothesis. The thermal and chemical non equilibrium zone extends 2 mm downwards the shock. The flowfield is not too far from equilibrium at 2cm downstream.

The emissivity peak occurs roughly between 1.2 and 1.5mm from the shock, in the non equilibrium region and is predominant for the $\Delta V=0$ transitions of the CN violet system.

3.3.2 Polyatomic species dissociation rate

The dissociation rate of the polyatomic species CH_4 was found to have a certain influence on the emissivity level in the equilibrium region. The reaction rates of dissociation for CH_3, CH_2, CH, are very fast (see Ref. 9,10). In our tentative to simulate the shock tube plasma, we either computed the complete sequence of CH_4 dissociation with associated finite rate, or we supposed a full dissociation of CH_4 in (CH ;3H) immediatly behind the shock. These two methods are referred as respectively "actual dissociation" and "CH_4 dissociated behind the shock".

Figure n°16 shows that the polyatomic dissociation rate (CH_4 actual dissociation in the plasma or the full dissociation of CH_4 at the shock) has no influence on the emissivity peak level, but it changes a bit the overshoot location. The main influence occurs after emissivity peak , where the CH_4 immediate dissociation at the shock hypothesis tends to reach quicker the equilibrium, and is, as a consequence, closer to the experimental values. The numerical reaction rates of the CH_4 dissociation are very high(#$10^{27}cm^3$/mole-s). The above results could mean that they are still unsufficiently high, though they are already numerically difficult to handle.

3.3.3 Relaxation law

Figure n°17 shows ε for the 3 different relaxation schemes.

The WOOD and SPRINGFIELD relaxation law is obviously not suitable for our case, as it gives a too low level of emissivities in the non equilibrium region.

Park's modification tends to give intermediate relaxation time between Millikan & White and Wood & Springfield and the resulting ε has a similar behaviour.

Emissivity peak occurs when the three temperatures collide. As the vibrational and electronic temperatures capability to rise up to the translational level is inversely proportional to the corresponding relaxation times in the energy exchanges processes, if τvt or τet is large (respectively relaxation time for vibrational-translational and electronic-translational exchange rates), the distance from the shock to collide is large. Moreover, the translational temperature decreases as we go far away from the shock. So if τ is large, the location where temperatures collide shifts farther from the shock, to a lower temperature level, and results in a lower emissivity overshoot.

This phenomenon is still amplified by the continuous decrease of the CN molar fraction from 1mm downward the shock.

The Millikan & White modelisation is found to give the emissivities which are the closest to the experimental values.

3.3.4 Vibration dissociation coupling

Figure n°18 shows the influence of the vibration dissociation coupling modelisation, which is accounted for in our modelisation.

3.3.5 Specific heat ratio behind the shock

Figure n°19 shows the influence of $\gamma_2=1.4$ or $\gamma_2=1.3$ behind the shock.

The overshoot distance from the shock remains unchanged, but the level slightly increases for $\gamma_2=1.3$ because this latter value gives higher pressure behind the shock, and then a greater number density of CN ($n=p/kT$).

3.3.6 Vibrational energy sharing

The vibrational energy sharing has been checked : N2 species alone was first considered to relax, the vibrational energy of all the poly- or di-atomic species being then in equilibrium with the translational mode. Then some cases were performed with all poly- or di-atomic species in vibrational non equilibrium. As the results are slightly the same, we will consider that all the poly- and di-atomic molecules relax like N_2, which is more realistic.

3.3.7 Ionization process

As the translational temperature of the plasma is very high, ionization occurs. The driving parameters of the ionization reactions have been assessed : catalysts of ionization reactions are either the free electrons alone(except for Ar $\iff Ar^+ + e^-$ catalysed by Ar and e^-) or free electrons plus heavy particles. Furthermore, these reactions are either driven by the translational temperature or by the electronic temperature.

By taking into account the heavy neutral species as catalyst for electron impact ionization reactions, we obviously increase the electron number density behind the shock, because heavy particles are always available to create electrons. At the opposite, when electrons alone are catalyst, a certain time elapses from shock crossing time to create electrons, which finally catalyse their own creation. The process is then amplified and known as the avalanche process.

Electrons increase the high energy levels population via non elastic collision, this results in emissivity increase.

It finally comes out, that within the cross checked theoretical models, two of them seem to be attractive :

1 Millikan & White plus Park's modification relaxation law
neutral species + electron as catalyst for ionization reactions (see fig. n° 20)
2.Millikan & White relaxation law
electron as catalyst for ionization reactions

For the two models : $\gamma_2=1.3$, vibration-dissociation coupling is modelized, CH_4 is dissociated at the shock and ionization reactions are driven by translational temperature.

However the model n°2 gives better results, especially in the overshoot region.

3.3.8. Best estimate theoretical hypothesis set

The reference model for the HUYGENS probe radiative heat flux calculations is then :

Millikan & White relaxation law
electron as catalyst for ionization reactions
ionization reactions are driven by translational temperature
$\gamma_2=1.35$
CH_4 is dissociated at the shock

Our numerical accuracy on the overshoot region lies within +/-3% for the main CN violet transitions, which is a fairly good result (see fig. n°21)

Conclusion

The analysis of the C.Park shock tube experimental results on a TITAN representative atmosphere have enabled us to find a best estimate set of kinetic hypothesis which is in good agreement with the measurements. This model is used as a reference for the HUYGENS probe radiative heat fluxes calculations.

The numerical calculations show Argon presence having a large effect on the radiative heat flux level : because Argon doesn't react with other species, it contributes to increase the shock layer temperature, and moreover, Argon is a strong catalyst for electron creation. Unfortunatelly, the C.Park thesis upstream gas mixture is very poor in Argon.

An experimental evidence of the Argon effect, including different upstream gas mixtures, was therefore needed, in order to assess the Argon effect, and to consolidate our radiative heat flux predictions. A dedicated shock tube campaign was therefore planned to take place at the Université de Provence facility TCM2.

Once a theoretical model was found to fit to the experimental data, in conditions close to flight ones, where radiative heat flux is significantly high, the radiative heat flux computations for TPS sizing can be undergone.

Obviously, the so called "best estimate" theoretical model is not thereby validated, but provides with reliable magnitude of the radiative heat flux. A margin policy has to be derived, which leads to about 75% uncertainty on the radiative heat flux.

The following paragraph describes the methodology for the calculation of the radiative heat flux on the entry module. This calculation takes into account different phenomena, like the absorptivity in the bow shock layer and the 3-dimensional calculation of the radiative heat flux.

4. COMPUTATION OF THE RADIATIVE HEAT FLUX ON THE HUYGENS ENTRY MODULE

4.1 Absorptivity effect

Radiative heat flux is due to incident photons emitted from particles that are deexcited. The total thickness of the shock layer in front of a probe surface point contributes to this phenomenon. The photons emitted by the zone immediatly behind the shock wave have to travel across the shock layer to reach the wall. As the gas medium in the shock layer is mainly composed of ground state molecules, these photons have non zero probabilities to be caught by these latter ones.

This phenomenon may be written under the form

$$\frac{\partial I^\lambda}{\partial x} = \varepsilon^\lambda(x) - k^\lambda(x) \cdot I^\lambda(x)$$

which describes the variation of the monochromatic radiative intensity I^λ in an arbitrary direction x in the gas medium,
ε^λ is the volumic monochromatic radiative emissivity,
k^λ is the absorption coefficient which includes the effects of bound-bound, bound-free and free-free transitions.

This equation may be integrated in a homogeneous gas medium:

$$I^\lambda = I_0^\lambda \cdot \varepsilon^{-\tau} + \frac{\varepsilon^\lambda}{k^\lambda} \cdot (1 - e^{-\tau})$$

(see ref. 16)

where τ is the optical depth $\tau = k^\lambda dx$,
dx is the width of the gas medium,
I_0^λ is the incident radiative intensity.

This equation is integrated numerically by considering that each point of the radiation code grid used to calculate the radiative heat flux is the center of an homogeneous gas medium receiving an incident radiative intensity I_0^λ emitted from the previous grid cell.

4.2 Curvature effect and radiative heat flux profile

In order to size the TPS, we need to know the radiative heat flux evolution versus time, or altitude, and its variation along the probe meridian.

As a radiative heat flux received on a point M of the probe surface is the result of the radiative intensity emerging from all directions seen from M, it requires to know the radiative power emitted from each point P of the plasma.

This emissivity is very CPU time consuming to compute as it needs to calculate the whole chemical and thermal non-equilibrium flowfield as well as the excitation process of each quantified energy level.

The simplest hypothesis consists in assuming a monodimensional plasma in front of the stagnation point. This leads to a simple expression of the radiative heat flux which implies to compute only the stagnation streamline. This gives us the stagnation point value. The radiative heat flux was assumed constant along the probe.

The following developments will show what is the complete expression of the radiative heat flux on a current point of the probe surface, and how it is related to the monodimensional assumption.

4.2.1 Formulation of radiative heat flux
4.2.1.1 Complete formulation of radiative heat flux

As the probe is entering TITAN atmosphere at very high velocity, a bow shock is created in front of the forebody. The high velocity upstream gas medium is changed in a high enthalpy plasma shock layer. The excited high energy levels population tends to increase (electronic, vibrational, rotational, translational) and in falling down to fundamental energy levels, emits high energy photons in whole space (4π steradians).

This is called radiative power or emissivity.

Let us call $d\varepsilon_\lambda$ the radiative volumic power emitted from P in the wavelength range (λ; $\lambda +$ $d\lambda$).

The power emitted from P is then:

$$d\varepsilon_\lambda \cdot dV$$

where dV is an elementary volume surrounding P

$$dV = r^2 \sin\theta \, dr \, d\theta \, d\phi$$

The radiative heat flux at M is then:

(1)

$$Qr(M) = \int_{\lambda=0}^{\infty} q_r^\lambda(M) \cdot d\lambda$$
$$= \int_{\lambda=0}^{\infty} \int_{r=0}^{\infty} \int_{\theta=0}^{\pi/2} \int_{\phi=0}^{2\pi} \frac{d\varepsilon_\lambda(r,\theta,\phi,\lambda)}{4\pi} \cdot \cos\theta \cdot \sin\theta \cdot dr \cdot d\theta \cdot d\phi \cdot d\lambda$$

4.2.1.2 Stagnation point radiative heat flux

The expression (1) should be used at each point of the probe.

Nevertheless, it is possible to reach a more simple expression for the stagnation point radiative heat flux when incidence is zero, as the flowfield is axisymetric. Then it comes

$$\frac{\partial E_\lambda}{\partial \phi} = 0$$

and therefore,

(2)

$$Q_r(0) = \frac{1}{2} \int_{\theta=0}^{\pi/2} dE(\theta) \cdot \sin 2\theta \cdot d\theta$$

where

$$dE(\theta) = \frac{1}{2} \int_{r=0}^{\infty} d\varepsilon(r,\theta) \cdot dr$$

and

$$d\varepsilon(r,\theta) = \int_{\lambda=0}^{\infty} d\varepsilon(r,\theta,\lambda) \cdot d\lambda$$

This expression n° 2 requires to know dE (θ) which is the summation of emissivities on a direction L inclined of an angle θ with respect to the longitudinal axis of the probe, for each θ in [0; $\pi/2$].

Q_R (0) is then the exact expression of the radiative heat flux which has been simplified due to the geometrical property of the flowfield.

4.2.1.3 Monodimensional approximation

It is then possible to still more reduce the emissivity flowfield to be calculated, by making a more restrictive hypothesis which consists in assuming that the bow shock in front of the stagnation point is normal.

This leads to a monodimensional plasma and then, if we note $\tilde{q}_R(0)$ the stagnation point radiative heat flux calculated with this monodimensional assumption, we have

(3)

$$\tilde{q}_R(0) = dE(\theta = 0)$$

It turns out that the monodimensional stagnation point radiative heat flux is equal to the summation of emissivities over the direction L for $\theta=0$.

This last expression is obviously very efficient to get in a faster way a stagnation point radiative heat flux, but is poor in that sense that it doesn't take into account the curvature effect at stagnation point. Because of the need of accuracy on radiative heat flux, it seemed useful to develop a methodology to implement the exact formulation (n° 1) in our radiative heat flux calculations, for stagnation point as

well as for a current point of the probe meridian.

4.2.2 Methodology applied to the HUYGENS probe
4.2.2.1 Stagnation point curvature effect

The practical way to proceed in order to predict a radiative heat flux is based on a decoupled approach which has been described earlier. This methodology requires the knowledge of the chemistry on the stagnation streamline.

The curvature effect at stagnation point using formulation (2) is available if one knows the chemical and thermal non- equilibrium plasma surrounding the probe. This computation has been undergone for some flight conditions and for different upstream chemical compositions. It becomes then possible to check the ratio $q_R(0)/\tilde{q}_R(0)$, i.e. the "curvature effect" at stagnation point ($\tilde{q}_R(0)$ is the radiative heat flux calculated with a monodim-approach).

$$q_R(0)/\tilde{q}_R(0) \; \# \; 0.8$$

Which means that the curvature effect at stagnation point results in a 20 % decrease of a monodimensional radiative heat flux calculation.

The upstream chemical composition has no appreciable influence on this coefficient for the stagnation point

4.2.2.2 Three dimensional radiative heat flux profile

The previous formula of radiative heat flux at a point M of the entry module surface, versus location of radiating elementary gas cell, enables a complete 3 dimensional radiative heat flux map to be computed, for the zero angle-of-attack trim condition of the entry module during Titan entry.

The figure n°22 shows the radiative heat flux profile versus curvilinear abscissa along the probe.

5. BACK-COVER RADIATIVE HEAT FLUX PROFILE
5.1 Experimental evidence of radiative base heating

The possibility that there may be substantial radiation in the afterbody region of a re-entry body at high entry speeds was first considered for the APOLLO program.

In 1965, STEPHENSON (see Ref. 17) launched axisymmetric blunt body models in a ballistic range at flight speeds up to 10 km/s: he succeeded in showing evidence of strong radiation in the wake and deduced a base-to-front-stagnation radiative heat flux ratio qb/qst of about 5 %.

In 1969, prior to APOLLO missions, a flight experiment of a 1/3 scale model of the APOLLO vehicle, named FIRE (see Ref. 18), was flown at a speed of 11.3 km/s to study the radiative heating phenomena on both the forebody and the afterbody regions. The measured radiative flux on the leeward side was determined by CAUCHON to be approximately equal to 5 % of that at the forebody stagnation point.

In the 1970s, experimental measurements were made by SHIRAI and PARK (see Ref. 19) to determine the magnitude of the radiative flux expected on the base region of the GALILEO JOVIAN entry probe: they obtained a base to front stagnation radiative heat flux ratio qb/qst of about 3.5 %.

According to the PARK theory (see Ref. 12), the ratio of the base to front stagnation point radiative heat flux, qb/qst, can be written approximately as:

$$q_b/q_{st} = 0.041 \cdot f^1(pb/pst) \cdot f^2(W/D) \cdot f^3(x/D) \cdot f^4(d/D)$$

where $f^1(pb/pst) = [(pb/pst)/0.023]^2$

$f^2(W/D) = [(W/d)/0.667]^2$

$f^3(x/D) = 1.5/(x/D)$

$f^4(d/D) = 0.0185/(d/D).$

In these expressions:

pb/pst is the volume averaged in the recirculating region to stagnation point pressure ratio,

W/D is the neck region to the cone frustum diameter ratio,

x/D is the neck position to the cone frustum diameter ratio,

d/D is the shock stand off distance to the cone frustum diameter ratio.

Although this formula has been developed for the Jovian entry conditions, it is believed to be valid approximately even when the radiating species are different from those in the Jovian case.

Furthermore, this correlation formula has given good comparisons with respect to experimental measurements done in different shock tube facilities (see Ref. 19).

The different arguments which are implied in the correlation formula can be evaluated from the NAVIER-STOKES computations done around the entry module.

The PARK correlation formula gives a 3 % ratio for the HUYGENS Entry Module base to front stagnation point radiative heat flux.

5.2 Computational results
5.2.1 Introduction

According to PARK works (see Ref. 12 and 19), there are 3 main radiative (active) zones which contribute to the radiative heat flux environment on the back-cover shape:

- the recirculation region, characterized by (usually) a low temperature environment, but close to the back-cover,

- the tip corner expansion region, characterized by chemical and vibrational freezing processes which may contribute to keep rather high levels of radiative species concentration,

- the neck region characterized by a recompression which tends to give a (rather) high pressure and temperature level region.

The plasma computation behind the HUYGENS entry module has been obtained from two different modelisations:

-a chemical equilibrium computation from pressure and temperature fields coming from a NAVIER-STOKES, perfect gas calculation ($\gamma = 1.2$),

-a chemical and vibrational non-equilibrium LAGRANGIAN type modelisation using the pressure and velocity fields from a NAVIER-STOKES, perfect gas computation ($\gamma = 1.2$).

These modelisations confirm PARK remarks: a neck region characterized by a temperature increase (see figure n° 13) and a tip corner expansion associated with (rather) high levels of CN concentration (see figure n° 23).

Experimental data of STEPHENSON (see Ref. 17) show that the high luminosity of the neck region extends over approximately 1 body diameter; then in the region downstream of the bright region, the luminosity attenuates gradually. For its theoretical afterbody flowfield modelisation, PARK has represented the neck region by a cylinder of uniform luminosity having a radius equal to the neck radius and a length equal to 1.5 body diameters.

This is coherent, for instance, with flowfield temperature distribution showed in figure n° 13 where the hot neck region extends over about 1.5 body diameters.

Conclusions:

Taking into account curvature effect and absorptivity, the base to stagnation radiative heat flux ratio represents about 3 % (in the worst case: chemical equilibrium), which is in agreement with PARK correlation results.

The radiative heat load will probably stay below this 3 % value along the back-cover profile and the decelerator leeward side; except for the back-cover face, inclined to 15° with respect to the axis of symetry direction, which is submitted to an important radiative emission coming from the frozen expansion flowfield around the tip corner (the radiative heat load represents about 20 % of the stagnation radiative heat flux level from a monodimensional calculation; by taking into account 3D effect, this value will be probably decreased down to 14 %).

This result is confirmed by PARK works on the JOVIAN probe (see Ref. 12): he calculated that the radiation flux emerging from the shoulder expansion region was about 5 times greater than the base level.

6. RADIATIVE HEAT FLUX MARGIN POLICY
6.1 Margin contents

The radiative heat flux margin policy is built in order to provide, from the knowledge of the nominal radiative heat flux, the range of variation which is known, for sure, to contain the radiative heat flux actually encountered by the probe during the mission.

The nominal heat flux is the result of a numerical calculation which is supposed to modelize all the physical processes involved in the emissivity phenomenon. The sizing procedure of the TPS thickness needs as an input the evolution of the radiative heat flux along a trajectory, which supposes to associate to each point of the trajectory all the parameters (such as velocity, density and so on) which are known to have some influence on the emissivity and are as a consequence the inputs of our numerical procedure.

This numerical approach handles with a certain set of theoretical hypothesis and the resulting model leads consequently to a certain level of accuracy. The input parameters may be themselves numerical results known within an associated dispersion. The margin assessment will first consists in quantifying the inaccuracies inherent to each step of the above procedure, then to associate them the resulting dispersion on the radiative heat flux, and finally the way to compose all these error sources to reach the total radiative heat flux margin.

Finally, a + 75 % margin on the radiative heat flux is considered.

7. Flight radiative heat flux database

In order to size the TPS thickness, we need to know the radiative heat flux evolution along

different trajectories. It is then necessary to have a formulae which fits, as closely as possible, the complete numerical {non equilibrium chemistry + Radiative heat flux code} calculations

$$Q_{R1} = C \cdot R_n \cdot (\rho_\infty / 1.225)^{d_1} \cdot (V_\infty / 3048)^{d_2}$$

$$Q_{R2} = C \cdot R_n \cdot (\rho_{\sigma} / 1.225)^{d'_1} \cdot (V_\infty / 3048)^{d'_2}$$

$$T_S = V_\infty^2 \cdot (0.167 + 0.83 / M_\infty^2) / 296$$

if $T_S > T_1$ then $Qr = Qr_1$

else if $T_S < T_2$ then $Qr = Qr_2$

else
$Qr = [(T_2 - T_S) Qr_1 + (T_S - T_1) Qr_2] / (T_2 - T_1)$

This formula is then used to provide the radiative heat flux versus altitude, for TPS thickness sizing.
Figure n°24 shows the radiative heat flux versus altitude.

As previously mentionned, experiments are needed, in order to assess the upstream mixture influence over the radiative intensity of the shock layer.
The following paragraph describes the radiation tests which were performed in the frame of the HUYGENS program

8. Experimental test set-up

The objective of the tests is to simulate the radiative environment of the probe, encountered during its hypersonic entry into the Titan atmosphere. This simulation is performed behind a normal shock wave, in a shock tube (see Ref. 23).

The shock tube is the powerful TCM2, located at Université de Provence, in Marseille, and is a free piston, reflected shock wind tunnel.

8.1 Performance of the Facility

The reflected shock free piston facility is nowadays the most powerful facility used for simulating thermochemical phenomena which are encountered during hypersonic entry of

space vehicles. This type of installation was first developed by R.J. Stalker, who demonstrated that several tens of MJ/kg enthalpy, typical of space vehicle hypersonic entry, can indeed be reached by free piston reflected shock facility, with more than 1 ms useful running time.

8.2 Functioning Principle of the facility

The principle of this facility is to generate a normal shock in the test gas medium, by the sudden expansion of the driver gas, typically Helium. The compression of the driver gas is provided by the kinetic energy of a free piston, which is due to the pressure difference between the compression chamber upstream of the piston, and the driver gas downstream of the piston.

The figure n°25 shows the free piston facility, and (x,t) diagram which describes its functioning :

The piston is initially at the beginning of the compression tube. The compression tube is filled with driver gas (He) at a pressure Pci, and the Air reservoir pressure is Pri, which is larger than Pci.

The inter diaphragm between Air reservoir and compression tube is broken, and the piston is thereby accelerated by the pressure difference (Pri-Pci). The piston kinetic energy is significantly increased (about 1 MJ), and when the pressure in front of the piston becomes greater than the Air reservoir one, the piston decelerates, and transfers its energy to the driver gas medium.

When the piston stops at the end of the compression tube, the temperature and the pressure of the driver gas are very high, pressure even higher than the initial Pri.

The inter diaphragm between the compression tube and the shock tube is tuned to break before the piston is pushed backward. The sudden expansion of the driver gas generates a normal shock in the test gas (Titan atmosphere representative gas mixture).

In the usual conditions, this normal shock reflects at the end of the shock tube, resulting in a further increase of the temperature and pressure of the test gas. The conditions in the facility are such that the interface between the driver gas and the test gas remain fixed with respect to the end of the shock tube (Taylor condition). The diaphragm between the shock tube and the nozzle is then broken, and the test gas expands in the nozzle test section.

In our case, we are interested in the thermal and chemical non equilibrium conditions behind a shock wave propagating in a Titan like atmosphere, at flight conditions, in term of velocity and density.

The measurements of radiative quantities (emission) behind a normal shock wave provide with monodimensional informations, which fulfil our investigation objectives. A nozzle expansion would imply freezing effect of vibrational temperature, and of chemical kinetics, which would complicate our investigations without additional informations.

8.3 HUYGENS tests

It was therefore chosen, for the HUYGENS tests, to use only the free piston shock tube part of the facility. The nozzle throat is taken away, and when the shock wave arrives at the end of the shock tube, the test gas freely expands in a vacuum vessel.

This configuration is more powerful than a classical shock tube, because of the preheating of the driver gas, during the compression by the piston, and this configuration enables a Mach number up to 17 to be reached, for an initial pressure in the test gas medium of 1 to 2 mBar.

A part of the shock tube has been changed with a test section (see figure 26). This test section is equipped with two 25 mm diameter windows, at both sides of the shock tube. Three heat flux probes are located along the longitudinal axis of the tube, in order to provide with the shock velocity, while a pressure sensor is used to verify the flow uniformity during the test.

8.4 Optical set up

Figure n°27 shows the optical set up used for the HUYGENS tests.

The radiative emission emitted by the gas behind the normal shock is focused by a lens on a rectangular optical fiber. The other end of the optical fiber is focused on the monochromator entrance slit area. The light is then refracted inside the monochromator and focused on three exit slits, the distance between each other corresponds to the three wavelengths that will be investigated during the tests (within the CN

violet system). The light which is collected at each of the exit slit, is gathered by a set of opical fiber, which are connected to the photocathods of photomultipliers tube (PMT). The resulting tension is recorded through an oscilloscope, by a micro computer.

The signal which is recorded by the oscilloscope on each wavelength, is proportional to the radiative emission of the plasma, and provides with the evolution of the radiative characteristics behind the normal shock versus time, which can then be converted versus distance behind the normal shock.

The signal for each wavelength is not pure monochromatic data, because the optical set up consists in several slit areas which filter the collected light. A spectrum $S(\lambda)$ as observed through an optical system with an entrance slit $A_1(\lambda)$ and an exit slit $A_2(\lambda)$, is the convolution of $S(\lambda)$ with the slit function $A(\lambda)$.
If $A_1(\lambda)$ and $A_2(\lambda)$ are rectangular area, of width λ_1 and λ_2 respectively, the slit function is a trapeze with a width $(\lambda_1 + \lambda_2)$ at the bottom, and $(\lambda_1 - \lambda_2)$ at the top.
The convolution of the spectrum is obtained by a slipping integral.

$$S_c(\lambda) = S(\lambda) \otimes A(\lambda)$$

A typical record for the wavelength $\lambda = 3879,7$ Angstroms is shown on figure n°28.

8.5 Results

Figure n°29 shows typical measurements, for the 0; 5; 10; 20% Argon, with 3,5% CH_4, for the $\lambda = 3869,58$ Angstroms wavelength.
The tests showed a lowered sensitivity of CN emission with respect to Argon concentration than theoretical prediction assessments.

CONCLUSION

During its entry into TITAN atmosphere, the HUYGENS probe, which is under ESA responsability, with Aerospatiale Espace & Defense as prime contractor, has to face large radiative and convective heat fluxes. The radiative compound is due the thermal and chemical non equilibrium feature of the stagnation region of the Entry Module, during

hypersonic entry, which results in CN creation, and enhanced radiative emissivities. A complete methodology for radiative heat flux predictions of the TITAN entry probe HUYGENS has been derived, in order to provide with reliable and conservative radiative heat flux predictions. This methodology accounts for 3-dimensional effects of radiative emission, absorptivity, and radiative heat flux emanating from both the front and rear part flowfield of the probe. Theoretical and experimental aspects are addressed.

REFERENCES

1. VINCENTI, W.G., KRUGER, C.H., "Introduction to physical gas dynamics", WILEY & sons, 1965

2. TREANOR, C.E., MARRONE, P.V., "Effect of dissociation on the rate of vibrational relaxation", *Physics of fluids*, vol 5,n°9, September 1962

3. TREANOR, C.E., MARRONE, P.V., "Chemical relaxation with preferential dissociation from excited vibrational levels", *Physics of fluids*, vol 6,n°9, September 1963

4. MILLIKAN, R.C., WHITE, D.R., "Systematics of vibrational relaxation",The *Journal of chemical physics*, vol 39, n°12, December 1963

5. WOOD A.D., SPRINGFIELD J.F., PALLONE, A.J., "Determination of the effects of chemical and vibrational relaxation on an inviscid hypersonic flowfield", *AIAA paper*, AIAA-63-441,1963

6. PARK,C.,"Assessment of two-temperature kinetic model for dissociating and weakly-ionizing nitrogen", *AIAA paper*, AIAA-86-1347,June 1986

7. PARK, C., "Assessment of two-temperature kinetic model for ionizing air", *AIAA paper*, AIAA-87-1574, Honolulu, June 1987

8. LEE, J., "Basic governing equations for the flight regimes of Aeroassisted Orbital Transfer Vehicles", *AIAA paper*, AIAA 84-1729, June 1984

9. NELSON, H.F., PARK, C., WHITING, E.E., "TITAN atmospheric composition by hypervelocity shock-layer analysis", *Journal of thermophysics and heat transfer*, vol 5, n°2, pp 157-165, April-June 1991

10. PARK, C., "Radiation enhancement by non-equilibrium during flight through the TITAN atmosphere", *AIAA paper*, AIAA-82-0878, St Louis, June 1982

11. PARK, C., BERSHADER, D., "Determination of the radiative emission of a hypersonic flow simulating the Cassini-TITAN atmospheric entry probe environment", *AIAA paper*, AIAA-90-1558, Seattle, June 1990

12. PARK, C., "Modeling of radiative heating in base region of Jovian entry probe", *AIAA paper*, AIAA-79-0039, New-Orleans, Jan. 1979

13. PALMER, G., "Enhanced thermochemical non-equilibrium computations of flow around the Aeroassist Flight Experiment vehicle", *AIAA paper*, AIAA Paper 90-1702

14. GNOFFO, P.A., "A code calibration program in support of the Aeroassist Flight Experiment", *AIAA paper*, AIAA Paper 89-1673

15. VENKATAPATHY, E., PALMER, G., PRABHU, D.K., "AFE base flow computations", *AIAA paper*, AIAA Paper 91-1372, Honolulu, June 1991

16. PARK, C., "Non-equilibrium hypersonic aerothermodynamics", WILEY interscience publication

17. STEPHENSON, J.D., "Measurement of optical radiation from the wake of ablating blunt bodies in flight at speeds up to 10 km per second", NASA TN D-2760, April 1965

18. CAUCHON, D.L., "Project Fire flight 1 radiative heating experiment", NASA TM X-1222

19. SHIRAI, H., PARK C., "Experimental studies of radiative base heating of a Jovian entry model", *AIAA paper*, AIAA-79-0038, New-Orleans, Jan. 1979

20. PARK, C., "Studies of radiative emission from the simulated shock layer of the HUYGENS probe", Dissertation for the degree of doctor philosophy, 1991

21. DROUIN, N., CORON, F., HOLLANDERS, H., LEMAIRE, D., MOULES, G., "Calculations of Non-equilibrium Real Gas Flows with the Finite Volume Euler/Navier Stokes Solver FLU3NEQV", *AIAA paper*, AIAA 94-0761, Reno, Jan. 1994

22. CHAPUT, E., DUBOIS, F., LEMAIRE, D., MOULES, G., VAUDESCAL, J.-L., "FLU3PNS : A Three Dimensional Thin Layer and Parabolized Navier-Stokes Solver using the MUSCL Upwind Scheme", *AIAA paper*, AIAA 91-0728, 1991

23. LABRACHERIE, L., " Détermination des Températures Rotationnelles et Vibrationnelles de CN à l'Aval d'un Choc Droit se propageant dans une Atmosphère de Titan Reconstituée", Mémoire de Thèse, Université de Provence, Oct. 1994

TABLEAU n° 1

COMPLETE CHEMISTRY

reaction	C cm3/mole·s	n	E/R K
CH4+M = CH3+H+M (M=CH4,N2,N,C,H,Ar)	2.25E+27	-1.87	52900.
CH3+M = CH2+H+M (M=CH3,N2,N,C,H,Ar)	2.25E+27	-1.87	54470
CH2+M = CH+H+M (M=CH2,N2,N,C,H,Ar)	2.25E+27	-1.87	50590.
CH+M = C+H+M (M=CH,N2,N,C,H,Ar)	1.13E+19	-1.00	40913.
CN+M = C+N+M (M=CN,N2,N,C,Ar,e-)	1.00E+23	-2.00	90000.
N2+M = 2N+M (M=N2,N,Ar,e-)	3.70E+21	-1.60	113200.
C2+M = 2C+M (M=N2,C2,N,C,Ar,e-)	9.68 E+22	-2.00	71000.
H2+M = 2H+M (M=H2,N2,N,H,Ar,e-)	1.47E+19	-1.23	51950.
NH+M = N+H+M (M=NH,N2,N,H,Ar,e-)	1.13E+19	-1.00	41820.
C2+N2 = 2CN	7.10E+13	0.00	5330
N2+C = CN+N	1.11E+14	-0.11	23000.
CN+C = C2+N	3.00E+14	0.00	18120.
N2+H = NH+N	2.20E+14	0.00	71370.
H2+C = CH+H	1.80E+14	0.00	11490.
CH4+H = CH3+H2	2.00E+14	0.00	5800.
CH3+H = CH2+H2	2.00E+14	0.00	5800.
CH2+H = CH+H2	2.00E+14	0.00	5800.
N+CN* = CN+N*	9.80E+12	0.00	40700
N2+C* = C+N2*	1.11E+14	-0.11	50000
N2+N* = N+N2*	1.11E+14	-0.11	50000.
C+N = CN*+e	1.00E+15	1.50	164440
2N = N2*+e-	1.79E-09	0.77	67500
H+M = H*+e-+M (M=H,H*,N,e-)	5.90E+37	-4.00	157600.
C+M = C*+e-+M (M=C,C*,N)	3.90E+33	-3.78	130000
C+M = C*+e-+M (M=e-)	2.89E+32	-3.00	130750
N+M = N*+e-+M (M=N,N*,N2)	2.50E-34	-3.82	168600
N+M = N*+e-+M (M=e-)	8.00E+37	-4.50	168600
Ar+M = Ar*+e-+M (Ar,Ar*,N)	2.50E-34	-3.82	181700
Ar+M = Ar*+e-+M (e-)	8.00E+37	-4.50	182800

TABLE n° 2

REDUCED CHEMISTRY

Set n° 1

$$k,f = C.(T^{**}n).exp(-E/RT)$$

REACTION	C cm³/mole·s	n	E/R R
CH4 + M = CH + H2 + M (M = CH4, N2, N, C, H, Ar)	2.25 E + 24	-1.87	52900.
CH + M = C + H + M (M = CH, N2, N, C, H, Ar)	1.13 E + 19	-1.00	40913.
CN + M = C + N + M (M = CN, N2, N, C, Ar, e-)	1.00 E + 23	-2.00	90000.
N2 + M = 2N + M (M = N2, N, Ar, e-)	3.70 E + 21	-1.60	113200.
H2 + M = 2H + M (M = H2, N2, N, H, Ar, e-)	1.47 E + 19	-1.23	51950.
N2 + C = CN + N	1.11 E + 14	-0.11	23000.
H2 + C = CH + H	1.80 E + 14	0.00	11490.

Set n° 2

REACTION	C cm³/mole·s	n	E/R R
N2 + M = 2N + M (M = N2, N, Ar)	3.70 E + 21	-1.60	113200.
CN + M = C + N + M (M = CN, N2, N, C, Ar)	1.00 E + 23	-2.00	90000.
H2 + M = 2H + M (M = H2, N2, N, H, Ar)	1.47 E + 19	-1.23	51950.
C + N2 = CN + N	1.11 E + 14	-0.11	23000

Figure n°1   MACH=19.75 , Z=253.75 km

COUPLED NS COMPLETE CHEMISTRY, THERMAL EQUILIBRIUM, 2% CH4

COUPLED NS SIMPLIFIED CHEMISTRY, THERMAL EQUILIBRIUM, 2% CH4

COUPLED NS SIMPLIFIED CHEMISTRY, THERMAL EQUILIBRIUM, 2% CH4 - 20% Ar
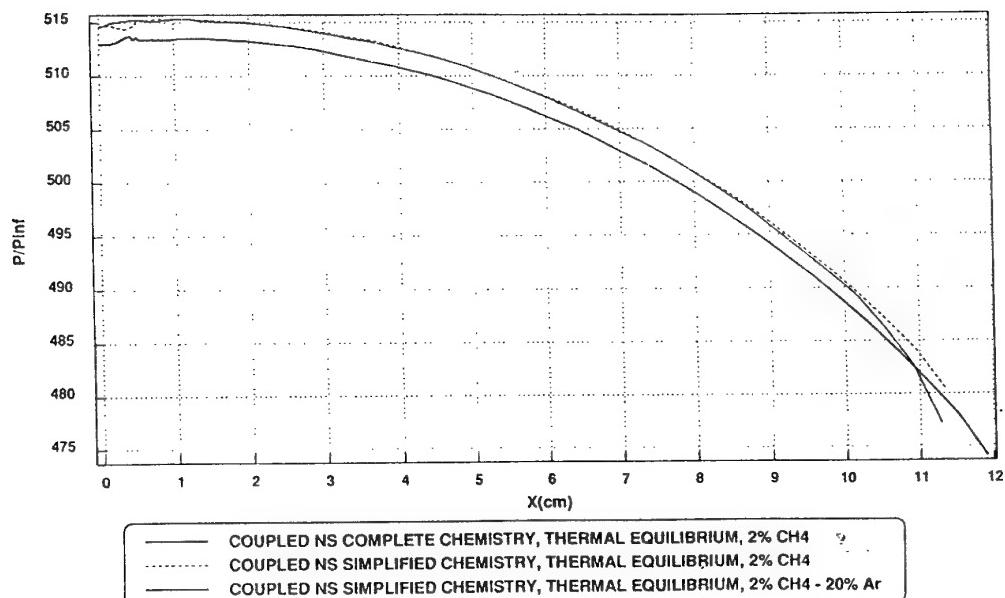
Figure n°2   MACH=19.75 , Z=253.75 km

COUPLED NS COMPLETE CHEMISTRY, THERMAL EQUILIBRIUM, 2% CH4
COUPLED NS SIMPLIFIED CHEMISTRY, THERMAL EQUILIBRIUM, 2% CH4
COUPLED NS SIMPLIFIED CHEMISTRY, THERMAL EQUILIBRIUM, 2% CH4 - 20% Ar

Figure n°3   MACH=19.75 , Z=253.75 km

COUPLED NS COMPLETE CHEMISTRY, THERMAL EQUILIBRIUM, 2% CH4
COUPLED NS SIMPLIFIED CHEMISTRY, THERMAL EQUILIBRIUM, 2% CH4
COUPLED NS SIMPLIFIED CHEMISTRY, THERMAL EQUILIBRIUM, 2% CH4 - 20% Ar

Figure n°4   MACH=19.75 , Z=253.75 km

COUPLED NS COMPLETE CHEMISTRY, THERMAL EQUILIBRIUM, 2% CH4
COUPLED NS SIMPLIFIED CHEMISTRY, THERMAL EQUILIBRIUM, 2% CH4
COUPLED NS SIMPLIFIED CHEMISTRY, THERMAL EQUILIBRIUM, 2% CH4 - 20% Ar

MACH=19.75 , Z=253.75 km

COUPLED NS COMPLETE CHEMISTRY, THERMAL EQUILIBRIUM, 2% CH4
COUPLED NS SIMPLIFIED CHEMISTRY, THERMAL EQUILIBRIUM, 2% CH4
COUPLED NS SIMPLIFIED CHEMISTRY, THERMAL EQUILIBRIUM, 2% CH4 - 20% Ar

Figure n°5

MACH=19.75, Z=253.75 km

EULER : 2%CH4, 20% Ar (with e-)   NS : 2%CH4, 20% Ar (without e-)
NS : 2%CH4, 20% Ar (with e-)

Figure n°6

M=16.43 Traj nom

N2 massique   H2 massique

CN massique   CH massique

△   BA89 equil. thermo G=1.30   O   VSL
♦   BA89 equil. thermo G=1.492.

Figure n°7

Wood et Springfield

Millikan et White

Millikan et White avec correction

Cas Vo. : Mach = 19.75
77% N2 , 3% CH4 et 20% Ar
P = 13.37 Pa
T = 145 °K
V = 4851 m/s

Figure n°8
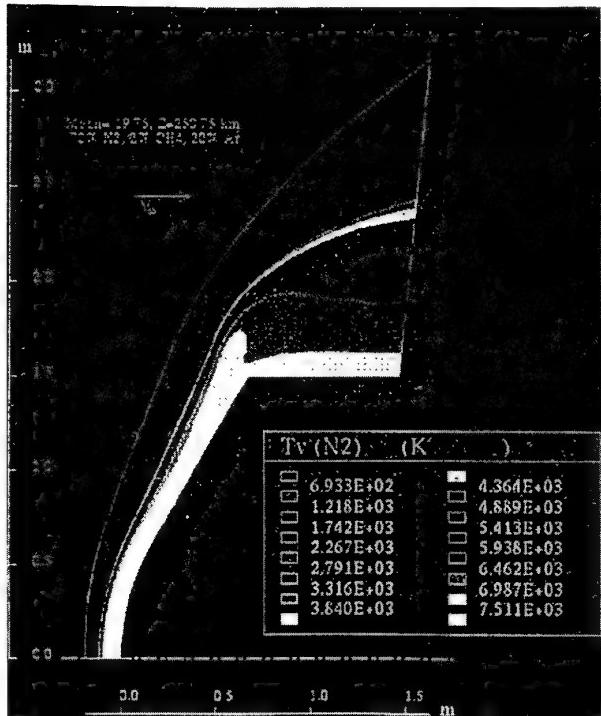
Figure n°9
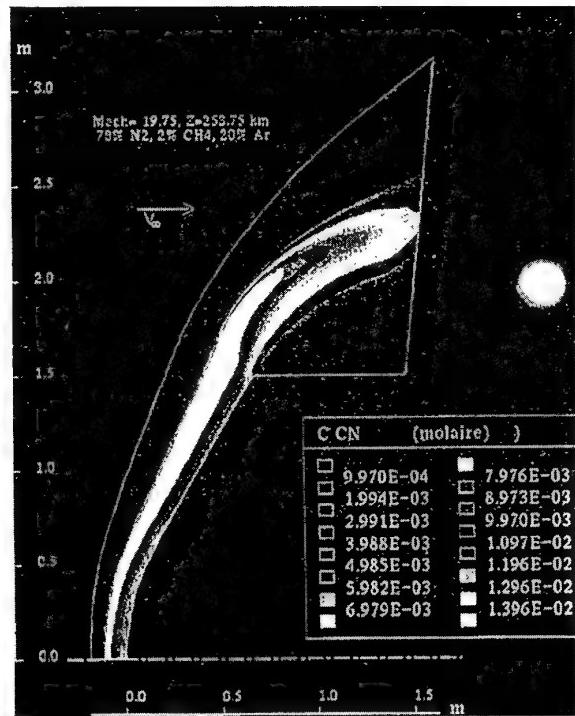

Figure n°10
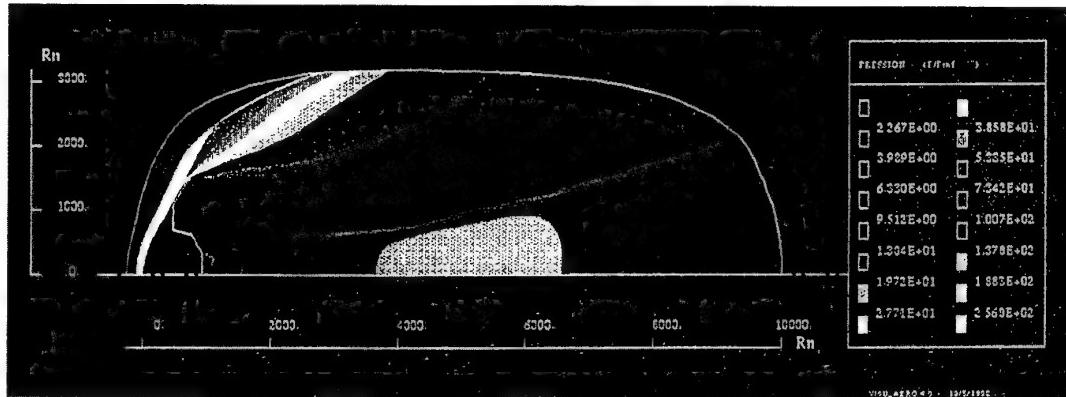
Figure n°11
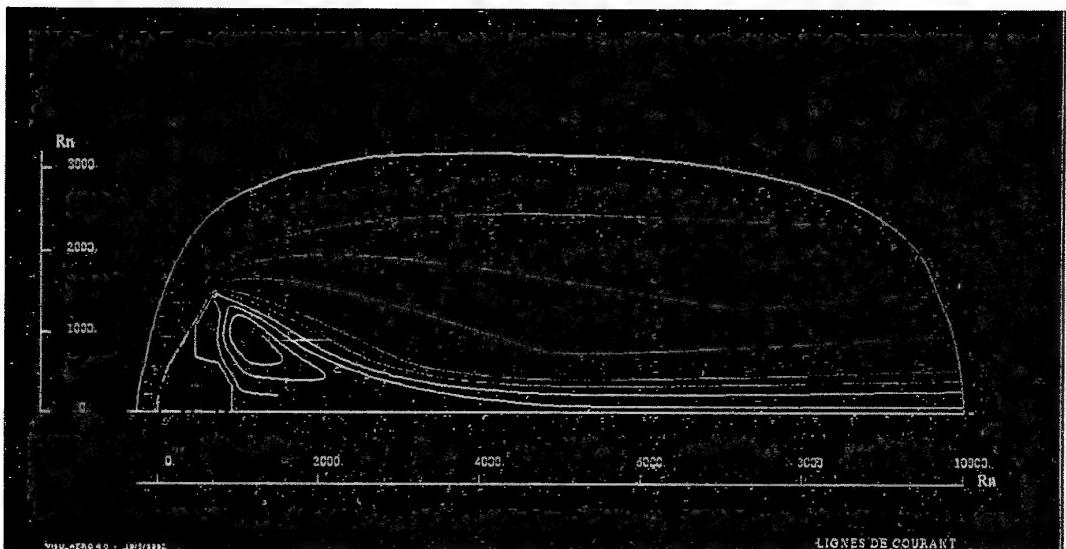
Figure n°12
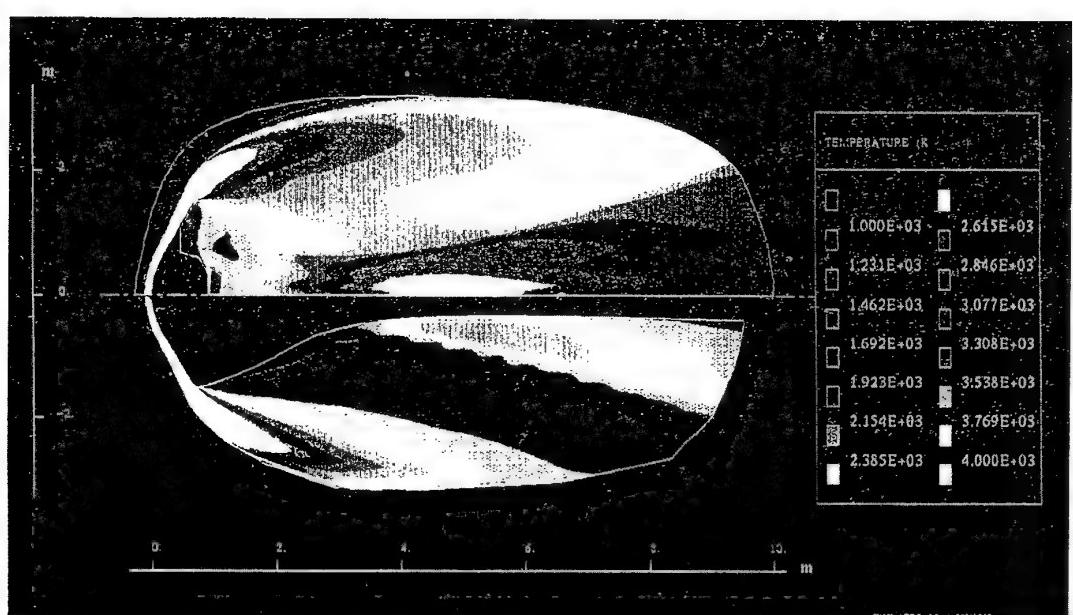
Figure n°13
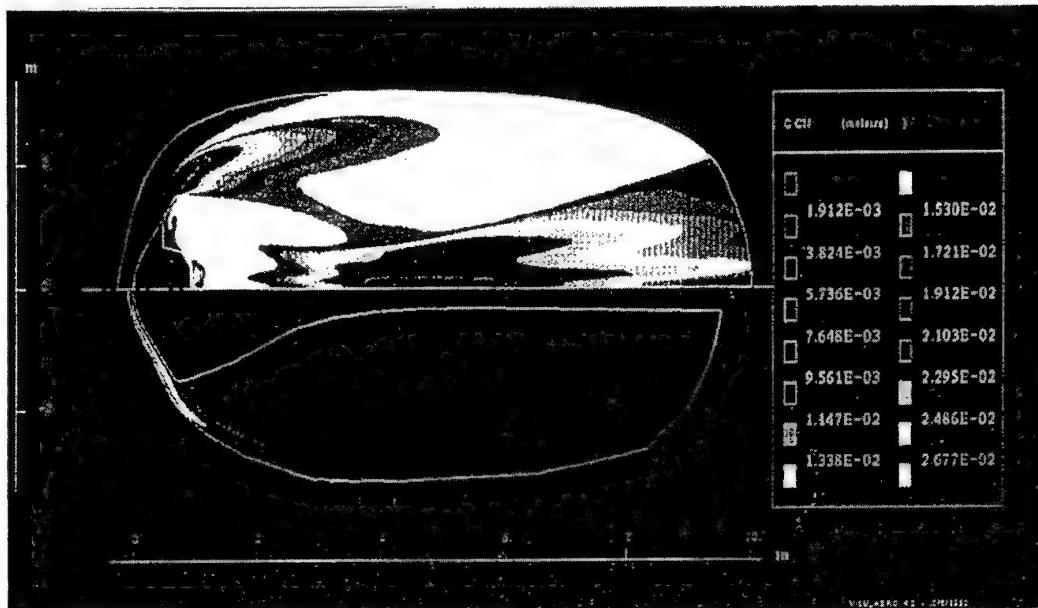
Figure n°14

Figure n°15

Figure n°16

γ=1.3 vibration / dissociation coupling
Te and Tv relaxation *(Millikan & White + Park)*

○ CH4 dissociated behind the shock
● CH4 actual dissociation
+ experiment

Figure n°17

γ=1.4 no vibration/dissociation coupling
CH4 dissociated behind the shock

○ *(Millikan & White + Park)*
● *(Millikan & White)*
▲ *(Wood & Springfield)*

Figure n°18

γ=1.3 CH4 actual dissociation
Te and Tv relaxation *(Millikan & White)*

○ vibration/dissociation coupling
● no coupling

Figure n°19

vibration/dissociation coupling - actual CH4 dissociation
Te and Tv relaxation *(Millikan & White + Park)*

○ =1.4
● =1.3

Figure n°20

γ=1.3 vibration / dissociation coupling
Te and Tv relaxation *(Millikan & White + Park)*
CH4 dissociated behind the shock
e- and neutral species catalysis for ionization reactions

Figure n°21

γ=1.35 vibration / dissociation coupling
Te and Tv relaxation *(Millikan & White)*
CH4 dissociated behind the shock
e- catalysis for ionization reactions

Figure n°22   △ 3D calculation
   + 3D calculation   + absorbtivity

Figure n°23

Figure n°24   HUYGENS PROBE - RADIATIVE HEAT FLUX EVOLUTION
Ve = 6.19 Km/s - D = 2.70 m - Tw = 1500 K

réservoir d'air   tube de compression   tube à choc   tuyère   enceinte à vide

Interdiaphragme D1 D2   piston   diaphragme D3   diaphragme D4

Pri   Pci   P1

Conditions initiales

u r   interface
            gazeuse

Prf   P4

                        onde de choc
L4   incidente

Rupture de D3
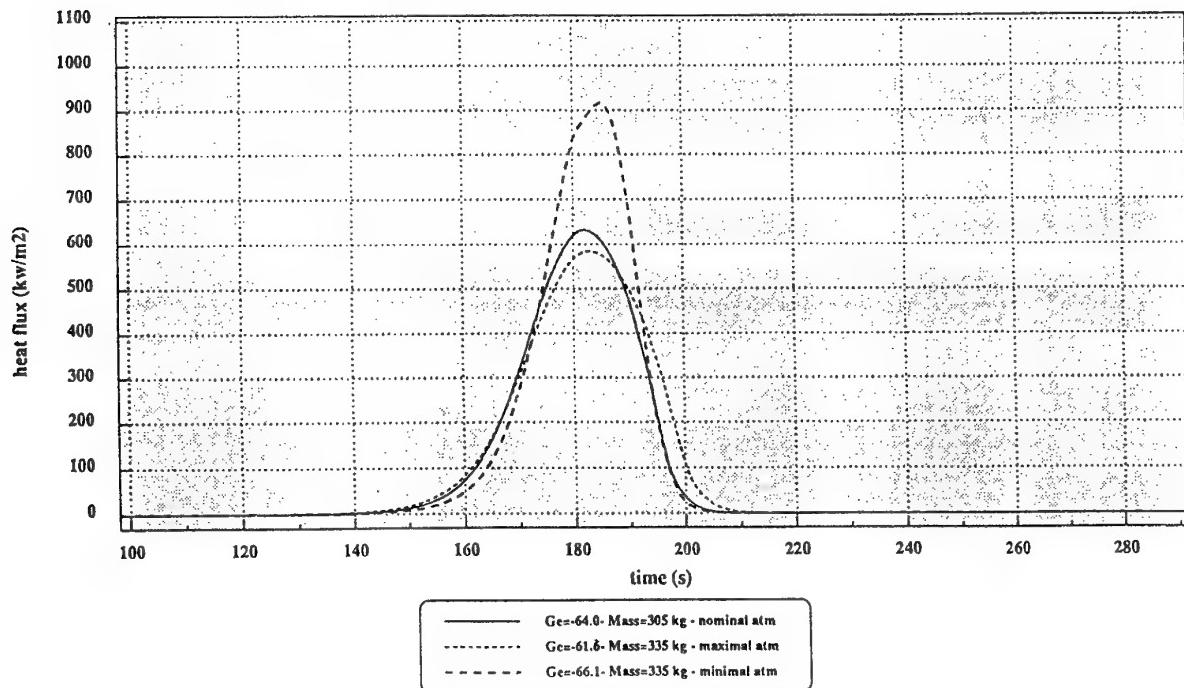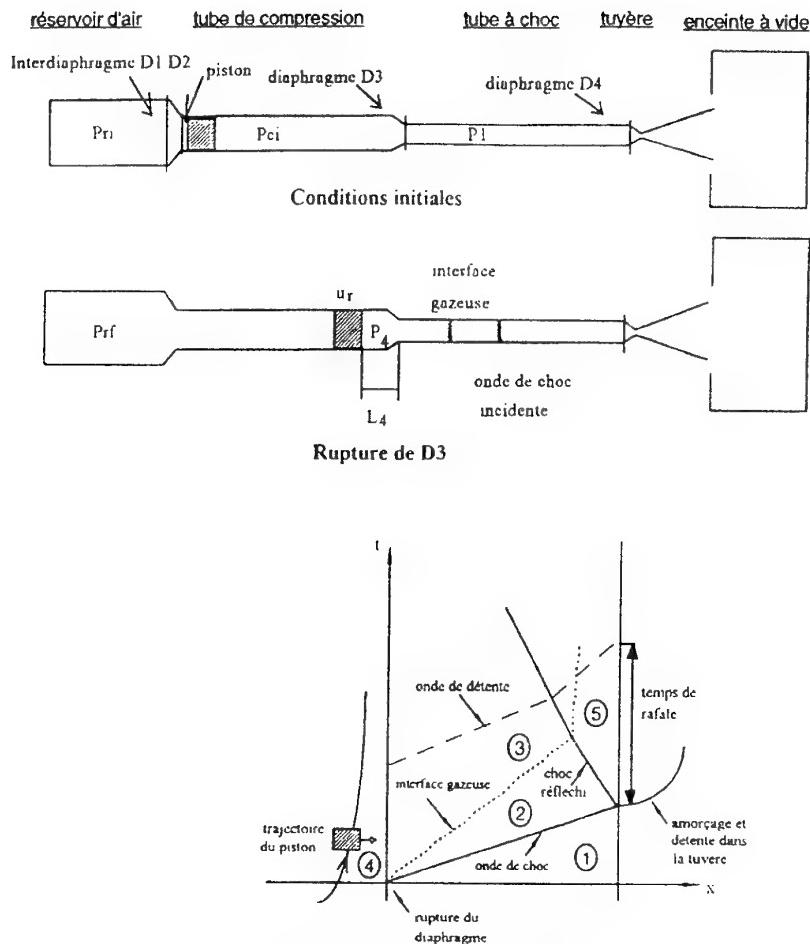

Figure n°25   Schémas et diagramme (x,t) d'une soufflerie à piston libre et à choc
   réfléchi
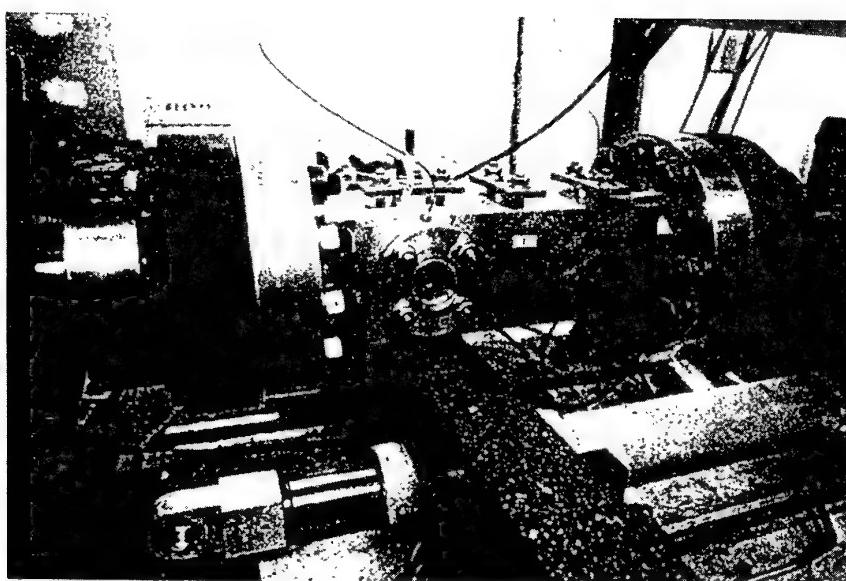
Figure n°26   Schéma de la chambre d'expérience dans le tube à choc
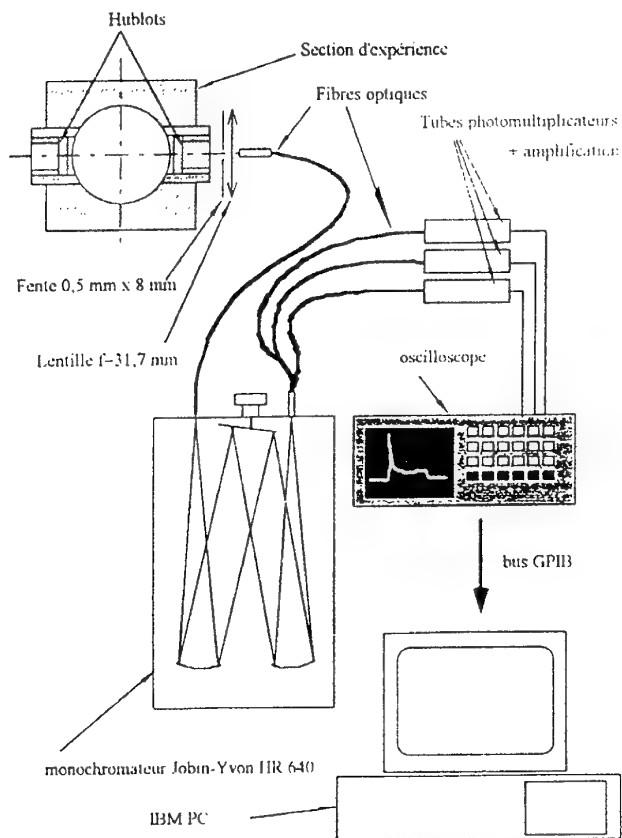
Figure n°27   Schéma général du montage optique pour les mesures d'émission
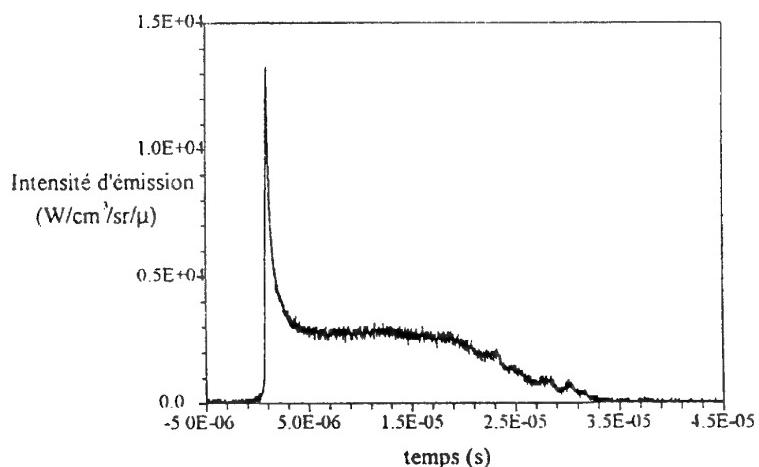

Figure n°28   Evolution expérimentale de l'intensité d'émission de CN à l'aval d'une
onde de choc droite dans le mélange N_2-CH_4 + 20% Ar
(λ=3879,7 Å)
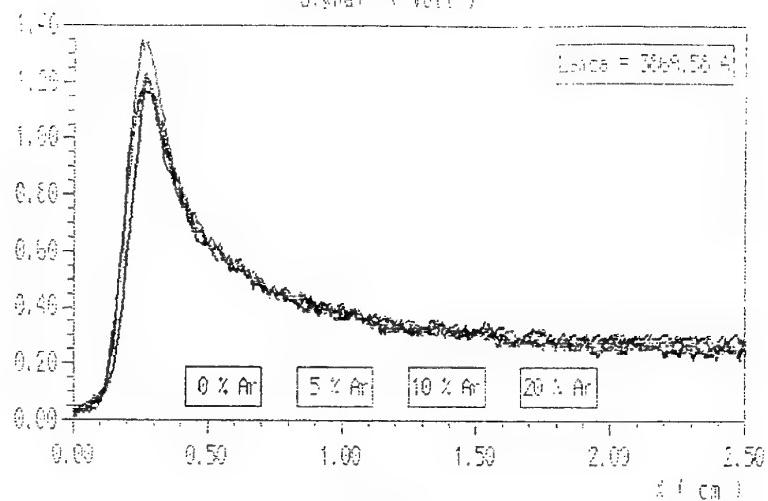
Figure n°29

COMMUNICATION BLACKOUT DURING EARTH-ATMOSPHERE ENTRY OF CAPSULES

M. Boukhobza
Aerospatiale Branche Espace & Défense
Centre Opérationnel Systèmes
Département Aérodynamique & Electromagnétisme
BP 2
78133 Les Mureaux Cédex
France

1. COMMUNICATION BLACKOUT PHENOMENOLOGY

1.1 Plasma

1.1.1 Description of phenomenons

During an hypersonic reentry, generally defined by altitudes lower than 120 km, the atmospheric drag converts a great part of the vehicle's kinetic energy into heat, mainly by compression at the front shock and also by viscous friction. This front shock significantly increases the temperature of the air which crosses it, that increase being all the more important since the body speed is great and since the direction with which the air reaches the shock is neighbouring the normal direction. The temperature within the shock layer rises to such magnitudes in the stagnation region, that the air dissociates and ionizes, which has the immediate consequence, since these reactions are endothermic, of bringing back these temperatures to lower values (decrease between temperatures of the order of 15,000 and 7,000 K for a speed of about 5,000 m/s).

The relaxation which occurs downstream along the body make decrease again the temperature, that thus results in an inversion of reactions which partially recombine the ions and electrons formed. These longitudinal variations of electronic densities go, for a vehicle entering with a great angle of attack, with important circumferential disparities (leeward side-windward side differences).

A typical flow pattern around a capsule entering in the atmosphere at hypersonic velocity with a great angle of attack is shown in figure 1. After the detached nose shock (1), one can distinguish the attached flow at windward side (2) (which possibly includes a local separation zone just downstream of the roundness) and the separation zone over vehicle leeward side (3) and base (4). The different directions of flow velocities associated to these last three regions result in vortex zones (5), which may exist too at the neighbouring of the junction between spherical and conical parts of the body.

According to the flight conditions, the plasma level may be influenced also by the body's wall. The heating undergone by the coating materials, especially in the front heatshield and windward side regions for a capsule, may bring about the emission of species by pyrolysis or ablation. In particular, the injection of easily ionizable species like alkaline species may result in an important increase of the electron density by adding a great amount of ions like Na^+ or K^+ to pre-existing ions of air such as $NO^+, O_2^+, N_2^+, O^+, N^+$.

The wall material intervenes also by its catalycity, which determines the degree of recombination of dissociated and ionized species at its contact.

Moreover, the presence of jets around the vehicle may modify the characteristics of the flow downstream, directly particularly by injection of easily ionizable species or indirectly by the change of catalycity of the wall following upon possible deposits.

1.1.2 Prediction tools used at Aerospatiale Espace & Défense, applications examples and difficulties of modelling

With regard to plasma characterization, Aerospatiale Espace & Défense, has a set of numerical codes for 2D or 3D calculations. These programs treat non viscous and viscous, laminar and turbulent flows with gases in thermochemical equilibrium and non equilibrium and take into account the influence of the wall (blowing and catalycity). In particular a 3D Euler/Navier-Stokes code, named FLU3NEQV, described in reference 1, is available. For the treatment of viscous flows this code allows to resolve the full, thin-layer or parabolized Navier-Stokes equations. It treats laminar and turbulent flows and the thermochemical non equilibrium modelling is made by means of a single module which allows to introduce any chemical kinetics. The influences of the catalycity of the wall and the injection of species from it are taken into account. The equations are resolved by an implicit finite-volume method.

The figure 2 presents comparisons of computed and measured electron densities on RAMC sphere-cone body for the altitudes of 61 km (Mach number 23.9) and 71 km (Mach number 25.9).

The electron densities predicted by the Euler and Navier-Stokes versions of FLUNEQV are in a quite good agreement with flight measurements.

Results of Euler version of FLU3NEQV obtained at a rear section of space vehicle Hermes for an altitude of 75 km, a Mach number of 20 and an angle of attack of 30 degrees are shown in figure 3. The calculated plasma frequencies (proportional to the square root of the electron densities) exhibit maximum values not only at the windward side, but also at the leeward side near the plane of symmetry, the lowest levels of plasma being predicted on the fuselage of the vehicle.

The maximal plasma frequencies obtained by the Euler version of FLU3NEQV and by an Aerospatiale PNS code on windward side and leeward side of the spaceplane Hermes at different altitudes between 85 and 52 km, extracted from reference 2, are presented in figures 4 and 5.
The Euler version with air in equilibrium is used around the Hermes 0.0 shape for the two realistic angles of attack of 30 and 40 degrees and the PNS version is applied to a simplified shape, named Bolide, with an angle of attack of 15 degrees and for air in thermochemical equilibrium, vibrational equilibrium and chemical non equilibrium and thermochemical non equilibrium.

These curves allow to appreciate the effect of the different hypotheses on the plasma levels. As regards the PNS calculations, as one passes from chemical equilibrium to chemical non equilibrium (without relaxation of vibration), the plasma frequency is moderately increased or decreased at the windward side and increased at the leeward side, where there occurs globally a relaxation, attenuated by a recompression in the plane of symmetry. As one passes from vibrational equilibrium to vibrational non equilibrium, the plasma frequency is decreased at the windward side, where the vibrational temperatures of O_2 and N_2 are lower than the translational temperature (lesser dissociation of these species) and globally increased at the leeward side where the vibrational temperatures of O_2 and N_2 are greater than the translational temperature (greater dissociation of these species). Of course these effects of chemical and vibrational relaxation tend to reduce as the altitude lowers.

With regard to Euler calculations, one can see a distinct rise in plasma frequency at the windward side and a lesser one at the leeward side where occurs a great increase in plasma thickness.

At the windard side, the plasma frequency obtained by the viscous calculations on the simplified shape becomes greater than the signal frequency of 1.5 GHz (approximate blackout entry) at an altitude varying of 2 km according to the thermochemical state of air hypothesis. At lower altitudes, where, unlike previously, the Euler calculations become more significant, the calculated plasma frequency is lower than 1.5 GHz (approximate end of blackout) at an altitude 5 km lower

for the angle of attack of 40 degrees in comparison with the one for the angle of attack of 30 degrees. At the leeward side, all the calculations result in a plasma frequency lower than 1.5 GHz, except the one with thermochemical non equilibrium hypothesis at the altitude of 74 km which is a little greater.

However plasma characteristics predictions generally must overcome a few difficulties.
First, the choice of a chemical kinetics for air. Apart from the selection of a set of species suited to the encountered temperatures of the considered flow, one comes up against the great disparities on reaction rates between the different authors. Moreover, these authors assume different dependences of the reaction rates towards the different temperatures of the flow. For instance, as given by Park in reference 3 for reactions like $O_2 + M \rightleftharpoons O + O + M$, where M is a heavy species, the forward reaction rate is a function of the vibrational temperature Tv_m of the diatomic molecule and translational temperature T of the impacting heavy particle, and more precisely, expressed with an average temperature $Ta = \sqrt{T \times Tv_m}$. The backward reaction rate depends only on the translational temperatures of the impacting particles (function of T). For the case where the impacting particle is an electron, the forward rate depends on the average of the vibrational temperature and the electron translational temperature: $Ta' = \sqrt{Tv_m \times Te}$ and similarly the backward reaction rate is governed by the temperature $Ta'' = \sqrt{T \times Te}$.

Otherwise difficulties arise for the modelling of wall effects.
The wall condition for a species i can be written:
$j_i + \dot{m}_i + (\rho v)C_i = (\rho v)_i$, where, at the wall,
j_i is the rate of diffusion, C_i is the mass concentration, (ρv) and $(\rho v)_i$ are the injected mass fluxes respectively total and for species i and $\dot{m}_i$ is the mass flux of recombination. This latter term is expressed as:

$$\dot{m}_i = \gamma_i \sqrt{\frac{kT}{2 \pi m_i}} (\rho C_i), \text{ where}$$

T is the temperature of the wall, m_i is the mass of species i, k is the Boltzmann constant, ρ is the density of the mixture and γ_i is the fraction of collisions at the wall which lead to a recombination. Unless the hypothesis is made of a wall fully non catalytic ($\dot{m}_i = 0$) or fully catalytic (for which the above relation at the wall is replaced by an equilibrium condition at the temperature of the wall), the coefficient γ_i has to be experimentally determined for each species and in function of the temperature.

Besides an evolution of the catalycity may occur during the flight by oxidation or degradation of the state of the surface.

But the main influence of the wall is of course the injection of species. These species may modify different parameters of the flow like the temperatures but above all may include, as mentioned above, easily ionizable species like alkaline species.

The first important difficulty is naturally to reach a sufficient characterization of the considered material in order to base the ablation or pyrolysis laws from which the injected mass fluxes of the different species can be obtained for the fluxes encountered at the wall.

The second one deals with the chemical kinetics to be used for the resulting mixture. In particular it is well established that the ionization-recombination reaction of alkaline species like Na or K is catalyzed by polyatomic molecules, these latter species so increasing greatly the ionization level. The process seems to go through Penning ionization (see reference 4):

$A + M^* \rightleftarrows A^+ + \bar{e} + M$ where A is the alkaline species and the vibrationally or electronically excited molecule M^* gives up its energy for ionization. So a representative chemical kinetics must be set up and the reaction rates obtained.

1.2 Radioelectric attenuations

1.2.1 Description of phenomenons

The ionized plasma which exists around antennas for tracking, navigation, telemetry and other communications directed towards receivers set out on ground, air planes or satellites may result in a modification of the radiation pattern and an impedance mismatching of these antennas and in an attenuation and a phase shifting of emitted waves.

The resultant attenuation may cause, in the most critical cases, a total interruption of communications.

This attenuation is a function of:
- the plasma characteristics, that is to say levels and spatial distributions of plasma frequency (proportional to the square root of the electron density) and electrons-neutrals collisions frequency; their great variations around the body make important the positioning of antennas,
- the path that the emitted wave must go through within the plasma, determined by the relative positions of the antenna and the receiver,
- the frequency of the emitted wave, only frequencies neighbouring or lower than the plasma frequency being subjected to an important attenuation,
- the polarization of the emitted wave.

1.2.2 Prediction tools used at Aerospatiale Espace & Défense

For characterizing the radioelectric effects of the plasma, Aerospatiale Espace & Défense has a set of numerical codes for 1D, 2D or 3D calculations. Among them is the 3D code AS-TEMMIS, described in reference 5, which allows to model the antenna functioning and the waves propagation in non homogeneous medium by resolving the time-dependent Maxwell equations by an explicit finite differences method. These codes have been commonly used for blackout studies relative to reentry of military objects as well as in the framework of studies on space vehicle Hermes.

About the difficulties encountered for calculation of radioelectric attenuations, one can mention the modelling of the interaction of the emitted wave with non stationary flow areas, natural or resulting from jets.

2. CONCERNED ALTITUDES RANGES AND ENCOUNTERED PROBLEMS DURING THE ATMOSPHERE ENTRY OF CAPSULES

As shown in figure 6, the reentries of capsules are characterized by very high velocities at high altitudes, which decrease very quickly below altitudes of 70-80 km. This deceleration induces a partial deionization of the plasma surrounding the vehicle which, associated to the electrons-neutrals collisions frequency increase going with the altitude lowering, strongly reduces the attenuation of the emitted waves.

The altitudes range where the blackout phenomenon may occur, depends of course on above mentioned parameters which determine the plasma characteristics and the radioelectric link, but may be approximately included in the altitudes range of 100-40 km.

Without use of technique allowing to reduce the plasma levels, as water injection at the vicinity of antennas, tested out on Gemini flights, which may reach an effective reduction of radioelectric attenuations but which is delicate to implement, the existence of a blackout zone during a reentry of a capsule is setting important problems which impose its precise determination.

For navigation and piloting, it is necessary to know the end of blackout position on the reentry trajectory in order to determine the point from which the links with NAVSTAR satellites and ground stations may be recovered for adjustment of the inertial navigation system and resumption of tracking of the vehicle.

The end of blackout may be also determining on the reentry guidance accuracy as shown in figure 7, extracted from reference 6. For a biconic shape and a capsule shape for which a beginning of blackout at an altitude of 90 km is assumed, the reentry errors at an altitude of 5 km are calculated by a Monte-Carlo statistical study consisting in random drawing on navigation errors, aerodynamic uncertainties and atmospheric disturbances and that for the three altitudes of end of blackout of 60, 50 and 40 km.

It can be seen that the reentry accuracy is more sensible to the altitude of end of blackout for the capsule shape than for the biconic shape, which has a greater lift-to-drag ratio, and that a deterioration of accuracy appears when the end of blackout is lowered from 50 km to 40 km.

Besides, the requirement of acquisition recovery by the ground stations from the very end of blackout leads to optimize the positioning of these stations, considering their limiting angles of observation. With regard to telemetry, one must determine the duration of interruption of communications with ground receivers or relay satellites in order to size the recorders.

3. EXAMPLES OF COMMUNICATION BLACKOUT OBSERVED DURING ENTRY OF APOLLO AND SOYOUZ VEHICLES

The figure 8, extracted from reference 7, shows the blackout appearance observed during the superorbital reentry of the command module APOLLO 6. This vehicle was fitted out with 4 S-band antennas (2.3 GHz) at the heatshield toroidal section.

The signal recorded by a receiver on airplane shows an abrupt decrase at about an altitude of 99 km, where the velocity of the vehicle was approximately 9,600 m/s, which begins less than one second before complete disappearance of signal. That altitude of blackout was confirmed by the observations made by a receiver on ship and the decrease of signal appeared not to be caused by other factors like receiving antennas pointing errors.

In figure 9, extracted from reference 8, the observed and calculated radioelectric attenuations during the reentry of SOYOUZ vehicles are shown.

The board antenna, of frequency 0.2 GHz, was installed at the base of the vehicle. The instant of end of communication, observed by a ground station, for the SOYOUZ TM-12 vehicle corresponds to an altitude of about 95 km. The calculations made with simplified methods show an attenuation for a frequency of 0.2 GHz approximately equal to the radioline potential at this altitude and so agree well with the flight data, that altitude of blackout having been observed on numerous SOYOUZ flights.

With regard to the end of blackout, the observed altitude for SOYOUZ TM-12 vehicle is around 35 km, which is lower than the calculated altitudes, for two angles of observation, of about 37-40 km. This discrepancy is imputed to a real angle of observation greater than $\varphi = 50$ degrees, and the altitude of communication restoring for the SOYOUZ TM-14 vehicle, for which the angle of observation is more surely in the 0-50 degrees range, agrees better with the calculated values.

Apart from end of blackout sensibility to angle of observation (altitude 3 km lower when φ increases from 0 to 50 degrees for 0.2 GHz frequency), these calculations allow to assess the change of signal frequency effects. For the same radioline potentials, when the signal frequency increases from 0.2 to 1 GHz, the altitude of communication terminating is about 8 km lowered and the communication restoring one is approximately 8 km too risen.

REFERENCES

1. N. Drouin, F. Coron, H. Hollanders, D. Lemaire, G. Moules
   Calculations of non equilibrium real gas flows with the finite-volume Euler/Navier-Stokes solver FLU3NEQV
   AIAA-94-0761 - January 1994

2. O. Driessens
   Prévision du blackout à la rentrée - Influence de la relaxation de vibration sur le plasma aérodynamique - Forme simplifiée
   Note Aerospatiale TK/AP n° 48 790 - February 1991

3. C. Park
   Assessment of two-temperature kinetic model form ionizing air
   AIAA Paper n° 87-1574 - 1987

4. T.J. Hollander, P.J. Kalff, C.T.J. Alkemade
   Ionization rate constants of alkali metals in CO flames
   Journal of Chemical Physics - Volume 39, Number 10 November 1963

5. E. Duceau, J.C. Stroch, F. Dubois
   Simulation numérique industrielle des équations de Maxwell par le code AS-TEMMIS
   Note Aerospatiale TX/C n° 109 637 - June 1993

6. P. Zgirski, E. Meloux, M.J. Bos
   CTV Studies - Phase 0 - Additional tasks
   Assessment of landing accuracy
   HV-TN-10-07-AS/T - December 1994

7. J.W. Marini, F.W. Hager
   APOLLO 6, 7 and 8 blackout test results
   X-550-69-277 - July 1969

8. V. Pochukaev, N. Ivanov, Y. Epishkin
   Study with Ts NII Mash concerning Hermes system aspects
   Contract n° 9912/92/F/TB - Word package 1
   Volume 2 - Experience and modelization of blackout phase during reentry
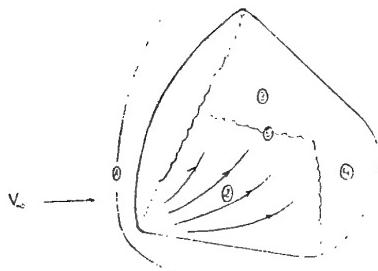
Figure 1
Flow pattern around a capsule entering in the atmosphere
at hypersonic speed
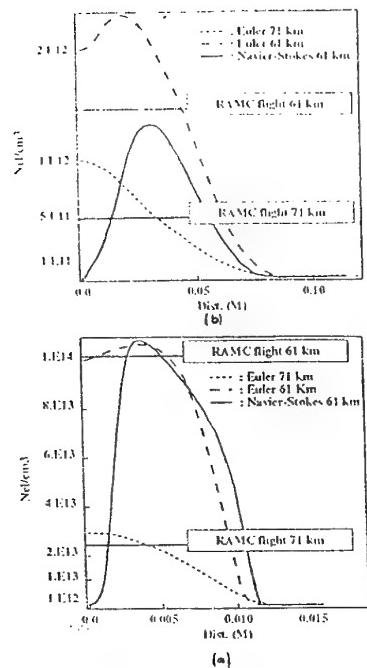
Figure 2
Comparison of computed and measured electron densities
on RAMC configuration vs body distance along the
stagnation line (a) and along the line at the axial
distance 0.22 meter from the nose (b)
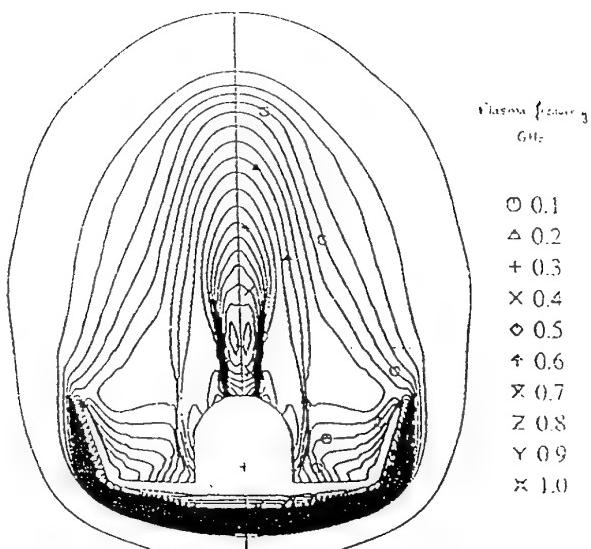
Figure 3
Plasma frequency iso-contours into a rear section of
space vehicle Hermes
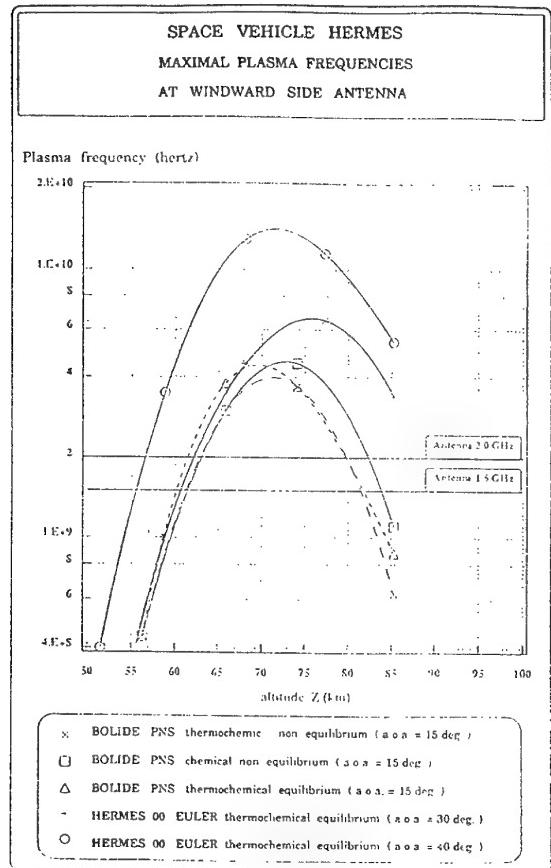
Figure 4
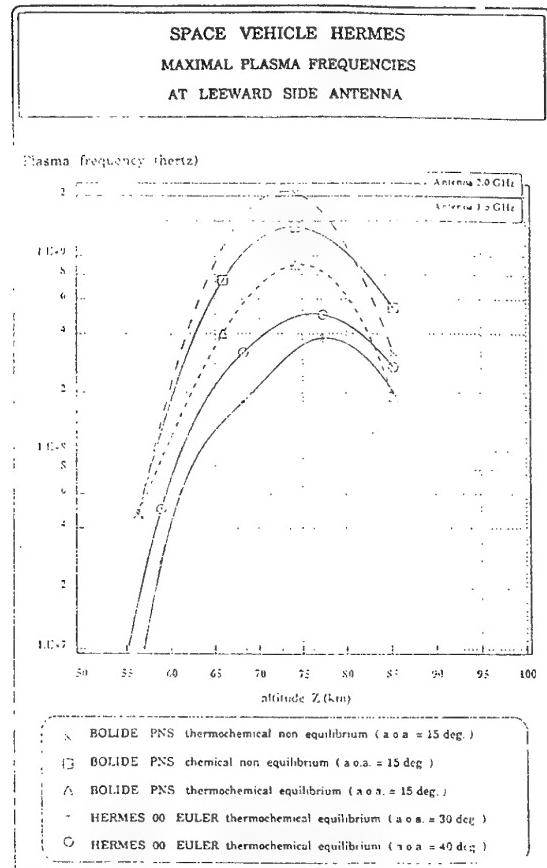
Figure 5
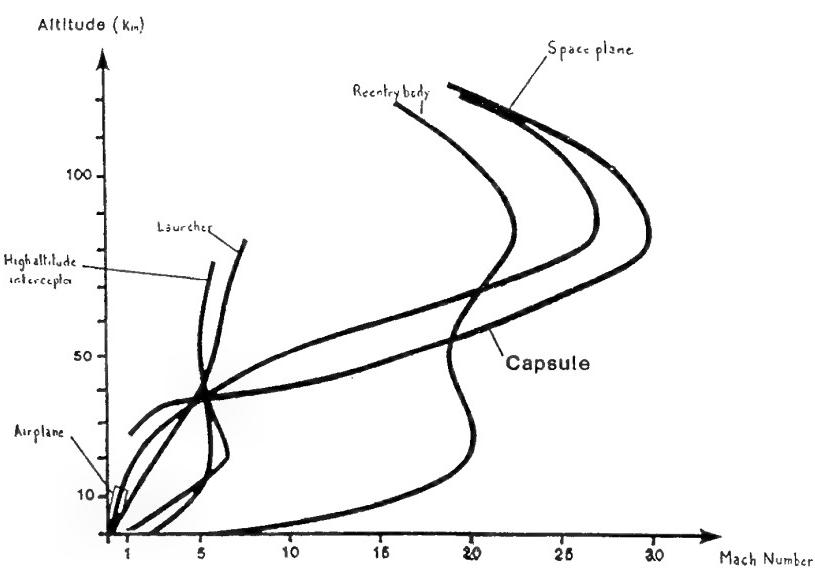

Figure 6
Flight domains
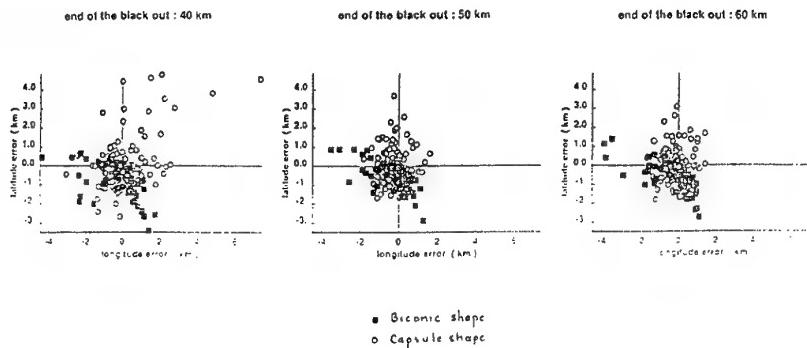
Figure 7
Reentry errors at an altitude of 5 km
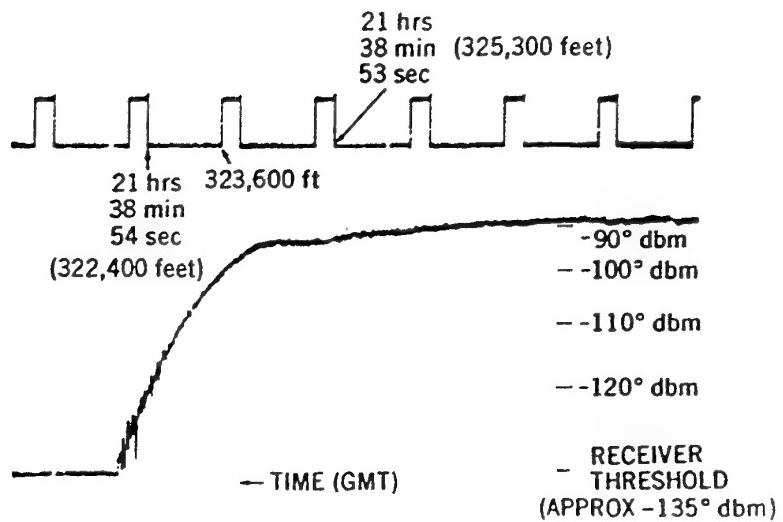
Figure 8
APOLLO 6 S-band signal strength
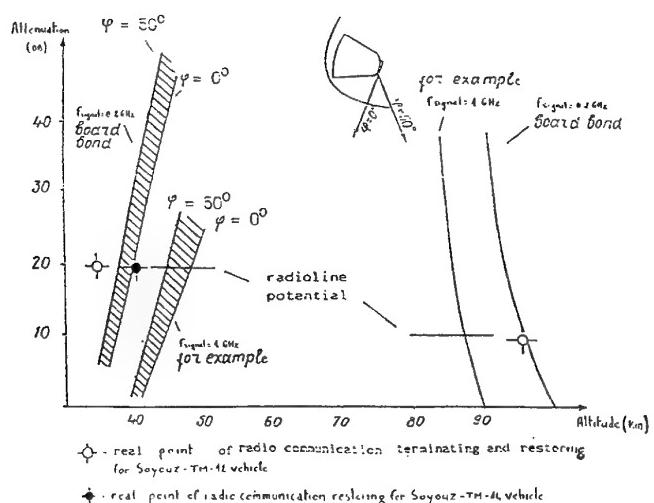
Figure 9
Comparison between calculated and flight data on radio
communication at plasma trajectory for SOYOUZ
vehicle

ABLATION

by

D. DEVEZEAUX, ONERA, BP 72, 92322 Châtillon, France
H. HOLLANDERS, AEROSPATIALE, Les Mureaux, France

1. Introduction

Why thermal protection system (TPS)?
When a vehicle is entering atmosphere at very large speeds, typically more than 4000m/s, the mixture of gas which surrounds the body is heated by compression mechanisms at its front, and by friction inside the boundary layer. The temperature gradients are strong enough to induce some large energy transfert through the wall.

One has to characterize the stiffness of this environment by the heat flux, an hypothetic wall at arbitrary temperature will receive, when isolated from the surrounding flowfield.
This heat flux is depending on the velocity, altitude, shape geometry and local point to be considered.
For a ballistic re-entry body, which has a drag force quite small with respect to its weigth, large velocity values are achieved until low altitude where density is rather high. The heat fluxes could reach values up to several hundred of MW/m2, for an isolated wall. None material can resist to such heatings.So, it needs the use of ablative materials, which disappear by means of physico-chemical processes with air.

2. Typical thermal protection systems.

2.1 Overview of materials. Fig. 1 gives an overview of materials suitable for thermal protection in the temperature range 400K to 3000K.
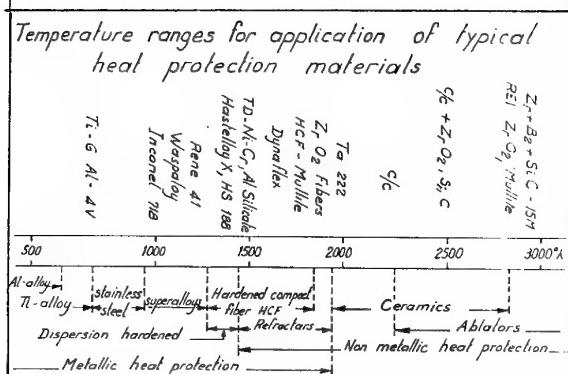
Fig.1 Temperature range for application of typical materials

Metallic materials operate up to 1800K, including refractors from 1400K. Above 1800K, non metallic materials are needed, including ceramics up to 2800K and ablators from 2300Kup tomore than 3000K.
Fig. 2 gives some examples of TPS for different types of missions, and different localisation along the vehicle.

Fig.2 Thermal protection systems

Fig. 3 shows some details of Mercury, Gemini and Apollo TPS. One can observe that the forebody TPS is made of phenolic resin or phenolic glass, which are pyrolysable materials and which are used for wall temperatures below 2500K.
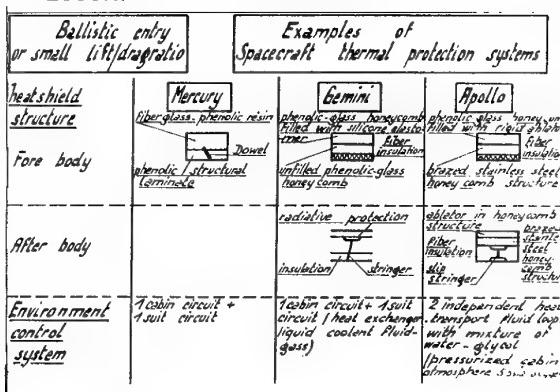
Fig.3 Examples of spacecraft TPS

2.2 Classification of materials. There are four types of materials :
1. Plastics and elastomers composits, including low density plastic or

elastomers composits, and high density composits,
2. Graphitic materials
3. Carbon-Carbon composits
4. Ceramics

2.2.1. Plastics & elastomers composits.
First of all, let us consider some examples, for plastics :
- polytetrafluorethylenes such teflon
- phenolic resins reinforced with organic materials (nylon), mineral (silica), or carbon,
and for elastomers :
-silicon elastomers in honeycomb,
  - polybutadiene - acrylonitric
+ phenolic resin.

Low density plastics. It is a large class of ablative materials with various heating responses depending on their chemical composition :
- depolymerization and vaporization for polytetrafluorethylens,
- pyrolysis and vaporization for epoxy and phenolic resins,
- degradation melting and vaporization for plastics reinforced with nylon fibers.
These materials have a low thermal conductivity and a good behaviour for heat shield.
The main disavantage is their high mechanical erosion when high skin friction occurs. However, their mechanical characteristics can be increased by injection of plastifiants.
For such materials, the control of density is done by adding empty micro spheres to the material.
For example, the teflon, which is used on ballistic missiles ablates by sublimation with depolymerization and gazeous injection in the boundary layer. The wall temperature is a function of the ablation velocity, and the external pressure. The following table gives its thermal characteristics :

T(K)	296	600	601	889
R(kg/m3)	2196	2172	1739	1085
Cp(J/kgK)	711	1213	1477	1536
K(W/mK)	0.336	0.540	0.429	0.373

Low density elastomers. Their advantages are :
- a low thermal conductivity,
- a low density,

- a low oxydation rate.
They are only used for typical missions where oxydation rate is low, and mechanical constraints are not too high. They are also included in honeycomb made in fiber glass. Addition of micro ballons and reinforcement fibers improve their thermal and ablative properties. As an example, Fig. shows the materila selected for Gemini heat shield.

The following table summarizes some properties of low density ablators :

Composit	Density (kg/m3)	Ablation heat (kJ/kg)
Porous Teflon	1392	11630
Low density silicon : silicon elastomer (75%) phenolic micro spheres (25%)	592	18608
Low density phenolic nylon : nylon powder (50%) phenolic resin (25%) phenolic micro spheres (25%)	592	34890
Cork (75%), phenolic plastic (25%)	480	16282

High density plastic composits. They are intensively used. For better mechanical properties, they are soon reinforced with silica, nylon, graphit or carbon, for approximately 70%. Silica composits are mechanically better than carbon ones, but when silica melts, the liquid phase is removed by friction.
Pyrolysis of the resin gives pyrolytic carbon, which is a good thermal protection.
The following table contains their typical properties :

Composit	Density (kg/m3)	Heat of ablation (MJ/kg)
Carbon phen.	1400	166
Graphit phen.	1360	90
Carbon polybenzimidanol	1340	83
Silica polybenzimidanol	1650	31
Silica phen.	1550	27

2.2.2. Graphitic materials. They have a sublimation temperature at about 4000K, and a low ablation recession rate. Among the most currently used, we have :

- the polycrystal graphite with a R value varying between 1700 and 1900 kg/m3, and where the characteristic parameter is the grain size of charge type of liant,
- the pyrolytic graphite, with R = 2000 kg/m3, and where carbon deposit is made at the wall of a prescribed shape by high temperature hydro-carbure environment.

Often used for multi layer deposition, the behaviour of this material is anisotropic, such that there is differences in values of K factor from one for the farest sublayer to two for the external one. This technique conducts to low mechanical resistance, brittleness, possibility of delamination and is difficult to machine.

The following table gives some characteristics of graphitic materials for a pressure of 8.1MPa and energy of 6MJ/kg :

Polycryst.alic graphits	Density (kg/m3)	Ablation rate (mm/s)
Large grain	1920	3.5
Middle grain	1760	4.1
Thick middle grain	1840	2.5
Fine grain	1840	2.0
Thick fine grain	2160	1.2

Under the same conditions, the phenolic carbon has an ablation rate of 6.5mm/s and the silica phenolic, 9mm/s.

Many studies have been done in US on ATJ graphite. The main results are :
- at temperatures below 2778K, only oxydation can occur, for pressure range 0.01 to 1MPa,
- at temperatures below 3700K, sublimation occurs with C3 as major species,
- at temperature above 3700K, the ablation rate is only a function of wall temperature (not of pressure), and grows up exponentially with Tw.

2.2.3. Carbon-Carbon composits. They combine good mechanical properties such as plastic composits, and a good ablative behaviour of graphite.

The process cycle to product carbon-carbon material from carbon-resin one is the following :
- carbon-resin is pyrolyzed under vacuum conditions, that results in porous carbon,

- this material is then impregnated with dense carbon resin,
and another previous loop is performed til achievement of a dense carbon material.

The following table gives some characteristics of carbon-carbon composits under 0.6MPa of pressure and 15MW/m2 of heat flux :

Type of carbon-carbon composits	Density (kg/m3)	Ablation H (MJ/kg)
CVD felt	1600	47
CVD graphit felt	1760	67
C/C matrix	1280	35
Short fiber composite	1570	94
Fine grain graphite	1840	38

Most often a layer of P.A.O. is added to the material.

2.2.4 Fireproof composits and ceramics
First, consider the fireproof composits, typically borates and carbids, which are essentially used for flights with long time duration and low heating. In order to prevent oxydation, materials are covered with a fireproof layer of oxyde (Molybden or Zirconium). The following table gives some details on composits :

Type of materials	Density	Q (MW/m3)
HfBr - SiC (80-20)	8970	7.5
HfC - C (85-15)	9050	6.5
HfC - C - SiC (55-30-15)	4645	5.5
C - ZrBr - SiC (45-40-15)	3010	4.5
ZrBr - C - SiC (56-30-14)	4520	5.0
Hf - Ta - Mo (65-20-15)	13455	4.0
Graphite	1795	5.5

In this table, Q is the heat flux necessary to have an ablation speed of 0.025mm/s when H=19MJ/kg and a pressure of 0,1 MPa.

Ceramics have good thermal performances. However, when thermal shocks occur, inducing some fissures in the material, their behaviour is quite surprising. So, this material is often filled in honeycomb or some polymers are injected in porous ceramics.

Among them, let consider : silica, zircon, alumina, carbides,..., which are manufactured by compression at high temperature, or injection and casting.

As far as we are concerned with applications, these materials are used

for optics : glass windows, or to prevent hydroerosion : metals as Tungsten, Molybden,...

The following table gives some characteristics of this type of materials

	W	WO3	W/Re	Mo	MoO3
density	19222	7160	20000	10235	7545
Tf (K)	3650	1745	3395	2889	1080
Hf (J/kg)	193	316	189	291	337
Hl (J/kg)	837	-2702	749	1221	-3991
emissi	0.4	0.4	0.4	0.4	0.4

3. Ablation process

The term ablation deals with the whole domain of physico-chemical processes acting on material constituting the wall and on chemical species belonging to the boundary layer. When these species come from air, they are diffused from the outer boundary layer to the wall. However, they should be originated from the wall as reacting products, and could be transported through the boundary layer til the outer part by convective and diffusive processes. Sometimes, the generated products can recondensate on the wall.

This system acts as a chemical reactor , exchanging matter with the external field.

In some cases, for example, with metals or silices, a liquid mixture appears such as metallic oxyde or liquid silice, which is brought by the flowfield as droplets, or pours along the wall, acting as chemical reacting species with the interface mixture.

In all cases, the volume of gas which is generated is larger than the one which is set apart from the boundary layer. This phenomenon induces some effect of injection at the wall, that is to say, causes some transversal velocity at the wall. This effect tends to sensitively decrease the convective fluxes.

A relatively well documented example of ablative materials is done with the carbone. At low temperatures, carbone combines with oxygen in order to create carbone dioxyde. This phenomenon is first piloted by the kinetics of the reaction, until the quantity of oxygen, provided by diffusion through the boundary layer, is insufficient in order to activated the reacting process.

Then, the ratio (m'/a) of absorbed oxygen mass rate per mass rate of the diffused gas at the wall is constant. This phenomenon is largely exothermic and , as a result, is not desirable. When temperature is increasing, the nitric monoxyde is producted, which is a stable component. Thus, the cycle of kinetics / diffusion processes is reoperated, until a plateau of m'/a value, which is double from the previous one, is reached.

At much higher temperatures, larger than 3500K, carbone is reacting with nitrogen of air, in order to product radicals such as CN, C2N2, C4N2, etc. At the same level of temperature, the material is sublimated through a production of Cn species, with n belonging to the range 1 to a very high value. C3 is the governing species when flowfield pressure is very high. This phenomenon is quite strongly endothermic, and as a result is seeked for consuming incident heat fluxes.

Fig. 4 (given in annex) shows the sketch of heat exchange balance at the wall.

For an inertial wall or a radiative material without pyrolysis and/or ablation, the heat exchange only concerns :
- convective heat flux coming from the boundary layer, augmented with incident radiating heat flux (solar, albedo, terrestrian, and eventually shock layer),
- wall re-emitted radiative heat flux.

The remaining heat flux is conducted through the material.

If the wall is pyrolysable, then, the previous heat exchange is completed with :
- outgasing effects which tend to decrease the level of heat fluxes,
- combustion effects of pyrolysis gases, which tend to increase the level of heat fluxes,
- roughness effects on heat fluxes, due to degradation of surface, which tend also to increase the level of heat fluxes.

As on the previous case, the remaining heat flux is conducted through the material.

As far as we are concerned with abalation process, the previous heat exchange is modified by introducing :
- outgasing effects of ablation products, which tend to decrease the level of heat fluxes,
- ablation heat effects, which can be exothermal (increasing effects), or endothermal (decreasing effects).
The final resulting heat flux is conducted through the wall.

Numerical modelling. One can notice two cases :
- pyrolysable materials, for which the two following phenomena must be taken into account ; surface abaltion and internal degradation.
- carbon-carbon and graphitic materials for which the only chemical process is the surface oxydization and sublimation.

For the first type of materials, a complete modelization of the chemical internal process is given by the example of the COKE code developed at ONERA The COKE code (ONERA)
We assume an unsteady one dimensional system.
The major restriction of the code is that it does not include ablation process at the wall. But the internal chemical process of pyrolysis of the resin is precisely taken into account.
For the energy equation, we assume that solid and gazeous phases are in thermal equilibrium.
Species conservation equations are written for each species.The continuity equation is written with a gazeous contribution including the mean percolation speed of the gas phase. The momentum equation includes the assumption of an homogeneous material and a low percolation velocity.

Gazeous reaction production rate evaluation

The resolution of the system of equations needs the knowledge of all the chemical production rates. The solid phase is composed of a reinforcement material (chemically non reacting) and a pyrolysable matrix.

With the help of experiments conducted with thermogravimetry technique, the mass loss can be written with a law similar to Arrhenius one, with temperature dependant coefficients.
The gaseous composition appearing by pyrolysis is obtained from mass spectrometry measurements.

Chemical model

The species retained in the COKE code are : H2, CH4, NH3, H2O, C2H4, CO, C2H6, CO2, C6H6.
The gaseous phase is supposed to be in chemical nonequilibrium. The reactions are the following :

2CH4 <-------> H2 + C2H6
C2H6 <-------> H2 + C2H4
C2H4 <-------> H2 + C2H2
C2H2 <-------> H2 + 2Cs
CH4 <-------> 2H2 + Cs
C6H5OH + H2 <---> C6H6 + H2O
C6H6 <-------> 3C2H2
C + H2O <-------> CO + H2
CO + H2O <-------> CO2 + H2
C + CO2 <-------> 2CO
2NH3 <-------> N2 + 3H2
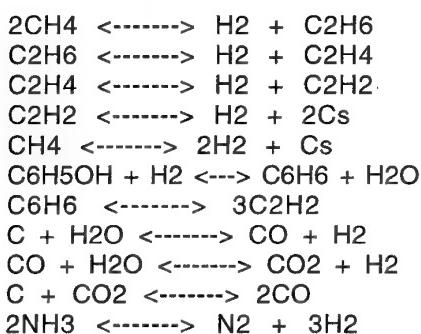
Numerical scheme :

The system is solved by finite difference technique with an explicit scheme.

Another modelization, including surface ablation is given by the example of Aerospatiale code :

One considers that the external wall receives an incident flux q_1 (convective and/or radiative heat flux). The internal wall receives a flux q_2.
The objective is to determine, with respect to the time under a heat flux effect:
• the temperature of the material,
• for pyrolysable and ablative material, the ablated thickness, the specific mass and the outgasing mass flow rate.

Thermal properties - conductivities and specific heats

After the pyrolysis, the material has the following properties r_c, g_c and C_c. One assumes that the caloric capacity r_c and the conductivity l_c are linear funtions of the specific mass r.

$$r.C(T) = A_1(T)r + A_2(T)$$
$$l(T) = B_1(T)r + B_2(T)$$

For the virgin material :
$r_v C_v(T) = A_1(T)r_v + A_2(T)$
For the pyrolysed material :
$r_c C_c(T) = A_1(T)r_c + A_2(T)$

Governing equations

• Surface recession :
  $S = S_{chem} + S_{mechan} + S_{hydroerosion}$

• For some types of material, the chemical erosion is linked to the specific mass of the pyrolised material, the convective coefficient a, the local pressure p_e and wall temperature T_w.

Energy equation for an ablative and pyrolisable environment

The quantity of heat received by an element of volume is equal to the change of enthalpy of this volume during an interval Dt.
The total heat flux received by an element of volume is the sum of :
• heat flux due to thermal conduction ,
• heat flux due to the flow of pyrolysis gases ,
• heat flux due to chemical reaction of pyrolysis .

Equation for pyrolysis :

The speed of decomposition follows an ARRHENIUS's type law :

$$-\frac{1}{\rho v}\frac{\partial \rho}{\partial t} = \left(\frac{\rho - \rho c}{\rho v}\right)^n . A.\exp\left(-B/T\right)$$

A, factor of decomposition - frequency, n order of the reaction of pyrolysis and B ratio of activation energy with respect to universal constant.

Balance equation of the walls

Ablative wall : the thermal balance takes into account :

a) the incidence flux, which includes :
  • convection $Q_c(t,T) = a (H_a - H_w)$, a being the convection coefficient, H_a the athermal enthalpy, H_w the enthalpy at the wall. Q_c is a function of time and wall temperature.
  • shock layer radiation $Q(t,T)$

b) radiation emitted or received by the wall

c) the injection of gas inside the boundary layer
  • pyrolysis gas,
  • gas produced by wall chemical reactions (chemical ablation)

d) absorbed or released heat flux at the wall
  • combustion of pyrolysis gas $m_g H_c$, H_c being the heat flux producted by combustion,
  • endo or exo-thermal heat flux produced from wall chemical reaction (ablation) $m_c H_v$, H_v being the heat of sublimation, combustion or vaporization.

e) internal conduction

Internal wall

The internal wall heat flux takes into account :
  • incidence flux,
  • radiative flux,
  • internal conduction.
If there is some interface between different layers inside the material, one has to add the following equations :
- continuity of flux density :
- introduction of a thermal resistance

The previous system of equations is then solved by an iterative procedure.

For the second type of materials, ground test experiments have been used for the evaluation of surface reference rate, and ablation enthalpy, as functions of wall temperature and static pressure.

Fig. 5 gives an example of these evolutions for graphitic materials.
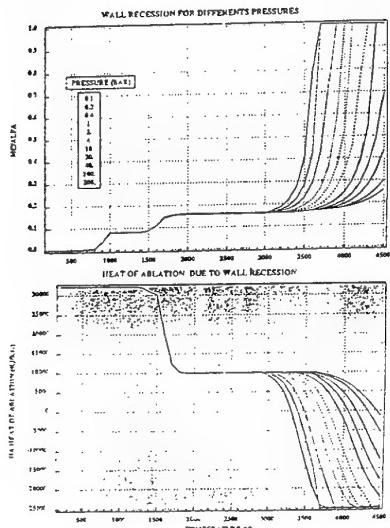
Fig.5 Ablation of carbon material

4. Aerothermal effects of ablation.

Phenomena due to ablation concern :
- injection of gazeous species in the flow field (passive blowing),
- degradation of the wall, which leads to roughness effects on transition and laminar and turbulent heatings,
- wall surface boundary conditions.

Effects of degradation of the wall.
Many studies have been performed for ballistic reentry nosetips and for the shuttle space plane. They are not summarized ih this paper, devoted more to material than to aerodynamics, but a list of references is attached.

Effects of injection of gazeous species.
The treatment of blowing inside the boundary layer needs the coupling of external flowfield and material thermal response. An example of such modelling given by J. Talandier (ONERA, 1994), is summarized below.
A bidimensional calculation has been performed using non-equilibrium boundary layer equations, and modelling of poreous materials.
The main characteristics of this numerical approach are the following :
- modelling of internal degradation process, which take into account oxydization of carbon material,

- outgasing of species , inducing modifications of the flowfield,
- boundary conditions between material and flowfield, which allow partial recombination process at the wall,
- possibility of modelling wall material inserts.

5. Ground tests

The main objectives of the ground test use are to quantify and characterize the fluid-material interactions and their consequences on the flowfield, which drive the processus of ablation. For the large temperature which are encountered during re-entry, it is required to dispose a hot wind tunnel, with a sufficiently long run time to provide adequate heating of the material. The traditional mean is the plasma jet which runs at high temperature levels, such as 5000K.
However, even if the installed power means are quite impressive, typically higher than a MWatt, it is not sufficient to reach flight conditions. For such a purpose, one has to properly select some parameters among all the possible ones, in order to simulate as close as possible the flight conditions, even if the simulation cannot be completely representative. Generally, pressure and heat fluxes are the two parameters which conduct the test conditions, allowing the experimentator to select either laminar or turbulent flowfield regime. In any case, the speeds of ablation are quite close to the flight ones.

Plasma jets. Ablation. The facility
consists on a wind tunnel, where operating air or gas mixture is heated by mean of an electrical arc heater, which runs in a continuous manner.
An example of this type of facility, which is used by Aerospatiale is presented in annex.

Laser/Wind-Tunnel. Ablation ONERA
has build such an installation, which includes a device for the generation of very high powerful CO_2 laser beam (l= 10.6 mm, 18KW max., duration : 10s, section 100mm2). The tests of ablation are conducted for the study of resistance of thermostructural materials

(C/resin, C/C, Kevlar, metals) to ablation effects. A sample is heated by laser beam and is subjected to aerodynamic constraints (Mach 2). Test conditions and ablation speeds are measured. Fig. 6 gives an example of results obtained in this facility.
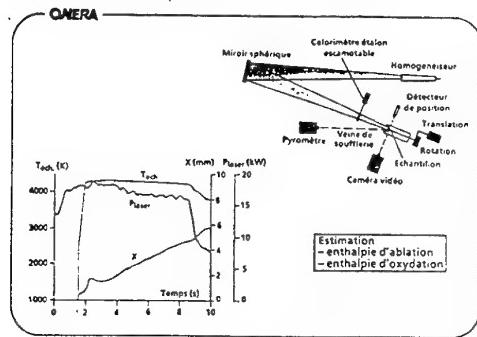

Fig. 6 Results of laser/WT for ablation tests

Blox facilities : oxydation. They consist of laser benches for the study of oxydation process. ONERA disposes of a serie of test facilties for the behaviour of thermostructural materials to oxydation (C/C, C/SiC,... composites). A sample is placed inside a pressurized room, is heated with a high pressure $CO2$ laser beam, and is weighed continuously during the test from several minutes to one day. The data are get and controlled by computer. Different mixtures of gas could be tested (O2 - N2 - Ar ...). Fig. 7 shows the experimental device for BLOX3 facility.
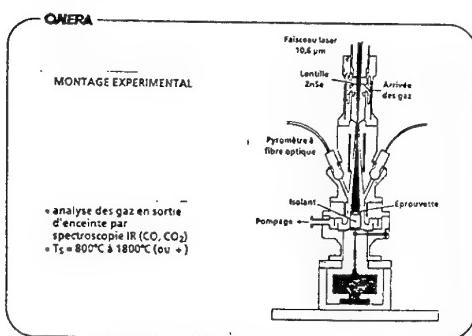

Fig. 7 BLOX3 device

Other facilities : Characterization of materials in high enthalpy conditions can also be performed using electric arc heater device such as SIMOUN facility of Aerospatiale the operating conditions

of which are shown in annex. One can notice that Italy is also preparing some new facility, named SCIROCCO, similar to SIMOUN one, at a larger scale in CIRA.

Finally, let us mention the plasmatron technology which uses a high frequency induction gas heating, and which delivers a cleaner flowfield than the previous facilities, since there is no electrod erosion. This type of device is often used for the characterization of catalytic properties.

6. In-Flight Measurements.

Flight measurements of the heat-shield recession on a re-entry body, have been well studied during the last 3 decades. A summary of techniques based on optical sensors and ultrasonic sensors is given in annex.

7. Conclusion

Ablative materials are needed in the case of intense heat fluxes, in order to build reliable thermal insulation of re-entry vehicles.

Many complex phenomena are involved in the ablation process :
- internal degradation, with appearance of gazeous phase,
- surface oxydization and sublimation,
- wall degradation and recession.
Furthermore, these phenomena act on the flowfield behaviour :
- blowing effects of ablative products,
- blocking effects of incoming heat fluxes on the materials,
- modification of boundary layer transition location, and increase of heat fluxes due to surface roughness.
Different typical materials can be chosen, depending on the type of mission (ballistic or gliding re-entry), and on the local level of fluxes.
Material modelling needs a complete characterization of material thermal properties and degradation.
As a result, ground tests are required and this leads to many different type of facilities, which unfortunately cannot entirely simulate the flight environment.
Finally, only partial results have been given by flight tests.

Fig. 4 Sketch of Heat Exchange Balance

$$Q_1 - \varepsilon_1 \sigma\left(T_{w1}^4 - T_{R1}^4\right) + \dot{m}g\left(H_c - \eta_1(H_a - H_w)\right)$$

$$+ \dot{m}_c[H_v - \eta_2(H_a - H_w)]] = -\lambda \frac{\delta T}{\delta x}$$

Outgasing $= \eta_1 \dot{m}_g (Ha - H_w)$

Pyrolysis gases

Combustion $= \dot{m}gHc$

Pyrolysis gases

Roughness effects

Convective

Resulting Wall

Δq

Conductive $\lambda \frac{\delta T}{\delta x}$

Pyrolysable Wall

Ablation Products $= \eta_2 \dot{m}_c (Ha - H_w)$

Outgasing

Exo

Ablation Heat

Resulting Wall

Endo $= \dot{m}_c H_v$

Ablation Heat

Ablative Wall

Radiative Wall

Resulting Wall

Radiative Ext

Convective Smooth Wall

Inertial Wall

Radiative Material

ABLATION AND TEMPERATURE SENSORS
FOR FLIGHT MEASUREMENTS IN REENTRY BODY HEAT SHIELDS

J.J. Cassaing, D.L. Balageas, A.A. Décom, J.C. Lestel

Office National d'Etudes et de Recherches Aérospatiales
Division de Thermophysique
ONERA, BP 72, 92322 Châtillon, France

ABSTRACT

Since 1977, ONERA has ground and flight tested different techniques for heat-shield recession : acoustic and combined temperature/ablation optical measurements.

This last technique uses a gage that views the radiation optically from a cavity embedded within the heat shield. Flight measurements, both of temperature and of passage of the ablation front, are compared with data generated by a predictive numerical code. The ablation and the heat diffusion into the instrumented ablator can be simulated numerically to evaluate accurately the errors due to the presence of the gage.

The ablation measurement alone of the reentry body nose is made by an acoustic gage.

The temperature measurement alone of the heat shield inner wall will be soon carried out by an optical sensor.

Keywords : Ablation, Optical sensor, Acoustic sensor, Temperature sensor.

1. INTRODUCTION

Flight measurement of the heat-shield recession on a reentry body, i.e. the phenomenom well known as ablation, is difficult. Since the beginning of the 1970s, two techniques have been used: ablation measurement by radio elements and ultrasonic ablation measurement. The first technique consists of measuring the variation in radioactivity of implants ablated with the material by means of a radiation detector. The second technique consists of determining the thickness of the receding material from the travel time of an ultrasonic wave reflected off the surface being ablated. These measurements, combined with the indications given by thermocouples implanted in the heat shield, are used for dimensioning the heat shield. However, it is obvious that each of these techniques has limitations, in particular thermocouples, which are destroyed when the temperature reaches 2300 K, whereas the ablation temperature may, in certain applications, be as high as 4000 K.

Ablation measurement by radio elements raises many technical problems and it has been supplanted by ultrasonic ablation measurement. In France, this radioactive technique on which research was conducted at ONERA as early as 1973 (Ref.1) was dropped after an inconclusive flight test. An ultrasonic ablation meter (Ref.2) has been in development for several years now at ONERA; two flight tests were successfully carried out in 1990 and 1991.

Between 1979 and 1985, ablation measurements in flight were made using an original sensor (Ref.3) on which development was started at ONERA in 1977. This sensor also measures the internal temperature of the heat shield as well as the ablation temperature.

2. THE COTA SENSOR

2.1 : Description and Concept of the COTA Sensor

The COTA sensor (*Capteur Optique de Température et d'Ablation*), illustrated schematically in Figure 1, consists of a very long cylindrical cavity, closed at one end, machined in the medium to be instrumented (Fig.1a). An optical fiber connected to a photodiode receives the radiation emitted by the cavity. In order to prevent ingress into the cavity of smoke and carbonized residues due to possible pyrolysis of the ablative material and to allow the sensor to be calibrated as a thermometer, the cavity was machined in a vitreous carbon cylinder inserted after calibration in the material to be instrumented (Fig.1b).
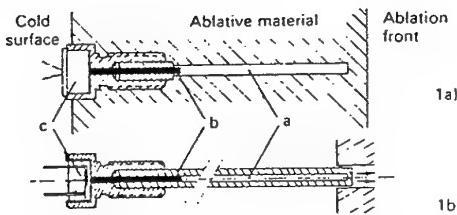

Figure 1 : Schematic view of COTA.

(a) cavity ; (b) optical fiber ; (c) photodiode

The typical dimensions of this vitreous carbon sheath are as follows: several tens of millimeters long, outer diameter 2 mm, inner diameter 0.8 mm and a thickness of 0.2 to 0.4 mm at the bottom of the cavity.

The vitreous carbon sensor is then inserted in a cylindrical cavity machined in the reentry body heat shield material, with the cavity axis parallel to the main heat flux direction. Several types of photodiodes can be used. A silicon diode was chosen as it has a spectral range of 400 to 1000 nm which allows temperature measurements from 1500 to 4000 K, i.e. the temperature range reached by the surface being ablated. Under the normal conditions of ballistic reentry, the medium is subjected to transient heating such that the cavity bottom is the hottest part and there is a strong thermal gradient along this cavity axis. Considering these thermal conditions and the sensor geometry, the radiation received by the photodiode is mainly that emitted by the practically isothermal bottom of the cavity, since the wall temperature decreases rapidly away from the bottom. It is therefore absolutely necessary for the diode (or the fiber) to be in direct view of the hot end. This was made possible by ultrasonic drilling of the vitreous carbon. The radiation received is therefore a function of the temperature at the cavity bottom.

To make a thermal sensor, it is sufficient to correlate this temperature with the current output by the photodiode.

Furthermore, if the bottom of the cavity is destroyed by ablation, there is a sudden drop in the signal, which allows detection of the ablation front passage time at the depth of the emitting hot wall (Figure 2). To follow the evolution of ablation with time, it is necessary to implant several COTA sensors at different depths.
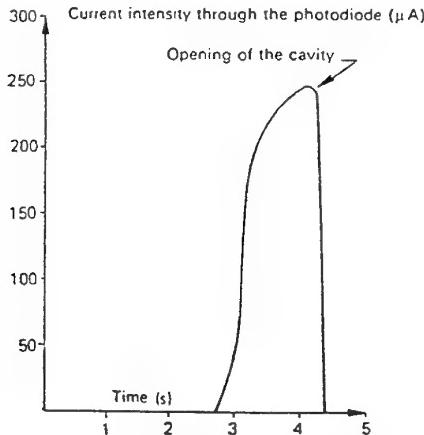

Figure 2: Detection of the ablation front passage time.

Figure 3 is a photograph of a COTA sensor before its insertion in a reentry body heat shield.

Figure 3: Photograph of the COTA sensor, flight model.

2.2 : Calibration of the Temperature Sensor

It is necessary to correlate the internal temperature T_{cota} at the bottom of the cavity with the current output by the photodiode. To do so, transient heating is carried out in a non-oxidizing environment by means of a 15 kW carbon gas cw laser.

The configuration during calibration is illustrated in Figure 4. An optical pyrometer measures the variation with time of the temperature T_{ex} of the external wall subjected to the laser flux. To determine the temperature T_{cota} corresponding to the measured temperature T_{ex}, it is necessary to simulate heating of the sensor in the calibration configuration by calculation. This is achieved by a 2D conduction program using a finite difference method, which gives the relationship between the emitting wall temperature and the current detected by the diode.
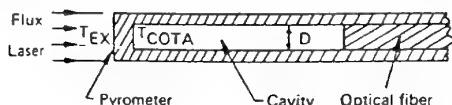

Figure 4: Principle of calibration and measurements made.

It is found that above 2 000 K, this relation is :

$$I = A.(T_{cota})^n, \quad n \cong 8,$$

where coefficient A depends on the optical properties of the vitreous carbon, the quality of the cavity machining and the cavity size.

The curve of Figure 5 is a typical COTA calibration curve. It relates the photodiode current to the average temperature T_{cota} of the emitting surface.

2.3 : Ground Testing

Ground tests were conducted in 1978 using the JP50 Plasma Generator of Aérospatiale, located in Aquitaine.

The flat samples of carbon/carbon and silica/resin composites with cavities directly machined in the materials were subjected to an air flow at very high enthalpy, causing heating and ablation of
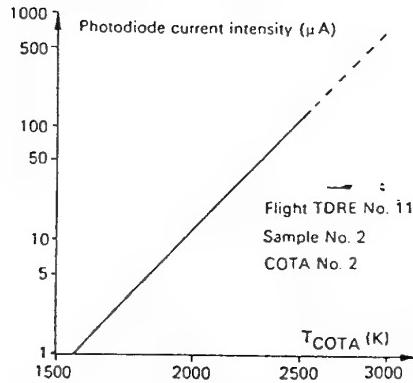

Figure 5: Calibration curve of a COTA.

the material. For charred materials, gases and liquid residues entered the cavity of the sensors, which caused high interference in the photodiode signal. Subsequent to these first tests, it was decided to make the cavity in a sealed vitreous carbon tube inserted in the material to be instrumented.

During the second test campaign, two tests were carried out, with six COTA sensors implanted in a silica/resin composite. For two COTA, the surface was continuously filmed during the test. Analysis of the films and the opening of these two COTA sensors gave an excellent comparison. The uncertainty on the opening of the COTA was ± 0.05 s. For the remaining sensors, their signals were compared with those from thermocouples located in their vicinity, slighty further back, since the thermocouples do not provide data above approximately 2300 K. As ablation occurs for the material around 2500 K, it was necessary for the opening of the cavities to slightly precede the loss of data from the thermocouple ; the uncertainty on the opening was between ± 0.05 s and ± 0.20 s.

2.4 : Correction of the Raw Measurements

The different thermal and ablative properties of the vitreous carbon and the instrumented ablative material, a phenolic silica material, as well as the presence of the cavity in the material to be analyzed make it necessary to evaluate the disturbances in the thermal field and the position of the ablation front induced by the presence of the COTA sensor.

As the vitreous carbon is a better heat conductor than the composite, it behaves like a heat sink in the location of the cavity. This affects the wall temperature of the heat shield, causing a local delay in ablation. The result is a protuberance and an increase in the convective fluxes which may be large. All these disturbance phenomena are specific to each COTA sensor, since they depend on the thermal history of the particular sensor in the ablative material.

A 2D conduction and ablation code prepared especially during development of the COTA sensor provides a general model of this geometry and the disturbances : the cavity, the various materials with thermal and physical characteristics depending on the temperature, the convective flux entering the material, the ablation temperature which varies along the trajectory, the mechanical and chemical ablation laws governing the temperature and rate of ablation of the materials, the increase in the aerodynamic flux (protuberance effect). This 2D program, using a finite difference method, is systematically applied to interpret the response supplied by the sensor during the flight test. It gives the following information :

- the delay ∂t between the cavity opening time t_{cota} and the time of passage t_{mat} of the ablation front in the material in the absence of a sensor, at depth Z_{cota} from the internal emitting surface of the cavity :

$$\partial t = t_{mat} - t_{cota}$$

($\partial t < 0$ if the ablative material is less conductive than the vitreous carbon).

- each time, for the same depth Z_{cota} and before opening of the cavity, the difference ∂T between temperature T_{cota} and temperature T_{mat} which would exist in the heat shield in the absence of the sensor :
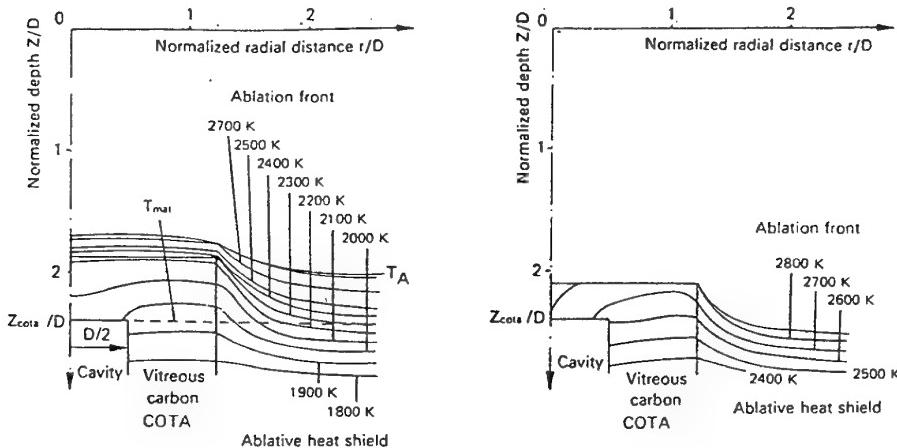
Figure 6: Simulation of heating and ablation of the heat shield instrumented by a COTA.

$$\partial T = T_{mat} - T_{cota}$$

- each time, the difference ∂T_{ablat} between temperature T_{cota} and the ablation temperature T_{ablat} of the ablative material of the heat shield in the absence of the sensor :

$$\partial T_{ablat} = T_{ablat} - T_{cota}$$

These differences, given by numerical simulation, are then used to correct the values measured during the flight test.

Figure 6 shows the results given by simulation at two times preceding opening of the cavity. In Fig.6a, the COTA sensor remains underneath the surface but already causes a slight protuberance ; in Fig.6b, it appears protruding on the surface a short time before opening the cavity.

The increase in the convective heat flux resulting from the effect of protuberance of the vitreous carbon in the boundary layer was modeled. Analysis of the results of tests conducted in a wind tunnel and bibliographic research made it possible to model the increase in heat flux according to the height k of the protuberance and the local momentum thickness Θ of the boundary layer (Figure 7) ; h is the convective heat transfer coefficient in presence of the protuberance and h_0 the same coefficient in the absence of protuberance. The minimum value of k/Θ may be as high as 2 or above. This quantity depends on the depth at which the COTA sensor is located and on the trajectory followed.
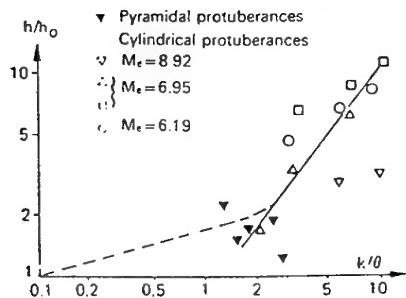

Fig.7: Increase in the heat flux due to protuberance effect.

2.5 : Flight Tests

Forty COTA sensors were implanted in the heat shield of eight ballistic reentry bodies. The sensors of the first flight (four COTA) were implanted too deeply for the cavity to open, and it was not possible to analyze the results of a flight test (involving six COTA) for reasons independent of the sensors. Accordingly, out of the thirty COTA sensors for which the flight test was satisfying, four did not give a signal, amounting to a failure rate of approximately 10 %, twenty-two were completely analyzed and four were not analyzed due to too low a signal-to-noise ratio.

The flight tests differed by the reentry trajectory followed, resulting in variation of the aerodynamic fluxes in a ratio of 1 to

10 at the time the sensor cavity opened. This means that the time during which the vitreous carbon was heated differed widely from one test to another and from one sensor to another depending on the depth at which it was located ; thus, for the lowest fluxes, the heating recorded lasted 4 seconds, whereas for the highest fluxes, it was only 0.5 seconds.

The 2D code described above was used to calculate the corrections to be made to the raw measurements gathered during the flight test, i.e. the sensor cavity opening time t_{vol} and the temperature T_{vol} before and at the time of opening the cavity.
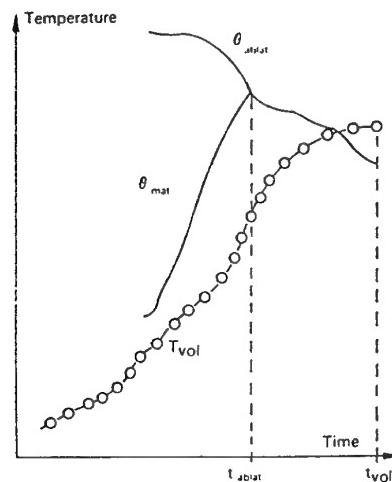
Figure 8: Example of interpretation of a flight test.

The quantities restored after analysis are the following :

- the time of passage t_{ablat} of the ablation front at depth Z_{cota} :

$$t_{ablat} = t_{flight} + \partial t$$

- each time, the internal temperature θ_{mat} of the heat shield at depth Z_{cota} :

$$\theta_{mat} = T_{flight} + \partial T$$

- during a certain lapse of time preceding time t_{ablat}, the ablation temperature θ_{ablat} of the heat shield :

$$\theta_{ablat} = T_{flight} + \partial T_{ablat}$$

Figure 8 shows an exemple of variation of the quantities restored: t_{ablat}, θ_{mat}, θ_{ablat} from the experimental results: t_{flight}, T_{flight}.

As was demonstrated, the larger the heat flux entering a heat shield, the smaller the difference ∂t. There is generally a delay of 1 to 1.5 seconds.

2.5.1 : Detection of the ablation front passage. The results obtained after analysis of the measurements given by the COTA sensors were compared with the numerical results given by the one-dimensional conduction and ablation code readjusted according to the parameters measured during launches (thermocouples, pressures, etc.). This code is used to dimension the heat shield. Figure 9 shows a comparison of the surface recession curve given by the 1D code with the interpreted results of four COTA sensors on which the cavity opened during a given flight test.

An average difference Δt of 0.2 s was found between the restored time of the ablation front passage and that given by the 1D code for 14 sensors included in four different tests. As the ablation rate in the material was between 0.9 and 1.5 mm.s^{-1} depending on the test, this difference corresponds to an uncertainty of 0.25 mm on the ablation front position.
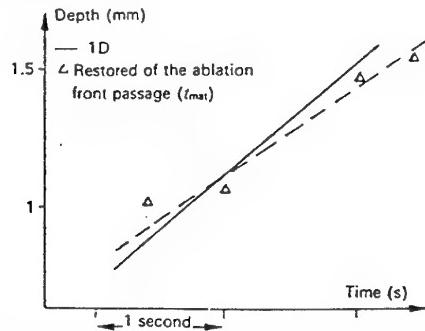

Figure 9: Comparison of the computed wall recession and that restored by four COTA included in the same flight test.

2.5.2 : Ablation temperature. For 13 sensors included in five flight tests, a difference of $\pm$ 120 K was found between the restored ablation temperature θ_{ablat} and the ablation temperature T_{ablat} given by the 1D code. As temperature θ_{ablat} is in the vicinity of 3 000 K, this difference is better than 5 %. A correlation is made on Figure 10 for three flight tests between this temperature difference $|\Delta T|$ and the difference $|\Delta t|$ between the time of the ablation front passage determined from flight measurements and that computed by the 1D code.
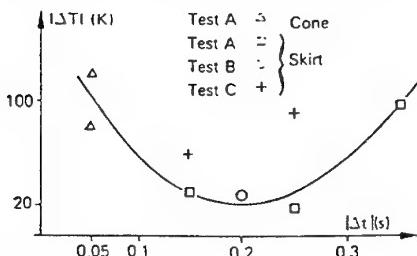

Figure 10: Correlation between temperature and time differences between the interpreted sensor response and the code results.

The restored ablation temperature before the time of the ablation front passage was compared with the heat shield surface temperature given by the 1D code. The curve of Figure 11 shows the results obtained for seven COTA sensors which opened during different tests.

The origin of the time axis is the cavity opening time given by the 1D code. It can be seen that the difference between the temperatures given by the code and those restored increases away from the time of opening of the cavity sensor.

2.5.3 : Measurement of the rate of ablation. The experimental results show that the time of opening of the cavity differs from the time of the ablation front passage at the same depth Z_{cota}. This difference can be up to 1 second and more ; it is necessary to use the 2D simulation code to correct the experimental values.

Considering two COTA sensors implanted in the same region of the heat shield at two different depths, it is observed that the difference between the times at which the two sensors open is very close to the difference between the times of the ablation
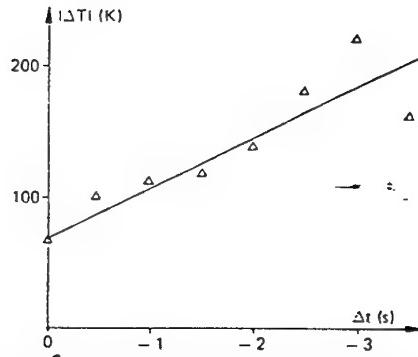
Figure 11: Variation in the difference between the calculated and restored temperatures of the surface subjected to ablation during the 4 seconds preceding opening of the cavity.

front passage at these two depths. This remarkable result, which allows the rate of ablation v_{ablat} of the heat shield to be determined directly :

$$v_{ablat} = (Z_{cota2} - Z_{cota1}) / (t_{cota2} - t_{cota1}),$$

is due to the fact that the two COTA were subjected to comparable heating during the trajectory. An example of this is shown in Figure 12 which corresponds to the case of four COTA sensors implanted at different depths but on the same measurement abscissa. The average computed rate of ablation is 0.85 mm.s^{-1} for the 3 seconds considered, whereas the rate of ablation determined from flight measurement is 1 mm.s^{-1}.

For all the flight tests, it was thus observed that the rate of ablation was restored from the raw measurements with an accuracy better than 20 %.
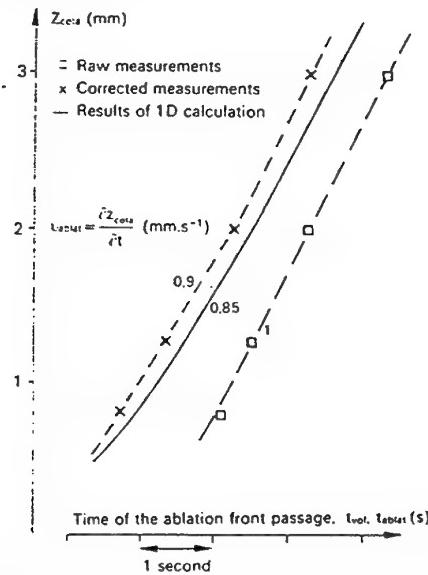
Fig.12 : Rate of ablation computed and determined from raw and corrected measurements.

3. THE COT SENSOR

This sensor, called *Capteur Optique de Température* (COT), is derived from the same principle as the COTA sensor, but it does not measure the ablation front passage because it is designed to measure the inner temperature of a heat shield wall.

The research was conducted with the support of Aérospatiale. Several COT sensors, manufactured by Aérospatiale, will soon be flight tested.

3.1 : Definition and Study of the Sensor

A numerical study was made to define the COT geometry and material. The code employed, ADINAT, uses a finite element method, applied in the 2D version.

Two sensors were possible, the first with a closed cavity to prevent obstruction of the cavity and the second with an open cavity which directly gives the inner wall temperature of the heat shield surface seen by the optical fiber and then by the photodiode (Figure 13). The calculations showed that very rapid high heating could not be restored by a closed cavity. The temperature difference (T_{ext} - T_{cot}) is about 1000 or 1500 K for a thickness e = 0.5 mm, which corresponds to an unacceptable time delay of about 4 s. An opened cavity with a graphite cylinder was therefore chosen .
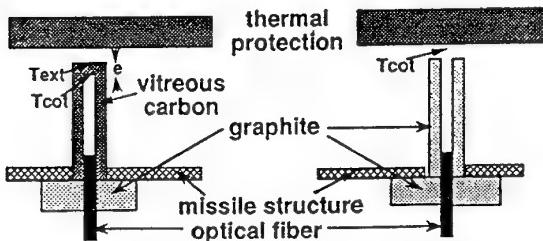
Figure 13: Schematic view of COT.

The dimensions of the COT sensor are as follows :

cavity diameter : 1 mm, graphite cylinder : 5 and 20 mm, cavity length : 30 mm.

Germanium or silicon photodiodes were suggested for the flight tests.

The 1 mm fiber diameter suggested is a flexible silica fiber.

The emitting wall sample is always seen with the same solid angle for a given COT sensor.

3.2 : Laboratory Tests

Samples of the heat shield were electrically heated in a vacuum furnace, which can reach 2600 K. A prototype COT sensor was made, using either a silicon or a germanium photodiode. The distance between the COT sensor and the emitted sample surface was adjustable.

3.2.1 : Calibration of the photodiode signal. Calibration tests are essential to define the output range of the photodiode current. Several tests were performed with the two types of photodiodes and the results are given in Figure 14. As used in the COTA approach, the relationship between the emitting wall temperature and the current detected by the diode is : $I = A.(T_{cot})^n$

n is about 8 for the silicon photodiode (test 1: n=8.3, test 3: n=7.9) and about 5.5 for the germanium photodiode (test 1: n=5.4, test 3: n=5.7). This difference can be explained by the fact that the sample temperature is not perfectly known during the heating (due to thermocouple ageing). Other tests with different photodiodes confirmed these uncertainties on coefficient n and thus showed that a calibration of each COT sensor coupled with its electonic circuit (amplifier, pins, etc.) is absolutely necessary. By reference with the COTA sensor calibration (silicon photodiode), it is demonstrated that the difference on the photodiode current for several ground tests is about 10 %, which leads to a relative error of ± 2 % on the temperature T_{cot}.

These tests also confirmed that the current is independent of the distance between the optical fiber and the emitting sample wall.

3.2.2 : Influence of the heat shield composite material. The 3DCC composite material is made of two phases (fiber and matrix) which may have different emissivities and different conductivities. Tests were conducted to quantify the importance of this phenomenon. The COT sensor could move in front of the sample wall and received the flux emitted by a 2 mm diameter surface. The COT sensor was successively aimed at the center of the middle line of the sample, then at abscissas : ± 0.5 mm, ± 1.5 mm and ± 2.5 mm. The photodiode current is given in Figure 15. A drift appears due to the furnace regulation and a relative error of ± 1.5 % on temperature T_{cot}. Another sample gave $\Delta T_{cot}/T_{cot}$ equal to 1 %.
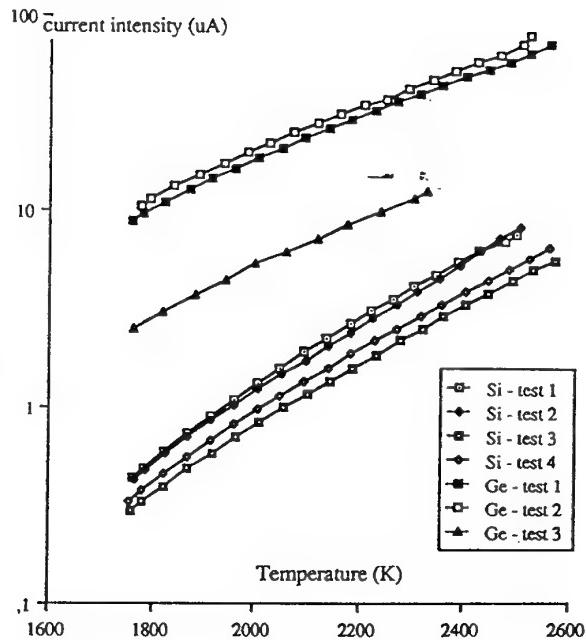
Fig.14: Preliminary calibration curves of a COT sensor.

3.3 : Project of a calibration bench.

For the calibration of the COT sensor and its electronic circuit, ONERA suggested Aérospatiale to manufacture a high temperature black body, operating between 1 500 and 2 300 K.

3.3.1 : Description of the bench. The black body, placed in a vacuum furnace, could include :

- a heating component consisting of a hollow graphite cylinder supplied by a current of 1000 A;

- a 2 mm diameter hole drilled in the graphite cylinder which would be sighted by the COT sensor ;

- an identical second hole for the aiming of the reference pyrometer.

3.3.2 : Calibration of the heat shield material emissivity. The calibration method assumeses the emissivity of the heat shield composite material well known. ONERA suggested to measure the emissivity in the solar furnace of ETCA (Etablissement Technique Central de l'Armement). The emitting surface of the heat shield sample can reach 2500 K. This temperature is measured with a pyrometer coupled to a hemispherical reflector. The relative emissivity error given by ETCA is about ± 5 %. This value leads to a relative temperature error of 0.5 %.

3.3.3 : Estimation of the restored temperature error. The relative error on the restored temperature of the inner heat shield wall is due to :
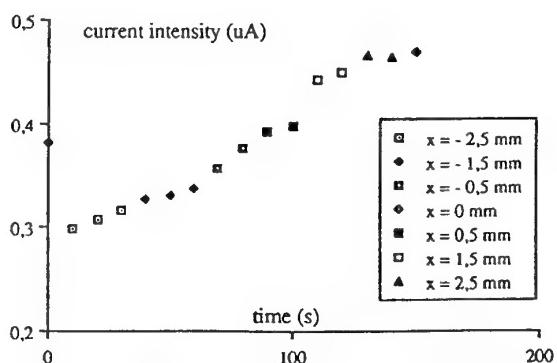
Figure 15: Influence of the composite material phases.

- uncertainty on the calibration reference temperature, estimated at 0.5 % ;

- uncertainty on the calibration curve of each COT sensor, estimated at ± 2 % ;

- uncertainty on the global composite material emissivity, estimated at ± 0.5 %, and on the emissivity and temperature gradient of the different phases, estimated at ± 0.75 %.

The total relative error is therefore about ± 4 %. For example, if the heat shield temperature is 3500 K, the absolute error on this temperature will be ± 140 K.

4 - ABLATION OF A REENTRY BODY NOSE

The research was conducted with the support of Commissariat à l'Energie Atomique (CEA/DAM).

4.1 : The COA Sensor

This sensor, called *Capteur Optique d'Ablation* (COA), is derived from the same principle as the COTA sensor, but it does not measure the temperature, as the cavity is drilled directly in a reentry body nose made of carbon/carbon reinforced composite (3DCC) without the use of vitreous carbon, making it impossible to calibrate the sensor. Its development was started in 1982.

Because of the cavity lenght in the nose, the optical fiber is much longer than in the COTA sensor and is sheathed in a nobium tube. The fiber is positionned in the cavity such that the end receiving the radiation (hot part) does not exceed 1300 K. The diameter of the cavity in the 3CDD is about 2 mm; it is necessary for the fiber hot end to be in direct view of the cavity end. The photodiode chosen was identical to those of the COTA sensor.

Two flight tests each involving two COA sensors were conducted, but it was not possible to interpret the results for reasons independent of the sensors. This optical technology has been abandoned for the benefit of an ultrasonic technology.

4.2 : The CUSA Sensor

4.2.1 : Concept of the CUSA Sensor : This sensor, called *Capteur UltraSonore d'Ablation* (CUSA), operates on the same principle as sonar : a train of acoustic waves is transmitted on the rear face of the reentry body nose and propagates to the apex where, considering the very high acoustic impedance ratio between the material and air, it is reflected completely back to the transmitter. The travel time can be related to the thickness crossed if the ultrasonic propagation speed is known. Althought the measurement principe is simple, application to thickness of several tens of centimers of a three-directional composite material such as carbon-carbon is more complicated.

The complexity of the material requires the use of relatively low propagation frequencies : a few hundred kHz. Fortunately, the large divergence of the sensors at these frequencies is decreased by the wave guidance phenomena related to the material structure. In order to increase the signal-to-noise ratio on the measurement as much as possible, the transmitted wave train is frequency modulated and detection is carried out by correlating the received signal with the emitted signal. The ultrasonic propagation speed was measured for the frequencies included in the transmission spectrum. The speed depends to a great extent on the propagation frequency.

The measurement system consists of an off-the-shelf piezoelectric sensor and an electronic system.

4.2.2 : Ground and Flight Tests : Ground tests were conducted by ablating samples of 3DCC material, first at reduced scale in a ONERA facility, then in full size on the Aérospatiale/Aquitaine JP200 plasma torch. The tests were sufficiently encouraging to initiate work on a flight ablatometer.

The flight system consists of a broadband sensor centered on 500 kHz, bonded to the rear tongue of the reentry body nose. The electric signal from the sensor is amplified, filtered and converted from analog to digital, then remotely measured on the ground during the test. The correlation processing is then conducted off-line on the ground. Figure 16 gives a comparison of the first flight ablatometer measurement with ablation computations.The difference observed with the prediction, increasing over time, is

due to the fact that the variation in the propagation speed versus temperature was not corrected. This effect will be taken into account later.
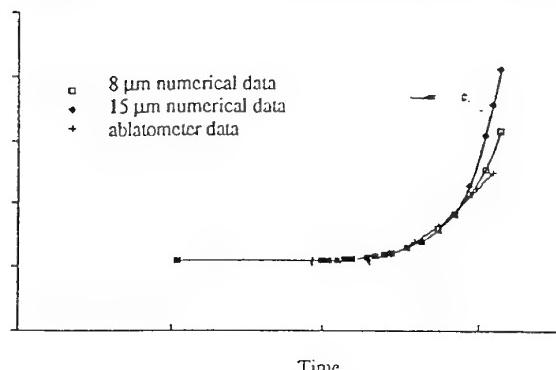
Fig.16 : First experimental flight - comparison of the ablatometer measurement with the corresponding ablation computations for two roughness height hypotheses.

5 - CONCLUSION

In France, since 1979, flight ablation measurements are made using two techniques developed at ONERA : an ultrasonic sensor (CUSA) for the reentry body nose and an optical sensor (COTA) which also measures the ablation temperature of the missile heat shield, which may be pyrolyzable.

The two physical parameters measured by the COTA sensor are, after data reduction, in good agreement with the computational predictions. The differences observed are equal to a few tenths of a second for the ablation time and in the vicinity of ± 100 K for the ablation temperature, which approaches 3 000 K in the flight tests. Direct analysis of the cavity opening times of several COTA sensors located on the same measurement abscissa at different depths in the heat shield gives a material ablation rate estimate with an error less than or equal to 0.2 mm.s^{-1}.

An optical sensor (COT) giving only the temperature of the inner face of an uncharring composite material was designed recently to be implanted soon in a reentry body.

The agreement between the computed ablation and the results given by the CUSA is rather good. Corrections taking into account the temperature effect on the propagation celerity will be done soon to try to improve the accuracy of measurements.

REFERENCES

1. Jalin 1973, Etude et réalisation d'un ablatomètre embarquable à radio-éléments, Rapport Technique ONERA n° 8/4234 SY.

2. Garnier 1984, Ablatomètre à ultrasons pour protection thermique en matériau composite 3DSR - Travaux 1983, Rapport Technique ONERA n° 25/3434 SY.

3. Cassaing et al. 1980, Temperature and ablation optical sensor, AIAA paper n° 80-1479 and Aerothermodynamics and Planetary Entry, Vol 77 of Progress in Astronautics and Aeronautics, 1981.

AEROASSIST KEY TO RETURNING FROM SPACE AND THE CASE FOR AFE

BY

LOUIS J. WILLIAMS
TERRILL W. PUTNAM
NASA HEADQUARTERS
300 E STREET, SW
WASHINGTON, DC 20546-0001

ROBERT MORRIS
NASA MARSHALL SPACE FLIGHT CENTER
ALABAMA 35812-1000

SECTION 1: RETURNING FROM SPACE—THE CASE FOR AEROASSIST (An Executive Summary)

The Aeroassist Flight Experiment (AFE) is important in the development of a substantial and cost-competitive space industry. It is a research program to develop the technology base needed to design a new class of advanced entry vehicles that will play a key role in establishing a mature U.S. space presence in the next century.

A dynamic and economical space program in the 21st century will include many operations involving the return of satellites, materials, and products from high Earth orbits (HEO), lunar bases, and planetary missions. The common and dominant characteristics of vehicles returning from such missions will be their very high speed as they approach the Earth. This high speed must be reduced substantially before the returning vehicle can be landed safely on Earth or placed in low Earth orbit (LEO), where the Space Shuttle operates now and the Space Station Freedom will operate in the future.

LEO is a strategic locale that will always play a critical role in any space program. Its location just beyond Earth's appreciable atmosphere can be reached from Earth with the lowest cost in energy, and it is the natural and convenient spaceport location. In the next century LEO will contain a broad complex of assembly, research, repair, and production facilities. Their effective and cost-competitive use will require a class of routine workhorse transportation vehicles whose importance might be overlooked at a time when dramatic space exploration is occurring. Yet it is these vehicles, the Aeroassisted Space Transfer Vehicles (ASTVs) that will provide the solid transportation base on which a productive space industry will grow.

The ASTVs will be assembled in orbit and will never return to the Earth's surface. They will be used to transfer people and material from high locations to LEO. They will reduce their high velocities in the region of LEO by flying into the outer reaches of the Earth's atmosphere where aerodynamic drag will slow them to the appropriate speed for LEO. They will then maneuver out of the atmosphere and into a desired orbit. The present consensus is that this is the only cost-effective method of reducing the

speed of such vehicles to the required level. For example, the cost savings of using aerodynamic drag over using retrorockets in returning from geosynchronous Earth orbit (GEO) is about 33%. Even greater cost savings can be obtained in moving material from the Earth's surface to LEO for missions to the Moon and Mars.

The ASTVs will operate at very high altitudes where the atmosphere is exceptionally thin and the flight data needed for their safe and efficient design are not adequately known. Much critical scientific research must be done to build the technology base needed to make such a design. The research program discussed in this publication, the AFE, is specifically aimed at acquiring the knowledge for this technology base.

The Future Space Program

One of the accepted goals of the space activities of the United States is to expand human presence and activity in space from low orbits around Earth out into the Solar System.

In 1986 the National Commission on Space recommended a bold national plan for the people of the United States. "To lead the exploration and development of the space frontier, advancing science, technology, and enterprise, and building institutions and systems that make accessible vast new resources and support human settlements beyond Earth orbit, from the highlands of the Moon to the plains of Mars."

Human expansion beyond Earth is an undertaking of great importance to the future of our species for which preparations should begin today. As a next step into the Solar System, the United States with international partners is developing Space Station Freedom to provide facilities for a permanent presence in LEO. A permanent presence in LEO permits humans to start building in space as they have built on Earth in the past. Crews based at a space station can assemble in space the advanced spacecraft needed for missions to the Moon and Mars. As a result of this and other international space station programs, we

will most likely witness early in the coming century the first humans landing on Mars and the first permanent research stations on the Moon with outposts there to develop lunar resources.

The United States and the Soviet Union, looking towards economic competition in the utilization of space, have each developed space transportation systems to move humans and materials to and from LEO. Other nations are also developing cost-competitive capabilities in the important region near Earth and aggressively laying the groundwork for their expansion into the Solar System.

Aeroassist

The next important stage of human expansion into the Solar System is to develop advanced transportation systems to move humans and cargo between GEO, where many important Earth support satellites are based, and LEO, and to provide capabilities for landing humans and cargo on the Moon and on Mars and returning them to LEO from such missions. Such vehicles must rely on aeroassist technology to be cost effective.

Aeroassist is a generic term employed when aerodynamic forces are used to assist a spacecraft to change direction or slow down while flying through a planet's atmosphere. Aeroassist allows spacecraft to be captured into an orbit around a planet or to be slowed sufficiently to change orbital parameters, e.g., from a highly elliptical orbit to a LEO or, in the extreme case, to a planetary landing, with a minimum or zero expenditure of rocket propellants. In fact, using atmospheric drag to slow space vehicles is regarded as one of the largest contributors to making both lunar and Mars missions affordable. Aeroassist reduces by 50% the amount of material that has to be carried to LEO from the Earth's surface for such missions.

Aeroassist Space Transfer Vehicle

Many case studies of future missions to the Moon and to Mars, especially manned missions, have concluded that these advanced transportation systems must use aeroassist to increase payloads and reduce rocket propellant requirements. Indeed, without aeroassist some of the missions are not practical with available technology. For example, a proposal to establish a manned lunar base early in the next century (Figure 1-1) depends upon aeroassist at Earth for returning vehicles. Also, a key feature of NASA studies of manned missions to the satellites of Mars and to the Martian surface (Figure 1-2) is the use of aeroassist at both Mars and Earth.

A reusable ASTV is the next logical major requirement in space to complement the Space Station Freedom and the Space Shuttle and expendable booster space transportation systems now used to move personnel and materials from the Earth's surface to LEO and return. The ASTV will be used initially to move payloads among LEO, HEO, and GEO. For example, one early application would be to move expensive telecommunications satellites in GEO back to LEO for servicing or upgrading. From LEO such satellites could be returned to Earth via the Space Shuttle if for some reason they could not be serviced in orbit.

Recent estimates are that a fleet of up to 80 ASTVs will be required to meet projected national and international needs in the coming decades, and the first such vehicle will be needed in the first decade of the next century. The design of this new type of vehicle must be started soon if the United States is to have a competitive edge on the international markets that will be served by such vehicles.

When bringing cargo or personnel from the Moon or from HEO, an ASTV will enter the Earth's upper atmosphere at a velocity of almost 25,000 miles per hour. It will fly through the atmosphere (Figure 1-3) above 250,000 feet long enough for atmospheric drag to slow it by about 6000 miles per hour. Then it will maneuver back into space to rendezvous with a shuttle orbiter or a space station. The ASTV is a cost-effective approach because it will be capable of carrying up to twice the payload of a vehicle that relies entirely on rocket braking.

However, there are many technical questions about high-speed ASTV flights. These questions must be answered satisfactorily before an efficient ASTV design can be defined and vehicles can be developed for production in the quantities required. Otherwise the ASTV would have to be overdesigned for safety, with enormous penalties in the amount of usable payload that could be transported by each vehicle.

A preferred concept of an ASTV is a vehicle with a large, blunt, lightweight aerobrake. The practicality of the aerobrake depends upon our being able to predict accurately the aerodynamic characteristics of the vehicle and the heating effects on it at hypersonic velocities. The most important technical questions relate to understanding the basic aerothermodynamics affecting the flow of atmospheric gases around the maneuvering ASTV. Considerable progress has been made in establishing the basic principles through the use of small models in ground-based tests (wind tunnels, ballistic ranges, shock tubes, and plasma jets), and through applications of
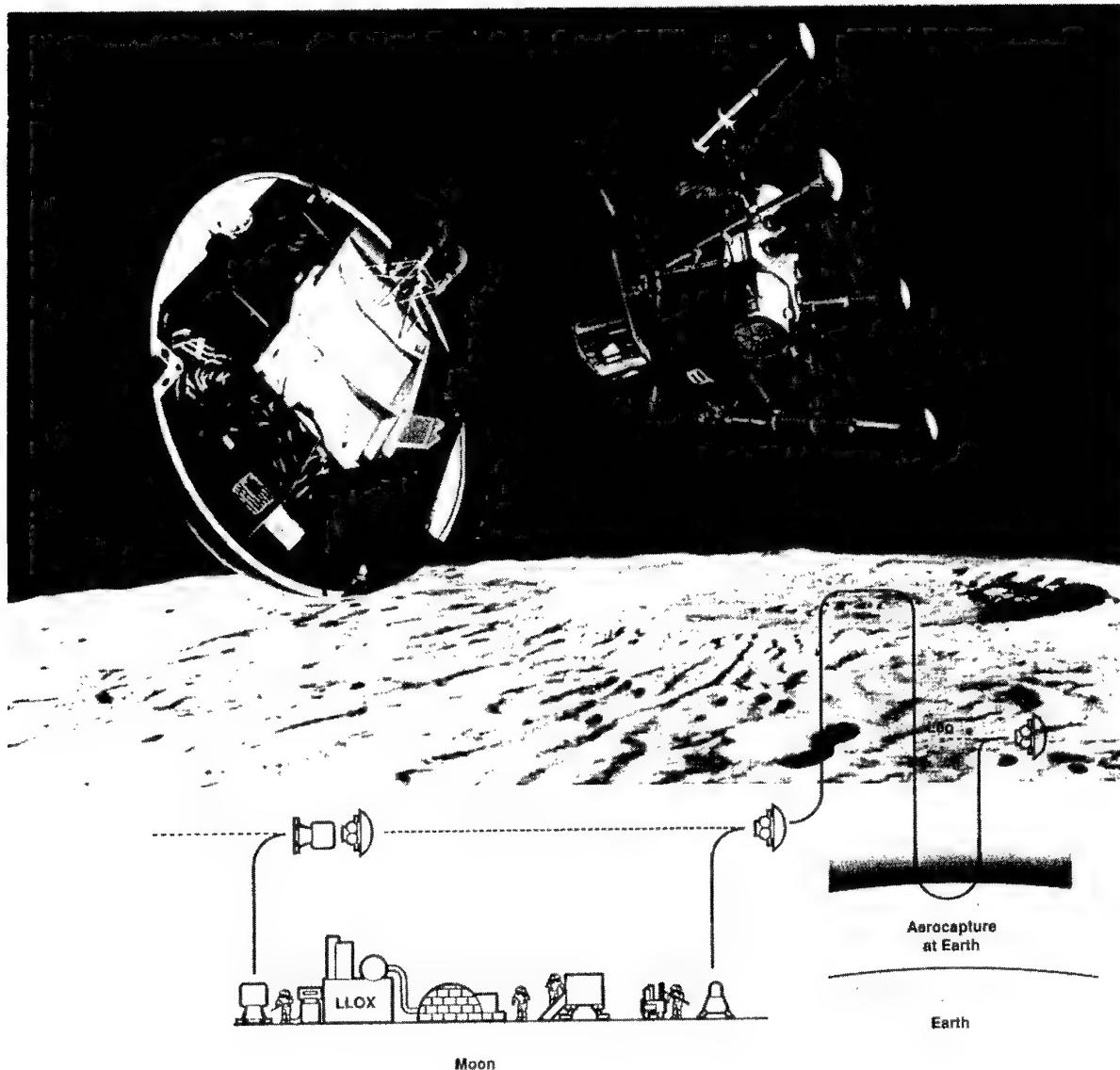
Figure 1-1. A permanent human presence on the Moon will depend on the use of aeroassist in Earth's atmosphere for return of personnel and materials to LEO.

computational fluid dynamics using supercomputers. However, flight test results are urgently needed over the range of hypersonic velocities that will be encountered by a spacecraft aerobraking from GEO to LEO to refine and validate the analytical methods to be used for design of the ASTV.

As an example, consider the aerobraking of a spacecraft returning to LEO from a deep space mission or from a high orbital mission such as from GEO. The maneuver will be at high altitude and at hypersonic speed. Under these circumstances the gas flow in front of the vehicle will be in a nonequilibrium condition; that is, an important part of the flow near the surface of the aerobrake will contain gas that is extremely hot (up to 45,000 K), and chemical reactions which would normally occur to cool the gas will not have time to proceed far toward completion because of the low densities. This nonequilibrated gas will radiate important amounts of heat to the aerobraking surface. For an ASTV returning from GEO, radiative heating to the forebody is nearly as large as convective heating.
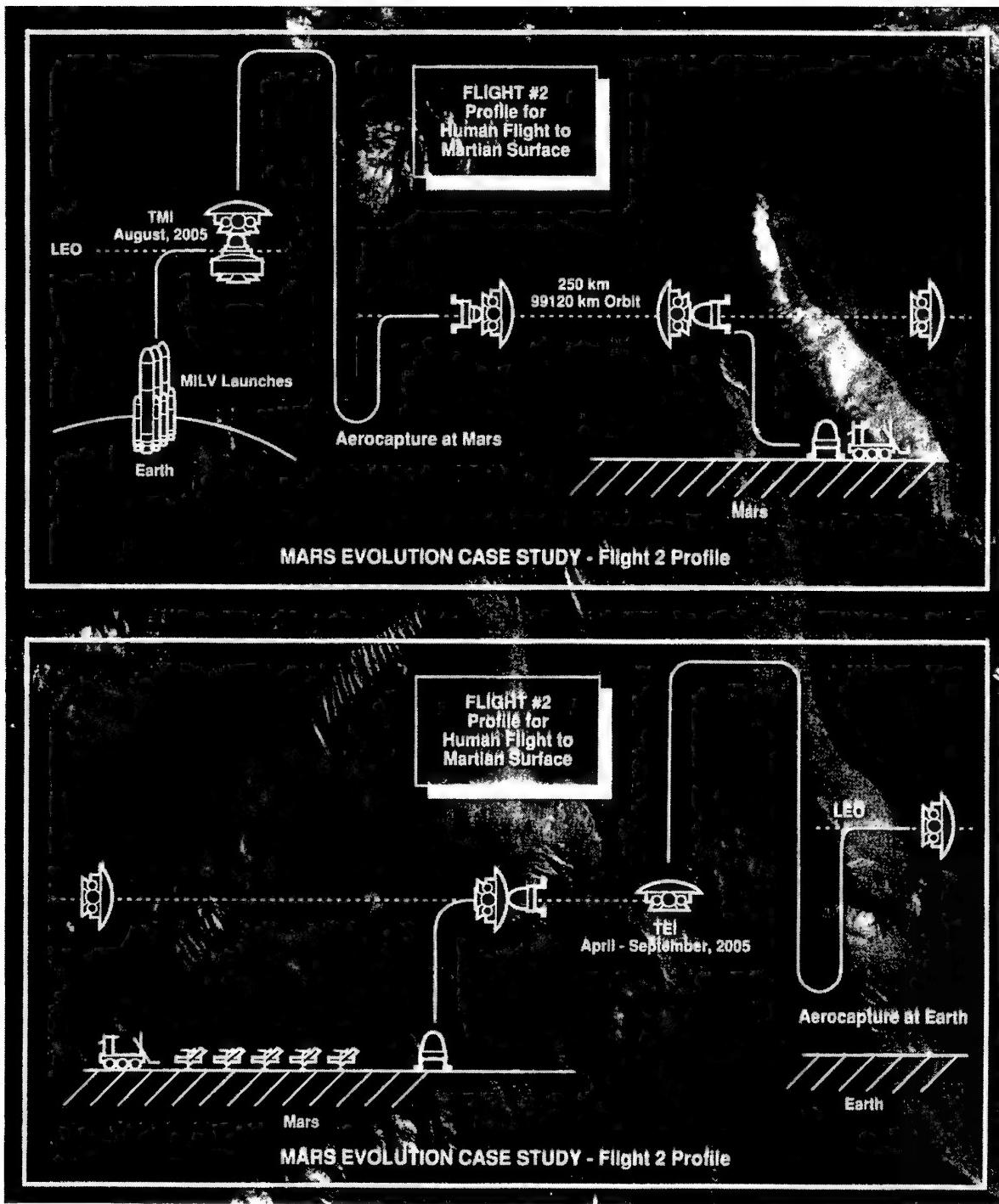
Figure 1-2. In several case studies for the establishment of human activities on the surface of Mars, considerable emphasis has been placed on the use of aeroassist at Mars and for return to LEO.
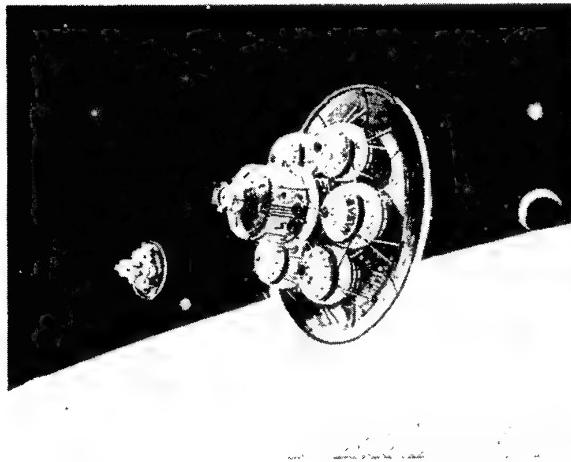
Figure 1-3. A concept for an ASTV employs a blunt aeroshell for atmospheric braking.

The heating is increased even further because of chemical reactions occurring on the wall of the spacecraft as a result of catalysis by the materials of the wall. This heating can increase the convective heating by about 40%.

Obviously there is a direct trade between thermal protection mass and payload mass. For spacecraft engineers to design an efficient and safe ASTV, the chemically reacting flow field and the resulting heating processes, and the material response of the thermal protection system (TPS) must be understood in detail. Preliminary computational models for these flow fields are being developed, but they currently use simplifications and approximations because of lack of basic science data. This is especially true in calculations of the amount of radiative heating. The problem is not only lack of physical data but also the complexity of the calculations relative to the capabilities of current computers. An ASTV designed with unvalidated analysis methods would of necessity include large safety factors and would thereby dilute or negate the advantage of aeroassist. The approximations and simplifications must be reduced and computational outputs must be verified by large-scale flight tests before the full potential of an ASTV can be realized. In addition, there are unpredictable variations of air density at the maneuvering altitudes so that guidance and control problems must be solved.

The AFE Program

The National Aeronautics and Space Administration has initiated the AFE to resolve these vital issues. The

AFE is a subscale vehicle of a size sufficient to validate scaling rules while fitting within the payload bay of the Space Shuttle Orbiter. It will be launched from an Orbiter and fly a representative aeroassist trajectory through Earth's high atmosphere during which it will gather detailed measurements of aerodynamic and aerothermodynamic phenomena. The AFE, a model of which is shown in Figure 1-4, will be recovered by the Orbiter for return to Earth and inspection after the flight to evaluate material and structural performance, and for possible reuse.

The AFE is designed to examine the requirements of efficient ASTV design for maneuvers that can use a non-ablating heat shield. These include orbital changes in the vicinity of Earth, e.g., GEO to LEO, return from the Moon to LEO, and orbital capture at Mars. The arrival at Earth from a planetary mission will be at much higher speeds and will require an ablating heat shield. What is learned from the AFE mission will need to be extended to include the effects of this kind of heat shield.

AFE Research Objectives

The proposed instrumentation for the AFE is extensive and involves a number of scientific disciplines to obtain data vital to the design of an efficient ASTV.

An important task is to determine radiative heating levels on the aerobrake, their spatial distribution, and the spectra of the radiation. New data are required to resolve different interpretations of available data and the spread in current prediction techniques which are major issues in the choice of a concept for an ASTV.

The performance of several advanced thermal protection materials, including their catalytic efficiencies, needs to be evaluated. Candidate materials offer potential for important mass savings if they can be demonstrated as usable in the ASTV environment. Also, since a low catalytic activity of the wall material of the aerobrake can result in a substantially lower heating rate than that of a highly catalytic surface, quantifying these effects is important to the design of an ASTV.

Aerodynamic performance characteristics of the vehicle are most important. Flying an aerobrake in the rarefied upper atmosphere requires an understanding of the effects of unpredictable irregularities in atmospheric density that are known to be present at high altitudes.

The flow around the base of the vehicle, behind the front heat shield, including heating effects from the wake
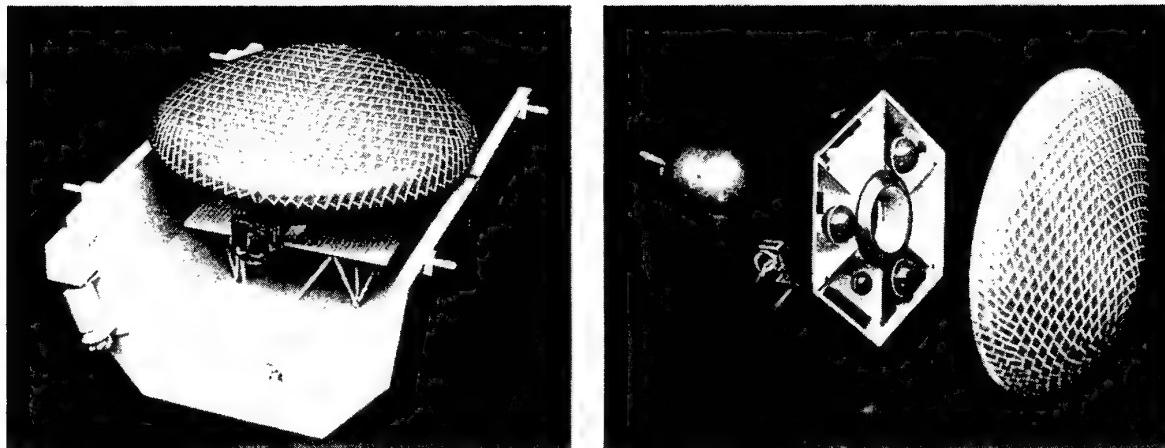
Figure 1-4. The AFE spacecraft and its experiments, a model of which is shown here, is designed to find answers to questions which must be solved to design an efficient ASTV system.

region, must be quantified. This is necessary to verify prediction techniques for the nonequilibrium base flow and wake region of a vehicle flying at high speed at high altitudes to determine the thermal and pressure loads needed for an efficient ASTV design.

Convective heating and pressure distribution on the aerobrake and characteristics of the plasmas generated in the flow field, including the concentrations of electrons, need to be measured.

Flight data must be provided to verify computational flow-field models which are needed to predict the performance and heating environment of future ASTVs and related vehicles.

Concurrent with and assisting the maturation of the AFE, a theoretical and experimental effort has been initiated to develop and validate computer codes to analyze the characteristics of ASTV flight. The AFE experiments will provide the critical flight data necessary to complete the validation of these modern computational codes which will be used to design a highly efficient ASTV capable of meeting the national need for high orbit (GEO to LEO) and cislunar (LEO to GEO to the lunar surface) space transportation systems.

Economics

The ASTV capability is needed for us to be competitive in forthcoming commercial space activities, as well as to keep our national position as a leader in Solar System exploration. The relatively inexpensive AFE mission will put the United States years ahead of a program that would incorporate a conservatively designed and instrumented operational ASTV which could provide the data to validate computer models. These early results are important to ensure that the first ASTVs will be efficient and competitive, and that the scientific basis will be available to continue development of our planetary programs. It is important to note that only a small amount of improved efficiency in an operational ASTV would make the early implementation of AFE a very economical and cost-effective program, even when applied over an initial small number of full-scale ASTVs.

Subsequent sections of this publication provide more details of the aeroassist concept and the rationale for its development. The immediate need for the AFE program is discussed. The flight mission and the vehicle and its instrumentation are described. Expected results are reviewed together with the future potential that can be realized to meet long-term national and international goals of expanding human activities into the Solar System.

SECTION 2: EVOLUTION OF THE AEROASSIST CONCEPT

In connection with the AFE program detailed in this booklet, aeroassist is defined as a generic term encompassing various maneuvers, including slowing, in which a vehicle enters the atmosphere, maneuvers using lift and drag forces, and exits without making a complete entry. The aeroassist technique in the present context involves the use of a large, saucer-shaped structure, the aerobrake, behind which is the main body of the spacecraft and its payload. The aerobrake also protects the cargo from aerodynamic heating. Large vehicles of this type will most likely be assembled in orbit. When, during an aeroassist mission, a planet's atmosphere is reached, the spacecraft uses the resistance generated by the planetary atmosphere on the aerobrake to slow the vehicle and maneuver it into orbit. Little propellant is expended during such a maneuver other than that required to control the attitude of the aerobraking vehicle relative to its flight path.

Aerobraking is important for spacecraft arriving at other planets, returning from the Moon to Earth, and transferring from HEOs (e.g., GEO), to the much lower orbits of Space Station Freedom and the Space Shuttle Orbiter. Various space missions (Figure 2-1) will require return to Earth at hypersonic speeds of 36,500 to 39,000 feet per second.

The potential benefits of aeroassisted velocity changes for orbital transfer have been recognized and studied since the beginning of the space age. For example, a study has shown that the amount of mass that must be lifted from the Earth's surface for a human mission to Mars can be nearly halved (Figure 2-2) if an aerobrake is used for atmospheric entry and landing on Mars and for later return to Earth orbit.

The ASTV flight regime involves higher velocities than the Space Shuttle and, in the region of significant aerodynamic heating, higher altitudes than the returning Apollo capsule. Although this high-altitude, high-speed flight regime is not unique to an ASTV, the flight of an ASTV will be entirely at high altitudes and thus in a region of low density. This is considerably different from the Apollo and Space Shuttle trajectories (Figure 2-3) which took these spacecraft rapidly through this
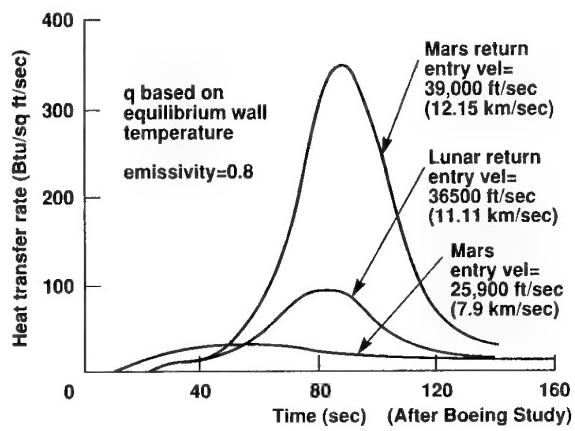

Figure 2-1. The range of velocities that will have to be encountered for aeroassisted vehicles in several space missions is shown, together with heat-transfer rates and the periods involved.
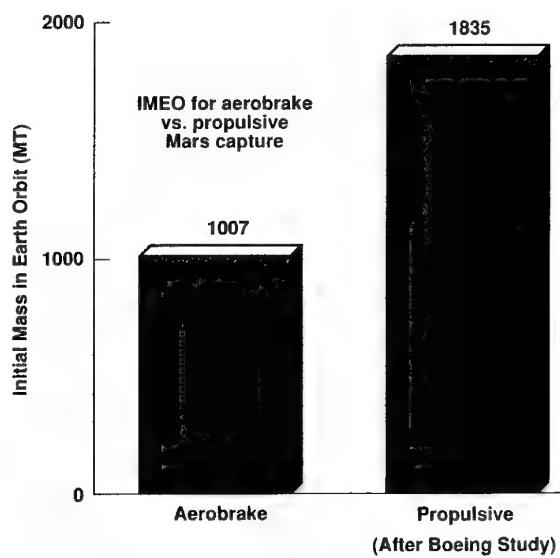

Figure 2-2. If aeroassist is used for human missions to Mars, the amount of material that has to be carried from the Earth's surface into LEO is almost halved.
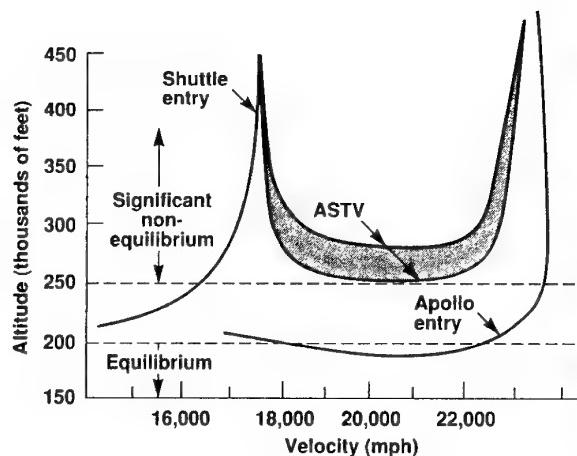
Figure 2-3. An ASTV using Earth's atmosphere must operate in a different regime from Apollo or the Space Shuttle Orbiter. As shown, the ASTV must operate at high velocities in the low-density upper atmosphere.

atmospheric region for a landing on the Earth's surface and thus had other design criteria. By contrast, the ASTV will maneuver for several minutes at about 250,000 feet.

ASTV Flow Field

For efficient ASTV design a detailed understanding of the heating processes is required. The flow environment on a large ASTV is in nonequilibrium and results from interactions of many dynamic processes, which have a wide range of times to achieve a steady condition.

A spacecraft returning from a deep space mission or from GEO must perform aerobraking maneuvers at hypersonic speeds where a shock wave forms in front of the vehicle as shown in Figure 2-4. As the shock wave passes through the atmosphere in front of the vehicle, the gas is abruptly compressed and heated to the condition of the shock layer. As a result, the gas in the most forward region of a maneuvering ASTV becomes extremely hot, up to 45,000 K, and presents a difficult technical challenge of protecting the vehicle. These high temperatures would normally cause energy-absorbing chemical changes in the atmospheric gas, which would cool it. But the high altitude (with its resulting low air density) at which the ASTV flies results in relatively infrequent collisions between gas molecules. This lengthens the time to complete the chemical changes. They are only partially completed during the time the gas resides over a specific region of the forebody of an ASTV. A shock layer with a
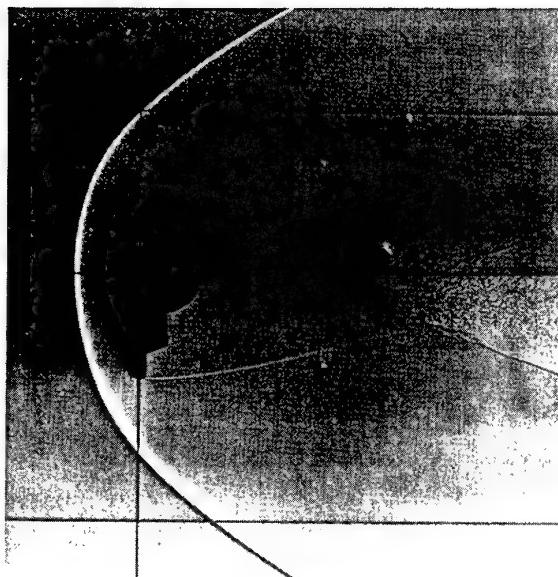
Figure 2-4. A detached bow shock is shown ahead of a blunt body at hypersonic velocity in a NASA ballistic range. Behind the shock the atmospheric gases are heated to high temperature and are in a nonequilibrium state.

substantial portion nonequilibrated is termed a nonequilibrium shock layer. The result of the lack of chemical equilibrium is that the energy which would be absorbed in the chemical reactions remains in the form of high gas temperature.

The high-temperature nonequilibrium gases radiate strongly, so that the radiative heating from the ASTV shock region will be about equal to the convective heating.

Nitrogen and oxygen molecules dissociate into their respective atoms, and other molecular species are formed. As the gas proceeds along streamlines around the vehicle, more gas collisions cause the gas to begin to equilibrate its chemical states. Some species ionize,and the temperature relaxes from the nonequilibrium value of 45,000 K to about 8000 K. This large temperature difference underscores the importance of chemical reactions in understanding the mechanics of energy transport in the shock layer of a maneuvering ASTV. During an ASTV maneuver some of the atoms from dissociated air molecules will diffuse to the wall of the spacecraft and catalytically recombine there to reform the parent molecules (Figure 2-5). These reactions can release additional heat directly to the wall. The catalytic effect of wall materials

Catalytic Wall

Low Catalytic Wall

Heat Release

Incoming atoms find partners - leave as molecules

Most incoming atoms leave as atoms
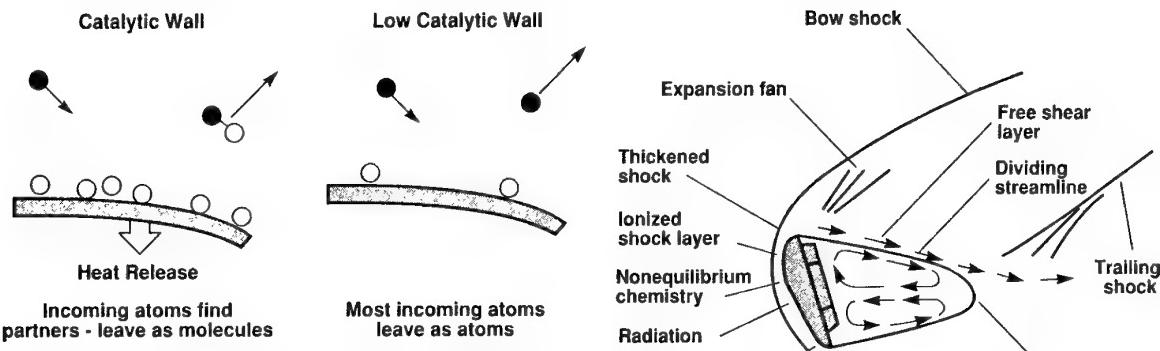
Figure 2-5. Materials of the aerobrake's wall surface can trigger reactions with the hot gases. Low catalytic materials can reduce the effects.

Bow shock

Expansion fan

Free shear layer

Thickened shock

Dividing streamline

Ionized shock layer

Nonequilibrium chemistry

Trailing shock

Radiation

Slip boundary conditions

Rear stagnation point

Figure 2-6. In the wake region, gas species recombine and produce radiation that could damage a payload behind the aerobrake. The photograph shows the complicated wake region of a model in a ballistic range.

on such heat-releasing reactions must also be thoroughly understood since this source of heat can account for as much as 40% of the convective heating.

NASA first encountered the problem of nonequilibrium radiation during the Apollo program. A great deal of ground-based experimentation was conducted before the launch of the first Apollo vehicle to determine the extent of radiative heating of the vehicle in the environment of high-speed entry into the Earth's atmosphere. When the results of the experiments were extrapolated to the flight conditions, a large amount of radiation was predicted. Later, in 1967, one-quarter-scale models of the Apollo vehicle, named Project Fire, were flown with radiometric instruments to verify the predictions. The flight experiment resulted in radiative heating rates much smaller than those predicted from the ground-based experiments. Since the heat shield for the Apollo Command Module was designed from the ground-based data, the process led to a substantial overdesign of the module, which reflected through the Apollo vehicle, and such overdesigning of the heat shield will lead to a heat shield that is too heavy, which would negate the advantage of aerobraking. It must be added here that, even today, there is no unique theory that alone can explain the data from Project FIRE: several different theories explain the data equally well.

In addition, conditions in the wake region must also be understood. The present understanding of this region is that it also is not in chemical equilibrium (Figure 2-6). The heating to the rear of the vehicle would not be as high as to the front, but it would be too high to expose a payload to without any protection. Unfortunately, very significant uncertainties exist in predicting these nonequilibrium processes associated with using aeroassist.

Thermal Protection

As mentioned earlier, compared with the relatively quick entries of Apollo and the Space Shuttle Orbiter, the aeroassist vehicle uses a much longer period of aerobraking above 250,000 feet. The intentions are, indeed, quite different. While the Orbiter and the manned capsules use aerobraking to penetrate into the lower and denser atmosphere and to reach the surface of the Earth relatively quickly, the aeroassist vehicle uses aerobraking in the rarefied upper atmosphere to enter into an orbit around Earth. Thus the aerobraking regimes are quite different in the dissipation of the kinetic energy and consequently how the TPSs have to be designed.

The excess kinetic energy of the entering vehicle which it has to dissipate to be captured into LEO has to be converted into heat, chemical energy, or radiation. An ideal would be for the gas to carry off or to radiate the energy without depositing it onto the vehicle's surface. This ideal cannot be met because while much energy is

carried away from the vehicle, some energy finds its way to the vehicle through radiative or convective heating, including catalytic reactions occurring on the surface. Accordingly, the aim is to minimize this unwanted energy flow and consequently to reduce the mass of material needed to protect the vehicle from excessive heating.

At the velocities to be experienced by an ASTV, thermal protection material may have to withstand a temperature of 1500 to 2000 K. Since current reusable thermal protection materials of the type used to protect the Space Shuttle Orbiter can withstand a temperature of up to 1800 K only, there is an urgent need to develop advanced materials for ASTVs. For example, a Mars sample return mission could use a high-drag aeroassist technique for landing on Mars, but would require a concurrent program to develop low-drag ablator aeroassist technology for capturing the returning, sample-carrying spacecraft into Earth orbit.

The three most practical types of heat shields are heat sink, ablative, and radiative. Heat sink thermal protection absorbs the heat in a large mass of material which never gets above a predetermined temperature. Heat sinks are generally very heavy and can lead to a fire hazard if they are not jettisoned before a spacecraft lands. At the beginning of the manned space program, ablative shields were most popular because they could be tailored for particular heating rates and total heat loads. However, they are efficient only at high heating rates. Early entry vehicles used materials that charred and ablated. Mercury, Gemini, and Apollo used an ablative material of sufficient thickness to protect the manned spacecraft during deceleration to a velocity at which a parachute system could be deployed for landing.

Later TPSs relied upon radiative protection. For example, the Space Shuttle Orbiter uses tiles of very low heat conductivity whose surface can reach a very high temperature without failing during the period of atmospheric deceleration. The hot surface radiates most of the heat away from the vehicle, and thereby reduces the amount of heat penetrating into its interior.

The ASTV will use radiative thermal protection since the accent in its design is reusability without having to return to the surface of the Earth. Moreover, the TPS for an ASTV must be highly reliable and require minimal servicing in space. Throwaway ablators are an easy solution for one-time missions, but clearly are not the way to go for an ASTV. However, a Mars return vehicle, which also would be expected to be retrofitted in LEO, might have to use ablators because of its high return velocity.

Computational Fluid Dynamics

Because of the deficiencies in ground test capability, the ASTV design must be based primarily on computational methods. Computational models are being developed for the ASTV flow fields. However, many approximations have to be used, especially in calculating the amount of radiation the surface will receive from the hot gases. These approximations are required because important physical data are lacking. The kinetic chemistry and the details of radiative phenomena are not fully understood. The consequence is that the present ability to predict the ASTV environment from small-scale tests in wind tunnels, ballistic ranges, arc-jet wind tunnels, and the like, must necessarily include large safety factors. A flight test is required to clearly define scaling factors from the small models used in ground-based tests to a full-scale ASTV.

The ASTV flow field presents a number of computational challenges which require significant advances over existing codes and procedures for predicting aerothermal loads and the responses of TPSs. Three-dimensional forebody and afterbody flows must be adequately resolved. Viscous terms must be included everywhere. Slip boundary conditions may have to be applied at the wall. An accurate model for wall catalytic efficiency is needed. Nonequilibrium flow must be computed reliably, and heat transfer due to radiation and convection within the TPS must be accurately modeled to minimize structural weight.

These computational techniques need to be developed. They will be reliable for system design and development, however, only if they have been verified by flight data. Such verification requires the use of a test vehicle with a representative blunt configuration capable of flying a realistic aerobraking trajectory in the high atmosphere to produce an aerothermodynamic environment like that to be experienced by an ASTV. The vehicle should fly a roll-controlled trajectory to obtain realistic flight-performance data. Recovery is also important for postflight inspection and analysis of the TPS.

Flight Tests, the Aeroassist Flight Experiment

Flight test experiments are needed to identify the various processes occurring during nonequilibrium flow. Valid tests cannot be done on the ground because the reaction time of various important interrelating dynamic processes compared to the flow time is important. Experiments with small models in arc jets and ballistic tunnels cannot simulate these interactions and show the overall flow field simultaneously. A large test vehicle is required so that the standoff distance of the shock wave will be

adequate for the nonequilibrium conditions to be distinct from the boundary layer, as will be the case with the ASTV. Also, it must have a TPS that will not contaminate the shock-layer flow; that is, the TPS must not ablate. The vehicle must be able to simulate a return mission from GEO to LEO, and travel through the Earth's upper atmosphere at a speed sufficient to induce distinct and measurable phenomena. The test vehicle must also be recoverable to allow for postflight analysis of the experiment, particularly the thermal protection materials.

This is the AFE, a productive, timely, and necessary step toward the ASTV fleet of the future. The reality of substantial chemical nonequilibrium in the flow field has led to the initiation of this AFE test program. The AFE is designed to collect a data base to develop and validate computational models for future ASTV design. This experiment consists of a spacecraft designed to function as an aerobrake. The AFE will be placed in orbit by a Space Shuttle Orbiter at an altitude used by the Orbiter and then will be driven by rocket propulsion into the Earth's upper atmosphere to simulate a return from GEO. The aeropass will be approximately 5000 miles long across the Pacific Ocean. The mission profile is designed to simulate important features of an actual ASTV maneuver. These include the influence of shock-layer nonequilibrium on the levels of radiation and convective heating, the influence of viscous and real gas effects on the aerodynamic characteristics of the vehicle, the ability of thermal protection materials covering the surface of the aerobrake to maintain low levels of catalytic activity, and the effects on guidance arising from unpredicted variations in air density. These key issues can be resolved only by obtaining flight test data.

The AFE is essentially an adequately large, instrumented platform whose primary purpose is to acquire fundamental aerothermodynamic data at the range of flight velocities and altitudes where an ASTV will operate. AFE is not a design for an ASTV. It is a means to provide the basic scientific data for such designs. That valuable data about the behavior of an ASTV flow environment can be obtained by instrumented bodies traveling at high speeds was demonstrated early in the 1970s by the Planetary Atmospheres Experiments Test (PAET). The entry vehicle was launched in June 1971 by a four-stage Scout rocket from Wallops Island, Virginia, to enter the atmosphere near Bermuda. Basically, the experiment demonstrated that the composition and structure of an unknown planetary atmosphere can be determined by measuring the interactions between an entry probe and the atmosphere. Of importance to the AFE mission, PAET showed that instruments can be designed to obtain important scientific information about atmospheric processes

caused when a blunt body travels at hypersonic velocity in the rarefied upper atmosphere, and that radiation from the shock layer can be analyzed in detail to identify and quantify the important radiating gas species.

The AFE is a recent new-start program of NASA. An Aerocapture Technology Working Group was formed in 1980, composed of representatives from nearly all NASA centers. In 1982 this group established the need for a flight test. Early in the 1980s NASA's Aeroassist Working Group identified the specific technologies and technical issues which must be addressed to meet the challenge of routine use of aeroassist to modify orbits by braking or maneuvering. Important milestones were reached during subsequent years. An AFE Steering Group was formed in 1983, and the initial concept was defined by November of the following year.

An initial Project Initiation Agreement was signed in 1985, and the Science Review Board established justifications for the AFE, namely, that technology development required for a future ASTV must precede the system definition and development. The nonequilibrium air environment required for understanding aerobraking and system performance can be achieved only in large-scale flight tests at sufficiently high velocities.

The Project Initiation Agreement was updated in 1986. This was followed a few months later by publication of an integrated science plan. In October 1987 the AFE program was given new-start approval, and a detailed project plan was published. The schedule established is for a flight test of the AFE in 1995.

Objectives of the Aeroassist Flight Experiment

The Science Review Board in a Science Rationale Document stated that the objectives of the AFE mission were to provide benchmark data to define the environment in which an ASTV must fly; radiative and convective heating effects both to the forebody and to the afterbody region of a blunt aeroshell; and the means to verify computational flow-field codes both through specific measurements of gas and wall parameters and through performance data obtained along its trajectory. An additional objective identified is to demonstrate the performance of state-of-the-art guidance techniques for flying a vehicle with a low lift/drag ratio (LID) in a variable-density atmosphere. It is known that the density of the upper atmosphere varies from location to location and from time to time somewhat unpredictably. Such variations could adversely affect the guidance and control of an ASTV moving through the upper atmosphere and lead to its being deflected from its path unless corrections were

made. Finally, the performance of candidate materials and surfaces for a TPS in the ASTV environment will be investigated.

Management of the Aeroassist Flight Experiment

NASA Headquarters, Washington, D.C., administers the AFE program, reports on the program to NASA management, and is the focal point for all external relations. It is also responsible for technical and financial management of the AFE program. The elements of the program include the aerobrake, the carrier vehicle, instrumentation, ground and airborne support equipment, and system test operations.

A Science Steering Group has been appointed by NASA Headquarters to provide advice on the program. It consists of scientists from NASA, universities, and industry.

Several NASA centers participate in the program under the direction of the Marshall Space Flight Center, Huntsville, Alabama, which has responsibility for project management. The Marshall project office has the responsibility for developing the AFE, integrating the total program, and operating the flight test.

Langley Research Center, Hampton, Virginia, is responsible for the development of certain instruments and for overall integration of the science experiments.

The Project Scientist at the Center is responsible for identifying science experiments and resolving issues regarding the experiments, and for ensuring that all the science objectives are met. Langley Research Center is also responsible for defining and coordinating the ground-based test program, including computational fluid dynamics (CFD), that supports the project office in planning the mission.

Johnson Space Center, Houston, Texas, is responsible for developing the aerobrake and some of the instrumentation. It also assists in developing algorithms for the guidance, navigation, and control software. The Center participates with other Centers in developing codes for CFD used to guide the design of the aerobrake and carrier vehicle.

Ames Research Center, Moffett Field, California, supports the AFE program in aerothermodynamics and thermal protection, and is responsible for some of the science experiments. The Center also supports the program in cooperation with other centers in mission planning and analysis, ground-based testing, and CFD analysis. It provides advanced computational work in support of the development of codes for the design of ASTVs.

The resolution of the major questions about the technology of aeroassist by the AFE program is discussed in section 4, where the various flight instruments are described.

SECTION 3: THE AEROASSIST FLIGHT EXPERIMENT (AFE) PROGRAM

Development

The AFE will be carried to, and recovered from, LEO by the Space Shuttle Orbiter. The test vehicle will be released on orbit at a nominal altitude of 160 nautical miles, and after appropriate on-orbit checkout will be accelerated downward into the Earth's atmosphere to a velocity of 33,800 feet per second at the nominal atmospheric entry point of 400,000 feet. This simulates a return from GEO. The perigee (closest approach to Earth) of the spacecraft's trajectory occurs at an altitude of approximately 250,000 feet above the Earth's surface. After leaving Earth's atmosphere at the end of the test flight, the test vehicle will be recovered by the Orbiter for return to Earth.

AFE development officially began in fiscal year 1988 aiming for a launch readiness date of 1995. A substantial part of the design of the spacecraft and instruments will be by civil service personnel at the various NASA Centers involved in the program. The aerobrake will be built by Johnson Space Center. The carrier vehicle will be designed by Marshall Space Flight Center, and McDonnell Douglas has been selected as the fabricator. Most of the other fabrication, assembly, and test of the AFE will be by contractors.

The AFE is a single-mission project. Its primary aim is to gather basic scientific data about the aeroassist environment. The spacecraft is defined as a class B payload for the Shuttle. Existing designs for subsystems will be used wherever possible with upgrades to high-reliability parts because instruments will not be duplicated. The basic TPS on the aerobrake will be the same type of tile used in the Space Shuttle Orbiter. No major technological developments or advancements in the state of the art are required to implement the AFE.

The AFE program requires the development of computational capabilities, ground-based testing with ballistic ranges and arc jets, and development of instruments. Limited redundancy of systems requires that high reliability be assured to achieve the same probability of success as a spacecraft with redundant systems.

Several major areas of NASA activities relate to and support the AFE. A development program for thermal protection materials and coatings at Ames Research Center is important to the project. At Langley Research Center, ground-based testing uses wind tunnels. Arc-jet and ballistic range tests take place at Ames Research Center and Johnson Space Center. Development of CFD is proceeding at these Centers as well as at Marshall Space Flight Center. The TPS research and the CFD analysis are funded separately from the AFE program.

The Flight Mission

The AFE vehicle is mounted on a spacecraft support structure in the bay of a Space Shuttle Orbiter which carries it into LEO (Figure 3-1). The vehicle is deployed from the payload bay and completes almost one orbit of the Earth while systems are checked and the AFE vehicle is maneuvered to the attitude needed for entry (Figure 3-2). A solid-propellant rocket motor is then fired, accelerating the AFE vehicle along a path that will carry it into the upper atmosphere for the hypervelocity test pass. When the desired velocity has been reached, the rocket motor casing is jettisoned and separates from the test vehicle.

The passage through the atmosphere (Figure 3-3) lasts approximately 10 minutes, during which the AFE vehicle descends to an altitude as low as about 250,000 feet. The descent into the atmosphere is at nearly constant velocity. The AFE vehicle then levels out and is decelerated at a roughly constant altitude. The most important data-gathering period is that during the transition from constant velocity to constant altitude. This is the region where heating peaks. During this period no maneuvering jets are fired unless they are required to save the mission. This quiescent period ensures that the wake flow is not contaminated by rocket exhaust gases. After the scientific and technical data have been gathered, the maneuvering jets will be used again to guide and control the vehicle through the atmosphere at hypersonic speeds. Later, when the AFE vehicle emerges from the atmosphere back into space, the maneuvering jets are used to circularize the orbit so that the vehicle can be recovered

Aerobrake

RMS Grapple Fixture

Carrier Vehicle
- Propulsion Tanks
- Pressurant Tank
- Trunnions
- Experiment Booms

RCS Clusters

Pallet Freon Pump Package

Pallet MDM Subsystem Electronics

Star 63FD SRM with Ejection System

Pre-deployment Support Ring

Spacecraft Support Structure

Latches, PRLA 3 places

2-Pallet Train
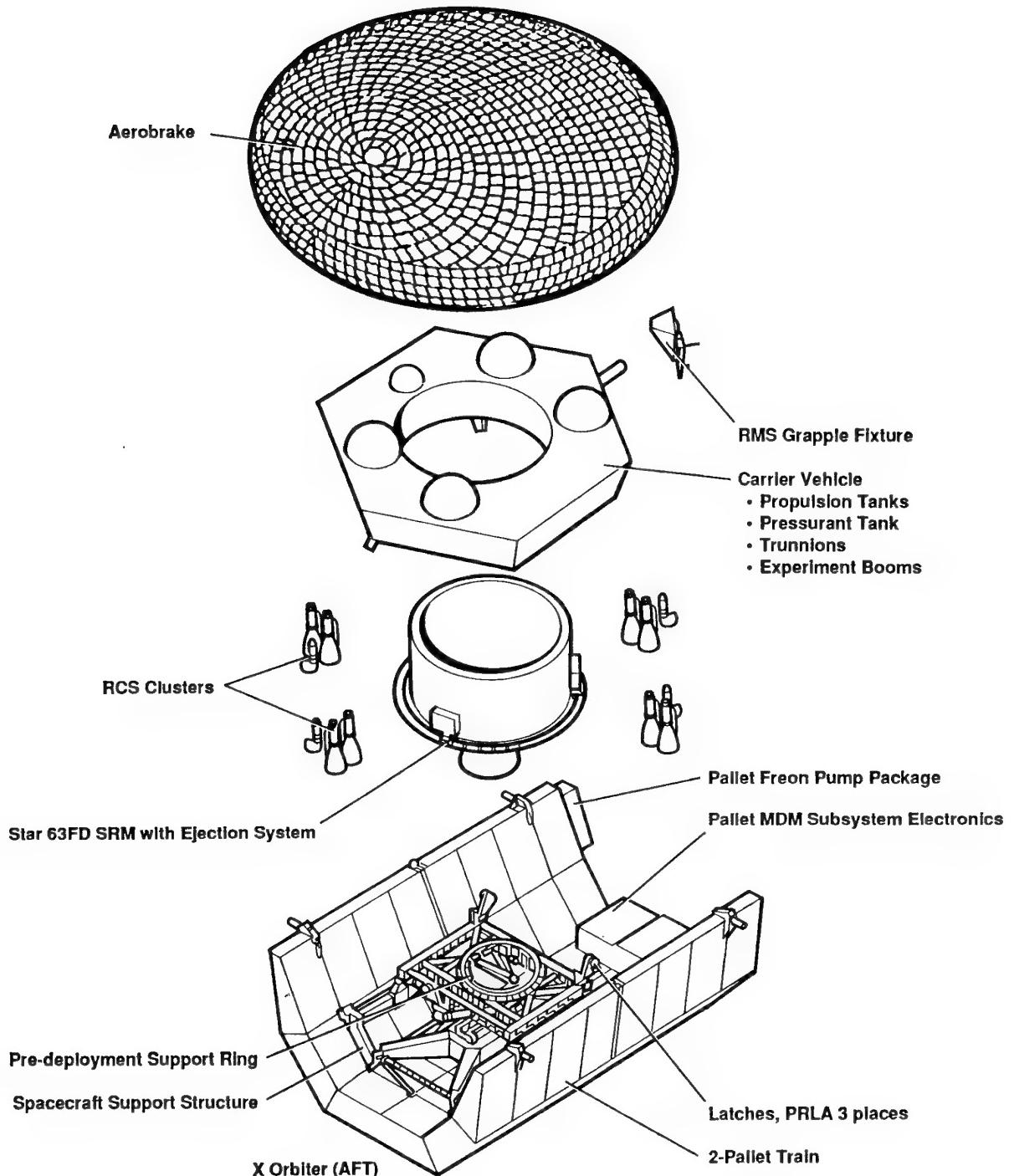
X Orbiter (AFT)

Figure 3-1. The aerobrake, the carrier vehicle, the solid-propellant rocket motor, and the supporting structure by which the spacecraft is carried on the pallet within the Space Shuttle Orbiter's cargo bay.
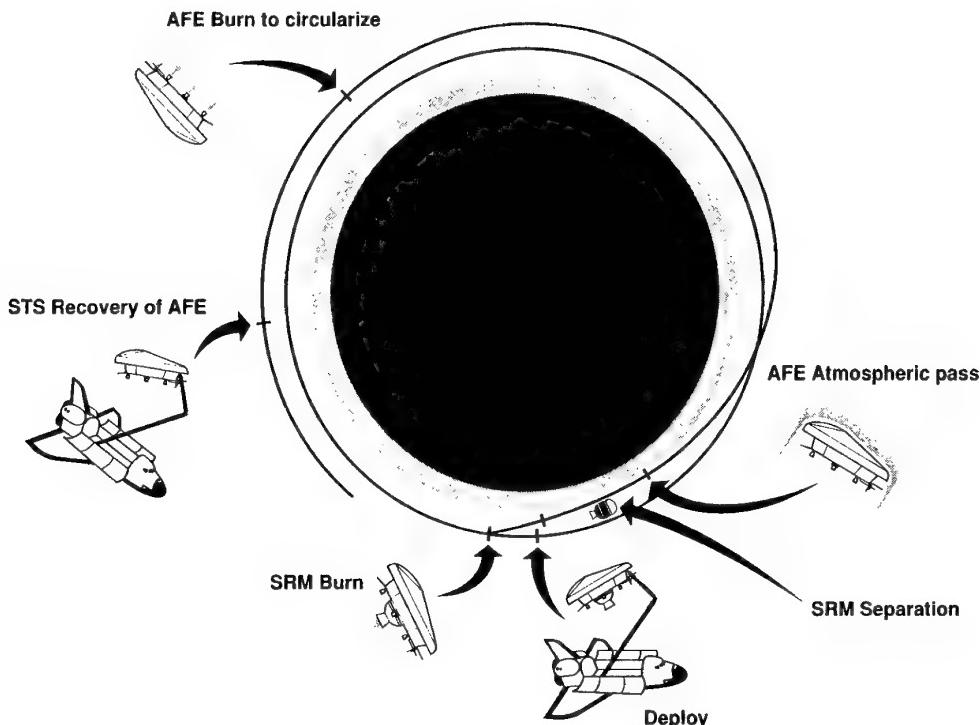
Figure 3-2. Operational sequence of the AFE mission with launch and recovery by the Orbiter.

by the Shuttle Orbiter. The sequence of deployment to recovery requires about 13 hours.

Recovery

Some mission objectives require recovery and return to the laboratory of the AFE vehicle. This is required to answer questions which cannot be instrumented for, and therefore require post-flight inspection and testing. This activity will provide the final set of data required to complete the technology data base to be provided by AFE for aeroassisted return from GEO and from lunar missions.

Primary technological benefits of recovery are related to the TPS experiments. Since ground-based experiments cannot duplicate the combined convective and radiative environment that ASTVs will experience in flight, the performance and re-flight capability of the baseline and advanced TPS materials can best be assessed through post-flight examination. This assessment will concern questions relative to the performance of a rigid TPS, such as coating behavior, (bubbling and melting, for example); optical property changes; and tile shrinkage and deformation. These cannot be assessed by the discrete thermocouple measurements that are the source of the flight data.

Other issues requiring post-flight examination are

1. The performance of the nonrigid TPS, as well as that of the associated adhesive.

2. Inspection of temperature-sensitive labels that will determine peak temperatures at many locations on the aerobrake structure to assess the impact of TPS on structure thermal performance.

3. Critical data interpretation considering how the instruments have been affected by the TPS (such as tile slumping around pressure ports and radiometer windows, thermocouple signal anomalies, and radiometer window contamination due to TPS material outgassing).

4. Post-flight calibration of experiment sensors (radiometers, pressure transducers, and accelerometers) to optimize critical data sets.

Recovery of the AFE vehicle will provide invaluable data from which unpredicted phenomena can be identified and resolved, as well as data to enhance the technology
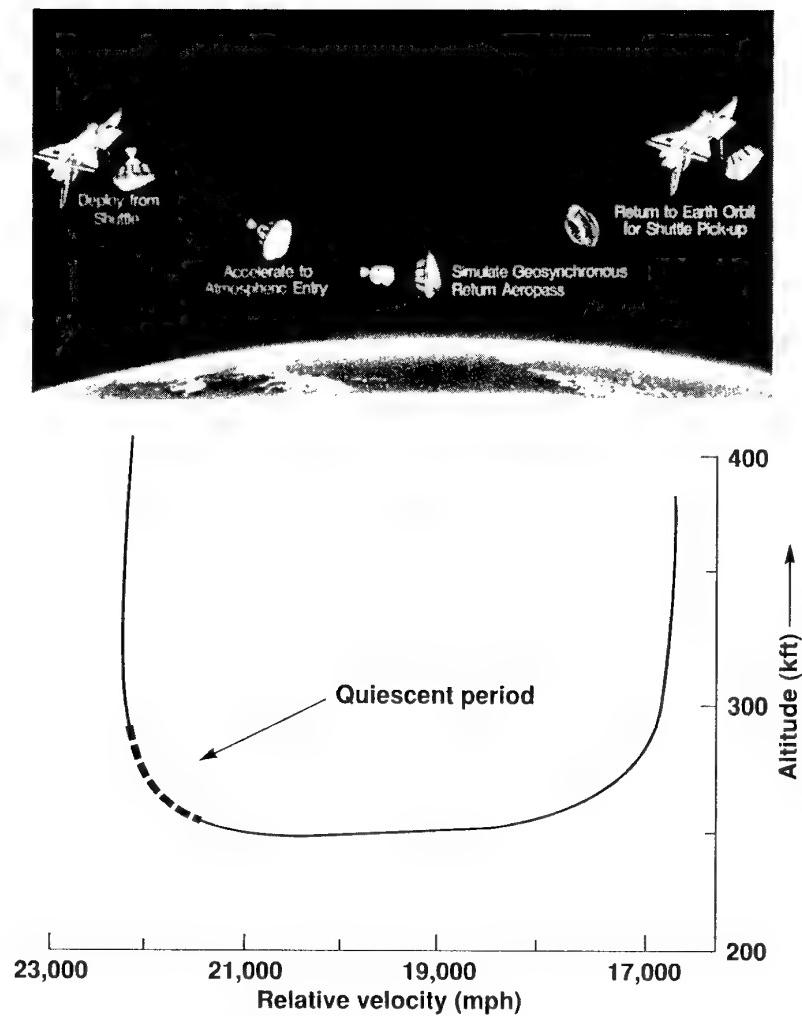
Figure 3-3. The flight regime of the AFE and its passage through the upper atmosphere. The altitudes and relative velocities are shown in the line diagram.

data base relative to predicted phenomena. This has been the experience with the recovery and post-flight inspection activities of the Space Shuttle Orbiter program. The Orbiter was, and continues to be, modified as a result of data and observations obtained only from post-flight inspections. It is expected that the "new" flight regime associated with ASTV will yield results that a priori instrument design will not obtain. The results therefore can be resolved only through post-flight evaluations. Consequently, the AFE objectives mandate recovery of the vehicle. Cost analyses indicate that this recovery of the AFE will be about 1% only of the total program's cost.

The ASTV Design Code Development

The motivation of the AFE is to develop the data base to support the design of a future ASTV. This includes validation of CFD codes. To gain maximum benefit from the flight experiment for this purpose, it is necessary to have a strong program in place for code development and phenomenological modeling. The codes and physical models will be necessary to interpret and evaluate the flight data and the flight data will, in turn, be used to validate the codes. The validated codes will be used in the analysis and design of future ASTVs. Particular code development emphasis is needed on the entire

thermochemical nonequilibrium flow field, i.e., the forebody region, the flow over the shoulder, and the unsteady flow in the base and wake regions. It is also important to further develop the codes to incorporate radiation fluxes.

Phenomenological models are in existence for the compressive flow regions, but they require the AFE data for improvement and validation. New models are needed for the expanding flow regions where there are inversions in energy level populations. And the present radiation codes need validation and must be incorporated into the flow-field codes.

The AFE instruments are designed to generate the data base required for the code development. The surface pressure and temperature measurements relate to vehicle performance and state of the gas in the AFE flow field. The surface heating rates, both convective and radiative, can be related to the state of the flow-field gas, surface catalytic effects, and the radiative energy transport of the flow field. The spectral content of the flow-field radiation is a potent indicator of the flow-field gas state. The frequency spectral content of the wake unsteadiness is a fundamental quantity of the wake dynamics, and a valid

CFD model must be able to reproduce these characteristics. All of these properties must be derived from the AFE flight event for development of efficient ASTV design codes.

A coordinated program has been initiated to develop codes needed to interpret and utilize the AFE data. This program also involves upgrading, and in some instances reactivating, some of NASA's high-enthalpy hypervelocity test facilities, such as shock tunnels and ballistic ranges, to be used for aerodynamic and aerothermodynamic testing. It also includes a focused computer code development program with direct application to the AFE's configuration and flight trajectory. The technology resulting from this program will be sufficiently mature when the AFE is performed to permit our gaining maximum benefit from the flight data. When the program is completed, a validated computational tool will exist, capable of use to achieve reliable design of ASTVs for return from GEO or from the Moon.

The next section of this publication describes the AFE vehicle and the instruments used to gather the important data concerning the hypersonic flight environment.

SECTION 4: THE AFE VEHICLE AND ITS INSTRUMENTS

There are two main approaches to designing a vehicle capable of entering an atmosphere and using that atmosphere to dissipate kinetic energy. One is a high L/D approach where convective heating dominates; the other is a low L/D approach where radiative heating dominates. The high L/D vehicle has a pointed shape; the low L/D vehicle has a blunt shape (Figure 4-1). High L/D vehicles are expected to be required for high maneuverability; e.g., in a manned mission to Mars requiring accurate control for landing at a specific location on the planet. Some studies, however, have suggested that low L/D aerobraking vehicles can be used for Earth return from Mars as well as for Mars landings.

For an AFE design a low L/D vehicle has advantages in investigating hypersonic flow conditions because the blunt shape pushes the shock front ahead of the vehicle and forms a sufficiently thick shock layer to evaluate nonequilibrium flow with minimum merging with cooler flow near the surface or contamination by the vehicle itself. Thus the basic physical principles of hypersonic flow can be investigated and defined for the blunt shape which is likely to be a model for a full-scale ASTV.

Various vehicle concepts (Figure 4-2) were considered for the ASTV. These included an aerobraking tug, an aeromaneuvering orbit-to-orbit shuttle, and a lifting brake. The lifting brake has received the most attention during the past decade because it requires less weight than the other approaches, thereby allowing a greater payload. The lifting brake has a large frontal area which produces a high drag. This allows deceleration to take place at a high altitude in the atmosphere. In turn, this permits the peak heating to be kept within limits that can be tolerated by lightweight heat-shield materials. The AFE vehicle is a lifting-brake vehicle.


Figure 4-1. Extreme classes of aeroassisted vehicles based on their ratios of lift to drag.
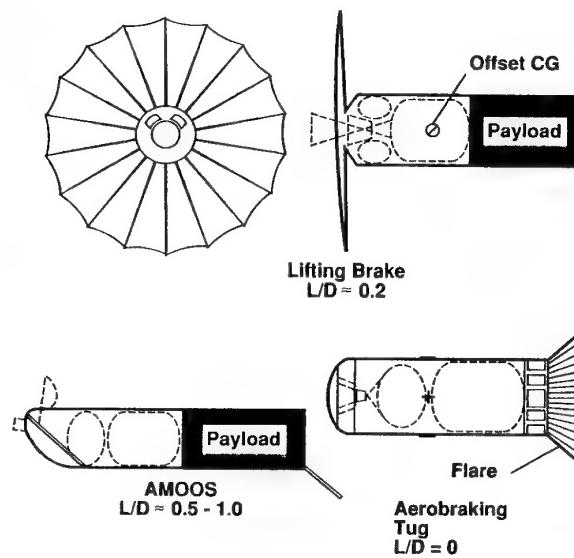
Figure 4-2. Various vehicle concepts that have been considered for ASTVs.

The basic control scheme for the lifting-brake AFE is to fly at a constant trim angle of attack while rolling the vehicle as required to direct the lifting force in the appropriate direction. This lifting force is used primarily to correct the trajectory for unpredictable variations in atmospheric density, which could cause the vehicle to follow a wrong trajectory. The lifting force is also used to place the trajectory higher in the atmosphere than would be possible with a purely ballistic flight, without the AFE vehicle exiting too quickly and not dissipating the required amount of kinetic energy for it to enter LEO.

Configuration of the AFE Vehicle

The AFE (Figure 4-3) is designed to test the blunt, lifting-brake concept using a roll-controlled guidance system. The diameter and effective nose radius are sufficient to produce the thick shock layer while fitting within the payload bay of a Space Shuttle Orbiter which will carry the AFE vehicle into orbit.
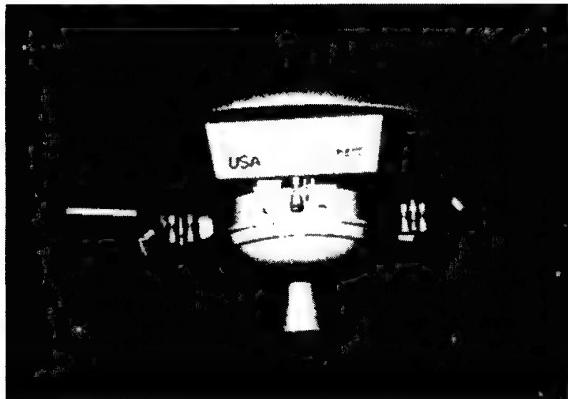

Figure 4-3. The AFE, shown here in a computer-generated concept, is designed to use the blunt-nosed, low L/D configuration.

The configuration resulted from a design study conducted at Johnson Space Center. The AFE's aeroshell is an elliptical cone blunted by an ellipsoidal nose. The cone is raked off at an angle of 17 degrees relative to the axis normal. The base profile in the rake plane is circular. The aeroshell's diameter is 14 feet.

The aerobrake support structure (Figure 4-4) is a low-temperature aluminum structure of the type used frequently in aeronautical construction. This instrumented structure is covered with a layer of fibrous refractory

Figure 4-4. This side view of a model of the AFE shows the special shape of the aerobrake structure to provide maneuverability as well as braking.

composite insulation tiles such as are used in many areas of the Space Shuttle Orbiter. The aerobrake weighs 725 pounds. The total weight of AFE without its solid propellant rocket motor is 4,100 pounds. It is important to note that the AFE is not intended to demonstrate light-weight construction, but is essentially an instrumented platform to acquire aerothermodynamic flight data.

The aerobrake is mounted on a hexagonal carrier vehicle whose diameter is less than that of the rake plane. The aerobrake thus overhangs the carrier. The carrier is a box-like spacecraft structure housing the reaction-control system, data-management system, communications, some instruments, and a solid-propellant rocket motor. The latter is a Thiokol Star-63 unit which develops the thrust needed to push the AFE vehicle into Earth's atmosphere at a velocity comparable to that which would be experienced by an ASTV returning from geosynchronous or cislunar orbit.

The AFE is fitted with a remotely manipulated system grapple fixture to permit it to be deployed and retrieved by the Space Shuttle Orbiter. Within the Orbiter's cargo bay, the AFE is carried on two standard Spacelab pallets.

Instrumentation of the AFE

The proposed experiments to be carried by the AFE use instrumentation located on the aeroshell and on the afterbody of the vehicle (Figure 4-5). These experiments are summarized in Table 1.

Forebody instrumentation

▨	Wall Catalysis	△	Heatshield performance
◈	ATPM	●	Pressure distribution
⧅	Total radiometer	▣	Air data system
⛧	High resolution spectrometer	x	Thermocouple
⊘	MRIS	▢	WCE pressure
		⊗	WCE thermocouple

Base region instrumentation

|			
☒	BFHE Tiles	x	Thermocouple
■	RAME	⧅	Total radiometer
c	Camera	⛧	High resolution spectrometer
●	Pressure tap		
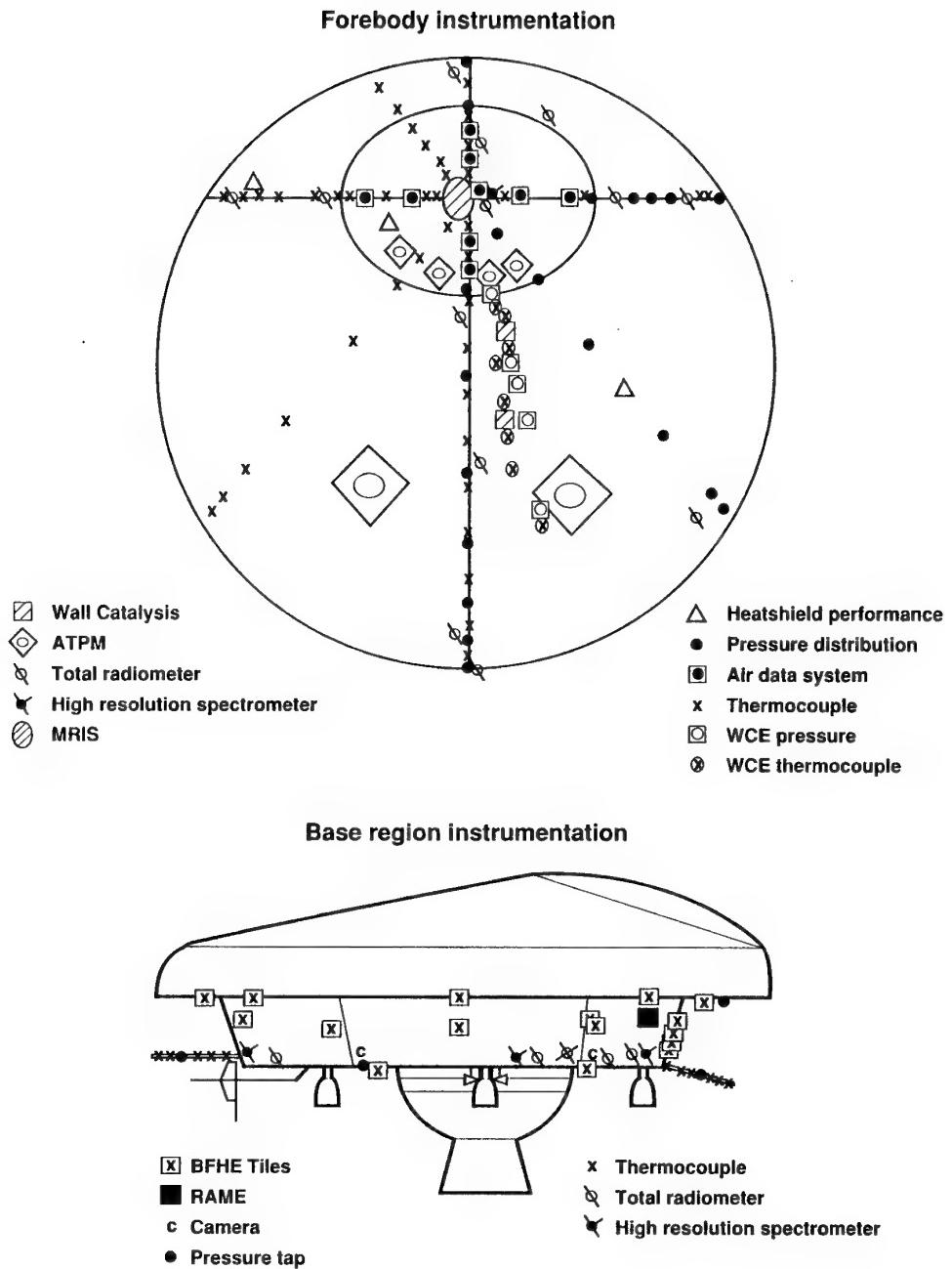
Figure 4-5. Locations of the many instruments to be used in the experiments carried aboard the AFE.

Table 1. Proposed AFE Experiments

Name (Acronym)	Principal Investigator	Center
1 Radiative Heating (RHE)	R. A. Craig	ARC
2 Wall Catalysis (WCE)	D. A. Stewart	ARC
3 Forebody Aerothermal Characterization (FACE)	L. Hartung, D. A. Throckmorton	LaRC
4 Pressure Distribution/ Air Data System (PD/ADS)	L.Gibson	LaRC
5 Base Flow and Heating (BFHE)	C. D. Scott, M. Jansen	JSC
6 Afterbody Radiometry (ARE)	W. C. Davy, A. W. Strawa	ARC
7 Microwave Reflec- tometer Ionization Sensor (MRIS)	R. Neece, P. Gnoffo	LaRC
8 Alternate Thermal Pro- tection Materials (ATPM)	M. A. Covington, D. Kourtides	ARC
9 Heat-Shield Perfor- mance (HSP)	D. E. Cagliostro, S. White	ARC
10 Aerodynamic Perfor- mance (APEX)	C. Cerimele	JSC
11 Rarefied Flow Aero- dynamic Measurement (RAME)	R. C. Blanchard	LaRC

Figure 4-6. The radiative heating experiment.

Overcoated tile with typical thermocouple locations
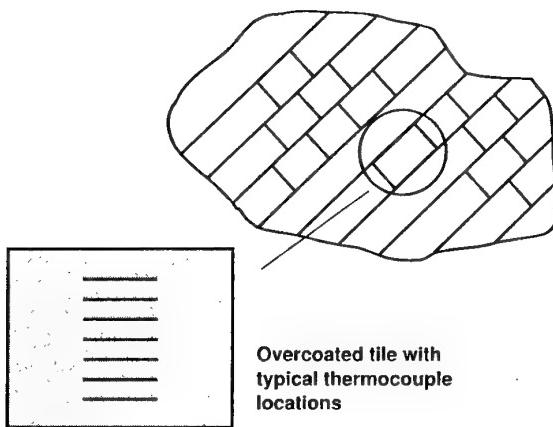
Figure 4-7. The wall catalysis experiment.

The **Radiative Heating Experiment** uses a number of spectrally integrating radiometers placed on the forebody to measure the distribution of radiation from the shock layer which reaches the aerobrake (Figure 4-6). A spectrometer will be located near the stagnation region, the region at the front of the AFE where the flow is virtually at a standstill with respect to the AFE. Another spectrometer will be located nearby, but in a cross-flow region. These instruments will be used to identify the relative contributions of various gas species in the radiation to the wall of the aerobrake. Some of these species may reach a temperature of 45,000 K during the entry of an ASTV. Characterizing these species is important to building a data base for the design of an efficient ASTV.

The **Wall Catalysis Experiment** will use a highly efficient catalytic coating on baseline TPS tiles at several locations on the forebody heat shield (Figure 4-7). By analyzing the heat-transfer data at these locations compared to baseline heating, the experimenters will determine the ability of coatings to change convective heating rates, and may also estimate the nonequilibrium nature of the flow in the boundary layer.

The **Forebody Aerothermal Characterization Experiment** uses thermocouples embedded below the glass-coated surface of the thermal protection tiles (Figure 4-8) to record the surface temperature of the heat shield during passage of the AFE vehicle through the atmosphere. This permits the local rate of heat transfer to be calculated. The convective heat-transfer rate can be
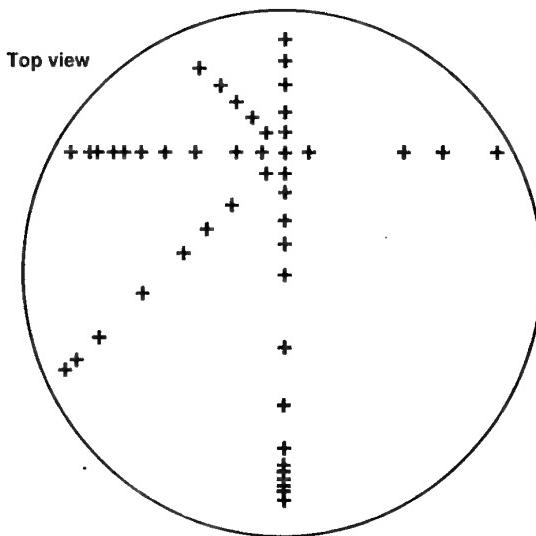
Figure 4-8. Thermocouple locations on FACE experiment.

extracted from the local heating using information from the Radiative Heating Experiment. This information is needed in the data base for the design of an efficient ASTV. The data will be used as fundamental information to validate codes used in CFD computations.

The **Pressure Distribution/Air Data System** measures surface pressure at locations on the forebody (Figure 4-9) to help analyze the flow and determine the attitude of the vehicle and the dynamic pressure on the aerobrake during flight. The data will provide fundamental information to validate codes used in CFD. Pressure data will be used to determine angle of attack, angle of sideslip, and free-stream dynamic pressure. The air data will be used to define the reference flight environment.

The **Base Flow and Heating Experiment** uses thermocouples and pressure transducers together with an imaging system mounted in the aft flow region of the spacecraft (Figure 4-10). Some instruments will be mounted on booms projecting into the flow region. The experiment is aimed at studying the nature of the base flow throughout the AFE's path through the atmosphere in an effort to resolve the complexities of this flow. The results will be used to define the shear layer, including the turning angle of the high-speed outer flow, and the location of the boundary which separates the high-energy outer flow from the low-energy recirculating inner flow. They will also be used to assess afterbody thermal loads.

The **Afterbody Radiometry Experiment** measures the volume radiation of the gas in the wake with spectral

PD/ADS pressure orifice locations
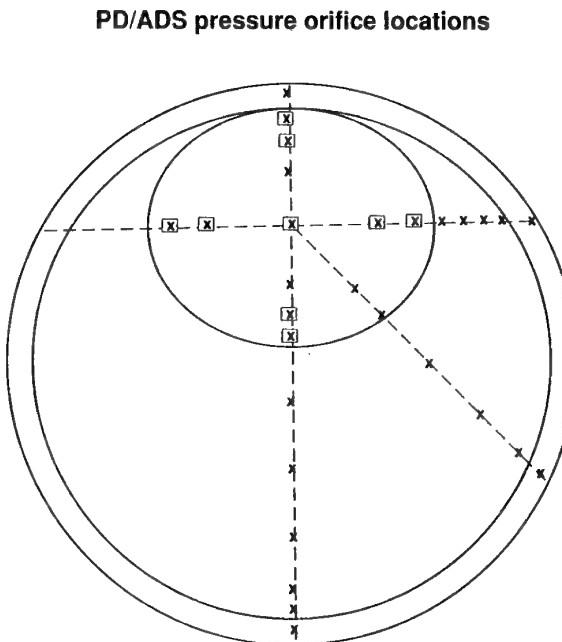

Figure 4-9. The pressure distribution/air data system.
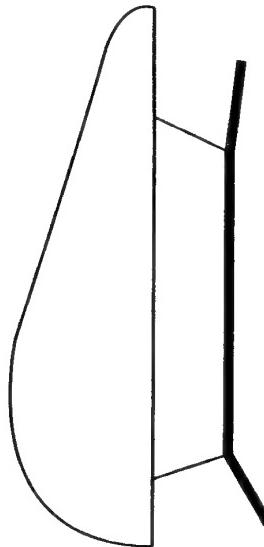
Figure 4-10. The base flow and heating experiment.

and integrating radiometers (Figure 4-11). The data will be used to determine the initial state of the wake flow gases and the chemical state at the downstream compression zone, and to determine the total radiation flux at selected locations on the afterbody. An additional

instrument is proposed to determine the dynamic behavior of the wake.

The **Microwave Reflectometer Ionization Sensor** measures the reflected power of microwave signals beamed outward from the vehicle (Figure 4-12) at four different frequencies. Significant reflected power will be an indication of free electrons reaching critical density—from which it can be determined the time of onset and disappearance of critical densities, as well as locations, in the shock layer. Such data will be important in supporting code validation of flow-field chemistry.

The **Alternate Thermal Protection Materials** experiment replaces the baseline TPS material at selected locations on the forebody with test samples (Figure 4-13) of various advanced and developmental thermal protection materials. The samples are instrumented with thermocouples to measure their heating. Postflight inspection is required to evaluate their performance.

The **Heat Shield Performance Experiment** measures the performance of the baseline tiles using thermocouples on the surface and buried within the tiles (Figure 4-14). Of particular interest is heating in the gaps between the tiles in the high-pressure-gradient region around the skirt of the heat shield where these gaps are somewhat shallower than those in the Space Shuttle Orbiter's TPS, and in the stagnation region where heating is most severe.

Figure 4-12. The microwave reflectometer ionization sensor.
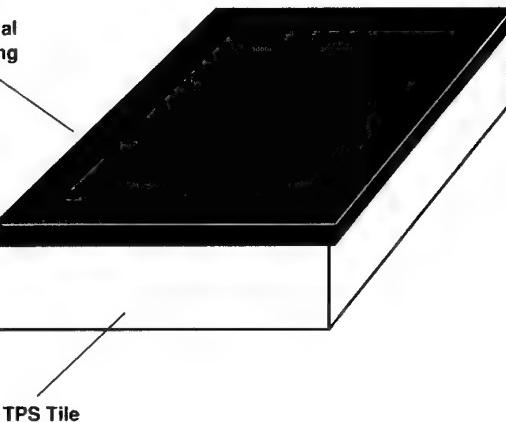
Figure 4-13. The alternate thermal protection materials experiment.

The **Aerodynamic Performance Experiment** will determine the values of the aerodynamic coefficients for lift, drag, and pitching moments (Figure 4-15) during the flight through the denser part of the atmosphere. This will provide a set of benchmark data which can be compared with predictions. Avionics accelerometers and angular rate gyroscopes of the guidance, navigation, and control system of the spacecraft will be used to derive aerodynamic forces and moments during the flight.

Figure 4-11. The afterbody radiometry experiment.

X - Thermocouple locations
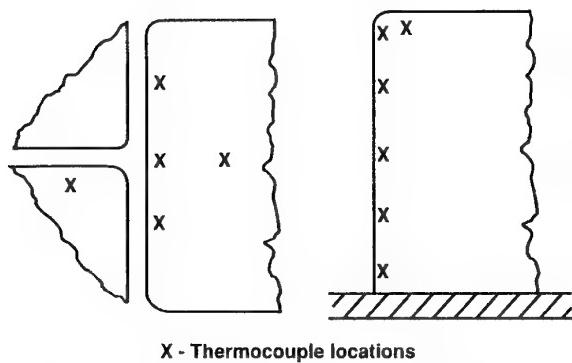
Figure 4-14. The heat shield performance experiment.
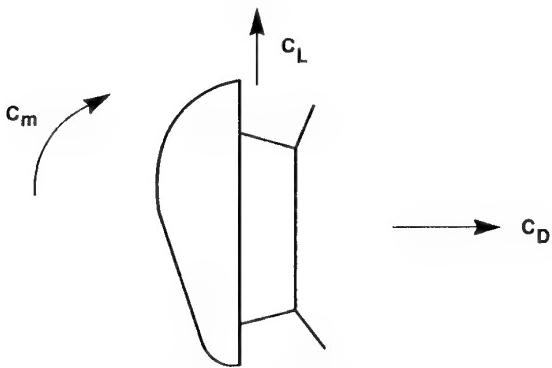
Figure 4-15. Aerodynamic performance experiment.

The **Rarefied Flow Aerodynamic Measurement Experiment** uses high-resolution accelerometers and rate gyroscopes aligned to the axis of the AFE to provide data in the transition and free molecular flow regimes (Figure 4-16) at altitudes above 300,000 feet, which are beyond the capability of the basic AFE avionics measurements. The data will be used to determine aerodynamic coefficients of the vehicle in these low-density viscous flight regimes. Ultimately, the experiment will provide data to validate spectral benchmark computer codes which are capable of bridging the gap between describing the aerodynamics of an "orbiting" spacecraft and of a "flying" spacecraft.

A major challenge in designing these experiments was in the placement of the instruments and the shaping the vehicle so that the flow past the AFE is not contaminated in ways that will invalidate the data. Another challenge has been that of making sure that the instruments can take measurements in situ when the carrier vehicle is moving at hypersonic velocity through the atmosphere. Most earlier in situ atmospheric measurements from spacecraft—such as Viking Landers and Pioneer Venus Probes—were made when the spacecraft was traveling slowly through an atmosphere. In this respect, for example, there will be several scientific spinoffs of new technology from AFE. One is the development of space-qualified instruments, such as radiometers and the microwave reflectometer ionization sensor, capable of gathering data while moving at high speed through an atmosphere to allow in situ atmospheric measurements at high speeds for planetary exploration probes. AFE, building on PAET, Project FIRE, and ongoing technology programs of NASA, will also introduce planetary exploration techniques comprising both the new instruments and the computational fluid dynamics to predict conditions in atmospheric gases.

Expected results of the experiments and their importance to future space transportation systems and space missions are described in the next sections of this publication.
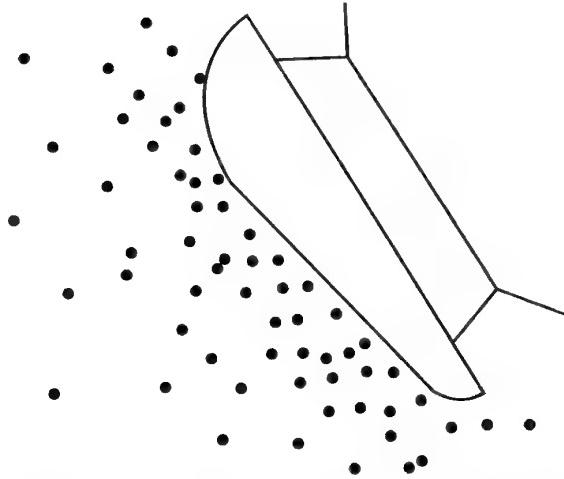

Figure 4-16. The rarefied flow aerodynamic measurement experiment.

SECTION 5: EXPECTED RESULTS FROM THE AFE
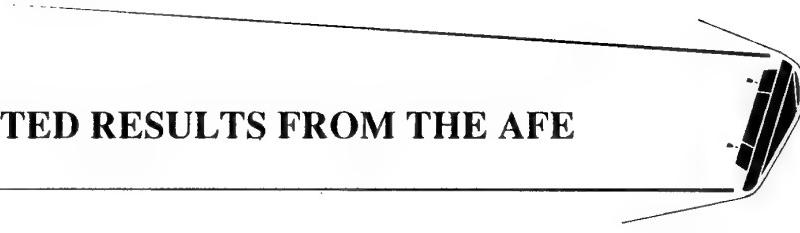
In meeting its mission objectives, the AFE program will resolve the major questions about radiative heating at hypersonic velocities. It will determine the effects of wall catalysis. This is very important for designing vehicles capable of traveling at high speeds in the upper atmosphere where nitrogen and oxygen atoms may play important roles in heating due to recombination at the wall of the aerobrake. Advanced TPS materials will be evaluated. Several different thermal control coatings will be tested on the basic TPS tiles. The wake flow and base heating will be defined, and the ability to control the vehicle in its flight through the atmosphere will be assessed. The new data base produced from the AFE program will provide a basis to develop and verify codes to be used in the computer design of other hypersonic vehicles, including the ASTV space transportation system.

Currently there are alternative interpretations of available data on the radiation from nonequilibrated shock layers, and the amount of radiation that will reach the wall of the TPS when no ablation gases are present and the shock layer is thick. The AFE program will provide data for a correct interpretation through its Radiative Heating Experiment.

At higher velocity and greater altitude than the region of main deceleration of the Space Shuttle Orbiter, nitrogen and oxygen dissociation, ionization, and recombination will affect the heat input to the TPS system. The magnitude of this effect will be determined by the AFE mission, and the measured heat-transfer rates with various wall coatings are expected to provide guidelines for designing materials having low catalytic activity coating for the ASTV.

Testing of advanced rigid and flexible thermal protection materials is expected to determine whether flexible ceramic blanket materials will perform adequately and whether new, high-temperature, rigid ceramic tiles can be used in the hypersonic entry environment. Reflective coatings will be tested that are expected to reflect more of the nonequilibrium radiation. These data will come from the Alternate Thermal Protection Material Experiment.

The base region heating and the flow environment behind a blunt-nosed body moving at hypersonic speeds in a low-density atmosphere is currently poorly understood. AFE will clarify the situation by providing information about the significance of wake radiation and ionization, and the distribution of convective heating over the aft portion of the aerobrake structure. These results will help define the safe ASTV payload envelope. Information of importance will be derived from the Base Flow and Heating Experiment and from the Afterbody Radiometry Experiment.

By flying AFE through the upper atmosphere while measuring its aerodynamic parameters and observing the ability of the guidance, navigation, and control system to direct its trajectory, designers will obtain much needed data about the performance of an aerodynamic, roll-controlled, lifting brake and the abilities of such a vehicle to handle dispersions in navigation and guidance. The necessary data will be derived from the Aerodynamic Performance Experiment, the Rarefied Flow Aerodynamic Measurement Experiment, and the Air Data System Experiment.

Because of the limitations of ground-test capability, ASTV design must be based primarily on computational methods. But even the most powerful supercomputers are useless unless they can be provided with reliable basic data with which to make computations. The ASTV presents a number of computational challenges which require a significant advancement over existing codes and procedures for predicting aerothermal loads and thermal and structural responses. For example, in CFD there is a good understanding of the important flow physics involved in thermochemical nonequilibrium, finite-rate chemistry, and molecular excitation, but input data are lacking to validate the codes in practical applications.

Basic data to confirm, develop, or validate computer models of high-speed flow are prerequisite to the design of the future ASTV fleet. Such data are expected to be derived from the measurements made from the AFE platform. Instruments involved in providing these data

include the Pressure Distribution Experiment, the Forebody Aerothermal Characterization Experiment, the Microwave Reflectometer Ionization Sensor Experiment, the Radiative Heating Experiment, and the Afterbody Radiometry Experiment.

As discussed earlier, the AFE will use a nonablating heat-shield material similar to the material used on the Space Shuttle Orbiter. This is an insulating ceramic material with a black coating to radiate away the heat. This kind of heat shield would be suitable for ASTVs used for orbital changes in the vicinity of the Earth (for example, from GEO to LEO, or return from the Moon to LEO) and

for orbital capture at Mars. However, the arrival at Earth from a planetary mission requires an ASTV with an ablative heat shield because of the much higher speeds. The presence of ablation on an ASTV would distort the flow field to such an extent that computational validation would not be possible on the basis of the AFE results. An ablating aeroassist flight experiment will, however, be required to complement the results of AFE. Although the AFE data will not directly apply to an ASTV returning from a Mars mission, they are needed to develop experiments for and interpret results from an advanced aeroassist experiment to support the design of such an interplanetary ASTV.

SECTION 6: INTO THE FUTURE
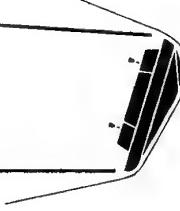
Information gained from the Aeroassist Flight Experiment program will be of enormous economic benefit to the United States in keeping abreast of new technologies which will begin to color international human expansion into space during the next century.

With increasing emphasis being placed on observing Earth from space with multispectral instruments, more complicated capital-intensive satellites will be placed in GEO. Such satellites will inevitably age or fall victim to advances in technology. While their basic structure may remain viable, their electronic systems and sensors will require upgrading as new technologies emerge. Economic benefits will accrue to that nation or nations with an ability to refurbish, repair, or upgrade such satellites. This requires transportation between GEO and LEO where facilities at space stations of the 21st century can be used to service or upgrade the satellites.

The use of aeroassist to dissipate the energy of return from GEO to enter into LEO is highly desirable from an economic standpoint since it considerably increases the payload-carrying capability of the transportation fleet. An efficient ASTV appears to be the key to commercially viable servicing operations based in LEO.

AFE results will make the design and development of an ASTV fleet practical without such a fleet suffering serious penalties of overdesign of heat shields or the addition of retrorockets to assure orbital transfer. While moving from orbit to orbit beyond LEO requires relatively low-energy expenditures, the transport of materials from the gravitational pit of Earth into LEO is energy-intensive. The less material that has to be transported into space, the smaller will be the fleet of Space Shuttles and expendable launch vehicles needed to initiate or service space operations.

Ultimately, it may be found opportune to establish manned stations in GEO. Again, the use of ASTVs to move personnel back to LEO for return to the Earth's surface via the Space Shuttle Orbiter will require an efficient human-rated ASTV fleet. The basic data

gathered by the AFE will be essential for designing any such ASTV.

In the next century it is most probable that the United States will return to the Moon and start to develop that world as a research base and as a source of raw materials. For example, deep-space radio astronomy can best be achieved by radiotelescopes based on the far side of the Moon where they are screened from electromagnetic pollution of Earth's many transmitters (Figure 6-1). A permanent research base on the lunar surface will also ultimately lead to the development of facilities to utilize lunar materials, possibly to support large space stations in orbit around Earth, or to construct interplanetary spacecraft. Moving material from the lunar surface to LEO requires less energy than moving an equivalent amount from the Earth's surface to LEO. In a developing space program beyond LEO, utilizing the resources of the Moon appears very attractive.

Such uses again require an efficient ASTV system to allow the freighters from the Moon to be captured into Earth orbit. This will provide another long-term benefit to the understanding of the basic aerophysics of aeroassist technology, the groundwork for which will be laid by the AFE program. This program is thus an important investment in the technological future of the nation.

Looking farther into the future, it seems inevitable that humans will journey to, land on, and establish a permanent presence on the planet Mars (Figure 6-2). There are many reasons for this which are beyond the scope of this publication, but which are discussed in recent literature including the Report of the National Committee on Space (1987), the Ride report on America's Future in Space (1988), and several Case for Mars study reports over the past 5 years.

Aerobraking and aeroassist technology will be essential for economical missions to Mars. They will be used to increase payload capacity, achieve maneuvers to specific landing locations, return science samples to Earth, and return personnel to Earth. If propellants are used to slow a
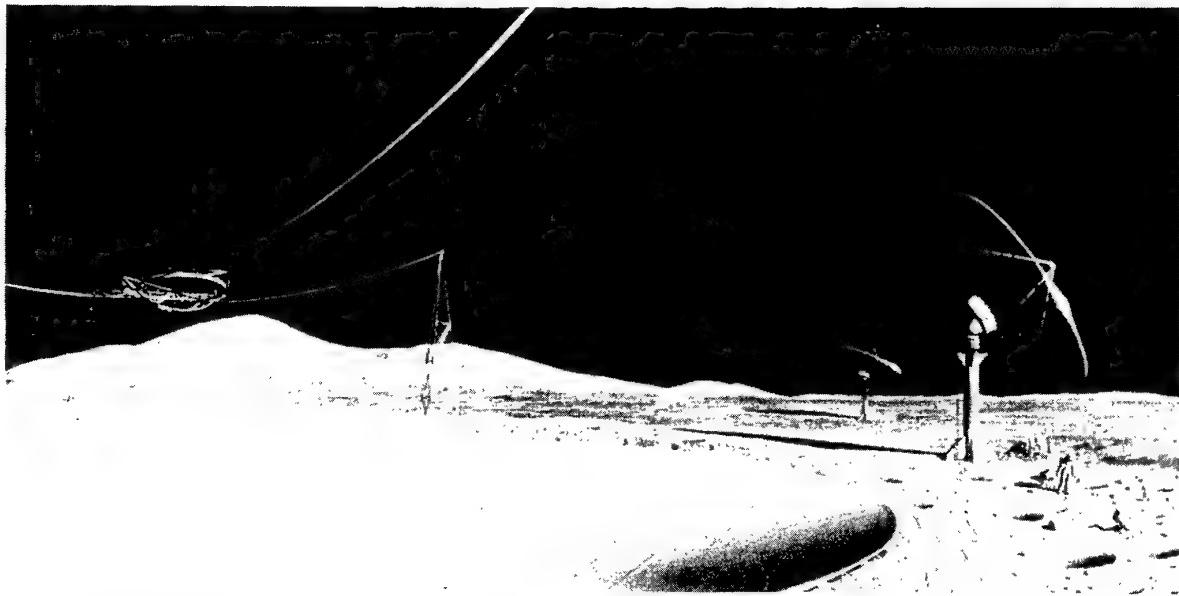
Figure 6-1. Establishment of research stations on the Moon, e.g., a radio astronomy station on the far side of the Moon will be economically possible only if aeroassist vehicles can be used for returning personnel and materials to LEO.
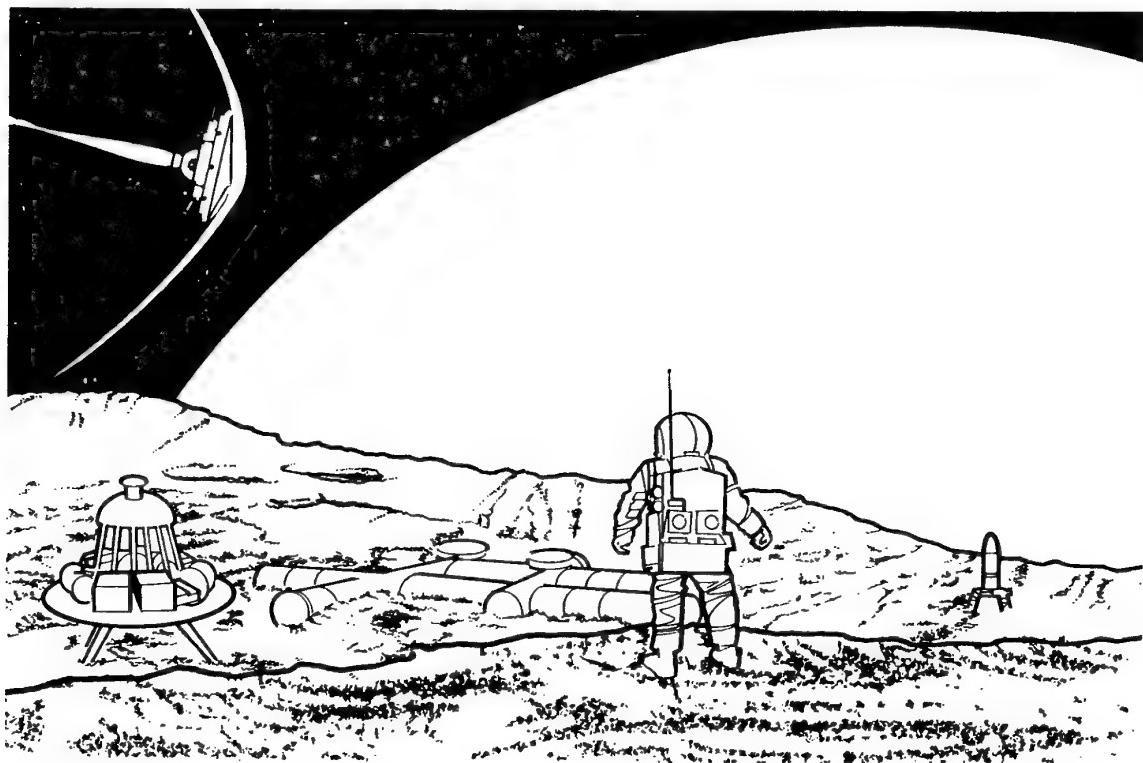
Figure 6-2. This artist's concept of human operations on Mars shows an aeroassist vehicle traveling through the upper atmosphere of the Red Planet. Aeroassist seems essential to making a human presence on Mars economically feasible.

spacecraft for a Mars mission, almost twice as much material has to be lifted from the Earth's surface to LEO. While some of these vehicles will require new technologies beyond those suggested for the ASTVs, they will rely basically on the same fundamental data concerning hypersonic flow and heat transfer under nonequilibrium flow conditions.

Winged gliders with sharp leading edges will be required in missions where high cross ranges are needed, such as landings in high latitudes. Biconic vehicles may be required for transportation of heavy freight, and blunt-nosed aeroassist vehicles will still be used in some scenarios for aerocapture at Mars and Earth. Each of these systems will need to be evaluated by CFD models which, as was mentioned in an earlier section, rely upon accurate data concerning all the parameters involved in hypervelocity flight, validated by flight data.

While the AFE program will provide data for many of these parameters, the wide range of aeroassist environments to be experienced in future space missions (Figure 6-3) require that additional concurrent research should take place using test vehicles with ablators and higher L/D ratios. Such vehicles, carried aloft and recovered by the Space Shuttle, would fly on missions similar to that of AFE vehicle, but at higher speeds of entry into the Earth's atmosphere and at different altitudes. These concurrent tests are needed if the nation is to keep up with and preferably lead in the important space transportation technologies which are capable of yielding great economic benefits to humankind in the 21st century.
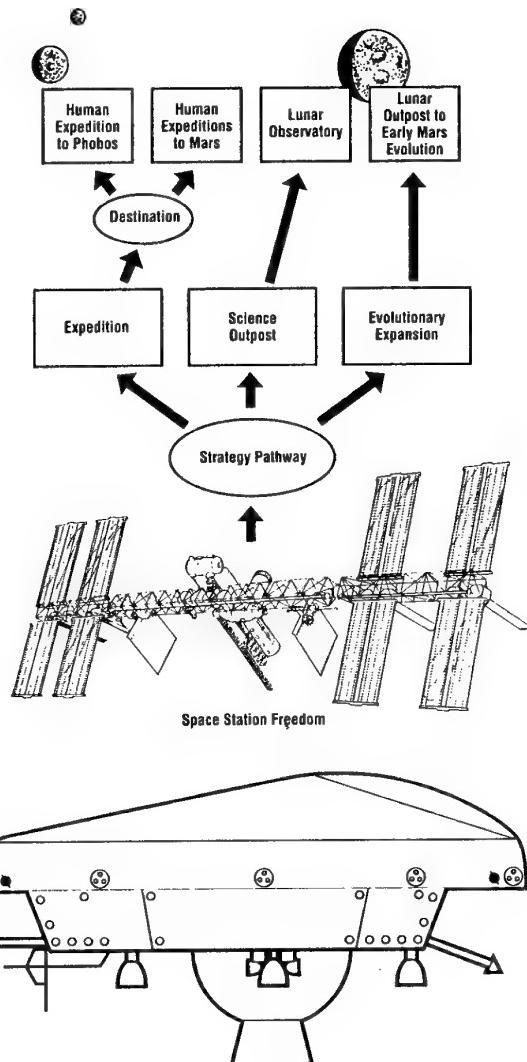

Figure 6-3. Human plans to expand into the Solar System through operations in LEO will be based on the firm foundation of an efficient ASTV system which, in turn, depends strongly on the basic science data to be obtained by the AFE mission.

GLOSSARY
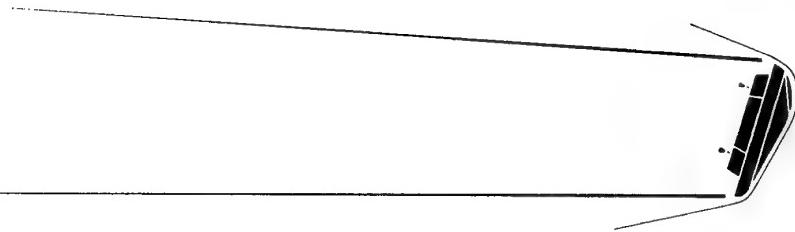
ABLATION: Erosion of material from a heat shield to absorb and transport heat away from a payload, usually by the removal of surface material by sublimation, vaporization, or melting.

AEROASSIST: Use of atmospheric lift and drag to maneuver a spacecraft.

AEROBRAKE: A structure to deflect airflow around a spacecraft and provide aeroassist.

AERODYNAMICS: The science dealing with the motion of air and other gaseous fluids, and of the forces acting upon bodies moving through such fluids.

AERODYNAMIC PARAMETERS: Nondimensional coefficients relating to aerodynamic forces or moments, such as a coefficient of drag or a coefficient of lift.

AEROPASS: Passage of a spacecraft through an atmosphere to utilize lift and drag forces.

AEROTHERMODYNAMICS: The thermodynamics of airflow moving around a body at very high speeds where the thermodynamic properties of the gas become important.

ARC-JET: A device to simulate high-speed airflow by creating an electrical discharge along a narrow channel to heat air or a test gas flowing through that channel.

BALLISTIC PATH: Path of a body moving freely in a gravitational field at less than orbital velocity, and acted upon solely by the gravitational field and the resistance of the medium through which it passes.

BALLISTIC RANGE: A test range in which a gun fires a projectile at high speed along a ballistic trajectory while its flight path and velocity are monitored and recorded.

BASE HEATING: Heating of the rear of a spacecraft.

BOUNDARY LAYER: The layer of air near a surface with an airflow over that surface which is affected primarily by the viscosity of the fluid; the flow may be laminar or turbulent. In aerodynamics the boundary layer is sometimes arbitrarily extended from the surface to a point at which the flow has 99% of the stream velocity.

CATALYSIS: Chemical reaction caused by a substance which itself does not enter into the chemical reaction or is changed by the reaction.

CISLUNAR: Space within the orbit of the Moon.

COMPUTATIONAL FLUID DYNAMICS (CFD): The science of computer simulation of the conditions within and patterns of a flow of fluids.

COMPUTATIONAL MODEL: Model developed through use of CFD to show how a spacecraft is expected to perform under a given set of conditions.

CONVECTIVE HEATING: Transfer of heat by mass motion of a fluid bringing to a surface heat which is transferred to that surface from the fluid.

EQUILIBRIUM: A state within a gas in which reactions between the components are proceeding equally in forward and backward directions so that the relative concentrations of the components would not change with time if so left at the condition.

FLUID DYNAMICS: The dynamics of the flow of gases around bodies immersed in them, such as a spacecraft traveling through an atmosphere.

FLOW FIELD: The region of gaseous flow around a body immersed in an atmosphere and moving relative to that atmosphere.

GAS SPECIES: The various chemical components of a gas.

GEOSYNCHRONOUS EARTH ORBIT (GEO): Strictly an orbit (circular or elliptical) in which a body completes a revolution in the same period that Earth rotates on its axis; more generally applied to a body moving in a geostationary circular orbit in Earth's equatorial plane in which the body remains stationary with respect to an observer on the surface of the Earth.

HEAT SHIELD: A protective device to block the transfer of unwanted heat into a spacecraft.

HIGH EARTH ORBIT (HEO): An orbit around Earth beyond LEO.

LIFTING BRAKE: A spacecraft aerodynamically shaped to provide some lift and much drag to change the path of a spacecraft through an atmosphere.

LOW EARTH ORBIT (LEO): An orbit, usually close to a circle, just beyond the Earth's appreciable atmosphere at a height sufficient to prevent the orbit from decaying rapidly because of normal conditions of atmospheric drag.

NONEQUILIBRIUM: A state within a gas mixture in which reactions have not reached equilibrium. The composition would change with time if left in the condition.

PHENOMENOLOGICAL MODELS: Computational models that describe the phonomena expected under a given set of circumstances.

PLASMA: A state of matter in which molecules and atoms are electrically charged and are not bound to each other chemically, and exist with a population of free electrons.

PLASMA JET: A jet consisting of charged particles to simulate conditions of very-high-speed atmospheric flow.

RADIATIVE HEATING: Transfer of heat by radiation without contact between the hot and the cold media.

RADIOMETER: An instrument to measure amount of radiation.

SHEAR LAYER: A layer along a flow field across which there occurs an abrupt change in velocity of the fluid.

SHOCK LAYER: A layer of fluid between the shock wave and the vehicle in which the velocity of the fluid has changed from supersonic or hypersonic to subsonic velocity.

SHOCK TUBE: A relatively long tube in which brief, high-speed gas flows are produced by the sudden release of high-pressure gas into the tube that produces a traveling shock wave along the tube with high-speed flow behind the shock.

SHOCK WAVE: A surface of discontinuity through which a fluid moving at high speed undergoes a finite decrease in velocity accompanied by an increase in pressure and temperature, or vice versa.

SPECTROMETER: An instrument to measure precisely and categorize radiation at different frequencies.

SUPERCOMPUTER: A modern digital computer possessing extremely high speed of operation, large storage of information, and typically with parallel processing to handle many computations very rapidly.

SURFACE CATALYSIS: Triggering of reactions within a gaseous mixture by the catalytic action of material in a surface in contact with that gaseous mixture.

THERMAL PROTECTION SYSTEM (TPS): A system designed to protect a vehicle such as a spacecraft from undesirable heating by rejecting, absorbing, or radiating unwanted heat.

THERMOCOUPLE: A device that generates an electrical potential by the effect of heat on dissimilar materials so that the temperature can be measured.

VISCOUS EFFECTS: Effects of the property of a fluid to support tangential stresses and resist being deformed.

WAKE REGION: The region of atmospheric flow behind a spacecraft traveling through an atmosphere.

AEROTHERMODYNAMIC REQUIREMENTS AND DESIGN OF THE HUYGENS PROBE

M. Baillion
Aerospatiale Branche Espace & Défense
Centre Opérationnel Systèmes
Département Aérodynamique & Electromagnétisme
BP 2
78133 Les Mureaux Cédex
France

SUMMARY

This paper presents the relationship between the main system requirements of the HUYGENS probe, derived either from mission analysis or from experiment related requirements, to the aerodynamics and aerothermo-dynamics studies.

The first part of the document will present the main mission and experiment related requirements, as they are expressed at the very beginning of the project, and which are derived from the specificity of the mission, without any direct link with aerothermodynamics.

The general system requirements of the HUYGENS probe, are the ones which are expressed by the customer ESA towards the industrial prime contractor Aerospatiale Space & Defense, and which correspond to the elementary requirements of feasibility of the mission, in terms of general objective : reach TITAN, survive a 7 years cruise in deep space, survive to the hypersonic entry in TITAN atmosphere.

The second part will show how these very general requirements are translated in terms of aerothermodynamics requirements.

The third part will show how these aerothermodynamics requirements are implemented in general aerothermodynamics studies and test plan, which has been actually performed in the frame of the HUYGENS project.

The choice of the shapes, the Computational Fluid Dynamics (CFD) and test plan, the related CFD and wind tunnel specificity and difficulties are addressed. The need for characterisation of the convective and radiative heat fluxes in an unknown environment is shown.

Finally very specific items like contamination and spin device are addressed.

LIST OF SYMBOLS

C_A	Axial force coefficient, (-Axial force)/Q S
C_N	Normal force coefficient, (-Normal force)/ Q S
C_D	Drag coefficient, $C_N \sin \alpha + C_A \cos \alpha$
C_L	Lift coefficient, $C_N \cos \alpha - C_A \sin \alpha$
C_m	Pitching moment coefficient, (Pitching moment)/Q S d
$C_{mq}+C_{m\alpha}$	Pitch damping coefficient, $\partial Cm/\partial(qd/V))+\partial Cm/\partial(\alpha \cdot d/V))$
Cp	pressure coefficient (p-pinf)/qinf
d	Diameter of the capsule, m
f	frequency of oscillation, Hz
M	Mach number
S, or A	Reference surface, m^2
Q	Dynamic pressure, $\frac{1}{2}\rho V^2$, Pa
V	Freestream Velocity, m/s
W	Mass of the probe, kg
Z	Altitude, km
γ	Specific Heat ratio, Cp/Cv
ξ	Dynamic stability parameter
ω	angular frequency, rad/s

subscripts

α	Static derivative with respect to incidence, *per rad*
inf	upstream conditions

1. INTRODUCTION

Within all the Solar system, the most exciting and interesting planet for exobiology, i.e. the study of extra terrestrial life, is Titan, the biggest moon of Saturn.

A unique satellite of Solar system with a dense atmosphere (pressure on Titan is 1.5 times the Earth one). Its atmosphere is composed mainly of Nitrogen with several percent of methane CH_4, Argon (up to 21%) and traces of hydrogen.

According to laboratory experiments, it should represent one of the most promising pre biotic atmosphere, which should contain many organic compounds, hydrocarbons and nitriles mainly.

Spectroscopic experiments performed during Voyager 1 mission in 1980 did confirm the presence of several nitriles which play a fundamental role in pre biotic chemistry on the Earth, like cyanhydric acid and cyanocetylen.

Analogy of Titan with the Earth is completed through the similar temperature profile (although much lower in magnitude), and surface properties, indeed Titan is probably partly solid and liquid (methane and ethane oceans).

The main difference between Titan and the Earth is the much lower temperature (96 K on surface, i.e. -179 °C).
Finally, even if life may not appear on Titan, because of its very cold atmosphere, Titan represents a full scale planetary field of investigation, which can provide to scientists the opportunity to understand the first steps of life appearance.
This has motivated the HUYGENS/CASSINI mission.

2. MISSION DESCRIPTION

The HUYGENS probe is part of the ESA scientific programs, devoted to the exploration of TITAN atmosphere.
The probe is passenger on-board MARINER-MARK II CASSINI SATURN Orbiter, which will be launched in October 1997 from Cape Canaveral by a TITAN IV/CENTAUR Launcher.
A large deep space delta-V manoeuvre is performed at about 60 days after launch, followed by two flybys of Venus at about 200 days and 620 days after launch respectively.
The spacecraft will then fly by the Earth at about 680 days after launch and will implement a Jupiter gravity assist in December 2000 (about 1200 days after launch). It will then be on a 3.5-year trajectory towards Saturn, with an arrival in June 2004 after a total flight duration of 6.7 years **(Cruise phase).**
The visualisation of CASSINI Orbiter and HUYGENS Probe trajectories are shown on figure n°1.
The CASSINI spacecraft will be inserted into a highly eccentric Saturn centered orbit (Saturn Orbit Insertion SOI). After 110 days past SOI, when the spacecraft is near the apoapsis of the capture orbit, a trajectory correction is achieved with a twofold objective:
- raise the periapsis radius from the Saturn radii (Rs) to about 8,2Rs
- target the CASSINI spacecraft for its encounter with TITAN
  About 22 days before TITAN encounter, the spacecraft will be oriented in the proper direction and the probe will be spun up and separated from the Orbiter **(Coast phase).**
  About two days after probe separation, the Orbiter deflection manoeuvre takes place with a twofold goal
- achieve adequate geometrical conditions for the probe relay link under the resulting TITAN flyby trajectory of the Orbiter
- achieve proper initial conditions for the subsequent Orbiter tour of the Saturnian system.

The probe will enter into the TITAN atmosphere in January 2005 with an entry velocity of about 6.2 km/s and a flight path angle of -64° **(Entry phase).**

After atmospheric braking, the atmospheric **Descent phase** begins with the activation of the parachute deployment device at an altitude of about 170 km, and a velocity of about 400 m/s (Mach 1.5).

At Mach 1.5, the mortar is fired and allows the deployment and inflation of the pilot chute. Two seconds later, the pilot chute removes the back cover and deploys the main chute which pulls the descent module out of the released front shield. One minute after beginning of the descent, measurements can start for scientific experiments. Science data are transmitted to the Orbiter, which will later send stored data to the Earth.
The total duration of the descent phase, limited by the Orbiter presence, shall be between 2 and 2.5 hours including dispersions of all natures (atmospheric density, zonal winds, radius and topography of TITAN, probe ballistic coefficient, probe mass, flight path angle, icing)
Entry and descent phase are shown on figure n°2.

In order to comply with this duration, the main parachute is jettisoned 15 minutes after start of Descent, and replaced by a stabilising parachute.
The stabiliser allows to maintain attitude required by experiments and transmission. Spin vanes attached to the fore dome of the descent module allow to obtain experiment required spin rate.

3. MISSION REQUIREMENTS

The objective of this document is to show how general requirements of the HUYGENS probe, considered as a general system, are derived to aerodynamic and aerothermodynamic requirements.
The general system requirements of the HUYGENS probe, are the one which are expressed by the customer ESA towards the industrial prime contractor, and which correspond to the elementary requirements of feasibility of the mission, in terms of general objective : reach TITAN, survive a 7 years cruise in deep space, survive to the hypersonic entry in TITAN atmosphere.
Within the general system requirements, one may distinguish the first level requirements which belong to the mission requirements (let us call them mxx for mission requirement n°xx).
The HUYGENS project, as part of the ESA scientific programs, presents several distinctive features and requirements, its synthesis makes it unique, such as:

m1) the probe is passenger on-board MARINER-MARK II CASSINI SATURN orbiter
m2) the probe shall survive a 7 year-long deep space dormant cruise phase at the end of which it is ejected alone in deep space

m3) the probe shall withstand a severe atmospheric entry at hypersonic velocity, entailing adverse mechanical and thermal conditions

m4) the probe shall accomplish its scientific mission during a short period of time (2 to 2,5 hours) inside a cold atmospheric environment, while sending all the acquired data to the Earth via the Orbiter cruising around SATURN.

m5) the coast, entry and descent phases are carried out in a fully autonomous and fault-tolerant mode, without involving any attitude or orbit active control.

4. EXPERIMENT RELATED REQUIREMENTS

Apart of these top level requirements, additional requirements are imposed by experiments.
The probe configuration is intended to provide accommodation for the following payload experiments:

ACP   Aerosol Collector Pyrolyser

DISR   Descent Imager Spectral Radiometer

DWE   Doppler Wind Experiment

GCMS   Gas Chromatograph and Mass Spectrometer

HASI   HUYGENS Atmospheric Structure Instrument

SSP   Science Surface Package

The HUYGENS Atmospheric Structure Instrument HASI will begin operations during the Entry phase, whilst the others are operational only after the start of the descent phase.
The particular interface requirements linked to this payload accommodation are listed hereafter (let us call them exx for experiment requirement n°xx):

e1) the HASI accelerometer requires to be close to the center of gravity of the entry configuration,

e2) the SSP accelerometer requires to be close to the impact point,

e3) the DISR requires a wide and extensive field of view ranging from the zenith to vertically downwards, covering most of the hemisphere,

e4) the ACP and GCMS require to be mounted close together, and both protruding through the aerodynamic boundary layer to collect atmospheric samples,

e5) the DISR and HASI require proper flow around optical windows and sensors to avoid imperfect measurements,

e6) contamination from decelerator ablative materials have to be minimized around ACP and GCMS inlets on one side, and DISR optical window on the other side (the accommodation is shown on figure n°3).

5. REQUIREMENTS IMPACT ON AERODYNAMIC/AEROTHERMODYNAMIC DESIGN

The following part describes how the requirements listed below are translated in terms of aerodynamic and aerothermodynamic studies.

5.1 Mission requirements

m1) the probe is passenger on-board MARINER-MARK II CASSINI SATURN orbiter

The requirement m1 defines the interfaces between the probe and its carrier, and thus imposes a certain number of geometrical constraints, which will at the end have impacts on aerodynamics. The maximum diameter of the decelerator is limited by the Orbiter interfacing constraints, and thereby gives a limit to the ballistic parameter $\beta=S.C_D/W$. As the altitude and velocity of the probe are defined at beginning of entry by the Orbiter velocity with respect to Titan, and are defined at beginning of descent, both in term of velocity (M=1.5) and altitude (170 km), the deceleration profile which is necessary to achieve these two constraints can be fulfilled by finding a large ballistic parameter β, and by tuning the initial flight path angle γ of the probe. The surface S is fixed by the 3 meters maximum diameter imposed by the Orbiter. The mass results from the payload, structure, Thermal Protection System, etc...
The last parameter is the drag coefficient C_D. A 60° half angle cone is a good compromise between the accommodation capabilities and the drag coefficient.
The flight path angle of the probe is constrained by the Orbiter position with respect to Titan, while it must not be too steep, in order to limit the heat fluxes during hypersonic entry, and must not be too shallow, elsewhere the probe could skip through the Titan atmosphere and return in deep space.

m2) the probe shall survive a long 7 years deep space dormant cruise phase at the end of which it is ejected alone in deep space

The requirement m2 has no direct consequence on aero/aerothermodynamic design. However, it puts severe constraints on the constituting elements of the probe which must withstand a deep space travel of 7 years. The pyrotechnic devices of the probe which are used to jettison the back cover must indeed be operational at the very time of TITAN entry, when Mach number 1.5 is detected. Furthermore this constraint is made more

difficult by the fact that after having survived at a very low temperature environment, these pyrotechnic elements have to withstand a rather hot one during hypersonic entry into TITAN atmosphere.

This long time cold environment is also of great importance for parachute design. Indeed, this latter one must remain packed and tightened in bags until the deployment phase begins, and at this time, the porosity, the mechanical integrity of the parachute must still be predictable for a reliable parachute sequence. Ageing effects must have been tested and qualified for all these mechanisms.

m3) the probe shall withstand a severe atmospheric entry at hypersonic velocity, entailing adverse mechanical and thermal conditions

The requirement m3 is of course of major concern for aerothermodynamics.

During hypersonic entry, the large amount of kinetic energy of the probe (arrival at 6.9km/s in TITAN atmosphere, at Z=1250 km) results in temperature increase behind the bow shock layer, which is formed in front of the probe, during braking of the HUYGENS entry module into the atmosphere of TITAN : the translational temperature just behind the bow shock layer is approximately 12000K and reaches 7000K close to the wall. This results in heat flux reaching the surface, because of convective process from the flowfield surrounding the probe to the wall of about 500kW/m2 at worst conditions. This heat flux is enhanced by diffusion process due to the recombination at the wall of the chemical species which were formed behind the bow shock. Moreover, due to the very high entry velocity of the probe, the characteristic time of the flowfield (time for a particle to travel along a characteristic length of the vehicle) is of the same order than the chemical relaxation time and the vibrational relaxation time. Therefore, when upstream chemical mixture passes through the bow shock, i.e. mainly N_2, some percent of CH_4 and Argon, the chemical reactions such as dissociation and recombination occurring in the shock layer cannot equilibrate. The shock layer is therefore in a metastable state, where chemical compounds such as CN are present. This particular species is known to be a very strong radiator. Furthermore, the translational-vibrational non equilibrium has been shown to enhance the radiative emission of the shock layer. The radiative heat flux, in these conditions is of the same order than the convective one. The additional difficulty is due to the large sensitivity of the radiative heat flux with respect to the upstream chemical mixture (small variation of CH_4 results in large change of radiative heat flux).

Therefore, from the aerodynamic/aerothermodynamic point of view, requirement m3 means that the convective and radiative heat fluxes must be characterised whatever the parameters which have an influence on heat fluxes may be (velocity, flight path angle, ballistic coefficient, atmosphere temperature and density profiles, atmosphere chemical mixture, etc...) and a proper thermal protection system must be designed.

Since the probe mass budget constraint would not allow it, gross oversizing could not be the only answer to mission robustness. Hence, a careful analysis of sensitivity and margins of the convective and radiative heat fluxes is needed to meet m3 thermal requirement.

The second part of m3 is the mechanical integrity of the probe during hypersonic entry. Indeed, the mechanical structure of the probe has to face 16 Earth g's of deceleration during entry.

The dimensioning aspects of this requirement are beyond the scope of this document, however, a good knowledge of aerodynamic drag forces is needed to insure a correct mechanical design. As a result, early aerodynamic database is built from literature, and specific aerodynamic wind tunnel tests are performed.

m4) the probe shall accomplish its scientific mission during a short period of time (2 to 2,5 hours) inside a cold atmospheric environment, while sending all the acquired data to the Earth via the Orbiter cruising around SATURN.

The requirement m4 imposes specific requirements on the duration of the scientific part of the mission. Some other requirements are dedicated to the altitude range of the scientific mission (the part of the mission where the experiments are switched on) , i.e. the descent phase begins at altitude Z=170km.

The requirement m4 imposes specific requirements on the conditions of the scientific part of the mission. Indeed, a radio link must be kept between the antenna of the experiment package and the Orbiter one. Hence, this leads to requirements put onto the attitude of the module which brings the experiments, and thereby constraints the descent control subsystem design.

The m3 and m4 requirements have been chosen to be answered independently, which leads to the choice of the concept of the HUYGENS probe. Indeed, the probe is constituted by a kernel carrying the scientific experiments operating during descent, surrounded by a shell which protects it during the coast and entry phases. During entry, the front shield reduces the probe speed while the other parts of the shell protect the kernel from aerothermal heating. The shell is automatically jettisoned on a deceleration criteria, around M=1.5, at an altitude of about 170km.

m5) the coast, entry and descent phases are carried out in a fully autonomous and fault-tolerant mode, without involving any attitude or orbit active control.

The requirement m5 may be split in three parts :
m5.1 the coast phase

m5.2 the entry phase

m5.3 the descent phase

The requirement m5.1 means that after the probe is released from the Orbiter, it has to reach the TITAN atmosphere (its upper layer will be considered here as the interface between coast and entry phase, i.e. Z=1270km) according to the desired flight path. Furthermore, the attitude of the probe at coast/entry phase interface must be compatible with the requirement m5.2 to have the probe reaching its trim angle-of-attack . Indeed, a too large incidence at beginning of entry may result in an angle-of-attack divergence during the first part of entry, because blunt body aerodynamics in rarefied flowfield is such that the center-of-pressure shifts towards the nose, the vehicle being then statically unstable at beginning of entry. Sensitivity studies of entry module behaviour during first part of entry have then been performed, in order to issue requirements related to probe attitude at beginning of entry.

The requirement m5.2 means that no reaction control system has to be used during braking of the entry module in TITAN atmosphere. Therefore, the entry module has to be statically stable, in order to reach its zero incidence trim angle-of-attack, which provides with the large drag necessary to achieve the deceleration from 6190m/s at beginning of entry down to 400m/s at required 170km altitude for beginning of descent phase. Furthermore, considering the heat fluxes, a zero trim angle-of-attack enables a pure axisymmetric shock wave and heat flux profile to be characterised, while a too large angle-of-attack would result in a stagnation point location on the conical part of the entry module, which would increase the bow shock distance, and further the radiative heat flux (roughly proportional to shock stand off distance).
The dynamic stability is required, in order to have safe parachute deployment conditions at entry/descent interface.

The descent module has to accommodate all the experiments located on the experiment platform, hence a blunt body of APOLLO type was chosen for the descent module, in order to have a good volumic efficiency. Although the static stability of such a vehicle is good, the dynamic stability in low subsonic is known to be poor (Ref. 1), large dynamic instability was evidenced by helicopter drops for similar blunt shapes. Some geometrical parameters were optimised in order to reduce this instability, and were tested in vertical wind tunnel. However **the requirement m5.3** imposes the use of a specific descent control subsystem, i.e. a dedicated stabiliser parachute (the size and the sequence of parachute are driven by descent time requirement m4).

5.2 Experiments related requirements

Let us now consider the experiment related requirements:

e1) the HASI accelerometer requires to be close to the center of gravity of the entry configuration

e2) the SSP accelerometer requires to be close to the impact point

The requirements e1 & e2 have impacts on accommodation of the experiments on the experiment platform, and have indirect impacts on aerodynamic related system studies. Indeed, the parachute deployment algorithm is based on deceleration level detection. Therefore, a dedicated accelerometer is used. As requirement e1& e2 imposes the experiment accelerometer to be located close the center of gravity, the T0 (time corresponding to deployment triggering) detection one has to take place at a certain offset with respect to the center-of-gravity location. An incidence oscillation will therefore result in a deceleration measurement oscillation, which will disturb the T0 detection algorithm. A careful analysis of the oscillation of the entry module in the transonic Mach number regime, i.e. prior to parachute deployment, had then to be performed, both in terms of amplitude and frequency. This analysis was undergone by the use of dedicated wind tunnel tests (dynamic derivatives measurements) and 6 degree-of-freedom simulations.

e3) the DISR requires a wide and extensive field of view ranging from the zenith to vertically downwards, covering most of the hemisphere

The requirement e3 is the most constraining experiment related requirement from the aerodynamic studies point of view. Indeed, the DISR has to cover the 360° field of view during descent, which imposes to have a descent module continuous rotation during descent. Furthermore, its rotation rate must be bounded within two limits. The higher one, because the DISR camera cannot rebuild the stored picture if the rotational motion of the descent module is too fast. The lower one, because of the need to cover the hemisphere a sufficient number of period of time.
Therefore, the descent module rotation is required to be controlled and in a required range of uncertainty (see § 10). While an active rotation rate control was not achievable in order to reach reliability, and to avoid excessive complexity, a specific aerodynamically controlled device was then designed, which consists in

36 spin vanes, which have a constant orientation with respect to the descent module centerline, but which provides, because of their conception, a self regulated rotation rate. The upper and lower limit requirement of rotation rate is achieved by the tuning of the spin vane angle and number. Such a design was performed by the use of specific wind tunnel tests and associated computer simulation of the rotation rate of the descent module in TITAN atmosphere (see §10).

e4) the ACP and GCMS require to be mounted close together, and both protruding through the boundary layer to collect atmospheric samples

The requirement e4 imposes the ACP and GCMS experiments to be located at an efficient location to collect atmospheric samples. The descent module stagnation point meets this requirement. Furthermore, boundary layer thickness calculations were performed, in order to size the length of the experiment tubes , as well as specific wind tunnel tests, in order to assess the sensitivity of the tubes to collect samples with respect to slight variations of descent module attitude.

e5) the DISR and HASI require proper flow around optical windows and sensors to avoid imperfect measurements

e6) contamination from decelerator ablative materials had to be minimied around ACP and GCMS inlets on one side and DISR optical window on the other side

The requirements e5 & e6 are related to the characterisation of the descent module surrounding flowfield. When the entry module enters the TITAN atmosphere, the upstream chemical mixture (N_2, CH_4 and Argon) is dissociated and ionised, and species recombine to form a collection of new species which can either deposit on the vehicle surface and eventually recombine, or can be captured in the wake of the entry module. Furthermore, the heat shield thermal protection system can be degraded when it is submitted to the high entry heat fluxes. These heat shield particles can be ejected from the surface and possibly captured also in the wake.

Now, even if the descent module is protected against the outer hypersonic flowfield, when the back cover is jettisoned, some of these contaminant species which have been trapped in the near wake of the entry module could deposit on the protruding DISR window, and stick to it. This would result in a signal loss for DISR, which can become unacceptable if too many particles stick to it.

The resulting requirement for DISR, is to have a limited number of particles on its surface.

The verification of this requirement has been performed first by aerodynamic/aerothermodynamic computations and studies of the surrounding flowfield of the probe, and has been finally met by designing a protective cover for the DISR optical window.

As a result, further aerodynamic studies were needed, in order to verify the correct ejection of this protective cover prior to DISR optical measurements.

The first part of this document has shown an overview of the mission requirements and scientific requirements. The second part shows the links between these requirements and aerodynamics and aerothermo-dynamics. The third part will show how these links are implemented in a coherent and comprehensive aerodynamic and aerothermodynamic studies and test plan, in order to fulfil these requirements.

6. HUYGENS AEROTHERMODYNAMIC DESIGN

6.1. Concept of the HUYGENS probe (m3&m4 related)

As explained in §5.1, it was chosen to ensure that the probe would withstand the hypersonic heat fluxes and accomplish its scientific mission independently. Indeed, the probe is constituted by a kernel carrying the scientific experiments operating during descent (the descent module), surrounded by a shell which protects it during the coast and entry phases.

Furthermore, during entry, the front shield reduces the probe speed while the other parts of the shell protect the kernel from aerothermal heating.

The kernel is constituted by two platforms supporting the experiments , while the jettisonable shell is constituted by a spheroconical front shield which extends as a 2.7 m diameter decelerator, and a back cover to complete thermal protection of the kernel during atmospheric entry.

The probe assembly is shown on figure n°4.

The shell is automatically jettisoned around M=1.5 at an altitude of about 170km, in order to enable the scientific mission of the descent module to be performed

This jettison is aerodynamically operated by inflating a main parachute large enough to put the kernel rearwards from the front shield. This main parachute itself is extracted, along with the back cover, by a smaller pilot chute whose deployment is triggered by an acceleration threshold, based on deceleration measurement.

6.2. Shape selection

6.2.1 Entry module

The HUYGENS entry module is required to decelerate in the TITAN atmosphere from its entry velocity at coast/entry phase interface, i.e. V=6190 m/s at Z=1250 km, down to the velocity compatible with descent module extraction from the entry shell, at the experiment switch-on required altitude, i.e. V=400 m/s at Z=170 km. Moreover, the probe must withstand the deceleration loads during entry.

Therefore, the drag coefficient of the entry module must be large, in order to provide an efficient braking in the upper layer of TITAN atmosphere.

The maximum deceleration load is driven by the initial velocity Ve, and the entry flight path angle γe at initial entry conditions (Z=1250 km), while the ballistic parameter has little influence on the maximum deceleration load.

Indeed, the maximum deceleration load may be expressed as follows :

$$\gamma max = Ve^2.sin\gamma e/C$$

where C is a constant.

On the other hand, the entry module must be fully autonomous, without any attitude control system. Therefore, an axisymmetric large angle blunt body was selected. Indeed, this kind of shape provides with large drag force coefficient, which is mainly due to pressure forces acting on the front face of the body, while it is statically very stable. This static stability ensures an efficient trim towards zero degree angle-of-attack, and then a reliable drag deceleration level.

A 60° half angle sphere cone was selected (see figure n°5) with the following geometrical parameters :
Nose radius Rn=1.25m, Diameter d=2.7m
Cone half angle θ=60° tip radius r=0.05m

The nose is blunted in order to decrease the stagnation point convective heat flux (roughly inversely proportional to square root of nose radius). The drawback of increasing the nose radius is that the shock stand off distance will increase as nose radius increases. The radiative heat flux which is roughly proportional to the shock stand off distance will then increase with nose radius. In hypersonic regime, the shock stand off distance of the HUYGENS probe is about 10cm.

The tip radius of the probe is expected to decrease the local overshoot of the convective heat flux which will appear at the external diameter of the entry module. Indeed, as the flowfield expands at the probe frustum, the boundary layer thickness decreases because of the flowfield acceleration. The gradient of velocity in the boundary layer will be steeper and the convective heat flux will therefore increase.

This phenomenum may be reduced by a local tip radius, which smoothes the velocity increase due to the flowfield expansion.

The drawback of this tip radius is a slight decrease of the static stability of the probe.

6.2.2 Descent module

The HUYGENS descent module (DM) is required to accomodate all the scientific experiments and provide reliable and stable attitude under parachute.

A truncated APOLLO-like shape was selected (see figure n°6).

6.3 Aerodynamic database

6.3.1 Preliminary Aerodynamic database

Early in the project, a complete aerodynamic database is needed in the whole range of entry conditions.

A large amount of data on large drag models are available in literature (see [R2] to [R7]). Furthermore a significant amount of CFD computations were performed in order to increase confidence in aerodynamic data, as no exactly similar shapes to HUYGENS one may be found in literature.

The advantage of such large drag, large half angle sphere cone shapes, is that not a too deep modelisation level of the computations is needed to assess reliable global aerodynamic coefficients in hypersonic.

Indeed, the geometry of the probe is simple, axisymmetric. Furthermore the aerodynamic forces are mainly pressure ones on the front heat shield, while the base pressures are accurately estimated by a simple pressure coefficient $Cp=-2/\gamma M^2$.

A first level of computation as a Newtonian representation of the pressure distribution over the front spherical heat shield leads to acceptable accuracy (see Ref. 5). The discrepancy is mainly due to the over estimation of pressure distribution near the maximum diameter of the probe, as this profile is influenced by the expansion at the frustum.

A further level of computation is achieved by an EULER modelisation. The EULER results lead to a very good accuracy, due to the very low magnitude of the viscous compound of the aerodynamic coefficients for this type of shapes.

From a system point of view, the capability to have reliable coefficient in a short period of time for a reasonable CPU time is very interesting, as aerodynamic database can be provided for mission analysis early in the project.

However, more accurate aerodynamic data are needed, as the design of the probe advances further in definition.
More sophisticated CFD level of modelisation and theoretical models must be used, while wind tunnel tests, for aerodynamic and aerothermodynamic data, must be performed.
Indeed, supersonic, transonic and subsonic data are more difficult to obtain from CFD analysis, while wind tunnel provides with extensive data in this Mach number range. However, the very blunted models of the HUYGENS probe present some specific features which had not been investigated previously in Europe, and which therefore made the exercise more difficult to handle within the technical, schedule and financial constraints of the program.
The next first paragraph will show the test and CFD plans for the HUYGENS probe, and the second one will describe some of the difficulties which were encountered from numerical and experimental point of view.

6.3.2 CFD & wind tunnel test plans

The complete aerodynamic database has to be generated for the selected Entry Module (EM), in the whole range of entry conditions.
To this end, both numerical and experimental aerodynamics are issued. However, as significant improvements of CFD predictive capabilities in terms of aerodynamic coefficients have been performed, and because of the challenge represented by a limited in time development phase of such a space vehicle, the ratio of CFD over wind tunnel (WT) experiments has significantly increased with respect to previous programmes like VIKING for example.

Of course, numerous lessons learned from VIKING programmes and related available literature participate to this trend.
The complementary aspects of both experimental/ theoretical studies have been issued on HUYGENS in the following topics :
- Static stability of the EM in the sub-trans-super-hypersonic range were performed in FFA (Stockholm) S4 and HYP-500 facilities
- Static stability of the DM in subsonic range in the LT1 FFA facility
In the meantime, CFD computations were performed in order to compare with WT and enable accuracy and related system margins to be derived.

Dedicated Euler, Navier Stokes in perfect gas, equilibrium and non equilibrium computations have been performed.

Apart from these classical Aerodynamic studies tests, some specific experimental and theoretical investigations were conducted during the HUYGENS development phase : the spin device, the dynamic tests and the radiation tests.
Indeed, dynamic stability tests were conducted for the EM in the sub-trans-supersonic range in FFA S4 facility and in ARA(Bedford) SWT and TWT facilities, and dynamic subsonic characteristics of the DM were measured in DRA(Bedford) 13x9 ft facility.
While determination of the aerodynamic coefficients in spinning motion for the DM during the descent were performed in the NLR Nord East Polder, LST facility, The Netherlands.

Qualitative tests of dynamic behaviour of the DM with/without parachute during descent, spin rate and parachute inflation characteristics were performed in the vertical wind tunnel of the Institut de Mécanique des Fluides (I.M.F.L.) in Lille, France.

Measurement of radiative emission properties of $(N2,CH4,Ar)$ plasma have been conducted in the shock tube facility TCM2 of the Université de Marseille.

On the other hand, high level of modelisation of accurate specific features like contamination problems of experiments were conducted theoretically.

The HUYGENS wind tunnel test plan is shown on table n°1 :

6.3.3 HUYGENS related CFD difficulties

As previously mentioned, the global aerodynamic coefficients of such large drag, large angle blunted cones are easily calculated with a fairly good accuracy in hypersonic regime, with simple theoretical models. However, as far as heat fluxes are concerned, or when local flowfield features are addressed, things become more severe, and need far deeper theoretical analysis.

Heat fluxes & level of modelisation
When the probe enters the atmosphere of TITAN, the hypersonic velocity of the entry module results in a strong bow shock in front of the sphero-conical heat shield. The upstream gas mixture is dissociated and ionised. Due to the low upstream pressure associated to the high velocity of the probe, the chemical reactions cannot equilibrate, as the collisions between particles are not numerous enough.

Furthermore, the kinetic energy of the probe is partly transferred to the plasma within the bow shock layer, and is therefore stored as internal energy of the plasma particles. This internal energy is shared among *translational energy* (thermic energy) of the particles, *rotational energy* of polyatomic species (potential energy of a group of rotating "spheres"), *vibrational energy* of polyatomic species (potential energy of an harmonic oscillator represented by the two, or more, atoms which composes the molecule, and which may be imagined as two spheres linked by a spring), and *electronic energy* (potential energy of the electron orbiting around the molecules or atoms).

The simplest hypothesis consists in assuming an equilibrium partition of the energy among these internal modes of storage (a Boltzmann partition). In this case, the energy of the flowfield in the bow shock layer may be represented as a unique temperature T, for a given location in the bow shock. This temperature will be a function of time and position in the shock layer.

However, as for the chemical state, in the case of HUYGENS entry, the pressure and velocity result in full non equilibrium internal state.

This means that after crossing the bow shock layer, each internal mode of energy storage will evolve according to a finite rate of exchange between translation and vibration, translation and rotation, translation and electronic, electronic and rotation, ...etc....

Hence, the energy state at a given position in the shock layer, will depend on time, and depend also on the non equilibrium partition of the energy which exists at a location immediately forward of this location (for a mono dimensional case). The state of the flowfield will then be described by a multiple temperature model : a translational temperature Tt, a rotational one Tr, a vibrational Tv and an electronic temperature Te-.

These temperatures, and chemical species will evolve towards an equilibrium state, at a certain rhythm which can be expressed by Landau Teller expression for example (see [R10] for example).

This phenomenum is called the relaxation of the chemical and of the internal energy across the shock layer.

An accurate non equilibrium representation of the flowfield in the bow shock layer is of primary importance for heat fluxes assessment. Indeed, as said before, strong radiators like CN molecules appear in these chemical non equilibrium state, although they would not be present, for the same conditions of temperature and pressure under chemical equilibrium assumption. Furthermore, the thermal non equilibrium (internal state non equilibrium) results in a large overshoot of the radiative spontaneous emission of CN (up to 3,5 times the equilibrium emission for the same translational temperature, see Ref. 9). Finally, the radiative heat flux may be as large than the convective heat flux (500kW/m2 convective 500kW/m2 for radiative).

In the case of a Earth re-entry, the radiative part of the total heat flux is less than 10% for velocity lower than 10 km/s.

Chemical non equilibrium features

Therefore, the radiative heat flux computations require a high level of theoretical modelisation, i.e. calculation of the non equilibrium chemistry, by computation of the finite chemical rate of a set of typically 20 reactions (forward and backward reaction rates). This calculation process uses first data on the reaction which can occur within the N_2, CH_4 and Argon plasma (see Ref. 9, 10 and 11), and indications on the reaction rates of these reactions, either the forward reaction rate kfi (endothermic reaction i, e.g. dissociation) or the backward reaction rate kbi (exothermic reaction i, recombination typically).

Typically, one of the two reaction rates, e.g. the forward, is given by an ARRHENIUS law such as :

$$kf = aT^b e^{-c/T}$$

Where T can be either the translational, vibrational or electronic temperature, or a combination of these temperatures (see Ref. 18,19).

A first remark should be stressed here : the available literature data have obviously a range of temperature and pressure over which they have been actually determined. The rigorous and reliable application of these data should therefore be strictly limited to the aforementioned temperature and pressure range. However, the flight conditions are often different from these experimental ones, and the engineer has often to "extend" the applicability of these data, by extrapolation. This, of course, can degrade the accuracy and reliability of the TPS design , at the end. The need of a continuous link between the design engineer and scientific research is obvious.

The backward reaction rate is computed from the simple relationship :

$$Ki = kfi^{eq\ vib}/kbi^{eq\ vib}$$

where Ki is the equilibrium constant, i.e. the constant which enables ,at equilibrium conditions , to calculate, together with conservation equations, the molar fractions of species.

This equilibrium constant Ki can be calculated from power series curve fit, within a certain range of temperature and pressure. However, in the HUYGENS case, where complete thermal non equilibrium occurs, the equilibrium constant is derived from the partition functions Q of the different chemical species implied in the reaction.

These partition function describe the fraction of molecules in any excited state of the different modes of internal energy storage :

$$N_j^i = \frac{N_j}{Q} C_i \exp(\frac{-\varepsilon_i}{kT})$$

Where Nj is the total amount of particle j

N_j^i is the number density of particles j in a given quantic energy ε_i level for translation, vibration, electronic or rotation, C_i is the number of possible representations of ε_i, k is the Boltzmann constant.

T is the corresponding temperature (for translation, vibration, electronic or rotation respectively), and the partition function Q is

$$Q = \sum_j \exp(\frac{-\varepsilon_i}{kT})$$

The expression of these partition functions is derived from statistical mechanics (see Ref. 8).

The chemical non equilibrium results indeed in a deep level of complexity, because of theoretical models and related computational representation, but also, because of the necessary analysis of the features of the plasma.

Indeed, the design engineer, has first to select a representative set of chemical reactions which can occur within the plasma, in order to "capture" all the species which may appear from the upstream mixture. Then, specific CFD problems can appear, which require performance of additional analysis.

In the very case of HUYGENS probe, the CH_4 dissociates just behind the shock, to form CH_3, CH_2, CH and C, H. This dissociation is so fast, in CFD wording : the equations are so steep, that a stagnation line computation of the HUYGENS entry module lasts for 2 to 4 hours of CPU time on a Cray YMP computer. This, of course, is constraining for aerothermodynamic analysis, because it can delay the heat fluxes delivery e.g., and furthermore, it increases the induced cost of the aerothermodynamic studies.

However, engineer analysis show that the reaction rate which involve CH_n compounds can be divided by 10^3, i.e. the reaction rate are much slower, whereas the molar fraction of the CH_n compounds are changed from 10^{-20} to 10^{-18}, i.e. the CH_n were almost zero and remain zero, which typically means that in any case the overall result is unchanged, from probe design point of view, whereas the CFD time for computations falls down to 2 ... minutes on the same Cray YMP!

Thermal non equilibrium features

The aforementioned thermal relaxation needs to be modelized as conservation equations for translational, rotational, vibrational and electronic energy.

Each of these equations may be expressed under the form:

$$dE_\xi/dt = (\text{exchange terms}) + (\text{source terms})$$

where ξ stands for t, r, v or e , i.e. translation, rotation, vibration and electronic respectively.

In this field, the difficulty is the selection of the exchange terms and the source terms.

The exchange terms are expressed typically under Landau Teller forms, let us take the translation vibration energy exchange term :

$$QT\text{-}v,j = \rho j \cdot \frac{evj(T) - evj}{\tau_j}$$

evj(T) is the vibrational energy of the species j calculated at equilibrium at the translational temperature T.
evj is the local vibrational energy.

The first term indicates that the rate of change of the vibrational energy is proportional to the vibrational nonequilibrium (dEv/dt proportional to (evj(T)-evj). The proportionality factor is equivalent to a time τj, which represents the characteristic time of this relaxation process.

Several different expression for this characteristic time can be found in literature. An expression developed by MILLIKAN and WHITE yields the vibrational relaxation time, τj (see Ref. 12). Two others laws have been checked : WOOD and SPRINGFIELD (see Ref. 13) and PARK's modification (see Ref. 14,15).

These different modelisations lead to different profiles of temperatures (see figure n°7).

Moreover, additional exchange terms must be taken into account, e.g. between electronic and vibrational energies, which is similar to the translational-vibrational exchange term, i.e., the rate of change of vibrational energy is proportional to the difference between the vibrational energy at equilibrium at electronic temperature Te- and the actual vibrational energy, and the exchange term which represents the tranfer of vibrational energy within the different vibration modes of the different polyatomic species.

Therefore, this does illustrate once more the need for high level of modelisation. Indeed, the relaxation rate of vibrational energy is driving the vibrational temperature profile in the bow shock layer.

Now, it turns out that the peak of radiative emission occurs when the translational, vibrational and electronic temperature collapse. The abscissa of this temperature collapse will then change the emissivity profile in the shock layer, and therefore it does change the radiative heat flux to the wall.

Sensitivity studies are needed to assess either the margins associated to the radiative heat flux computations, or the model which leads to the best comparison with experiments (see §8).

Within the source terms, we can note the following :

$$(\text{source term}) = - \rho j \cdot \frac{\text{Ev}(T;Tvj) - \text{evj}}{Cj} \left[\frac{d\ Cj}{dt} \right]_f +$$
$$\rho j \cdot \frac{\text{Gv}(T) - \text{evj}}{Cj} \left[\frac{d\ Cj}{dt} \right]_b$$

where Cj is the mass fraction of the species j.
The first and second terms represent the source terms, which are respectively the loss of vibrational energy due to the dissociation whereas the second term represents the gain of vibrational energy due to the recombination. Ev and Gv are developed in Ref. 16,17.

Some CFD amazing features
Apart of the difficulties of numerical computations related to the high level of theoretical modelisation which is required for heat fluxes calculation for example, some difficulties may arise from the feature of the numerical solution itself.

Let us take the example of the computation of the large wake of the HUYGENS entry module in supersonics.

This wake is characterised by the shoulder expansion around the tip corner, the free shear layer between this expansion area and the large recirculation zone, emanating from the probe frustum, and extending rearward down to 1.5 diameter from the base (see figure n°8).
A recompression shock occurs at the rearward stagnation point (closure of the recirculation zone), which is characterised by high temperature level, which is also called the neck region (see fig. n°9).

Some laminar, perfect gas Navier Stokes computations of this recirculation zone were needed at Mach=15 and M=21, in order to assess the convective heat flux profile on the back cover of the entry module. These Mach numbers correspond to the following conditions on the Entry Module trajectory : the altitude Z, upstream pressure P, upstream temperature T are respectively (Z=226 km; P=27,3 Pa; T=145 K) and (Z=260km; P=11,4 Pa; T=145 K). The specific heat ratio g=Cp/Cv

was fixed to 1.2, in order to take into account the decrease of the temperature due to real gas effect (The grid for this calculation is shown of figure n°10).

Figure n°11 shows the pressure field in the recirculation zone, which shows that a recirculation shock takes place immediately downward of the top of the back cover. Indeed, the flow in the recirculation region becomes supersonic when it impiges the top of the bach cover. Therefore, a normal shock must take place on the top of the back cover, to reach zero velocity at the stagnation location. This unexpected numerical feature results in a convective heat flux increase at the top of the back cover. Indeed , the recirculation shock results in temperature increase in front of the top of the back cover.

This kind of feature has already been observed in numerical simulation performed by Gnoffo (see Ref. 20,21), however it has not been observed in experiments on similar kind of vehicles (see Ref. 22,23), and this effect disappears when a non zero angle-of-attack is computed (see Ref. 21,24).

This recirculation presence is questionnable, and could be explained by several hypothesis:

it can be due to a grid axis effect for the particular zero degree angle-of-attack computation case,

this shock can represent a particular solution at the very zero degree angle-of-attack case, and could vanish for a slightly different incidence. It is indeed possible that when the flow is forced to be axisymmetric, the afterbody streamlines configuration present a saddle point at the neck, where the velocity cancels, resulting in a strong recompression wake core, which drives the base flow to be supersonic. When incidence increases, this convergent streamline structure is broken, resulting in a better homogeneisation of the base flow,

the Navier Stokes computations were performed in laminar condition. A realistic case would be turbulent (a very low Reynolds number, about 2000, based on body radius, triggers the transition in the shear layer, see Ref. 25). It is clear that a turbulent viscosity model in the Navier Stokes calculations will result in a greater dissipation in the recirculating flow, and a corresponding atenuation of the recirculation shok wave,

the Navier Stokes solution corresponds to the steady state solution of the time dependent equations. Whereas experimental test seem to show the base flow to be unsteady, which tends to homogeneize the wake flow.

Several reasons therefore exist, which lead to think that the recirculation shock is not realistic. However the thermal protection system of the probe must be reliable.
The amazing behaviour of this numerical solution puts here a strong question directed towards the design engineers of the vehicle.

It was therefore chosen to use a semi-empirical formula to calculate the base heat flux of the HUYGENS entry module along the trajectory (Navier Stokes calculations cannot be performed all along the trajectory). This formula was shown to agree with the Navier Stokes data on the major part of the base of the entry module.
The heat flux data on the top of the back cover were multiplied by a safety factor 2, in order to take into account the Navier Stokes data.

CFD towards complexity
Besides the questions that can arise from the numerical solutions, CFD provides with the capability to answer quickly to very complicated problems that designers have to face during the development of the vehicle, and which are related to the increase of the complexity of the system, resulting from the completion of its definition along the time schedule of the program.
One example taken here is the influence of the presence of several protrusions on the descent module, on the performance of the spin vanes.
Figures n°12 and 13 show the Navier Stokes computations of the streamline around the descent module, for different arrangements of the maximum diameter geometry of the descent module.
Informations on the position and inclination of the vanes can be derived from these calculations, although experimental assessment of this topics would lead to complex wind tunnel tests arrangements, much increased time schedule with respect to the CFD computation time, which could be unaffordable within the time and financial constraints of the development program.

Another example will be derived in the contamination topics depicted hereafter.

6.3.4 HUYGENS related experimental difficulties

The difficulties which were met in the frame of the HUYGENS program can be split in two sorts of problems :
- either the needed material and/or experience related to required experimental investigation was not mature in Europe, but had been experienced in US (e.g. VIKING program),
- or, the specific features of the HUYGENS mission led to the need of very innovative experimental investigations.

The static and dynamic derivatives investigation tests can be put in the first item, while the radiative spontaneous emission tests can be put in the second one. All of them were conducted in the frame of the HUYGENS project.

The first item will be discussed here, while the radiative tests will be described in paragraph 8.

No previous experience on very blunt shape like HUYGENS entry module was available in European wind tunnels. The main drawback concerns the existing hardware, and especially the balance. Indeed, the existing balance sensitivity was adapted to aircraft or slender cones aerodynamic loads (small axial force / large lateral force-pitching moment) which are the opposit of blunt large angle cone ones (large axial force / small lateral force-pitching moment). The accuracy on the aerodynamic coefficients was therefore not optimized. However, the required accuracy on the drag coefficient for example, is not so stringent for HUYGENS probe than for an aircraft (typically less than 1% required accuracy).

The drawback of the lack of experience was more critical on the dynamic experimental investigations. Indeed, a limited number of available wind tunnel facilities were found to have made dynamic measurements in EUROPE. The available experience was limited to aircraft dynamic measurements, or slender cone shapes.
As a limitation arising from this specificity to slender bodies, the dynamic rigs (composed of the balance, the flexures and the forcing mechanism in case of forced oscillation technique) were designed to fit into the aircraft models, and were consequently long, and could not be accomodated into the scaled HUYGENS entry module model. The available sting diameter was consequently large compared to the maximum allowable size of the probe model, and the actual test oscillation center was located behind the model, which is not representative of the actual flight conditions. Furthermore, this involves the use of transport formulae which increase the uncertainty in the damping coefficients calculation process.

In addition to the existing hardware limitations, the specific features of the HUYGENS entry module add some strong requirements on experimental devices.

The dynamic instability of the probe is by a matter of fact, present even in the case of static tests (the probe definitely ignores that it undergoes static tests...). The model excites the sting, especially in transonic regime, and results in stiffness requirement onto the sting, in order to avoid significant oscillations, and possibly damages, of the model set-up.

The wake of the large angle cones is also to take into account for wind tunnel tests. Indeed, because a large subsonic region is contained within the wake of the blunt model, informations of the downstream region of the wind tunnel can possibly affect the model base pressure distribution.

The model must therefore be suitably placed in the wind tunnel, in order to avoid this effect.

7. DRAWBACKS OF THE SELECTED SHAPES ON SYSTEM

7.1 Dynamic behaviour of the entry module and related T0 constraints

When entering the TITAN atmosphere, the entry module is submitted to aerodynamic torque, which results in the case of a statically stable vehicle, to a precessing elliptic motion of probe longitudinal axis around the velocity vector. The total incidence of the EM describes then an oscillatory motion, with first a converging amplitude towards a constant trim angle-of-attack.

The angle-of-attack at beginning of entry is less than 10° at Mach number M>20, which becomes less than 2° in supersonics.

This convergence is the result of the static stability of the 60° half angle entry module in hypersonics.

Early in the project, dynamic stability tests were performed in sub-trans and supersonic Mach number range, which showed that the entry module was dynamically unstable for Mach number 2 and lower, at moderate angle-of-attack ($\alpha \leq 15°$), with an increasing instability with decreasing Mach number.

These tests were performed with forced oscillation test technique for small amplitude oscillations (1.2° amplitude) with existing rig adapted to aircraft dynamic stability investigation (see §6.3.4). As a result, the sting was large, which resulted in interferences with the flowfield. Moreover, the center-of-oscillation of the test could not be located inside the model. Therefore, dedicated transport formulae had then to be used in order to derive the damping coefficients at the model scaled center-of-gravity location (see Ref. 26) and led to poor accuracy of the results.

However, VIKING tests had shown that interference effect were not significant for Mach number 2 (see Ref. 27), and Schlieren pictures of the EM tests at small incidence did not show evidence of near wake disturbance, in terms of neck diameter and/or neck distance to the EM frustum, when compared to CFD Navier Stokes computations (these two parameters were investigated in VIKING dynamic tests sensitivity studies with respect to sting interference).

Consequently, this unexpected dynamic instability was taken into account in dynamic database used for 6 degree-of-freedom computations of EM entry into TITAN atmosphere.

The dynamic stability of the EM for Mach numbers larger than 2, up to hypersonic regime, was fitted to VIKING one, which predict a stabilising trend in the range Mach number 2 to 3 (see Ref.27). A conservative slight dynamic instability was however kept in hypersonics for very small incidence ($\alpha \leq 2°$), based on free flight test results of flat base 60° half angle cones (see Ref. 28).

This unexpected supersonic dynamic instability had a large negative impact on the system.

Indeed, 6 degree-of-freedom simulations showed that hypersonic to supersonic dynamic instability resulted in a small limit cycle, associated with a transverse rate in high supersonic. These conditions revealed to be very unfavourable in low supersonic, because the transverse rate, associated to the dynamic instability peak in transonic resulted then in a fast rise of incidence, up to unacceptable value for safe parachute deployment (more than 30° at Mach number M=1.5).

Further experimental investigations were needed, in order to verify the supersonic stabilising trend, and the actual dynamic behaviour of the EM in high supersonics.

A different facility and test set up were used in ARA(Bedford), in order to avoid the identified sources of discrepancies, and add confidence in results which should be measured by two different ways.

The free oscillation test technique was used. This technique provides the experimenter with a simple and reliable way to assess the dynamic behaviour of a model. Indeed, no balance is used, the sting is then far simpler and smaller.

Moreover, the direct output of strain gage located on the flexure which is the center-of-oscillation of the tests, and is designed to be placed at the scaled center-of-gravity of the model, gives the incidence versus time history, and so far, immediate evidence of dynamic stability or instability.

Figure n°12 shows the incidence versus time of the EM at Mach number M=2.9.

The quickly damped amplitude of oscillations shows that the EM is dynamically stable at this Mach number, with a $Cmq+Cm\alpha = -0.19$.

The free oscillation tests have shown that the EM is actually dynamically unstable for Mach numbers $M \leq 2.4$,

with an increasing instability for decreasing Mach numbers, for very small range of angle-of-attack ($\alpha \leq 3°$). The stabilising trend from Mach number M=2 to M=3 was confirmed, and a very small dynamic instability is kept in the hypersonic database for very small angle-of-attack ($\alpha \leq 2°$).

The complete new issue of the dynamic database was then used to compute EM trajectories in the TITAN atmosphere, and led to a safe angle-of-attack lower than 5° at parachute deployment (M=1.5).

8. HEAT FLUXES CALCULATION IN AN UNKNOWN ENVIRONMENT

Maybe the most important feature of this mission is the fact that the mission objective is to determine the atmospheric chemical compounds, the temperature and pressure profiles, while these parameters have a strong impact on the design of the probe. Indeed, as it will be seen later, the radiative heat fluxes have been shown to exhibit a strong sensitivity with respect to the upstream chemical composition of the atmosphere. Hence, design drivers like heat fluxes, or deceleration loads must be determined with a conservative approach, while a too pessimistic prediction would lead to mass penalties, which of course must be avoided.

This paragraph will show how the heat fluxes need to be determined whatever the parameters which have an influence on heat fluxes level may be, and how a conservative, but not oversizing methodology has been derived.

The Titan entry module enters the Titan atmosphere with a velocity of 6190m/s, with a flight path angle of -64°.

This extremely high velocity results in dissociation and ionisation of the upstream gas mixture in the forebody shock layer. Moreover, the relaxation times of chemical and thermal processes involved are of the same magnitude than the characteristic time of the flowfield, the shock layer being so in full non equilibrium.

As the Titan atmosphere major constituents are N_2 (more than 77% in molar fraction), CH_4 (from 0 up to 3,5%) and Argon which may exist up to 20%, non equilibrium reactions result in CN creation which is known to be a strong radiator.

The probe heat shield has then to face both large convective and radiative heat flux. Very early in the thermal protection system design process, designers have to be provided with reliable maximum heat fluxes, in order to issue a robust TPS, while TPS thickness must not be too large (too conservative) in order to avoid mass penalties.

Up to now, the exact composition of Titan atmosphere is unknown and cannot therefore be treated by statistical approach. The total heat fluxes must then be calculated for the upstream gas mixture chemical composition which gives the maximum level.

Sensitivity of both convective and radiative heat fluxes with respect to upstream gas mixture chemical composition was then studied theoretically.

Convective Heat Flux

The convective heat flux is the summation of the part proportional to temperature gradient (Fourier law), and the part which corresponds to the diffusion of the enthalpy of the species to the wall :

$$Q_c = \frac{\partial T}{\partial y}\Big|_{y=0} - (\sum_i j_i h_i)_{y=0}$$

where $\frac{\partial T}{\partial y}\Big|_{y=0}$ = thermal gradient at the wall

λ = gas conductivity

j_i = mass diffusion flux of species i

h_i = specific enthalpy of the species i

The studied upstream gas mixtures were in the range 0-5-10-15-20% Argon, 0 to 5% CH_4 in molar fraction, and N_2 to complete.

Stagnation convective heat flux computations were performed by use of Euler plus boundary layer, thin layer Navier Stokes and Viscous shock layer codes, either in equilibrium or non equilibrium (see chemistry in Ref. 29), with catalytic wall conditions, for different upstream gas mixtures and for different points along the trajectory.

The observed trend of variation of stagnation convective heat flux versus upstream chemical composition is similar in all conditions : a methane increase decreases the convective heat flux level and an Argon increase results in a convective heat flux increase (see figure n°15).

Radiative Heat Flux

Radiative heat flux sensitivity with respect to upstream chemical composition was first determined theoretically.

Within the potential radiator species, the main contributor to the radiative heat flux is first of all the CN violet band system in the range 0.3 - 0.5μm and the CN red system (0.5μm and higher). The monoatomic Nitrogen N radiates, but is about completely self absorbed. Other species like HCN are in negligible amount.

The methodology used consisted in calculating first the chemical and thermal characteristics of the bow shock layer, then calculating the excitation and radiative properties on the stagnation line, in order to derive a stagnation radiative heat flux with a thin slab assumption, which led to conservative values of radiative heat fluxes.

The global chemical and thermal properties of the bow shock layer were determined using either Euler full non equilibrium computation for calculating the global species number densities, temperatures and pressure, or a Parabolized Navier Stokes with perfect gas assumption giving the stagnation line pressure evolution, and a streamline chemistry was performed on this stagnation line.

Then, excited state populations of radiator molecules calculation was performed using a quasi steady state assumption, and finally radiative emission calculation was performed.

A non linear evolution of radiative heat flux versus methane molar fraction was then observed. Indeed, the radiative heat flux level first increases from 0 to a small amount of CH_4 molar fraction (2-3%), it reaches a maximum, and then decreases for larger CH_4 molar fractions.

The CH_4 molar fraction corresponding to the maximum radiative heat flux depends on the upstream Mach number: it increases with increasing upstream Mach number.

This behaviour may be explained as follows: an upstream gas mixture without methane radiates to a negligible extent. When little CH_4 is introduced, CH_4 dissociates very quickly behind the shock wave and with dissociated N_2 creates CN, which in turn radiates.

The radiation heat flux then increases with increasing CH_4, as more CH_4 results in more CN radiator.

However, as CH_4 dissociation is an endothermic reaction, the enthalpy of the shock layer decreases when CH_4 fraction increases. As a result, the temperature of the shock layer decreases, and at a certain time, more CH_4 leads to less radiative heat flux.

When upstream Mach number increases, as the upstream enthalpy is higher, more CH_4 may be dissociated to create more CN before the available enthalpy decreases too much.

Figure n°16 show this behaviour for M=19,75.

More Argon was found to increase the radiative heat flux, and increases the CH_4 molar fraction which corresponds to the maximum radiative heat flux.

Total Heat Flux

Finally, heat fluxes are calculated for the worst upstream chemical composition, which leads to the maximum total heat flux level, i.e. a 3.5% CH_4, 20% Ar and 76.5% N_2.

Finally, computations of total heat flux are performed for nominal and extremes trajectories in terms of flight path angle (-66°/-64°/-60°), atmosphere (min/max density and temperature according to Lelouch Hunten model), for the worst upstream chemical composition.

This leads to approximately the same level of maximum convective than radiative heat flux versus altitude :

500 kWm2 convective / 500kW/m2 radiative (see figure n°17).

The features of both types of heat flux are however different, as the radiative heat flux curve versus time, or altitude, is very sharp, the level of it is of great importance for the TPS integrity (a heat flux higher than the maximum allowable could lead to significant mechanical and/or physical degradation). On the other hand the convective heat flux curve versus time or altitude is more smooth and is the main factor for TPS thickness sizing.

Experimental evidence of both the choice of the worst chemical upstream gas mixture, and of the level of predicted heat fluxes was then needed.

Convective heat fluxes have been predicted theoretically and measured in flight on re-entry vehicles for at least two decades in Aerospatiale. The knowledge of convective heat flux is accurate within +-10%.

No dedicated tests have been performed in the HUYGENS program for convective heat flux measurements.

Meanwhile, the radiative heat flux is very specific of TITAN entry, since the powerful radiative emission of the bow shock layer is strongly dependent on the non equilibrium chemistry of the N2/CH4/Ar gas mixture. Indeed, Park has shown that non equilibrium conditions lead to peak of radiative emission (see reference n°6). Our theoretical calculations show indeed this phenomenum, of a fast rise of the radiative emission of mainly the CN violet system, behind the shock, when the electronic, vibrational and rotational-translational temperature collapse.

Our first comparisons with experimental material was performed by using Chung Park shock tube experiments (see Ref. n°9).

Many comparisons were performed with different assumptions on theoretical models, which enable a best estimate model to be found out, to be used for our flight predictions of radiative heat fluxes.

This model was a Millikan & White relaxation model, with three temperatures model (Tt, Tv, Te-).

Figure n°18 shows the comparisons between calculated and measured emission versus distance behind the shock, for one of the CN violet transition, which shows a good agreement.

Associated with radiative heat flux level prediction, a margin analysis was performed, which led to a +-100% uncertainty.
This seems reasonable and not too conservative, with respect to the large number of influencing parameters which are not very well known (electron number density, electronic temperature, collision sections, ...etc...). Chul Park proposes the same in reference n°30.
Although, significant improvements have been performed in theoretical predictions of radiative emission (our models use a three temperature scheme), dedicated WT tests were needed.

The powerful TCM2 Université de Provence shock tube facility was selected.
The test program consisted in performing shock tube tests of measurements of selected wavelengths radiative emission, for different upstream gas mixture within 0/5/10/20%Ar ; 3.5% CH4 and N2 to complete.
The upstream pressure was requested to be in the range 1-2mBar, which is low for shock tube tests (problem arise from boundary layer growth on the shock tube, and not enough emission), but still 10 times larger than the TITAN conditions in flight at the same Mach number. The main difference resulting is the 10 time smaller non equilibrium zone of the shock tube plasma behind the shock wave, with a peak non equilibrium which occurs at 1.5mm downstream of the shock in the shock tube, and approximately 2-3 cm in flight. As this non equilibrium zone is our main interest in flight because it sizes the radiative heat flux in the stagnation region, one of the requirement of the tests is to have a high time resolved accuracy in these 1.5mm behind the shock, i.e. having roughly 100 measurements sample in the zone immediately behind a shock wave travelling at 5600m/s.
Moreover, the slit area of the optical apparatus was requested to be as thin as possible, in order to be able to derive the vibrational temperature from the ratio of selected wavelengths within the $\Delta V=0$ and $\Delta V=1$ of the CN violet system. The slit area is then about 0.8Å.

The tests results show a sensitivity of measured emissivities versus Argon which is less than expected from theoretical calculations, and is difficult to determine. Indeed, a slight variation of shock velocity and/or a slight leakage of air in the shock tube can vary the emissivity profiles in a magnitude comparable to Argon effect (air brings O_2, which dissociates and creates CO instead of CN with dissociated CH_4).

Hence significant experimental efforts have been made in order to discriminate these effects, which means that the tests are requested to be very accurate, and are therefore very difficult to master.
Finally, experimental results show that the emissivity profiles in the CN violet system behind normal shock, are maximum for the 20% Argon case within the tested mixtures, which confirms the choice of the worst case for heat flux calculation process.

9. PARACHUTE PHASE DESCRIPTION

The main specifications of the descent subsystem are:
- to control the descent (sink and spin rates),
- to stabilize the probe attitude in order to insure a good radio up-link to the CASSINI orbiter during the descent and to guaranty good conditions for the descent imager.

The conditions at the end of the reentry phase are very severe: supersonic regime at low dynamic pressure (between 210 and 440 Pa at M = 1.5) and incidence of the probe, less than 15°, although the module possesses weak dynamic stability in a low divergent dynamics.

The descent sequence, initiated by g-sensing, allows the deployment and inflation of the pilot parachute, which extracts the back cover and the bag of the 8 m diameter main parachute. After its inflation, the main parachute stabilizes the probe through the transonic flight regime and allows the front shield to separate. Fifteen min. later, the main parachute is separated and in turn deploys the 2.8 m stabilizer for the remaining 2 hours descent phase (see figure n°21).
This scenario has been derived from the GALILEO probe one.

The three parachutes are Disk-Gap-Band parachutes. This type has been chosen because it inflates at very low dynamic pressure in supersonic regime. It has been already chosen for the Viking mission.

The pilot chute is sized in order to separate the back cover from the entry module.

The main parachute is sized to allow a front shield separation from the descent module. The second goal from the main parachute is to stabilise the probe during the transonic phase, the angle of attack oscillation having to be damped in the (0-15°) range for a clean separation.

The stabiliser is sized to provide to the descent module the remaining 2 hours of the descent phase.

On the roll axis, a swivel discouples parachute from descent phase motions.

Moreover, the descent time duration requirement, the descent system has to stabilise the descent module in order to maintain the attitude of the probe with respect to the local vertical under 10°.

The whole system and especially the link between the parachute and the load has been optimised (see ref. 31 and 32).

Simulation of the probe attitude during the descent has been carried out to assess the fulfilment of the requirement. For these simulations, a special wind gust model, associated to the LELOUCH-HUNTEN atmosphere model (p, t), has been set up (see ref. 33).

All the separation phases have been carefully studied by multibody trajectory simulations. Most of the effort has been put on the front shield separation for which a special model with 4 bodies and 21 DOF has been developed to assess its clean separation.

During the development phase, these 3 parachutes have been characterized during wind tunnel tests at sub-, trans- and supersonic regimes in European and American facilities (IMFL, ARA Bedford, AEDC) by measuring static aerodynamic coefficients (drag and normal forces, and pitching moment), and unsteady coefficients for the inflation phase.

The qualification of the descent system will be achieved by:
- flight drop tests of each parachute,
- an air balloon drop test for the whole descent sequence,
- simulations of the probe attitude, during the descent in the Titan atmosphere.

10. SPIN DEVICE

During the descent phase, the scientific experiments are switched on, while DM descends gently under the parachutes.
At this time, probe spin is required basically by the imaging instrument, the Descent Imager/ Spectral Radiometer (DISR). Indeed, as it is expressed by the requirement n°e3, the DISR requires a wide and extensive field of view ranging from the zenith to vertically downwards, covering most of the hemisphere.

The associated quantitative requirement is to get a spin in the range 1 to 15 rpm during most of the descent, and to get back to 1 to 3 rpm under 10 km altitude.
In order to meet this requirement, a spin eject device (SED) first provides the EM with spin at orbiter

separation (nominally 7rpm). This initial spin provides gyroscopic stiffness in the outer space during the so called coast phase (see mission description : probe released by orbiter but still not in TITAN atmosphere, which lasts for 22 days).
This contributes to have a reliable small angle-of-attack at beginning of entry, and improves slightly the EM stability during entry.
However, disturbances like viscous roll damping and center-of-gravity offset coupling with inertial and aerodynamic dissymetries may alter significantly the initial spin in the range respectively of +0/-1rpm and +1/-1rpm at beginning of descent.
Moreover, erratic spin behaviour may not be excluded.

Hence, a specific aerodynamic spin device was designed in order to meet the DISR spin requirements during descent.

This spin device consists in 36 spin vanes located approximately at outer diameter of the descent module. These spin vanes are oriented to have an incidence with respect to upstream flowfield of 87.8°.
This large incidence results in a positive motor torque for zero roll rate up to increasing roll rate until the local incidence of the vane decreases to zero.

When spin rate increases, the local incidence becomes negative and results in a negative torque which will force the spin to an equilibrium state (for constant upstream conditions).
Figure n°6 shows the spin vanes design and location.
Dedicated WT tests were performed in NLR Nord East Polder facility in order to measure the spin vanes torque for various configurations (12/24/36 spin vanes for 2 locations on the DM).
Additionally, separation zone around the DM was determined using pitot rake, and was compared to Navier Stokes computations

Viscous damping was also derived from free spinning tests.

As a result, the descent computations enable a suitable design of the spin vanes setting to be determined, in order to meet the experiment roll rate requirement (see figure n°19).

11. CONTAMINATION STUDIES

Within the requirements related to experiments, the e5 &e6 ones stress the need to have clean optical windows for DISR. Indeed, this latter one is very sensitive to loss of signal due to the deposition of contaminants on the DISR window.

Two types of contaminants can deposit on the window:

- either particles coming from the thermal protection of the probe, after burning of the surface due to the high heat fluxes of the hypersonic entry
- or the particles which can be formed due the chemical reactions which occur behind the bow shock within the upstream chemical mixture.

Indeed, although the DISR is protected from the external flowfield during hypersonic entry, the back cover has to be removed at beginning of the descent phase. This jettison occurs at Mach number 1.5 when the heat fluxes have decreased to almost zero (the heat fluxes become negative during descent, i.e. the descent modules releases heat to the outside), the process of degradation of the heat shield should then have stopped, while the production of contaminant particles issued from the external flowfield should also have stopped, as the energy released by the entry module to the surrounding flowfield is too small to enable chemical reaction to occur.

However, the DISR, mounted on the rear conical part of the descent module, is located inside the rear recirculation zone of the entry module.

During hypersonic entry, some particles coming either from the degraded heat shield, or from the chemically active bow shock, can be trapped in the recirculating base region. Furthermore, the degraded particles released by the rear part of the heat shield are directly inserted in this "dead water" region.

The question is therefore, can some of these particles remain trapped in the recirculating region until back cover release, and within these trapped particles, how many of them will impact and will be stick on the DISR window?

The answer is not so obvious.

The first type of particles may arise either from the front face heat shield, or from the back cover of the probe. Within the front face particles, one should know how many will be captured in the boundary layer of the conical part, and will be injected in the recirculation zone through the frustum shear layer. This information can be obtained if the size and mass of the particles is known (in terms of statistics). While a Navier Stokes calculation with two phases capability may provide the trajectory of the particles, for a given surrounding flowfield. Furthermore, once they are trapped, and the velocity of the probe decreases, how will these particles behave? Does a balance process exist between the particles coming in and particles going out of the recirculating region through the shear layer.

Within the second type of particles, some can be trapped which came from the bow shock layer, or some can be

directly created in the recirculating zone. The characteristics of these particles can be obtained if dedicated Navier Stokes calculations are able to simulate the non equilibrium chemistry which occurs all around the entry module : dissociation , ionisation in the bow shock layer, freezing at the edge frustum, recombination in the recirculating region. Furthermore, as we are interested in particles behaviour, the calculation should be able to handle a two phases flow and two phases chemistry.

Then, the same question appears as for heat shield particle during deceleration of the probe : how does the balance process through the shear layer look like?

Of course, the scientist who is responsible for the DISR, has to be provided with reliable informations concerning the amount of pollutants which can alter the DISR capabilities.

The first idea is then to make a simple and conservative assumption, which assumes that all of the out coming particles which are created during the hot hypersonic phase (roughly 40s) from the heat shield stick on the DISR window. This **very** pessimistic assumption is not at all realistic, but would enable not to worry about contamination from the heat shield if the answer would have been "even in this pessimistic case DISR is OK".

Unfortunately, this is not the case, as the quantitative requirement for contamination is violated by a factor of 100.

More sophisticated analysis is therefore needed.

Experimental attempts have been made to characterise the adhesive properties of the heat shield particles. However, a complete simulation of the hot entry phase, including hypersonic velocity, heat fluxes, representative flowfield topology, deceleration and extraction of the descent module is not possible.

Furthermore, as for any topics related to HUYGENS probe development phase, the answer to this problem has to be addressed in a cost and time schedule plan which is not extendible.

Navier Stokes calculation have then been performed, by simulating the particles by a gas medium, ejected from the rear part of the entry module (direct insertion into the recirculating zone), with a representative mass flow rate equivalent to the thermal protection particle jettison process, in order to try to bring a partial answer to the global question : within the trapped particles (assumed to be equivalent to a perfect gas in here), what is the balance process through the shear layer, and where do the trapped particles migrate within the recirculation zone?

Figure n°20 shows the density of pollutants within the recirculating zone, and the equivalent location of the DISR window.

The preferred location of the pollutant gas is the DISR location, as they all gather to this region !

A very interesting feature was provided by the time dependent scheme of this calculation. Indeed, the calculation shows that an equilibrium balance process is reached after a couple of seconds of physical time.
This would indicate that no more than the amount of pollutant which is created in a couple of seconds can remain in the recirculating region, for a given Mach number. This would enable to decrease the maximum pollutant quantity from the overall amount which is outcome from the heat shield, down to:

$$n.Q.S$$

where n is the n second needed time to reach this equilibrium situation
Q is the mass rate of injected pollutant
S is the surface over which the pollutant is injected

However, it must be kept in mind, that particles will not behave like equivalent gas, and therefore this calculation provides with rough indications and trend only.

In parallel, a non equilibrium chemistry Navier Stokes calculation was performed, in order to assess the species which could be trapped in the recirculating zone. This calculation was performed with a mono phase capability. The simulation shows the presence of atomic Carbon in the recirculating zone, which could be transformed in graphite, which could deposit on the DISR window.
This possibility has been verified in IRS (Institut für Raumfahrtsysteme, Stuttgart University, Germany), during thermal tests of the heat shield material, it was evidenced that solid carbon was created due to the cracking process of the upstream CH_4 molecules.

Finally, the amount of stick pollutant could not be for sure determined in such a way that the DISR capabilities would be guaranteed not to be reduced significantly.

Therefore, a dedicated protective cover has been designed for the DISR window, in order to guarantee the integrity of its surface.

The integration of the development of this protective cover, which had not been planned at the beginning of the project, creates new work at system level, while the ejection of this cover asks for new aerodynamic studies, in order to prove the reliability of its jettison phase, which has to occur after back cover release, and before scientific beginning of the descent phase.

CONCLUSION

The HUYGENS project led to very innovative development in Aerodynamics and Aerothermo-dynamics, due to the specificity of both the environment of the probe, the TITAN atmosphere, and the shape of the entry and descent modules.

This document stress the continuous link between the design of hardware, such that sizing of the thickness of the Thermal Protection System, and the fundamental research in Aerothermochemistry.

REFERENCES

1. Sommer, S.C., Short, B.J., Compton, D.L., "Free-Flight Measurements of Static and Dynamic Stability of Models of the Project MERCURY Re-Entry Capsule at Mach Number 3 and 9.5", NASA TM-X 373.
2. Owens, R.., "Aerodynamic Characteristics of Spherically Blunted Cones at Mach numbers from 0.5 to 5", NASA TN D-3088
3. Campbell, J.F., "Longitudinal Aerodynamic characteristics of several High Drag Bodies at Mach numbers from 1.5 to 4.63", NASA TN D-3915, April 1967
4. Campbell, J.F., "Supersonic Aerodynamic characteristics and Shock stand-off distances for Large Angle Cones with and without cylindrical Afterbodies", NASA TN D-5334, Aug. 1969
5. Campbell, J.F., Howell, D.T., "Supersonic Aerodynamics of Large Angle Cones", NASA TN D-4719, Aug.1968
6. Deveikis, W.D., Sawyer, J.W., "Effects of Cone angle, base flare angle and corner radius on Mach 3.0 Aerodynamic characteristics of large-angle cones", NASA TN D-5048, March 1969
7. Campbell, J.F., Howell, D.T., "Supersonic Lifting capabilities of large angle cones", NASA TN D-5499, Oct.1969
8. Vincenti, W.G., Krufer, C.H., "Introduction to Physical Gas Dynamics",Wiley & Son's editor, 1965
9. Park, C., "Radiation enhancement by non-equilibrium during flight through the Titan atmosphere", *AIAA paper*, AIAA 82-078, June 1982
10. Park, C., Bershader, D., "Determination of the radiative emission of a hypersonic flow simulating the CASSINI-TITAN atmospheric entry probe environment"
11. Nelson, H.F, Park, C., Whitting, E., "Titan atmospheric composition by hypervelocity shock layer analysis", Journal of Thermophysics and Heat Transfer, Vol. 5, n°2, April-June 1991, pp 157-165

12. Millikan, R.C., White, D.R., "Systematics of Vibrational Relaxation", The Journal of Chemical Physics, Vol 39, n°12, Dec. 1963

13. Wood, A.D., Springfield, J.F.,Pallone, A.J., "Determination of the effects of chemical and vibrational relaxation on an inviscid hypersonic flowfield", *AIAA paper*, AIAA 63-441, 1963

14. Park, C., "Assessment of two temperature kinetic model for dissociating and weakly ionizing Nitrogen", *AIAA paper*, AIAA 86-1347, 1986

15. Park, C., "Assessment of two temperature model for ionizing air", *AIAA paper*, AIAA 87-1574, 1987

16. Treanor, C.E., Marrone, P.V.,"Effect of dissociation on the rate of vibrational relaxation", Physics of Fluids, Vol 5, n°9, Sept. 1962

17. Treanor, C.E., Marrone, P.V., "Chemical relaxation with preferential dissociation for excited vibrational levels", Physics of Fluids, Vol 6, n°9, Sept. 1963

18. Méolans, J.G., Brun, R., Mouti, M., Llorca, M., Chauvin, A., "Vibration-dissociation coupling in high temperature nonequilibrium flows",Second European Symposium on Aerothermodynamics for Space Vehicles, ESTEC, Noordwijk, Te Netherlands, 21-25 Nov. 1994

19. Brun, R., Llorca, M., "Vibration-Dissociation Coupling Revisited by a Chapman-Enskog Procedure", 19th RGD Symposium, Oxford, 1994

20. Gnoffo, P.A., "Complete Supersonics Flowfields over Blunt Bodies in a generalized orthogonal coordinate system",NASA TM 81784, 1980

21. Gnoffo, P.A., Price, J.M., Braun, R.D., "On the Computation of Near Wake, Aerobrake Flowfields", *AIAA paperI*, AIAA 91-1371, Honolulu, June 1991

22. Zappa, O.Z., Reinecke, W.G., "An Experimental Investigation of Base Heating on typical Mars Entry Body Shapes", NASA CR-1920, 1971

23. Murthy, S.N.B., Osborn, J.R., "Base Flow Phenomena with and without Injection : Experimental Results, Theories, and Bibliography", Progress in Astronautics and Aeronautics: Aerodynamics of Base Combustion, Vol 40, AIAA, New York, 1976, pp. 7-210

24. Venkatapathy, E., Palmer, G., Prabhu, D.K., "AFE Base Flow Computations", *AIAA paper*, AIAA 91-1372, Honolulu, June 1991

25. Strawa, A.W., Park, C., "Radiometric Investigation of the Wake Flow of the forthcoming Aeroassist Flight Experiment", *AIAA paper*, AIAA 91-1408, Honolulu, June 1991

26. Wehrend, W.R., "An Experimental Evaluation of Aerodynamic Damping Moments of Cones with different Centers of Rotation", NASA TN D-1768, 1963

27. Steinberg, S., Uselton, B., Siemers, P.M., "Viking Configuration Pitch Damping Derivatives as influenced by Support Interferences and Test Technique at Trans and Supersonic Speeds", *AIAA paper*, AIAA 72-1012, 1972

28. Sammonds, R.I., "Aerodynamics of Mars Entry Probe Lander Configuration at Mach number 10", NASA TN D-5608, 1970

29. Baillion, M., Taquin, G., Soler, J., "HUYGENS Probe Radiative Environment", IUTAM symposium, 1992

30. Park, C., "Problems of Rate Chemistry in the Flight Regimes of Aeroassisted Orbital Transfer Vehicle", *AIAA paper*, AIAA 84-1730, 1984

31. Underwood, J., "A 12 Degree-of-freedom Parachute/Payload Simulation of the Huygens Probe", 12th RAeS Aerodynamic Decelerator Systems Technology Conference and Seminar, London, 1993

32. Moulin, J., "Recovery System Simulation : Link Modelization", 12th RAeS Aerodynamic Decelerator Systems Technology Conference and Seminar, London, 1993

33. Moulin, J., "Wind Influence on Recovery System Performances", *AIAA paper*, AIAA 95-1579 13th AIAA Aerodynamic Decelerator Systems Technology Conference and Seminar, Clear Water, 1995, to be issued.

WIND TUNNEL	WIND TUNNEL TEST OBJECTIVES	WIND TUNNEL CONDITIONS	WIND TUNNEL FACILITY	PLANNING
WT 11	• Determination of the dynamic behaviour of the descent module (with and without drogue) during the descent. • Determination of the spin rate level with different spin vanes geometry for low free stream velocity • Determination of the dynamic behaviour of the main parachute during inflation	→ 10 m/s < V < 40 m/s → 5 m/s < V < 22 m/s	Institut de Mécanique des Fluides Lille - France	09.1991
WT 12	• Determination of the aerodynamic coefficients in spinning motion for the descent module during the descent.	→ 20 m/s < V < 75 m/s	NLR - Nord East Polder LST tunnel Holland	11.1992
WT 13	• Determination of the aerodynamic static coefficients for: - the descent module in subsonics - the front shield in subsonics, - the entry module in subsonics, transonics, and supersonics. • Determination of the aerodynamic dynamic coefficients for: - the front shield in transonics - the entry module in transonics	→ Mach = 0.2 → → Mach = 0.5 → → 0.5 < Mach < 2. → → Mach = 4.7 → → Mach = 0.5 → → Mach = 0.8 → 2.0 →	FFA - Stockholm - Sweden LT1 Tunnel S4 Tunnel S4 Tunnel Hyp500 Tunnel S4 Tunnel S4 Tunnel	10-12.1992 01.1993
WT 14	• Determination of the aerodynamic dynamic coefficients for: - the descent module in subsonics	→ Mach = 0.2 →	DRA - Bedford - England 13*9 ft tunnel	07.1992
WT 15	• Determination of the aerodynamic dynamic coefficients for the entry module from subsonics up to supersonics.	0,2 < Mach < 1,4 → 1,4 < Mach < 3 → 4 < Mach < 5 →	ARA - Bedford England TWT tunnel SWT tunnel M4T tunnel	09.1993
WT 16	• Determination of the integrated emissivity behind a shock wave travelling inside a (N2, CH4, Ar) mixture in a shock tube.	→ V = 5 000 m/s	Université de Provence TCM2 Shock Tunnel Marseille - France	04-07.1993

Table n°1
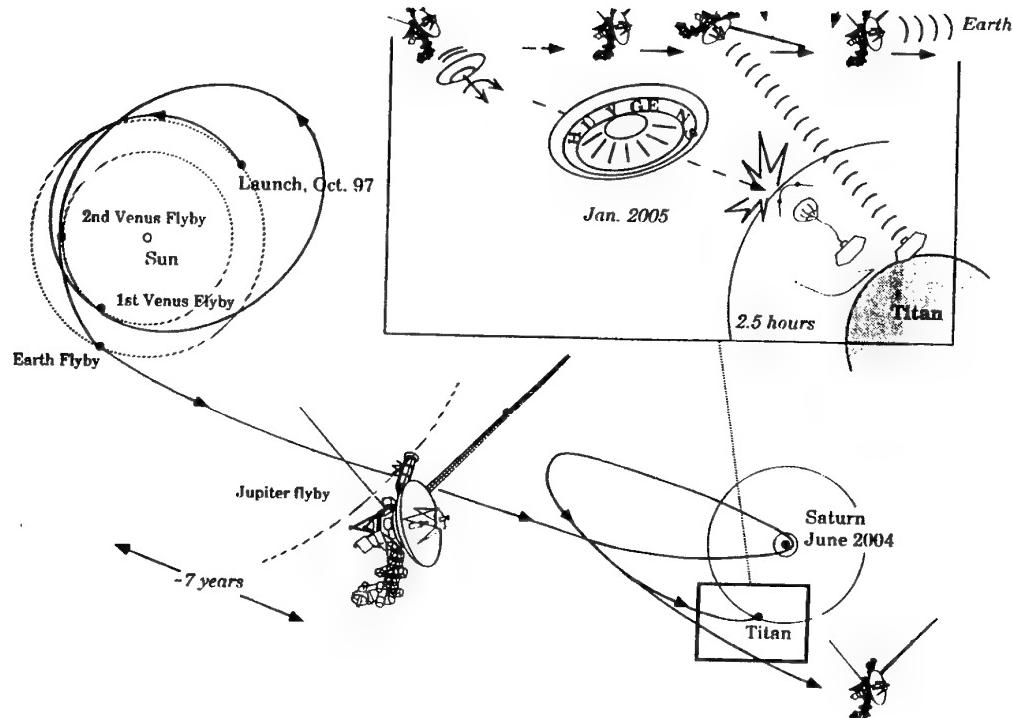
Figure n°1CASSINI/HUYGENS Probe trajectories
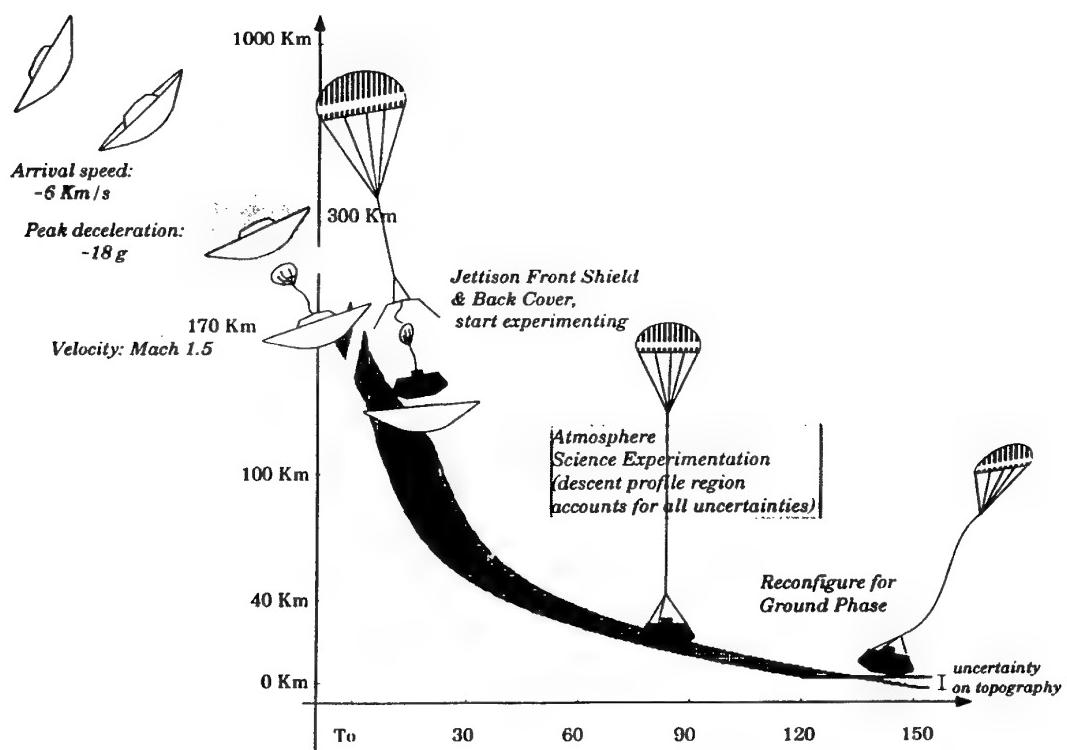
Figure 2. Entry and descent phase
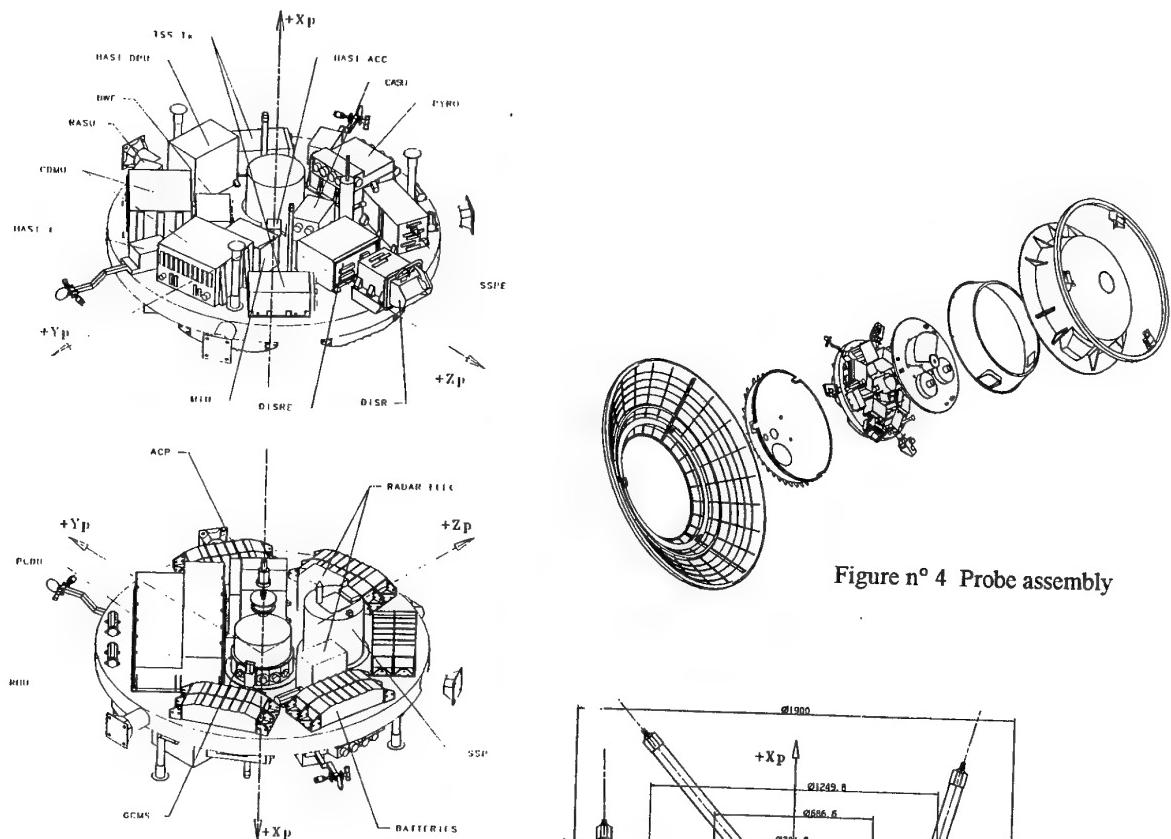
Figure n°3 Experiment platform

Figure n° 4 Probe assembly
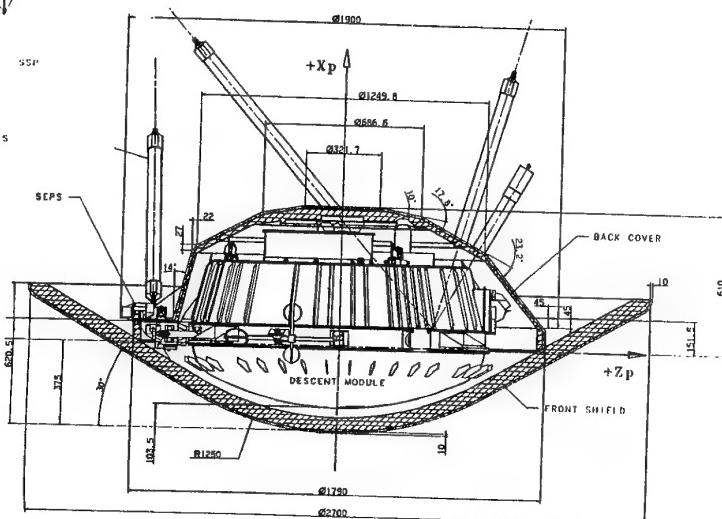
Figure 5. Entry Module external geometry
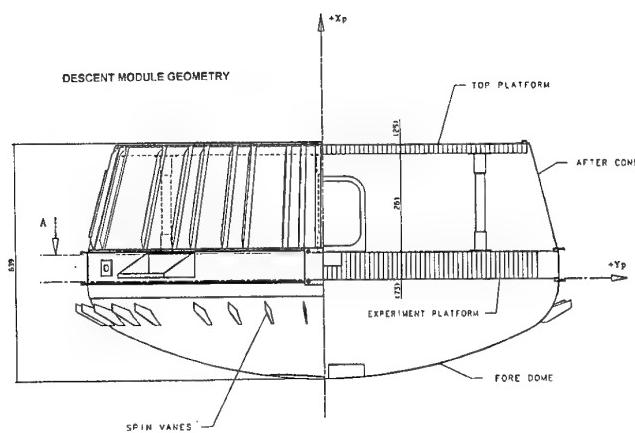
Figure 6. Descent Module geometry

V = 5550 m/s * T = 293 K * P = 2 mBar
3 % CH4 - 10 % Ar - 87 % N2
Evolution des Températures (K)
Ancien processus E-T
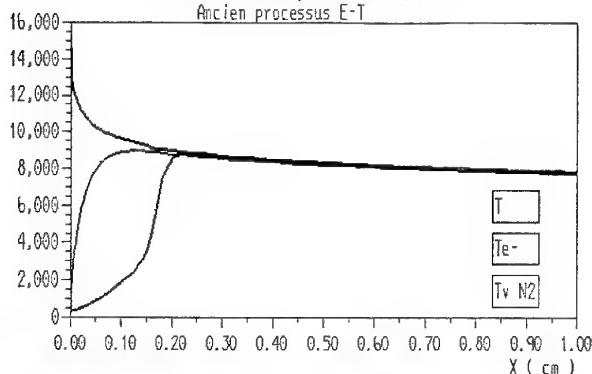
Figure 7. Temperatures profiles in the shock layer

Figure 8. Entry Module wake
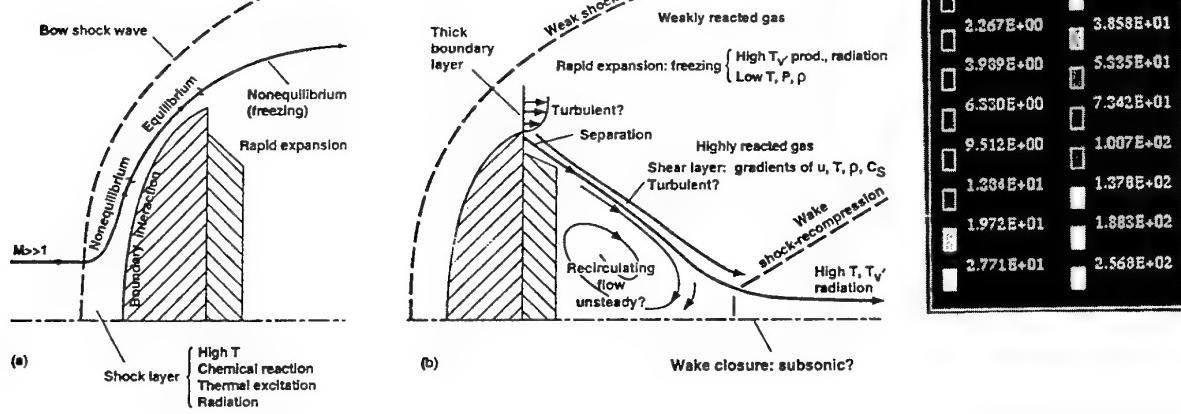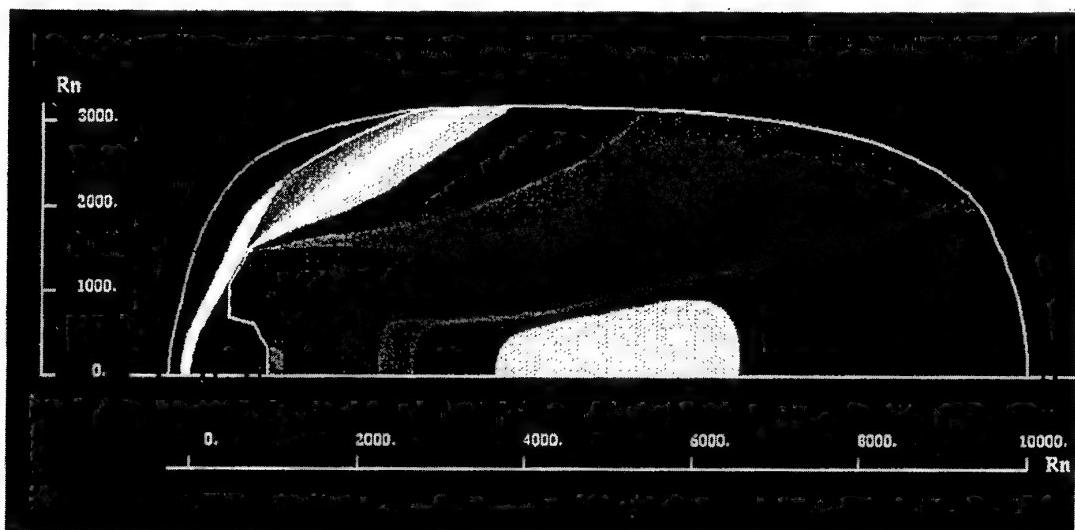
Figure 9. Probe rear flowfield pattern
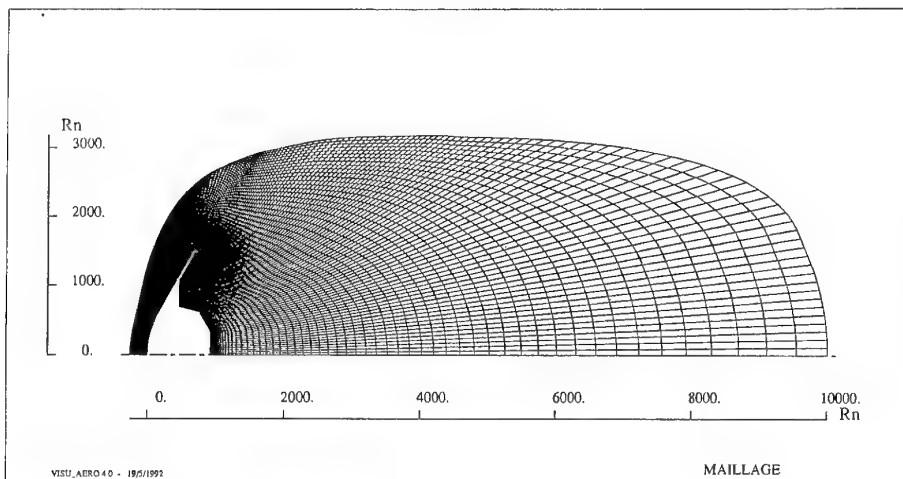
Figure 10. Navier Stokes grid
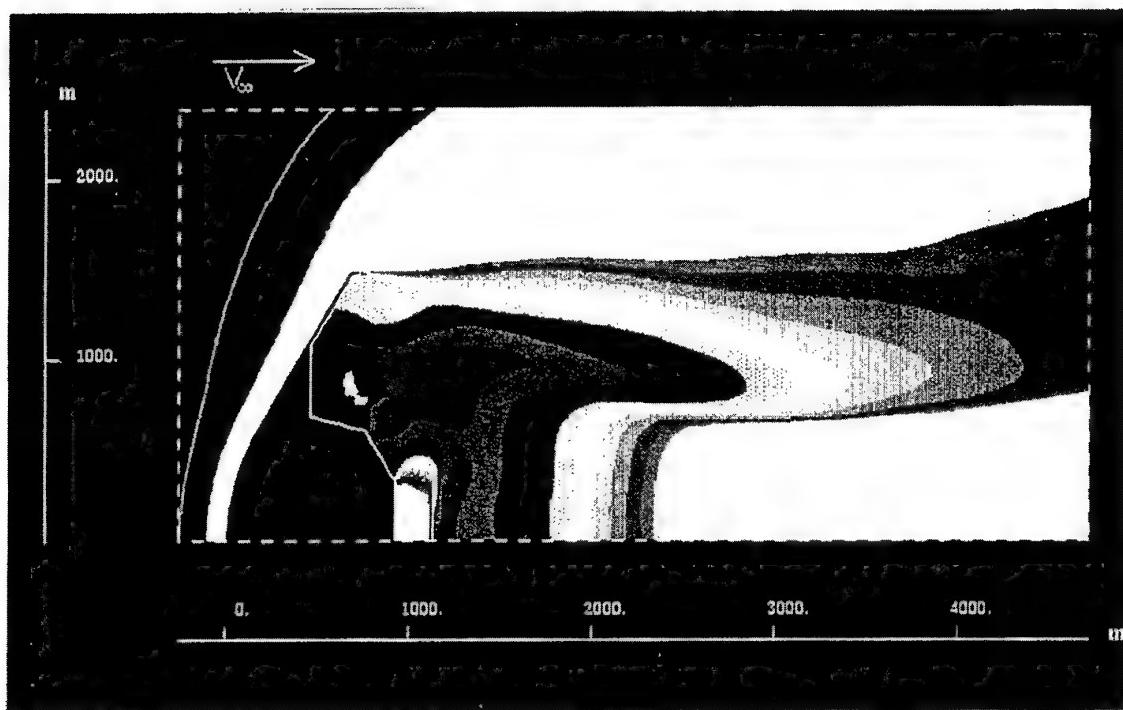
Figure 11. iso-pressure lines in the probe near wake
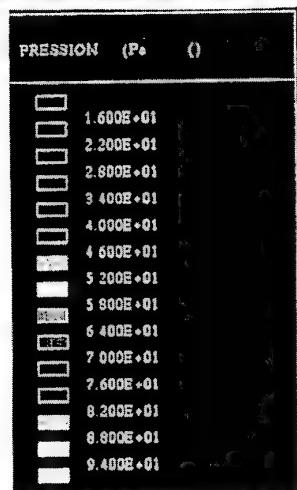
Figure 12. Streamlines around Descent Module config. 1
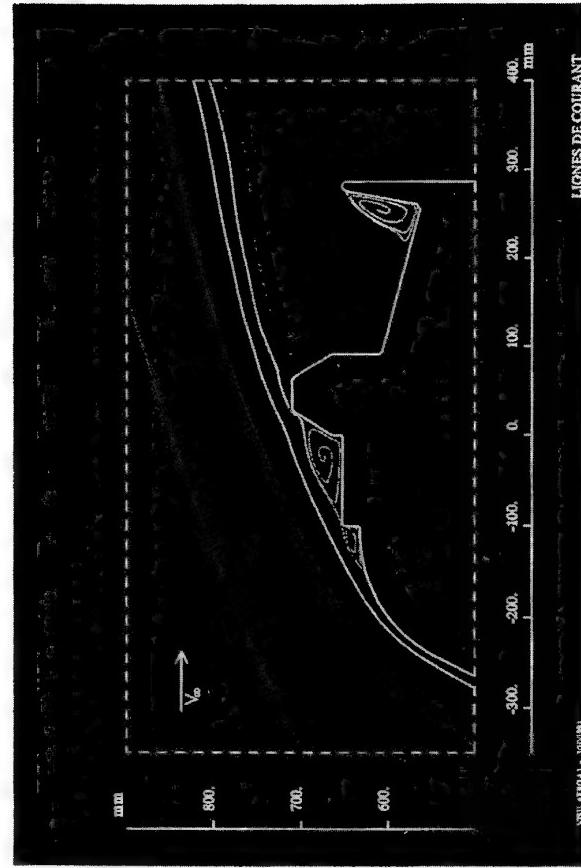

Figure 13. Streamlines around Descent Module config. 2
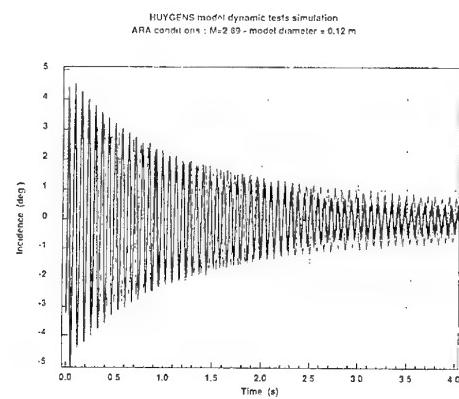

Figure 14. θ(t) at M=2,9
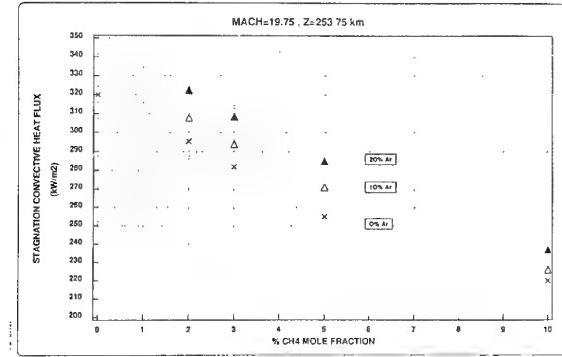
Figure 15. Convective heat flux sensitivity vs Argon
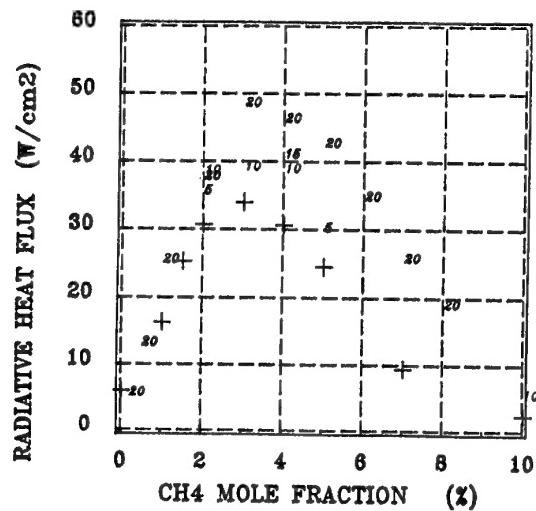
Figure 16. Radiative heat flux sensitivity vs CH4

HUYGENS PROBE - RADIATIVE HEAT FLUX EVOLUTION

Ve = 6.19 Km/s - D = 2.70 m - Tw = 1500 K

HUYGENS PROBE - CONVECTIVE HEAT FLUX EVOLUTION

Ve = 6.19 Km/s - D = 2.70 m - Tw = 1500 K
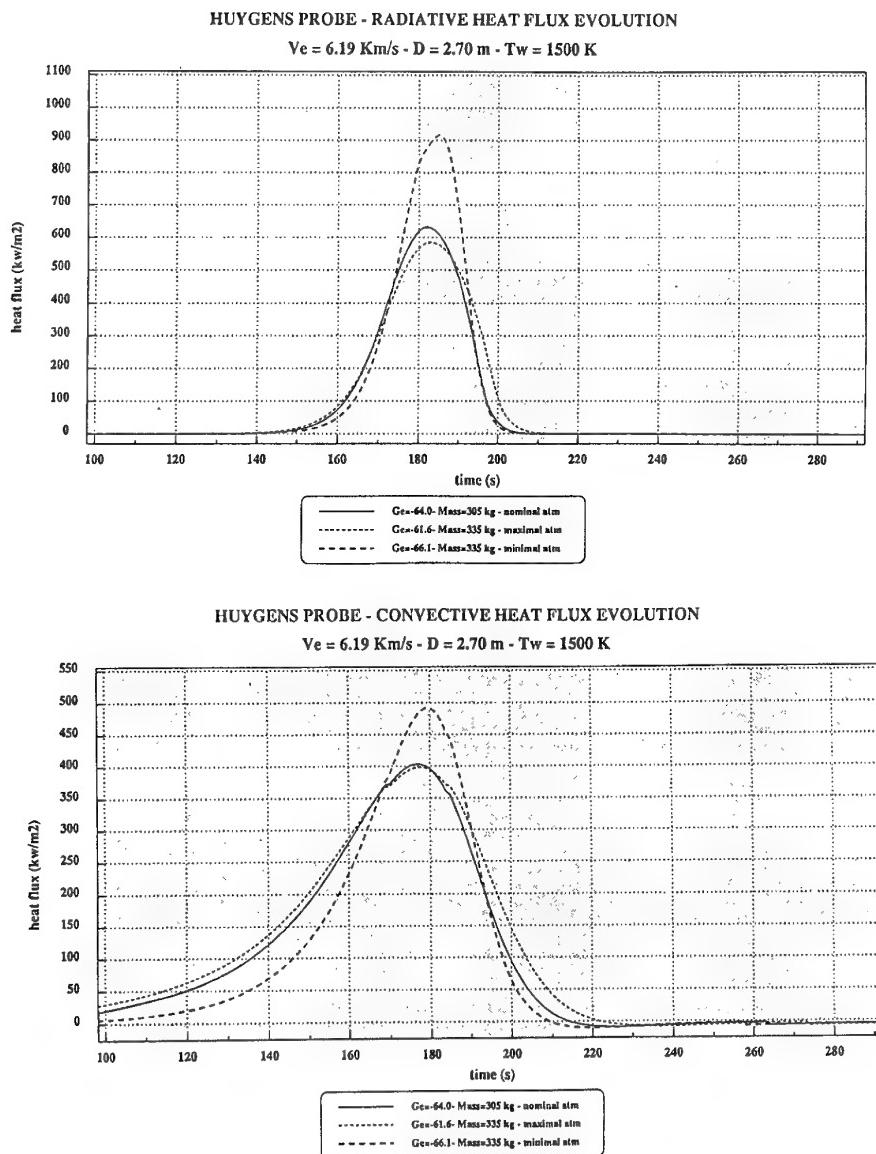
Figure 17. Radiative and convective heat flux vs time
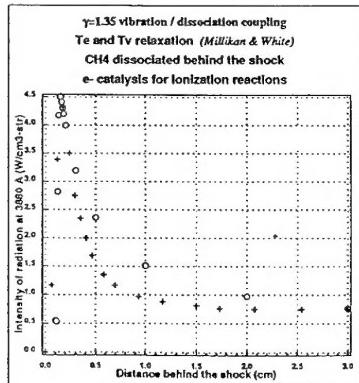
Figure 18. Predicted and measured CN emission vs distance behind normal shock

spin rate profile - 36 spin vanes design
descent time duration = 136. mn

nominal profile , incidence 87.8 deg
profile with dispersions
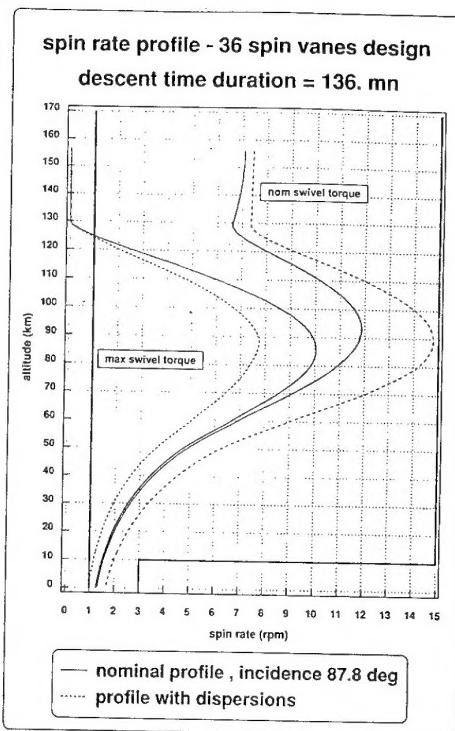
Figure 19. DM Roll rate during TITAN descent

HUYGENS INJECTION ESPECE 20 g/M
ROesp * V

ROesp*V   (Kg/M2/s   )

2.707E-03
5.414E-03
8.121E-03
1.083E-02
1.354E-02
1.624E-02
1.895E-02
2.166E-02
2.436E-02
2.707E-02
2.978E-02
3.248E-02
3.519E-02
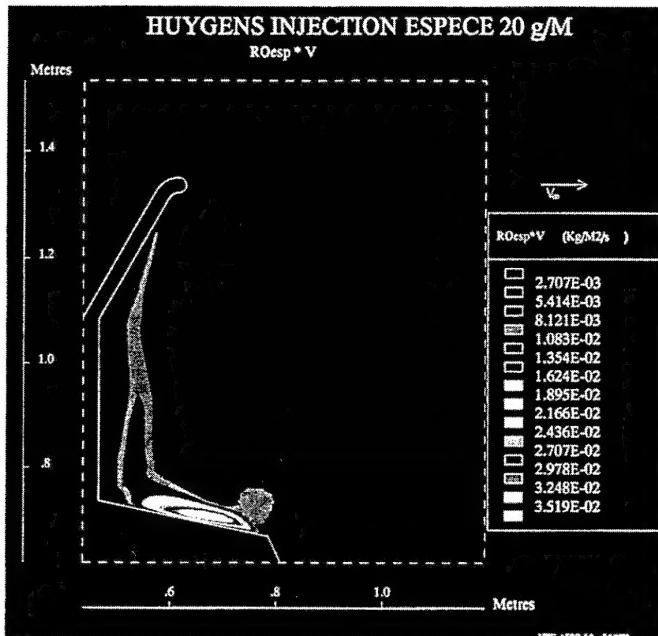
Figure 20. Pollutants in the probe near wake
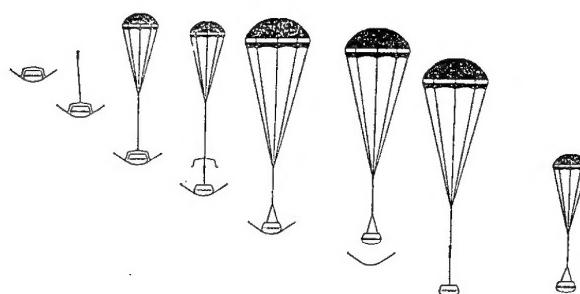


Figure 21. Huygens descent scenario

REPORT DOCUMENTATION PAGE

1. Recipient's Reference	2. Originator's Reference	3. Further Reference	4. Security Classification of Document
	AGARD-R-808	ISBN 92-836-1053-9	UNCLASSIFIED/ UNLIMITED

5. Originator	Advisory Group for Aerospace Research and Development North Atlantic Treaty Organization 7 rue Ancelle, 92200 Neuilly-sur-Seine, France

6. Title	Capsule Aerothermodynamics

7. Presented at/sponsored by
AGARD FDP Special Course on "Capsule Aerothermodynamics", held at the von Kármán Institute for Fluid Dynamics Panel (FDP) in Rhode-Saint-Genèse, Belgium, in March 1995.

8. Author(s)/Editor(s)	9. Date
Multiple	May 1997

10. Author's/Editor's Address	11. Pages
Multiple	296

12. Distribution Statement	There are no restrictions on the distribution of this document. Information about the availability of this and other AGARD unclassified publications is given on the back cover.

13. Keywords/Descriptors

Aerothermodynamics	Design
Heat transfer	Reentry vehicles
Rarefied gas dynamics	Ablation
Space probes	Hypersonic flow
Reentry	Space capsules
Aerodynamics	

14. Abstract

Lecture notes for the AGARD Fluid Dynamics Panel (FDP) Special Course on "Capsule Aerothermodynamics" have been assembled in this report. Aerodynamic design aspects related to planetary probe and capsule configurations are covered, as well as critical phenomena occurring during the different regimes of flight. The impact of real gas and rarefaction on capsule aerothermodynamics, and in particular on forebody and wake flow, is addressed.

The material assembled in this report was prepared under the combined sponsorship of the AGARD Fluid Dynamics Panel, the Consultant and Exchange Program of AGARD, and the von Kármán Institute (VKI) for Fluid Dynamics.

AGARD

NATO ⊕ OTAN

7 RUE ANCELLE • 92200 NEUILLY-SUR-SEINE

FRANCE

Télécopie 0(1)55.61.22.99 • Télex 610 176

DIFFUSION DES PUBLICATIONS

AGARD NON CLASSIFIEES

Aucun stock de publications n'a existé à AGARD. A partir de 1993, AGARD détiendra un stock limité des publications associées aux cycles de conférences et cours spéciaux ainsi que les AGARDographies et les rapports des groupes de travail, organisés et publiés à partir de 1993 inclus. Les demandes de renseignements doivent être adressées à AGARD par lettre ou par fax à l'adresse indiquée ci-dessus. *Veuillez ne pas téléphoner.* La diffusion initiale de toutes les publications de l'AGARD est effectuée auprès des pays membres de l'OTAN par l'intermédiaire des centres de distribution nationaux indiqués ci-dessous. Des exemplaires supplémentaires peuvent parfois être obtenus auprès de ces centres (à l'exception des Etats-Unis). Si vous souhaitez recevoir toutes les publications de l'AGARD, ou simplement celles qui concernent certains Panels, vous pouvez demander à être inclu sur la liste d'envoi de l'un de ces centres. Les publications de l'AGARD sont en vente auprès des agences indiquées ci-dessous, sous forme de photocopie ou de microfiche.

CENTRES DE DIFFUSION NATIONAUX

ALLEMAGNE
Fachinformationszentrum Karlsruhe
D-76344 Eggenstein-Leopoldshafen 2

BELGIQUE
Coordonnateur AGARD-VSL
Etat-major de la Force aérienne
Quartier Reine Elisabeth
Rue d'Evere, 1140 Bruxelles

CANADA
Directeur - Gestion de l'information
(Recherche et développement) - DRDGI 3
Ministère de la Défense nationale
Ottawa, Ontario K1A 0K2

DANEMARK
Danish Defence Research Establishment
Ryvangs Allé 1
P.O. Box 2715
DK-2100 Copenhagen Ø

ESPAGNE
INTA (AGARD Publications)
Carretera de Torrejón a Ajalvir, Pk.4
28850 Torrejón de Ardoz - Madrid

ETATS-UNIS
NASA Center for AeroSpace Information (CASI)
800 Elkridge Landing Road
Linthicum Heights, MD 21090-2934

FRANCE
O.N.E.R.A. (Direction)
29, Avenue de la Division Leclerc
92322 Châtillon Cedex

GRECE
Hellenic Air Force
Air War College
Scientific and Technical Library
Dekelia Air Force Base
Dekelia, Athens TGA 1010

ISLANDE
Director of Aviation
c/o Flugrad
Reykjavik

ITALIE
Aeronautica Militare
Ufficio del Delegato Nazionale all'AGARD
Aeroporto Pratica di Mare
00040 Pomezia (Roma)

LUXEMBOURG
Voir Belgique

NORVEGE
Norwegian Defence Research Establishment
Attn: Biblioteket
P.O. Box 25
N-2007 Kjeller

PAYS-BAS
Netherlands Delegation to AGARD
National Aerospace Laboratory NLR
P.O. Box 90502
1006 BM Amsterdam

PORTUGAL
Estado Maior da Força Aérea
SDFA - Centro de Documentação
Alfragide
2700 Amadora

ROYAUME-UNI
Defence Research Information Centre
Kentigern House
65 Brown Street
Glasgow G2 8EX

TURQUIE
Millî Savunma Başkanliği (MSB)
ARGE Dairesi Başkanliği (MSB)
06650 Bakanliklar-Ankara

Le centre de distribution national des Etats-Unis ne détient PAS de stocks des publications de l'AGARD.

D'éventuelles demandes de photocopies doivent être formulées directement auprès du NASA Center for AeroSpace Information (CASI) à l'adresse ci-dessous. Toute notification de changement d'adresse doit être fait également auprès de CASI.

AGENCES DE VENTE

NASA Center for AeroSpace Information
(CASI)
800 Elkridge Landing Road
Linthicum Heights, MD 21090-2934
Etats-Unis

The British Library
Document Supply Division
Boston Spa, Wetherby
West Yorkshire LS23 7BQ
Royaume-Uni

Les demandes de microfiches ou de photocopies de documents AGARD (y compris les demandes faites auprès du CASI) doivent comporter la dénomination AGARD, ainsi que le numéro de série d'AGARD (par exemple AGARD-AG-315). Des informations analogues, telles que le titre et la date de publication sont souhaitables. Veuiller noter qu'il y a lieu de spécifier AGARD-R-nnn et AGARD-AR-nnn lors de la commande des rapports AGARD et des rapports consultatifs AGARD respectivement. Des références bibliographiques complètes ainsi que des résumés des publications AGARD figurent dans les journaux suivants:

Scientific and Technical Aerospace Reports (STAR)
publié par la NASA Scientific and Technical
Information Division
NASA Langley Research Center
Hampton, Virginia 23681-0001
Etats-Unis

Government Reports Announcements and Index (GRA&I)
publié par le National Technical Information Service
Springfield
Virginia 22161
Etats-Unis
(accessible également en mode interactif dans la base de données bibliographiques en ligne du NTIS, et sur CD-ROM)

Imprimé par le Groupe Communication Canada Inc.
(membre de la Corporation St-Joseph)
45, boul. Sacré-Cœur, Hull (Québec), Canada K1A 0S7

𝔸𝔾𝔸ℝ𝔻

NATO ⊕ OTAN

7 RUE ANCELLE • 92200 NEUILLY-SUR-SEINE

FRANCE

Telefax 0(1)55.61.22.99 • Telex 610 176

DISTRIBUTION OF UNCLASSIFIED

AGARD PUBLICATIONS

AGARD holds limited quantities of the publications that accompanied Lecture Series and Special Courses held in 1993 or later, and of AGARDographs and Working Group reports published from 1993 onward. For details, write or send a telefax to the address given above. *Please do not telephone.*

AGARD does not hold stocks of publications that accompanied earlier Lecture Series or Courses or of any other publications. Initial distribution of all AGARD publications is made to NATO nations through the National Distribution Centres listed below. Further copies are sometimes available from these centres (except in the United States). If you have a need to receive all AGARD publications, or just those relating to one or more specific AGARD Panels, they may be willing to include you (or your organisation) on their distribution list. AGARD publications may be purchased from the Sales Agencies listed below, in photocopy or microfiche form.

NATIONAL DISTRIBUTION CENTRES

BELGIUM
Coordonnateur AGARD — VSL
Etat-major de la Force aérienne
Quartier Reine Elisabeth
Rue d'Evere, 1140 Bruxelles

CANADA
Director Research & Development
Information Management - DRDIM 3
Dept of National Defence
Ottawa, Ontario K1A 0K2

DENMARK
Danish Defence Research Establishment
Ryvangs Allé 1
P.O. Box 2715
DK-2100 Copenhagen Ø

FRANCE
O.N.E.R.A. (Direction)
29 Avenue de la Division Leclerc
92322 Châtillon Cedex

GERMANY
Fachinformationszentrum Karlsruhe
D-76344 Eggenstein-Leopoldshafen 2

GREECE
Hellenic Air Force
Air War College
Scientific and Technical Library
Dekelia Air Force Base
Dekelia, Athens TGA 1010

ICELAND
Director of Aviation
c/o Flugrad
Reykjavik

ITALY
Aeronautica Militare
Ufficio del Delegato Nazionale all'AGARD
Aeroporto Pratica di Mare
00040 Pomezia (Roma)

LUXEMBOURG
See Belgium

NETHERLANDS
Netherlands Delegation to AGARD
National Aerospace Laboratory, NLR
P.O. Box 90502
1006 BM Amsterdam

NORWAY
Norwegian Defence Research Establishment
Attn: Biblioteket
P.O. Box 25
N-2007 Kjeller

PORTUGAL
Estado Maior da Força Aérea
SDFA - Centro de Documentação
Alfragide
2700 Amadora

SPAIN
INTA (AGARD Publications)
Carretera de Torrejón a Ajalvir, Pk.4
28850 Torrejón de Ardoz - Madrid

TURKEY
Millî Savunma Başkanliği (MSB)
ARGE Dairesi Başkanliği (MSB)
06650 Bakanliklar-Ankara

UNITED KINGDOM
Defence Research Information Centre
Kentigern House
65 Brown Street
Glasgow G2 8EX

UNITED STATES
NASA Center for AeroSpace Information (CASI)
800 Elkridge Landing Road
Linthicum Heights, MD 21090-2934

The United States National Distribution Centre does NOT hold stocks of AGARD publications.

Applications for copies should be made direct to the NASA Center for AeroSpace Information (CASI) at the address below.
Change of address requests should also go to CASI.

SALES AGENCIES

NASA Center for AeroSpace Information
(CASI)
800 Elkridge Landing Road
Linthicum Heights, MD 21090-2934
United States

The British Library
Document Supply Centre
Boston Spa, Wetherby
West Yorkshire LS23 7BQ
United Kingdom

Requests for microfiches or photocopies of AGARD documents (including requests to CASI) should include the word `AGARD' and the AGARD serial number (for example AGARD-AG-315). Collateral information such as title and publication date is desirable. Note that AGARD Reports and Advisory Reports should be specified as AGARD-R-nnn and AGARD-AR-nnn, respectively. Full bibliographical references and abstracts of AGARD publications are given in the following journals:

Scientific and Technical Aerospace Reports (STAR)
published by NASA Scientific and Technical
Information Division
NASA Langley Research Center
Hampton, Virginia 23681-0001
United States

Government Reports Announcements and Index (GRA&I)
published by the National Technical Information Service
Springfield
Virginia 22161
United States
(also available online in the NTIS Bibliographic
Database or on CD-ROM)

Printed by Canada Communication Group Inc.
(A St. Joseph Corporation Company)
45 Sacré-Cœur Blvd., Hull (Québec), Canada K1A 0S7